THE UNIVERSITY OF ADELAIDE

DEPARTMENT OF MECHANICAL ENGINEERING

RELATIONSHIP BETWEEN INTERNAL SOUND GENERATION AND CHARACTERISTICS OF FLOW IN A REGION OF FLOW SEPARATION DUE TO DISTURBANCE OF FULLY-DEVELOPED TURBULENT FLOW IN A PIPE

by

NAVAL KISHORE AGARWAL, M.Tech.

Thesis for the Degree of Doctor of Philosophy

November, 1985.

Awarded 24/3/87

SUMMARY

Mean flow characteristics in the fully-developed turbulent pipe flow approaching an orifice plate, in the region of separated flow and in the flow downstream of reattachment up to and beyond the point where an undisturbed pipe flow regime is again established, for a wide range of flow speed and orifice sizes ($0.62 \leqslant D_0 \leqslant 0.83$), have been studied. Mean positions of separation and reattachment points have been determined using a surface fence gauge. The development of the free jet shear layer in the separated flow region downstream of the orifice and recovery of the attached flow to the fully developed state are discussed. Time-histories of the streamwise fluctuating velocity very close to the wall have been obtained by means of a probe incorporating three wires. The mean position of the reattachment point deduced from these measurements is compared with the results obtained with surface fence gauge and surface hot film.

The effects of shear flow on the transmission of sound waves in a hard-walled pipe are theoretically investigated. A fully developed turbulent velocity profile, where various regions are appropriately represented, has been used. Results for the effect of shear flow on the acoustic pressure and radial velocity distribution, cut-off frequency and modal phase speeds are discussed.

Measurements of the power spectral density and rms value of the wall pressure fluctuations, p' in the initially undisturbed flow, in the separated-flow region and in the re-established fully-developed pipe flow have been made. Scalings for p' and the spectra in the various regions have been suggested. Higher-order acoustic modes in the wall-pressure spectra upstream and downstream of the orifice, have been identified. Attenuation and variation of cut-off frequencies of higher-order modes with the orifice size and flow rate are discussed. Measurements of the axial velocity fluctuations in the separated flow, far

downstream and upstream of the orifice plate are presented. Flow regions where higher order modes are detectable have been identified, and variation of their cut-off frequencies with flow rate is compared with the results obtained with the wall pressure measurements.

STATEMENT OF ORIGINALITY

This thesis contains no material which has been accepted for the award of any other Degree or Diploma in any University. To the best of the author's knowledge and belief, this thesis contains no material previously published or written by another person, except where due reference is made in the text.

NAVAL KISHORE AGARWAL

CONSENT FOR LOAN AND PHOTOCOPYING

The Author consents to the thesis being made available for photocopying and loan if accepted for the award of the degree.

NAVAL KISHORE AGARWAL

ACKNOWLEDGEMENTS

The author wishes to express his sincere gratitude to Dr. M.K. Bull, who supervised the work, for his interest, constant encouragement and time given throughout the course of the research and especially during the preparation of this thesis. It was a pleasure to work with him and his help was invaluable to say the least.

The assistance of Instrumentation, Electronics and Engineering Workshops, and their help with the construction of various probes, electronic circuits and various pipe sections, is gratefully acknowledged.

The author is indebted to his wife, Shashi, and daughter, Ruchi, for their tremendous patience and support during the difficult times of the work and especially during the preparation of the thesis.

Finally, the author gratefully acknowledges the financial support from the University of Adelaide in the form of a post-graduate research scholarship and also a tutorship in the Department of Mechanical Engineering.

LIST OF CONTENTS

Page

LIST OF FIGURES

NOMENCLATURE

a	Pipe radius
a'	Constant in Equation 2.29
a_r	Speed of sound in the reservoir
A	Area ratio (area under shear flow velocity profile/ area under uniform flow velocity profile)
$A(f)$	Amplitude at frequency f
A_{mn}	Amplitude constant in Equation 2.4
b'	Constant in Equation 2.29
B	Constant in logarithmic law (=5.0)
Be	Equivalent resolution bandwidth
c	Constant in Equation 2.30
c	Speed of sound in the fluid
c_e	Speed of sound in the fluid corresponding to M_e
c_ϕ	Modal Phase speed
C	Constant in Equation 2.2
C_1 & C_2	Constants in Equation 2.44
C_f	Skin friction coefficient $(\tau_\omega/(\frac{1}{2}\rho U_0^2)$
c_g	Group velocity of an acoustic mode
C_p	Pressure coefficient $(p-p_{min})/(p_{max}-p_{min})$
Cp	Specific heat of the air at constant pressure
d	Pipe diameter
d_0	Orifice plate hole diameter
D	Thickness of the backflow velocity
D_0	$= (d_0/d)$
d_c	Choke throat diameter (mm)
D_c	$= (d_c/d)$
$E(f)$	Energy spectrum function
f	Frequency

f	Friction factor (=4 C_f)
$F(M_o)$	Function defined by equation 5.9
$F_2(M_o)$	Function defined by equation 5.6
$F_4(M_o)$	Function defined by equation 5.13
G	Clauser Parameter (equation 5.26)
h	Orifice radial height
h	Fence height
h	Sampling or digitizing interval
h_+	$(= hU_\tau/\nu)$
H	Shape factor $(= \delta^*/\theta)$
He	Helmholtz Number
$\bar{j}$	Average mass flow rate per unit area
j_0	Mass flux per unit area on the pipe centreline
j_*	Mass flow rate per unit area
J	j/j_*
J_0	j_0/j_*
J_m	m^{th} order Bessel function of first kind
k	Wave number $(= \omega/c)$
k_x	Axial wave number component
K	$(\kappa^2{}_{mn} + k_x{}^2)^{1/2}$
K	Constant in logarithmic law equation (=0.41)
K	Constant
K	Fence gauge calibration constant
K	K_x/Ω $(= \nu c/\omega)$
K_x	$= k_x.a$
L	Distance of maximum shear stress from wall
ℓ	Length
m	Integer representing the number of diametral nodal planes of m^{th} acoustic mode
M	Mode order
M	Local Mach number of flow

M_E	Centreline Mach number just upstream of the choke
M_e	Effective flow Mach number
M_J	Maximum jet Mach number
M_0	Centreline Mach number
M_I	Pipe centreline Mach number at X = -3.8
M_ϕ	Phase Mach number
$M_{\phi 0}$	Phase Mach number for no-flow case
n	Integer representing the number of nodal circles
N	Number of averages
p	Pressure distribution associated with the acoustic wave
p	Static pressure
p_{min}	Minimum static pressure
p_{max}	Maximum static pressure
p_1	Static pressure ahead of shock wave
p_2	Static pressure behind shock wave
p_4	Initial pressure in high pressure chamber of shock tube
$\overline{p^2}$	Overall mean wall pressure fluctuations
p'	Overall root mean square wall pressure fluctuation $(\overline{p^2})^{1/2}$
p_{ac}	Acoustic pressure fluctuation
p_h	Hydrodynamic pressure fluctuation
$p_m(t)$	Power spectral densities of the combination of tranducer output (equation 6.10)
P_{mn}	$1 - m^2/\kappa^2{}_{mn}$
$P(r)$	Radial variation of pressure amplitude
p_T	Total pressure as measured by pitot tube
$p(\tau_\omega)$	Probability density function of wall shear stress
q_I	Dynamic pressure at x = -3.8
q_J	Dynamic pressure corresponding to maximum jet Mach number
p_r	Indicated total pressure

q_0	Dynamic pressure
q_m	Mean dynamic pressure
r	Radial coordinate
(r, θ, x)	Cylindrical polar coordinates (fig.2.1)
R	Non-dimensional radius (= r/a)
R	Mean reattachment point
R	Characteristic gas constant
R_s	Constant in Equation 2.34
R_e	Reynolds number (= $U_0\ d/\nu$)
R_{eh}	Reynolds number based on U_I and orifice plate radial height (= $U_I h/\nu$)
R_s	= Ru_τ/ν_T
S_1	Mean primary separation point
S_2	Mean secondary separation point
S_{T_t}	Total temprature sensitivity coefficient (Equation 7.2)
$S_{\rho u}$	Mass flux sensitivity coefficient (Equation 7.2)
t	Time
t	Orifice plate thickness
T	Time period
T	Local static temperature of the fluid
T_o	Stagnation (total) temperature
Tr	Sample length (=Nh)
T_r	Reservoir (atmosphere) temperature
u ,v ,w	Velocity components in x,r,θ directions
u'_0	Velocity fluctuations at the pipe centre in axial direction
u'_{max}	Maximum value of velocity fluctuations in axial direction at a given streamwise position
u^*	Speed of the sonic flow
u	Acoustic particle velocity

u', v', w'	Velocity fluctuations in x, r, θ directions
u_{ac}	Axial component of acoustic fluctuations (Equation 7.1)
u_h	Axial component of hydrodynamic fluctuations (Equation 7.1)
U_J	Flow velocity in the jet just downstream of the orifice
$U(r)$	Mean flow velocity
U_o	Mean pipe centreline velocity
U_c	Convection velocity
U_I	Velocity upstream of orifice at $X = -3.8$
U_M	$(= \sqrt{\tau_m/\rho})$
U_N	Maximum reverse velocity
U_S	Velocity scale for Perry and Schofield defect law
U_s	Effective axial velocity for shear flow
U_τ	Friction velocity $(= \sqrt{\tau_\omega/\rho})$
U^+	$(= U/U_\tau)$
x	Streamwise distance
x'	Quantized digital signal
$\overline{x}$	Mean value
x_{s1}, x_{s2}, x_R	Distance of primary, secondary separation and reattachment points
X	$(=x/d)$
X_R	$(=x_R/d)$
X_{S1}	$(=x_{S1}/d)$
X_{S2}	$(=x_{S2}/d)$
y	Distance from pipe wall in radial direction
y'	Quantized digital signal
y_N	Distance of Maximum reverse velocity from pipe wall
Y	$(1-R)$
Y_a	Y^+/a'
Y^+	$(= y\, U_\tau/\nu)$

∇^2	Laplacian operator $\left(\frac{\partial^2}{\partial r^2} + \frac{1}{r}\frac{\partial}{\partial r} + \frac{1}{r^2}\frac{\partial^2}{\partial \theta^2} + \frac{\partial^2}{\partial r^2}\right)$
α	Constant in equation 5.30
α	$(= 1/KR_s)$
α_{mn}	Characteristic number for Bessel function
β	Specific wall admittance
β	Parameter in Equation 2.39
γ	Ratio of specific heat of a gas at constant pressure to the specific heat at constant volume
γ_p	Percentage downstream flow
ν	Propagational constant
ν	Kinematic viscosity of fluid
σ	Standard deviation
δ	Boundary layer thickness
δ^*	Displacement thickness
θ	Momentum thickness
$\phi(f)$	Phase at frequency, f
$\phi h(\omega)$	Power spectral density of the turbulence pressure fluctuations
$\phi p(f)$	Power spectral density of wall pressure
Φ_p	Non-dimensional power spectral density of wall pressure
$\phi_u(f)$	Power spectral density of axial velocity fluctuations
Φ_u	Non-dimensional power spectral density of axial velocity fluctuations
$\phi_s(f)$	Power spectral density of wall static pressure fluctuations
ρ	Density
ρ_o	Density at pipe centre line
ρ^*	Density of the sonic flow
τ_m	Maximum shear stress
Π	Wake parameter, equation 5.28

τ_w	Wall shear stress
$\overline{\tau_w}$	Mean wall shear stress
$\overline{\tau'^2_w}$	Mean square fluctuation of wall shear stress
ε_r	Normalized standard error (= $\sqrt{1/Be.Tr}$)
ξ	(= r/a)
ε_x, ε_y	Aperture time error
κ_{mn}	$\pi\alpha_{mn}/a$ (= $(\omega_{co})_{NF}/c$)
Ω	Frequency parameter (= $\omega a/c$)
Ω	Strouhal number (= $\omega a/U_I$ or $\omega a/U_0$)
Ω_{co}	Cut-off frequency
ω	Radian frequency (= $2\pi f$)
Δ	(=2.88 $\delta^* U_0/U_S$, equation 5.35)
ΔP	Pressure difference across the fence
ΔP	Pressure drop across the shock front (p_4-p_1)

Suffix

b	Buffer layer
co	Cut-off
e	Effective
E	Just upstream of the choke
f	Fluid
r	Radial
NF	No flow
0	Centreline value
UF	Uniform flow
w	Wall
I	Measurements upstream of the orifice at X = -3.8

CHAPTER 1

INTRODUCTION

1.1 General Introduction

There is an increasing emphasis on reducing the noise levels in the industrial environment, and this has given rise to a large amount of noise legislation; a long exposure to very high noise levels can be a health hazard leading to a permanent hearing loss. Use of fittings in pipe-lines with moving fluid is unavoidable, and it has been recognised that pipe fittings can contribute significantly to the overall noise level in an industrial situation. The flow disturbance caused by these pipe fittings excites the higher order acoustic modes in the fluid, thus generating an internal pressure field which is the sum of turbulent and acoustic pressure fluctuations. These pressure fluctuations excite pipe-wall vibration which transmits the acoustic energy to the atmosphere.

The acoustic energy propagates both upstream and downstream, the propagation being governed by the convected-wave equation. The solution of this equation applied to fully-developed turbulent flow leads to a set of characteristic pressure patterns across the pipe, the so-called higher-order acoustic modes. The lowest (plane-wave) mode propagates at all frequencies but the higher order modes propagate only at frequencies above their cut-off frequencies. In the real situation, the noise generated by flow separation in the pipe covers a wide frequency range with many modes simultaneously propagating.

Previous investigations by Karvelis (1975), Walter (1979), Rennison (1976), Norton, (1979) and Hyland, (1978) have been concerned with the effects of pipe fittings, e.g. bends, valves and orifice plates, on vibrational response and acoustic radiation from a pipe with fully-developed turbulent flow. The work reported here is concerned with detailed mean-flow measurements and the generation and propagation of higher order acoustic modes in fully-developed turbulent pipe flow with separation caused by an orifice plate.

1.2 Literature Review

Flow separation in a fully-developed turbulent pipe flow is a matter of concern to designers as it poses difficulties for mathematical modelling, and understanding of it is poor because of the inability of conventional instrumentation to measure in reversing flows.

The flow structure associated with separation and reattachment of a turbulent shear layer is important in a large number of engineering applications. The flow, after separation, becomes a free shear layer which grows into the adjacent recirculating flow, so that finally the separated shear layer curves sharply towards the wall, where part of the fluid is deflected upstream. The separated-flow region seems to be dominated by low frequency oscillations, and, in order to understand the separated flow, one should understand the behaviour of reattaching flows. Until recently, few reliable quantitative data on the structure of separated flow were available, owing to difficulties with measurement. The quality of available data is now improving, with increasing use of the laser anemometer and multi-wire probes.

Most of the studies of the reattaching shear layer are confined to two-dimensional flows, such as steps and sudden expansions; good reviews of the available data have been presented by Bradshaw and Wong (1972) and Eaton and Johnston (1981). Langren and Sparrow (1967) reported some measurements on the streamwise static pressure variation for an end-cap orifice in a tube, and derived the length of the separated-flow region from these measurements. McGuinness (1978) studied the large-eddy structure in a separated flow behind an orifice at the entrance of a pipe. No detailed measurements of flow structure after the separation caused by an orifice plate are reported in the literature. To the author's knowledge the only data on the length of the reattachment downstream of orifice plates are those compiled by Dyban and Epik (1972), but they did not study the effects of Reynolds number.

Beyond the reattachment, the boundary layer again begins to develop and after many pipe diameters (40-50) downstream the flow returns to the fully-developed undisturbed state. Numerous measurements of flow structure downstream of the disturbed flow are reported, but again almost all of them are for backward-facing steps and sudden expansions (Bradshaw and Wong (1972), Ethridge and Kemp (1978), Smyth (1979), Eaton and Johnston (1980)).

It has been established (Stratford (1959)), that the logarithmic law of the wall is valid just before separation and also beyond re-attachment. Stratford observed the existence of a half-power law in the separated-flow region, while according to Schofield (1981) this extends to the whole region of adverse pressure gradient; beyond reattachment the extent of the half-power law decreases and that of the logarithmic region increases. These studies and those of Perry and Schofield (1981, 1983), Simpson, Strickland and Barr (1977), Simpson, Chew and Shivaprsad (1981), Perry and Fairlie (1975) and

Schofield (1981) are related to two-dimensional flow. Simpson (1982) proposed a correlation for the backflow mean-velocity profile, based on the maximum reverse velocity and its distance from the wall. Schofield (1982) used the distance of the point of zero velocity from the wall instead of maximum reverse velocity and obtained an improvement on Simpson's correlation. No such comprehensive mean-flow measurements for the fully-developed turbulent pipe flow, with flow disturbance caused by an orifice, are available.

It is established (Karvelis (1975), Norton (1979)) that flow separation in fully-developed pipe flow, caused by pipe fittings, generates an intense internal fluctuating pressure field which is the sum of the turbulence and acoustic pressure fluctuations. The pressure and velocity spectra of the internal sound field show a strong plane-wave component at low frequencies and the presence of higher-order acoustic modes at the higher frequencies. In the plane-wave range the spectra have peaks at characteristic frequencies and the higher-order acoustic modes are most intense at frequencies close to their cut-off frequencies. The acoustic modes thus generated travel with small attenuation in the direction of flow and upstream.

Acoustic energy is also dissipated to the atmosphere through the pipe wall, by means of vibration excited by the internal wall-pressure field. Theoretical studies of acoustic plane-wave and multi-mode transmission in pipes with no flow have been made by Cremer (1956), Heckl (1958) and Morfey (1971). Vibrational response of the pipe to the random wall-pressure field, due to the flow separation caused by the pipe fittings, has been investigated by Karvelis (1975), Rennison (1976), Hyland (1978), Norton (1979) and Walker (1979). Kuhn (1974), and Kuhn and Morfey (1976) investigated the transmission loss of sound through pipe walls. Norton studied the excitation of the pipe wall and sound power radiation from a pipe carrying fully-developed turbulent flow with various valves and fittings. Karvelis's work is mainly an experimental investigation of the wall-pressure fluctuations in piping containing control valves.

To the author's knowledge, no systematic experimental study of the propagation of higher-order acoustic modes in the pipe with fully-developed turbulent flow, or the variation of cut-off frequency with the flow speed, is reported in the literature. It is known that the cut-off frequencies of the higher-order acoustic modes are reduced by a factor of $\sqrt{1-M_0^2}$ with uniform mean flow (Mason (1969)). In a pipe carrying fully-developed flow, the mean-flow velocity varies over the cross-section even when the flow is undisturbed, and considerably higher flow velocities exist in the separated-flow region and in the vicinity of it. Now the interesting question is what is the flow Mach number which determines the factor by which the cut-off frequencies are reduced. How do the cut-off frequencies change with flow speed? Cut-off frequency for a propagating mode may change with streamwise distance; therefore the cut-off frequency of a given mode must correspond to the Mach Number at one particular streamwise position.

In order to study the variation of cut-off frequency and modal amplitude one needs to separate the higher order acoustic modes. Various researchers have separated the higher order modes in a duct with mean flow (Bolleter and Chanaud (1970), Mugridge (1969), Bolleter and Crocker (1972), Moore (1972-79), Karvelis (1975), Norton (1979)).

In the above cases, cross-correlation between two hot-wire anemometers or two pressure transducers has been used to separate the various order modes. Cross-correlation techniques, which can be used to determine whether the acoustic energy being transmitted is in the plane-wave or a higher-order mode, were used by Karvelis and more recently by Norton. Norton extended the technique to identify the contribution of plane-waves and higher order modes to the wall-pressure fluctuations in various frequency bands. However, in general, separation of radial mode orders in addition to the circumferential ones, requires traversing the measuring instrument across the radius or making measurements at more than one radius.

Kerschen and Johnston (1980, 1981a,b) developed a technique which separates broadband noise propagating inside a circular pipe into the higher-order acoustic modes. The technique uses combinations of the instantaneous outputs of microphones located around the pipe circumference. It has some advantages over the cross-correlation method: the instantaneous values of the modal coefficient can be studied (cross-correlation technique produces the power spectral densities of the modal coefficients), and considerable simplification in measurements occur when the various circumferential modes are not correlated. This technique has been used in the present investigations.

Beatty (1950), Ingard and Singhal (1974) and Howe (1979) studied the attenuation of sound in circular pipes. In all these cases, only the plane-wave mode was studied and Beatty did not consider the effect of flow. Ingard and Singhal derived an expression for the attenuation of the plane-wave mode. Doak and Vaidya (1970), using perturbation methods, obtained analytical expressions for the attenuation of higher-order and plane-wave sound propagation, as a function of frequency, for nearly hard-walled pipes. They included the effects of the uniform mean flow but not of shear.

Fricke and Stevenson (1968), Fricke (1971), Norton (1979) and Bull and Norton (1981) have studied pressure fluctuations in separated flows. Fricke and Stevenson and Fricke from their measurements in flow over a fence concluded that the total rms wall pressure fluctuations are associated with the convected turbulence in the shear layer and ruled out any significant contribution from acoustic waves. Bull and Norton and Norton made measurements in fully-developed turbulent pipe flow through a 90° mitred bend. They showed that, after about 12 pipe diameters, the total rms pressure reaches an asymptotic value, higher than that found in undisturbed flow; the difference was attributed to the contribution from the higher-order acoustic modes. Mabey (1972) summarises various measurements of wall-pressure fluctuations in separated flow, and demonstrates that spectra for various flow geometries show similarity when plotted in terms of a frequency parameter based on the reattachment length.

As discussed earlier, the total rms pressure will be composed of the turbulence and acoustic pressure fluctuations, and both will contribute to the particle velocity, u . Both the turbulence and acoustic pressure vary with streamwise distance x, and therefore u will also vary with x. Hence the velocity spectrum may, at certain streamwise locations, show spectral peaks corresponding to the higher-order acoustic modes, and may also show up radial modal patterns at a given x, depending on the relative amplitudes of turbulence and acoustic contributions to u . In the present investigation, extensive hot wire measurements have been made to identify the higher-order acoustic modes from the velocity spectra.

So far, the literature review has been concentrated on the mean-flow measurements, measurements of the pressure fluctuations and separation of acoustic modes. In order to predict the cut-off frequencies of the higher-order acoustic modes and their relative magnitude at various radial locations, one needs to know precisely the variation of acoustic pressure and cut-off frequencies in the fully developed turbulent pipe flow. After a classic paper by Pridmore-Brown (1954) on the propagation of acoustic waves in a two-dimensional duct with flow, numerous publications have appeared in the literature. The earlier studies were limited to the two-dimensional duct, but later Mungur and Plumblee (1969) derived an equation for the sound propagation in a circular duct with mean flow. Studies by Mungur and Plumblee and others (e.g. Savkar (1971), Shankar (1972a,b), Ko (1972-73), Mikhail and Abdelhamid (1973a,b)) were limited to annular ducts or to the use of a mean-velocity distribution given by a power law or a boundary layer with uniform flow in the core. An excellent review of the available literature is presented by Nayfeh, Kaiser and Telionis (1975). In the present work, results for the sound propagation in circular duct with hard walls using a fully-developed turbulent flow profile have been obtained.

1.3 Aims of the Present Investigation

As discussed in the preceding section, little work on the detailed structure of the separated flow caused by an orifice plate in a pipe, or on the reattaching layer, is reported in the literature. Extensive experimental data on the vibrational response of the pipe and the acoustic radiation from it, for various flow disturbances, have been collected. Almost all of the available literature on noise due to internal flow disturbances in pipes is concerned with the process of conversion of the pressure fluctuations associated with a given internal acoustic field, by their interaction with the pipe wall, into externally-radiated acoustic energy. No comprehensive measurements in fully-developed turbulent pipe flow of the propagation of higher-order acoustic modes, or of the variation of their cut-off frequencies and modal-amplitude attenuations with flow speed, size of obstruction and streamwise distance are available.

In this investigation comprehensive measurements of the flow resulting from the separation of a fully-developed turbulent pipe flow, caused by an orifice plate, have been made.

The general aims of the investigation can be defined as follows:

(i) The development of an analytical method for the solution of the convected-wave equation for sound propagation in fully-developed turbulent pipe flow (with the appropriate mean velocity profile), for use in the study of

(a) modal cut-off frequency,

(b) acoustic pressure, axial particle velocity and radial particle velocity variation across the pipe radius,

(c) modal phase speed,

and their variation with sound frequency and flow Mach number.

(ii) To measure mean-velocity profiles downstream and upstream of the orifice plate and the positions of the separation and reattachment points, and hence to study the flow development through separation and reattachment.

(iii) To study the wall-pressure characteristics, spectrum levels and generation of higher order modes for various sizes of orifice plate and flow speeds. It is also intended to study the variation of modal amplitude and cut-off frequency with streamwise distance for various flow conditions, and to establish the effective Mach number of the flow system by which the cut-off frequencies are scaled.

(iv) To study the turbulence properties and velocity spectra for various flow speeds and orifice sizes, and to identify the regions in the flow where the higher order acoustic modes are detectable. It is also intended to study the variation of the modal amplitude of the axial component of acoustic particle velocity across the pipe radius, and the variation of cut-off frequency with flow Mach number, and to relate them to the wall-pressure and theoretical results.

(v) To study the fluctuations in the line of flow reattachment.

CHAPTER 2

PROPAGATION OF ACOUSTIC WAVES IN FULLY-DEVELOPED TURBULENT PIPE FLOW WITH HARD WALLS

2.1 Introduction

Disturbances to fully-developed turbulent pipe flow which cause flow separation are responsible for the generation of a strong sound field in the flow which propagates throughout the fluid in the piping system. The pressure spectrum of the sound field shows a strong plane wave component at low frequencies and the presence of higher order acoustic pipe modes at higher frequencies. Earlier studies of acoustic wave propagation in circular and annular ducts with hard walls were limited to axisymmetric modes. In the study of external noise radiation from piping systems, resulting from pipe wall vibrations excited by internal acoustic fields, it is important to know the propagational characteristics of both symmetrical and asymmetric acoustic modes. It is also important to know the modal cut-off frequencies fairly accurately to enable modes to be identified in pressure and velocity spectra and also for the prediction of "coincidence" (phase speeds of structural and acoustic modes being equal) frequencies excited by flow disturbances.

Various aspects of acoustic wave propagation in circular and annular ducts with soft and hard walls containing shear flow have been studied by a number of investigators : Mungur and Plumblee (1969), Doak and Vaidya (1970), Eversman (1971, 1972, 1973), Ko (1972 and 1981), Savkar (1971), Shankar (1972a,b), Mikhail and Abdelhamid (1973a,b). An excellent review of the work has been presented by Nayfeh, Kaiser and Telionis (1975). In almost all cases the mean velocity profile of the shear flow has been taken as that of fully developed laminar flow or as a uniform core flow with a thin boundary layer at the wall.

However Savkar, Shankar and Eversman have given results for a $1/7^{th}$ power law velocity distribution. This distribution gives an infinite slope at the wall; and hence the resulting wave equation is singular at the wall. In the present study a three-region (viscous sublayer, logarithmic region and central core region) mean velocity distribution has been used. The results have been obtained by numerical solution of the convected-wave equation, for flow Mach numbers up to 0.6. The numerical scheme, for any specified acoustic mode, flow speed and pipe wall impedance, allows the determination of the cut-off frequency of the mode, and, for any specified values of the frequency parameter $\omega a/c$, the propagation constant of the mode and the radial distribution of acoustic pressure and velocity. Although the scheme is applicable to both hard-walled and soft-walled pipes, only results for hard-walled pipes, which are relevant to vibration of and acoustic radiation from industrial piping systems, have been included. Centre-line Mach numbers up to 0.6 and values of $\omega a/c$ up to 30 have been considered adequate to cover cases of interest. Total temperature has been taken to be constant across the pipe diameter.

2.2 Acoustic Wave Propagation in a Pipe for the Cases of Stationary Internal Fluid and Uniform Flow

The wave equation governing propagation of acoustic pressure waves inside a circular pipe containing stationary fluid is,

$$\frac{1}{c^2}\frac{\partial^2 p}{\partial t^2} - \nabla^2 p = 0, \tag{2.1}$$

In the solution to this equation for harmonic waves in a hard-walled pipe of constant cross-sectional area, the pressure can be represented in the form (in the coordinate system illustrated in Figure 2.1)

$$p = CP(r)e^{i(k_x x+m\theta- \omega t)} . \tag{2.2}$$

The solution must be continuous at $\theta = 0$ and $\theta = 2\pi$, and therefore m must be an integer. The function P(r), representing the radial variation of pressure amplitude, is then given by the Bessel equation

$$\frac{d^2P}{dr^2} + \frac{1}{r}\frac{dP}{dr} + (\kappa_{mn} - \frac{m^2}{r^2})P = 0 . \tag{2.3}$$

The solution satisfying the wall boundary conditions and remaining finite on the pipe axis can then be expressed in the well known form (see e.g. Morse and Ingard (1968))

$$p(r,\theta,x) = \sum_m \sum_n (A_{mn} \cos m\theta + B_{mn} \sin m\theta)J_m(\kappa_{mn} r)e^{i(k_x x-\omega t)}. \tag{2.4}$$

The κ_{mn} are eigenvalues which satisfy the hard-wall boundary condition

$$J'(\kappa_{mn} a) = 0, \tag{2.5}$$

where the prime denotes differentiation of the Bessel function with respect to its argument, and the axial and transverse wave number components are related to the frequency by

$$\kappa^2_{mn} + k^2_x = (\frac{\omega}{c})^2. \tag{2.6}$$

The dispersion relation between k_x and ω can therefore be written in non-dimensional form as

$$K_x = \pm \sqrt{\Omega^2 - (\kappa_{mn}a)^2} , \tag{2.7}$$

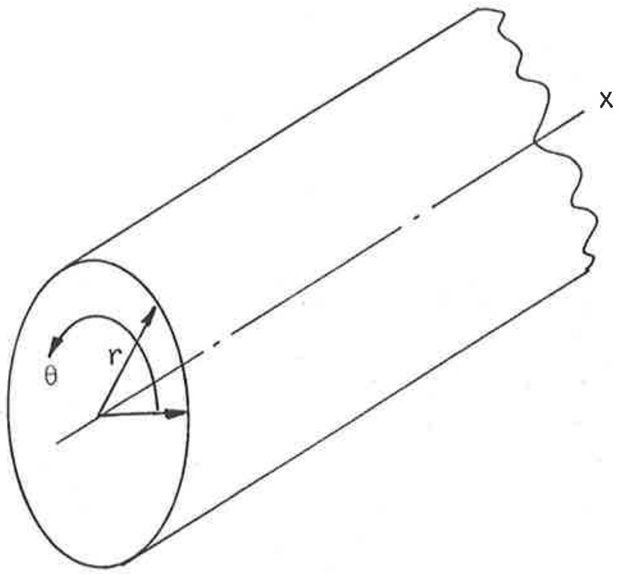

FIGURE 2.1 : COORDINATE SYSTEM

where $K_x = k_x a$, $\Omega = \omega a/c$, and the plus and minus signs correspond to wave propagation in the positive and negative axial coordinate directions respectively.

The (m,n)th acoustic mode has m plane diametral modal surfaces and n cylindrical nodal surfaces concentric with the cylinder axis; it can propagate only at frequencies above its cut-off frequency which is given by

$$(\Omega_{co})_{mn} = \kappa_{mn} a \ . \tag{2.8}$$

The modes can be classified as plane waves ($m = n = 0$), symmetric higher order modes ($m = 0$, $n \geqslant 1$) or asymmetric higher order (spinning) modes ($m \geqslant 1$, $n \geqslant 1$).

At cut-off there is no propagation of sound energy along the pipe and therefore the axial group velocity is zero. As frequency increases above cut-off, the wave form begins spiralling down the pipe, finally approaching plane wave velocity in both phase and group velocity.*

For the case in which the fluid inside the pipe is in uniform axial motion with velocity U and Mach number M, the governing equation is formally the convected-wave equation

$$\frac{1}{c^2}\frac{\partial^2 p}{\partial t^2} + \frac{2M}{c}\frac{\partial^2 p}{\partial t \partial x} + M^2 \frac{\partial^2 p}{\partial x^2} - \nabla^2 p = 0 \ . \tag{2.9}$$

For harmonic waves the variables are again separable and the pressure can be represented by equation (2.2). The radial distribution function is again given by equation (2.3), the solution can still be expressed by equation (2.4), and the eigenvalues κ_{mn} are given by the boundary condition equation (2.5). This is to be expected

* (see e.g. page 70, Stephens and Bate (1966) for definitions of phase velocity and group velocity)

since the system of acoustic modes in a stationary fluid is simply being translated relative to the space-fixed coordinate reference frame at mach number M. Equation (2.6) is, however replaced by

$$\kappa_{mn}^2 + k_x^2 = \left(\frac{\omega}{c} - M k_x\right)^2 , \qquad (2.10)$$

the term $M k_x$ being associated with the Doppler frequency shift experienced by a stationary observer as a result of the fluid motion. The non-dimensional dispersion relation follows from equation (2.10) as

$$k_x = \frac{-M\Omega \pm \sqrt{\Omega^2 - (\kappa_{mn}a)^2(1-M^2)}}{(1-M^2)} , \qquad (2.11)$$

which replaces equation (2.7).

Positive and negative values of k_x, (which do not coincide exclusively with the positive and negative signs in equation (2.11)) correspond to downstream and upstream propagation respectively. The cut-off frequency is modified to

$$(\Omega_{co})_{mn} = (\kappa_{mn}a)\sqrt{1-M^2} , \qquad (2.12)$$

and is associated with a wave propagating upstream and having an axial wave number of

$$K_x = -\frac{M}{\sqrt{1-M^2}}(\kappa_{mn}a) . \qquad (2.13)$$

2.3 The Convected-Wave Equation in Cylindrical Polar Coordinates for Fully-Developed Shear Flow

When the pipe contains a shear flow the convected-wave equation which then governs acoustic propagation does not admit simple analytical solutions as in the two limiting cases which have been referred to. The complexity introduced by the combined effect of convection and refraction resulting from transverse velocity gradients necessitates numerical solutions. Numerical results for various aspects of propagation in circular or annular ducts have been obtained by Mungur and Plumblee (1969), Eversman (1971a, 1973), Shankar (1972), Ko (1973, 1981) and Mikhail and Abdelhamid (1973a,b) Doak and Vaidya (1970). A comprehensive review of methods of calculating wave propagation in ducts carrying shear flows is given by Nayfeh, Kaiser and Telionis (1975).

The derivation of the wave equation governing propagation of sound in a fully-developed duct flow in cylindrical polar coordinates is given by Mungur and Plumblee (1969). The term fully-developed, as used here, implies that the mean flow is confined to the axial direction (the mean flow velocity components in both the circumferential and radial direction are zero) and that the mean flow velocity at a given radial position is independent of the axial coordinate. The only mean shear is therefore that associated with the variation of axial mean velocity U with the radial coordinate, namely $\partial U/\partial r$. The effects of viscosity are neglected except in so far as they govern the mean-velocity distribution. Under these conditions the equations obtained by first order perturbation of the Navier-Stokes equations and the continuity equation, linearisation by subtraction of the time averaged quantities, and neglect of products of perturbation velocities are given by Mungur and Plumblee as

$$\frac{\partial u}{\partial t} + v\frac{\partial U}{\partial r} + U\frac{\partial u}{\partial x} = -\frac{1}{\rho_0}\frac{\partial p}{\partial x} \tag{2.14}$$

$$\frac{\partial v}{\partial t} + U\frac{\partial v}{\partial x} = -\frac{1}{\rho_0}\frac{\partial p}{\partial r} \tag{2.15}$$

$$\frac{\partial w}{\partial t} + U\frac{\partial w}{\partial x} = -\frac{1}{\rho_0 r}\frac{\partial p}{\partial \theta} \tag{2.16}$$

and

$$\frac{\partial \rho}{\partial t} + U\frac{\partial \rho}{\partial x} + \rho_0\left(\frac{\partial u}{\partial x} + \frac{\partial v}{\partial r} + \frac{1}{r}\frac{\partial w}{\partial \theta}\right) + \rho_0\frac{v}{r} = 0 \quad . \tag{2.17}$$

In addition to the neglect of viscous effects, it is assumed that the effects of thermal conductivity of the fluid are negligible; this allows the pressure and density fluctuations to be isentropically related so that

$$p = \rho c^2 \quad . \tag{2.18}$$

In Munyur and Plumblee's analysis the temperature of the fluid is taken to be uniform throughout, in which case c is constant.

Addition of the three equations obtained by differentiation of equations (2.14), (2.15) and (2.16) with respect to x, r and θ respectively, and the use of equations (2.15), (2.17) and (2.18), leads to the convected-wave equation in the form

$$\frac{1}{c^2}\frac{\partial^2 p}{\partial t^2} + 2\frac{M}{c}\frac{\partial^2 p}{\partial x \partial t} + M^2\frac{\partial^2 p}{\partial x^2} - 2\rho_0 c\frac{\partial M}{\partial r}\frac{\partial v}{\partial x} - \nabla^2 p = 0 \quad . \tag{2.19}$$

For the uniform flow case $\partial M/\partial r = 0$ and the equation reduces to equation (2.9), while for stationary internal fluid M = 0 and the equation further reduces to equation (2.1).

For a harmonic wave propagating in the direction of flow, with p and u proportional to $\exp[i(\nu x-\omega t)]$, where ν is a propagation constant,

$$\begin{aligned}\left(\frac{\partial}{\partial t} + U\frac{\partial}{\partial x}\right) &= i(\nu U-\omega)\\ &= -\,i\omega(1-MK)\end{aligned} \tag{2.20}$$

where $K = \nu c/\omega$ and $M = U/c$ is the local flow Mach number. Here ν is allowed to be complex, so that its real part is the axial wave number component k_x and its complex part gives the spatial attentuation of the acoustic wave. Equations (2.20) and (2.15) allow the radial acoustic velocity component to be expressed as

$$v = \frac{1}{i\ \rho_0\omega(1-MK)} \cdot \frac{\partial p}{\partial r} \quad . \tag{2.21}$$

Substitution of equations (2.20) and (2.21) in equation (2.19) then leads to

$$\frac{1}{c^2}\frac{\partial^2 p}{\partial t^2} + 2\frac{M}{c}\frac{\partial^2 p}{\partial x \partial t} + M^2\frac{\partial^2 p}{\partial x^2} - \frac{2K}{(1-MK)}\frac{\partial M}{\partial r}\frac{\partial p}{\partial r} - \nabla^2 p = 0 \quad . \tag{2.22}$$

Separation of all variables is again possible, and the acoustic pressure can be expressed in the form

$$p = CP(r)e^{i(\nu x+m\theta-\omega t)} \quad . \tag{2.23}$$

Combination of equations (2.22) and (2.23) and introduction of the non-dimensional variables $\Omega = \omega a/c$ and $R = r/a$ yields the equation for the radial distribution function $P(R)$:

$$\frac{d^2P}{dR^2} + \left(\frac{1}{R} + \frac{2K}{1-MK}\frac{dM}{dR}\right)\frac{dP}{dR} + \Omega^2\left[(1-MK)^2 - K^2 - \frac{m^2}{\Omega^2 R^2}\right]P = 0 \ . \tag{2.24}$$

The boundary conditions to be satisfied are that

(i) $\left.\begin{array}{r} dP/dR = 0 \text{ for axisymmetric } (m=0) \text{ modes} \\ P = 0 \text{ for asymmetric } (m \geq 1) \text{ modes} \end{array}\right|$ at $R = 0$ (2.25)

and

(ii) $\beta = \rho_0 c\ v/p$ at $R = 1$, where β is the specific acoustic admittance of the pipe wall.

From equations (2.21) and (2.23) the latter condition is equivalent to

$$\frac{dP}{dR} = i\,\Omega\beta[(1-MK)P]_{R=1} \quad , \tag{2.26}$$

which, for the case in which the mean flow satisfies the no slip condition at the pipe wall ($M = 0$, at $R = 1$), becomes

$$\frac{dP}{dR} = i\,\Omega\beta P \text{ at } R = 1. \tag{2.27}$$

For a hard-walled duct ($\beta = 0$), this boundary condition further reduces to $v = 0$ or

$$\frac{dP}{dR} = 0 \text{ at } R = 1 \quad . \tag{2.28}$$

The singular nature of equation (2.24) at $R = 0$ prohibits application of the boundary condition (2.25) at the centre of the pipe. Eversman (3) has dealt with the problem by shifting the centre to a point η, where $\eta << 1$. In the present study also, the boundary conditions are applied at a point close to the centre (e.g. $\eta \leqslant 0.001$).

Mungur and Plumblee (1969) derived equation (2.24) and devised an iterative trial and error process for determining the K eigenvalues, utilising a fourth-order Runge-Kutta numerical integration scheme. They present results for the shapes of axisymmetric ($m = 0$) modes in annular ducts with rigid walls containing fully-developed laminar flow with a parabolic distribution of mean velocity.

The same equation has also been solved numerically by Eversman (1970) using similar techniques. The results given by Eversman are for the effect of shear flow on the attenuation of axisymmetric acoustic waves in a soft-walled circular pipe with a mean axial-velocity distribution consisting of a central region of uniform flow and a boundary layer region adjacent to the pipe wall in which the mean velocity drops sinusoidally (over a quarter-wave) from the core-flow value to zero at pipe wall.

Eversman [1972] used a $1/N^{th}$ power law velocity profile to solve the same equation for the case of lined annular ducts. He derived a method to avoid another singularity (due to infinite slope of the velocity) at the wall because of $1/N^{th}$ power law.

Propagation of plane waves in a two dimensional duct containing subsonic flow was considered by Shankar [1972]. He solved the initial value problem in time and space within the framework of a perturbation scheme about uniform flow. Though his scheme can be used for weakly sheared flow, it cannot be used for boundary layer type flow e.g. no slip boundary.

Shankar (1972a) has also obtained numerical solutions to equation (2.25) for hard-walled circular pipes and annular ducts with a 1/7 power distribution of axial mean velocity over the flow cross-section. Results are given for mode shapes and propagation constants (both real and complex, the latter corresponding to cut-off modes in a hard-walled duct), but again the analysis is confined to axisymmetric ($m = 0$) modes.

Mikhail and Abdelhamid (1973) give results of numerical solutions for annular ducts for both axisymmetric and asymmetric modes for the same form of mean velocity distribution as used by Eversman (1970) for incompletely-developed flow and for a parabolic profile of fully-developed flow. They have considered the effects of mean-flow Mach number and frequency parameter on mode shapes and propagation constant for both upstream and downstream wave propagation. The results indicate that the acoustic waves are refracted towards the wall for downstream propagation and away from it for upstream propagation, and that the effect is greater the greater is the mean flow Mach number and the greater is the difference between the frequency of the wave and its modal cut-off frequency.

In the analysis of the response of the wall of a hard-walled pipe to excitation by an internal acoustic field in the presence of shear flow, and the external acoustic power radiated by the vibrating wall, non-axisymmetric modes ($m \neq 0$) may be as important, if not more important than, axisymmetric modes. It will be noted that in a pipe with stationary internal fluid the non-axisymmetric modes (1,0), (2,0) occur at lower frequencies than the lowest-frequency axisymmetric mode, the (0,1).

Since the level of pipe wall response to excitation by these acoustic modes depends on the degree to which their phase velocities and wave numbers match those of flexural waves in the pipe wall at a given frequency, it is important to be able to calculate the effects of a shear flow (and in particular that corresponding to fully-developed turbulent pipe flow) on mode shapes and phase velocities of both axisymmetric and non-axisymmetric acoustic modes.

To this end, the convected-wave equation derived by Mungur and Plumblee, equation (2.24) has been solved numerically for both upstream and downstream wave propagation, over a range of values of the non-dimensional frequency parameter $0 < \Omega < 30$ and for a range of flow conditions. In all cases, a radial distribution of mean axial velocity corresponding in detail to that of fully-developed turbulent pipe flow has been used in the analysis (although no account is taken of the effects of the turbulent motion itself on acoustic wave propagation). Calculations have been made for flows with various values of M_0, the centre-line Mach number, in the range $0 \leqslant M_0 \leqslant 0.6$. Results will be presented for all modes with $0 \leqslant m \leqslant 5$ and $0 \leqslant n \leqslant 5$ (see Figure 2.2).

However before results are considered, details of the mean velocity profile used and of the techniques used to obtain the numerical solutions will be given.

2.4 Mean Velocity Profile

So that the mean velocity profile used in the calculations is truly representative of fully-developed turbulent pipe flow at all radial positions, three regions are distinguished - the viscous sublayer and buffer layer, the logarithmic region and the central core region, each with its own form of velocity distribution, with appropriate matching conditions at the limits of the regions.

2.4.1 Wall region : $0 < Y^+ < 33.2$

The basic relation for the velocity distribution in this region, which includes the viscous sublayer and the buffer layer, has been based on the velocity gradient distribution given by Bull (1969), namely

$$\frac{\partial U^+}{\partial Y^+} = [1 + \frac{Y^+}{a'} + \frac{1}{2}(\frac{Y^+}{a'})^2 + \frac{1}{b'}(\frac{Y^+}{a'})^6]\, e^{-Y^+/a'}, \qquad (2.29)$$

where a' and b' are constants with the values a' = 4.0 and b' = 1300. This relation yields the appropriate limiting form of velocity distribution at small Y^+ namely

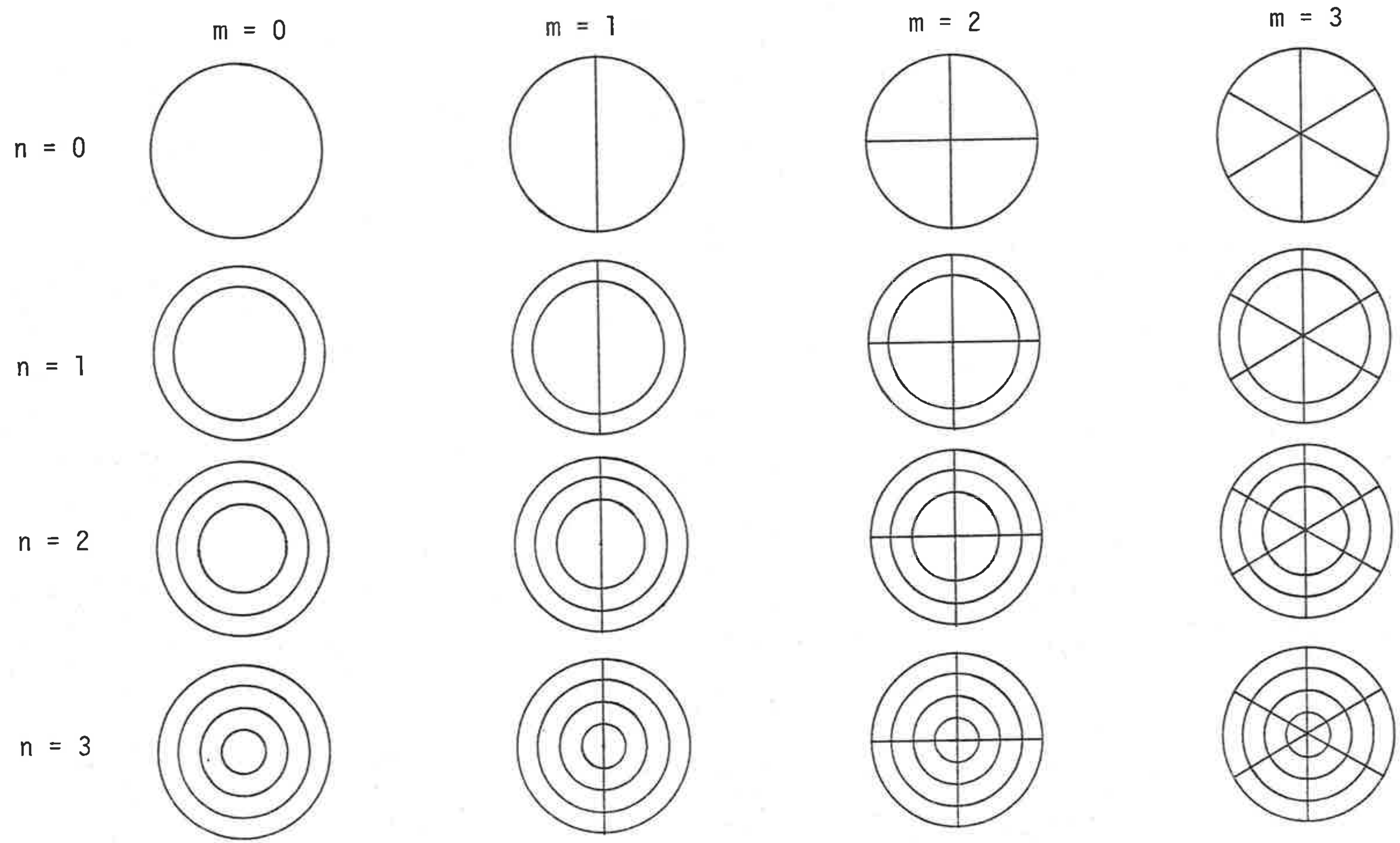

FIGRUE 2.2 : PHYSICAL INTERPRETATION OF THE MODE NUMBERS IN THE (m,n) MODES

$$U^+ = Y^+ + cY^{+4} + \ldots , \tag{2.30}$$

where c is a constant, and at very small Y^+ reduces to the sublayer variation

$$U^+ = Y^+. \tag{2.31}$$

Integration of equation (2.29) leads to the velocity distribution for this region, which will be denoted by U_b^+, given by

$$U_b^+ = a\{(3 + \frac{720}{b'}) - [\frac{1}{b'}(720+720Y_a+360Y_a^2+120Y_a^3+30Y_a^4+6Y_a^5+Y_a^6)$$
$$+ (3+2Y_a+\frac{1}{2}Y_a^2)]e^{-Y_a}\}, \tag{2.32}$$

where $Y_a = Y^+/a'$. This is in close agreement with the distribution recommended by Coles (1954) for this region (see Shubert and Corcos (1967)) and at $Y^+ = 33.2$ matches the logarithmic profile as given below in Section 2.4.2 with $B = 5.0$.

2.4.2 Logarithmic region

Once Y^+ exceeds 33.2, it is assumed that the velocity distribution is logarithmic with the basic form

$$U^+ = \frac{1}{K} \ln Y^+ + B , \tag{2.33}$$

with $K = 0.41$ and $B = 5.0$.

2.4.3 Composite velocity profiles

Calculations have been made with two different forms of composite velocity distribution, one based on the velocity distribution in the central core region of the flow given by Townsend (1976, p.149) and the other based on the correction function proposed by Allan (1970).

For the core region, Townsend gives the parabolic distribution

$$U^+ = U_o^+ - \frac{1}{2} R_s(1 - y/a)^2, \tag{2.34}$$

valid for $\alpha \leqslant Y/a \leqslant 1$. This distribution follows from the linear variation of shear stress with radial distance which characterises fully-developed turbulent flow together with the assumption of constant eddy viscosity ν_T over the central region of the flow. The flow constant for the central region R_s is given by $R_s = RU_\tau/\nu_T$. The value of α corresponds to the point where the eddy viscosity in the equilibrium region of the turbulent boundary layer at $Y/a < \alpha$, which is given by $KU_\tau Y$, becomes equal to the constant value ν_T of the core region. This leads to

$$\alpha = 1/KR_s \quad . \tag{2.35}$$

With Townsend's value of $R_s = 15.2$ and $K = 0.41$, $\alpha = 0.160$. For $Y/a < \alpha$ (but outside the buffer layer), the logarithmic relation of equation (2.33) applies. The composite profile is thus

$$U^+ = \begin{cases} U_b^+ & \text{for } 0 \leqslant Y^+ \leqslant 33.2 \quad (2.36a) \\ \frac{1}{K}\ln Y^+ + B & \text{for } 33.2\ \nu/U_\tau \leqslant y \leqslant 0.16a \quad (2.36b) \\ U_o^+ - \frac{1}{2}R_s(1 - \frac{y}{a})^2 & \text{for } 0.16 \leqslant y/a \leqslant 1.0 \quad (2.36c) \end{cases}$$

The relation between the friction velocity and the centre-line flow velocity is obtained by equating the logarithmic and core distributions at $y/a = \alpha$ as

$$U_o^+ = \frac{1}{K}\ln\left(\frac{\alpha Re}{U_o^+}\right) + B + \frac{1}{2}R_s(1-\alpha)^2, \tag{2.37}$$

where the Reynolds number $Re = U_o a/\nu$.

The distribution given by Allan applies to all radial positions outside the buffer layer. For a pipe with a smooth internal wall, it takes the form

$$U^+ = \frac{1}{K}\ln Y^+ + B + K'f_c(\frac{y}{a}, K'), \qquad (2.38)$$

with K' = 0.7 and the "correction" function

$$f_c(\frac{y}{a},K') = \frac{1 - \cos(\beta y/a)}{1 - \cos \beta}. \qquad (2.39)$$

The parameter β is the solution of the equation

$$\frac{\beta \sin \beta}{1-\cos \beta} = - \frac{1}{KK'}. \qquad (2.40)$$

With K = 0.41 and K' = 0.7 its numerical value is β = 4.4666 (a value slightly different from that given by Allan, owing to a slightly different choice here of the value of K). Equation (2.38) then becomes, with B = 5.00,

$$U^+ = \frac{1}{K} \ln Y^+ + 5.563 - 0.5630 \cos(4.4666\ y/a). \qquad (2.41)$$

For $Y^+ \leqslant 33.2$ the values of $K'f_c(y/a, K')$ are insignificant compared with the values of U_b^+ given by equation (2.32), and hence the correction function can be applied at all y. The composite distribution in this case therefore becomes

$$U^+ = K'f_c(\frac{y}{a}, K') + \begin{cases} U_b^+ & \text{for } 0 \leqslant Y^+ \leqslant 33.2 \\ \frac{1}{K} \ln Y^+ + B & \text{for } 33.2\ \nu/U_\tau \leqslant y \leqslant a \end{cases} \qquad (2.42)$$

The expression for U_0^+ is given by the second relation of equation (2.42) with y = a, or by equation (2.41), and is

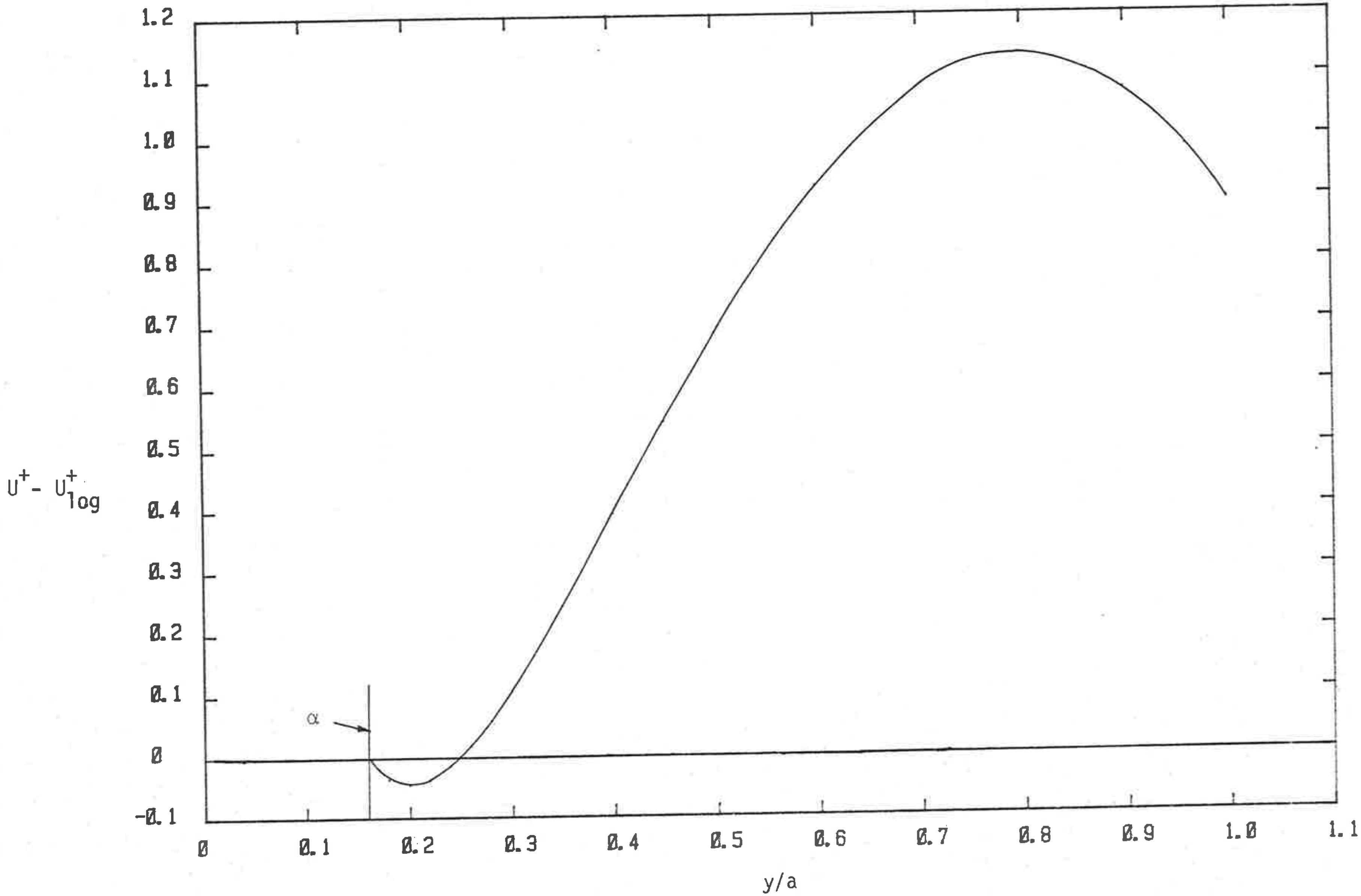

FIGURE 2.3 : COMPARISON OF LOGARITHMIC-LAW PROFILE WITH TOWNSEND'S PARABOLIC PROFILE FOR $y/a > \alpha$

$$U_o^+ = \frac{1}{K}\ln\frac{Re_o}{U_o^+} + B + K'f_c(1,K')$$

$$= \frac{1}{K}\ln\frac{Re_o}{U_o^+} + 5.70 \qquad (2.43)$$

For calculation purposes, where the centre-line flow velocity Mach number is assigned a chosen value, it is necessary to solve either equation (2.37) or (2.43) by iteration to determine the value of U_o^+, and hence U_τ, to allow all parameters in equations (2.36) or (2.42) to be evaluated.

Of the two profiles considered above, equations (2.36) and (2.42), because the former based on Townsend's parabolic distribution in the core region has a discontinuity in slope at $y/a = \alpha$, and falls below the logarithmic-law line (as shown in Figure 2.3, in which $U^+ - U^+_{log}$, the difference in U^+ given by equations (2.36b) and (2.36c) has been plotted), the latter has been preferred. Although results for both profiles have been obtained, only those obtained using Allan's profile function are presented.

U_o^+ and then U_τ were evaluated by iteration of equation (2.43), for M_o between 0.05 to 0.6.

2.5 Numerical Procedure

Equation (2.24) has been solved numerically, as an initial value problem, by means of a forward integration procedure employing the fourth-order Runge-Kutta method (Kreyszig, 1972).

Equation (2.24) may be rewritten as

$$\frac{d^2P}{dR^2} + \frac{C_1(R)}{R}\frac{dP}{dR} + \frac{C_2(R)}{R^2}P = 0 \quad , \qquad (2.44)$$

where the coefficients $C_1(R)$ and $C_2(R)$, which are dependent on R through the Mach number variation across the pipe, are given by

$$C_1 = 1 + \frac{2KR}{1-MK} \cdot \frac{dM}{dR} \qquad (2.45)$$

and

$$C_2 = (R\Omega)^2[(1-MK)^2 - K^2] - m^2 \; .$$

The boundary conditions for a hard-walled pipe are

$$\frac{dP}{dR} = 0 \text{ at the wall } (R=1)$$

and those given by equation (2.25) at R = 0.

Equation (2.44) may be rewritten as pair of first-order equations

$$\frac{dP}{dR} = Q$$

and

$$\frac{dQ}{dR} = -\frac{C_1(R)}{R}Q - \frac{C_2(R)}{R^2}P \; . \qquad (2.46)$$

If the region $0 \leq R \leq 1$, where the solution is required, is divided into N steps with a step width h (not necessarily constant), then P_{N+1} and Q_{N+1}, the the values of P and Q at R = (n+1)h, can be obtained from the corresponding values P_n and Q_n at R = nh from the relations

$$P_{n+1} = P_n + h(Q_n + K_n)$$

and

$$Q_{n+1} = Q_n + K_n^*, \qquad (2.47)$$

where

$$K_n = 1/3\;(A_n + B_n + C_n)$$

$$K_n^* = 1/3\;(A_n + 2B_n + 2C_n + D_n)$$

and

$$\left.\begin{aligned}
A_n &= 1/2\ h\ f(R_n,\ P_n,\ Q_n), \\
B_n &= 1/2\ h\ f(R_n + 1/2\ h,\ P_n + \beta_n,\ Q_n + A_n), \\
C_n &= 1/2\ h\ f(R_n + 1/2\ h,\ P_n + \beta_n,\ Q_n + B_n), \\
D_n &= 1/2\ h\ f(R_n + h,\ P_n + \delta_n,\ Q_n + 2C_n), \\
\beta_n &= 1/2\ h\ (Q_n + 1/2\ A_n), \\
\delta_n &= h\ (Q_n + C_n).
\end{aligned}\right| \qquad (2.48)$$

Equations (2.47) and (2.48) with the initial values for P_0 and Q_0 allow Equation (2.44) to be integrated numerically over the pipe radius from R = 1 to R = 0 and the value of P_n at R = 0 (subject to qualification for the singularity at R = 0 discussed below) obtained. The procedure for solving Equation (2.44) is then as follows (and as values of P and K are complex for soft-walled ducts and in some cases, discussed later, for hard-walled ducts also, it is done in complex mathematics). Values are chosen for

(i) centre line flow mach Mumber M_0,

(ii) circumferential mode order, m ,

(iii) radial order, n, and

(iv) non-dimensional frequency parameter, Ω.

The initial value of dP/dR is zero at R = 1 (i.e. $Q_0 = 0$). The initial value of P at R = 1 can be arbitrarily assigned and is here taken to be $P_0 = (1+i)$ (and this does not affect the eigenvalue K, of the equation (2.44)).

A value of K is then assumed for the given m, n, M_0 and Ω and the integration using Equations (2.47) and (2.48) carried out across the pipe radius starting at the wall. Smaller steps are taken in the sublayer and buffer layer regions, $Y^+ < 33.2$ (h=0.0005) than in the logarithmic and core region of the velocity profile (h=0.02).

The integration is continued to the point $Y = 1-\varepsilon$ ($\varepsilon \ll 1$) just short of the pipe centre-line (it cannot be taken right to the centreline, $Y = 1$, because of the singularity associated with the terms $(1/R)\,(dP/dR)$ and m^2/R^2 at $R = 0$). If the boundary condition at the centre line ($Q_n = 0$ for $m=0$ modes or $P_n = 0$ for $m \geq 1$ modes) is not satisfied (which generally will be the case), the integration is repeated with a new value of K. A good initial guess for K (as suggested by Shankar (1972a)) is the value corresponding to uniform flow with Mach number M_o, for the given m,n and Ω. As the K value for the sheared flow lies between the uniform and no-flow values, the initial guess for K (in increments ΔK) is moved towards the no-flow value and the variation of P and Q (i.e. dP/dR) across the pipe radius calculated till the pressure distribution exhibits the appropriate number of sign changes (namely n) between $Y = 0$ and $Y = 1-\varepsilon$, and satisfies the boundary condition. In practice, to reduce the computing time, P and dP/dR are not calculated across the complete radius for an assumed value of K, but a check is kept on the number of sign changes in the pressure and if this number exceeds the required one, the integration is restarted from the wall with a new guess.

The situation is complicated in the case of a soft-walled pipe or when K is complex for a hard-walled pipe (discussed later in this section), as the check on sign has to be kept for both the real and imaginary values of P and dP/dR; and to complicate the situation further, a change in the guess requires a change in both the real and imaginary parts of K.

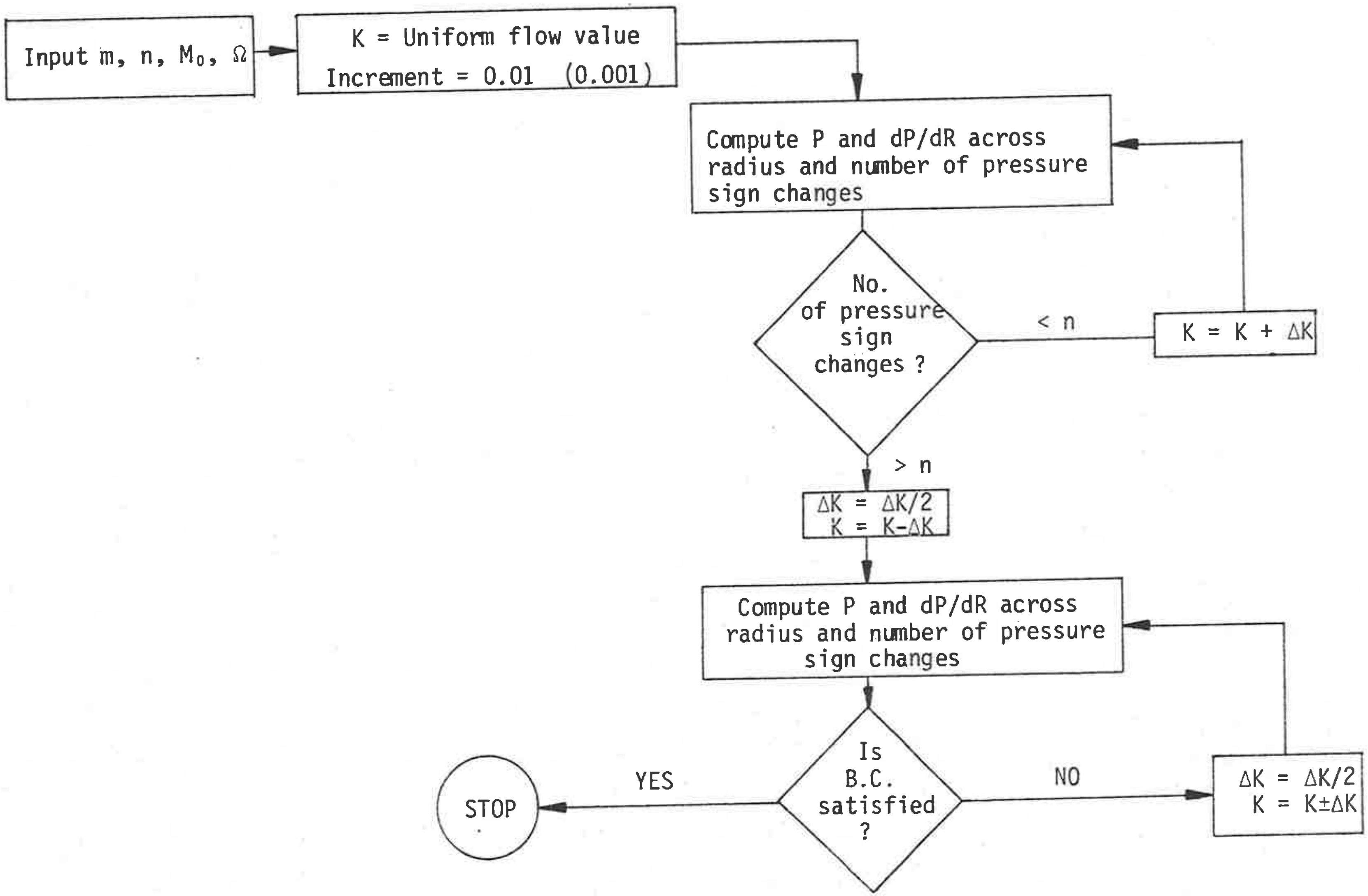

FIGURE 2.4 : SCHEME FOR THE LOCATION OF EIGENVALUES

After the range of K is established, the increment is cut to half and the integration is repeated. The increment is again cut to half, and added to or subtracted from the previous value depending upon the number of sign changes in P (or dP/dR for the m=0 case). The process is repeated until the boundary condition at the centre is satisfied. The integration is then stopped and the guess is the required value of K. Integration is also stopped if the increment becomes less than a specified limit (a value of 10^{-10} is used). In real arithmetic it is almost impossible to achieve a value of zero for P and dP/dR for the boundary conditions to be satisfied, and hence a value of 10^{-4} is normally used as the limit. This procedure for finding the roots of equation (2.44) is illustrated in Figure 2.4. A step size of 0.01 has been found to be adequate for $\Omega \geqslant (\kappa_{pq}a)$, but for $\Omega_{co} \leqslant \Omega \leqslant (\kappa_{pq}a)$ a smaller step size (0.001) is required.

For each value of the frequency parameter Ω, there will be two values of K which will satisfy equation (2.44), one corresponding to downstream propagation and other to upstream propagation (see Figure 2.6). The effect of shear is not to change the frequency (given by $\kappa_{mn}a = (\Omega_{co})_{NF}$) corresponding to zero axial wave number k_x, and therefore for $\Omega < (\Omega_{co})_{NF}$ both the values of K will be negative, i.e. both will correspond to upstream propagation.

Values of K will be real (imaginary part zero), for frequency greater than the cut-off frequency Ω_{co} of the mode, but for $\Omega < \Omega_{co}$, K will be complex, i.e. the acoustic wave will be attenuated with distance. Therefore, Ω_{co} is the limiting frequency, above which K will be real.

Table 2.1

$M_0 = 0.2$, $\Omega = 20$, $A = 0.90842$ Modes (2,n)

n	Ω_{co}	K (= K_x/Ω)		Values for uniform flow, AM_0		% difference	
		Real	Imaginary	Real	Imaginary	Real	Imaginary
0	3.00930	0.85352	-	0.83452	-	-2.226	-
1	6.59636	0.79062	-	0.78842	-	-0.278	-
2	9.80387	0.71436	-	0.71349	-	-0.123	-
3	12.95096	0.60045	-	0.60014	-	-0.051	-
4	16.07541	0.42726	-	0.42736	-	+0.023	-
5	19.18925	-0.10318	-	0.10376	-	+0.565	-
6	22.29792	-0.18898	0.50937	-0.18788	0.50935	+0.582	-0.006
7	25.40463	-0.18905	0.80962	-0.18788	0.80928	+0.619	-0.042
8	28.51170	-0.18947	1.05028	-0.18788	1.04952	+0.839	-0.073
9	31.62116	-0.18975	1.26586	-0.18788	1.26454	+0.985	-0.100

Table 2.1 shows a typical set of results for the values of K, in this case for the (2,n) modes for $M_o = 0.2$ and $\Omega = 20$. It is evident that when $\Omega < \Omega_{co}$, the K have non-zero imaginary parts. (Calculations for the (0,n) modes with $M_o = 0.3$ and $\Omega = 20$ and with a mean-velocity distribution corresponding to a $1/7^{th}$ power law reproduced the results of Shankar (1972b) accurate to three decimal places.)

2.6 Cut-Off Frequency Calculations

The following properties of the cut-off frequency of an acoustic mode are used in the scheme for its location.

(i) At frequencies below the cut-off frequency propagation is not possible and K then has a non-zero imaginary part.

(ii) At the cut-off frequency, the two solutions of equation (2.44) become identical.

(iii) At the cut-off frequency the group velocity $d\Omega/dK$ is zero.

But its calculation is much more cumbersome than the calculation of K, because here for each assumed value of frequency parameter Ω, both the eigenvalues of the equation (2.44) have to be calculated using the procedure described in section 2.5. Then the process has to be repeated for other assumed values of Ω.

The first trial value of Ω is chosen between $(\Omega_{co})_{NF}$ and $(\Omega_{co})_{UF}$ and K is calculated (both the eigenvalues if K is real). Now the frequency step size, which is half the difference between $\kappa_{mn}a$ ($=\Omega_{co}$) and $(\Omega_{co})_{UF}$, is halved, and added to the previous trial value of Ω if the K calculated has a non-zero imaginary part (subtracted, if K is real) to form the new trial Ω. The process is repeated until

(i) K is real and the two eigenvalues are the same, and

(ii) the frequency step size is less than the specified tolerance (10^{-10}).

This scheme is illustrated in Figure 2.5.

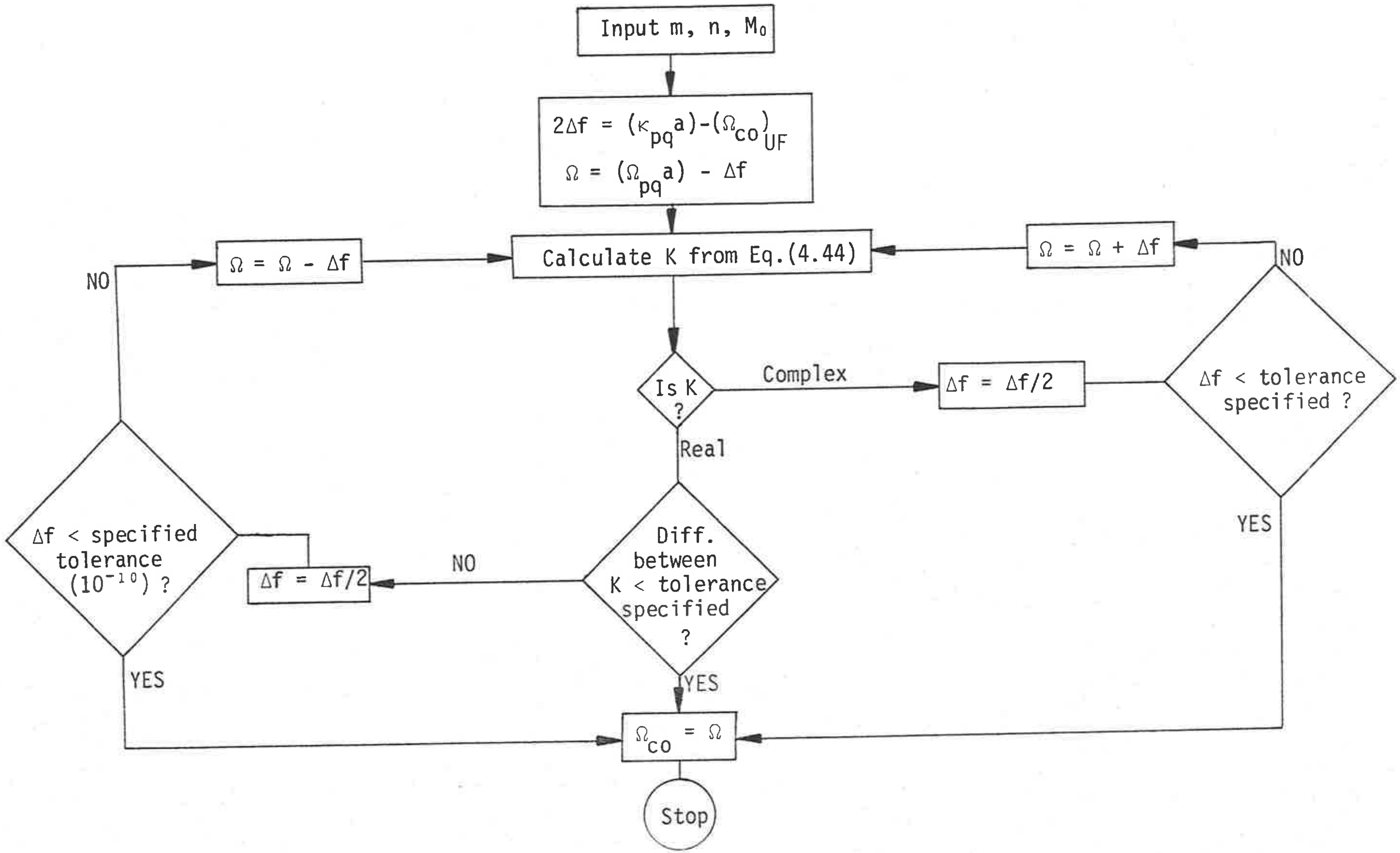

FIGURE 2.5 : SCHEME FOR THE CALCULATION OF MODAL CUT-OFF FREQUENCIES

2.7 Effect of Shear Flow

The effect of shear flow on acoustic wave propagation in an annular duct has been discussed by Mungur and Plumblee (1969), Mikhail and Abdelhamid (1973a,b) and Shankar (1972a,b) for the case of a mean-velocity profile made up from a thin boundary layer and a uniform core flow. Here, the effects of shear, with a velocity profile given by equation (2.42), on phase speed, acoustic pressure and radial velocity profiles, and modal cut-off frequencies have been investigated.

2.7.1 Dispersion Curves

Typical dispersion curves (K_x v. Ω), derived from real numerical solutions for $K(K_x = \Omega K)$, those for the (0,0), (2,3) and (5,4) modes, are shown in Figure 2.6 for M_0 = 0, 0.2 and 0.6, together with curves for no flow and uniform flow with $M = M_0$. The curves for shear flow lie between those for no flow and uniform flow. The effect of flow is to translate the dispersion curve towards lower frequencies and lower values of the axial wave number component. The shape of the curve for the fully-developed shear flow is similar to that of the no-flow and uniform flow curves, but the curve is shifted less than the uniform-flow curve. Compared with the no-flow case, the effect of flow is therefore, in particular, to reduce the cut-off frequency and to displace the axial wave number at which it occurs to a negative value. Shear-flow cut-off frequencies are higher than the uniform-flow values.

For $K_x = 0$ i.e. $K = 0$, equation (2.24) reduces to

$$\frac{d^2P}{dR^2} + \frac{1}{R}\frac{dP}{dR} + [\Omega^2 - \frac{m^2}{R^2}]P = 0 \qquad (2.49)$$

i.e.

$$\frac{d^2P}{d(\Omega R)^2} + \frac{1}{(\Omega R)}\frac{dP}{d(R\Omega)} + [1 - \frac{m^2}{(\Omega R)^2}]P = 0 \ , \qquad (2.50)$$

whose solution is given by $J_m(\Omega R) = 0$; (2.51)

and the boundary condition to be satisfied is

$$J'_m(\Omega R) = 0 \ . \qquad (2.52)$$

This is the same as for the no-flow and uniform-flow cases. Therefore, for a given mode, the shear-flow value of Ω corresponding to $K_x = 0$ is the same as that for no flow and uniform flow, and is independent of both flow Mach number and its radial distribution. The dispersion curves for the three cases therefore pass through the same point at $K_x = 0$, as shown in Figure 2.6.

In the case of the plane wave (0,0) mode, K for uniform flow ($M = M_o$) is independent of frequency and equal to $1/(1 \pm M)$. Shear flow not only increases the value of K but also makes it frequency dependent, i.e. even the plane wave becomes dispersive (see Table 2.2).

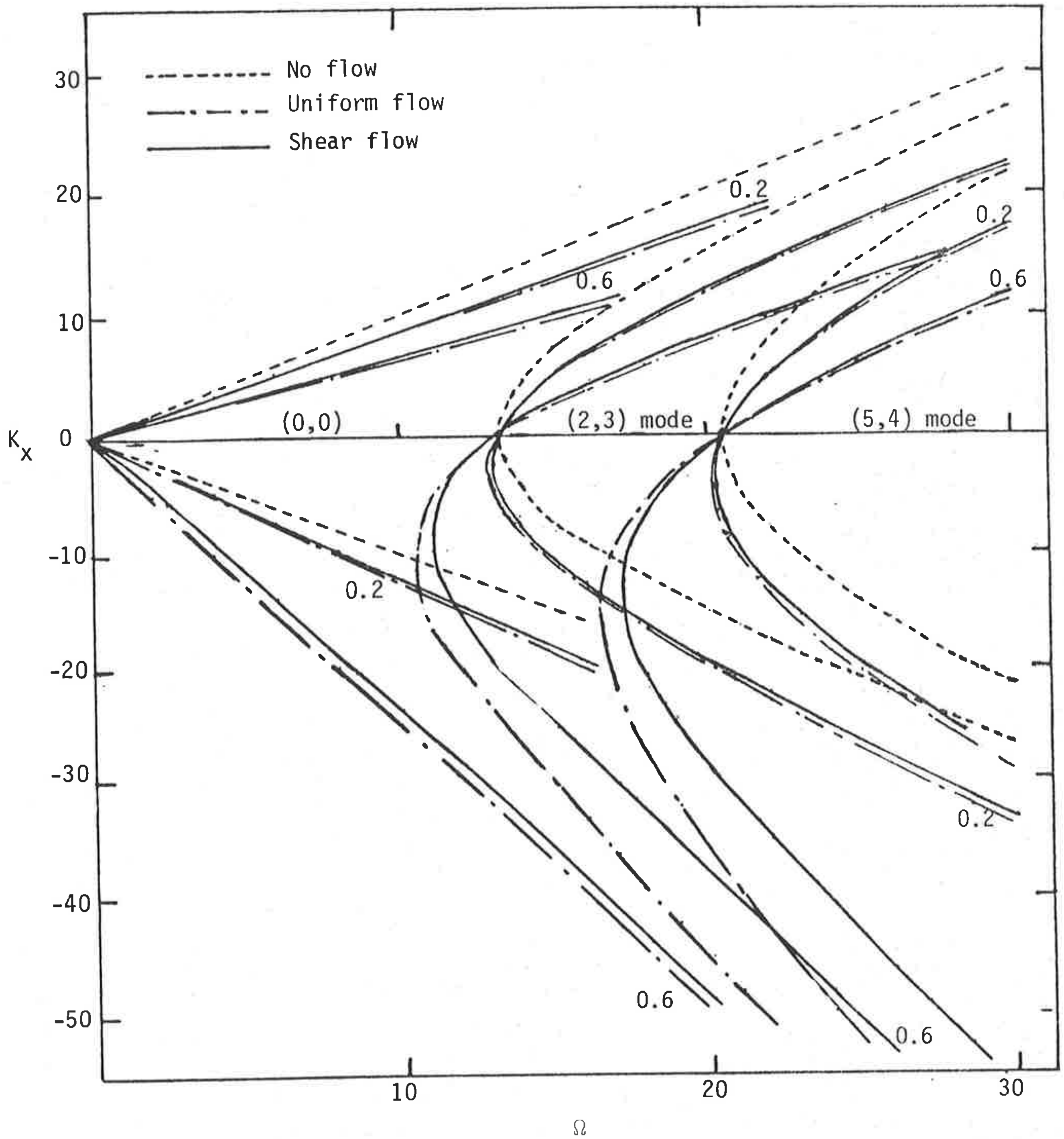

FIGURE 2.6 : DISPERSION CURVES

Table 2.2

Numerical solutions for K : (0,0) Mode; M_0 = 0.2, Downstream Propagation

Ω	$K = 1/(c_\phi/c)$		
	Uniform flow	Sheared flow	U.F. Approx. for shear flow
≈ 0	0.83333	0.85334	0.84625
1	"	"	"
2	"	0.85339	"
4	"	0.85373	"
6	"	0.85423	"
8	"	0.85493	"
10	"	0.85579	"
12	"	0.85678	"
14	"	0.85786	"
16	"	0.85898	"
18	"	0.86010	"
20	"	0.86121	"
22	"	0.86227	"
24	"	0.86328	"
26	"	0.86424	"
28	"	0.86515	"
30	"	0.86602	"

2.7.2 Modal cut-off frequency

Cut-off frequencies have been calculated for twelve values of M_0 in the range 0.05 to 0.6, for modes with $0 \leqslant m \leqslant 5$ and $0 \leqslant n \leqslant 5$; these values are shown in table 2.3. They are lower than the corresponding no-flow values, but somewhat higher than those for uniform flow with $M = M_0$ (in which case the cut-off frequencies are reduced from the no-flow values by a factor $\sqrt{1-M^2{}_0}$). These effects are illustrated for typical cases in Figure 2.7. In general, the progression of cut-off frequencies follows that for no flow. However, it is interesting to note that in two cases, those of the (4,0) and (1,1) modes, the order of progression is reversed.

The numerical scheme for the calculation of cut-off frequency described in section 2.6 takes a very large amount of computing time, as trial values have to be selected for both frequency Ω and K; and the computing time increases with the mode order and the Mach number of flow. However, as illustrated in Figure 2.8 by the values for (0,1), (2,3) and (5,4) modes, the ratio of cut-off frequency to the no-flow value is very nearly a unique function of Mach number (although there is a suggestion that the ratio increases slightly with increasing mode order at a given Mach number). In fact, as found by Mikhail and Abdelhamid (9,10), the cut-off frequency can be closely approximated by that in uniform flow with an effective Mach number $M_e = AM_0$ obtained by averaging over the shear flow Mach number profile, where

$$A = \frac{1}{M_0}\int_0^1 M(R)\, dR. \qquad (2.53)$$

(<u>Note</u> that M_e is not a mass-weighted average Mach number over the pipe cross section.)

Table 2.3

(a) Ω_{co} for M_o = 0.05

n \ m	0	1	2	3	4	5
0		1.83979	3.05157	4.19780	5.31352	6.41104
1	3.82782	5.32858	6.69953	8.00755	9.27374	10.51038
2	7.00839	8.53400	9.95954	11.33480	12.66969	13.97411
3	10.16299	11.70600	13.15742	14.57168	15.94885	17.29681
4	13.30978	14.86358	16.33202	17.77210	19.17842	20.55712
5	16.45362	18.01553	19.49570	20.95432		
6	19.59569					

(b) Ω_{co} for M_o = 0.10

n \ m	0	1	2	3	4	5
0		1.83422	3.04327	4.18717	5.30078	6.39626
1	3.81679	5.31203	6.67922	7.98386	9.24688	10.48059
2	6.99025	8.50742	9.92888	11.30038	12.63173	13.93278
3	10.13943	11.66958	13.11676	14.52703	15.90041	17.24467
4	13.28264	14.82155	16.28148	17.71742	19.11979	20.49476
5	16.42443	17.96996	19.43535	20.88972		
6						

(c) Ω_{co} for M_0 = 0.15

n \ m	0	1	2	3	4	5
0		1.82482	3.02920	4.16907	5.27896	6.37092
1	3.79634	5.28411	6.64492	7.94378	9.20145	10.43005
2	6.95311	8.46256	9.8772	11.24221	12.56754	13.86286
3	10.08580	11.60811	13.04811	14.45160	15.81857	17.15672
4	13.21257	14.74356	16.19616	17.62508	19.02076	20.38936
5	16.33794	17.87550	19.33346	20.78064		
6	19.46382					

(d) Ω_{co} for M_0 = 0.2

n \ m	0	1	2	3	4	5
0		1.81158	3.00930	4.14339	5.24795	6.33488
1	3.76744	5.24461	6.59636	7.88703	9.13706	10.35841
2	6.90059	8.39911	9.80387	11.15987	12.47665	13.76373
3	10.00993	11.52114	12.95096	14.34485	15.70269	17.03204
4	13.11343	14.63321	16.07541	17.49439	18.88056	20.23989
5	16.21555	17.74183	19.18925	20.62625		
6	19.31819					

(e) Ω_{co} for $M_o = 0.25$

n \ m	0	1	2	3	4	5
0		1.79446	2.98348	4.11002	5.20758	6.28795
1	3.72992	5.19330	6.53327	7.81325	9.05333	10.26529
2	6.83236	8.31666	9.70868	11.05284	12.35847	13.63495
3	9.91135	11.40812	12.82469	14.20608	15.55204	16.87008
4	12.98459	14.48979	15.91846	17.32450	18.69829	20.04571
5	16.05649	17.56809	19.00179	20.42554		
6	19.12891					

(f) Ω_{co} for $M_o = 0.3$

n \ m	0	1	2	3	4	5
0		1.77340	2.95164	4.06879	5.15765	6.22977
1	3.68348	5.12978	6.45513	7.72186	8.94958	10.14979
2	6.74789	8.21455	9.59076	10.92024	12.21203	13.47541
3	9.78924	11.26811	12.66826	14.03412	15.36535	16.66928
4	12.82497	14.31209	15.72398	17.11396	18.47239	19.80499
5	15.85939	17.35280	18.76950	20.17680		
6	18.89434					

(g) Ω_{co} for M_o = 0.35

n \ m	0	1	2	3	4	5
0		1.78436	2.91366	4.01953	5.09796	6.16015
1	3.62784	5.05364	6.36146	7.61228	8.82516	10.01127
2	6.64661	8.09211	9.44934	10.76118	12.03636	13.28381
3	9.64281	11.10017	12.48059	13.82783	15.14135	16.42821
4	12.63350	14.09891	15.49064	16.86134	18.20133	19.51622
5	15.62292	17.09447	18.49076	19.87831		
6	18.61288					

(h) Ω_{co} for M_o = 0.40

n \ m	0	1	2	3	4	5
0		1.71926	2.86942	3.96205	5.02821	6.07877
1	3.56265	4.96438	6.25163	7.48379	8.67926	9.84885
2	6.52786	7.94850	9.28343	10.57456	11.83023	13.05913
3	9.47101	10.90311	12.26037	13.58572	14.87846	16.14540
4	12.40880	13.84871	15.21676	16.56481	17.88314	19.17720
5	15.34537	16.79125	18.16355	19.52791		
6	18.28248					

(i) Ω_{co} for M_o = 0.45

n \ m	0	1	2	3	4	5
0		1.68601	2.81873	3.89610	4.94811	5.98524
1	3.48745	4.86138	6.12489	7.33550	8.51087	9.66139
2	6.39077	7.78267	9.09183	10.35902	11.59215	12.79956
3	9.27258	10.67548	12.00594	13.30600	14.57470	15.81856
4	12.14918	13.55961	14.90026	16.22214	17.51542	18.78530
5	15.02462	16.44081	17.78537	19.12290		
6	17.90060					

(j) Ω_{co} for M_o = 0.5

n \ m	0	1	2	3	4	5
0		1.64849	2.76139	3.82139	4.85729	5.87910
1	3.40173	4.74390	5.98032	7.16634	8.31878	9.44754
2	6.23433	7.59337	8.87308	10.11293	11.32031	12.50316
3	9.04600	10.41551	11.71533	12.98647	14.22771	15.44533
4	11.85263	13.22932	14.53868	15.83059	17.09524	18.33766
5	14.65813	16.04036	17.35318	18.66004		
6	17.46417					

(k) Ω_{co} for M_0 = 0.55

n \ m	0	1	2	3	4	5
0		1.60657	2.69714	3.73755	4.75525	5.75978
1	3.30485	4.61106	5.81682	6.97504	8.10156	9.20571
2	6.05732	7.37910	8.62544	9.83432	11.01254	12.16764
3	8.78944	10.12106	11.38616	12.62452	13.83464	15.02247
4	11.51667	12.85510	14.12894	15.38690	16.61909	17.83022
5	14.24282	15.58652	16.86333	18.13541		
6	16.06567					

(l) Ω_{co} for M_0 = 0.6

n \ m	0	1	2	3	4	5
0		1.56004	2.62564	3.64412	4.64143	5.62657
1	3.18513	4.46179	5.63309	6.76008	7.85748	8.93404
2	5.85364	7.13806	8.34681	9.52083	10.66625	11.79008
3	8.48856	9.78960	11.01554	12.21699	13.39206	14.54632
4	10.99208	12.43364	13.66742	14.88712	16.08275	17.25869
5	13.58829	15.07522	16.31142	17.54429		
6	16.39769					

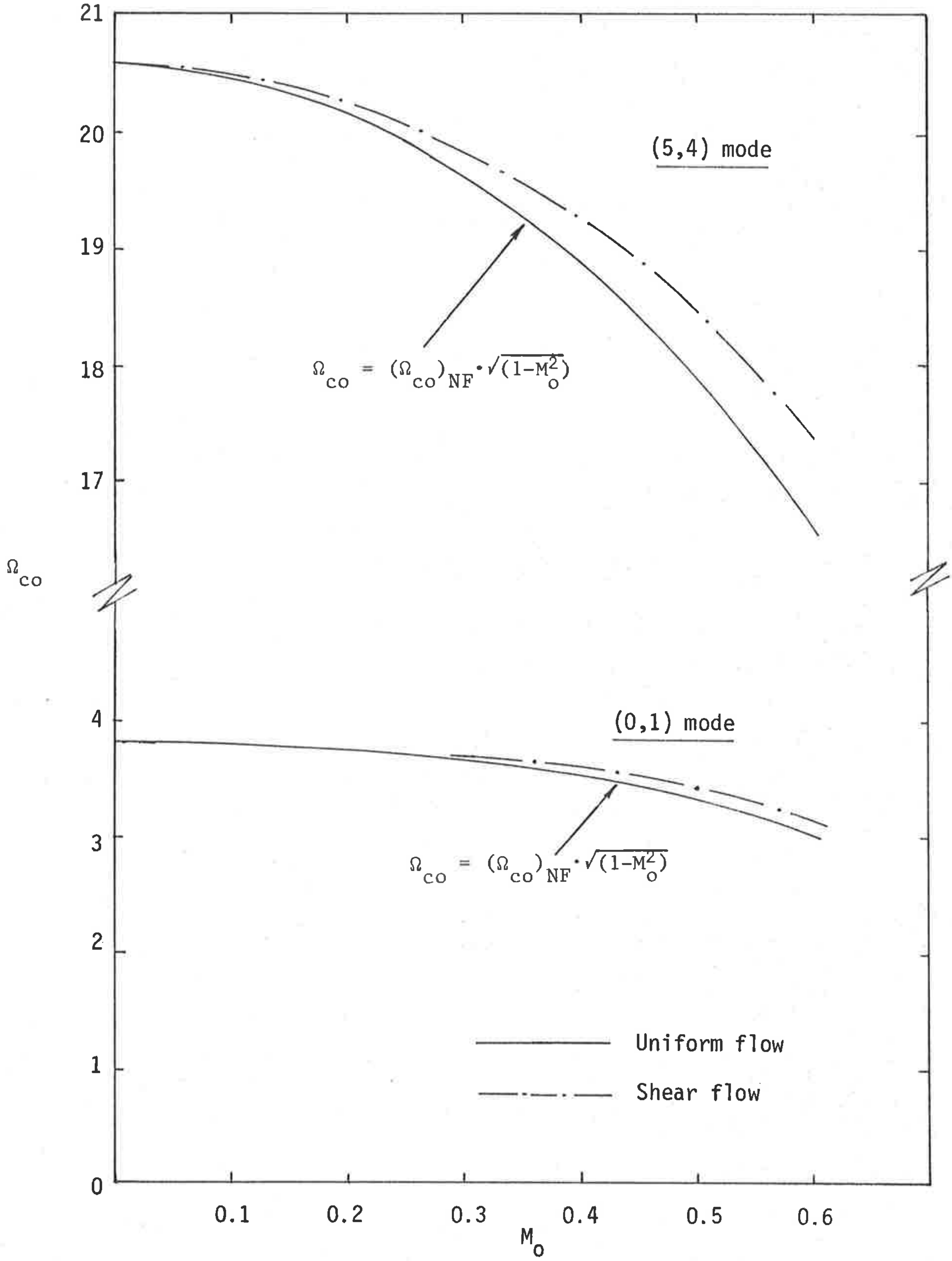

FIGURE 2.7 : VARIATION OF CUT-OFF FREQUENCY WITH MACH NUMBER FOR UNIFORM FLOW AND FULLY-DEVELOPED PIPE FLOW

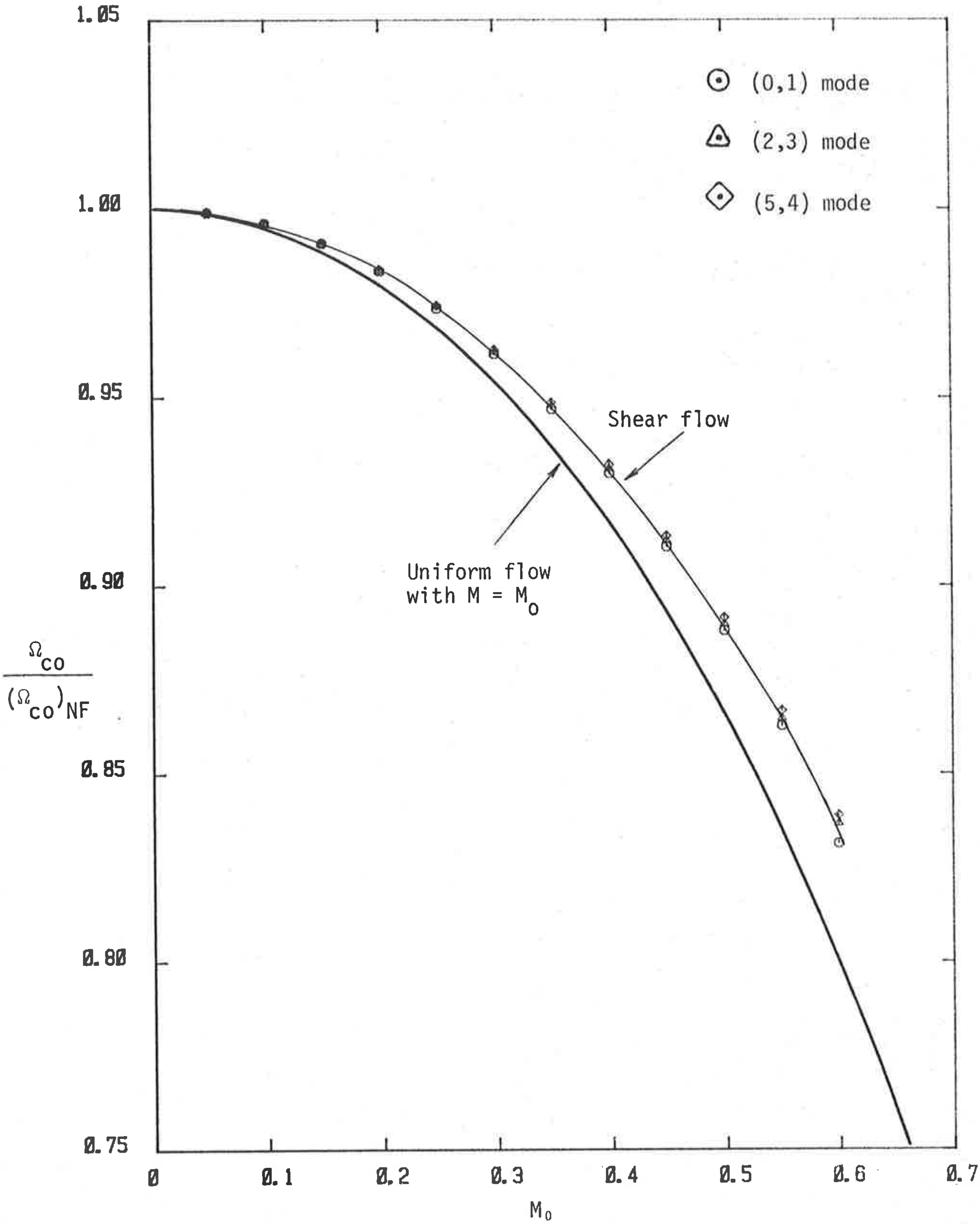

FIGURE 2.8 : VARIATION OF MODAL CUT-OFF FREQUENCY WITH MACH NUMBER

Values of A can readily be obtained from the velocity profiles by analytical integration for $Y^+ \geq 33.2$, together with numerical integral (Simpson's Rule) for the range $0 \leq Y^+ \leq 33.2$. As an example, values of M_e and cut-off frequency for the (1,0) and (2,3) modes obtained in this way and the corresponding cut-off frequency obtained by the numerical procedure are given in in Table 2.4. It can be seen that there is very close agreement between the two values of cut-off frequency at all Mach numbers. In general, the difference between them increases with Mach number and decreases with the mode order.

Similarly, a good approximation to the value of K can be obtained by treating the shear flow as uniform flow with effective Mach number $M_e = AM_0$, as shown in Table 2.1, for real as well as complex K. The error in the imaginary part is much lower than in the real part; for the (2,n) modes, the greatest error is 2.2% for the (2,0) mode. In the case of (0,0) mode the uniform flow approximation gives a K value independent of frequency but this is still a fairly good representation of the frequency-dependent shear flow value provided the frequency parameter Ω is not too high.

2.7.3 Acoustic Pressure profiles

Mungur and Plumblee (1969), Pridmore-Brown (1954), and Mikhail and Abdelhamid (1973a,b) have considered the effect of shear flow on acoustic pressure distribution, but their studies are confined to two-dimensional or annular ducts.

The general effect of shear flow on sound waves is to refract waves propagating downstream towards the wall and waves propagating upstream towards the pipe centre-line. The extent of the refraction which occurs depends on both flow Mach number and frequency.

Table 2.4

Cut-off frequencies for (1,0) and (2,3) mode

M_o	$A = M_e/M_o$ (Equ. 2.53)	M_e	Mode (1,0)			Mode (2,3)		
			Ω_{co}	Ω_{co} from UF approx.	% diff.	Ω_{co}	Ω_{co} from UF approx.	% diff.
0.05	0.89566	0.04478	1.83979	1.83933	-0.0249	13.15742	13.15716	-0.0020
0.10	0.90254	0.09025	1.83422	1.83366	-0.0301	13.11676	13.11662	-0.0010
0.15	0.90608	0.13591	1.82482	1.82409	-0.0393	13.04811	13.04816	+0.0004
0.20	0.90842	0.18168	1.81158	1.81054	-0.0566	12.95096	12.95117	+0.0016
0.25	0.91015	0.22754	1.79446	1.79288	-0.0855	12.82469	12.82490	+0.0016
0.30	0.91151	0.27345	1.77340	1.77100	-0.1303	12.66826	12.66838	+0.0010
0.35	0.91262	0.31942	1.74836	1.74473	-0.1972	12.48059	12.48043	-0.0013
0.40	0.91356	0.36542	1.71926	1.71385	-0.2940	12.26037	12.25952	-0.0069
0.45	0.91437	0.41147	1.68601	1.67810	-0.4297	12.00594	12.00380	-0.0178
0.50	0.91509	0.45754	1.64849	1.63715	-0.6158	11.71533	11.71092	-0.0376
0.55	0.91572	0.50365	1.60657	1.59061	-0.8666	11.38616	11.37802	-0.0715
0.60	0.91629	0.54977	1.56004	1.53796	-1.1991	11.01554	11.00139	-0.1285

-52-

For the plane wave mode, shear flow changes the uniform or no-flow pressure distribution to the distributions shown in Figures 2.9, 2.10 and 2.11, with the pressure at the wall becoming higher than at the centre for downstream propagation and lower for upstream propagation. At a given Mach number, the departure from the uniform-flow or no-flow distribution increases with sound frequency (Figures 2.9 and 2.10). Mode shapes for upstream propagation are more strongly affected by increases in Ω than those for downstream propagation. Figure 2.11, for downstream propagation, shows that for a given frequency the refraction effect becomes greater as Mach number is increased.

The influence of Mach number on the extent of refraction, in downstream propagation, for $m = 0$ modes with nodal circles is shown by Figures 2.12 and 2.13 for the (0,1) and (0,3) modes respectively. The indication is that the greater the number of nodal circles, the less the pressure distribution changes from the no-flow distribution.

For asymmetric acoustic modes ($m \geqslant 1$), the effect of shear flow is strongly dependent on Ω. At or near the modal cut-off frequency the mode shape is almost unaffected by the shear flow, but the effect of the shear flow increases with Ω and the Mach number as shown in Figure 2.14(a) and Figure 2.14(b) for the (2,3) mode. (It appears that, in general, the effect increases with the difference between Ω and the modal cut-off frequency, Ω_{co}). At high Mach numbers, the effect becomes very large, and the acoustic pressure amplitude away from the wall becomes much higher than the value at the wall (see Figures 2.14(a), (b)).

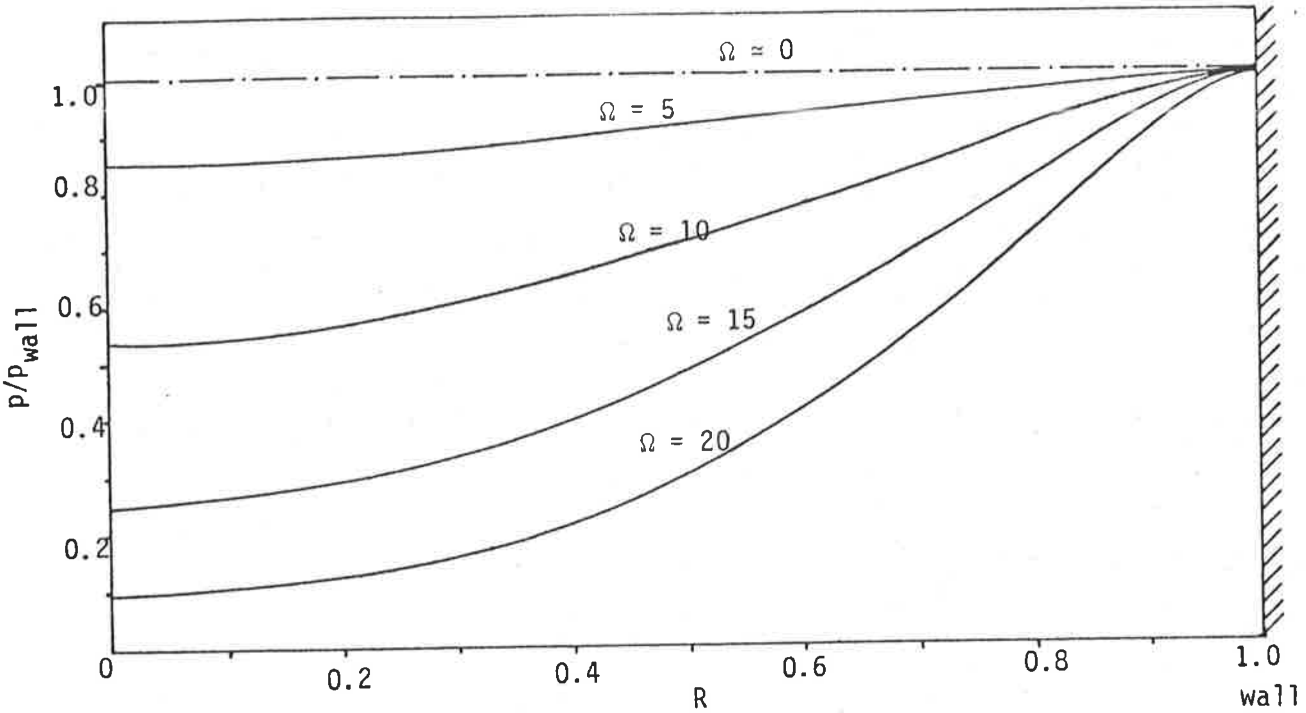

FIGURE 2.9 : ACOUSTIC PRESSURE PROFILES, (0,0) MODE, $M_o = 0.2$; DOWNSTREAM PROPAGATION

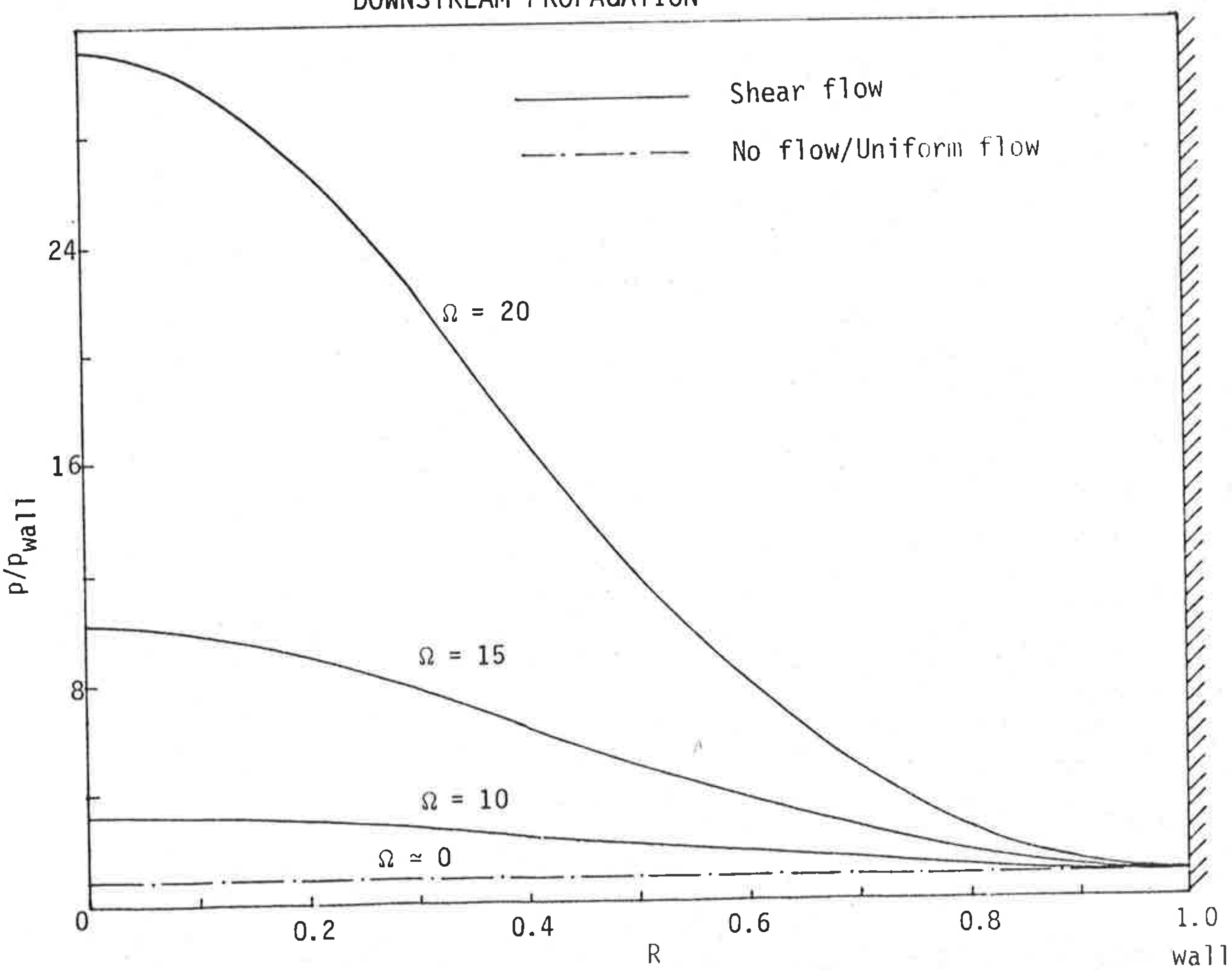

FIGURE 2.10 : ACOUSTIC PRESSURE PROFILES, (0,0) MODE, $M_o = 0.2$ UPSTREAM PROPAGATION

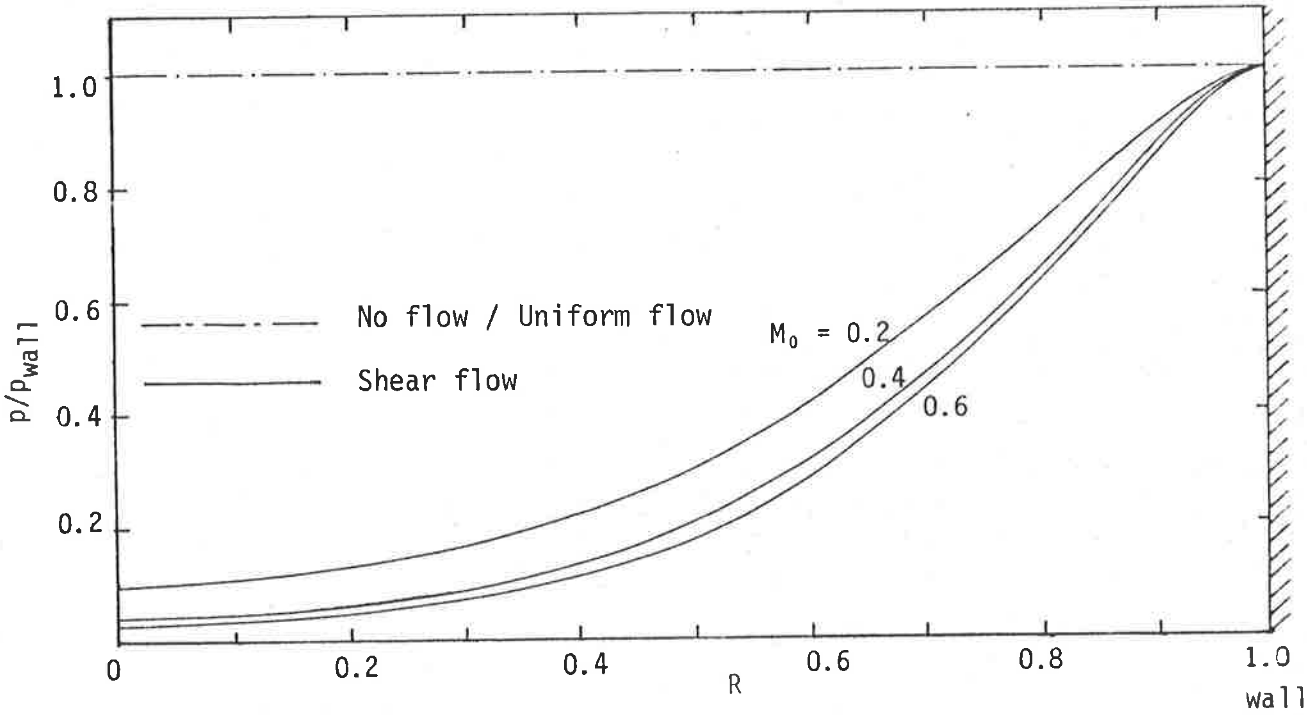

FIGURE 2.11 : ACOUSTIC PRESSURE PROFILES, (0,0) MODE, Ω = 20; DOWNSTREAM PROPAGATION

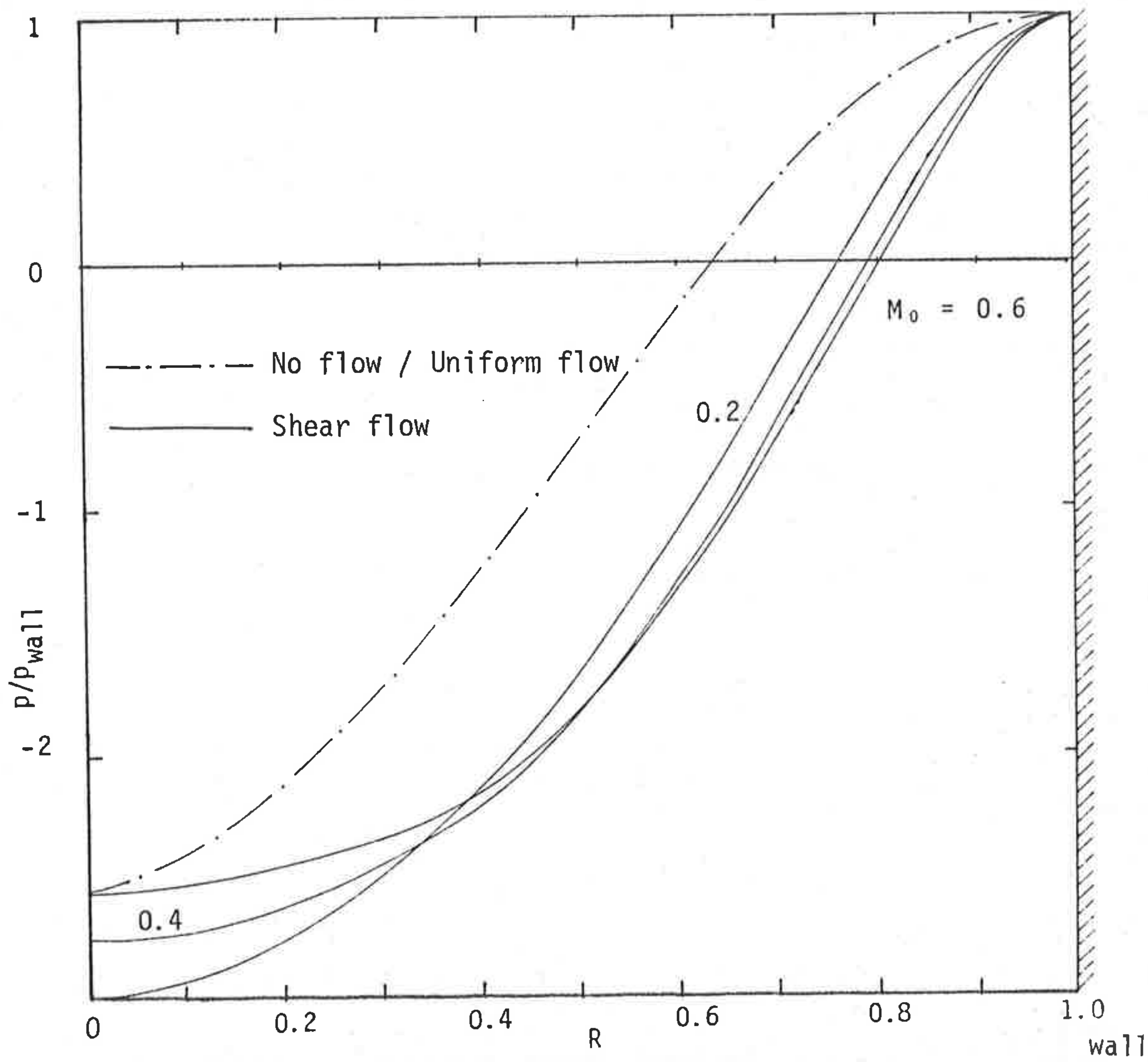

FIGURE 2.12 : ACOUSTIC PRESSURE PROFILES, (0,1) MODE, Ω = 20; DOWNSTREAM PROPAGATION

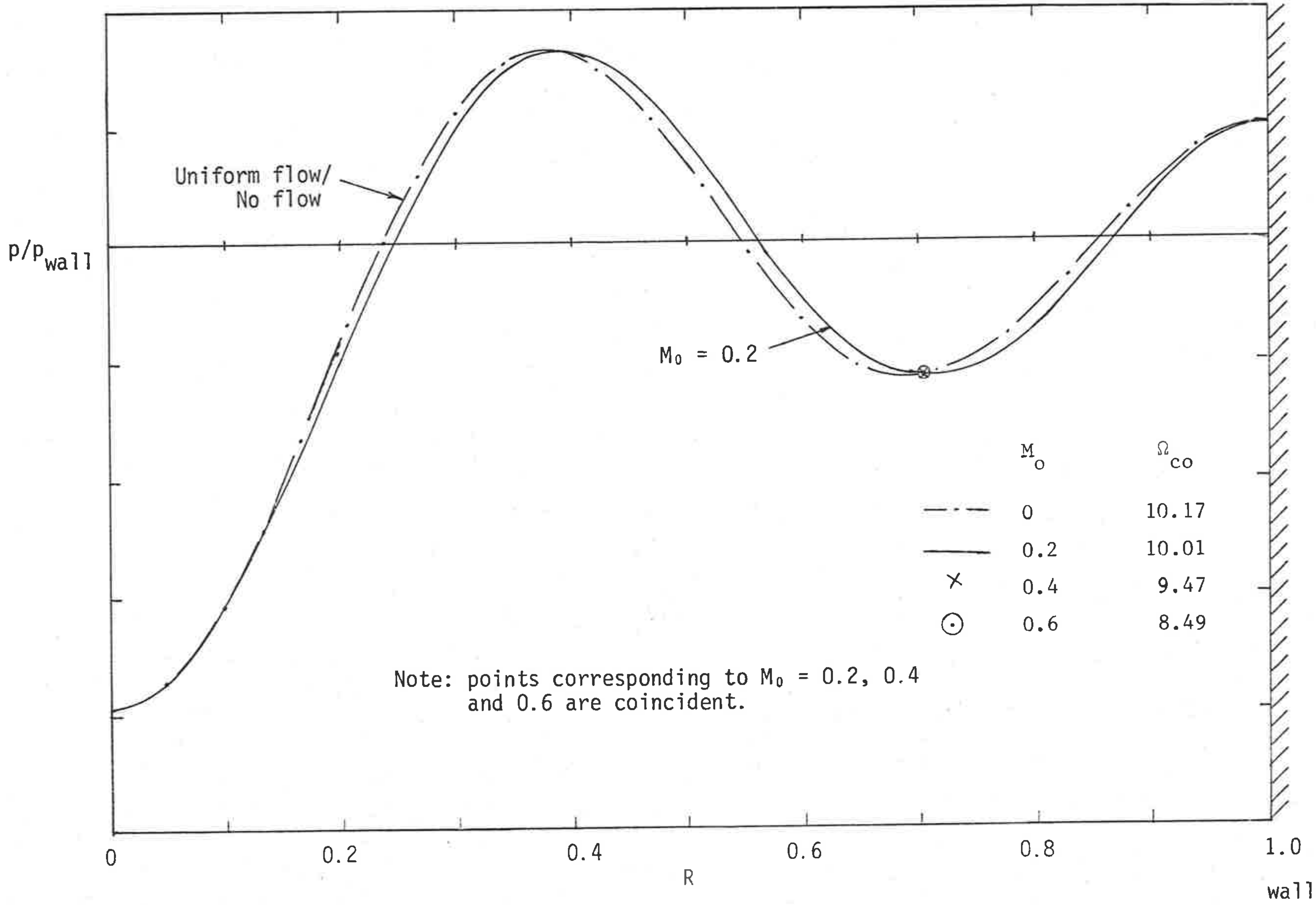

FIGURE 2.13 : ACOUSTIC PRESSURE PROFILES, (0,3) MODE, Ω = 20; DOWNSTREAM PROPAGATION

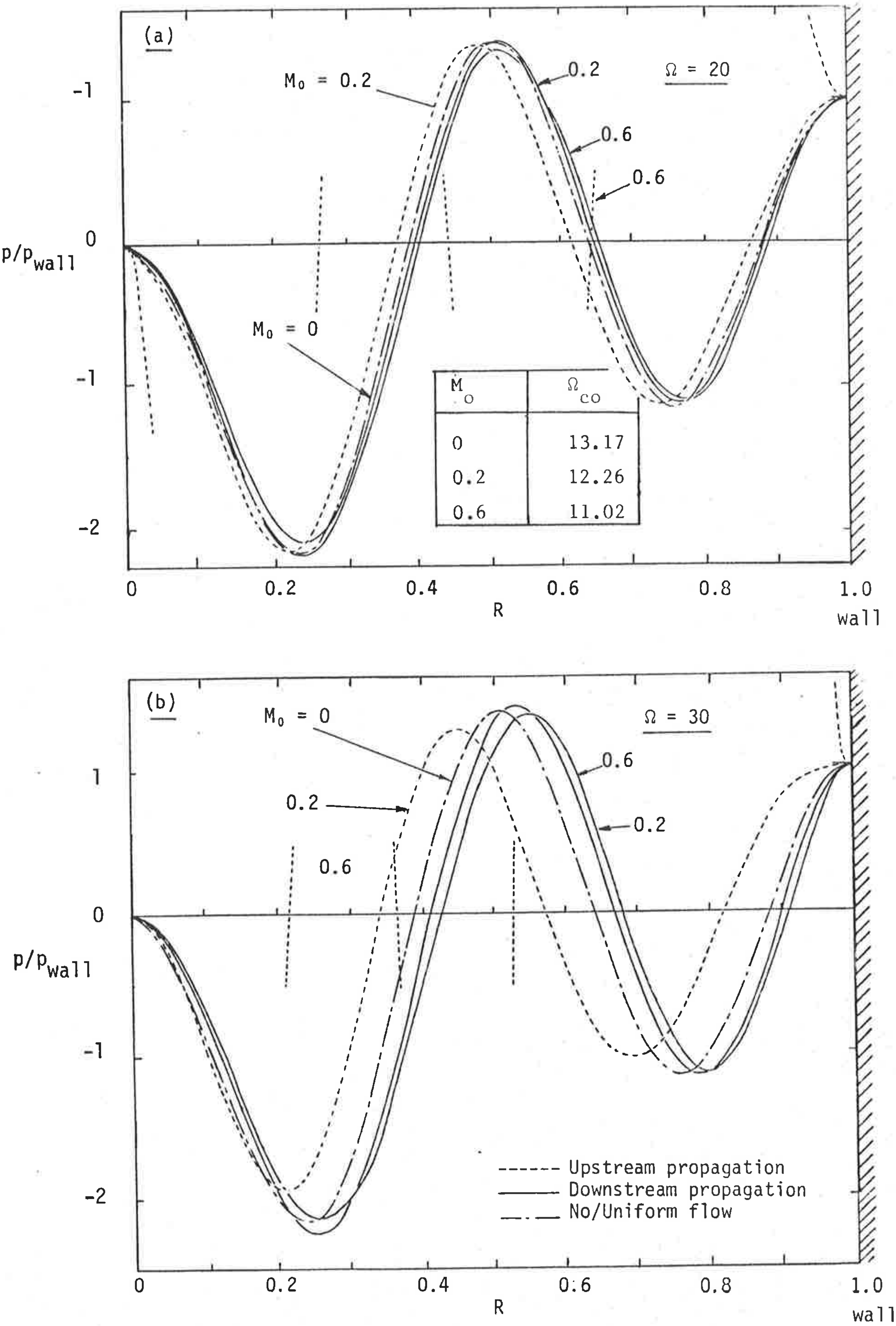

FIGURE 2.14 : ACOUSTIC PRESSURE PROFILES, (2,3) MODE

As discussed earlier, when Ω is lower than the modal cut-off frequency, K is complex. In such a situation the acoustic pressure distribution across the duct will have a non-zero imaginary part. The pressure profile for the (2,7) mode (which has a cut-off frequency of $\Omega_{co} = 25.40$), at $M_0 = 0.2$ and $\Omega = 20$, is shown in Figure 2.15. The total pressure amplitude at any point in the duct will be given by the modulus of the resultant complex quantity. It is interesting to note that imaginary pressure profile also satisfies the criterion that the number of pressure sign changes equals the number of nodal circles.

2.7.4 Radial Velocity Profiles

The relation between the acoustic pressure profiles and the profiles of the radial component of particle velocity is given by equation (2.21). The radial velocity distribution will therefore be subject to refraction effects similar to those affecting the pressure.

For downstream plane wave propagation, the radial velocity increases slowly from zero at the centre to a maximum value at about 80-85% of the pipe radius and then decreases to zero at the wall. The effect of shear flow is to displace the maximum value towards the wall and to increase its magnitudes to an extent which increases with Mach number (Figure 2.16). As in the case of acoustic pressure, frequency has a strong effect on the distribution (Figure 2.17), the displacement of the maximum towards the wall and its magnitude both increasing with increasing Ω. For upstream propagation, similar effects are observed but the radial velocities are generally larger, as can be seen in Figures 2.16 and 2.17.

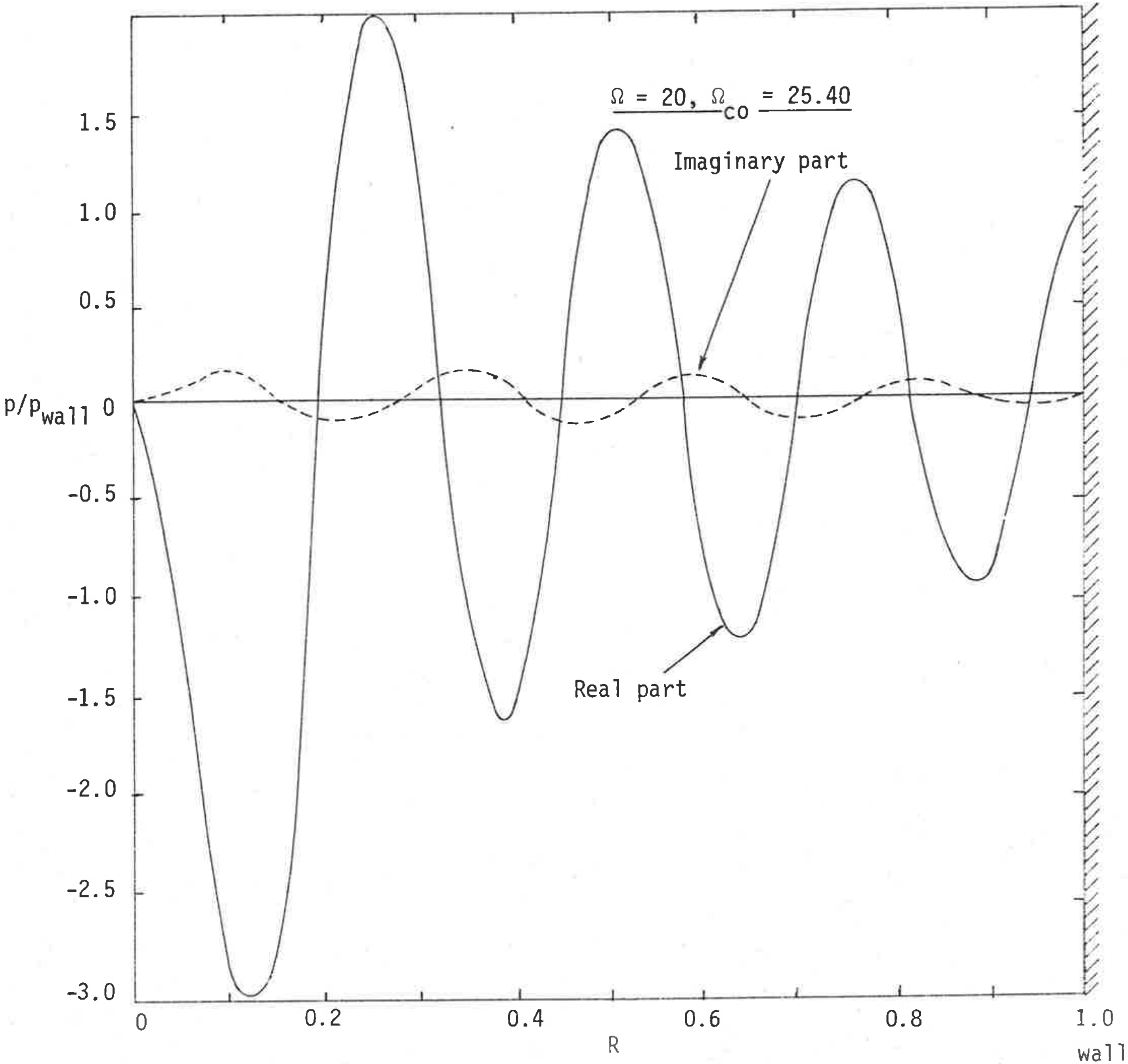

FIGURE 2.15 : ACOUSTIC PRESSURE PROFILES, (2,7) MODE, M_o = 0.2

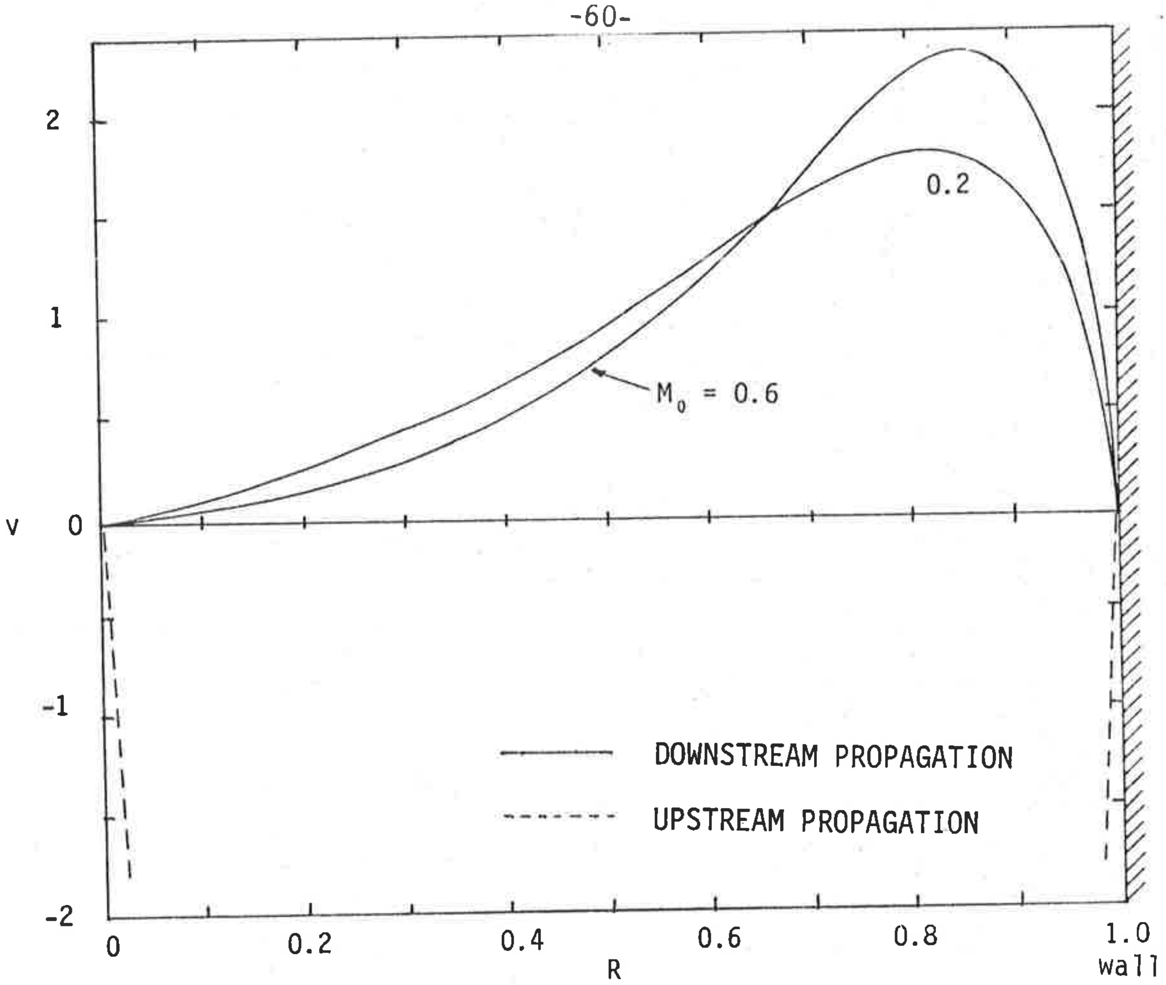

FIGURE 2.16 : RADIAL VELOCITY PROFILES, (0,0) MODE, Ω = 20

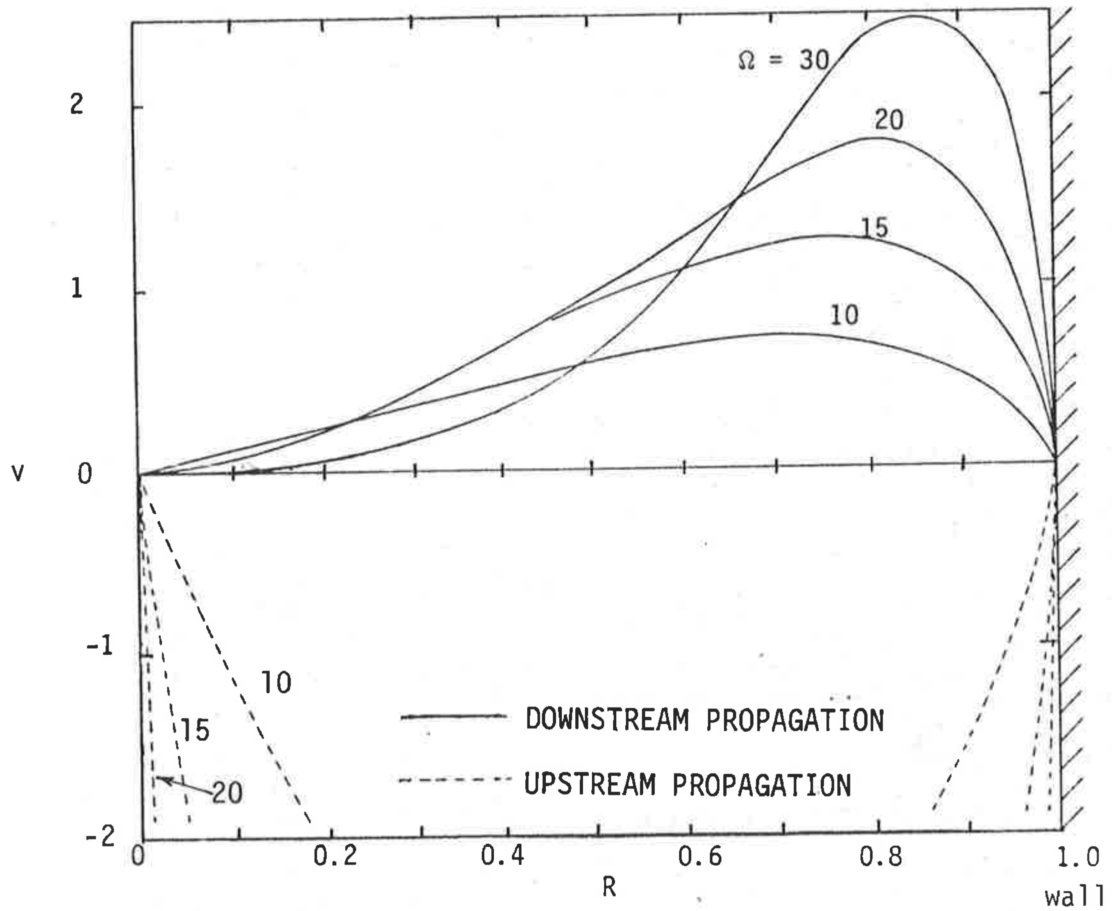

FIGURE 2.17 : RADIAL VELOCITY PROFILES, (0,0) MODE, M_0 = 0.2

The behaviour of the (0,1) symmetrical mode, with one nodal circle (Figure 2.18), is similar to that of the plane wave; but, as for the acoustic pressure distribution, the effect of shear becomes much less marked for the symmetrical modes with more than one nodal circle, as illustrated by Figure 2.19 for the (0,3) mode.

The effect of shear on asymmetrical modes is again very similar to that on the acoustic pressure, and increases with $(\Omega - \Omega_{co})$. For downstream propagation, the velocity distribution is displaced towards the wall to an extent which increases with both Mach number and Ω (as shown in Figure 2.20). For upstream propagation the effect is to displace the radial velocity towards the centre and the Mach number has a big influence on the velocity amplitudes as shown in Figures 2.20(a) and 2.20(b).

2.7.5 Axial Particle velocity

In the wave described by equation (2.4) the relation between acoustic pressure and axial component u of the particle velocity is given by equation (2.14) as

$$\left(\frac{\partial}{\partial t} + U\frac{\partial}{\partial x}\right)u + v\frac{\partial U}{\partial r} = -\frac{1}{\rho_o}\frac{\partial p}{\partial x}. \qquad (2.54)$$

From equation (2.4)

$$\frac{\partial p}{\partial x} = ik_x p \quad , \qquad (2.55)$$

and substitution of this and equations (2.20) and (2.21) in equation (2.54) leads to

$$u = \left[K\frac{p}{\rho_o c} - \frac{1}{\rho_o \omega^2(1-MK)} \cdot \frac{\partial p}{\partial r} \cdot \frac{\partial U}{\partial r}\right]/(1-MK) \ . \qquad (2.56)$$

For a hard-walled pipe, equation (2.56) reduces exactly in the case of uniform flow and approximately in the case of shear flow (if the second term on the RHS is small) to

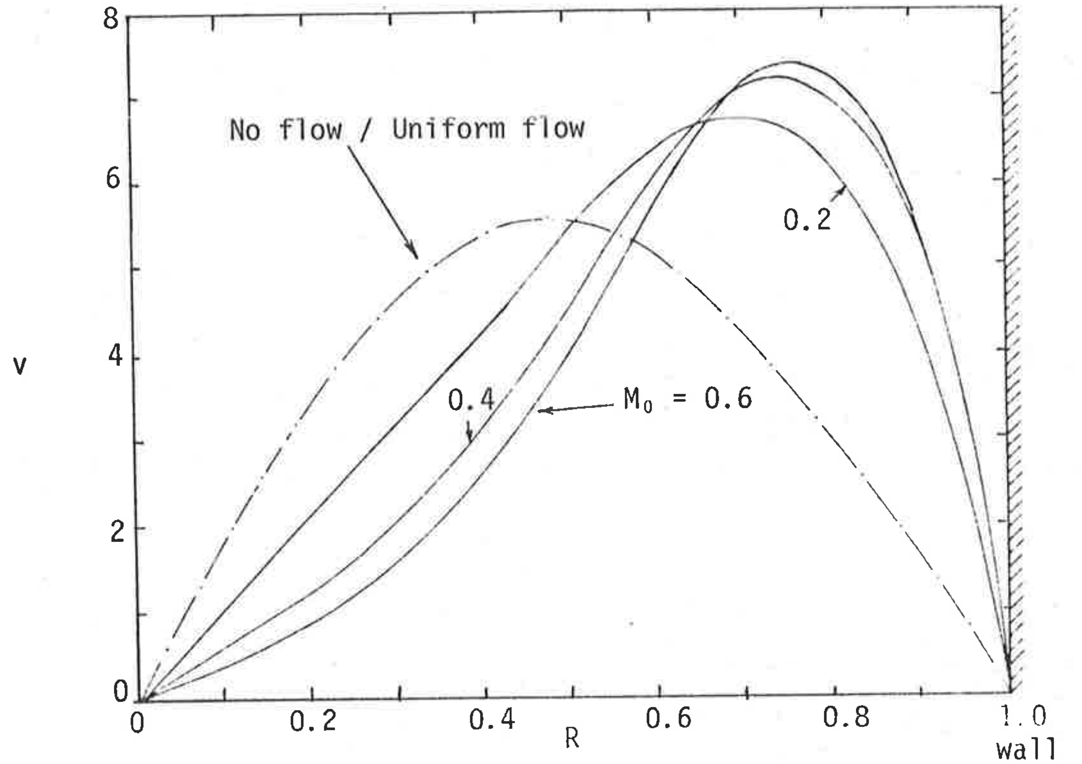

FIGURE 2.18 : RADIAL VELOCITY PROFILES, (0,1) MODE, Ω = 20; DOWNSTREAM PROPAGATION

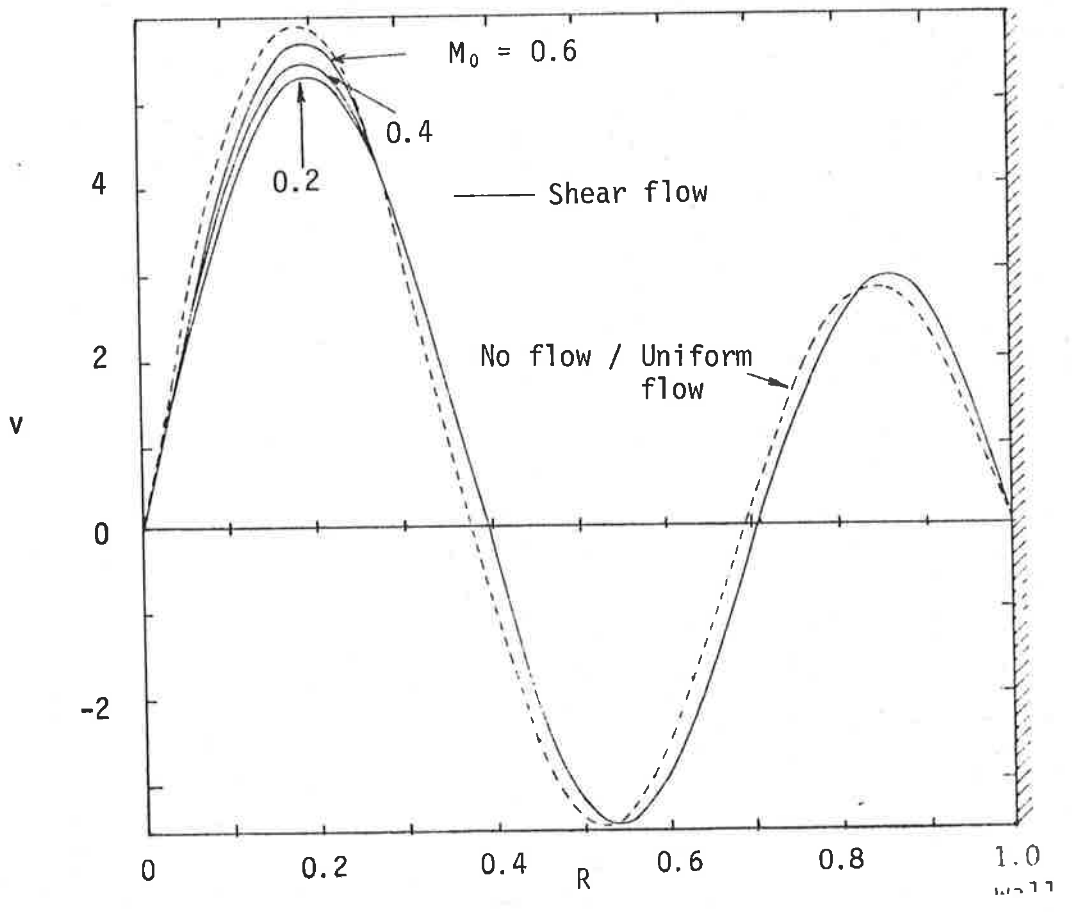

FIGURE 2.19 : RADIAL VELOCITY PROFILES, (0,3) MODE, Ω = 20; DOWNSTREAM PROPAGATION

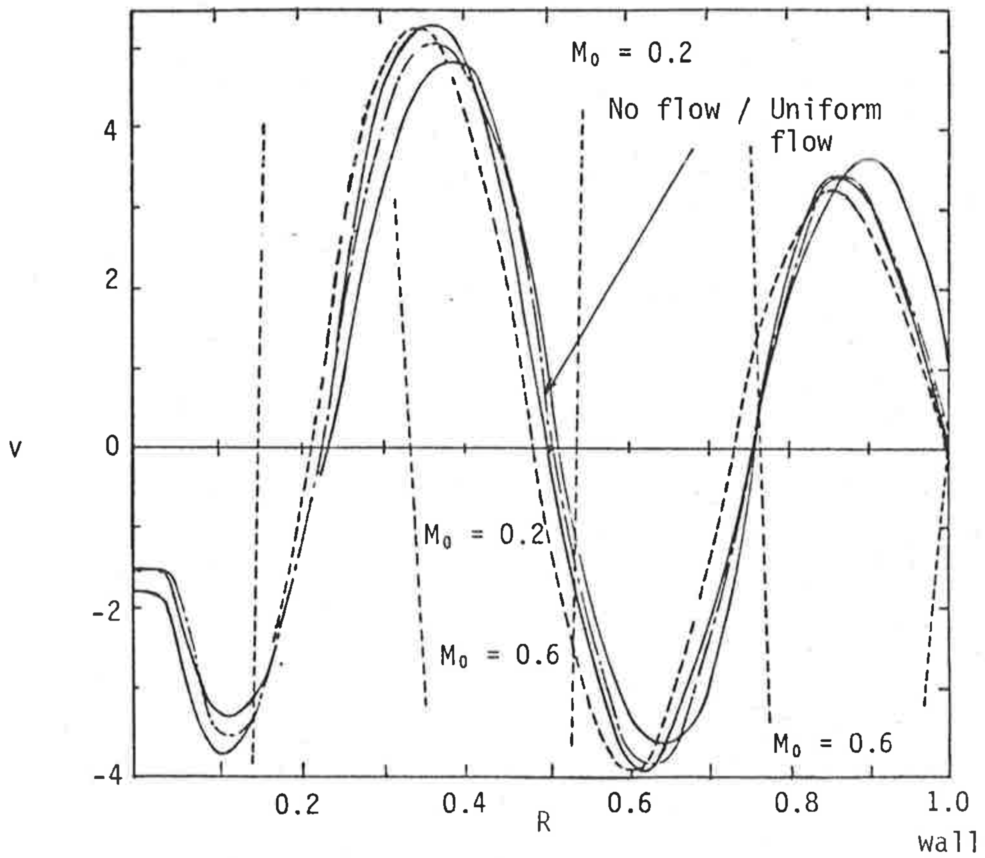

FIGURE 2.20a : RADIAL VELOCITY PROFILES, (2,3) MODE, Ω = 20

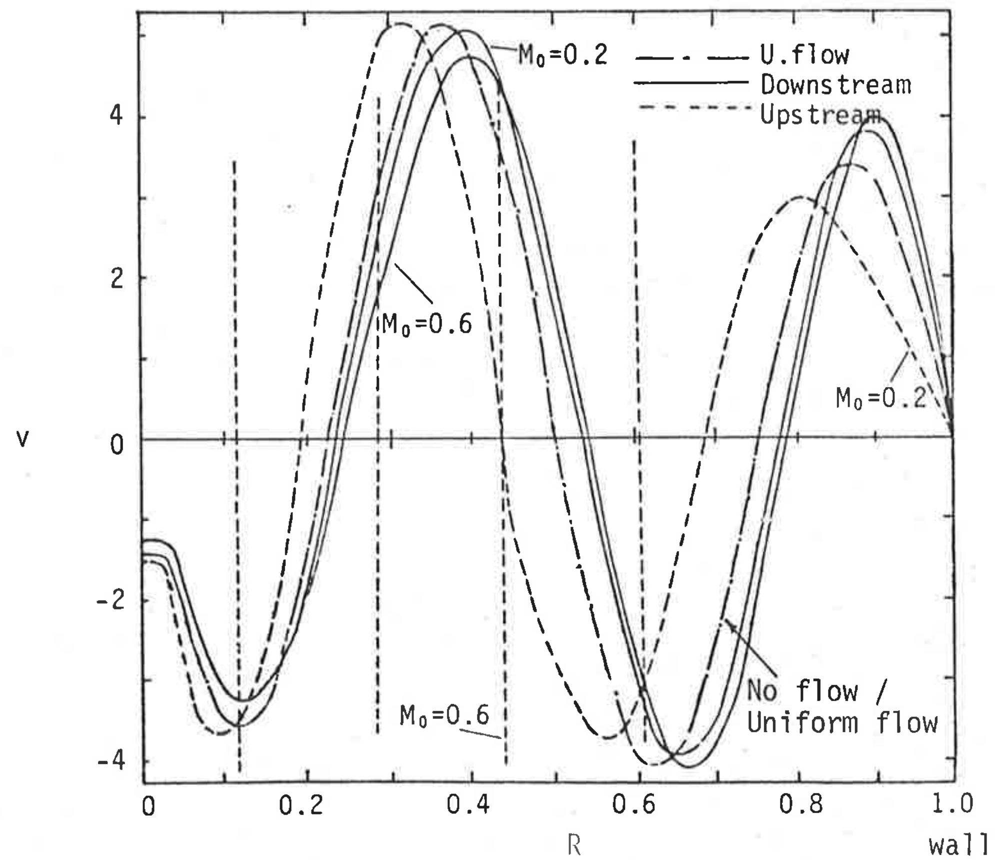

FIGURE 2.20b : RADIAL VELOCITY PROFILES (2,3) MODE, Ω = 30

$$u = \frac{p}{\rho_0(c_\phi - U)} \qquad (2.57)$$

(where c_ϕ is the phase velocity ω/k_x) in which case the axial particle velocity is proportional to the acoustic pressure. Hence the effect of shear flow on axial particle velocity will be similar to that on the acoustic pressure if the second term in equation (2.56) is small.

2.7.6 Phase Velocity

The phase velocity c_ϕ of an acoustic wave in the pipe is given by

$$c_\phi = \frac{\omega}{k_x}, \qquad (2.58)$$

and hence the phase Mach number M_ϕ is given by

$$M_\phi = \frac{c_\phi}{c} = \frac{\Omega}{K_x} = \frac{1}{K}. \qquad (2.59)$$

The dispersion relationship between K_x and Ω therefore also determines the variation of c_ϕ with frequency. At a given frequency, as can be seen from Figure 2.6, the effect of shear flow is to increase K_x above its uniform-flow value, thereby decreasing the phase velocity compared with the uniform-flow phase velocity for $K_x > 0$ and increasing it (in magnitude) for $K_x < 0$ (see Figure 2.21). In a uniform mean flow with axial velocity U and Mach number M, the no-flow phase velocity and phase Mach number are augmented by U and M respectively; in the case of shear flow they are augmented by some effective axial velocity less than the maximum axial velocity U_0 and some effective Mach number less than M_0.

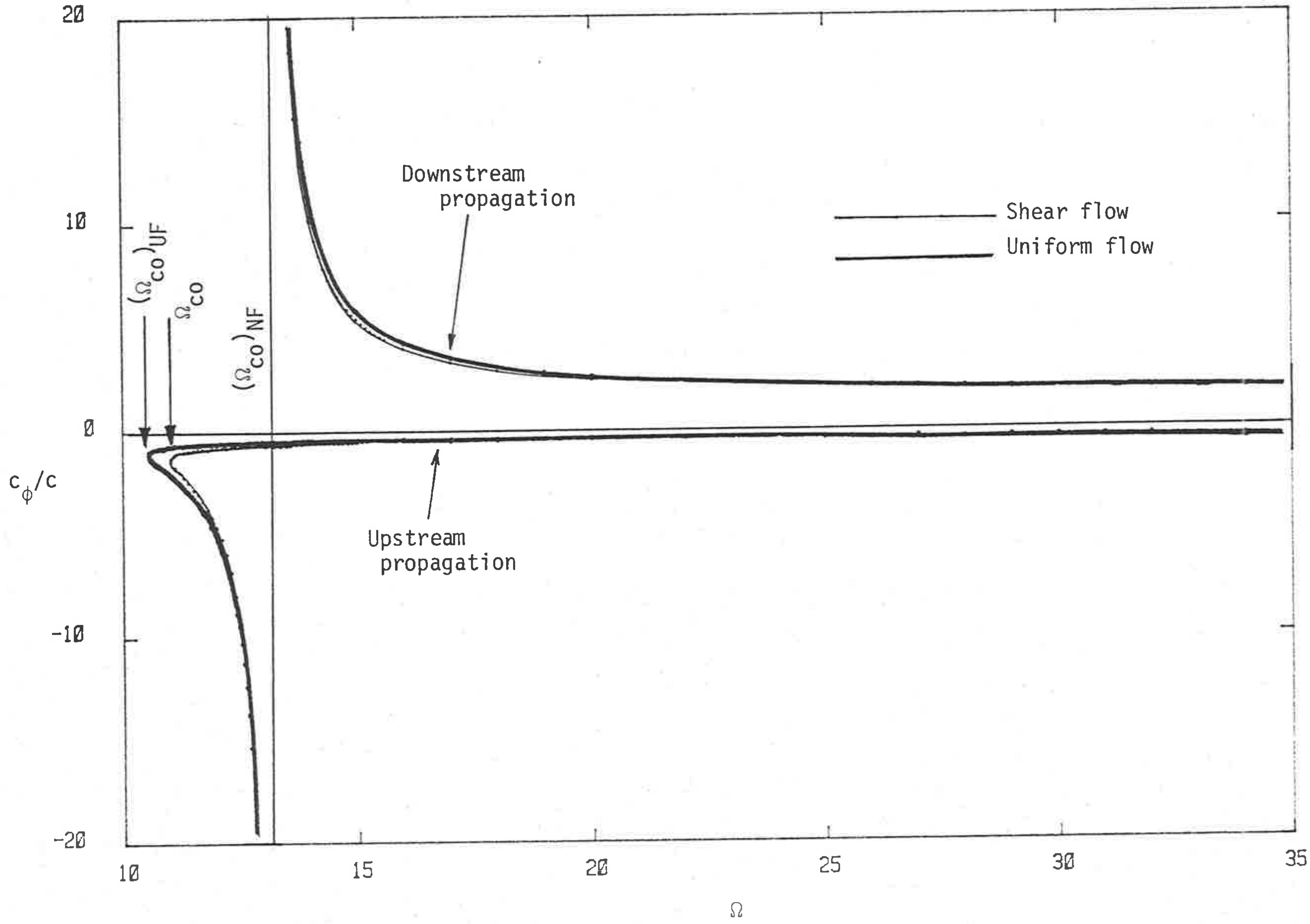

FIGURE 2.21 : PHASE SPEED OF A HIGHER ORDER MODE, (2,3) MODE AT M_o = 0.6

A measure to the extent to which the shear flow augments the no-flow phase velocity is given by the parameter $\Delta M_\phi/M_o$, where $\Delta M_\phi = (M_\phi - M_{\phi o})$ and M_ϕ and $M_{\phi o}$ are respectively the phase Mach numbers for the shear-flow and no-flow cases, at the same axial wave number. For the (m,n)th mode, it is given by

$$\Delta M_\phi/M_o = [(\Omega/K_x) \mp \sqrt{1 + (\kappa_{mn}\, a/K_x)^2}]/M_o, \qquad (2.60)$$

where - and + refer to downstream and upstream propagation. For uniform flow it has the value unity. For the shear flow its value is roughly the ratio of average flow Mach number to M_o i.e. A as given by equation (2.53), but its detailed variation with Ω depends on mode order, M_o and the direction of wave propagation - as illustrated in Figures 2.22-2.25 for plane wave, (0,n), (m,0) and (m,n) modes respectively. The effect of Mach number M_o on $\Delta M_\phi/M_o$ is greater for upstream than for downstream propagation, as shown by Figures 2.26-2.28 for the (0,1), (1,0) and (2,1) modes respectively.*

As $\Omega \to \Omega_{co}$, $\Delta M_\phi/M_o$ for the higher order acoustic modes appears to approach the same value for downstream and upstream propagation; but for the plane wave mode $\Delta M_\phi/M_o$ has different limiting values for downstream and upstream propagation as $\Omega \to 0$.

This difference in the limiting $\Delta M_\phi/M_o$ values is further illustrated in Figure 2.29, where $\Delta\Omega$, the difference in Ω for shear flow and no flow for the same value of K_x, is plotted against K_x, for the (0,0), (1,0) and (2,3) modes. It is evident from the figure that the $\Delta\omega$ vs. K_x lines for the (1,0) and (0,0) modes, are discontinuous at $K_x = 0$:

* (For each case i.e. (0,n), (m,o) and (m,n) modes, effect of Mach number is shown only for one higher order mode, as other modes show the similar trend.)

the lines corresponding to upstream and downstream propagation have different slopes. The effect is larger for the (0,0) than the (1,0) mode, and if the (2,3) mode has a discontinuity it is almost impossible to detect. This seems to suggest that the magnitude of the discontinuity in augmentation of the phase velocity between upstream and downstream waves at the cut-off frequency decreases very rapidly with increasing mode order.

A similar discontinuity at $\Omega = U$ follows from the approximate analytical result obtained by Hersh and Catton (1971) for plane wave propagation in a two-dimensional duct with shear flow.

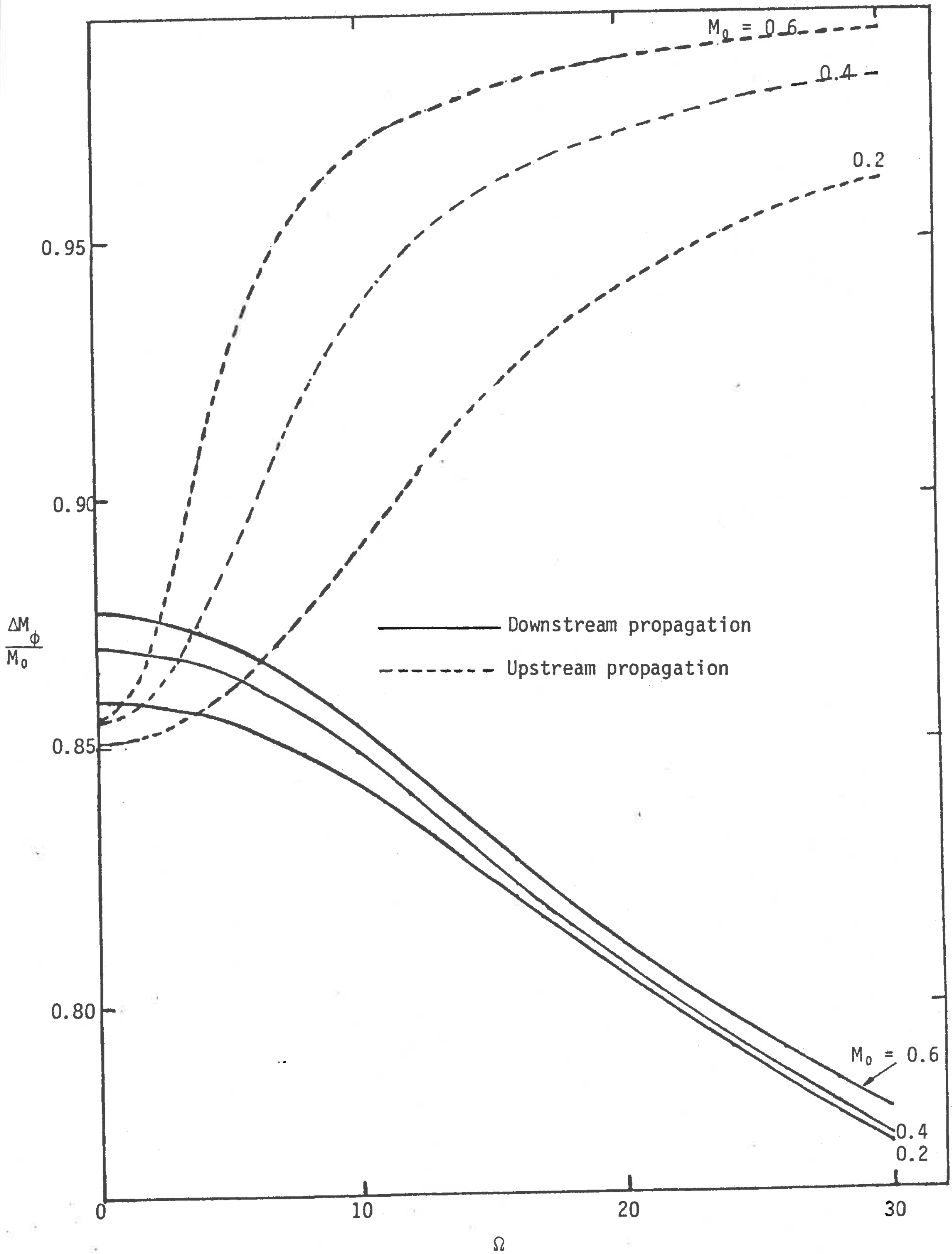

FIGURE 2.22 : PHASE MACH NUMBER CHANGES, (0,0) MODE

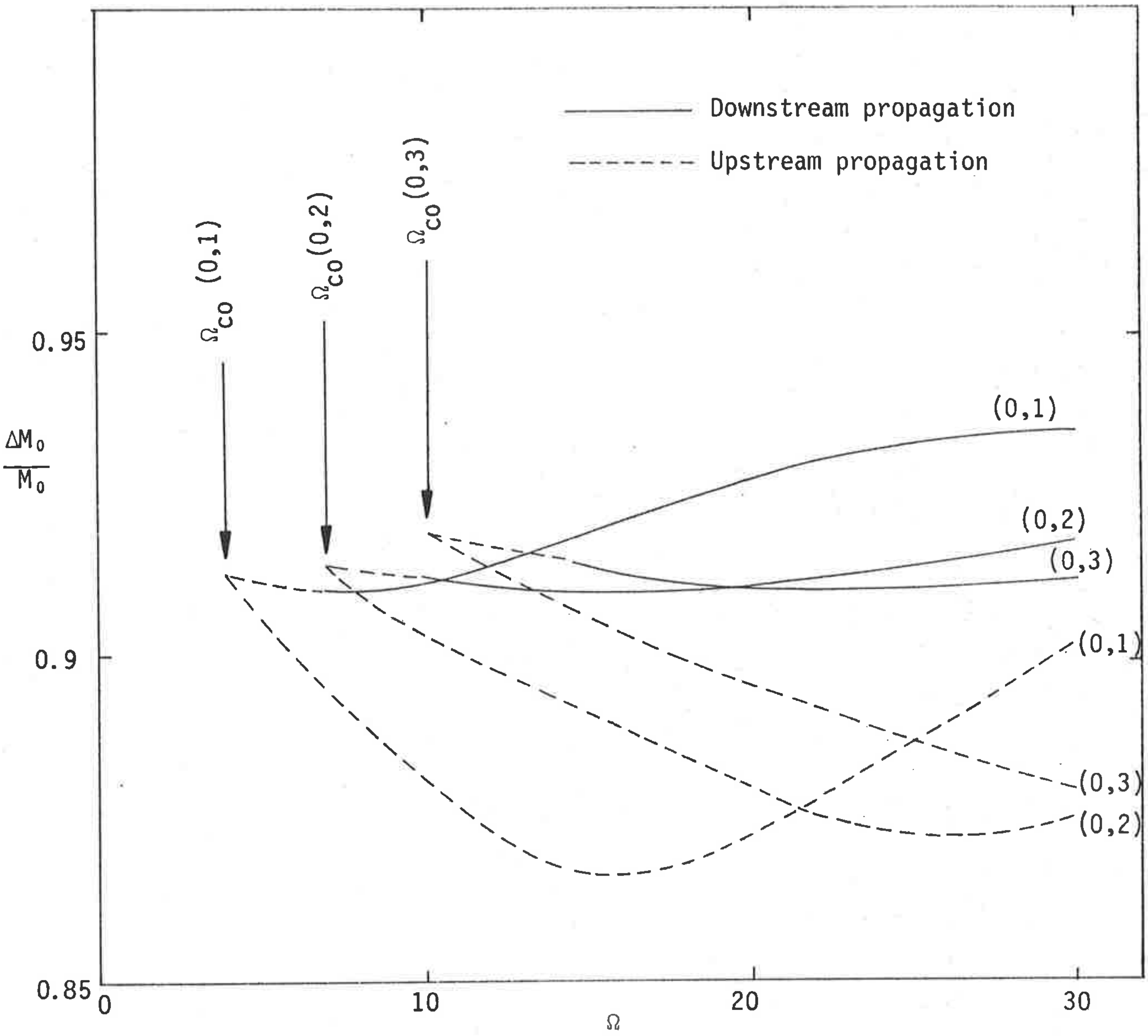

FIGURE 2.23 : PHASE MACH NUMBER CHANGES (0,n) MODES, M_o = 0.2

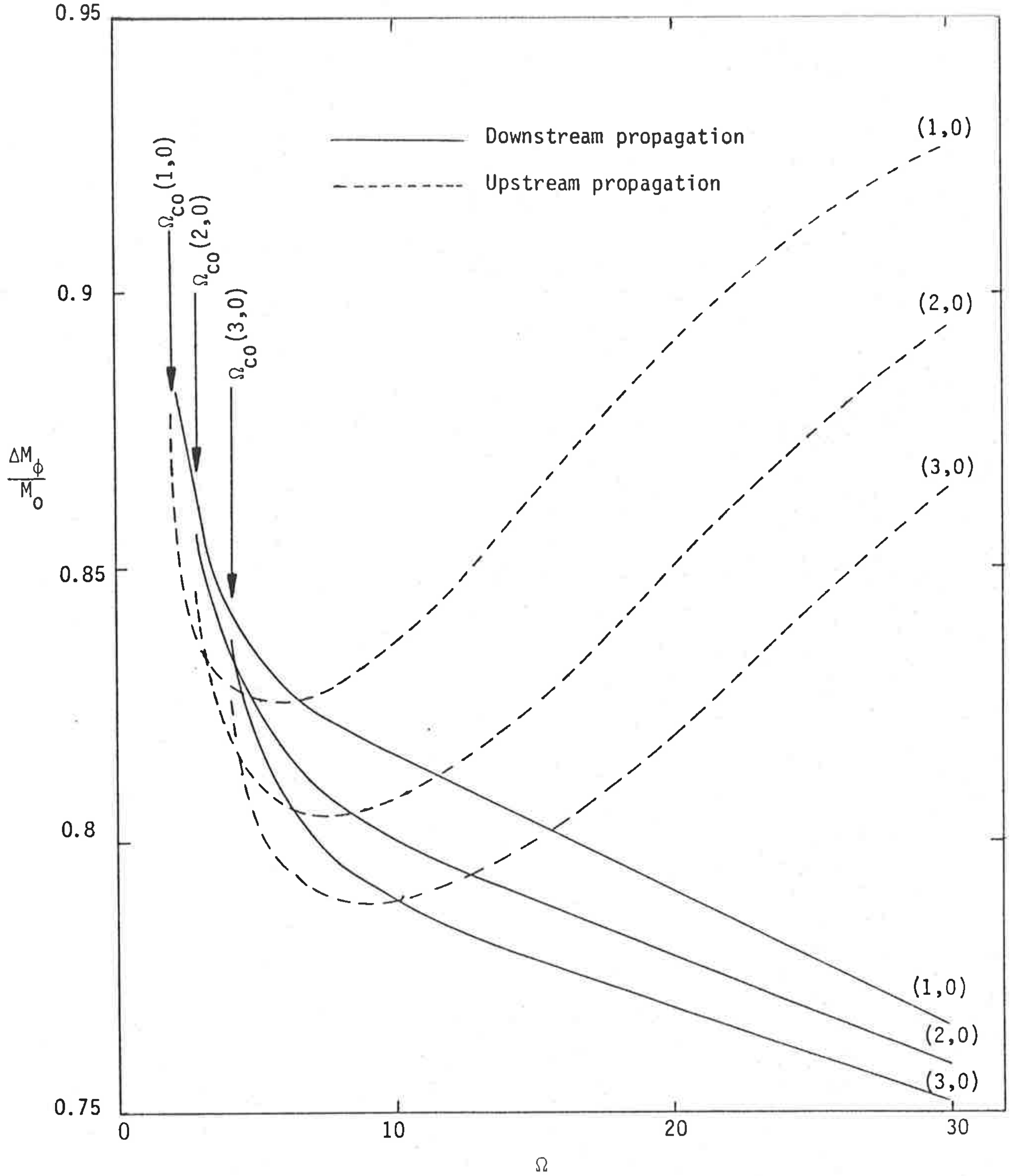

FIGURE 2.24 : PHASE MACH NUMBER CHANGES (m,0) MODES, $M_o = 0.2$

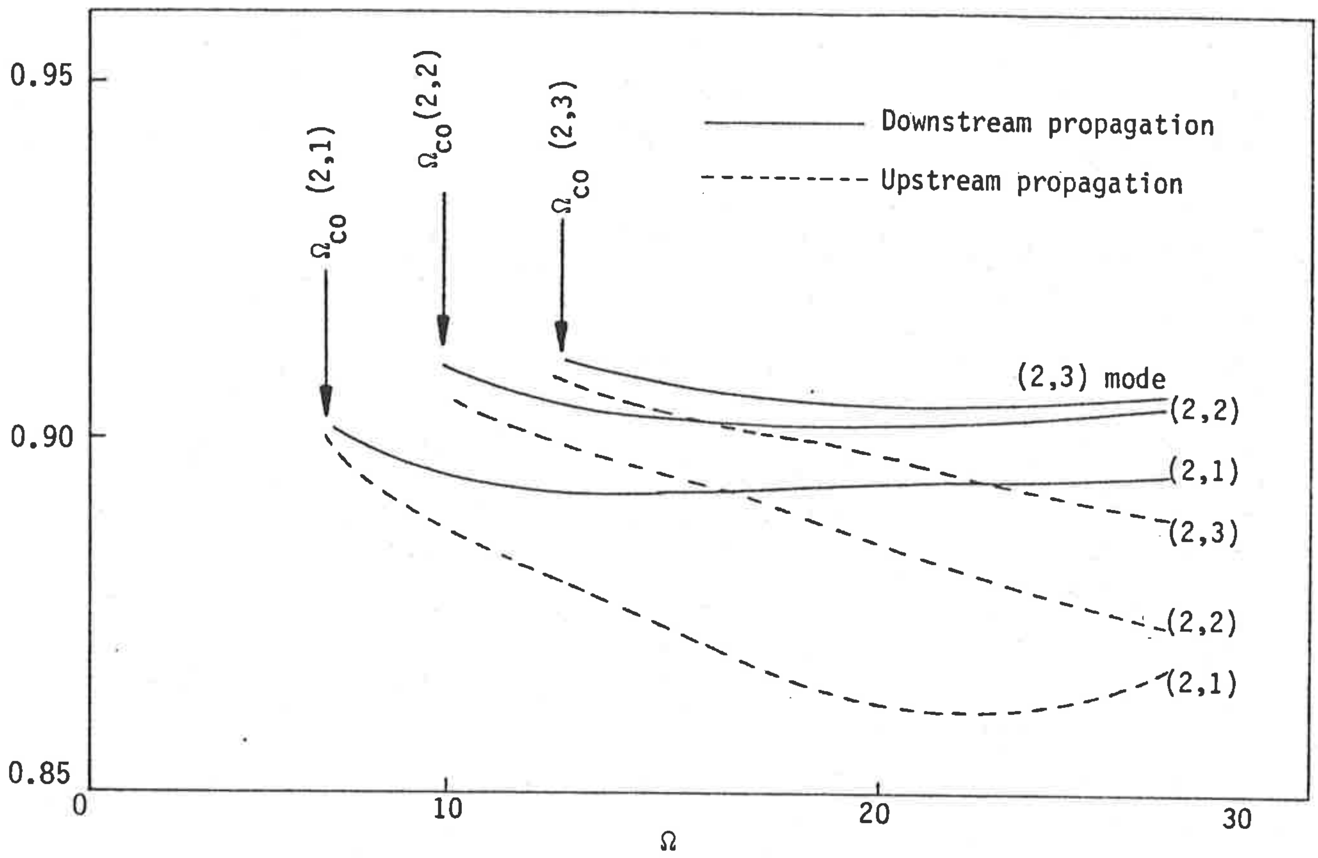

FIGURE 2.25 : PHASE MACH NUMBER CHANGES (m,n) MODES, M_o = 0.2

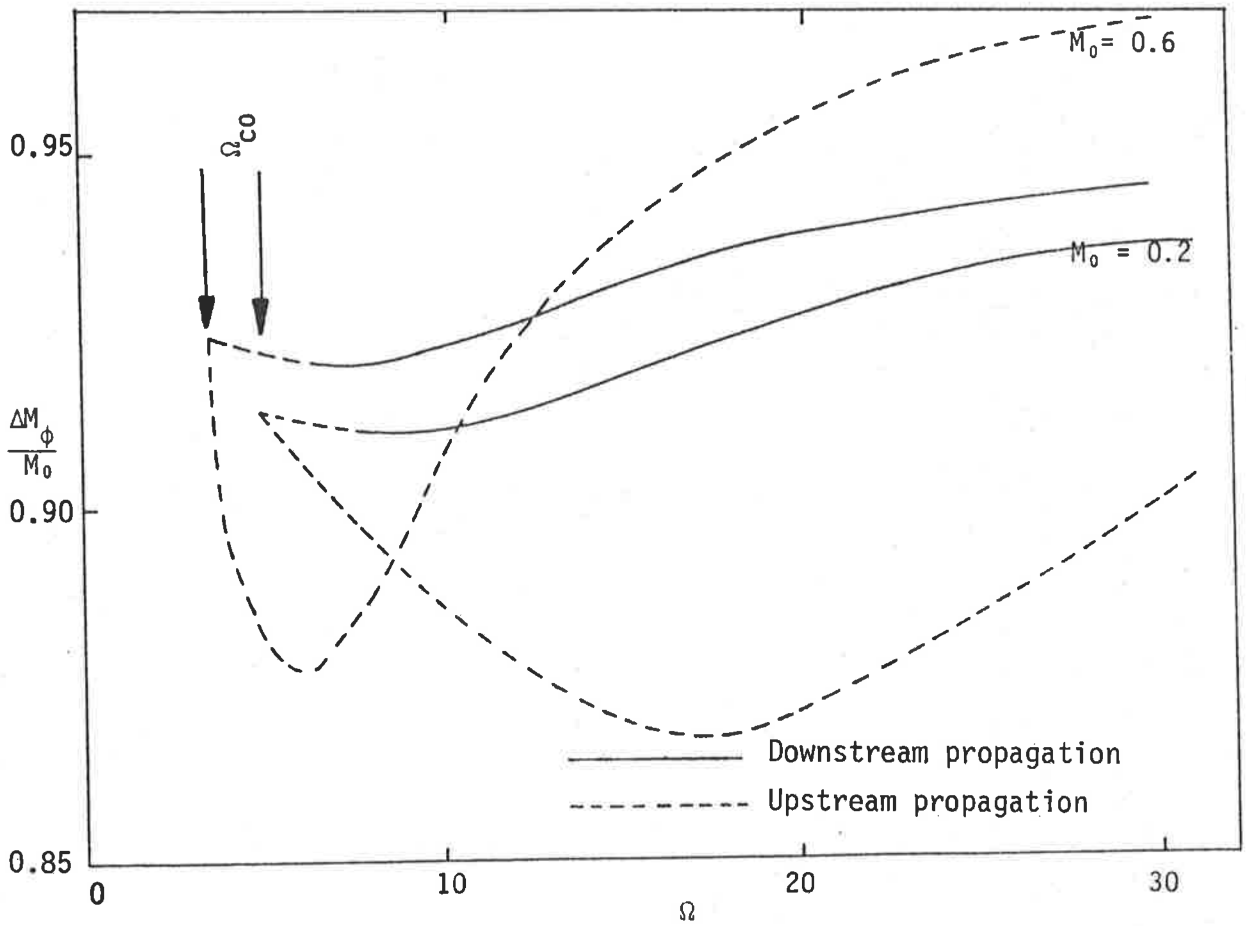

FIGURE 2.26 : PHASE MACH NUMBER CHANGES, (0,1) MODE; EFFECT OF MACH NUMBER

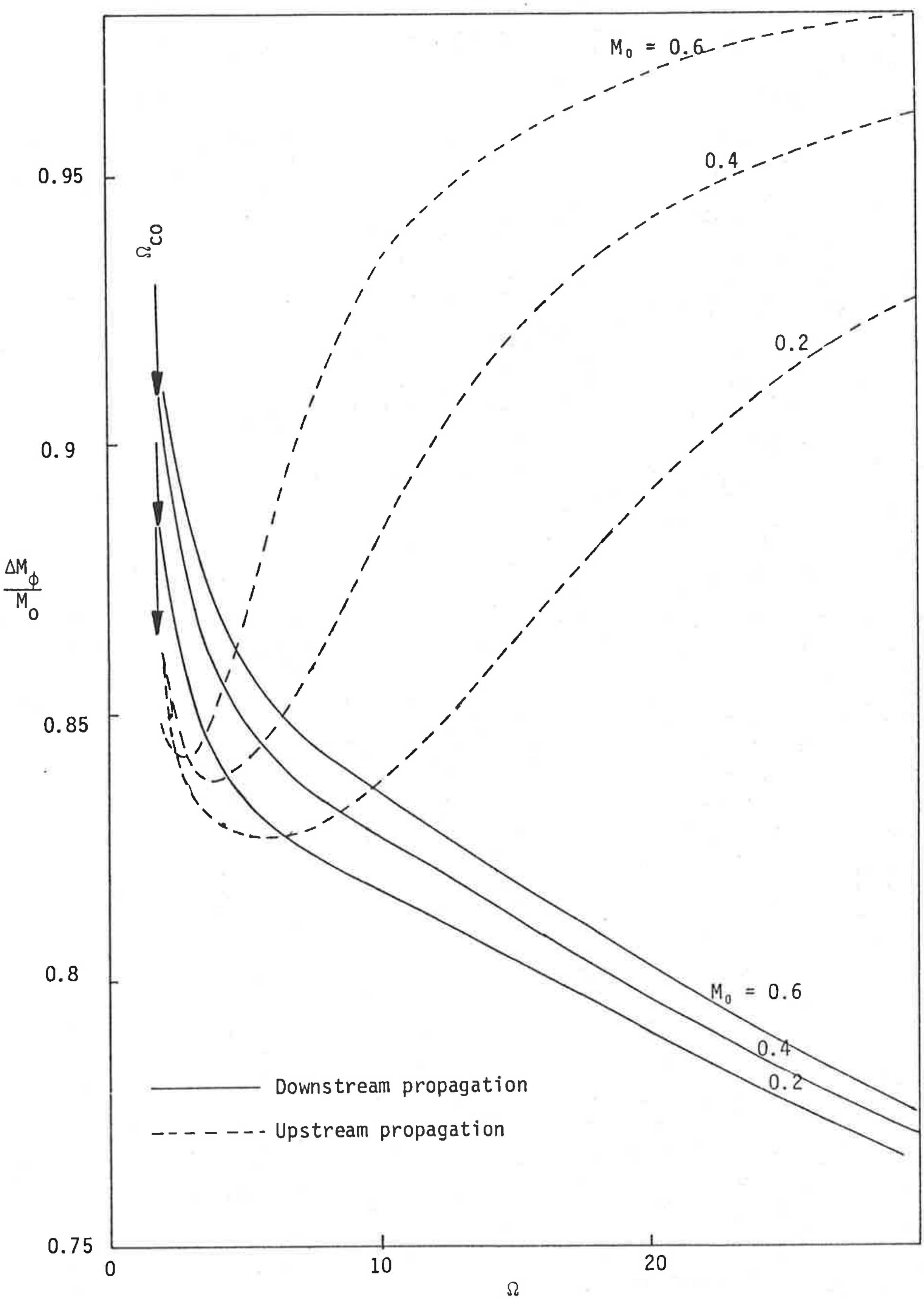

FIGURE 2.27 : PHASE MACH NUMBER CHANGES, (1,0) MODE; EFFECT OF MACH NUMBER

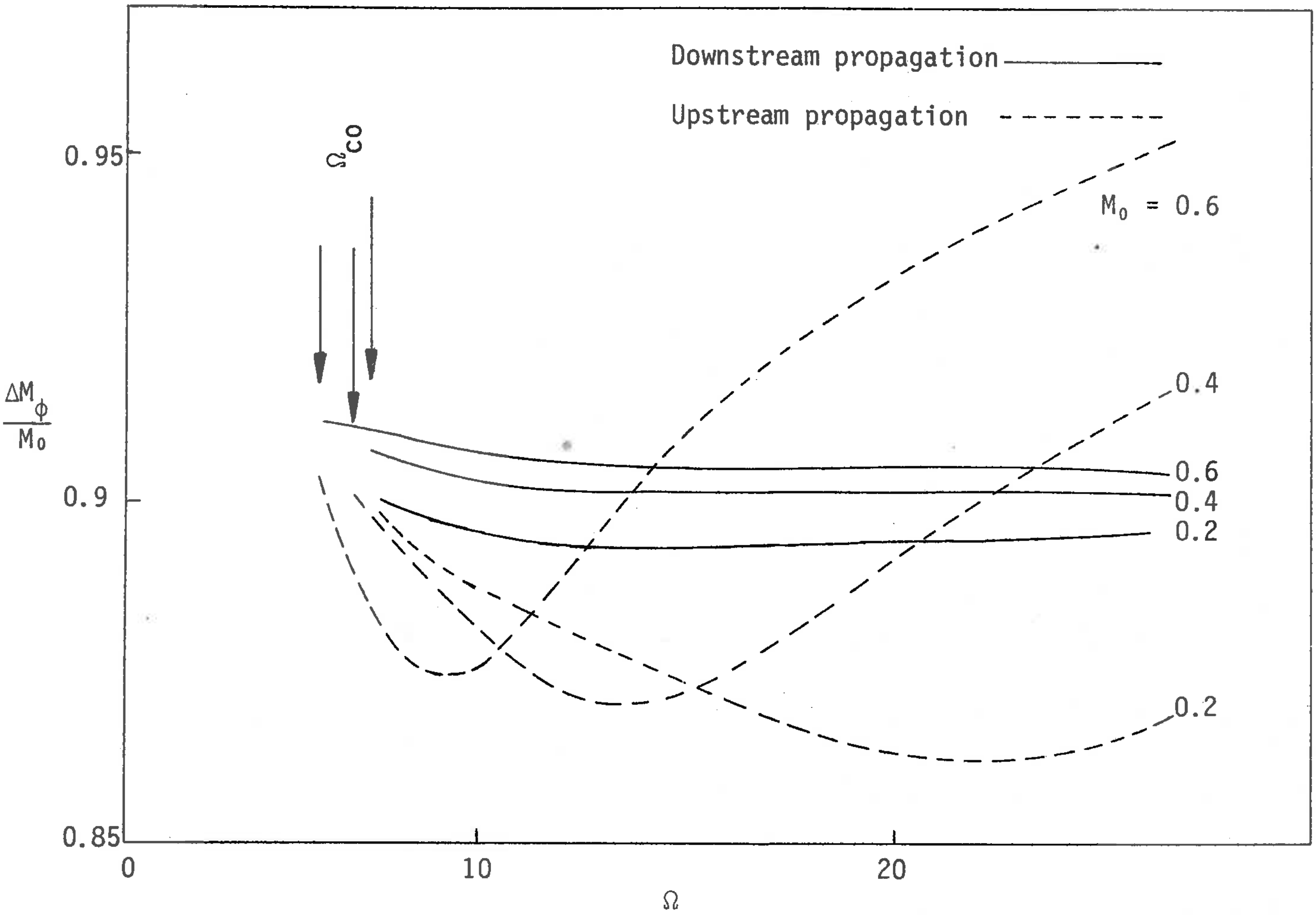

FIGURE 2.28 : PHASE MACH NUMBER CHANGES, (2,1) MODE; EFFECT OF MACH NUMBER

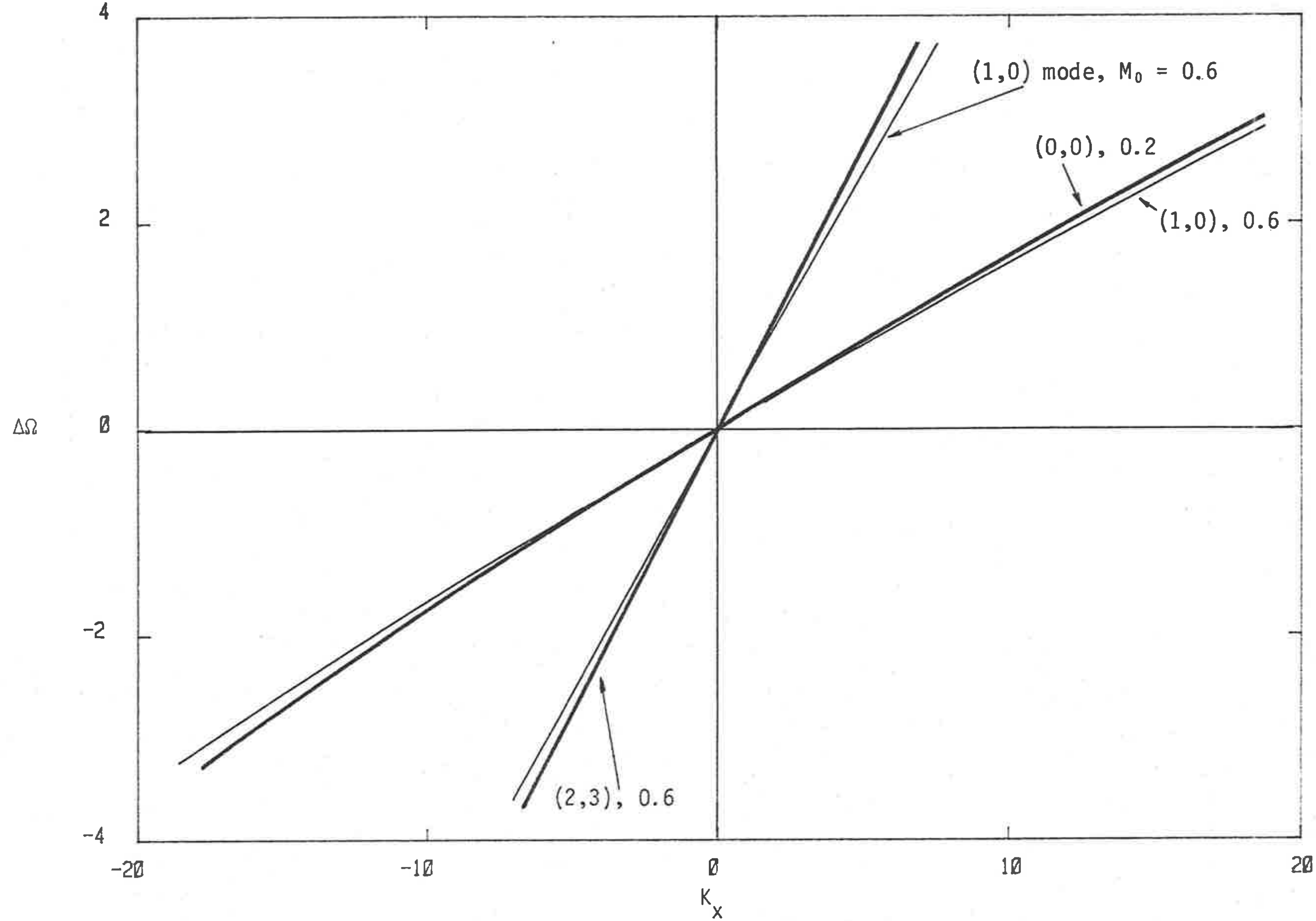

FIGURE 2.29 : VARIATION OF $\Delta\Omega$ WITH K_x

2.8 Summary and Conclusions

The main aim of the work presented in this chapter is the numerical solution of the convected-wave equation in cylindrical polar coordinates, for acoustic wave propagation in a circular pipe, in the presence of fully-developed turbulent flow. A mean-velocity profile model, consisting of wall, logarithmic and core regions, truly representative of such flows has been used. The fourth order Runge-Kutta method of solution to obtain the radial distribution of acoustic pressure and particle velocity, the modal phase speed and cut-off frequency for any given mode and flow Mach number has been described. On the basis of the numerical results obtained, the effect of shear flow can be summarized as follows.

(1) The plane wave (0,0) modes becomes dispersive.

(2) Compared with uniform flow with $M = M_0$, the modal cut-off frequencies are increased and the axial wave number at cut-off although still negative is reduced in magnitude.

(3) The frequency for $K_x = 0$ is the same as that for the uniform-flow and no-flow cases, and is independent of the flow Mach number and its radial distribution.

(4) The cut-off frequency can be closely approximated by that of a uniform flow with a profile averaged Mach number AM_0.

(5) Sound waves are refracted towards the wall for downstream propagation and away from the wall for upstream propagation. This results in displacement of the radial distributions of acoustic pressure and particle velocity towards or away from the wall. The effect is small at or near the cut-off frequency and increases with the $(\Omega - \Omega_{co})$ and increasing flow Mach number.

(6) ΔM_ϕ, which gives a measure of the extent to which the shear flow augments the phase velocity from the no-flow case at the same K_x, depends very much on mode order, M_0 and the direction of the propagation. Extensive calculated results for various modes have been presented.

(7) Variation of acoustic particle velocity u with radial position may in some circumstances be similar to that of acoustic pressure.

CHAPTER 3

EXPERIMENTAL FACILITY, INSTRUMENTATION AND CALIBRATION

3.1 Introduction

As indicated earlier the flow system chosen for the investigation of the relationship between the characteristics of a disturbed internal flow and the resulting sound field in the flow is that of fully-developed turbulent flow in a pipe of circular cross-section, disturbed by an orifice plate. The study requires

(i) the overall definition of the flow in terms of the streamwise and radial variation of mean flow parameters (total pressure, static pressure, flow speed, flow Mach number, wall shear stress, etc.) over a region extending from the undisturbed approach flow far upstream of the disturbance, through the disturbed region, to the re-established flow downstream of the disturbance;

(ii) identification of points of flow separation and re-attachment;

(iii) a knowledge of the variation throughout the flow of fluctuations in the flow parameters (pressure, velocity, and wall shear stress fluctuations, and fluctuations in the position of re-attachment of the flow to the pipe wall after the separation caused by the orifice plate); and

(iv) detailed knowledge of the acoustic field (both plane waves and higher order modes) in the fluid inside the pipe.

In this chapter, the experimental pipe flow facility and various special pipe sections used in it, the orifice plate sizes and geometry, instrumentation and instrument calibration are described and discussed.

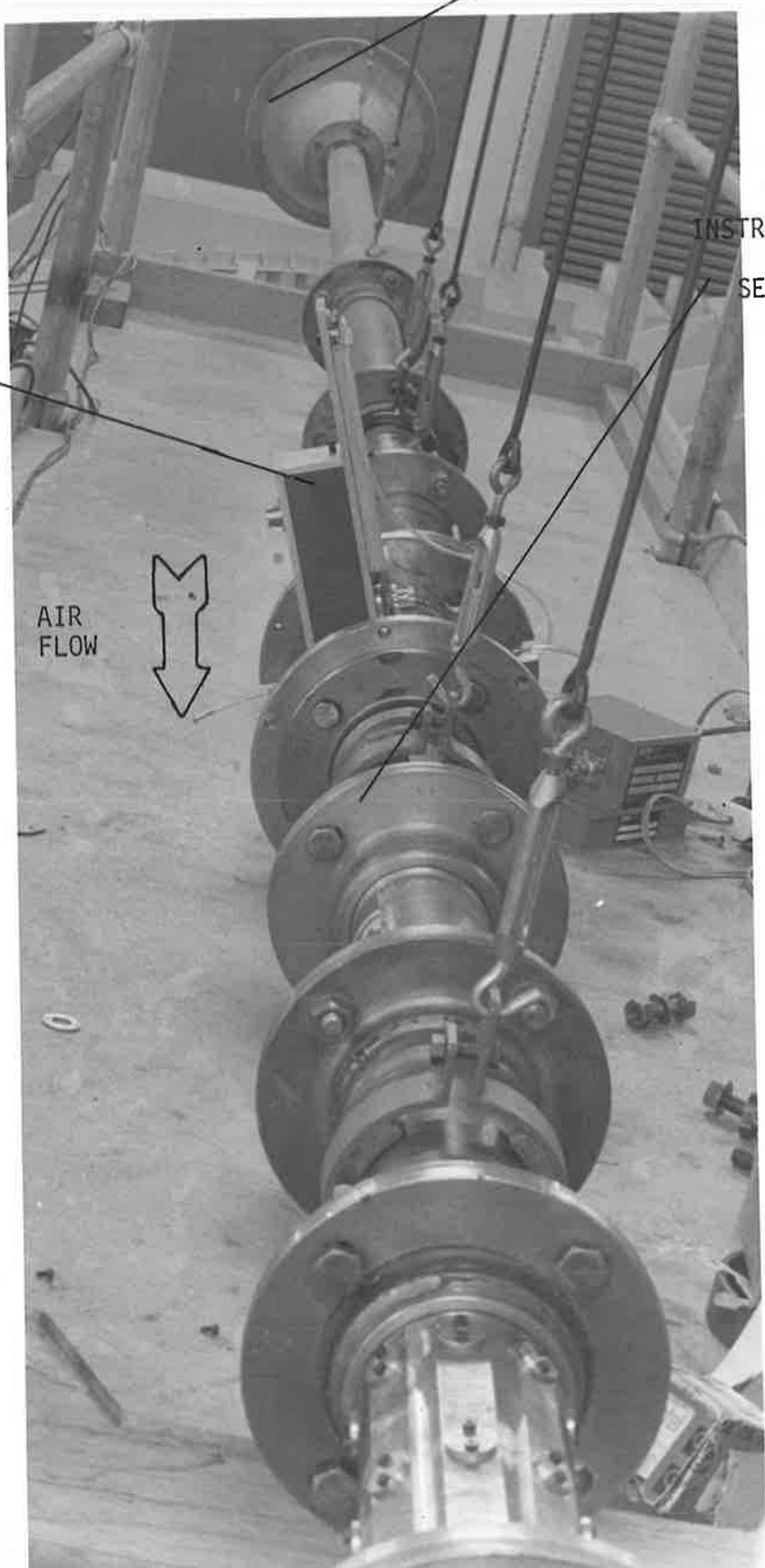

FIGURE 3.1(a) : EXPERIMENTAL PIPE FACILITY

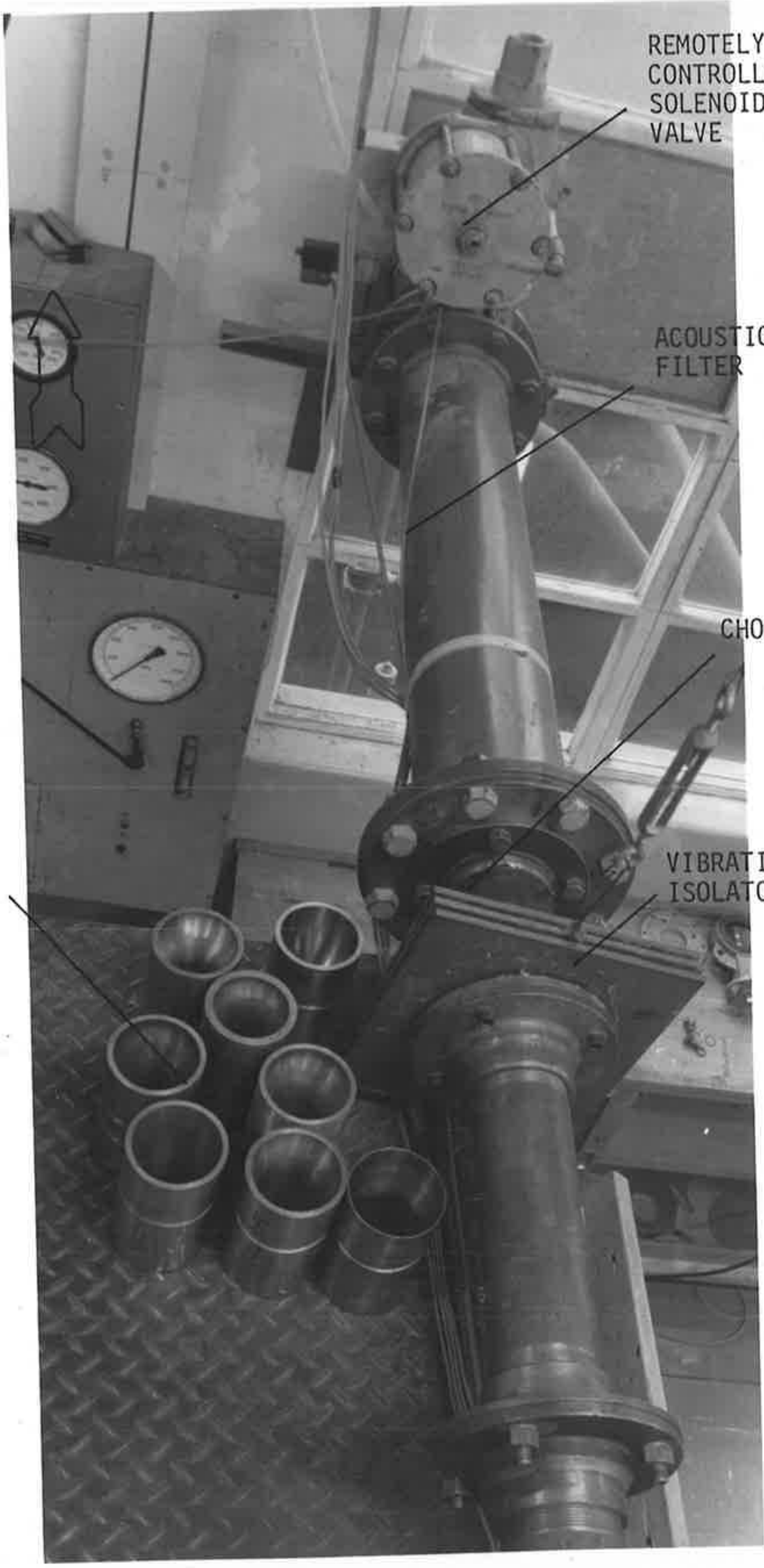

FIGURE 3.1(b) : EXPERIMENTAL PIPE FACILITY

3.2 Experimental Facility

The pipe flow facility, shown in Figures 3.1(a) and 3.1(b), is, with minor modifications, that used previously by Rennison (1976) and Norton (1979). The pipe itself, is made up from smooth cold-drawn interchangeable sections of steel tubing with internal diameter 72.54mm and wall thickness 6.35mm, with an overall length of 12m. The bores of the various pipe sections are accurately matched, and mating pipe sections are joined by flanges located by a system of spigots. There is an '0' ring seal between flanges to prevent leakage. The orifice plate under test is mounted about 4m (~ 55 pipe diameters) downstream of the pipe entrance, leaving a length of about 110 pipe diameters downstream of the orifice plate. Air enters the pipe from atmosphere through a bell mouth extending over 10 pipe diameters.

The pipe rig is suspended over its entire length by a series of soft elastic supports, and the downstream end of the pipe is connected through a vibration isolator, a sonic choke, and a remotely controlled quick acting valve to two large ($17m^3$) vacuum tanks. This arrangement effectively isolates the pipe from external vibration and from both vibrational and acoustic disturbances occurring downstream of it when the flow is on.

The vibration isolator is a low pass mechanical filter to prevent vibration generated near the sonic choke from being transmitted to the test section. It consists of four steel plates (6.5mm thick and 250mm square) separated from each other and the enclosing flanges by soft rubber rings 6mm thick, moulded from silastic. The internal diameter of rubber rings and enclosing flanges is the same as the pipe diameter. The pipe flow facility is shown schematically in Figure 3.2.

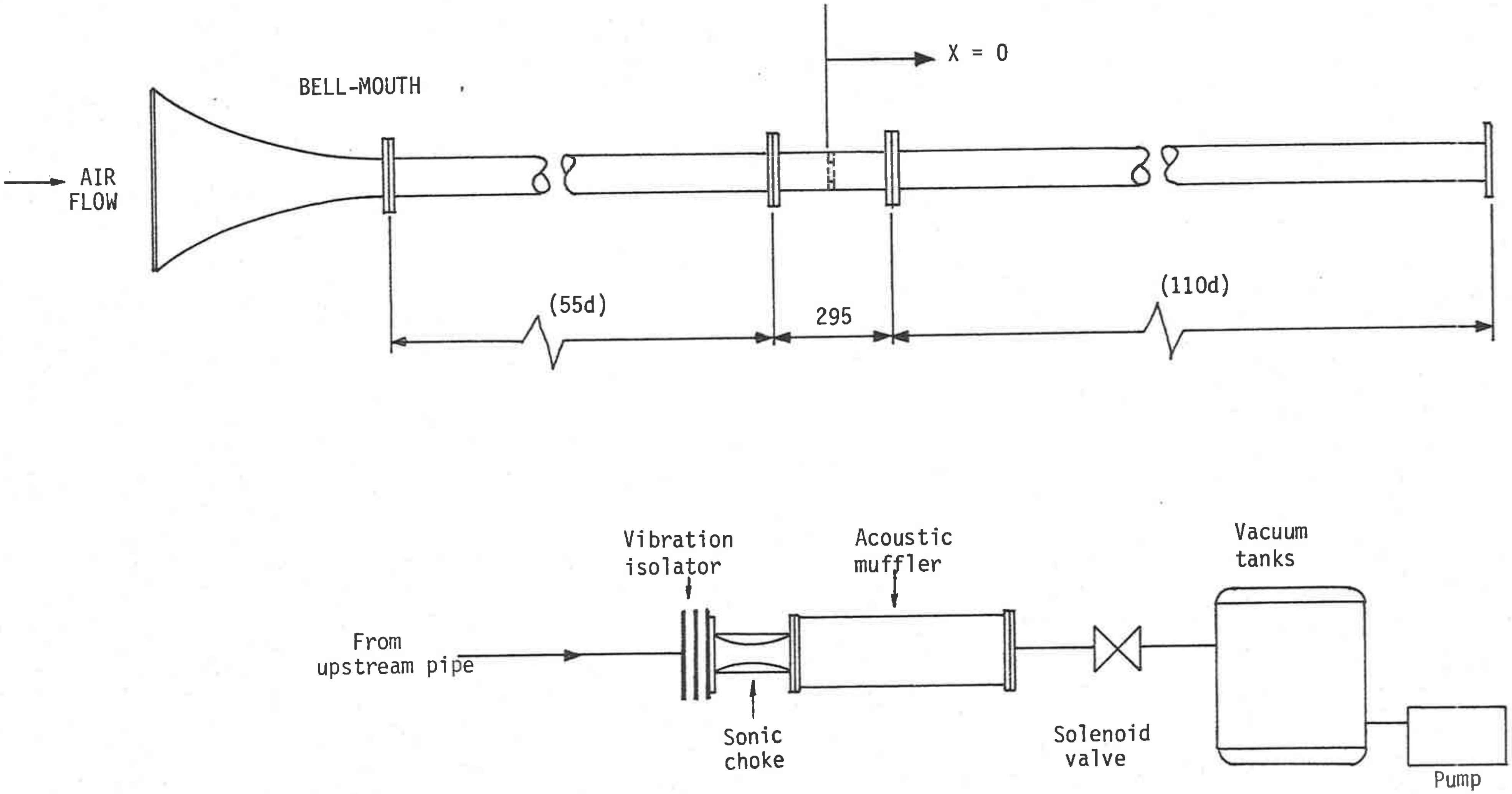

FIGURE 3.2 : DETAILS OF TEST RIG

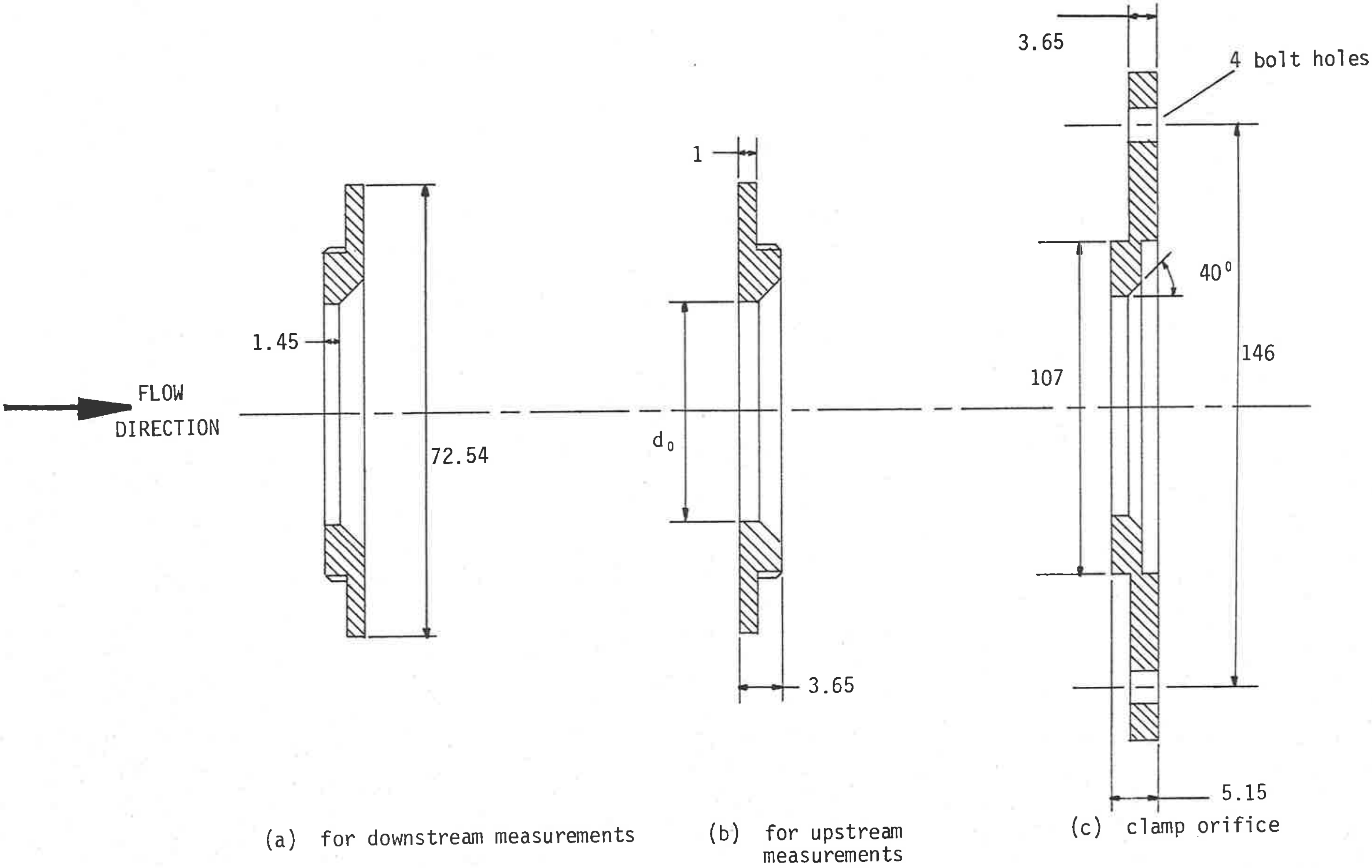

FIGURE 3.3 : ORIFICE PLATES (all dimensions in mm)

When the remotely controlled valve is opened, air flows from the atmosphere through the piping system to the vacuum tanks. Mass flow rate and the flow velocity in the pipe system are determined by the combination of the throat area of the sonic choke and the size of the installed orifice plate. Each choke nozzle is characterised by its throat diameter d_C, non-dimensionalised by pipe diameter d, i.e. by $D_C = d_C/d$. Similarly each orifice plate is characterised by its hole diameter, d_0 non-dimensionalised by pipe diameter, i.e. by $D_0 = d_0/d$.

Ten interchangeable sonic choke inserts with D_C values in the range 0.39 to 0.86 and four orifice plates with D_0 values in the range 0.62 to 0.83, dimensional details of which are given in Tables 3.1 and 3.2, are available. The various D_0 and D_C combinations allow flow velocities in the range of 30 to 155 m/sec and corresponding times of steady running from 40 to 6 seconds to be obtained.

Because of the short running times, the operation of the rig and data acquisition (the procedures and equipment for which are described in Chapter 4) are computer controlled.

The four orifice plates conform to British Standard 1042, Part I (1964). Their geometries are shown in Figure 3.3. Each can be mounted between pipe flanges, but, in order to allow the streamwise position of instrumentation in the flow to be varied continuously in relation to the orifice plate, a second set is available which can be mounted on a movable internal cylindrical brass sleeve of 1.0mm wall thickness. The sleeve and orifice plate can be moved axially by an external screw mechanism (see Figure 3.4-3.5). It is possible to reverse the sleeve so that the orifice plate can be mounted at either its upstream or downstream end. In this way measurements close to the orifice plate can always be made in a flow occupying the full pipe diameter.

Table 3.1

Choke Throat Sizes

Choke Number	Throat diameter d_c (mm)	D_c
1	28.0	0.39
2	35.5	0.49
3	38.0	0.52
4	42.0	0.58
5	45.5	0.63
6	49.0	0.68
7	52.0	0.72
8	55.0	0.76
9	58.0	0.80
10	62.5	0.86

Table 3.2

Orifice sizes

Orifice number	Hole diam. d_0 (mm)	D_0
1	45	0.62
2	50	0.69
3	55	0.76
4	60	0.83

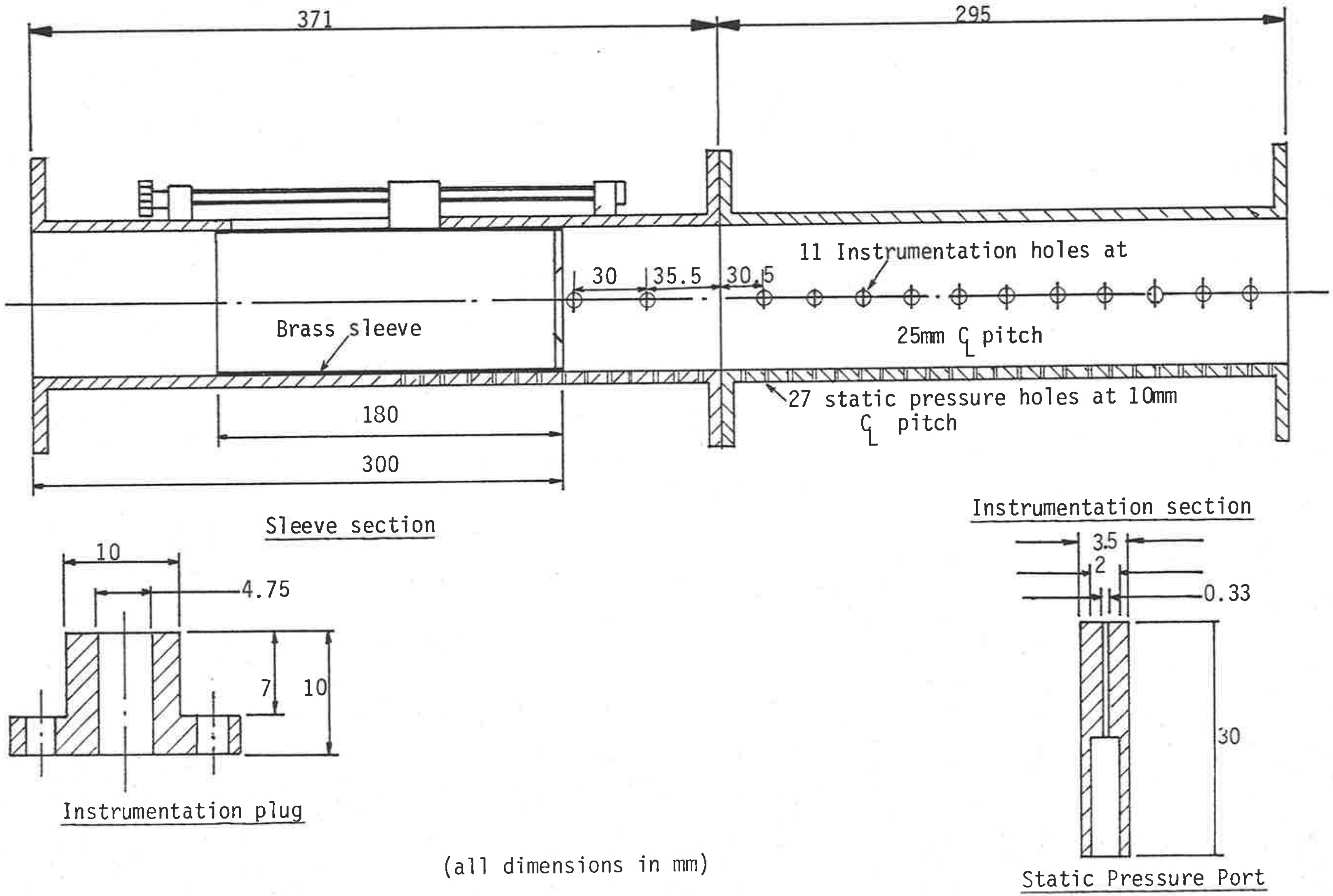

FIGURE 3.4 : DETAILS OF MOVABLE ORIFICE PLATE (not to scale)

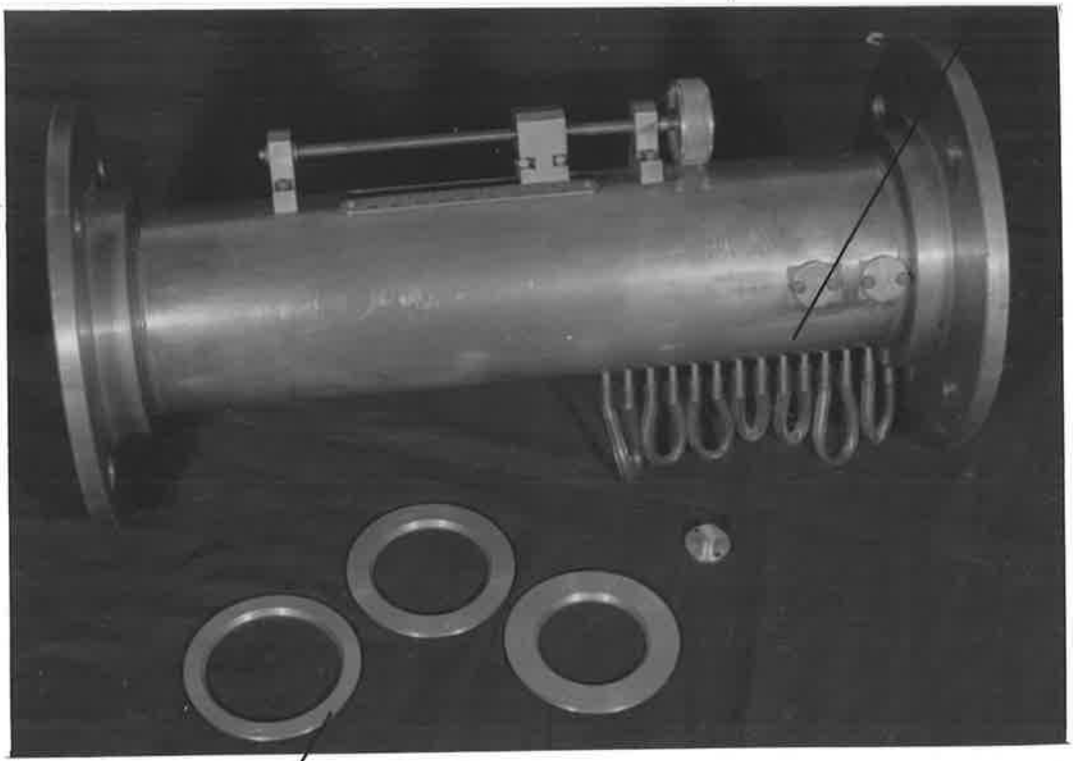

FIGURE 3.5 : ORIFICE SLEEVE SECTION

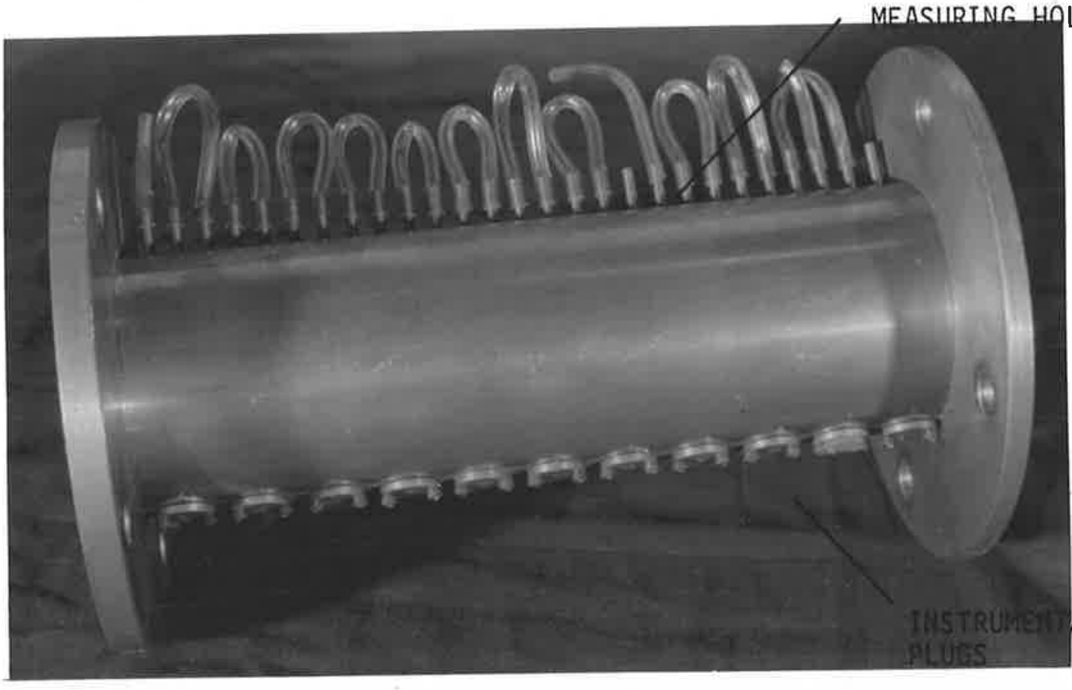

FIGURE 3.6 : INSTRUMENTATION SECTION

Several instrumentation pipe sections, of the type shown in Figures 3.4 and 3.6, all of length 295mm, which can be inserted anywhere in the rig in relation to the orifice, are used for mounting the various pieces of instrumentation. They are fitted with removable 10 mm diameter brass plugs, which are interchangeable with similar plugs having a central hole of diameter 4.75mm. The latter can accommodate fence gauges, hot film probes, pitot tubes or piezoelectric pressure transducers (all of which have bodies 4.75mm in diameter). A set screw in the brass plug keeps the instrument body in place. The instrumentation sections are also provided with static pressure tappings, the static pressures being measured by 0.33 mm diameter holes in the wall. Construction details are shown in Figure 3.4. The instrumentation sections have been carefully honed internally with the various instrumentation brass plugs in place.

3.3 Mean Velocity and Mach Number Measurement

Mean velocities and Mach numbers are obtained from total pressure measured by a pitot tube of 1.25mm OD and 0.8mm ID and the wall static pressure measured at the same axial location as the pitot tube entry. Total and static pressures relative to atmosphere are each measured by Datametrics Barocel manometers of 1000/100 Torr range. According to the manufacturer's specification, the Barocel has a time response of about a millisecond; this has been confirmed by measuring the pressure in an air jet interrupted by a disk segment rotating at known speed.

Static pressure measurements are always made with the pitot tube removed from the pipe. Standard compressible flow relations, in conjunction with the assumption that the total temperature in the flow at any point is equal to the reservoir (atmospheric) temperature, are used to evaluate the Mach number and other parameters from the total and static pressure measurements.

Although the pitot tube can be mounted in an instrumentation plug for measurements at a fixed radial location, radial profiles of Mach number and static pressure can be obtained by mounting it on a traverse drive attached to a special instrumentation section, which is shown in Figure 3.7. The traverse drive can be mounted on any of the three holes in the section (Figure 3.6); and at each position one static pressure hole is located at the same streamwise position as the pitot tube entry. With this arrangement the pitot tube support runs completely across the pipe diameter to avoid asymmetric blockage effects. A resistance potentiometer in the traverse rig produces a voltage, proportional to the probe position, which is fed to an analogue-to-digital converter.

3.4 Instrumentation and Calibration

The various instruments used - surface fence gauge, hot film shear gauge, hot wire anemometer and wall pressure transducers (piezoelectric and condenser microphone) - and their calibration will now be described.

3.4.1 Surface fence gauge

Mean positions of separation and reattachment points, where the wall shear stress τ_w is zero, have been determined by means of a surface fence gauge (Figure 3.8) of the type described first by Konstantinov and Dragnysh (1955) and later by Vagt and Fernholz (1973). Basically, the "fence" consists of a rectangular projection of very small height positioned normal to the wall and to the flow direction. The difference ΔP in the pressure on the pipe wall between the front and rear of the projection is related to the wall shear stress τ_w and changes sign when the direction of the stress is reversed.

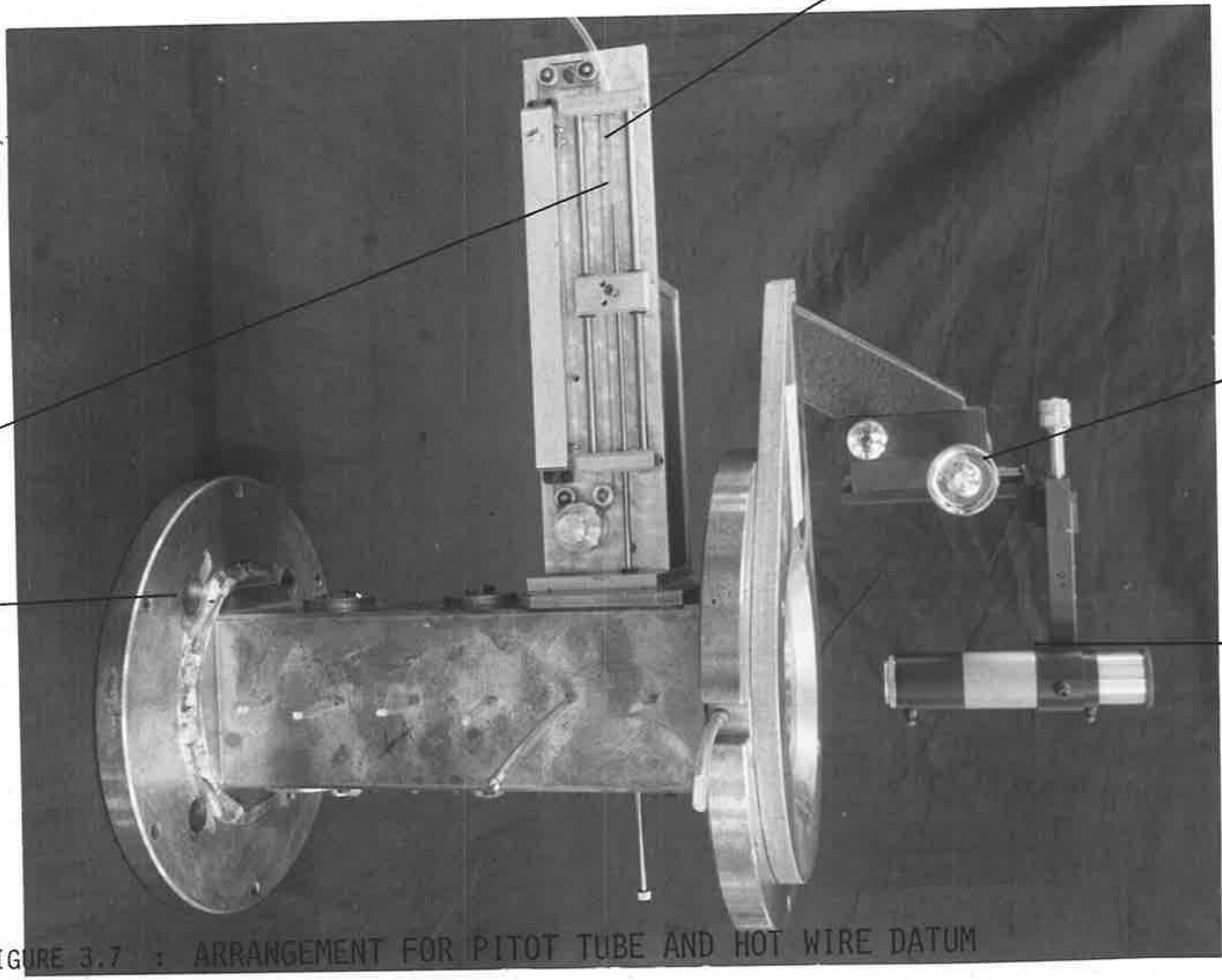

FIGURE 3.7 : ARRANGEMENT FOR PITOT TUBE AND HOT WIRE DATUM
POSITION MEASUREMENT

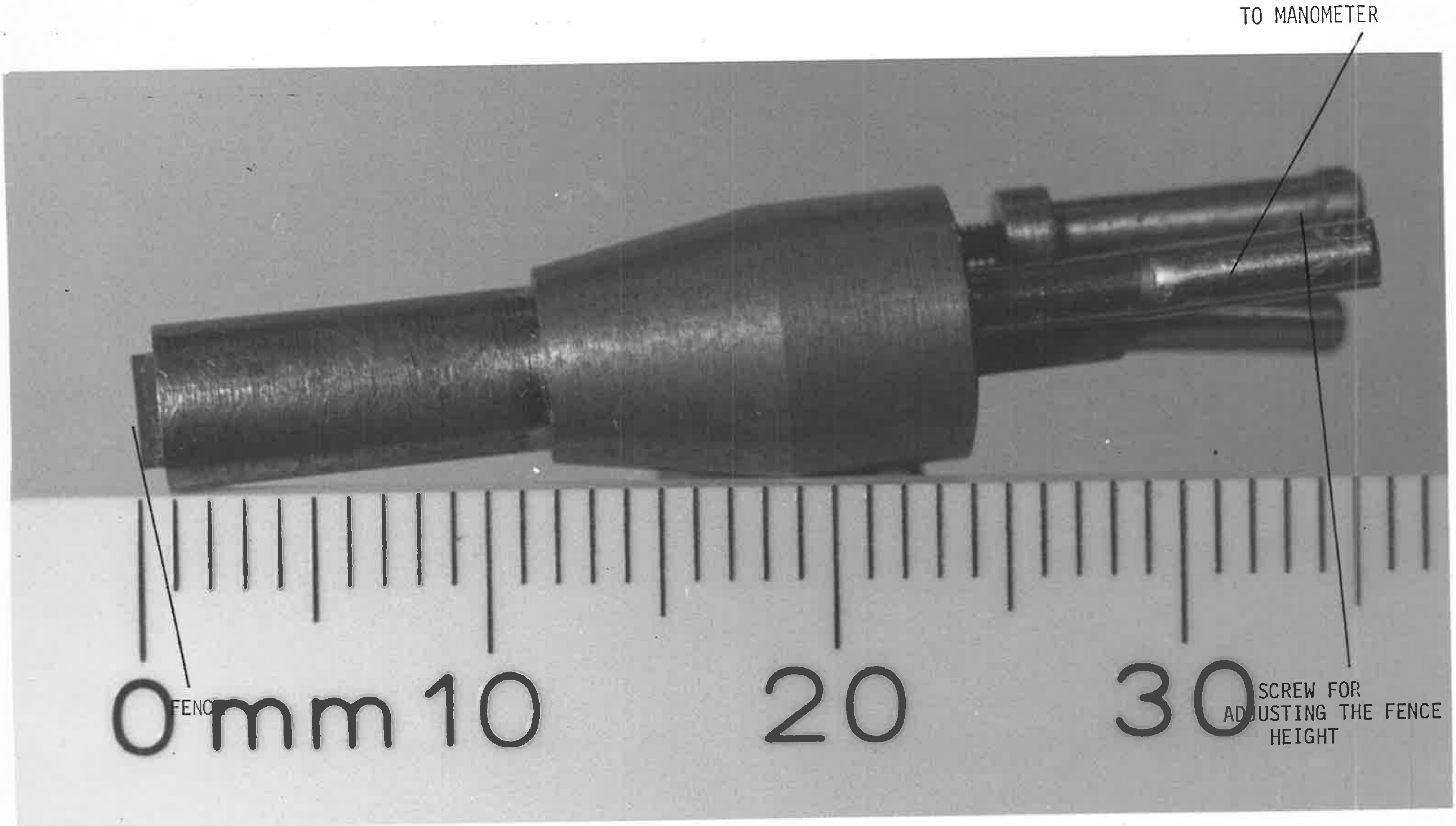

FIGURE 3.8 : SURFACE FENCE GAUGE

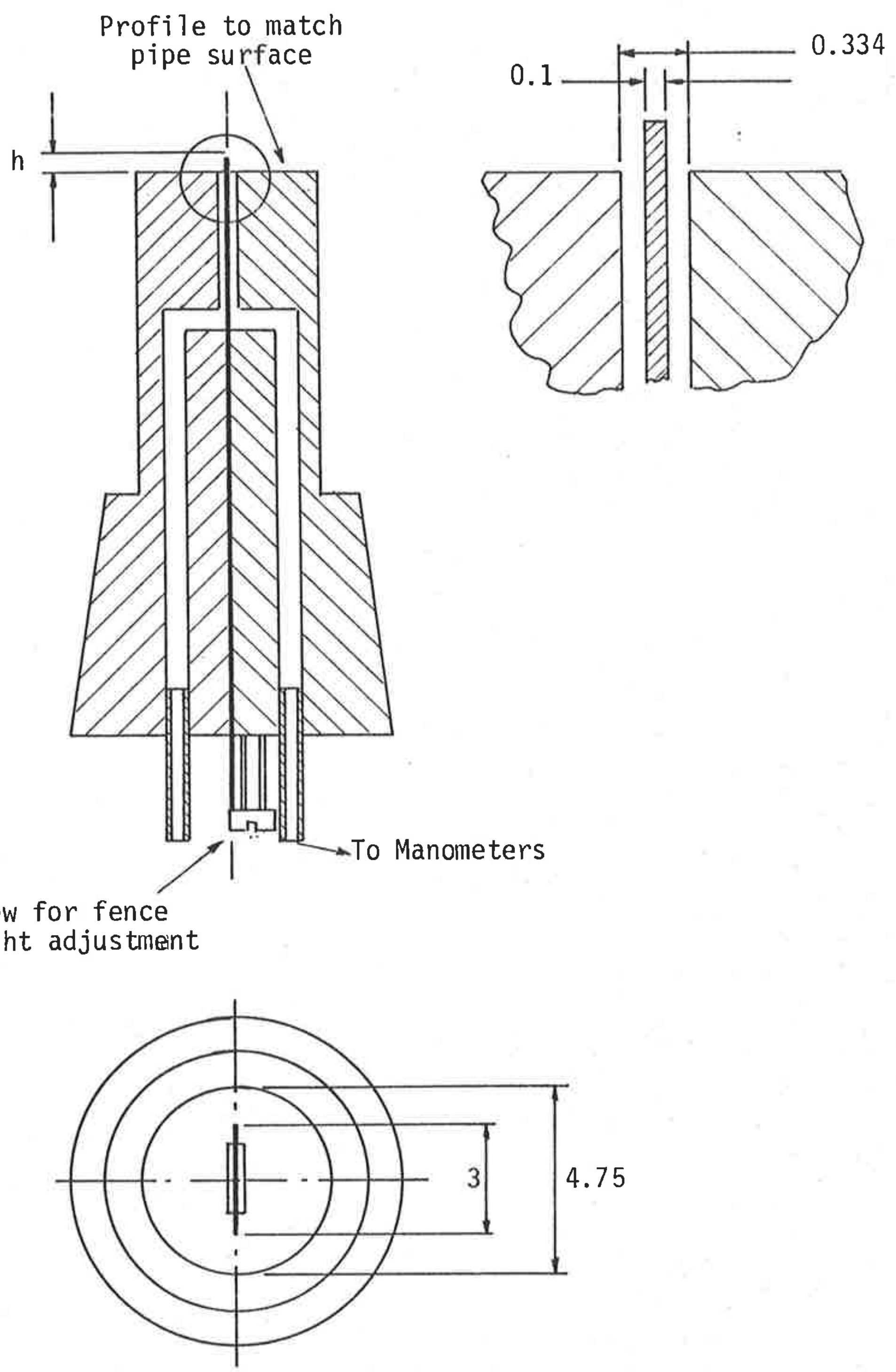

(all dimensions in mm)

FIGURE 3.9 : DETAILS OF A SURFACE FENCE GAUGE

The gauge is therefore suitable for measurement in regions of flow separation and reattachment, where both forward and reverse flows are encountered.

The results of Konstantinov and Dragnysh indicate that for very small projection heights ($h_+ = hU_\tau/\nu \lesssim 3$) Δp and τ_w are linearly related for a fixed value of h, i.e.

$$\Delta p = K\tau_w \quad , \tag{3.1}$$

but with K dependent on and increasing with form height. Later work (see Winter, 1977) suggests that more generally

$$\frac{\Delta p}{\tau_w} = f(h_+) \quad . \tag{3.2}$$

The construction of the gauge used in the present investigation is shown in Figure 3.9. A 3mm wide and 0.1mm thick section of razor blade is used as the fence. The pressure-measuring slots on either side of it are connected to 'L' shaped holes of about 1mm diameter which lead to the base of the instrument. Interference-fit steel extension tubes are used to make connections, by flexible tubing, to an electronic manometer. The gauge is made from brass in two halves which are clamped together by the threaded base cap; silicone grease is applied to the two halves before assembly to ensure perfect sealing without leakage between the slots on either side of the fence. A screw mechanism allows adjustment of the fence height. The top surface of the gauge body which is exposed to the flow and the fence are carefully machined to match the pipe profile. The body of the gauge fits in the 4.75mm diameter hole in the instrumentation plug and a grub screw in the plug keeps the gauge in place.

The gauge has been found to be quite sensitive to small irregularities in matching the profile of its exposed surface with the profile of the instrumentation plug (the instrumentation plug itself being accurately matched with the pipe profile as a consequence of honing the instrumentation section with the plug in position). Therefore, with the fence retracted below the gauge surface, the gauge and the plug profiles were polished with a very fine emery paper to remove the surface irregularities at the hole in the plug; then the height of the blade was adjusted and measured under a microscope. Once mounted the surface fence gauge was not removed from the instrumentation plug.

In the present work a series of tests with different fence heights in the range $0.05 \leqslant h \leqslant 0.5$ showed that the location of the point at which $\tau_W = 0$, as indicated by the gauge, is insensitive to the fence height. A value of 0.1mm, corresponding to $10 \leqslant h_+ \leqslant 30$ over the range of the experimental flow speeds, rather larger than normally used for wall shear stress measurements, has therefore, for convenience, been used throughout the investigation. The value of K for the present experimental conditions is about 70.

The pressure differential is measured with a Datametric Barocel electronic manometer of 100 Torr range. To obtain a stable value of ΔP in the separated and re-attaching flow region downstream of the orifice plate, a long averaging time is necessary. For each streamwise location 1000 samples were taken over a total running time of 30 seconds. Geometrical symmetry of the gauge was checked by repeating measurements with the gauge rotated through 180°; the averaged values of ΔP for 30 seconds run time were found to be within 0.5% (see Figure 3.10) of each other.

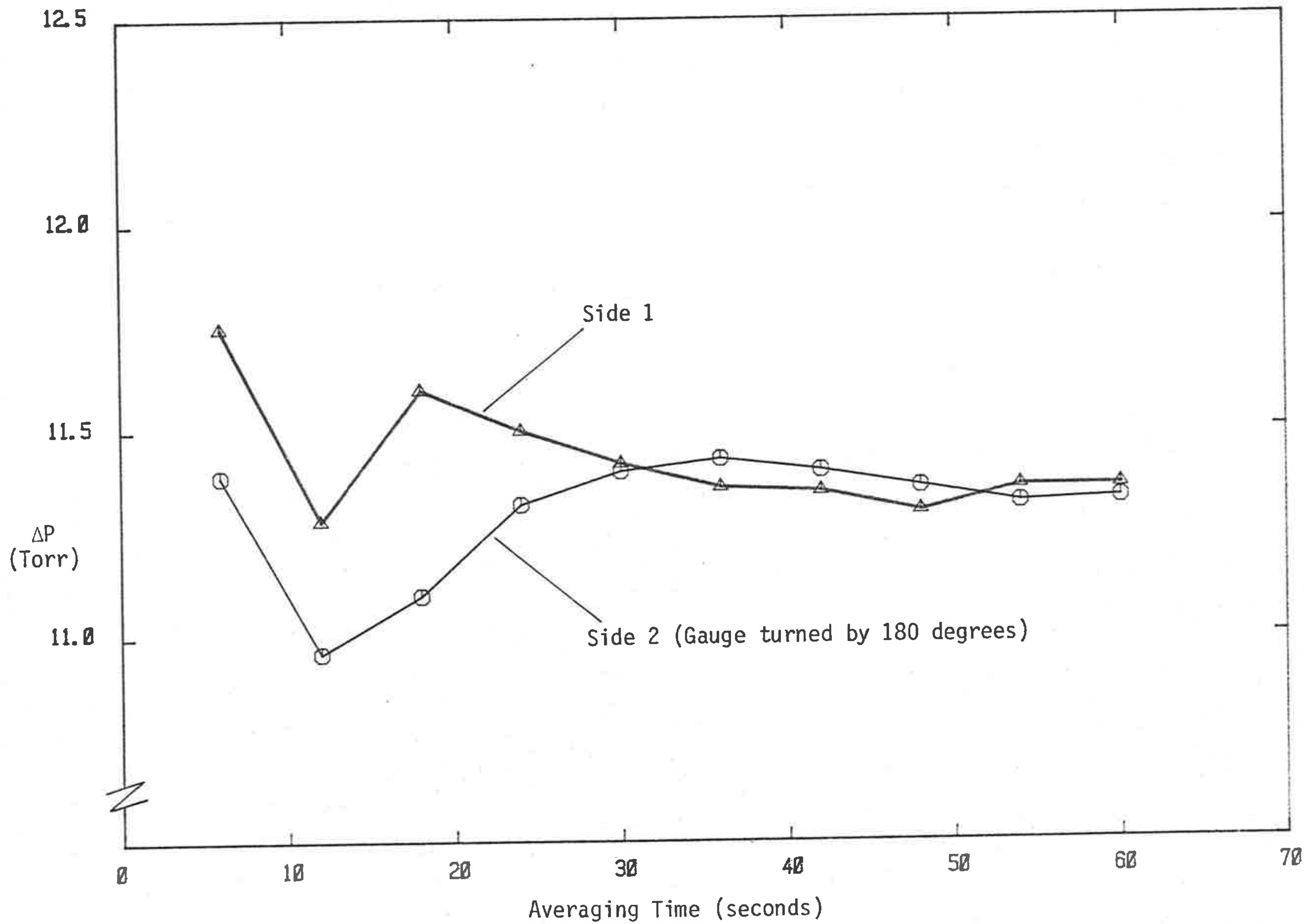

FIGURE 3.10 : FENCE GAUGE MEASUREMENTS

3.4.2 Mean and Fluctuating Velocity and Shear Stress Sensors

Hot wire anemometer

A single-wire constant-temperature anemometer has been used to measure the velocity profile across the pipe and the streamwise component of velocity fluctuations. The probe used for this work is shown in Figure 3.11.

The hot wires are formed by copper plating 5 μm diameter tungsten wire leaving an unplated central active portion 1.2-1.3mm long (giving a length to diameter ratio ℓ/d of 240-260). The copper plated ends of the wire are soft soldered to stainless steel needles, allowing a small amount of slack in the wire to avoid strain gauging. A typical wire resistance is 6.5 ohms.

It has been found advantageous to make the portion of the probe carrying the wire as a removable plug-in tip. Several interchangeable tips with different needle configurations (e.g. bent for measurements closer to the pipe wall) were used. This arrangement also facilitates quick wire replacement in the case of breakage. The hot-wire probe can be mounted in the same traverse gear as the the pitot tube.
As one use of the results obtained from hot-wire measurements is the determination of sharp spectral peaks in velocity fluctuations associated with acoustic modes in the flow, the unsupported length of the needles was carefully selected so that the needles have a very high natural bending frequency (> 25 kHz). During use, frequent checks were made on the velocity spectrum in undisturbed flow (without orifice plate) to be sure that no such natural frequencies in the range of interest developed due to probe deterioration.

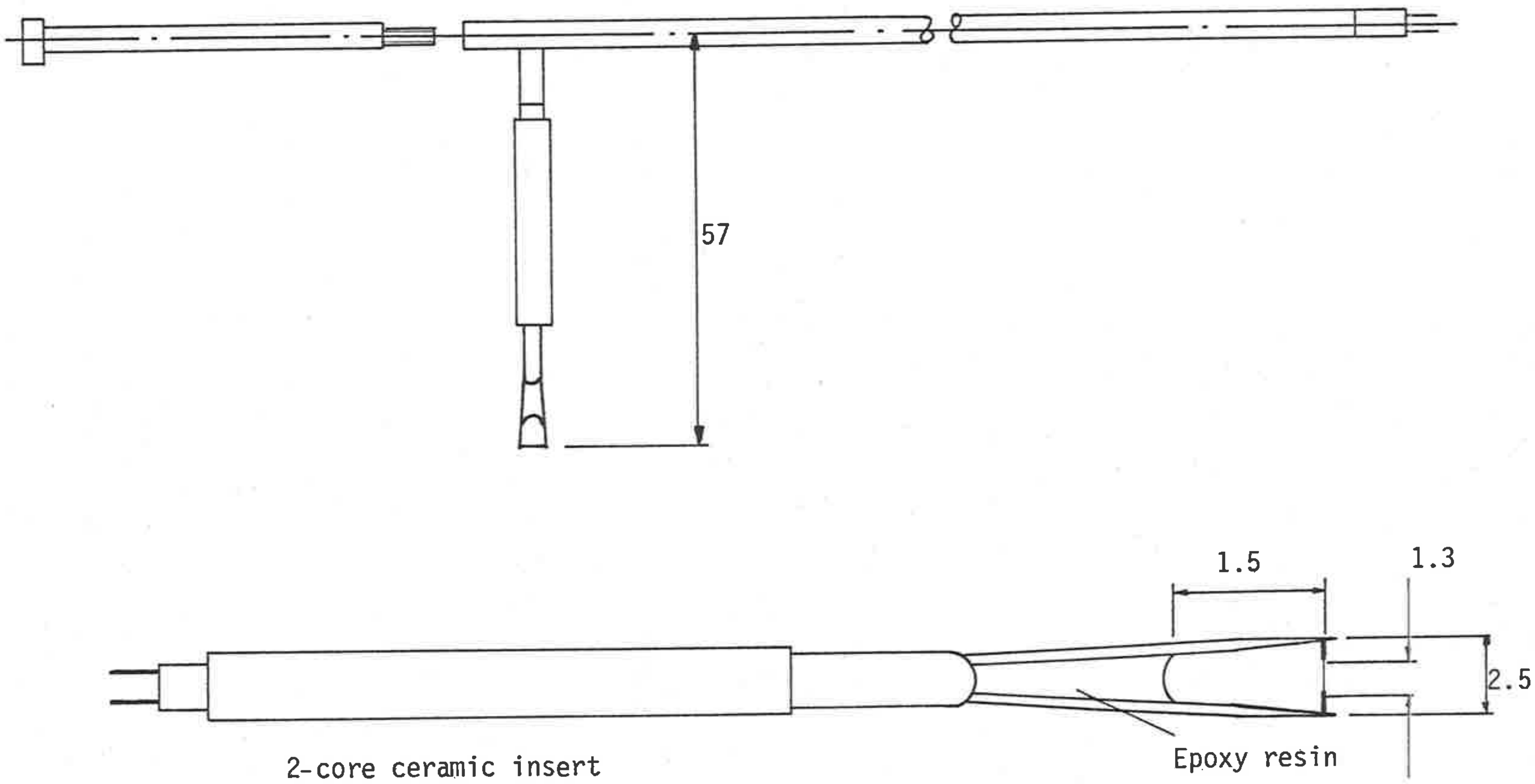

FIGURE 3.11 : HOT WIRE PROBE (not to scale)
(all dimensions in mm)

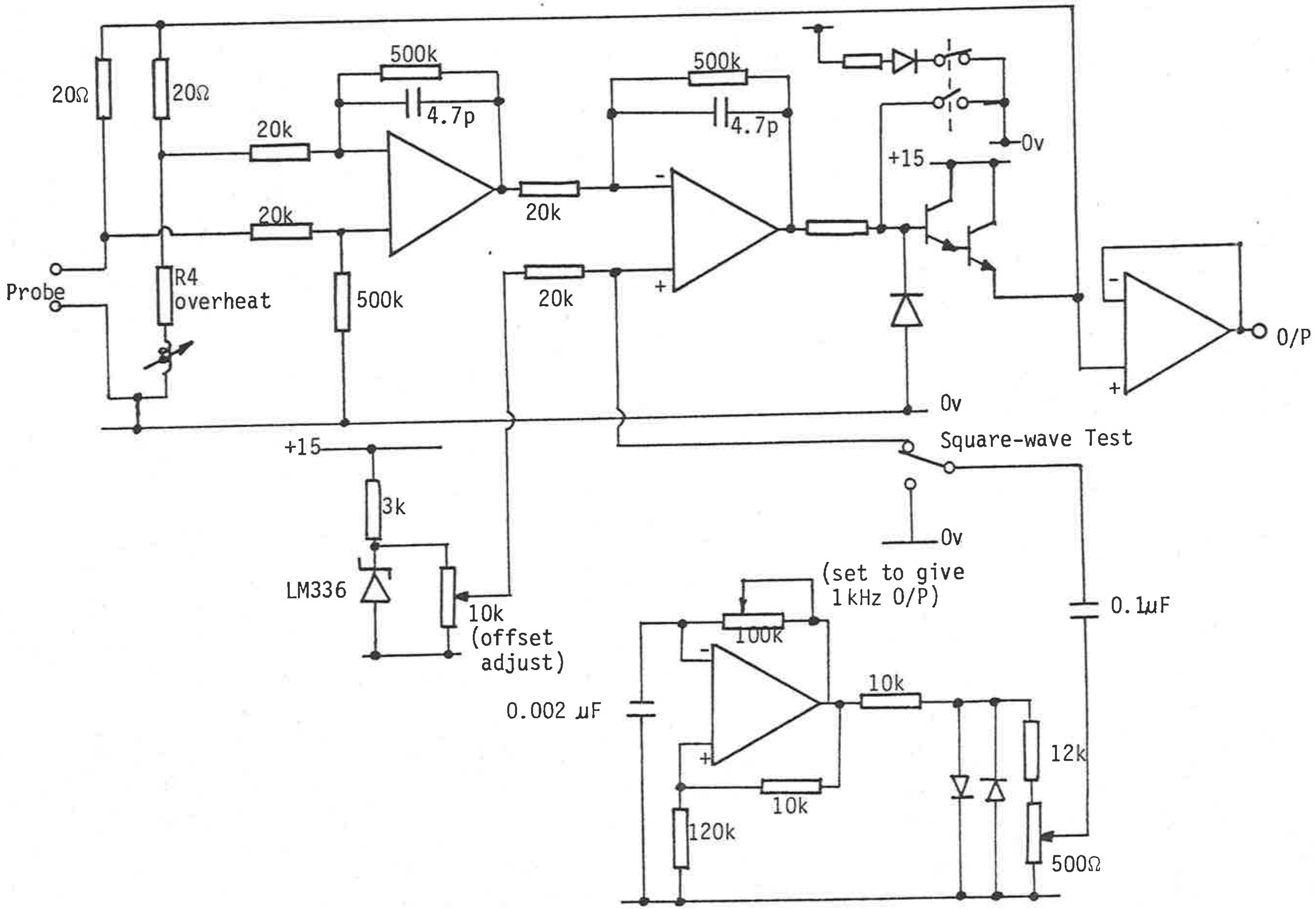

FIGURE 3.12 : CONSTANT TEMARATURE ANEMOMETER BRIDGE

A telescope in the rig, shown in Figure 3.7, is used to align the wire correctly in the pipe section, and to measure the distance of the wire from the pipe wall at the traverse extremities. The telescope is carried by a micro-manipulator (capable of motion in three perpendicular directions), mounted on a stainless steel plate which can be bolted to the pipe section. The plate is located relative to the pipe bore by a spigot similar to the one used on the pipe sections.

The hot wire is operated at an overheat ratio of 1.5 in the constant temperature anemometer bridge, shown in Figure 3.12. Prior to measurement, the time response of the wire and associated feedback loop is adjusted by changing the offset to give a square-wave-test frequency response of the system of at least 40 kHz.

The hot wire was calibrated over the full range of pipe flow-speeds in the pipe rig, in situ, by locating it on the pipe centre-line and altering the flow speed by changing the sonic chokes. Velocities at the position of the wire in the flow were already known from previous pitot tube measurements. Calibration in the low velocity region was also checked by calibrating the wire in the core region of a circular jet.

The difficulties of making accurate hot wire measurements in compressible flows are well known. Therefore, in the present work, quantitative velocity and turbulence measurements have been confined to cases where the Mach number does not exceed ~ 0.25.

Where power spectral density measurements of velocity fluctuation are required only for identification of the frequencies of spectral peaks, measurements with the uncalibrated wire are adequate.

Hot Film Shear Gauge

Mean and fluctuating wall shear stresses have been measured by means of a hot film gauge of the type described in detail by Thomas (1977). Nickel was chosen for the film material because of its relatively high temperature coefficient of resistivity ($6.7 \times 10^{-3}/°C$) and also because of its high adhesion on glass which is used as a substrate. The dimensions of the rectangular film parallel to and at right angles to the flow direction are 0.25mm and 0.5mm respectively. The gauge, shown in Figure 3.13, has a 4.75mm diameter steel body, and can be flush mounted with the pipe wall using the same brass instrumentation plugs as for pitot tube and fence gauges.

Bellhouse and Schultz (1966) used heated platinum films for mean and dynamic friction measurements in both laminar and turbulent flows and verified the applicability of the one third power calibration law (heat transfer rate proportional to $\tau_w^{1/3}$). Brown (1967) again verified the one third power calibration law and obtained identical mean calibrations from his experiments in laminar and turbulent flows. This has been further confirmed by later work of Owen and Bellhouse (1970), Rebesin, Okuno, Mateer and Brosh (1975) and Murthy and Rose (1978).

In early work, the hot film gauges were calibrated in the laminar boundary layer in a wind tunnel, their output being

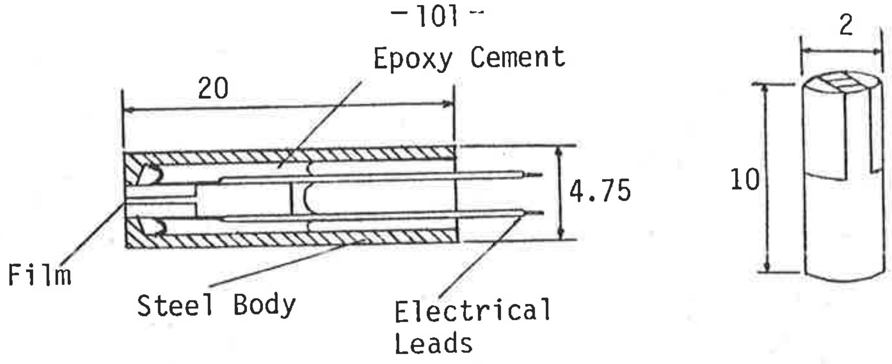

FIGURE 3.13: DETAILS OF A HOT FILM

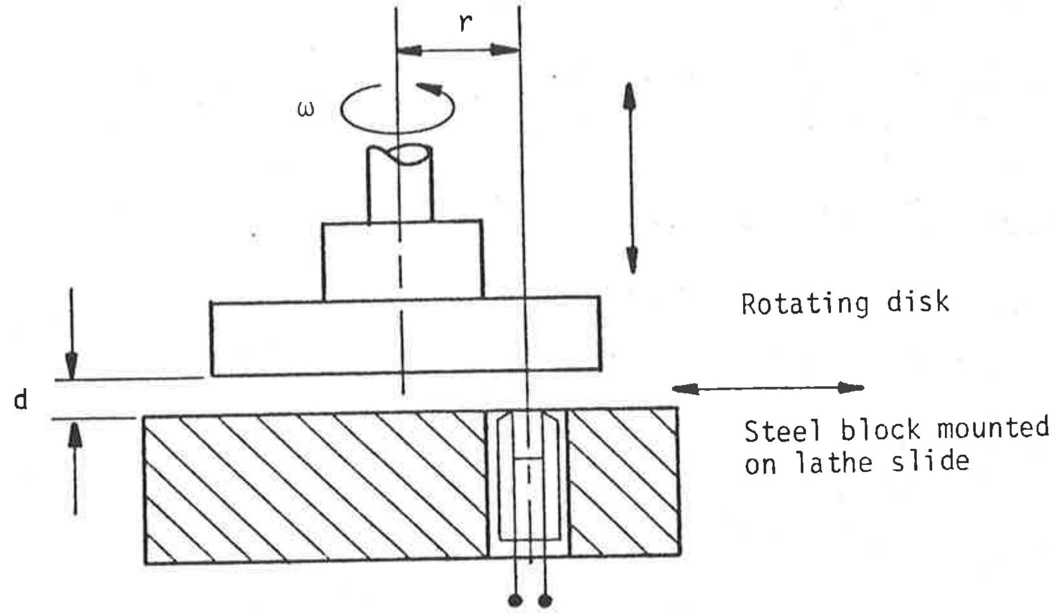

FIGURE 3.14: SPINNING DISK ARRANGEMENT FOR CALIBRATING THE HOT FILM

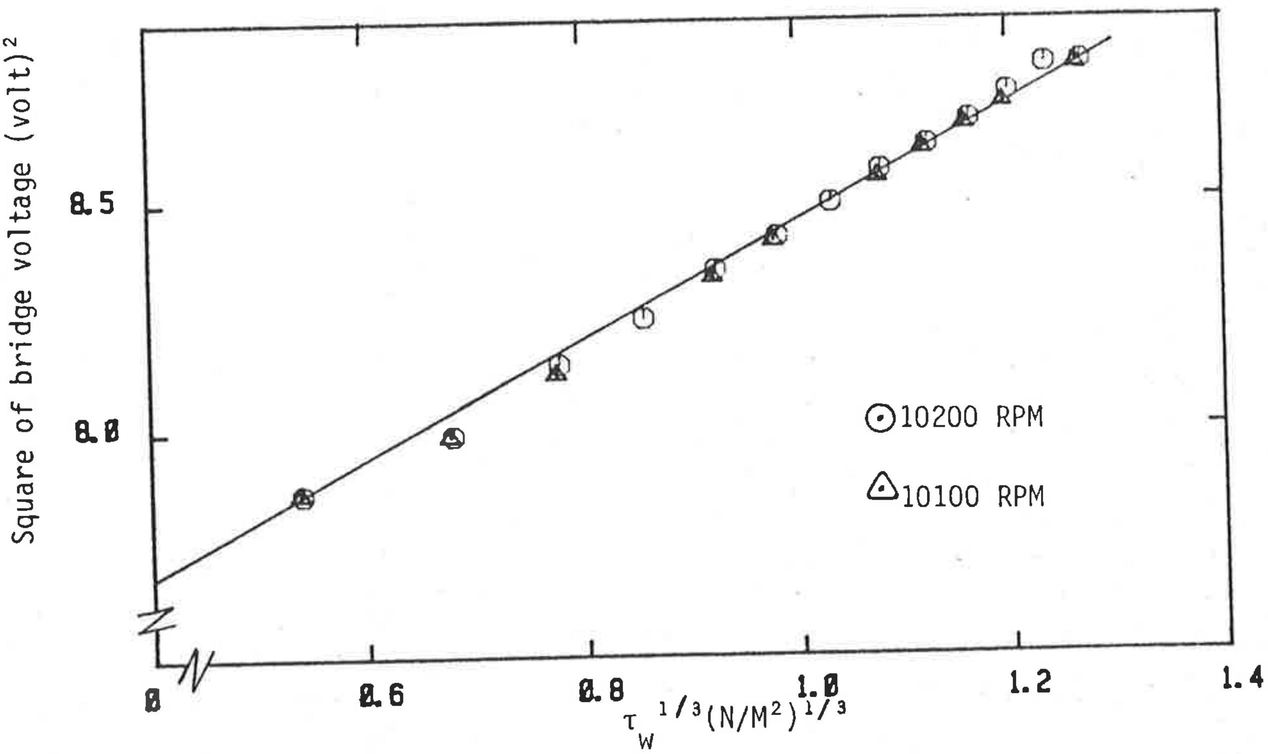

FIGURE 3.15 : A TYPICAL HOT FILM CALIBRATION CURVE

compared with that of a Preston tube. An alternative method of calibration, utilising the flow between a flat plate and a disk rotating in a plane parallel to it and calculated values of τ_w, was introduced by Brown and Davey (1971). In the present work, a similar calibration rig was used (Figure 3.14). In this rig, the hot film is flush mounted in a 150mm × 80mm × 30mm steel block, the top surface of which has been carefully ground flat. The spacing between the block and rotating disk (also accurately ground flat) mounted above and parallel to it can be varied. The block can be traversed radially beneath the disk to vary the shear stress at the film. A spacing of 0.25mm and speed in the range of 8500 to 10500 rpm is normally used for calibration.

The basis for the calibration is the theoretical solution for the shear stress in the flow between the plate and the steel block. For an angular velocity, ω and gap, d and small Reynolds number ($= \omega d^2/\nu$), the magnitude of shear stress at the film is given by (Brown and Davey, 1971),

$$\tau_w = \mu(\omega r/d)(1+Re^2/1050+\ldots) \qquad (3.3)$$

For Re less than 5, the first term gives τ_w within 3%.

Typically a hot film has a resistance of about 5 ohms, and is operated in a constant temperature bridge at an overheat ratio of 1.2. A typical calibration curve of such a gauge is shown in Figure 3.15.

3.4.3 Wall Pressure Transducers

Piezoelectric transducers and Bruel and Kjaer (1/4" - 6.35mm) condenser microphones were used to measure the wall pressure fluctuations.

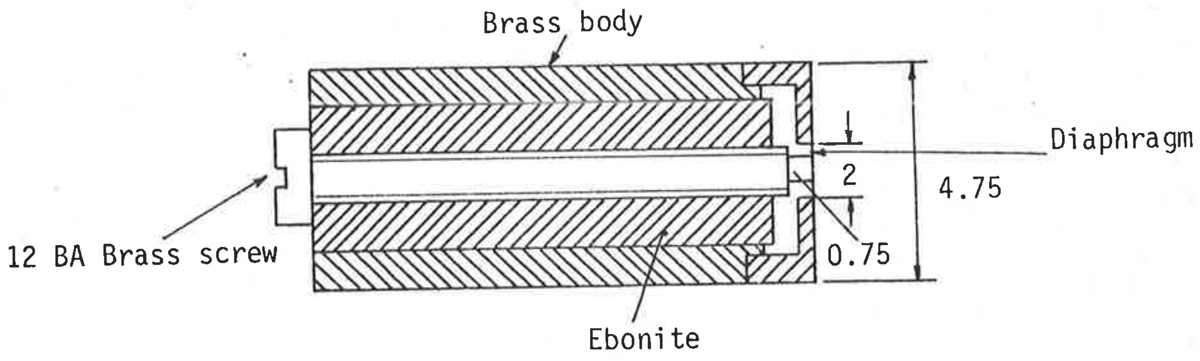

FIGURE 3.16 : DETAILS OF THE PIEZOELECTRIC PRESSURE TRANSDUCER (all dimensions in mm)

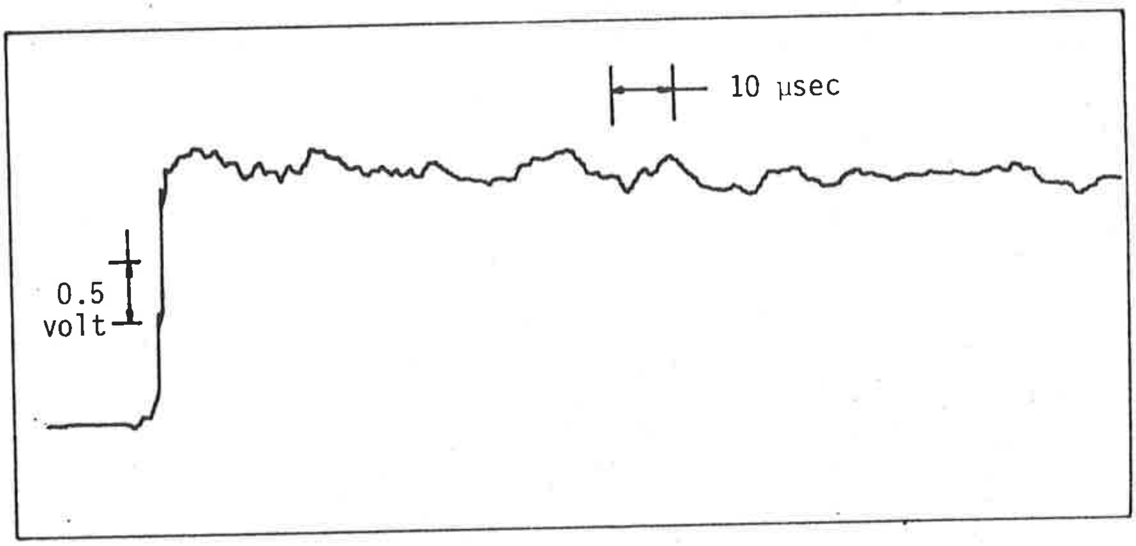

FIGURE 3.17 : A TYPICAL OSCILLOSCOPE TRACE OF THE RESPONSE OF THE PRESSURE TRANSDUCER IN A SHOCK TUBE

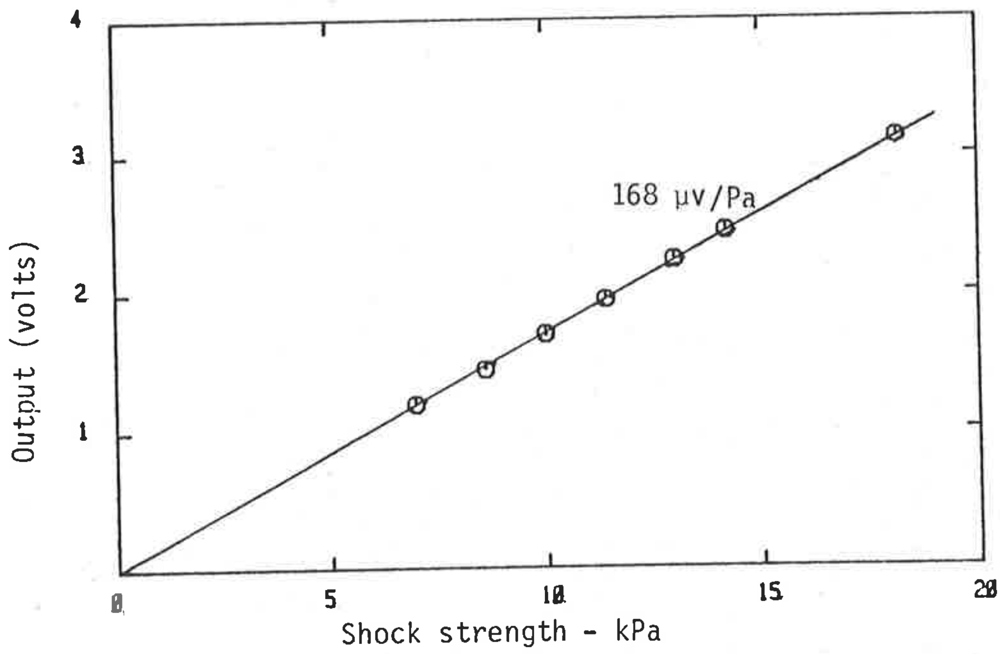

FIGURE 3.18 : A TYPICAL SHOCK TUBE CALIBRATION CURVE

Piezoelectric Pressure Transducers

Initially piezoelectric transducers were used in preference to the condenser microphones because of their simplicity, higher attainable frequency response characteristics and smaller sensing area. The transducers used in the present work are of the type described by Bull and Thomas (1976) and can be mounted in the brass instrumentation plugs. However, piezoelectric transducers are sensitive to vibration, and this coupled with electronic noise can contaminate the true wall pressure fluctuation signal. Therefore, the pressure transducer is always dampened with plasticine⊛, Its response to vibrational effects of the rig was investigated by comparative measurements with the transducer exposed to the flow and with it pulled back in the instrumentation plug by 2-3mm and blanked off from the flow with a steel plug. The spectral density of the signal obtained from the latter configuration is always less than 1% of that obtained from the former. The spectral density of the electronic noise is generally 40-80 dB less than that with flow, depending on the flow disturbance. Details of the piezoelectric transducer used (from Bull and Thomas (1976)) are shown in Figure 3.16.

Two methods are used to calibrate the transducers:

(i) measurement of its response to the passage of a shock wave of known strength over its face, and

(ii) comparison of the response of the transducer with that of a calibrated microphone when both are mounted in an acoustic coupler.

In the first method, the transducer is mounted flush with the wall of a 40mm × 65mm rectangular shock tube and shocks

⊛ placed around the transducer stem.

of various known strengths are passed over the face of the transducer, to determine its sensitivity, linearity and frequency response. The voltage rise at the transducer output is determined from oscilloscope traces.

The magnitude of the pressure rise across the shock may be calculated from the initial conditions in the shock tube by using the approximate shock tube relation (Bannister and Mucklow, 1948)

$$\left[\frac{p_2}{p_1}\right]^{1/7} = \frac{2}{1 + (p_1/p_4)^{1/7}} \tag{3.4}$$

where

p_1 = static pressure ahead of shock,

p_2 = static pressure behind the shock,

p_4 = initial pressure in the high pressure chamber of the shock tube, and

ΔP = (p_2-p_1) = pressure drop across the shock front.

(Note that ΔP can also be evaluated by computing the speed of the shock from the time it takes to pass between two timing transducers in the wall of the shock tube. Checks were made with this method to show that both yielded similar results, timing being measured by a Systron Donner Counter Timer Model 6150. A typical oscilloscope trace and calibration curve are shown in Figures 3.17 and 3.18 respectively. The progressive fall of the output voltage, after the initial rise due to the shock is attributable to the lack of low frequency respone of the transducer-amplifier combination.

In the second calibration procedure the pressure transducer and a 1/8" Brüel and Kjaer microphone are both subjected to acoustic pressures, generated by an electromagnetic acoustic

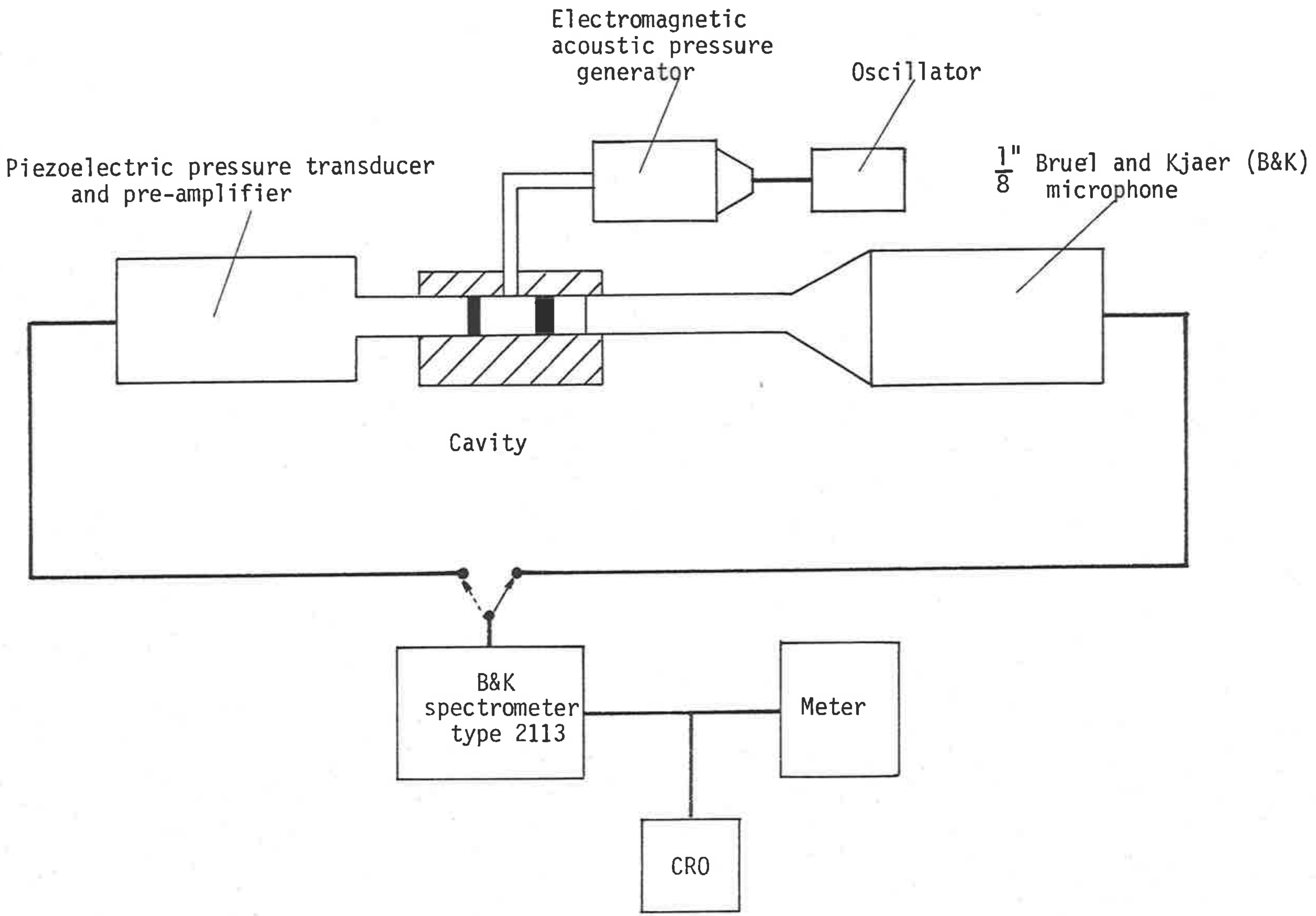

FIGURE 3.19 : SCHEMATIC OF ACOUSTIC COUPLER CALIBRATION

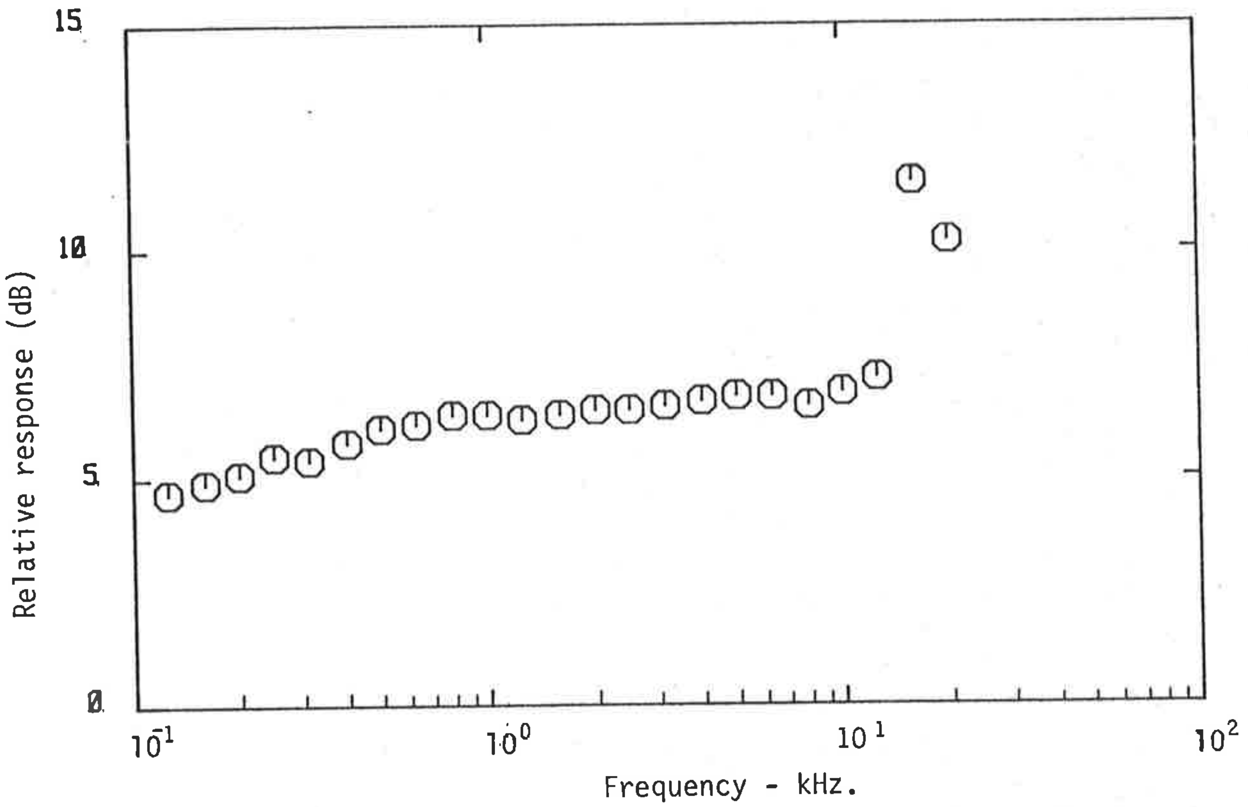

FIGURE 3.20 : FREQUENCY RESPONSE OF A PIEZOELECTRIC TRANSDUCER USING A BRUEL & KJAER (1/8") MICROPHONE WITH AN ACOUSTIC COUPLER

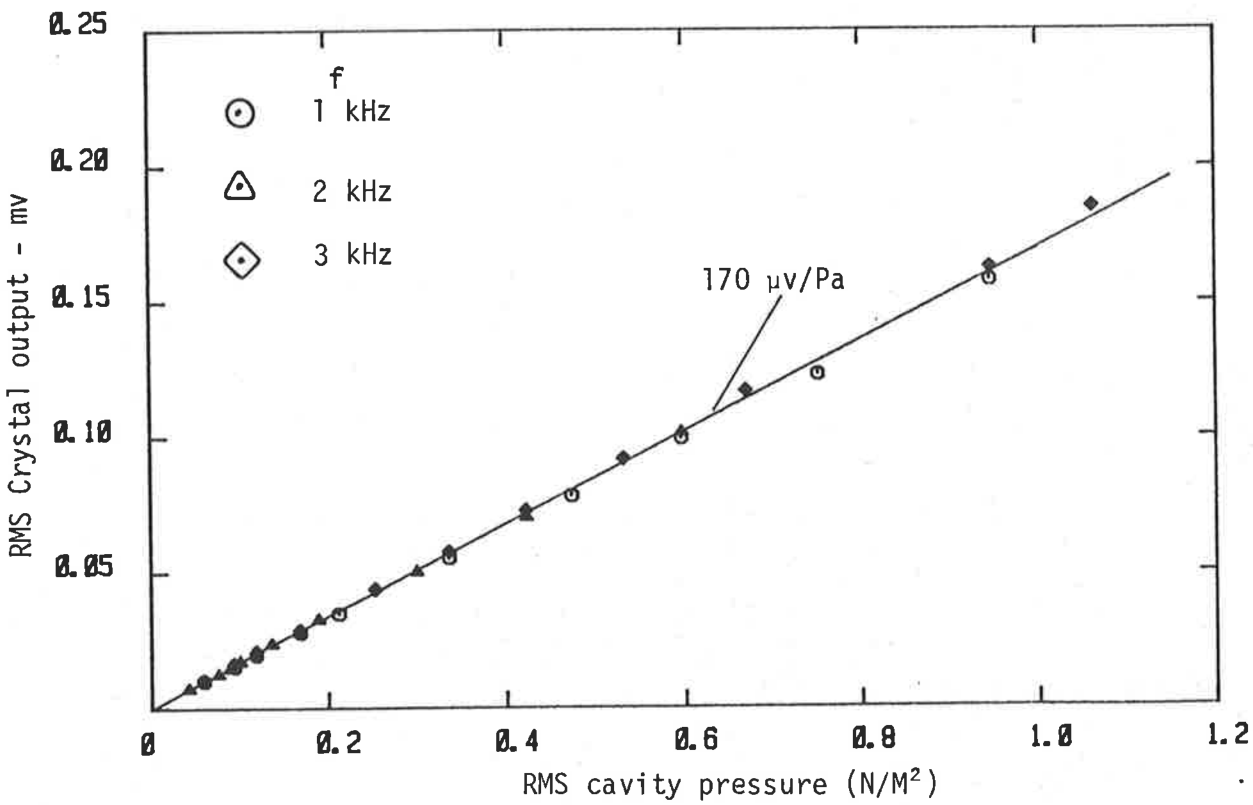

FIGURE 3.21 : PRESSURE TRANSDUCER CALIBRATION WITH ACOUSTIC COUPLER

pressure generator driven by an oscillator at discrete frequencies, in a cavity 3.5mm in diameterand 1.5mm in length. A diagram of the arrangement is shown in Figure 3.19.

Silicone grease is used to seal the joints to make sure that no air leaks are present. Calibration measurements are made at one-third octave intervals, and the cavity is sufficiently small to allow calibration to be made at frequencies in the range $20 \leq f \leq 10{,}000$ Hz. This calibration procedure is similar to that used in previous investigations by Bull and Thomas (1976) and Bull and Langeheineken (1981). It can be seen from Figure 3.20 that a flat response is obtained for frequencies from about 80 Hz to 10 kHz with small deviations occuring at higher frequencies owing to wave effects in the cavity. Figure 3.21 shows the linearity of the pressure transducer with pressure amplitude at frequencies 1, 2 and 3 kHz. The transducer sensitivity obtained in this way is generally within 2% of that obtained with the shock tube.

The piezoelectric transducer is mounted in a brass instrumentation plug, so that on its centreline parallel to the flow direction it is accurately flush with the pipe surface. There is then a discontinuity between the flat face of the transducer and the cylindrical surface of the pipe, varying around the circumference of the transducer face from zero at upstream and downstream extremities to a maximum of 0.07mm on the centreline of the face transverse to the flow direction. Bull and Langeheineken investigated the effect of this cavity (which was 0.13mm in their case) and found that results were not altered by its presence. Measurements were therefore made with the transducer mounted in the plug as shown in Figure 3.22.

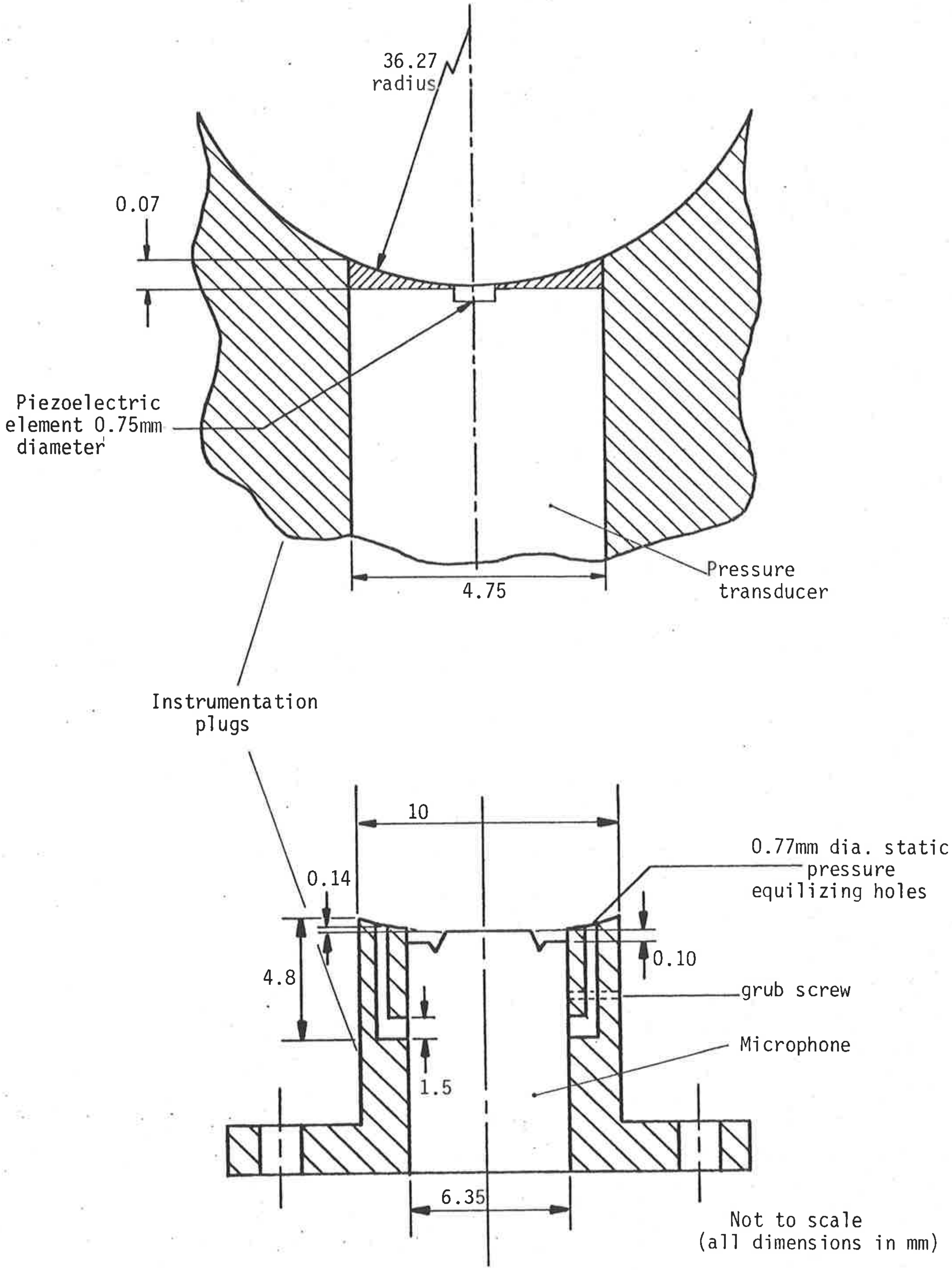

FIGURE 3.22 : INSTALLATION OF A PIEZOELECTRIC TRANSDUCER AND A MICROPHONE IN PIPE WALL SURFACE

Microphone transducers

Condenser microphones offer a higher sensitivity than piezoelectric transducers and are less sensitive to structural vibration. In the initial stages of the investigation, they were used as a check on the results obtained with piezoelectric transducers, but later they were used in the separation of higher order acoustic modes in the pipe. For the latter purpose, Brüel and Kjaer 6.35mm, (1/4") condenser microphones can be mounted in brass instrumentation plugs, fitted to a special instrumentation pipe section, shown in Figure 3.23. The pipe section has three sets of eight circumferentially equispaced instrumentation plugs.

The condenser microphone is used with its diaphragm (sensitive area diameter 4.2mm) directly exposed to the flow and is mounted in the plug with the face of the diaphragm flush with the pipe surface on the centreline in the direction of flow; this results in a discontinuity varying from 0 to 0.14mm around its circumference. However, the flat face of the diaphragm does not extend right to the edge of the microphone body (Figure 3.22), and as a result there is also a double discontinuity on the longitudinal centreline, up to 0.1mm deep. Tests by Langeheineken (1977) established that these irregularities have negligible effect on the measured power spectral density of the wall pressure.

Because the microphones are required to operate in a region of mean static pressure below atmospheric it is necessary to make provision for equalisation of the mean static pressure across the microphone diaphragm. For this purpose

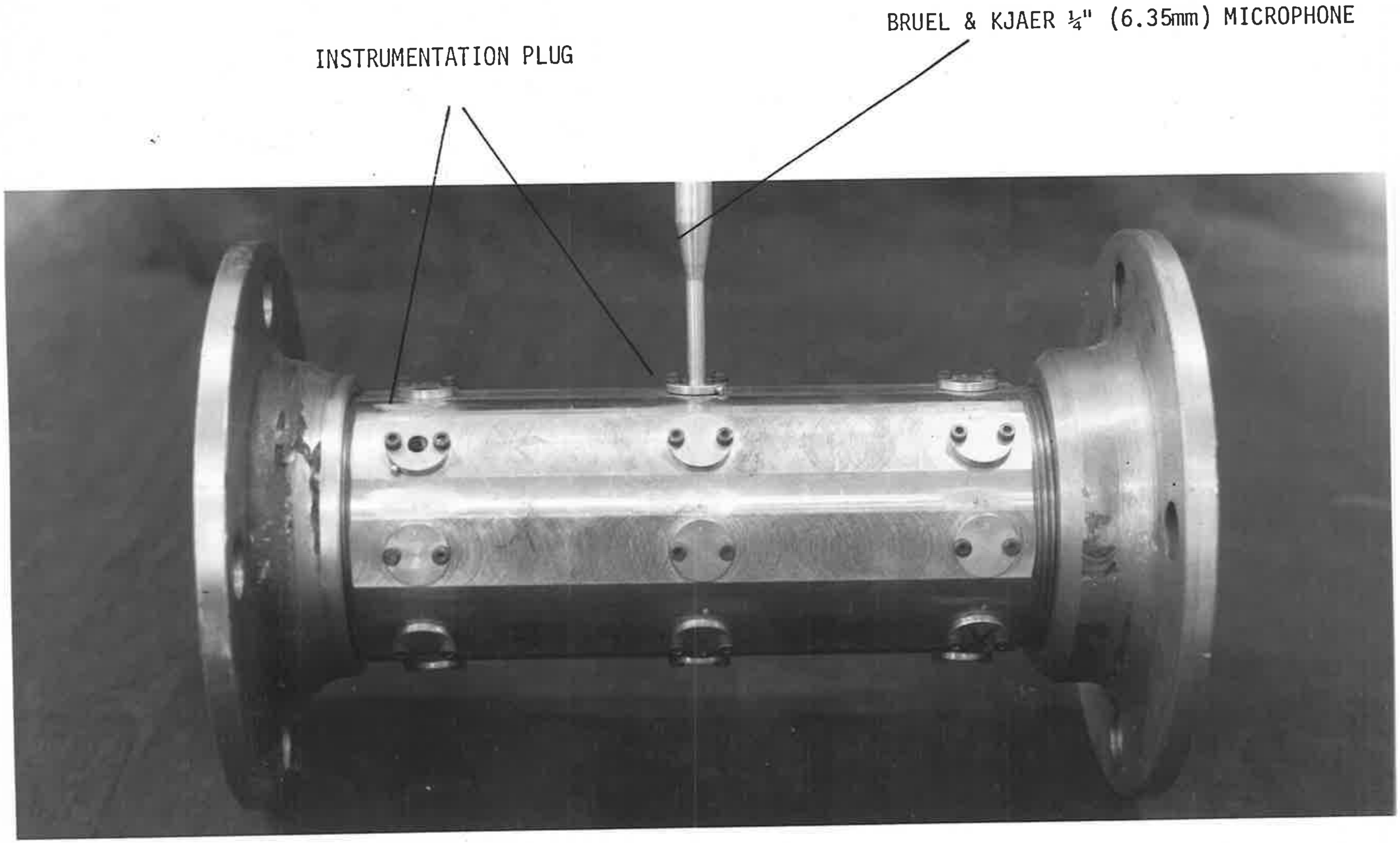

FIGURE 3.23 : INSTRUMENTATION SECTION WITH WALL MICROPHONES

a 0.77mm hole was drilled on either side in the instrumentation plug leading to the pressure equilization holes in the microphone (refer Figure 3.22). The frequency response of the condenser microphones is assumed to be in accordance with the manufacturer's open circuit pressure response calibration, which shows it to be constant over the range $20 < f < 25{,}000$ Hz. Microphones are used in conjunction with the Brüel & Kjaer pre-amplifier (type 2619) and spectrometer (type 2112), on linear frequency range (20 Hz to 200,000 Hz). The calibration of the microphone - pre-amplifier - spectrometer combination was always checked with a pistonphone (Brüel and Kjaer, type 4230).

CHAPTER 4

DATA ACQUISITION AND ANALYSIS

4.1 Introduction

In this chapter techniques used for the data acquisition and analysis are discussed.

All data (except those relating to modal separation, where the analogue signals were recorded on a F.M. Tape recorder), were obtained by direct digitization and stored for further processing. Since the time for which the flow in the pipe remains choked is small (e.g. 6 seconds with choke D_C = 0.86), it is necessary to acquire the data as soon as the flow has stabilized after the quick-acting solenoid valve is opened. It is also required to start various instruments at the same time as the data acquisition starts, and to turn them off at the end of the data acquisition. Therefore it is convenient to control the data acquisition by means of a mini-computer; parameters such as sampling frequency, number of samples, interval between sets of samples, traverse drive time and time delay between successive triggerings of the Hewlett-Packard spectrum analyser are controlled through software.

Most of the mean flow data have been acquired using a 10-bit analogue-to-digital (A/D) converter in conjunction with a PDP 11/34 computer. A 12 bit A/D converter and an LSI 11 computer have been used for wall pressure fluctuation and velocity fluctuation measurements. Mean flow data were analysed on the PDP 11/34 computer operating on the Unix-system, and the fast Fourier transforms and cross-correlation calculations were performed on 64 bit Control Data Corporation Cyber 173 computer.

4.2 PDP 11/34 and 10 Bit Converter

The DEC PDP 11/34 system of the Department of Mechanical Engineering at the University of Adelaide is a 16 bit machine with two RK05 hard discs, and is interfaced with a 10 bit analogue-to-digital (A/D) converter. The A/D converter is connected through a multiplexor to 16 data channels, and is capable of making measurements at up to 30,000 samples per second [Fig. 4.1]. A maximum of 3 channels were used for the present work (e.g. for measurements of velocity profile across the pipe: Ch.1, static pressure; Ch.2, total pressure; Ch.3, position monitor). TTL signals from the PDP 11/34 are used for operating the solenoid valve, probe traverse (either in continuous mode with the traverse moving continuously and signal samples being taken at set time intervals, or in the stop/start mode in which the traverse moves for a specified distance and then stops for a specified time to acquire a specified number of samples) and the H.P. spectrum analyser. The time required for the HP analyser to acquire and process one set of samples depends on the frequency span setting; it varies from about 0.5 seconds for a 25 kHz span to about 10 seconds for a 25 Hz span. It was used in its external triggering mode for the spectral measurements, using a TTL pulse to initiate collection of each new set of samples, within the duration of choked flow. A typical data acquisition procedure used is shown in Figure 4.2. Data were stored on an RK05 disk, and later copied on to magnetic tape for further processing on the Cyber.

4.3 12 Bit A/D Converter and LSI-11 System

While the 10 bit A/D converter is adequate for mean flow measurements, a faster converter with better resolution is required for measurements of fluctuating quantities, and for this purpose a 12 bit A/D converter in conjunction

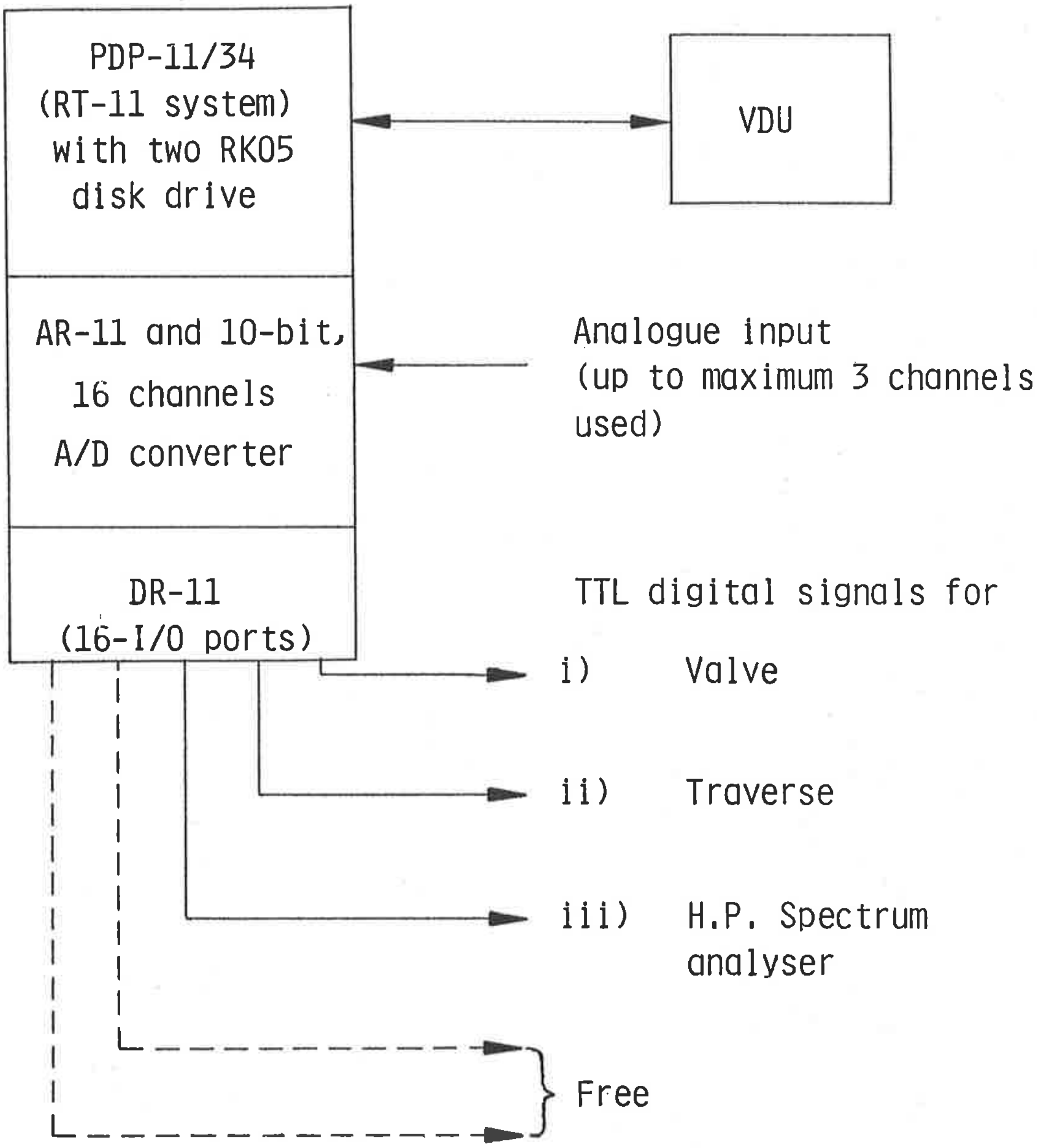

FIGURE 4.1 : PDP 11/34 AND 10-BIT (16 channels) A/D CONVERTER DATA ACQUISITION SYSTEM

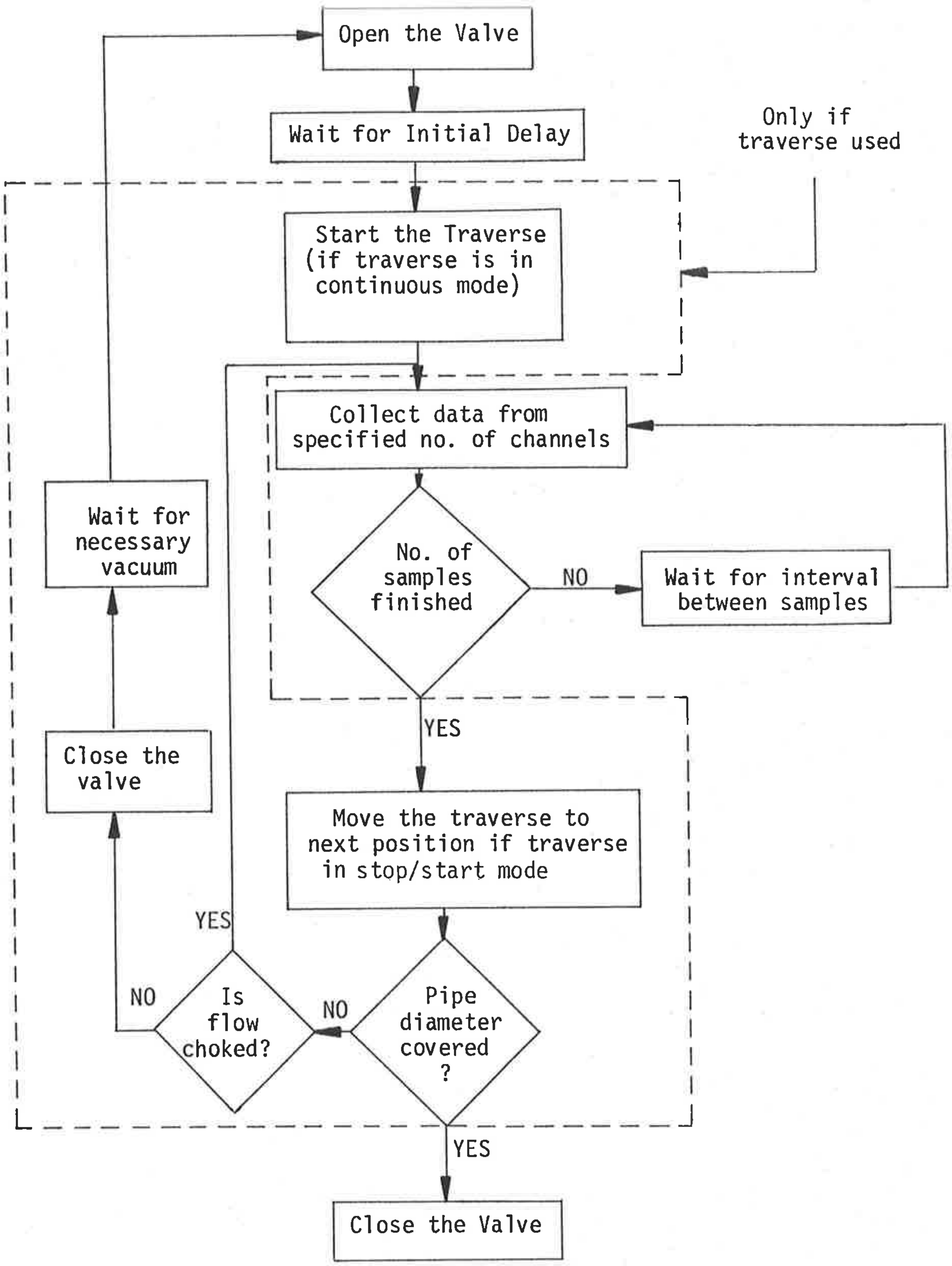

FIGURE 4.2 : A TYPICAL DATA ACQUISITION PROCEDURE

with a microprocessor (Type MPF-I, manufactured by Multitech, USA) and an LSI-11 minicomputer, as shown in Fig. 4.3, is used. The microprocessor has 2 programmable PIO's (Peripheral input/output ports), one of which is used for hand-shaking with the LSI-11 and the other for obtaining 5 volt TTL signals for operating various devices. There are three input and output ports (8 bits each), which are used to set the A/D converter and send the start/convert pulse to it. A diagram of the data acquisition system, various ports and front view of the microprocessor is shown in Figure 4.4. A crystal clock of frequency 1.79 MHz in conjunction with 4 independent counter timers in the microprocessor is used to generate various waveforms for the sampling frequency, interval between sample sets, initial delay, timing for traverse and valve operation. A typical example of waveform generation for data acquisition at the rate of 2000 per second from three channels with the traverse in continuous mode is shown in Figure 4.5.

A series of instructions written in Z80 code to operate the microprocessor in one of the following modes is loaded into the memory of the microprocessor through its keyboard.

Mode	Device in Use
1	Valve + A/D converter
2	Valve + Traverse (in continuous mode) + A/D converter
3	Valve + Traverse (in stop/start mode) + A/D converter
4	Valve + A/D converter + HP analyser
5	Valve + HP spectrum analyser

The microprocessor is controlled by the software running on the LSI-11 through an 8 bit line (one way); for example, the first 8 bit block sent might contain information such as mode of operation, number

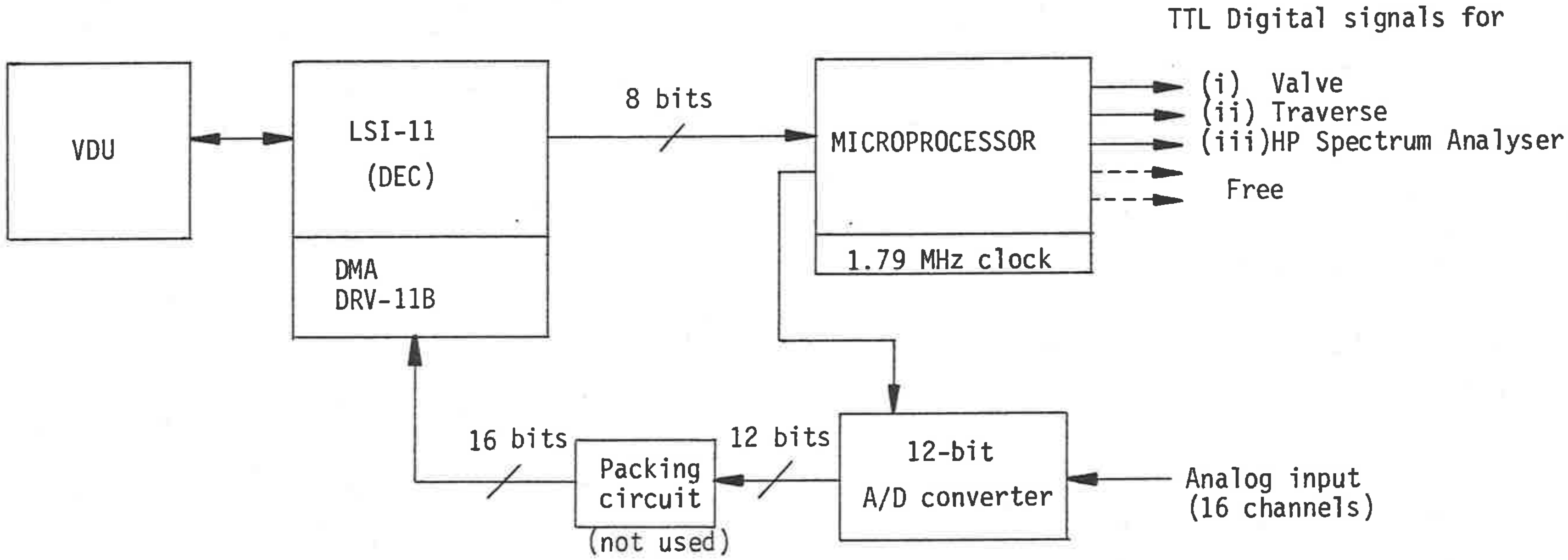

FIGURE 4.3 : LSI-11 AND 12-BIT A/D CONVERTER DATA ACQUISITION SYSTEM

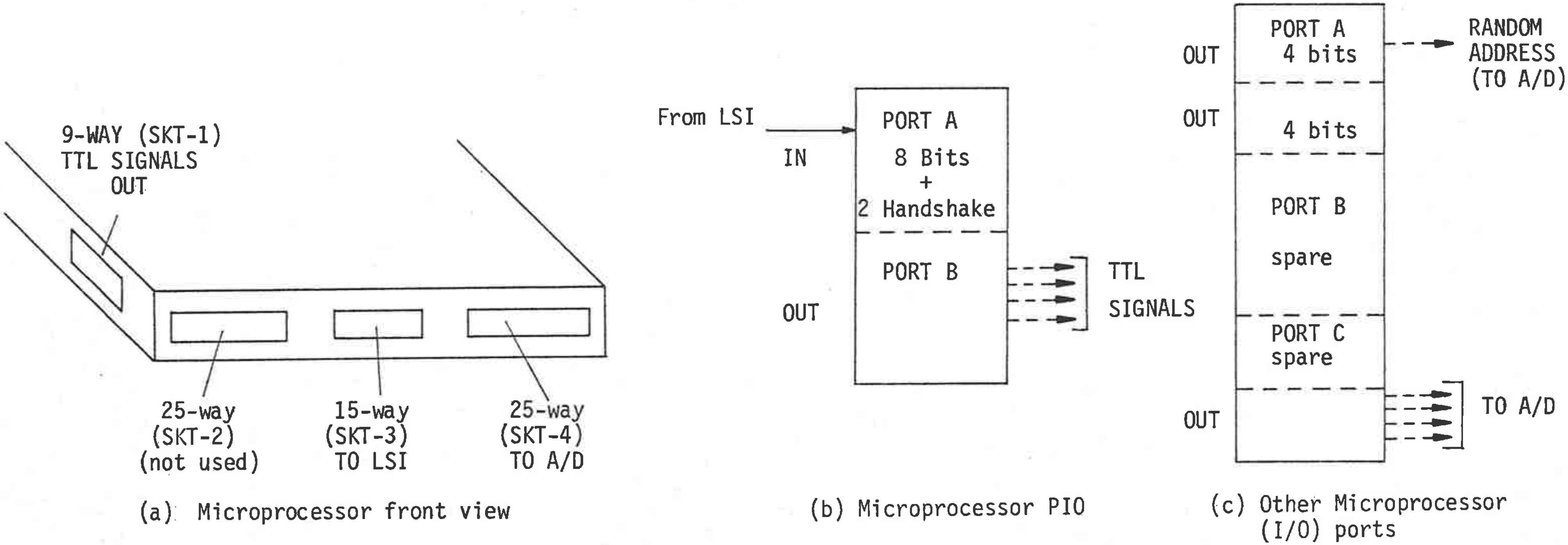

FIGURE 4.4 : MICROPROCESSOR DETAILS

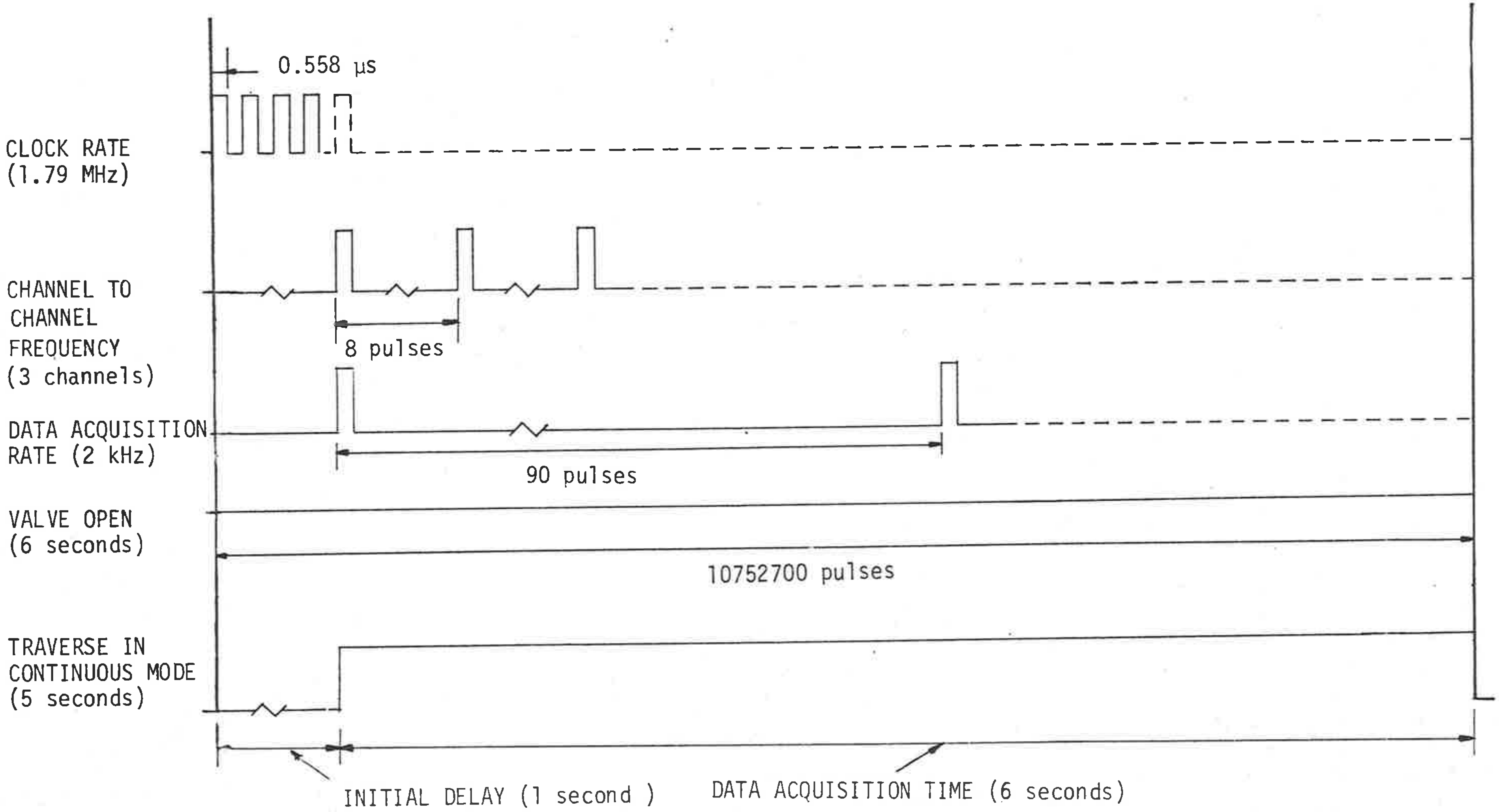

FIGURE 4.5 : A TYPICAL WAVE-FORM FOR SAMPLING THREE CHANNELS WITH TRAVERSE IN CONTINUOUS MODE

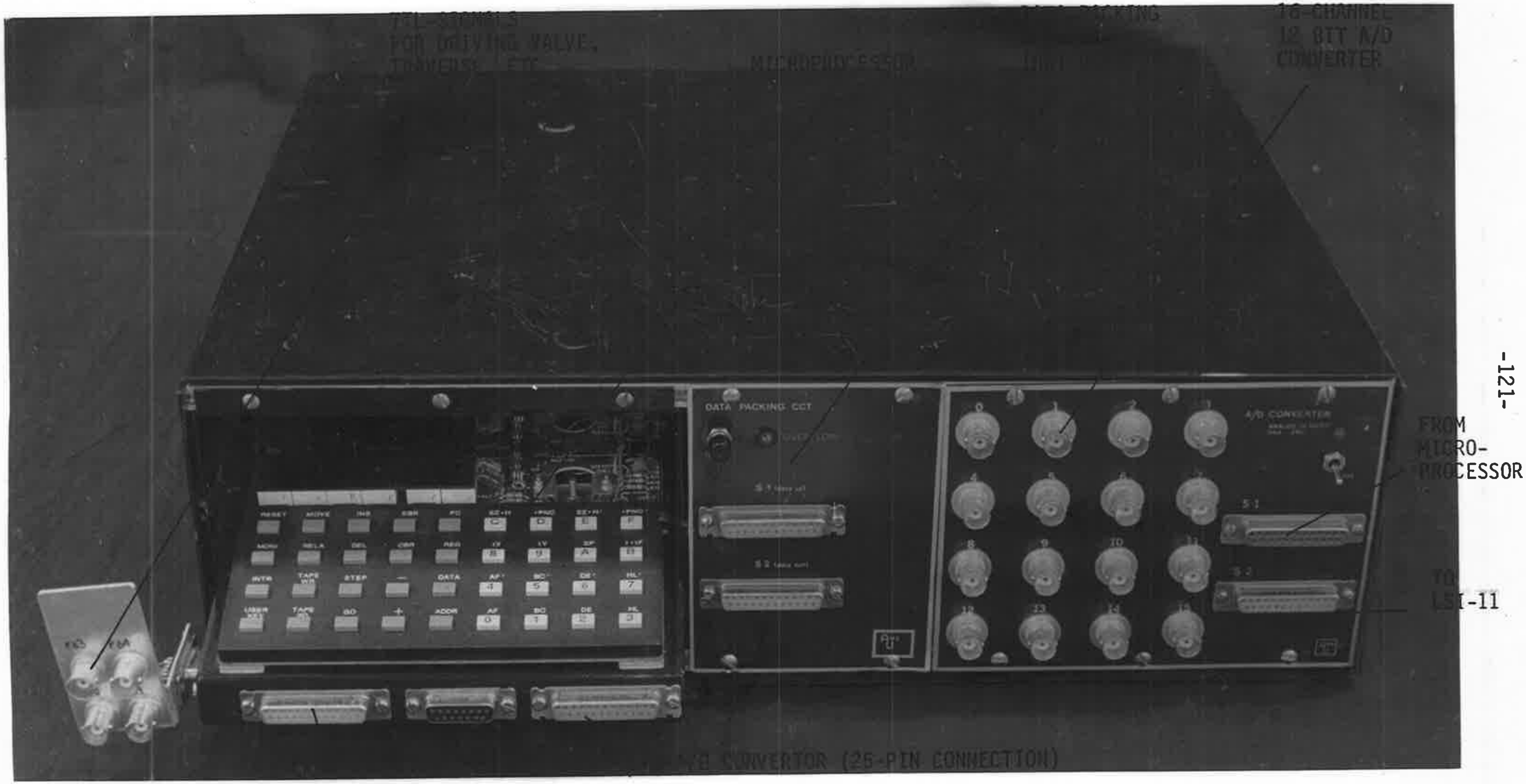

FIGURE 4.6 : DATA ACQUISITION SYSTEM

of samples, sampling frequency etc., while the next block might indicate the end of the data. Data samples are sent directly to the LSI-11's memory via a DMA (direct memory access) card. The data acquisition system is shown in Figure 4.6.

4.4 Offset Amplifier

The 12 bit A/D converter is set to operate on 0 to -10 volts and since most of the signals measured are positive, it is necessary to offset the signal to suit the range of the A/D converter. To obtain maximum resolution, variable gain is required to make use of the full range of the A/D converter (e.g. for a signal between +1.5 and +2.5 volts, an offset of -2.5 and gain of 10.0 would yield a signal of 0 to -10 volts).

Each of the A/D channels has an offset amplifier with the circuit shown in Figure 4.7. Electrical noise from the amplifiers is less than the resolution of the A/D converter (~ 2.5 milli volt) and maximum offset of ± 7.5 volts and gain up to 100 are possible. The offset amplifiers were always calibrated before use, and calibration of the A/D converter was constantly checked using a highly stable (± 0.1mv) DC voltage source (Datel DVC 8500). The offset amplifiers have a flat frequency response up to at least 50 kHz, at a gain of 100, and even better at lower gains.

4.5 Simultaneous Acquisition of Multichannel Data

Where strictly simultaneous acquisition of several data channels (up to four in fact) was required, the data were recorded on a 7-channel RACAL 'Store' FM tape recorder. Later the data were digitized, one channel at a time, using the LSI-11 data acquisition system.

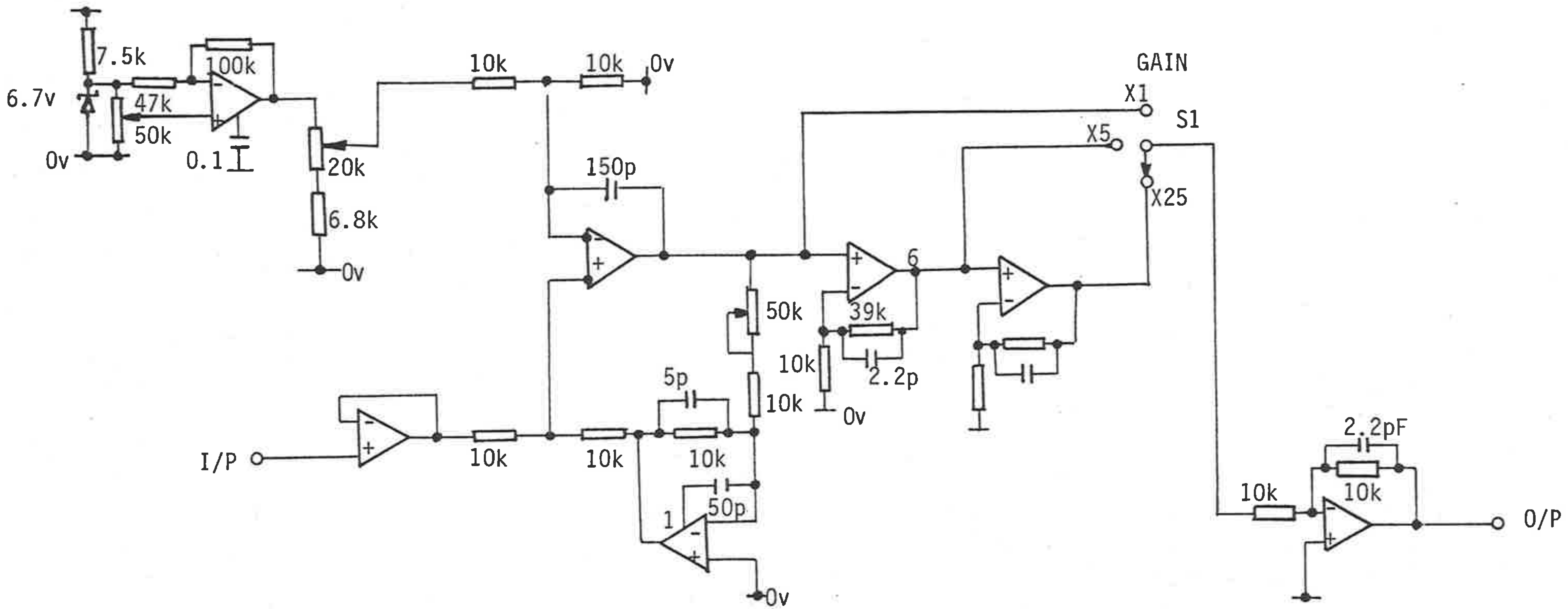

FIGURE 4.7 : OFFSET AMPLIFIER

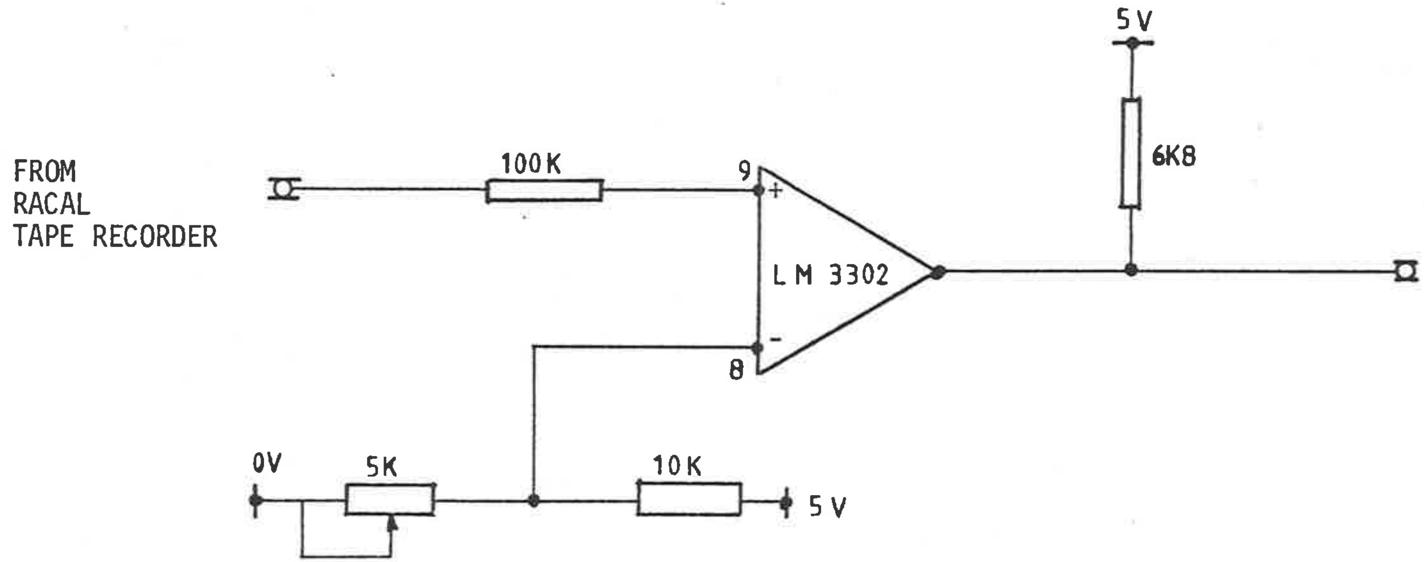

FIGURE 4.8 : SCHMITT TRIGGER

For this purpose a sine wave of 20 kHz is recorded on one of the spare channels slightly after the beginning of the analogue data, at the time of data recording. During play-back the sine wave is converted to a square wave using a Schmitt-trigger (refer to Figure 4.8), and the latter used as a start/convert pulse for the A/D converter.

A long analogue record is digitized in several runs, the tape being rewound to the beginning of the record each time. Because of the memory limitation of the LSI to about 20K, the procedure is as follows.

The microprocessor is not used and the A/D converter is set in the required mode by means of hard switches mounted on the A/D converter. After the first 20K samples have been digitized, the tape is rewound to the beginning and again the digitization started at the start of the pulse, but this time the first 20K samples acquired are overwritten by the next 20K samples, and so on. This process is repeated for each channel till the required length of signal is digitized. A schematic diagram of the play-back loop is shown in Figure 4.9.

As the analogue data and sine wave are recorded on the same tape, they are locked together, and the method gives the same results every time the same channel is digitized. The system is checked by processing a single channel of data recorded in this way and also using the H.P. spectrum analyser at the time of recording. Similar results are obtained as shown in Figure 4.10; the spectra are essentially the same except for some low frequency deviation. The Racal FM tape recorder provides a 0-20kHz frequency responce bandwidth at a tape speed of 60 inches per second with an FM centre carrier frequency of 108 kHz and a signal-to-noise ratio of 48 dB. Before being recorded, the

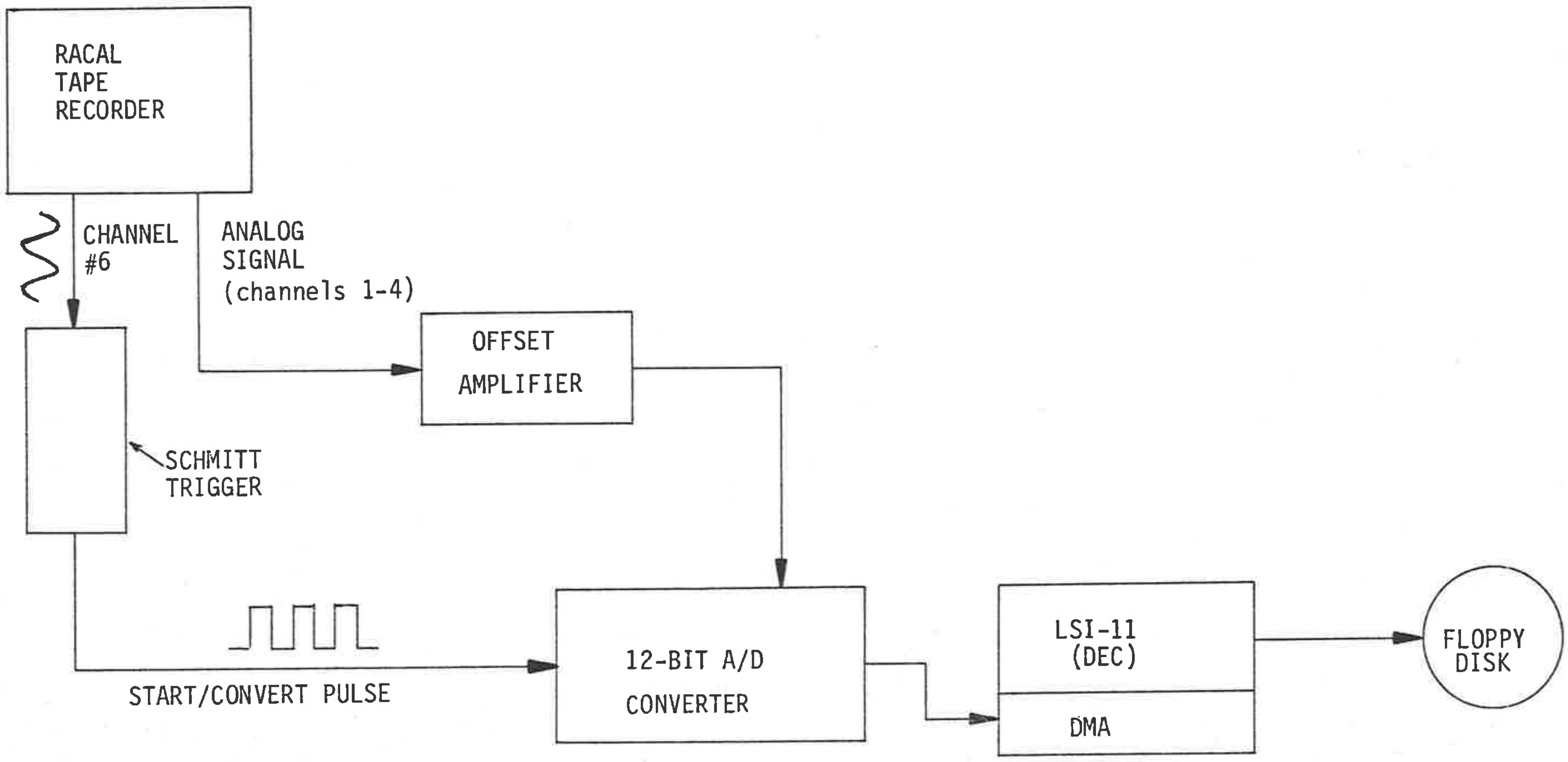

FIGURE 4.9 : TAPE PLAY-BACK LOOP

analogue signals are passed through an analogue dual 4-pole Butterworth low-pass filter with a cut-off frequency of 10 kHz. The signals are digitized at the rate of 20 kHz (limited by frequency response of tape recorder as the recorded and later modified sine wave signal is used as the start/convert pulse for the A/D converter) corresponding to a Nyquist or folding frequency (f_N) of 10 kHz, where

$$f_N = \frac{1}{2h} \tag{4.1}$$

and h is the sampling or digitizing interval. The analogue pre-filtering is necessary to avoid errors resulting from the "aliasing" phenomenon, described by Bendat and Piersol (1966) and Harris and Ledwidge (1974). Therefore, for the data analysed this way, the maximum frequency is limited to 10 kHz. Signals directly digitized were always low pass filtered at the maximum frequency of interest.

4.6 Frequency Analysis

The frequency spectrum of the fluctuating signal, as indicated in Section 4.4, is obtained by two methods. In the first method, the digitized signal (directly digitized in the case of single channel data or through recording on the Racal FM tape recorder in the case of multichannel data) is processed by using an efficient fast Fourier transform algorithm based on the Cooley-Tukey technique (1965) on the Cyber 173. In the second method, the fluctuating signal is fed to the H.P. spectrum analyser type 3582A, which is capable of analysing signals with frequency up to 25 kHz. Up to 256 averages are obtained (by running the rig several times) to get the required statistical accuracy. The HP analyser is interfaced with the LSI using the HP-IB interface (which is Hewlett Packard's implementation of IEEE Standard 488) provided with the instrument. Once the required number of averages is obtained, the trace of the spectrum consisting of digital data points at each of 256 frequencies (e.g. 100 Hz spacing over 25 kHz span) is transferred to the LSI memory.

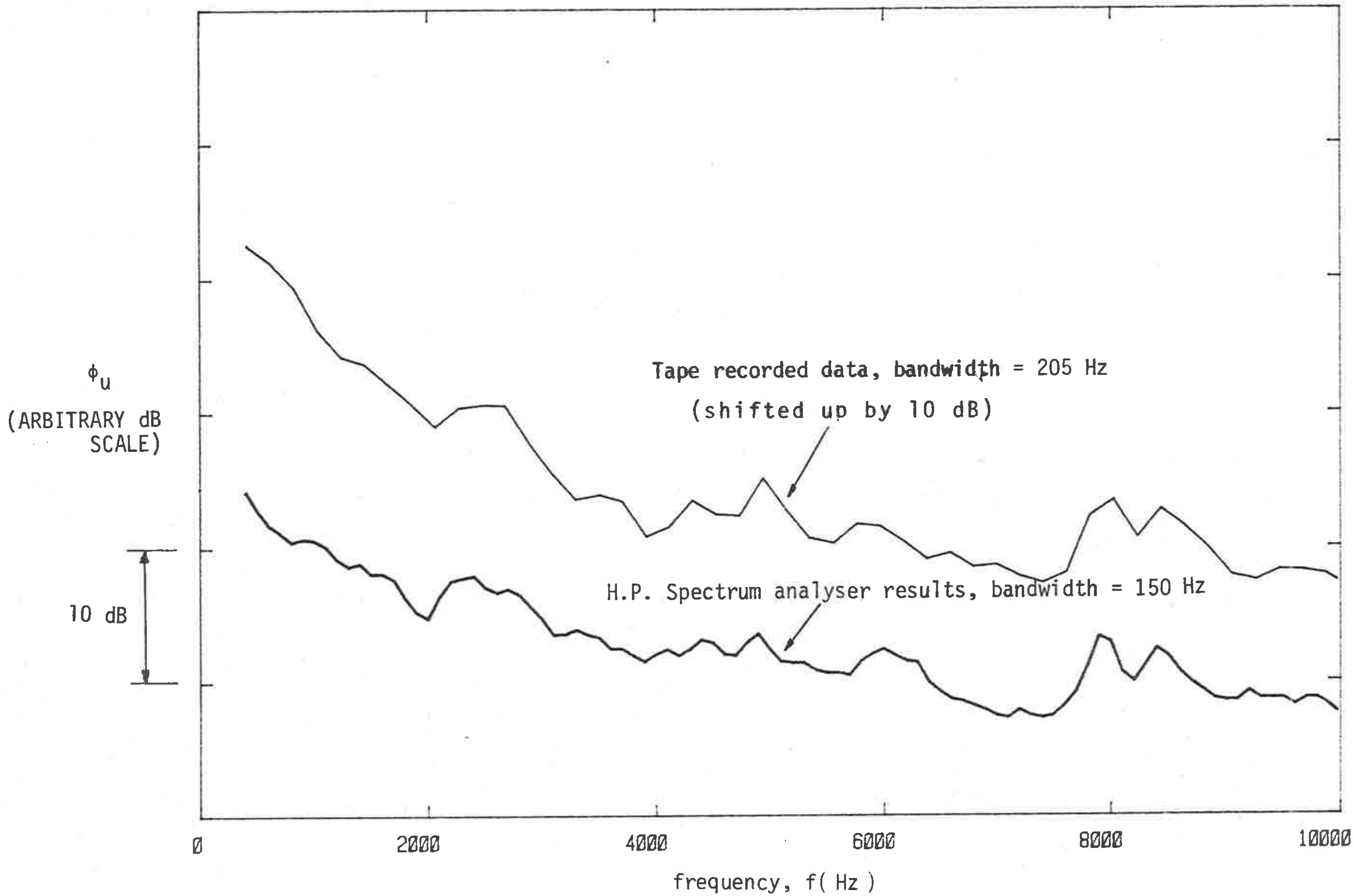

FIGURE 4.10 : A TYPICAL VELOCITY SPECTRUM OBTAINED WITH H.P. SPECTRUM ANALYSER AND TAPE RECORDED DATA FOR THE SAME SIGNAL

Together with the 256 digital data, information such as bandwidth, frequency span, and vertical scale, displayed by the analyser with the trace, is also retrieved and kept with the data file. The analyser is always used in the RMS averaging mode with a 'Hanning' passband window, which offers a compromise between 'flat top' and 'uniform passband windows' with maximum uncertainty of 1.5 dB. The RMS averaging mode combines each new spectrum with the previous partial result on a point-by-point basis using an RMS calculation. At any point in the cycle the amplitude A(f) at frequency f is given by

$$A(f) = \sqrt{\frac{1}{n}[A_1^2(f) + A_2^2(f) + \ldots + A_n^2(f)]} \,, \tag{4.2}$$

and the phase by

$$\phi(f) = \frac{1}{n}[\phi_1(f) + \phi_2(f) + \ldots + \phi_n(f)] \,, \tag{4.3}$$

where n is the number of averages.

The same method of averaging is used on the data analysed on the Cyber 173: a continuous record obtained by one run of the rig is processed and averaged with the subsequent runs of the rig. A diagram of the interface of the LSI-11 with the HP analyser, which requires a separate DMA card, is shown in Figure 4.12. A typical comparison of the spectrum obtained by the two methods is shown by Figure 4.10.

The 12 bit analog-to-digital converter used is Datel's DS-250 with an acquisition time of 1.35 microseconds, a conversion time of 2 microseconds, and a total throughput period of 4 microseconds (i.e. throughput rate 250,000 samples per second). A negligible amount of energy exists in wall pressure and velocity fluctuations at the frequency corresponding to this conversion time. For 12 bit

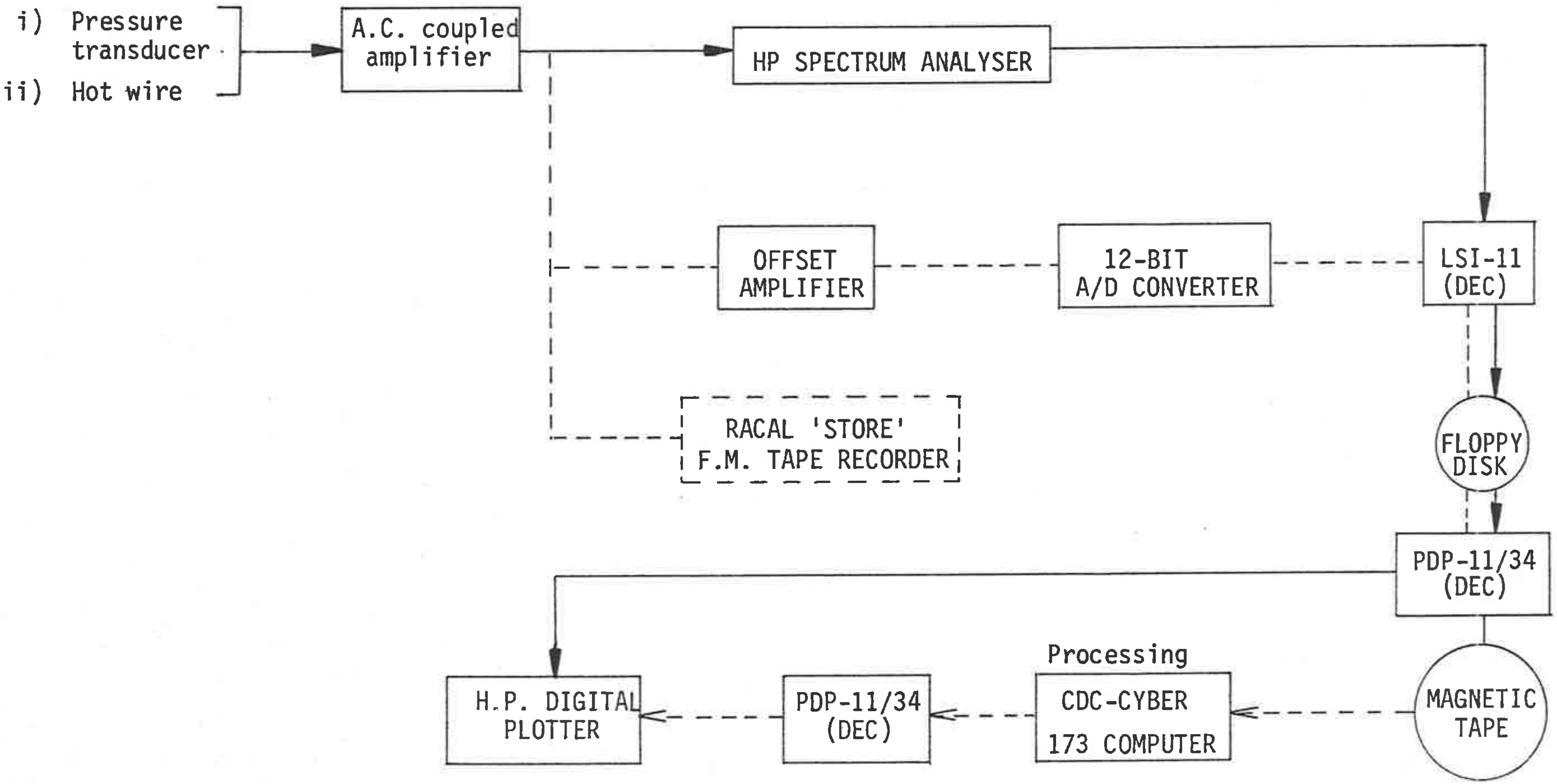

FIGURE 4.11 : DATA ACQUISITION PROCEDURE

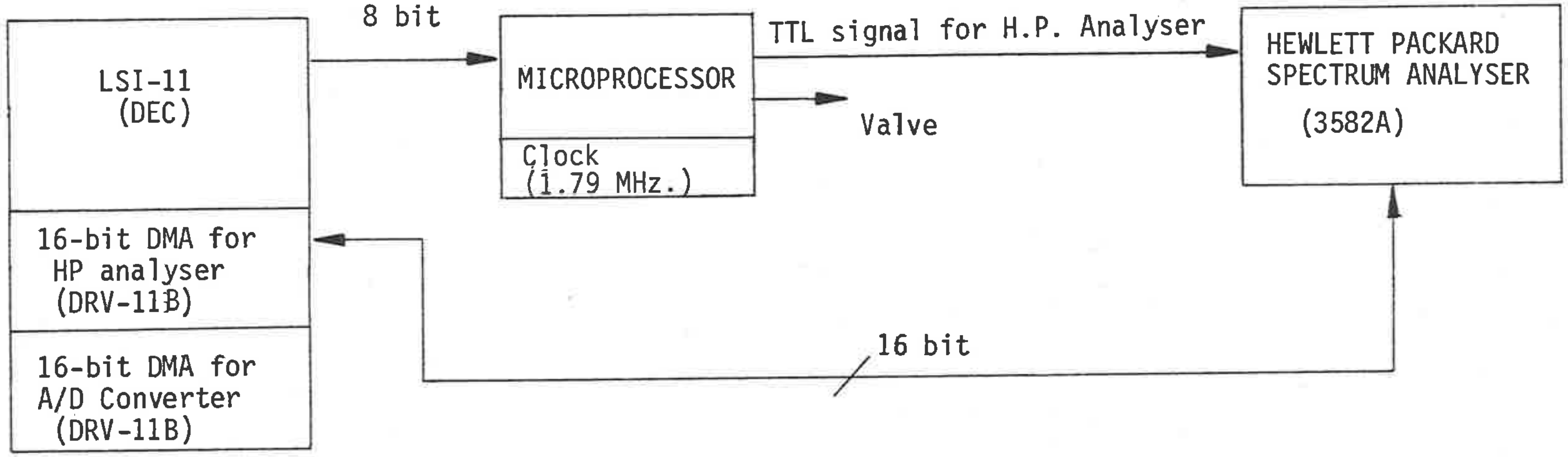

FIGURE 4.12 : LSI-11 INTERFACE WITH H.P. SPECTRUM ANALYSER

resolution, quantization errors are negligible (before digitizing the fluctuating signals are passed through an AC coupled amplifier to remove the DC component) and quantization and conversion time errors are essentially uncorrelated with the signal and with themselves (Windrow, 1956 and Watts, 1962). As discussed by Norton (1979), if we consider the quantitized signal x' (or y') to be the original signal x (or y) plus an additive εx (or εy) due to quantization and conversion time errors such that,

$$x' = x + \varepsilon x$$

and (4.4)

$$y' = y + \varepsilon y \ ,$$

then the normalized correlation coefficient between the two quantized variables is

$$\rho_{x'y'}(\tau) = \rho_{xy}(\tau) + \rho_{x\varepsilon y}(\tau) + \rho_{y\varepsilon x}(\tau) + \rho_{\varepsilon x\varepsilon y}(\tau)$$

$$= \rho_{xy}(\tau) \quad , \tag{4.5}$$

since $\rho_{x\varepsilon y} \approx \rho_{y\varepsilon x}(\tau) \approx \rho_{\varepsilon x\varepsilon y}(\tau) \approx 0$.

4.7 Statistical Considerations

To achieve the desired degree of statistical certainty relating to the spectral measurements, it is necessary that the record length, T_r, be large enough for the chosen analysis bandwidth, B_e. The relation between T_r and B_e is discussed in detail by Bendat and Piersol (1971, p.208) and Harris and Ledwidge (1974). If bias errors are neglected, the record length required to keep the normalized standard error to a predetermined level is given by

$$\varepsilon_r = 1/\sqrt{B_e T_r} \quad . \tag{4.6}$$

A normalized standard error of $\varepsilon_r = 0.1$ was chosen for the present work, corresponding to 95% certainty that a measured value lies within 2% of the true mean value. The required condition on bandwidth and record length is then

$$B_e T_r > 100 \tag{4.7}$$

Thus, small bandwidths require large averaging time and vice versa.

Where the spectrum is obtained by averaging a number of spectral samples, each derived from a short fixed time-length record of signal, equation (4.7) gives the total record length required.

CHAPTER 5

THE MEAN FLOW

5.1 Introduction

In this chapter the results of measurements made to define the mean flow in the piping system in the presence of an orifice plate are presented. The flow has the general character shown in Figure 5.1. It can, as shown in Figure 5.1, be usefully divided into the following five characteristic zones.

Zone 1, $X \lesssim -0.8$

A region of undisturbed fully-developed turbulent pipe flow extending to large distances upstream of the orifice plate.

Zone 2, $-0.8 \lesssim X < 0$

A region of small streamwise extent just upstream of the orifice plate, in which the primary separation of the flow from the pipe wall occurs at the point S_1, quite close to the orifice plate. The separated shear layer encloses a small recirculation region between the separation point and the upstream face of the orifice plate.

Zone 3, $0 < X \lesssim 1.4$

A region of separated and recirculating flow downstream of the orifice plate. This region is characterised by a central, turbulent axisymmetric free shear layer or jet originating at the sharp upstream edge of the orifice plate. The shear layer grows radially with increasing downstream distance until it reaches and reattaches to the pipe wall. In the process of reattachment, part of the shear layer fluid is deflected upstream, along the pipe wall, under the influence of the strong adverse pressure gradient which exists in this vicinity, to form the recirculation region. The flow in this zone is very unsteady : the reattachment point and the rate of entrainment of fluid from the recirculating flow into the free shear layer (which

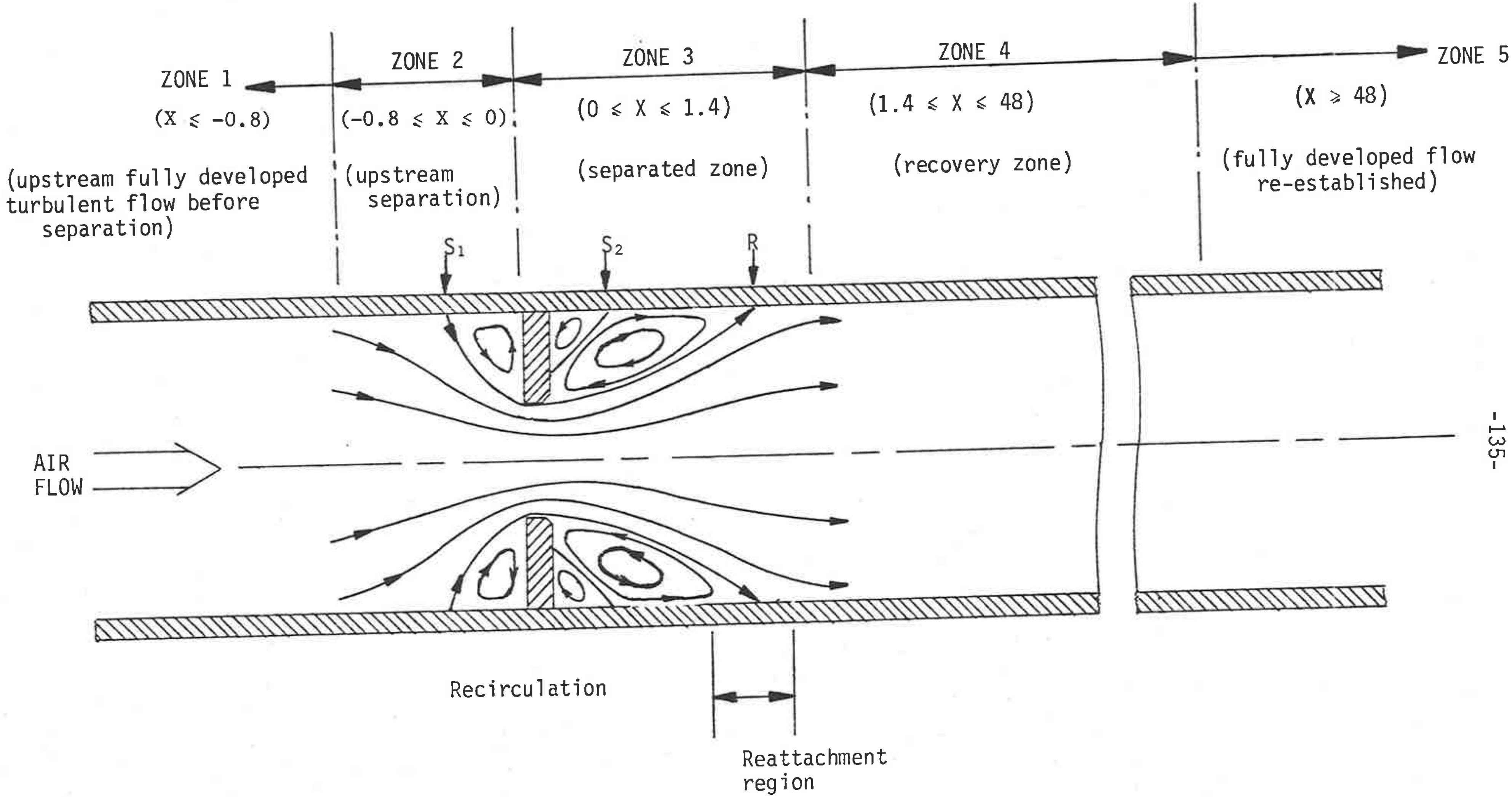

FIGURE 5.1 : ORIFICE FLOW

is directly related to the reattachment length, i.e. the distance between the orifice plate and the reattachment point [Kim, Kline, and Johnston, 1980]) both fluctuate with time.

Within the recirculation region, a secondary separation, of the reverse flow, from the pipe wall, occurs at the point S_2 (Figure 5.1) giving rise to a secondary recirculation region close to the downstream face of the orifice plate.

<u>Zone 4, $1.4 \lesssim X \lesssim 48$</u>

The region downstream of reattachment where the disturbances produced by the orifice plate die out and the flow undergoes recovery towards an undisturbed equilibrium state.

<u>Zone 5, $X \gtrsim 48$</u>

The region of re-established fully-developed turbulent flow at large distances downstream of the orifice plate.

Results will now be given, for various combinations of orifice plate and choke, in the ranges $0.62 \leqslant D_0 \leqslant 0.83$ and $0.39 \leqslant D_C \leqslant 0.86$, for

(i) the mass flow rate and Mach number of the undisturbed flow in Zone 1;

(ii) the centreline flow Mach number at the downstream end of the pipe;

(iii) the mean position of separation and reattachment points in Zones 2 and 3;

(iv) the streamwise variation of mean values of wall static pressure, centreline flow velocity and centreline Mach number throughout the flow;

(v) radial profiles of static pressure;

(vi) mean wall shear stress in Zones 1, 3, 4 and 5;

(vii) radial profiles of mean velocity in Zones 1, 3, 4 and 5; and

(viii) streamwise turbulence intensity.

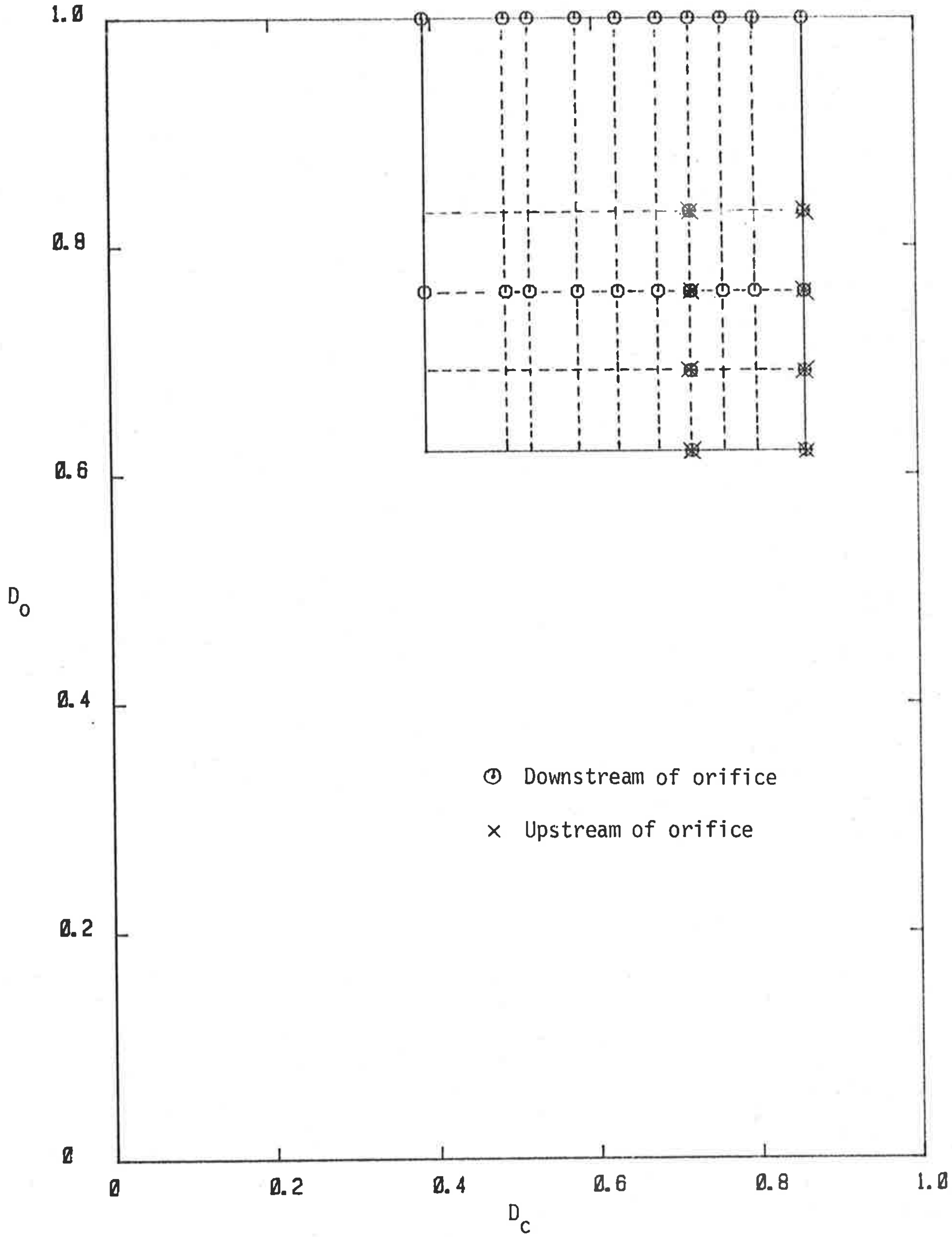

FIGURE 5.2: RANGE OF MEAN FLOW MEASUREMENTS

Table 5.1

Instrumentation and Range of Application

Instrumentation	No orifice	With orifice plate: Upstream $-22.7<X<-0.83$ (Zone 1)	$-0.83<X<0$ (Zone 2)	Separated region $X < X_R$ (Zone 3)	Recovery region $X_R < X < 48$ (Zone 4)	Re-established Fully-developed flow $X > 48$ (Zone 5)
Fence gauge	✓	✓	✓	✓	✓	✓
Wall Static pressure	✓	✓	✓	✓	✓	✓
Total pressure tube	✓	✓	✓	✓	✓	✓
Static pressure tube	✓			✓	✓	
Hot film shear-gauge	✓			✓	✓	
Hot-wire	✓	✓		✓	✓	✓
Piezoelectric wall-pressure transducer	✓			✓	✓	✓
1/4" Bruel & Kjaer wall microphones	✓	✓		✓	✓	✓
Three wire probe				✓	✓	

A summary of the regions of the flow, where measurements with the various pieces of instrumentation described in Chapter 3 have been made, is given in Table 5.1

The particular combinations of orifice plate and choke used for each of the measurements (i)-(vi) listed above are shown, in the appropriate section of the text, as a table or on a parameter space plot (D_o V. D_c) such as Figure 5.2.

5.2 Specification of Flow Conditions

Over the period during which the pressure in the vacuum tanks is low enough to produce choked flow at the nozzle throat at the downstream end of the pipe, the flow is completely determined by the combination of orifice plate and choke which are installed. Thus specification of D_0 and D_C specifies the flow. But these combinations need to be related to various flow parameters.

The flow is essentially a subsonic compressible flow of the Fanno type, that is an adiabatic flow subject to the effects of wall friction. Friction is responsible for the flow speed and Mach number increasing in the flow direction, while at the same time static temperature, static pressure and static density decrease.

In the pipe flow rig used for the present work, the effect of the choke is to accelerate the fully-developed flow at the downstream end of the pipe to a sonic condition within a very short axial distance. Provided that conditions are not too close to those at which frictional effects become overwhelming and frictional choking occurs in the pipe, frictional effects over the acceleration region are not very significant. The acceleration therefore is very nearly isentropic; and hence, provided that the mean velocity profile in the fully-developed flow in this region does not vary significantly with the mass flow rate through the pipe, the centre-line flow Mach number M_E in the pipe immediately upstream of the choke will be determined only by the ratio of the throat area of the choke to the cross-sectional area of the pipe, i.e. by D_c^2. On this basis the centreline Mach number M_E can be expected to have the same value for a given choke, irrespective of orifice plate which is installed further upstream. Thus we expect

$$M_E = M_E(D_c), \text{ and independent of } D_0, \tag{5.1}$$

and it will be seen this is confirmed by the experimental measurements.

Variation of the orifice size D_0 affects the flow as a result of the corresponding variation in flow resistance; for a given D_c, reduction of D_0 gives increased flow resistance, and increased static pressure drop between the reservoir (atmosphere) and the downstream end of the pipe. Thus a decrease in D_0 produces reduced fluid density at the downstream end of the pipe at the same flow Mach number M_E, and hence reduced mass-flow rate.

If the assumptions are made that

(i) the radial distribution of mean velocity in the pipe just upstream of the choke is similar for all mass-flow-rates;

(ii) total temperature in the fluid is constant and equal to the reservoir (atmospheric) temperature T_r, and

(iii) static pressure p is constant over the cross-section,

then the average mass flow rate per unit area over the cross-section $\bar{j}$ is given by

$$\bar{j} = \frac{\dot{m}}{\pi a^2} = \frac{2}{a^2}\int_0^a \rho U r dr$$

$$= \frac{2pU_0}{RT_r}\int_0^1 \frac{f(\xi)\xi \, d\xi}{(T/T_r)}, \tag{5.2}$$

where $\xi = r/a$, the radial distribution of mean velocity is represented by $f(\xi) = U/U_o$, and T is the local static temperature of the fluid. Consistent with the above assumptions the local static temperature can be expressed as

$$T = T_r - \frac{U^2}{2C_p} = T_r[1 - \frac{U_o{}^2}{2C_pT_r} f^2(\xi)]$$

$$= T_r[1 - k^2 f^2(\xi)], \tag{5.3}$$

where

$$k^2 = \frac{U_o{}^2}{2C_pT_r} = \frac{\frac{\gamma-1}{2} M_o^2}{(1 + \frac{\gamma-1}{2} M_0^2)} = k(M_0). \tag{5.4}$$

With these relations and the speed of sound in the reservoir expressed as $a_r = (\gamma RT_r)^{1/2}$, equation (5.2) can be written as

$$\bar{j} = \frac{\gamma p M_o}{a_r(1 + \frac{\gamma-1}{2} M_0^2)^{1/2}} F_2(M_0), \tag{5.5}$$

where

$$F_2(M_0) = 2 \int_0^1 \frac{f(\xi)\xi \, d\xi}{[1 - k^2 f^2(\xi)]} \tag{5.6}$$

It is convenient to express $\bar{j}$ in non-dimensional form a $\bar{J} = \bar{j}/j_*$, where j_* is the mass-flow rate per unit area which would be produced by isentropic expansion from the given reservoir conditions to sonic velocity a_* with corresponding density ρ_*. j_* is given by

$$j_* = \rho_* a_* = \frac{\gamma p_r}{a_r} (\frac{2}{\gamma+1})^{(\gamma+1)/2(\gamma-1)}, \tag{5.7}$$

where p_r is the reservoir pressure.

Equations (5.5), (5.6) and (5.7) give

$$\bar{J} = p/p_r \; F(M_0), \tag{5.8}$$

where

$$F(M_0) = \left(\frac{\gamma+1}{2}\right)^{(\gamma+1)/2(\gamma-1)} \frac{M_0}{\left(1 + \frac{\gamma-1}{2} M_0^2\right)^{1/2}} F_2(M_0) \qquad (5.9)$$

In a flow such as the present one, where the fluid experiences large changes in state between inlet and outlet, $\overline{J}$ is an important parameter providing an overall characterisation of the flow.

The mass flux per unit area on the pipe centreline j_0 $(=\rho_0 U_0)$ can be shown to be given by

$$j_0 = \frac{\gamma p M_0 \left(1 + \frac{\gamma-1}{2} M_o^2\right)^{1/2}}{a_r}; \qquad (5.10)$$

and hence

$$J_0 = \frac{j_0}{j_*} = \left(\frac{\gamma+1}{2}\right)^{(\gamma+1)/2(\gamma-1)} \frac{p}{p_r} M_0\left(1 + \frac{\gamma-1}{2} M_0{}^2\right)^{1/2} \qquad (5.11)$$

It follows that

$$\overline{J} = F_4(M_0)\, J_0, \qquad (5.12)$$

where

$$F_4(M_0) = \frac{F_2(M_0)}{\left(1 + \frac{\gamma-1}{2} M_o^2\right)}. \qquad (5.13)$$

Calculated values of the functions $F(M_0)$ and $F_4(M_0)$ based on $f(\xi)$ given by Equation (2.42) are shown in Figure 5.3. These allow $\overline{J}$ to be evaluated from measured static pressures and centreline Mach numbers (in regions of fully-developed flow) by Equation (5.8) or Equation (5.12).

To complete the specification of the flow, we require to specify also the initial state of the fully-developed pipe flow, upstream of the orifice plate, before it is subjected to disturbance. An appropriate parameter is some centreline Mach number characteristic

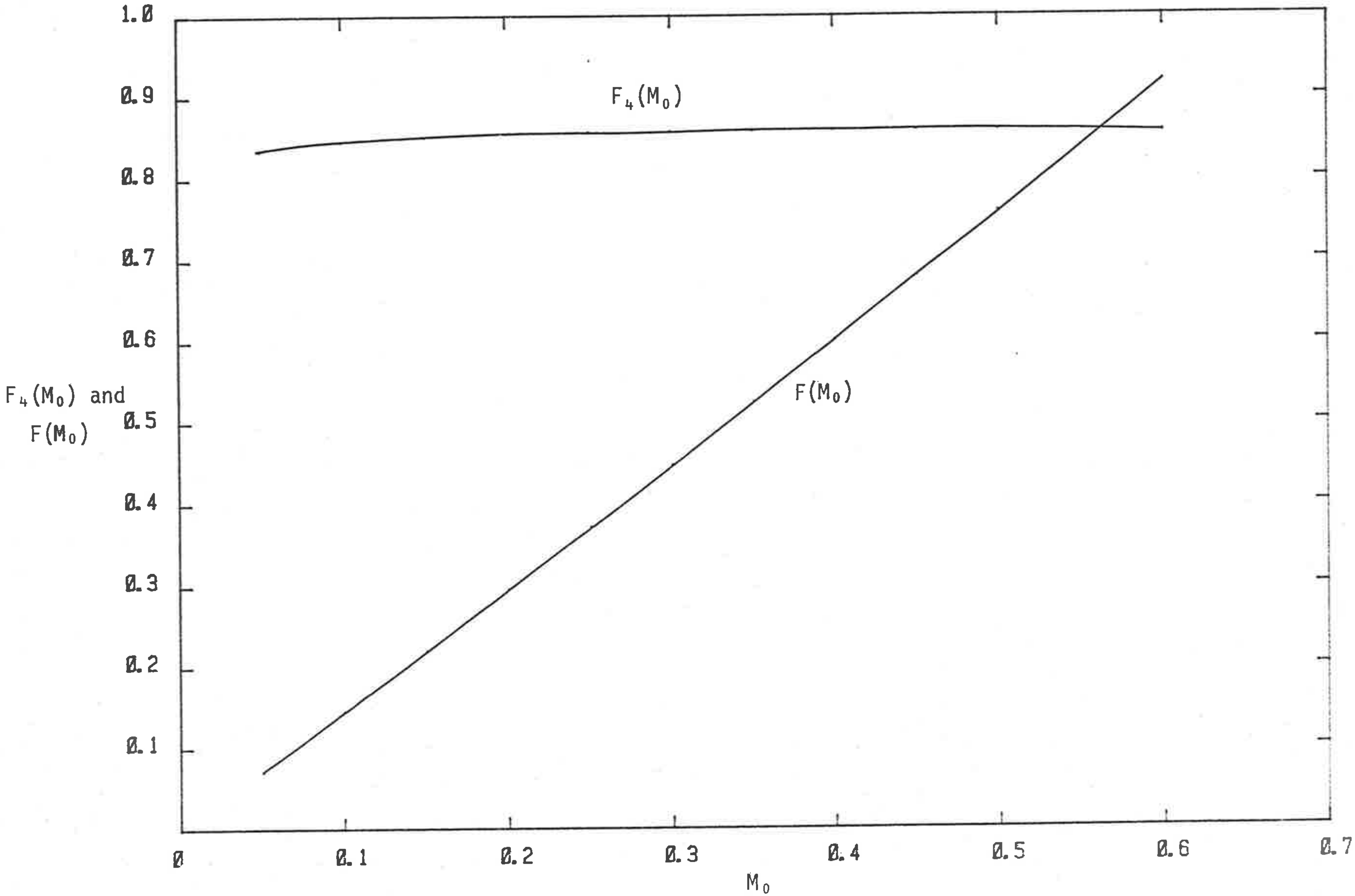

FIGURE 5.3 : VARIATION OF $F_4(M_0)$ AND $F(M_0)$ WITH MACH NUMBER

of the flow in this region. Since, in this region, flow speeds and Mach numbers are low and frictional effects cause them to vary only slowly with axial distance, it is adequate to specify the centreline Mach number at an (arbitrary) convenient distance upstream of the orifice plate. A point 275mm upstream of the orifice plate ($X = -3.8$) is used throughout for this purpose; the centreline Mach number at this point is designated M_I and the corresponding velocity U_I.

Provided that the assumptions listed earlier in this section are valid, specification of $\bar{J}$, and M_I (determined in turn by D_0 and D_c), together with the atmosphere reservoir conditions, completely specifies the flow which is being subjected to disturbance.

An expression for estimating the Mach nubmer M_E just upstream of the choke can also be obtained, based on the same assumptions given above for the derivation of mass-flow rates, with the additional assumption that, in each annular streamtube entering the choke, the flow is accelerated from its fully-developed turbulent state at the downstream end of the pipe to a sonic condition at the throat section of the choke (implying that $M = 1$ at all radii at the throat, but that other fluid properties vary with radial position). Thus the fluid flowing through the annular area $2\pi r dr$ in the pipe is assumed to pass through the corresponding area $2\pi r dr\ (A_*/A)$ of the throat, where (A_*/A) represents the area ratio in a one-dimensional flow for flows with Mach numbers unity and M, and is given by

$$\frac{A_*}{A} = \frac{M}{\left[\frac{2}{\gamma+1}\left(1 + \frac{\gamma-1}{2} M^2\right)\right]^{(\gamma+1)/2(\gamma-1)}} \qquad (5.14)$$

The choke area associated with pipe flow with $M_0 = M_E$ is therefore

$$\frac{\pi d_c^{\,2}}{4} = 2\pi \int_0^a r\left(\frac{A_*}{A}\right) dr. \qquad (5.15)$$

The local Mach number in the pipe flow is given by

$$M^2 = \frac{U^2}{\gamma RT} \quad ;$$

and with Equation (5.3) this can be expressed as

$$M^2 = \frac{2}{\gamma-1} \frac{k^2 f^2(\xi)}{[1 - k^2 f^2(\xi)]}. \tag{5.16}$$

Substitution of equation (5.14) and (5.16) in equation (5.15) leads to

$$D_c^2 = 2\left(\frac{\gamma+1}{2}\right)^{(\gamma+1)/2(\gamma-1)} \frac{M_E}{\left(1 + \frac{\gamma-1}{2} M_E^2\right)^{1/2}}$$
$$\times \int_0^1 [1 - k^2 f^2(\xi)]^{1/(\gamma-1)} \,.\, \xi \,.f(\xi)\, d\xi \,. \tag{5.17}$$

With k^2 as in equation (5.4) with $M_0 = M_E$, this equation allows the value of D_c corresponding to any given value of M_E to be calculated.

5.3 Experimental Values of $\bar{J}$, M_I and M_E for Various D_0/D_c Combinations

As a preliminary to examination of the flow in the presence of orifice plates, the development of the flow in the absence of an orifice plate was investigated. Fully-developed turbulent flow velocity profiles exist at X = 0 (taken as 55 diameter downstream of the pipe entrance) at all speeds. The velocity profiles are presented in the universal form in Figure 5.4 for the flow speeds given by the chokes D_c = 0.39 and 0.86. They compare well with the logarithmic distribution given by Equation (2.33) and 1/7th power velocity distribution derived from Blasius's resistance formulae. Good agreement is found between friction velocities calculated from the pressure drop along the pipe and those obtained from the measured velocity profiles using Clauser (1954) charts.

With an orifice plate installed, measurements were in general not made at positions further upstream of the orifice plate than X = -4.1.

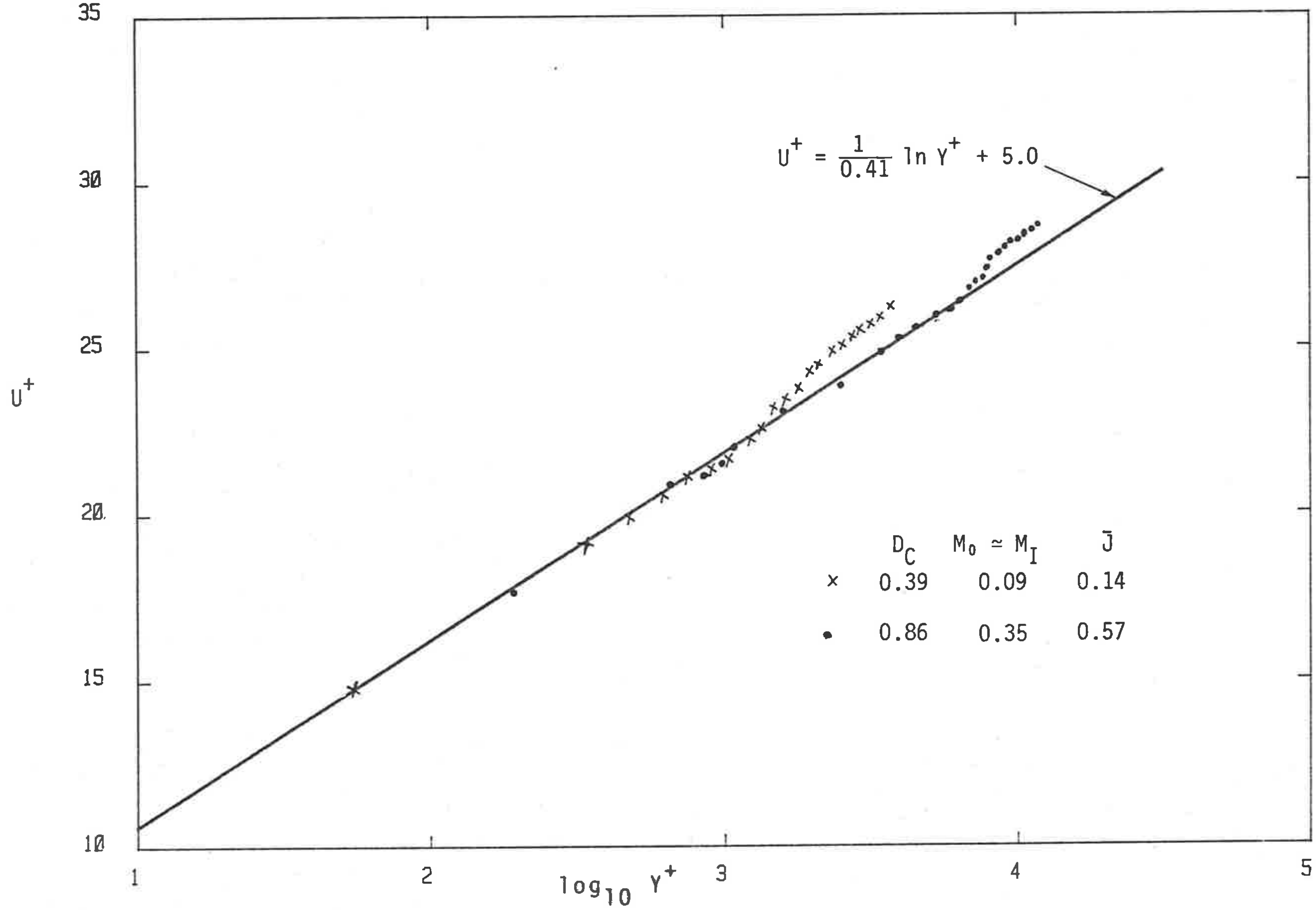

FIGURE 5.4 : UNIVERSAL VELOCITY PROFILES (UNDISTURBED FLOW, X = 0)

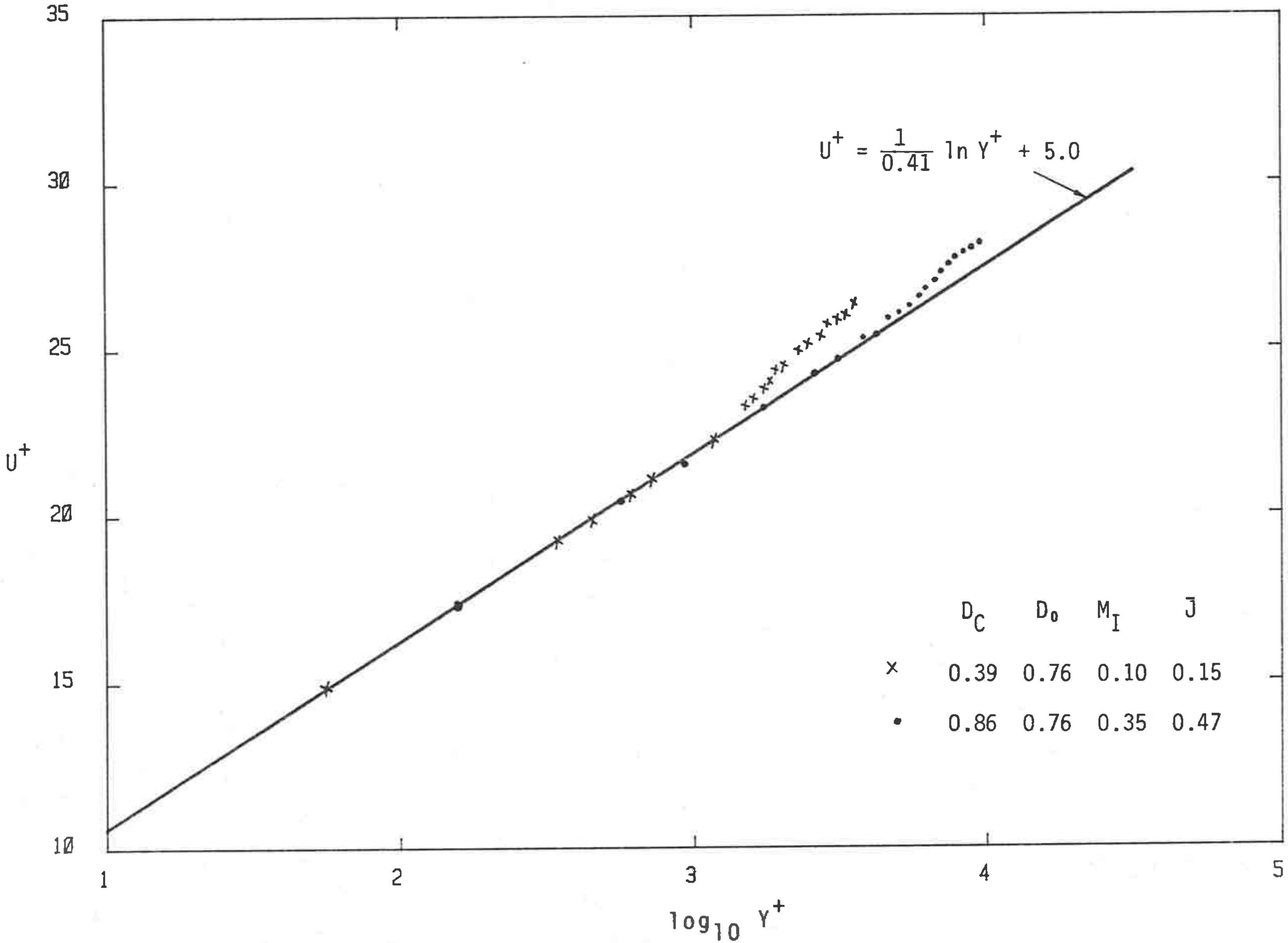

FIGURE 5.5 : UNIVERSAL VELOCITY PROFILES (UPSTREAM OF THE ORIFICE PLATE, X = -8.27)

For all orifice plate/choke combinations used in the experiments, the flow is fully-developed at this position. In the one or two cases in which measurements were made further upstream, fully-developed flow was found at positions significantly beyond $X = -4.1$. Typical measured velocity profiles, at $X = -8.27$ for flows with the orifice $D_0 = 0.76$ and chokes $D_C = 0.39$, 0.86 are shown in Figure 5.4 It can be seen that they are in close agreement with fully-developed profiles represented by Equation (2.33).

Comparative measurements were made to determine the effect of introducing the internal sleeve to carry the orifice plate. The presence of the sleeve produces small differences in mass-flow rate and initial Mach number compared with the flow with an orifice plate of the same geometry clamped between pipe flanges. However, at most, the changes amount to ± 2% of M_I or $\bar{J}$; and generally they are considerably less than this. Consequently, no attempt is made, in the data presented, to distinguish values corresponding to the different methods of mounting the orifice plate.

Values given for the mass-flow rate parameter $\bar{J}$ have been obtained from measured centreline values J_0 and values of $F_4(M_0)$ calculated from Equation (5.13), or equivalently from the measured static pressure and $F(M_0)$ calculated from Equation (5.9). This procedure appears to give consistent results for $\bar{J}$ irrespective of the particular location in the system (provided that the flow there is fully-developed) at which the measurement is made. Values of centreline Mach number and $\bar{J}$ obtained from measurements at $X = 0$ and 102 in undisturbed flow (no orifice plate, $D_0 = 1.00$) are given in Table 5.2 for all chokes. The values of M_0 at $X = 0$ are essentially the M_I values for this case, while the M_0 values at $X = 102$ correspond to M_E. Similar data for all flows with the $D_0 = 0.76$ orifice, derived from measurements at $X = -3.8$, with the orifice plate mounted at the upstream end of the sleeve, and at X = 102 with the orifice plate mounted on the downstream end of the sleeve, are given in Table 5.3. The values in Tables 5.2 and 5.3 illustrate both the consistency referred to above and the small effect of differences arising from different orientations of the orifice plate and the sleeve.

M_I, $\overline{J}$ and M_E values for all four orifice plates in combination with the chokes D_C = 0.58, 0.72 and 0.86 are presented in Table 5.4.

It can be seen that the centreline flow Mach number at X = 102, M_E, as discussed earlier in this section, is independent of D_0 for any given choke, in accordance with Equation (5.1).

The dependence of M_I and $\overline{J}$ on D_0 and D_C is shown graphically in Figure 5.6 and 5.7. The former also shows the measured variation of M_E with D_C, and the close agreement between these values and those calculated by Equation (5.17). As can be seen from these figures, the mass-flow rates fall in the range of about 15 to 58% of the uniform isentropic flow rate, the centreline Mach number M_I in the undisturbed flow varies between 0.1 and 0.4, and the corresponding Mach number M_E at the downstream end of the pipe, where the flow has recovered from the disturbance, varies between 0.1 and 0.56.

Table 5.2

Centreline Mach number and flow rates obtainable with various chokes

Undisturbed flow $D_0 = 1.00$

Choke No.	D_C	X = 0: $M_O \simeq M_I$	X = 0: ρu (kg/m^2. sec.)	X = 0: $\rho u/\rho^* u^*$	X = 0: $\bar{J}$	X = 102: $M_O \simeq M_I$	X = 102: ρu (kg/m^2. sec.)	X = 102: $\rho u/\rho^* u^*$	X = 102: $\bar{J}$
1	0.39	0.094	38.5	0.161	0.136	0.102	41.49	0.173	0.146
2	0.49	0.157	63.3	0.266	0.226	0.165	65.51	0.274	0.233
3	0.52	0.178	72.7	0.300	0.256	0.189	73.92	0.309	0.264
4	0.58	0.223	88.4	0.368	0.315	0.236	89.90	0.376	0.322
5	0.63	0.254	101.6	0.419	0.359	0.276	102.20	0.427	0.366
6	0.68	0.298	115.2	0.481	0.412	0.323	115.30	0.482	0.413
7	0.72	0.324	125.8	0.525	0.450	0.366	126.20	0.527	0.452
8	0.76	0.363	135.9	0.568	0.487	0.410	135.90	0.568	0.487
9	0.80	0.400	146.2	0.611	0.524	0.463	145.90	0.610	0.523
10	0.86	0.451	160.9	0.670	0.574	0.559	160.18	0.669	0.573

Table 5.3

Centreline Mach number and flow rates obtainable with various chokes with the orifice plate, $D_0 = 0.76$

Choke No.	D_C	X = -3.8				X = 102			
		$M_O = M_I$	ρu (kg/m^2.sec.)	$\rho u/\rho^* u^*$ J_O	J	$M_O = M_E$	ρu (kg/m^2.sec.)	$\rho u/\rho^* u^*$ J_O	J
1	0.39	0.102	41.8	0.175	0.148	0.102	41.1	0.172	0.146
2	0.49	0.159	64.7	0.270	0.230	0.165	63.5	0.265	0.226
3	0.52	0.181	72.5	0.304	0.259	0.188	70.9	0.296	0.253
4	0.58	0.214	85.2	0.356	0.304	0.235	84.9	0.355	0.304
5	0.63	0.240	94.7	0.396	0.339	0.276	94.9	0.396	0.339
6	0.68	0.268	104.7	0.437	0.374	0.322	104.5	0.437	0.375
7	0.72	0.290	111.6	0.466	0.399	0.366	112.1	0.469	0.402
8	0.76	0.311	119.0	0.497	0.426	0.410	118.1	0.494	0.424
9	0.80	0.328	124.5	0.520	0.446	0.463	123.5	0.516	0.442
10	0.86	0.348	130.9	0.547	0.469	0.561	130.5	0.547	0.468
		orifice plate at upstream end of sleeve				orifice plate at downstream end of sleeve			

Table 5.4

Centreline Mach number and flow rates obtainable with various size orifices and flow speeds at X = 102

Orifice Size	D_o	Choke # 4					Choke # 7					Choke # 10				
		$M_o = M_E$	ρu (kg/m² sec)	$J_o = \rho u/\rho^* u^*$	$\bar{J}$	M_I	$M_o = M_E$	ρu (kg/m² sec)	$J_o = \rho u/\rho^* u^*$	$\bar{J}$	M_I	$M_o = M_E$	ρu (kg/m² sec)	$J_o = \rho u/\rho^* u^*$	$\bar{J}$	M_I
45	0.62	0.234	73.3	0.306	0.262	-	0.363	86.09	0.360	0.309	0.217	0.559	91.81	0.384	0.329	0.230
50	0.69	0.235	80.2	0.335	0.287	-	0.366	100.6	0.42	0.360	0.260	0.559	110.0	0.464	0.397	0.290
55	0.76	0.235	84.9	0.355	0.304	-	0.366	112.1	0.469	0.402	0.290	0.561	130.5	0.547	0.468	0.348
60	0.83	0.235	87.5	0.366	0.313	-	0.366	119.5	0.499	0.428	0.311	0.562	145.8	0.609	0.521	0.394
No Orifice	1.00	0.235	87.9	0.376	0.322	0.223	0.366	126.2	0.527	0.452	0.324	0.559	160.2	0.669	0.573	0.451

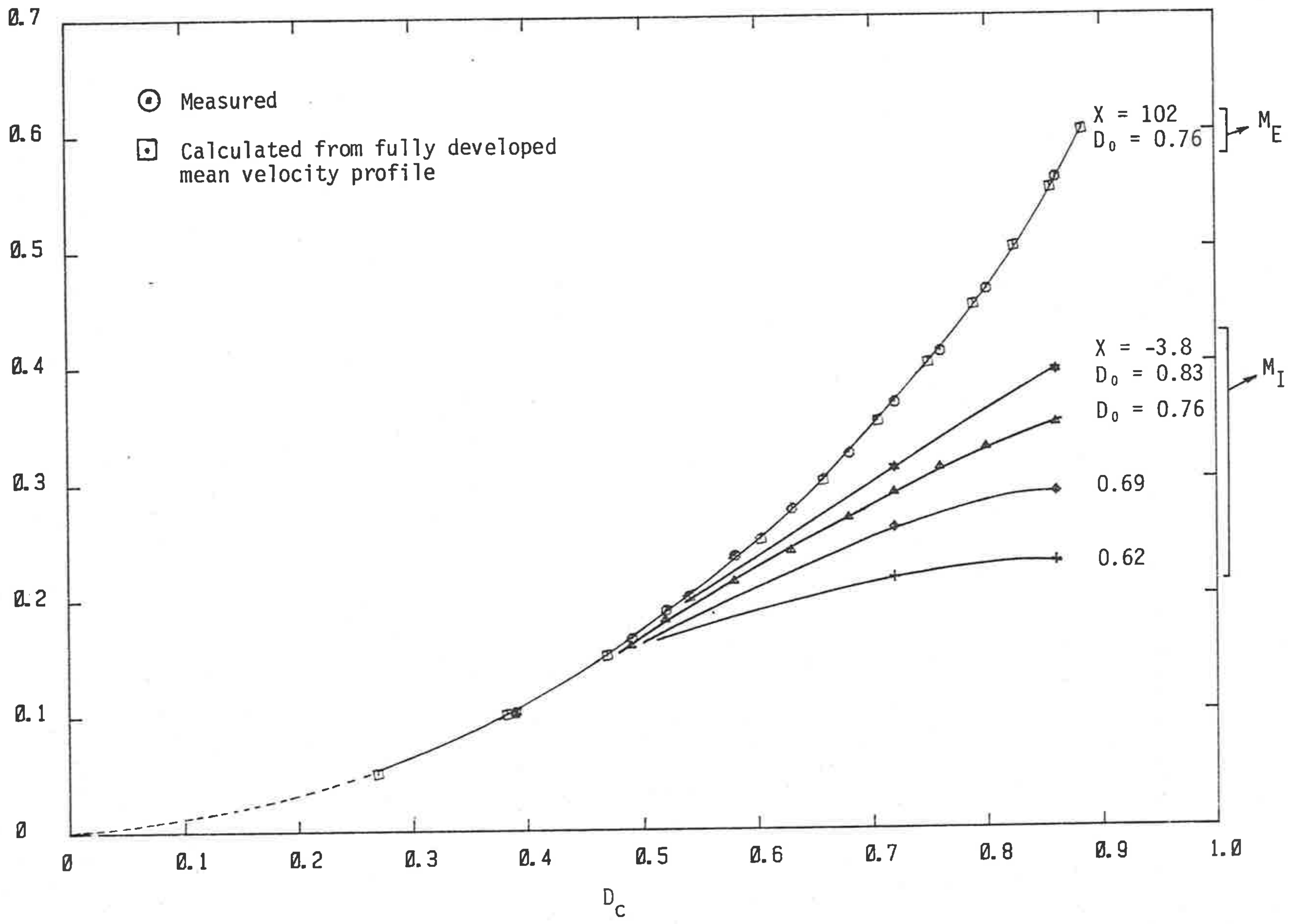

FIGURE 5.6 : VARIATION OF M_E AND M_I WITH D_c AND D_O

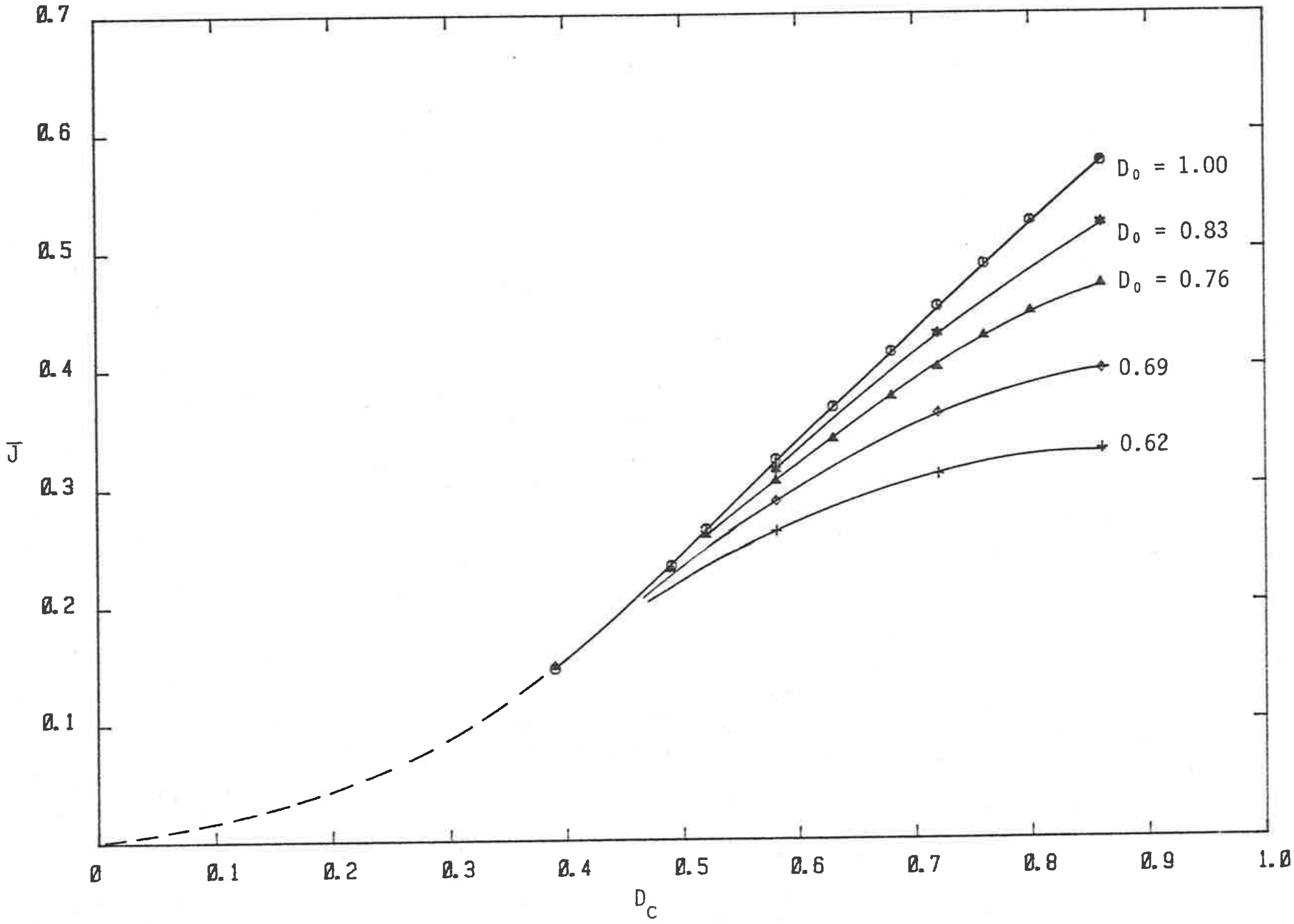

FIGURE 5.7 : VARIATION OF $\bar{J}$ WITH D_C AND D_O

5.4 Separation and Reattachment Positions

Typical variation of the pressure differential, ΔP, indicated by a fence gauge (with a fence height of 0.1mm) mounted in the pipe wall, through the separated-flow region and slightly beyond for an orifice plate with $D_0 = 0.76$ with three different flow rates (corresponding to the chokes $D_C = 0.58, 0.72, 0.86$) is shown in Figure 5.8. The zero-crossings of the curves of Δp against X gives the positions of points of zero mean wall shear stress: thus the mean position of the primary separation can be identified as $X_{S1} \simeq -0.08$, that of reattachment X_R in the range 1.3-1.4, and that of secondary separation as $X_{S2} \simeq 0.17$.

Figure 5.9 shows the results, from Figure 5.8 and similar plots for other orifice plates, for the coordinates of the primary separation, reattachment and secondary separated points non-dimensionalised by the pipe diameter. In these terms, all three points move towards the orifice plate as D_0 increases (i.e. as the radial height of the obstruction decreases). The effect of increasing flow rate (increasing D_C) is also to move the points towards the orifice plate; the effect is very small on X_{S1}, somewhat greater on X_{S2} and largest on X_R, and increases as D_0 is reduced. Lines of constant x_R/h are also shown on Figure 5.9. These indicate that the reattachment length expressed in terms of h is less strongly dependent on D_0 than is X_R.

Some measurements were also made of the wall shear stress in the separated and reattached flow regions with hot film gauges. For this application these gauges have two well-known problems:

(1) the gauge responds only to the magnitude of the wall stress and gives no indication of the direction of the stress, and

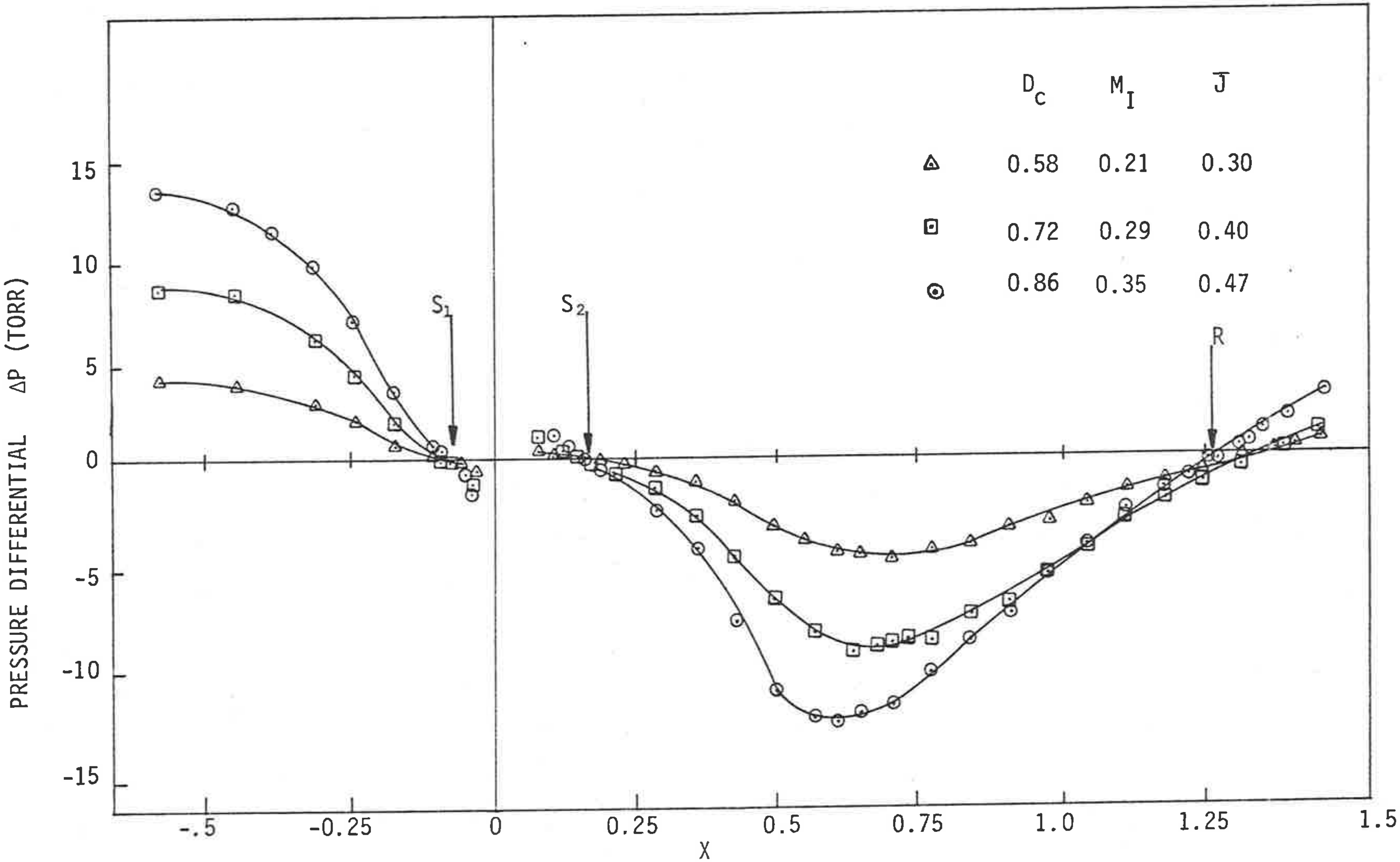

FIGURE 5.8 : SURFACE FENCE GAUGE PRESSURE DIFFERENTIALS, D_0 = 0.76

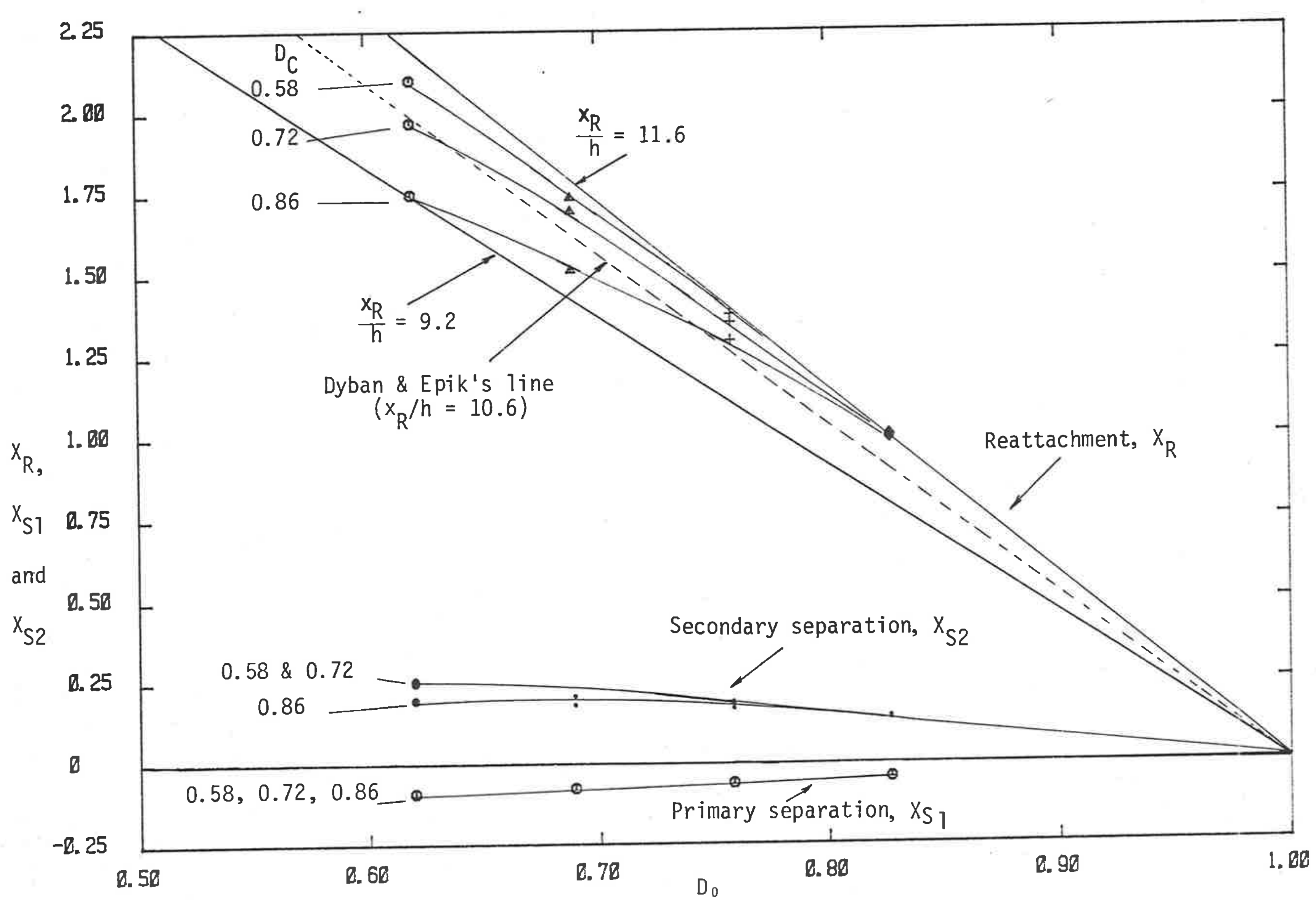

FIGURE 5.9: VARIATION OF REATTACHMENT AND SEPARATION LENGTHS WITH ORIFICE SIZE

(2) the intercept on the Nusselt number axis obtained by extrapolating the linear Nu v. $\tau_w^{1/3}$ calibration curve to $\tau_w = 0$ does not give a true indication of the gauge response at $\tau_w = 0$ (see McCroskey and Durbin, 1972).

A comparison of the type of result obtained with the hot film and that given by the fence gauge is shown by Figure 5.10. It can be seen that minima in the hot film values correspond quite closely to the $\Delta p = 0$ values from the fence gauge. However, the magnitudes of the stress indicated by the hot film at these points are not the same. This difference appears to be a result of the fact that the hot film output in regions of fluctuating stress corresponds to $(\tau_w^2 + \overline{\tau_w'^2})^{1/2}$, where $\overline{\tau_w'^2}$ is the mean square fluctuation, and that the level of fluctuation is significantly different at the two $\tau_w = 0$ points.

Thus, while, with care, the hot film measurements can be used to obtain the separation and reattachment positions, the procedure is less satisfactory than that based on the fence gauge. For this reason hot film measurements for this purpose were not persisted with.

Figure 5.11 shows that when the same measured distances of separation and reattachment points from the orifice plate are expressed in terms of the radial height of the obstruction presented by the orifice plate, $h = (d-d_0)/2$, they show a considerably weaker dependence on D_0. The position of primary separation X_{S1}/h appears to be independent of D_0, while X_{S2}/h and X_R/h increase slowly with increasing D_0.

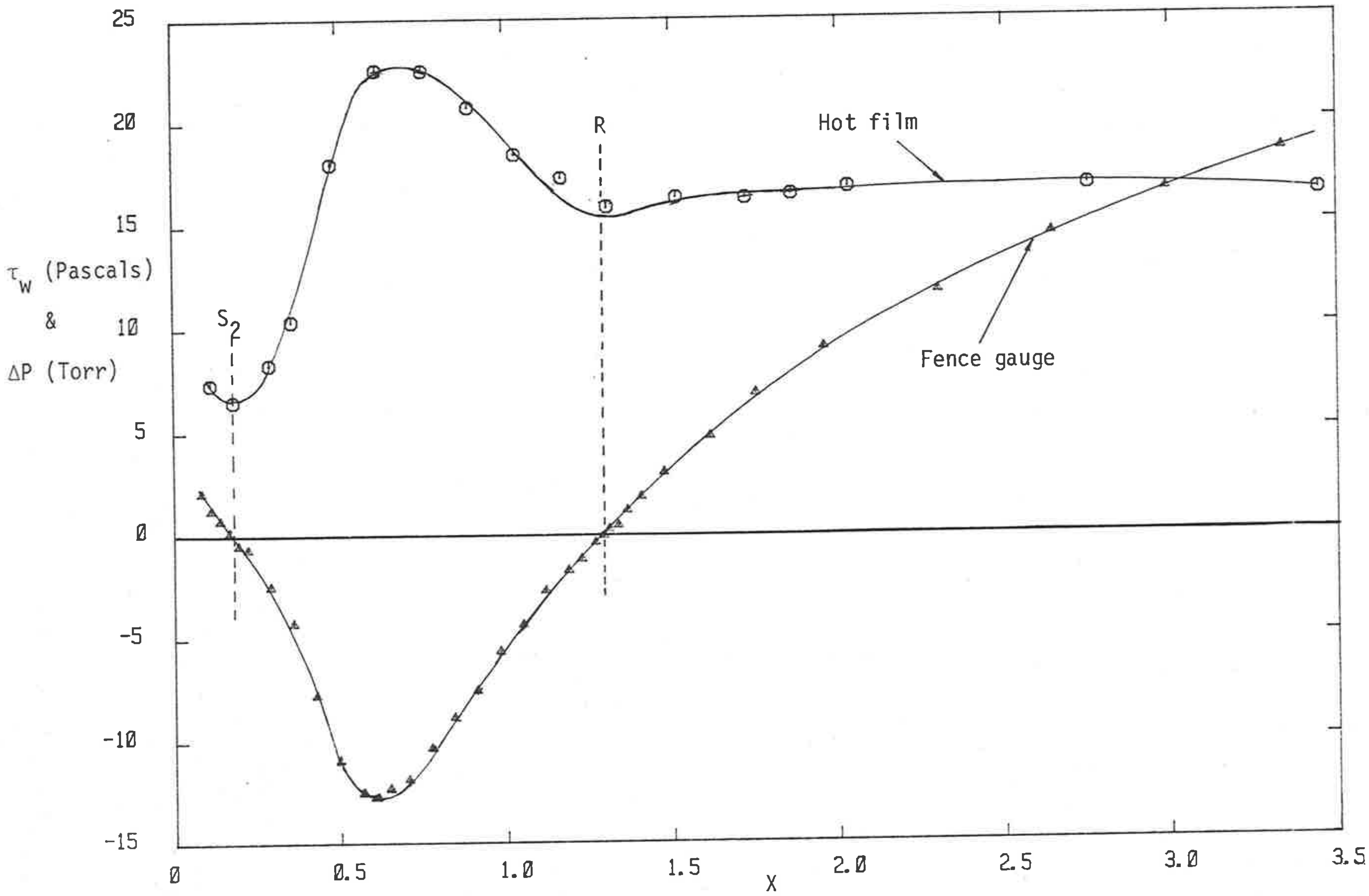

FIGURE 5.10 : HOT FILM SHEAR GAUGE AND FENCE GAUGE MEASUREMENTS

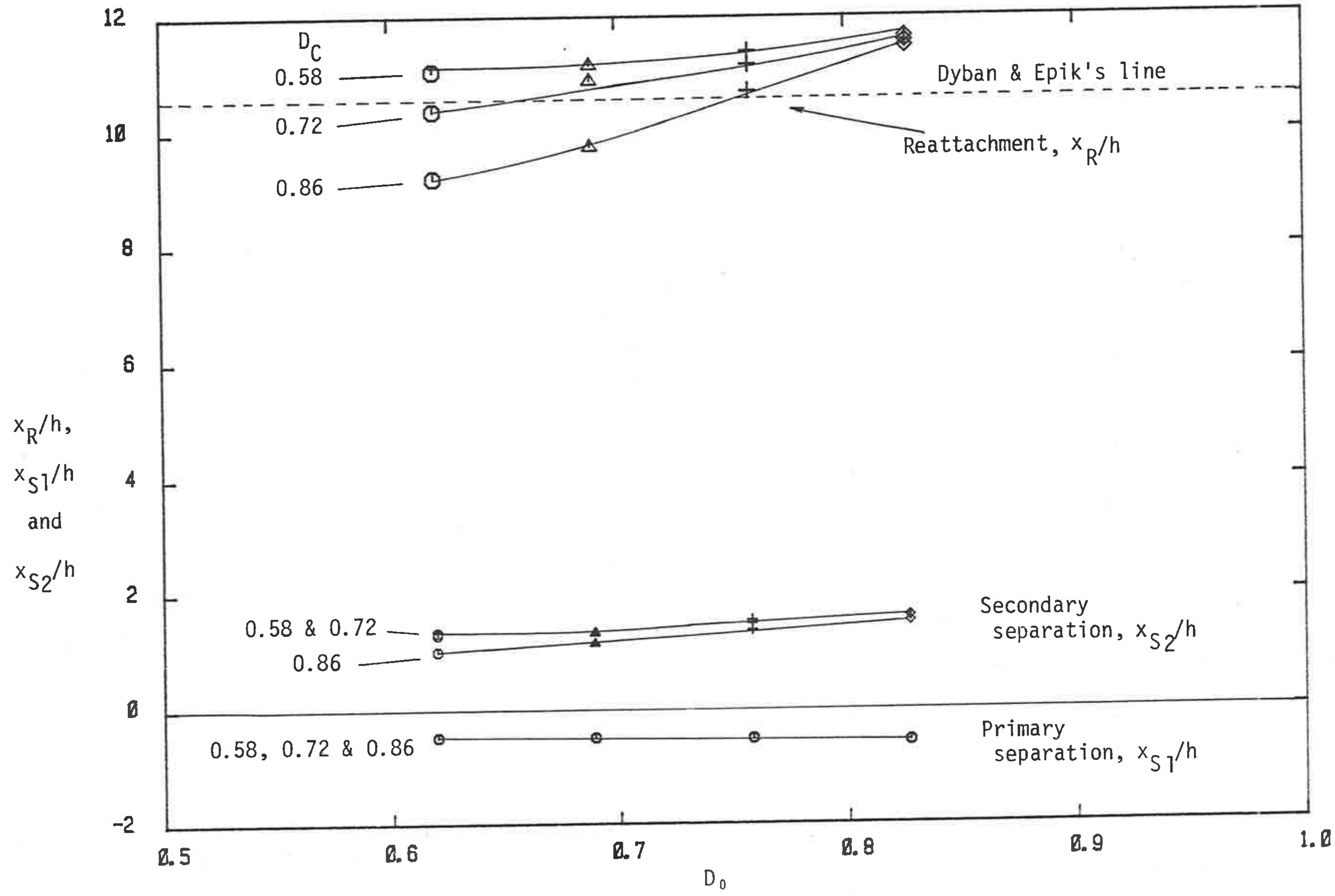

FIGURE 5.11 : VARIATION OF REATTACHMENT AND SEPARATION LENGTHS WITH ORIFICE SIZE

On the assumption that compressibility effects are insignificant, and for a given orifice geometry (sharpness of edges, etc.), dimensional analysis would indicate that

$$X_{S1},\ X_{S2},\ X_R = \text{function}\ (D_0\ ,R_e) \qquad (5.18)$$

or

$$x_{S1}/h,\ x_{S2}/h,\ x_R/h = \text{function}\ (D_0\ ,R_e), \qquad (5.19)$$

where R_e is a Reynolds number characteristic of the orifice flow. A fairly good collapse of the data can be obtained if h is used as the length scale and the values plotted as a function of the Reynolds number $Re_h = U_I h/\nu_I$ (Figure 5.12), where U_I is the undisturbed centre-line velocity upstream of the orifice and ν_I the corresponding kinematic viscosity. Thus Figure 5.12 suggests that over the, admittedly rather small, Reynolds number range of the present experiments, equation (5.19) reduces to

$$x_{S1}/h,\ x_{S2}/h,\ x_R/h = \text{function}\ (Re_h)\ . \qquad (5.20)$$

Most of the previous experimental determinations of the reattachment length for an orifice plate in a circular pipe have been made indirectly, the position of reattachment being identified with the position of maximum heat transfer rate in a heated pipe or with that of maximum turbulent axial velocity fluctuation. Dyban and Epik (1970) have attempted to correlate such data, which cover orifice sizes $0.25 \leqslant D \leqslant 0.88$ and a Reynolds number range of $10^3 \leqslant Re_h \leqslant 4.0 \times 10^4$. The data show no systematic variation with Reynolds number and considerable scatter, values of x_R/h as low as 5 and as high as 18 being observed. Dyban and Epik give a mean line for the variation of X_R with D_0, which is shown in Figure 5.9; it is equivalent to $x_R/h = 10.6$. This can be compared with the x_R/h values in the present case in the range 9.2 to 11.6, for just slightly higher Reynolds numbers.

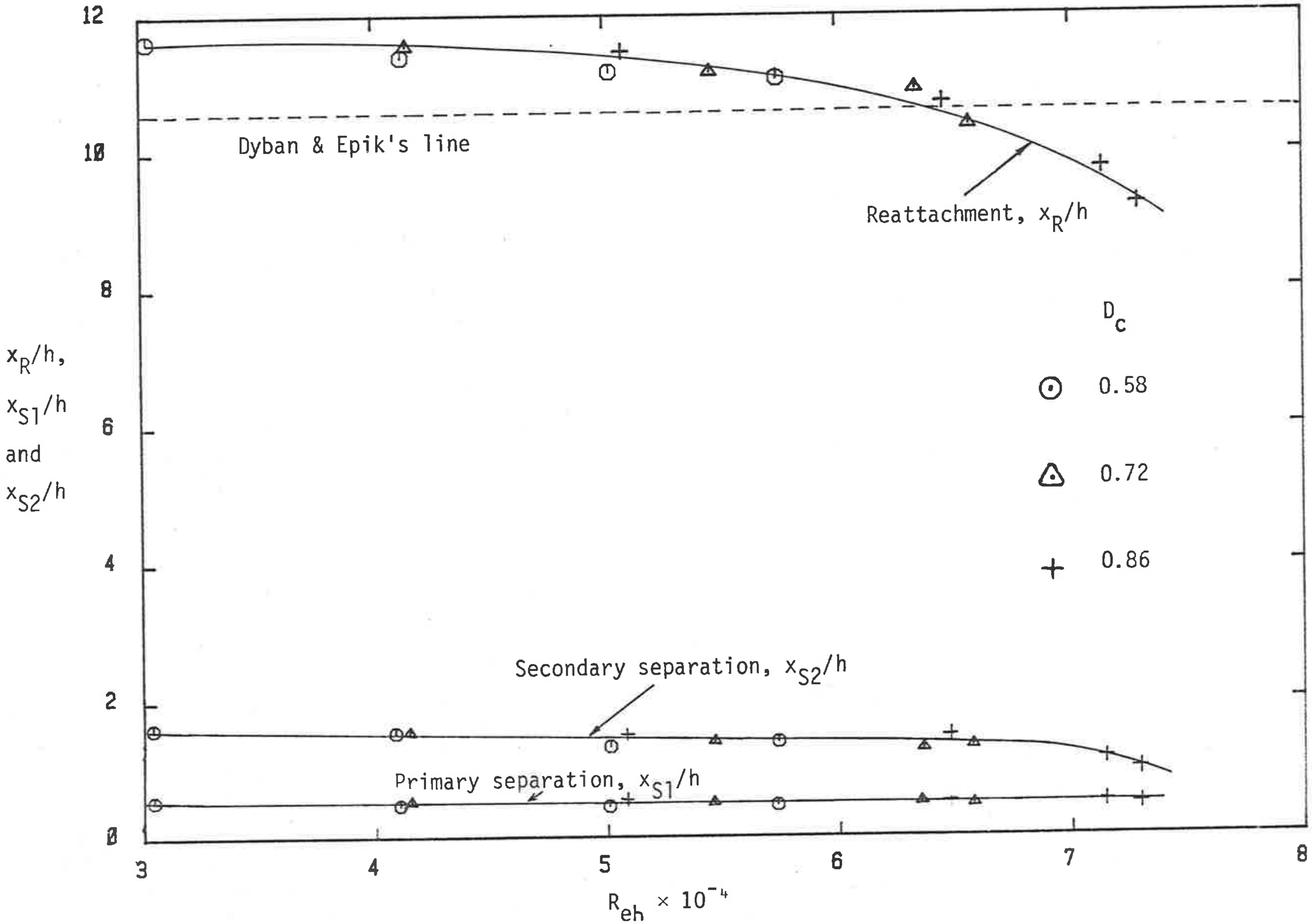

FIGURE 5.12 : VARIATION OF REATTACHMENT AND SEPARATION LENGTHS WITH REYNOLDS NUMBER

Back and Roschke (1972) have measured reattachment lengths (by flow visualisation) in the flow through a sudden expansion (diameter ratio 0.39) in a circular pipe, but only for flow with a thin boundary layer upstream of separation. At Re_h values of the order of 3×10^3 the boundary layer is turbulent and $x_R/h \simeq 10$.

The reattachment length for orifices in circular pipes expressed as x_R/h seems to be rather higher than the corresponding value for separation of a turbulent boundary layer from a backward-facing step in two-dimensional flow. From the data surveyed by Eaton and Johnston, (1980) the latter ranges from 5 to 8.2.

Very little experimental information is available on either X_{S1} or X_{S2}. Adams, Johnston and Eaton (1984) used a pulsed wire probe in their two-dimensional flow downstream of a backward-facing step, with a step height Reynolds number, Re_h, of 36000 and measured the separation of the reversed flow at $x/x_R = 0.1$, which is a slightly lower value than measured here, namely $(x_{S2}/x_R) = 0.13$ at a Reynolds number based on the orifice plate radial height h of $Re_h = 30350$.

The results obtained here for separation and reattachment locations are therefore broadly consistent with previously published work and appear to represent a more direct and systematic set of measurements than any previously obtained for orifice plates in circular pipes.

5.5 Streamwise Variation of Wall Static Pressure and Centre-line Velocity and Mach Number

The streamwise variation of total pressure, velocity and Mach number on the pipe centreline and the wall static pressure has been measured for the orifice-choke combinations shown in Table 5.5.

Table 5.5

Range of Measurements for Streamwise Variation of Wall Static Pressure and Velocity

D_C	D_0			
	0.62	0.69	0.76	0.83
0.58			✓	
0.63			✓	
0.72	✓	✓	✓	✓
0.76			✓	
0.80			✓	
0.86			✓	✓

The measurements cover streamwise distances $-5.5 \leqslant X \leqslant 8.5$, except for the case with $D_C = 0.86$, $D_0 = 0.76$ where the measurements cover the wider range $-16.7 \leqslant X \leqslant 91.5$.

The typical form of the streamwise variation of the flow parameters is shown for two flow cases: $D_0 = 0.76$, $D_C = 0.86$ in Figure 5.13(a) and $D_0 = 0.83$ and $D_C = 0.72$, in Figure 5.13(b).

Figure 5.14 shows the same data as in Figure 5.13(a) in greater detail in the range of X from -5.5 to 8.5. The flow zones defined in Section 5.1 are shown on the figures.

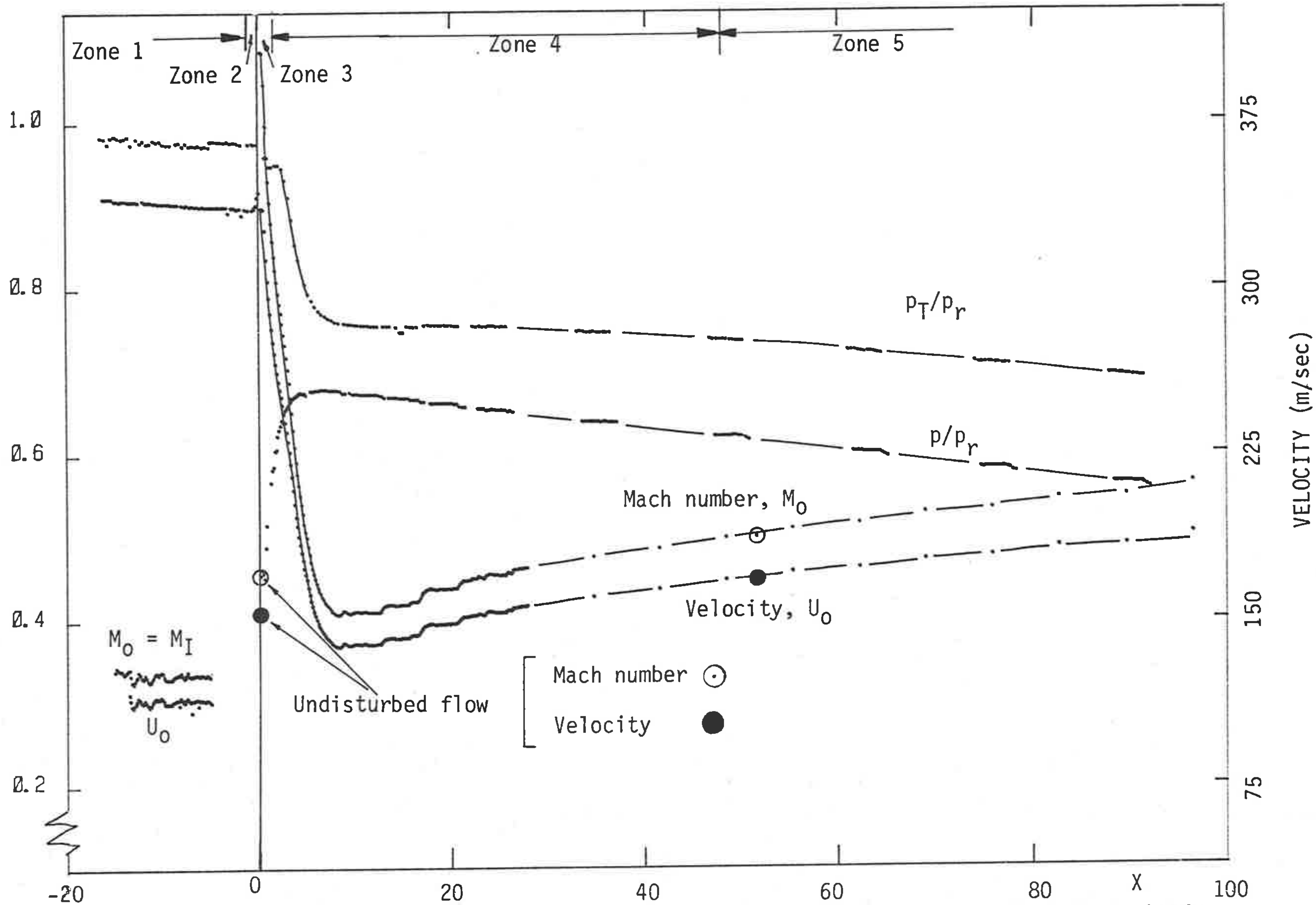

FIGURE 5.13a : AXIAL VARIATION OF STATIC PRESSURE, TOTAL PRESSURE (INDICATED), MACH NUMBER, AND VELOCITY

$D_C = 0.86$, $D_0 = 0.76$, $M_I = 0.35$ $\bar{J} = 0.47$

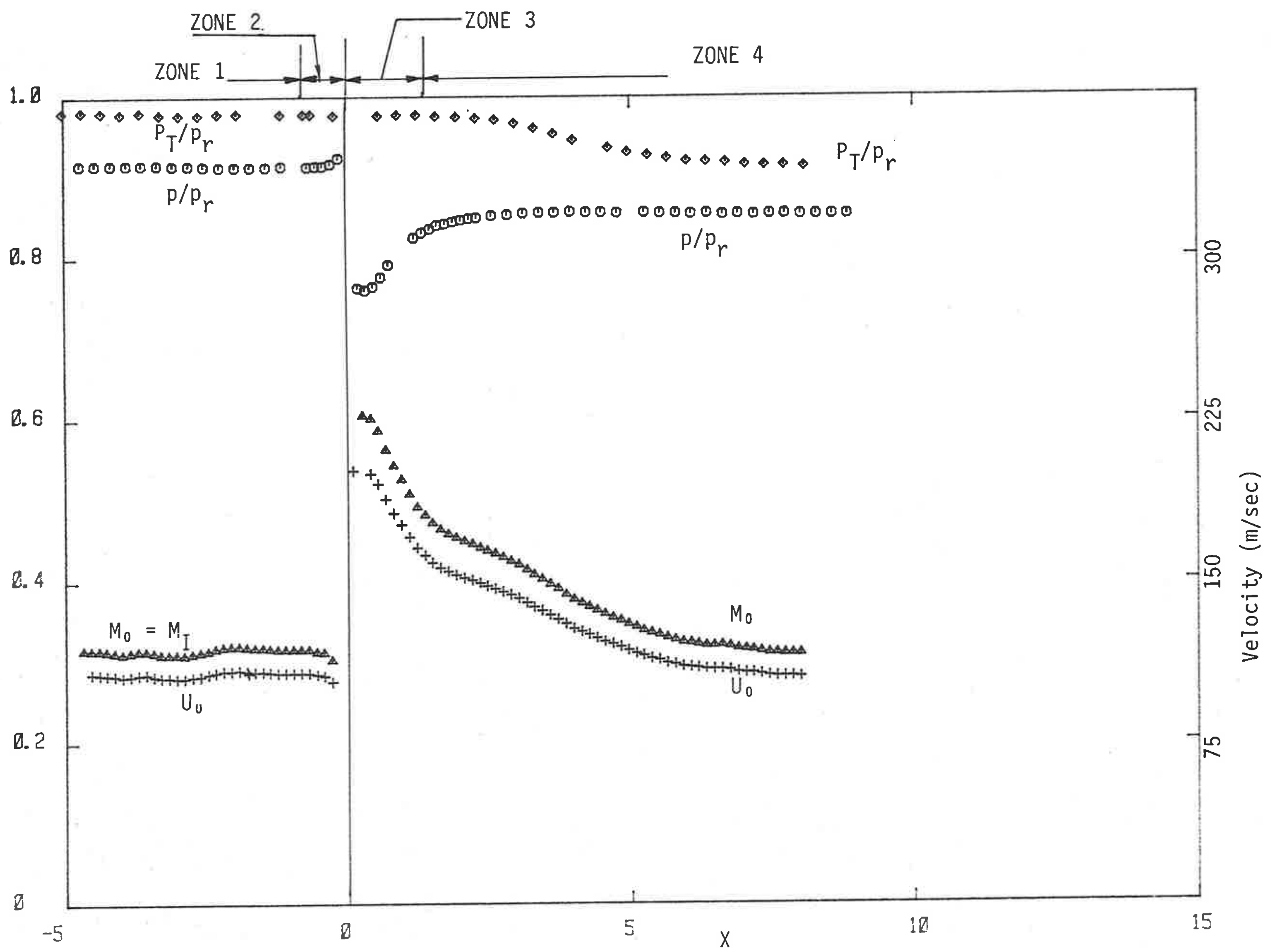

FIGURE 5.13b : AXIAL VARIATION OF STATIC PRESSURE, TOTAL PRESSURE (INDICATED), MACH NUMBER AND VELOCITY

$D_c = 0.72$, $D_o = 0.83$, $M_I = 0.29$, $\bar{J} = 0.40$

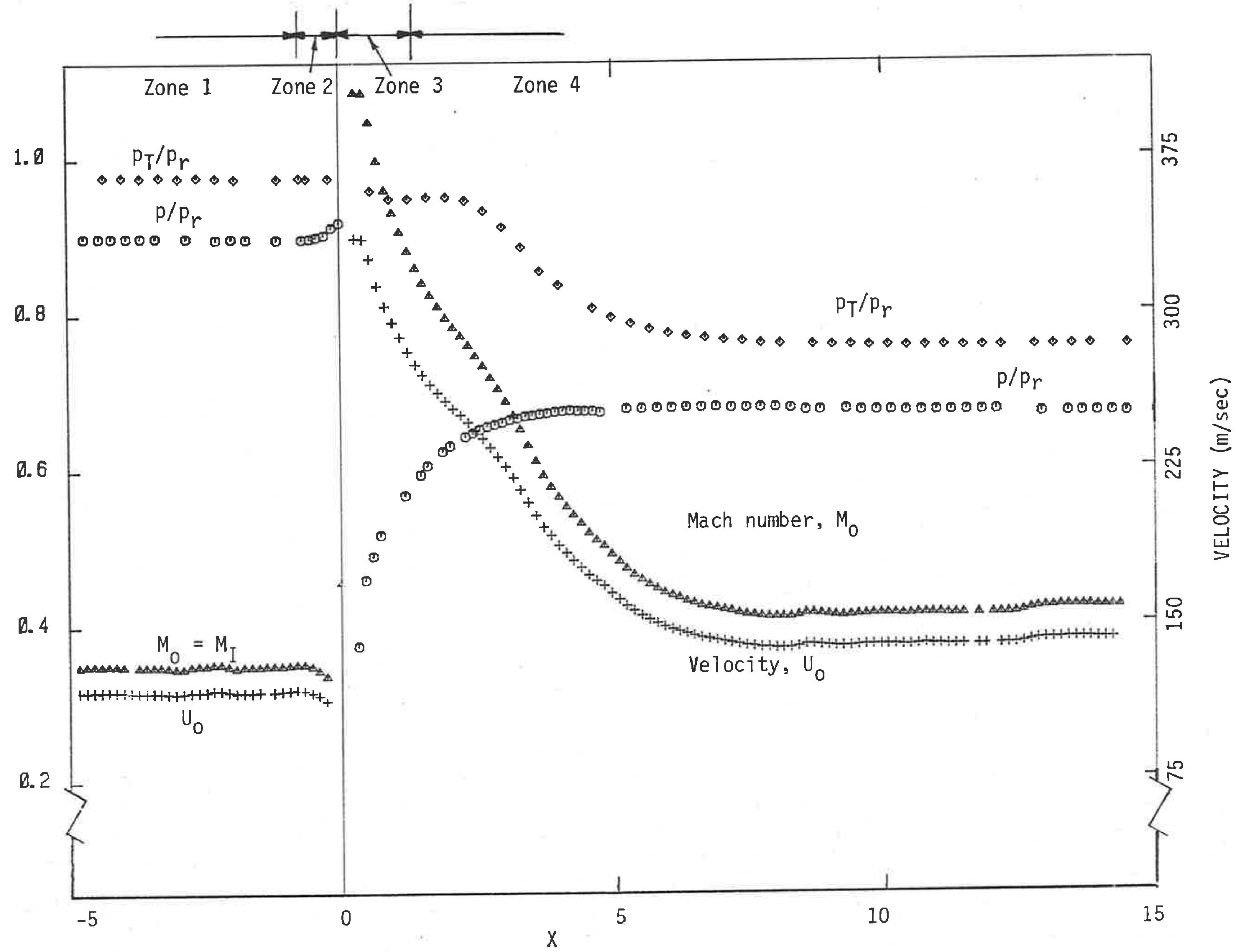

FIGURE 5.14: AXIAL VARIATION OF STATIC PRESSURE, TOTAL PRESSURE (INDICATED), MACH NUMBER AND VELOCITY

$D_C = 0.86$, $D_0 = 0.76$, $M = 0.35$, $\bar{J} = 0.47$

Consider first the flow with $D_0 = 0.76$ and $D_C = 0.86$. Figures 5.13(a) and 5.14 show that the centreline Mach number remains essentially constant in zone 1 (at $M_I = 0.35$) for some considerable distance upstream of the orifice plate.

In the the disturbed flow region, zones 2 and 3, between the point of separation of flow from the pipe wall upstream of the orifice and the point of reattachment downstream, the centreline Mach number shows - as would be expected considering that the cross sectional area of the orifice is only 57% of the pipe area - a large and rapid variation. Immediately upstream of the orifice, in zone 2, it falls slightly below M_I and then rises rapidly as the flow contracts to pass through the orifice. Just downstream of the orifice ($X = 0.34$, or $x/h = 2.9$), the Mach number reaches its maximum value (in this case slightly greater than unity) at the vena contracta of the free jet formed by separation of the flow from the upstream edge of the orifice plate. It then falls very rapidly as the free jet grows to fill the pipe at reattachment; it continues to fall, in zone 4, at the commencement of the recovery process in the now reattached flow, reaching a local minimum value of 0.41 at $X = 7.14$, $x/h = 59$. With further increase in X it rises, at first in zone 4 more rapidly than frictional effects can account for, and finally in zone 5, for $X > 48$ or $x/h > 400$, at a rate determined entirely by frictional effects.

It should be noted that the total pressure shown in the figures corresponds to the pitot tube reading. Just downstream of the orifice where the Mach number is slightly in excess of unity, this indicated total pressure is the stagnation pressure behind the normal shock formed ahead of the pitot tube. In such cases M_0 is obtained from the true total pressure, calculated using the Rayleigh Supersonic Pitot formula [see, e.g. Liepman and Roshko, 1957, p.149].

As can be seen from Figure 5.13(a) and 5.14, the variation of centreline velocity U_0 with X closely parallels that of M_0.

The streamwise variation of static pressure on the pipe wall is complementary to that of the Mach number and velocity. Upstream of the orifice plate the static pressure decreases very slowly due to frictional effects, and close to the upstream edge of the orifice it is slightly increased as part of the impact pressure on the orifice plate is conveyed to the wall. Across the orifice plate it undergoes a step reduction, and further decreases downstream to a minimum where the velocity is maximum. It then increases as the cross-sectional area of the free jet increases, and continues to increase steeply beyond the point of flow reattachment. It reaches a maximum value downstream of reattachment, at about X = 4.4. At reattachment, the static pressure has risen by about 56% of the overall pressure rise from the minimum value to the maximum value. This is a considerably smaller percentage than the 75% which is observed in the case of reattachment behind a two-dimensional backward facing step (Kim, Kline and Johnston (1980)) or the 71% for the 90° mitred bend in pipe flow (Bull and Norton (1981)).

With increase in X, beyond 4.4 the static pressure drops slowly at first and beyond $X \geq 48$ at a slightly faster rate, now determined only be frictional effects.

A similar sequence of parameter changes, although of different magnitudes can be followed in Figure 5.13(b) for the second representative flow case, $D_0 = 0.83$, $D_C = 0.52$.

The form of the wall static pressure variation over the separated flow and reattachment region (zones 3 and 4) is shown in more detail in Figure 5.15, where the data have been plotted in the form of the pressure coefficient

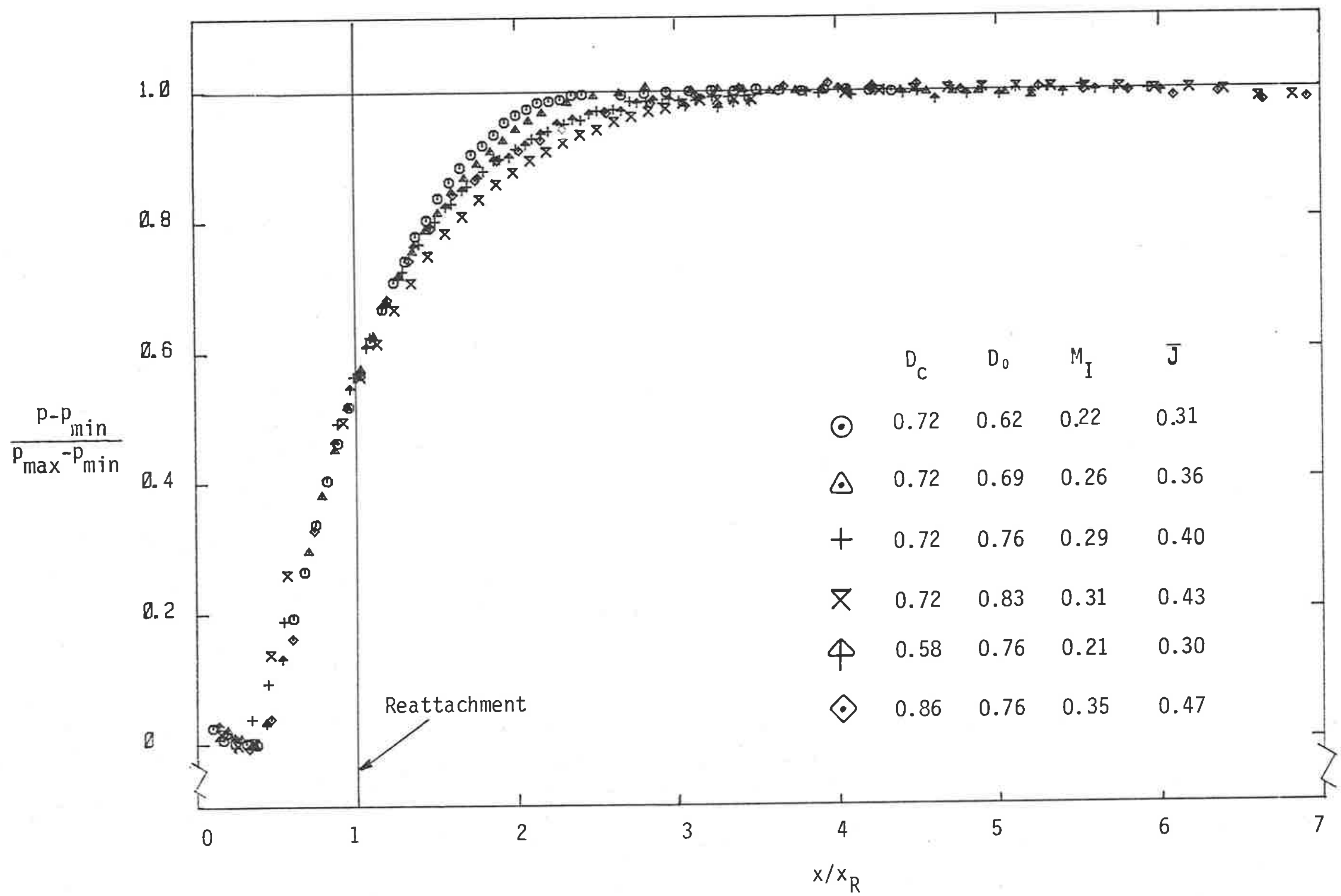

FIGURE 5.15 : STREAMWISE WALL STATIC PRESSURE VARIATION

$$C_p = \frac{p - p_{min}}{p_{max} - p_{min}}, \qquad (5.21)$$

and the X coordinate has been non-dimensionalized by the length of the reattachment region, x_R. Results are shown for one orifice, $D_0 = 0.76$, in combination with three different chokes, $D_c = 0.58$, 0.72, and 0.86, and also for four different orifice plates $D_0 = 0.62$, 0.69, 0.76, 0.83 in combination with one choke $D_c = 0.72$. With this normalization those of the former set collapse well on to a single curve; but for those of the latter, the rate of pressure recovery, particularly just after reattachment in the region $1.3 < X < 3.6$ is a function of the orifice size, recovery being faster the smaller the orifice. The precise shape of the pressure recovery curve therefore appears to be determined by the orifice size, irrespective of the flow rate.

5.6 Static Pressure Profiles

The results for flow velocities and Mach numbers in the preceding sections have been derived from measurements of total pressure and the static pressure at the wall at the same streamwise location. The assumption has been made that the static pressure is essentially constant over a given transverse cross-section of the flow - or, at least, that the static pressure has the same value on the centre-line as on the wall. The assumption is valid in the flow upstream of the orifice plate and also well downstream of it ($X > 6.5$). However, in the separated flow region immediately downstream of the orifice the streamlines of the flow exhibit appreciable curvature; this gives an increase in pressure with distance from the centre of curvature and the effect increases with the flow speed. In addition, the turbulence causes a variation of static pressure across the pipe diameter. Turbulence effects for the case of undisturbed fully developed turbulent flow can be calculated using the data of Laufer (1954). The radial variation of mean static pressure is given by the appropriately reduced form of the Navier-Stokes equation (refer to Goldstein, 1938, p.254):

$$r \frac{d}{dr}\left(\frac{\overline{p}}{\rho} + v'^2\right) = (w'^2 - v'^2) \ , \qquad (5.21)$$

where v' and w' are the rms radial and circumferential turbulence velocities; since v' and w' are zero at the wall, this equation can be integrated to give

$$\overline{p} = p_W - \rho v'^2 - \int_r^a \rho \frac{w'^2 - v'^2}{r} dr \ . \qquad (5.22)$$

Therefore the effect of turbulence can be calculated if v' and w' are known. Based on Laufer's data for Re = 500,000, at a centre line Mach number of 0.32, the maximum effect of turbulence would be about -1.1 Torr at $r/a \approx 0.97$; this would give a maximum -0.2% variation in static pressure or at the most +0.04% variation in the local Mach number. However, in the separated region where the turbulence intensities are high, effects due to turbulence are likely to be greater.

Measurements made with a small traversible static tube in flows with D_0 = 0.62 and 0.72 and D_C = 0.58, 0.72 and 0.86 show that the static pressures at the wall and the pipe centre-line are essentially the same except in the case region before the vena contracta, where the centre -line value is higher than the wall value. The maximum difference of 7 Torr is found at X = 1.3, and corresponds to a 1.6% under- -estimation of the Mach number; the effect diminishes to 1 Torr at X = 5.5, corresponding to 0.14% difference in the Mach number. These figures give an indication of the errors inherent in the data for the flow close to the orifice.

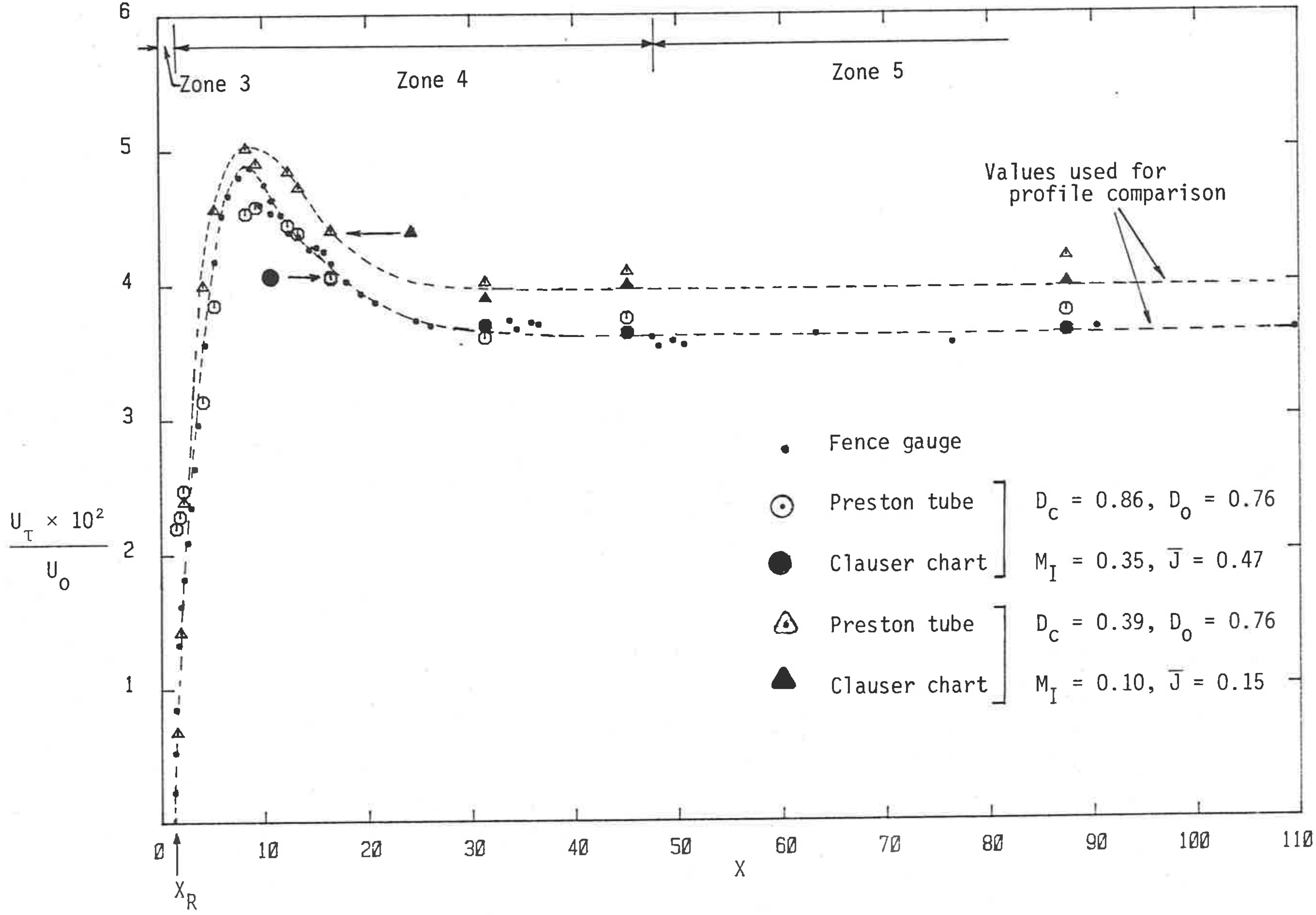

FIGURE 5.16 : WALL SHEAR STRESS MEASUREMENTS

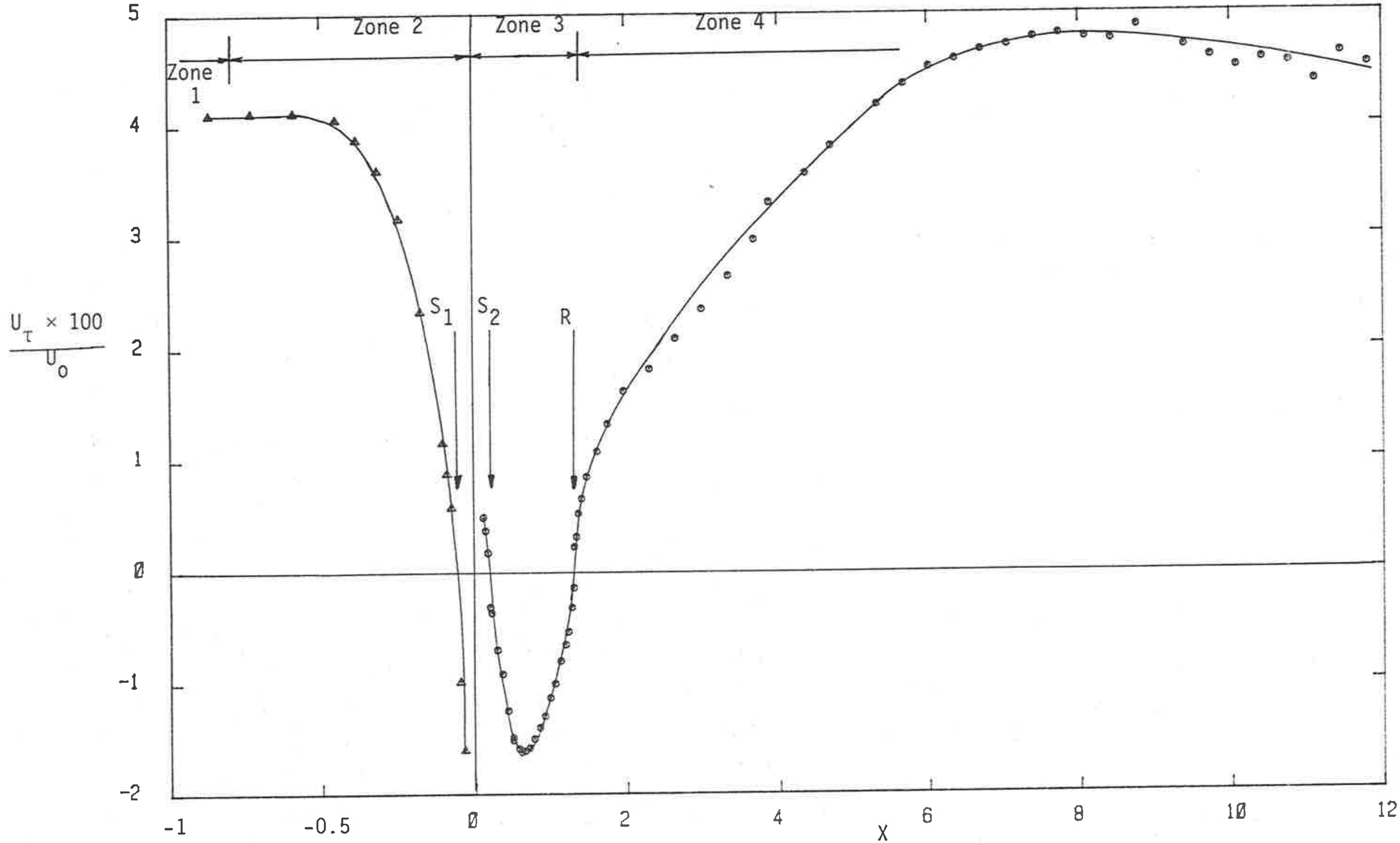

FIGURE 5.17 : WALL SHEAR STRESS MEASUREMENT; FENCE GAUGE RESULTS $D_c = 0.86$, $D_o = 0.76$, $M_I = 0.35$, $\overline{J} = 0.47$
(Note different scale ; upstream and downstream)

5.7 Mean Wall Shear Stress

Measured values of the mean wall shear stress τ_W, throughout the flow downstream of the orifice plate, are required for analysis of mean velocity profiles and their development, to be discussed later. These values have been obtained from

(i) Preston tube measurements,

(ii) surface fence gauge measurements, and

(iii) Clauser charts.

Clauser (1954) charts have been used to determine values of the ratio U_τ/U_0 of friction velocity $U_\tau = \sqrt{\tau_W/\rho}$ to centreline flow velocity at locations downstream of flow reattachment where recovery of the flow from the disturbance has progressed sufficiently for the measured mean velocity profiles (see Section 5.8 below) to show well-defined logarithmic regions. Such values, for $X \geqslant 16.5$, for flows with $D_0 = 0.76$ and $D_C = 0.39$ and 0.86, are shown in Figure 5.16.

For the flow with $D_0 = 0.76$ and $D_C = 0.86$ surface fence measurements have been made at closely spaced points over the whole of the region downstream of the orifice plate $0.08 \leqslant X \leqslant 109.6$. In this case, the Clauser chart values have been used to determine the calibration constant $K = \Delta p/\tau_W$ of the fence gauge in the region $X \geqslant 16.5$. This value (actually 72.7) has been assumed to apply also to the regions of separated, reattaching and recovering flow $0 \leqslant X < 16.5$. The values of U_τ/U_0 shown for the surface fence in Figure 5.16 have been obtained in this way. The validity of this procedure is confirmed by the quite good agreement (within a few percent) obtained between the Clauser chart and fence gauge values and corresponding values from Preston tube measurements which are also shown in Figure 5.16. The values of U_τ/U_0 which are used later in discussion of the development of the mean velocity profiles during recovery are shown by the broken line in Figure 5.16.

For the flow with $D_0 = 0.76$ and $D_C = 0.39$, for which no surface fence measurements were made, Clauser chart and Preston tube results are also consistent for $X \geq 16.5$. The values of U_τ/U_0 for velocity profile comparisons, shown in Figure 5.16, are based on these values and the Preston tube data for $0 \leq X \leq 16.5$.

It can be seen from Figure 5.16 that, as observed by Bradshaw and Wong (1972) in the case of reattachment and relaxation of separated boundary layers, the wall shear stress and U_τ/U_0 do not return monotonically to their equilibrium values after the disturbance. Here, as X increases downstream of reattachment, the value of U_τ/U_0 rises from zero at reattachment to a maximum value at $X \simeq 7.7$, about 25% higher than that for the undisturbed flow; it then falls off, regaining values typical of undisturbed flow at $X \simeq 30$.

The variation of U_τ/U_0 with X over zones 2, 3, and 4 for flow with $D_0 = 0.76$, $D_C = 0.86$, is shown in Figure 5.17.

In the separated flow region (zone 3) $0 \leq X \leq 1.4$, as in the corresponding region in two-dimensional flow over a backward-facing step investigated by Eaton, Jeans, Ashjaee and Johnston (1979), quite large negative values of skin friction associated with the reversed flow are observed. The largest negative value corresponds to $U_\tau/U_0 \simeq -0.016$, some 40% of the undisturbed flow value. Closer to the orifice plate, in the region $0 \leq X \leq -0.06$ upstream of the secondary separation, small positive shear stress values are again observed.

Upstream of the orifice plate U_τ/U_0 falls rapidly in zone 2, from its undisturbed flow value in zone 1 to zero at the primary separation point. Between S1 and the orifice plate it assumes negative values of similar magnitude to those in the separated flow downstream of the orifice plate.

5.8 Mean Velocity Distributions

Variation of the mean-velocity profile across the pipe from its initial undisturbed fully-developed state well upstream of the orifice to its re-established fully developed state well downstream, over the range $9.3 \leqslant X \leqslant 87$, has been investigated for the flows with $D_0 = 0.62$ to 0.86 and $D_C = 0.39$ to 0.86. The measurements were made with a pitot tube, and for $D_C = 0.39$ velocity profiles were also measured with a hot wire anemometer. Data obtained by the two methods compare well as shown in Figure 5.18. The pitot tube and hot wire were always set with their axes parallel to the pipe axis.

Data were recorded digitally, and mean values obtained as an average of 100 samples (1000 samples with hot wire) over a period of 1 second at each radial location.

Velocities in the reversed flow were obtained from total pressure measurements, with the mouth of the pitot tube facing in the opposite direction to the main flow. Static pressure was taken from the tapping in the pipe wall at the same axial location as that of the pitot tube entry. The pitot tube was always removed from the pipe before measuring the static pressure. In the mean velocity values presented no account is taken of any local inclination of the mean flow to the pipe axis. Errors from this source will be greatest in the vicinity of separation and reattachment points where streamline curvature is highest.

Total pressure measurements are subject to additional error in the unsteady flow which occurs near a reattachment point, as a result of reversals in flow direction during measurement. Kim, Kline and Johnston (1980) estimate that such effects introduce uncertainties of about 10% of measured velocities.

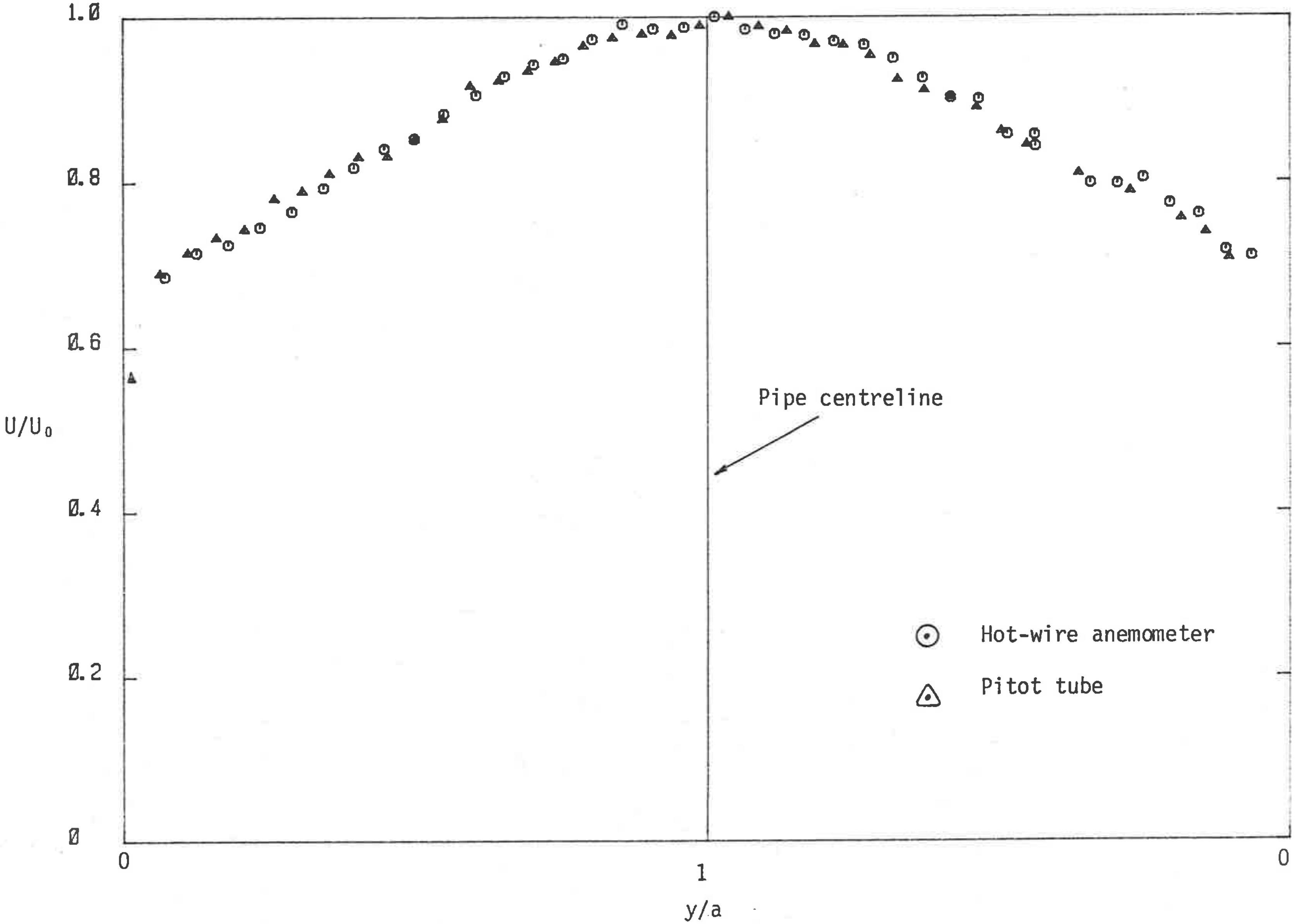

FIGURE 5.18 : MEAN VELOCITY PROFILE USING PITOT TUBE AND A HOT-WIRE ANEMOMETER, X = 4.18
(D_c = 0.39, D_0 = 0.76, M_I = 0.10 , $\bar{J}$ = 0.15)

Profiles for flows with $D_0 = 0.76$ and $D_C = 0.39$ and 0.86, are shown in Figure 5.19. In the flow approaching the orifice, a fully developed velocity profile exists at $X = -8.27$, but divergence from it is evident at $X = -1.83$*,

In the region of reversed flow downstream of orifice plate $0 \leq X \leq X_R$, profiles are shown for four values of X, viz. 0.34, 0.55, 0.90 and 1.21. The variation of the maximum reverse velocity U_N, its distance from the wall and the distance of the point of zero velocity from the wall with streamwise distance x non-dimensionalised by x_R, is shown in Figure 5.20. The maximum backflow velocity occurs slightly less than half-way along the separation bubble and has a value approaching 27% of the corresponding centreline velocity, which is slightly higher than that measured for the flow over a two-dimensional backward-facing step - 20% by Bradshaw and Wong (1972), 21% by Kim, Kline and Johnston (1980), 18% by Etheridge and Kemp (1978) and the 21% measured by Back and Roschke (1972) for a sudden expansion in a circular pipe.

The distance from the wall of the position of zero velocity (i.e. the point above and below which the fluid is moving in opposite directions) is slightly greater than the height of the orifice plate just downstream of the orifice (at $x/x_R \approx 0.1$), and the data for the two cases collapse fairly well on a single curve against streamwise distance normalized with the reattachment length.

As X increases beyond X_R, the velocity profiles develop two points of inflexion; this can be clearly seen in those for $X = 1.52$ to 4.18. In this region the mass flow distribution is displaced towards the pipe centreline as compared with that of an undisturbed flow velocity profile, as shown in Figures 5.21(a) and (b) for the

* i.e. close to the point, where the flow starts separating from the pipe wall.

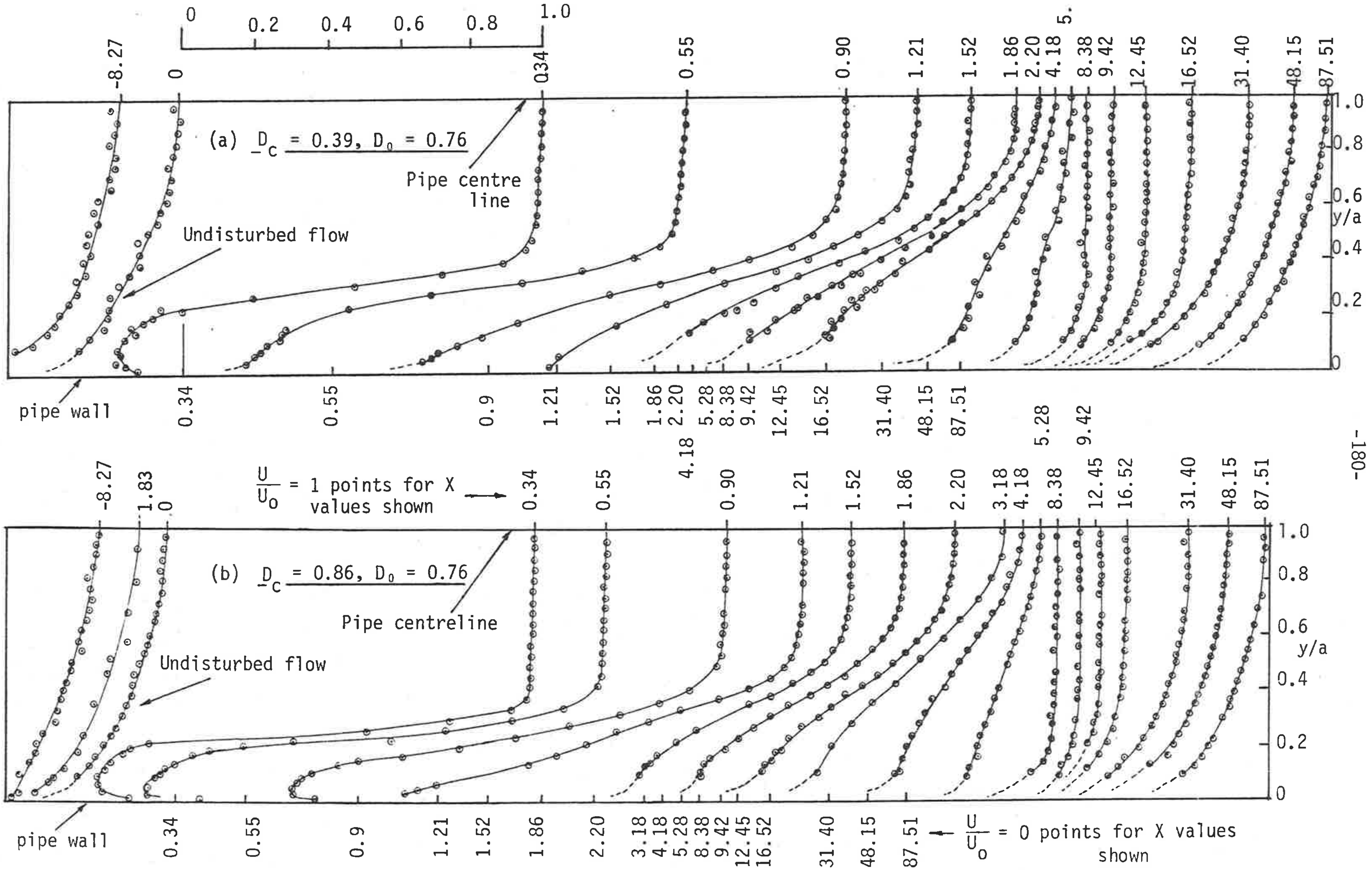

FIGURE 5.19 : VELOCITY PROFILES

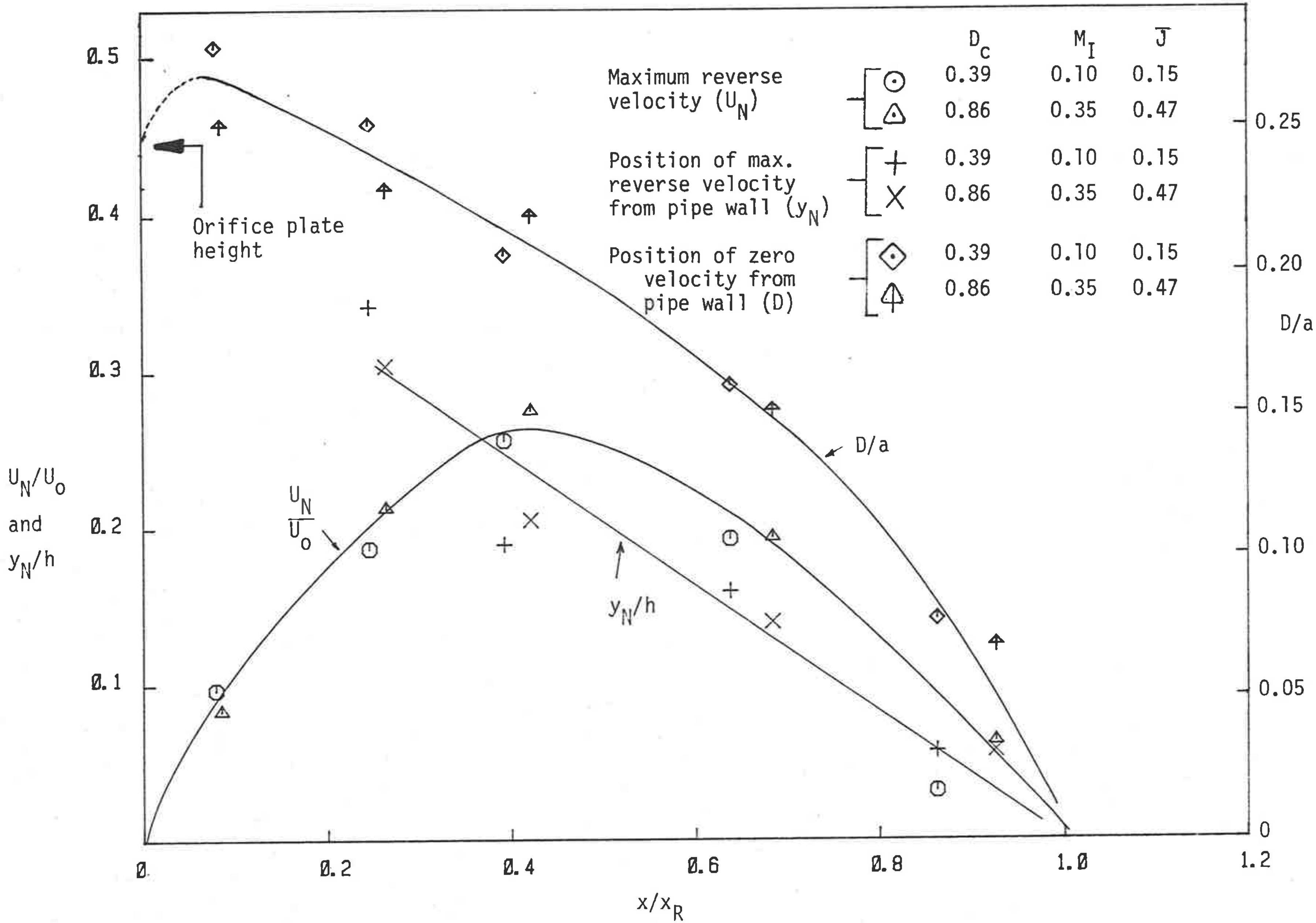

FIGURE 5.20 : MEASUREMENTS IN THE SEPARATED REGION, D_o = 0.76

flow $D_0 = 0.76$, $D_C = 0.86$. [Note: the mass flow rate profiles are at slightly different streamwise distances from those of velocity profiles.] As X is further increased, the inflexional character becomes less marked; it is still perceptible at X = 8.38 but not at X = 12.45. At this stage, the velocity profile has become very flat and the mass flow distribution is now displaced toward the pipe wall (refer again to Figure 5.21). With yet further increases in X, the profiles approach the undisturbed profile. The final stage involves the redistribution of mass flow back towads the pipe centreline, which seems to be essentially complete at X ≃ 48. The variation in mass flow distribution with X follows the changes in direction of the radial centrifugal force to which the fluid is subjected as a result of reversal in streamline curvature between points upstream and downstream of the reattachment points.

Profiles of mass flow rate per unit area shown in Figure 5.21(a) are ρU profiles non-dimensionalised by the centreline value of $\rho_0 U_0$. The total mass flow rate at a given streamwise location is given by $2\pi \int_0^a \rho U \, r \, dr$; ρUr profiles (non-dimensionalised by $\rho_0 U_0 a$, for the flow $D_0 = 0.76$, $D_C = 0.86$ are shown in Figure 5.21(b).

The total (net) mass flow rate, obtained from the areas under these curves is essentially the same at all stations throughout the pipe, as it should be.

The development of the free jet shear layer in the separated flow region (zone 3) downstream of the orifice and the recovery of the attached flow to the fully developed state (zones 4 and 5) are also quite clearly shown by the streamwise variation of the displacement thickness δ^*, momentum thickness θ and shape factor H of the forward flow. In this case δ^* and θ are appropriately defined by the relations

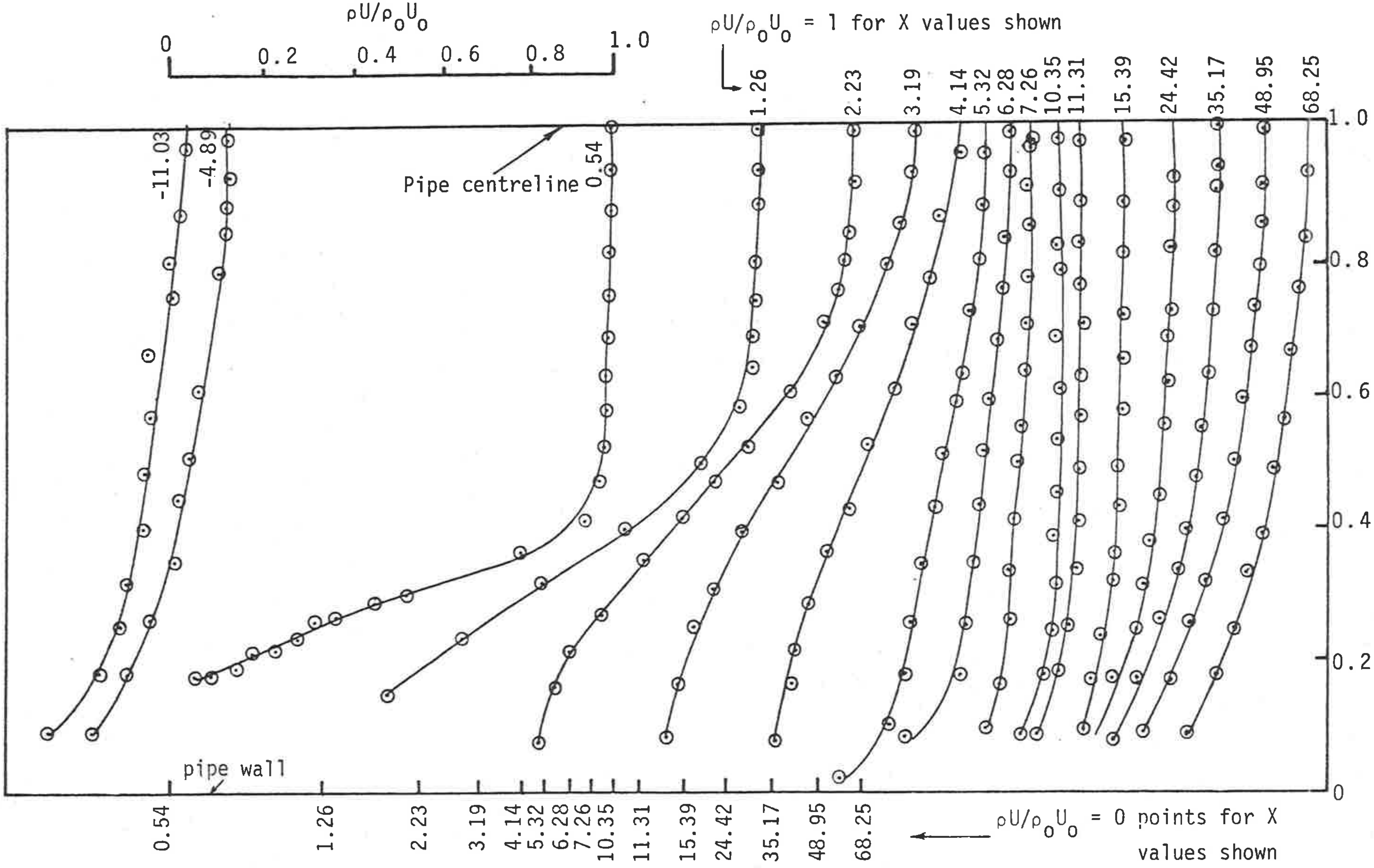

FIGURE 5.21a : MASS FLOW PROFILES (D_o = 0.76, D_c = 0.86, M_I = 0.35, $\bar{J}$ = 0.47)

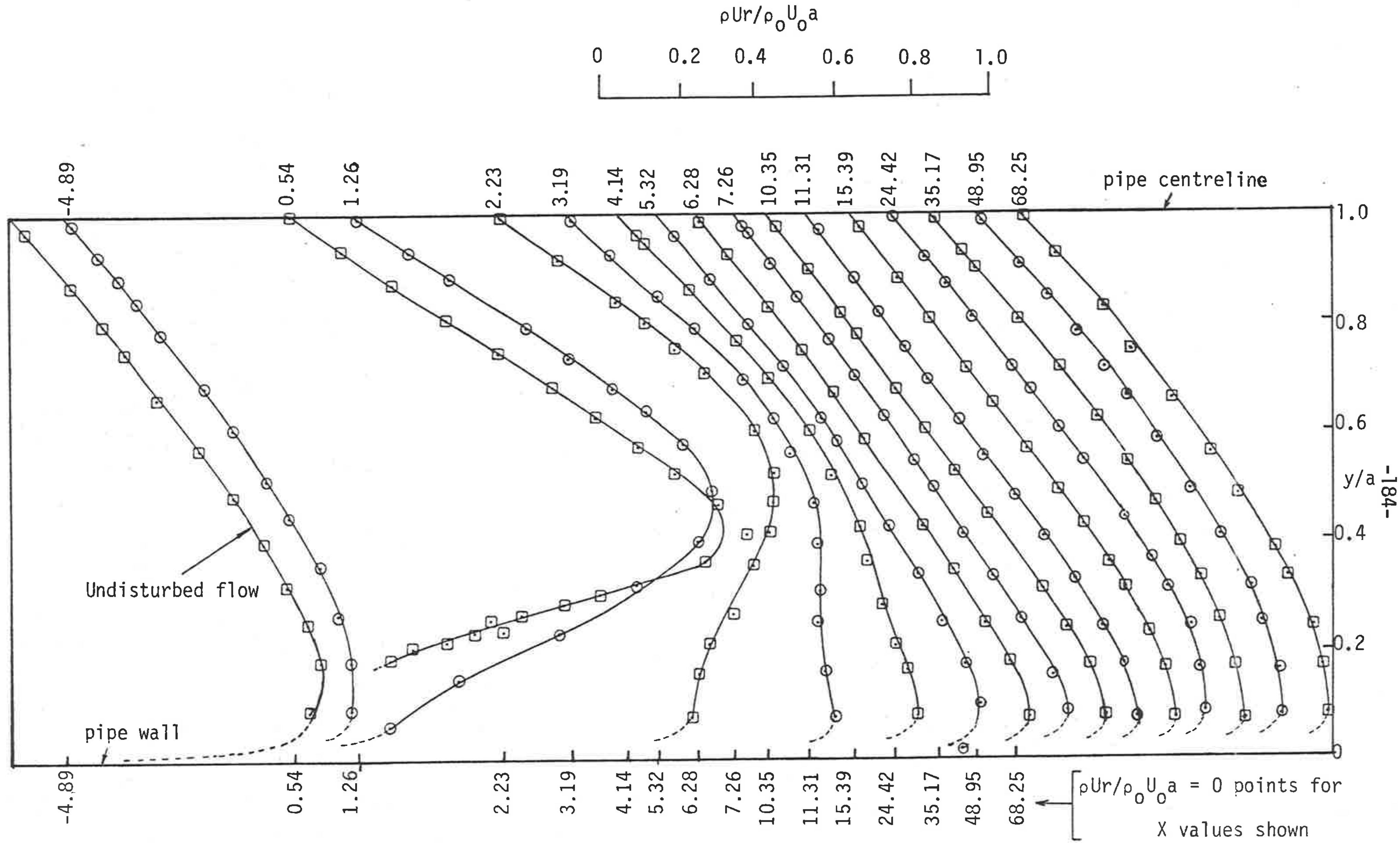

FIGURE 5.21b : MASS FLOW PROFILES (D_o = 0.76, D_c = 0.86, M_I = 0.35, $\overline{J}$ = 0.47)

$$\frac{\delta^*}{R} = \frac{R}{R_0} \int_0^{R_0/R} (1 - \frac{U}{U_0})\frac{r}{R}\, d(\frac{r}{R}) \ , \tag{5.23}$$

$$\frac{\theta}{R} = \frac{R}{R_0} \int_0^{R_0/R} (1 - \frac{U}{U_0})\frac{U}{U_0}\, \frac{r}{R}\, d(\frac{r}{R}) \ , \tag{5.24}$$

and

$$H = \delta^*/\theta \ , \tag{5.25}$$

where R_0 is the radius in the separated-flow region at which the mean flow velocity is zero and beyong which the flow is in the reverse direction. In the recovery region $X > X_R$, where there is no reverse flow, $R_0 = R$. Values of these parameters are shown in Figures 5.22(a), (b) and (c). δ^* and θ both have small values in the nearly uniform flow through the orifice at $X = 0$. They both increase fairly linearly with X, over the separated-flow region, reaching a maximum at about $X = 4.2$, then decrease to a minimum at about $X = 13.4$ where the mean velocity profile is very flat over a substantial part of the pipe radius, and finally rise slowly towards the fully-developed-flow values which are reached at $X \gtrsim 48$.

The shape factor rises from about 1.7 at $X = 0$ to a maximum of 2.4 near re-attachment, then rapidly drops off reaching a value of 1.34 typical of undisturbed flow at $X \simeq 6$; thereafter it remains very nearly constant at this value.

The progress towards a re-established equilibrium state can also be followed in the variation of the Clauser parameter G, given by

$$G = (\int_0^{\delta} (U_0-U)^2 \ dy/u_\tau^2\delta)/(\int_0^{\infty} (U_0-U)dy/u_\tau\delta)$$

$$\equiv (\frac{2}{C_f})^{1/2} \ (H-1)/H, \tag{5.26}$$

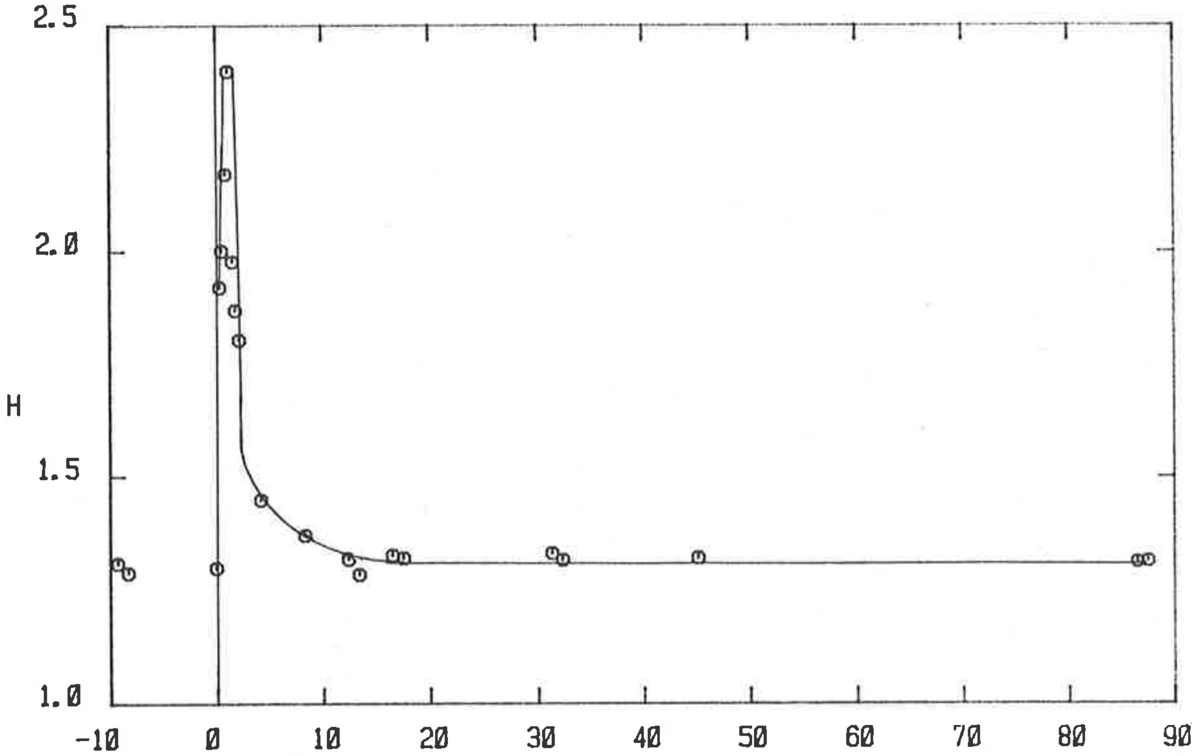

FIGURE 5.22(a) : DEVELOPMENT OF SHAPE PARAMETER , H

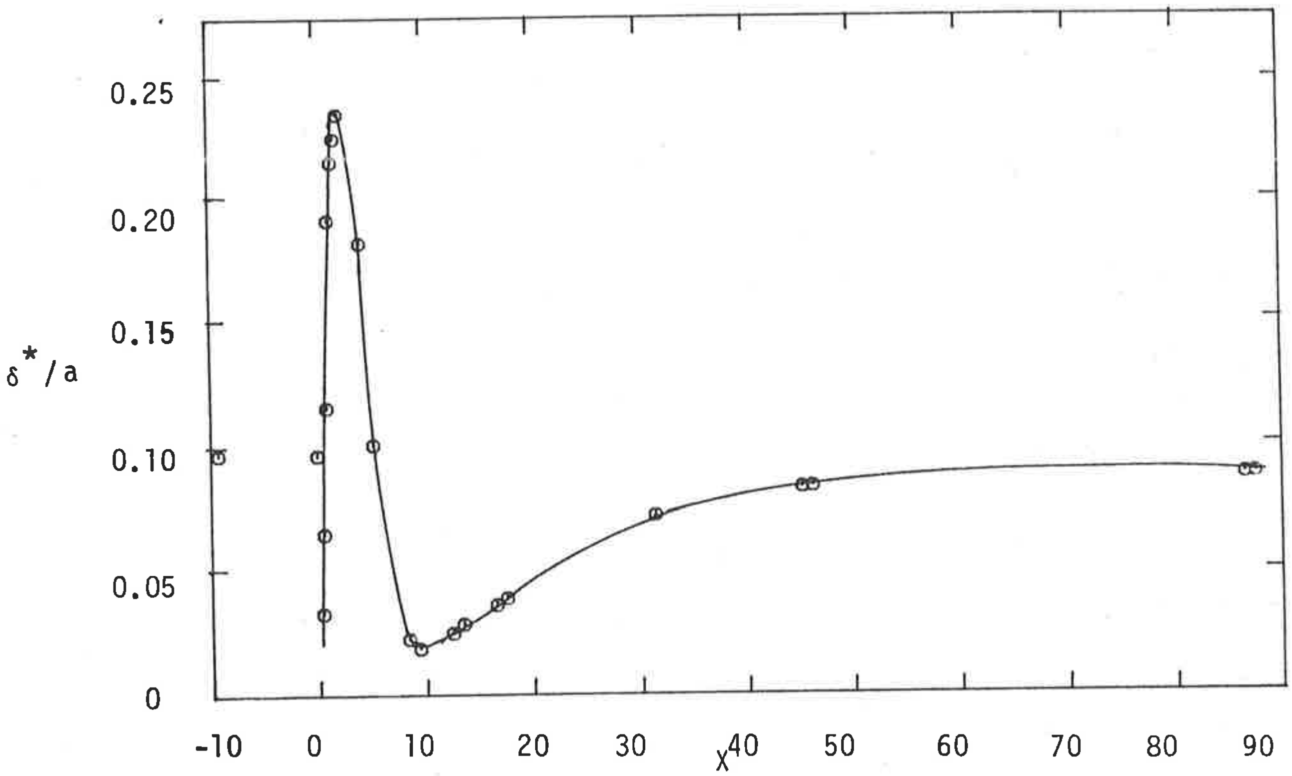

FIGURE 5.22(b) : DEVELOPMENT OF DISPLACEMENT THICHNESS, δ*

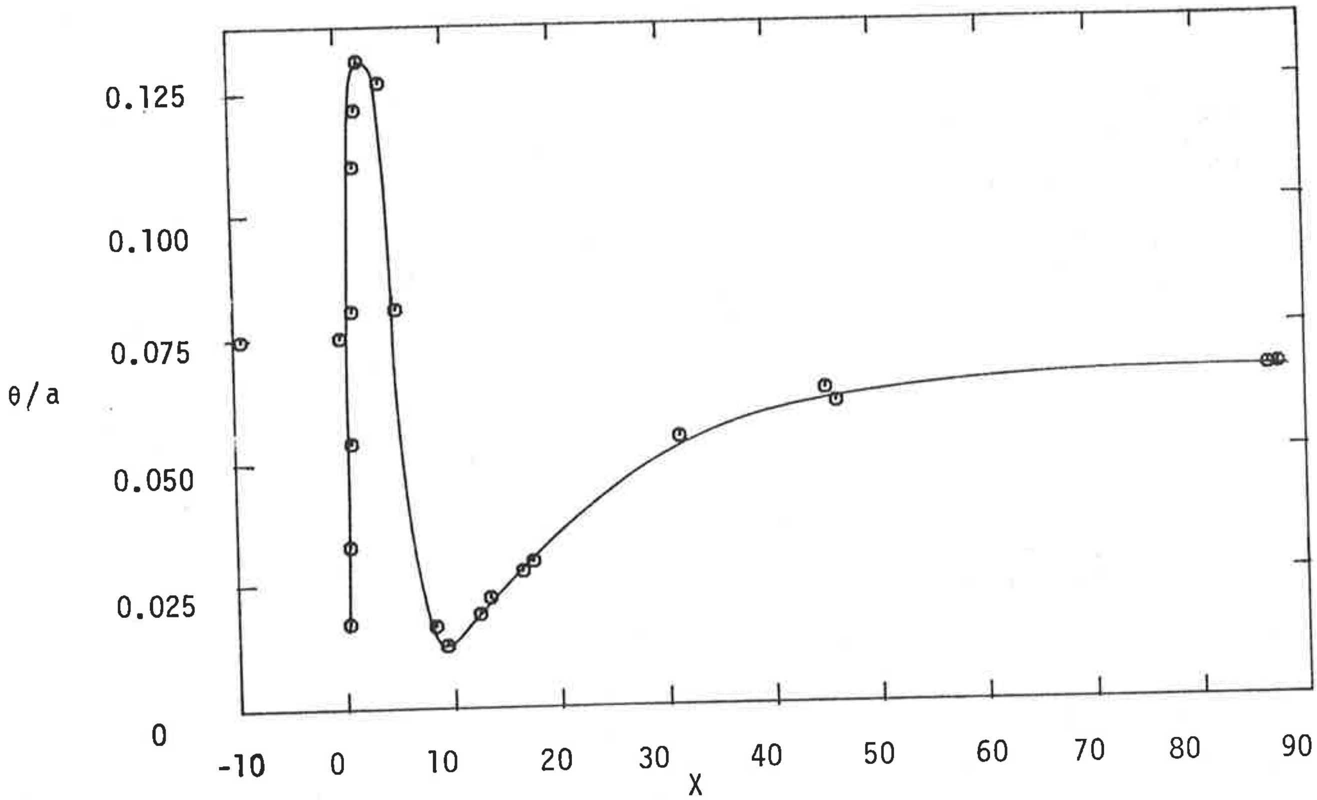

FIGURE 5.22(c) : DEVELOPMENT OF MOMEMTUM THICKNESS, θ

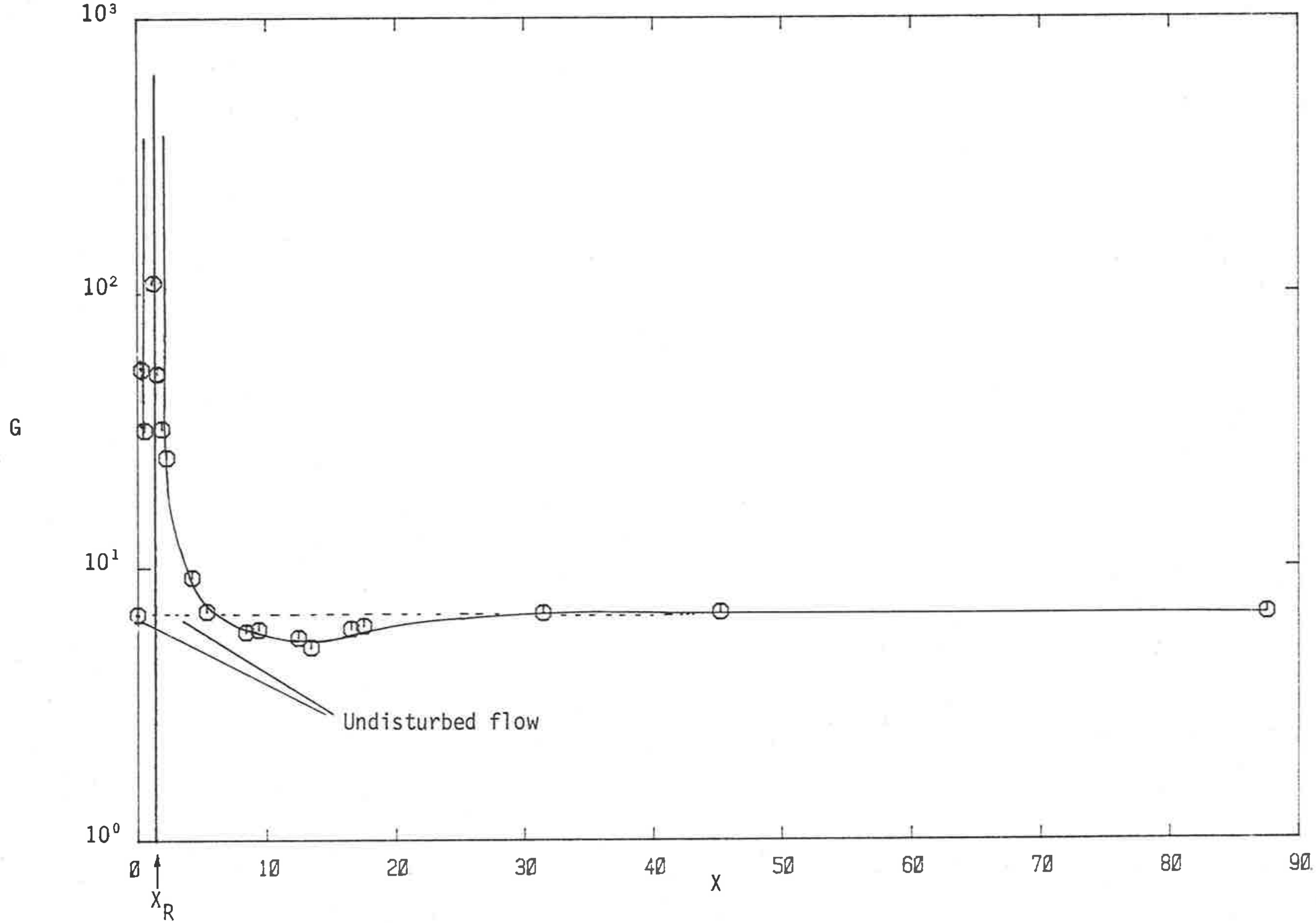

FIGURE 5.23 : VARIATION OF CLAUSER PARAMETER G WITH STREAMWISE DISTANCE (D_C = 0.86, D_O = 0.76, M_I = 0.35, $\overline{J}$ = 0.47)

which gives a measure of the departure of a turbulent boundary layer from equilibrium (see also Bradshaw and Wong, 1972).

Calculated values of G (based on C_f obtained from the surface fence gauge results) are shown in Figure 5.23. G rises to large values near reattachment (at $X = X_R$, $C_f = 0$) and then sharply decreases to a minimum in the recovery region (zone 4) at $X \sim 13$. It then rises slowly to the constant equilibrium value typical of the undisturbed flow, reaching it at $X \sim 48$ ($x/h \sim 370$).

The preceding results describe the general character of the flow before and after disturbance and of its subsequent recovery to an equilibrium fully-developed state. Some consideration will now be given to the forms of similarity exhibited by the mean velocity profiles.

The applicability to the separating, separated and reattaching two-dimensional turbulent boundary layer of the well-established logarithmic form of the law of the wall,

$$U/U_\tau = U^+ = \frac{1}{K} \ln Y^+ + B \tag{5.27}$$

(where $Y^+ = yU_\tau/\nu$), of extensions to it such as the Coles (1956) law-of-the-wall/law-of-the-wake formulation,

$$U_+ = \frac{1}{K} \ln Y^+ + B + \frac{\Pi}{K} w(y/\delta_c) \ , \tag{5.28}$$

and of alternative forms such as the similarity relations proposed by Perry and Schofield (1973) has been fairly extensively investigated and reported. Because of the general similarities between turbulent boundary layer flow and fully-developed turbulent pipe flow, it would not be too surprising if some of the characteristics of separating and reattaching boundary layers were also found in the corresponding pipe flows.

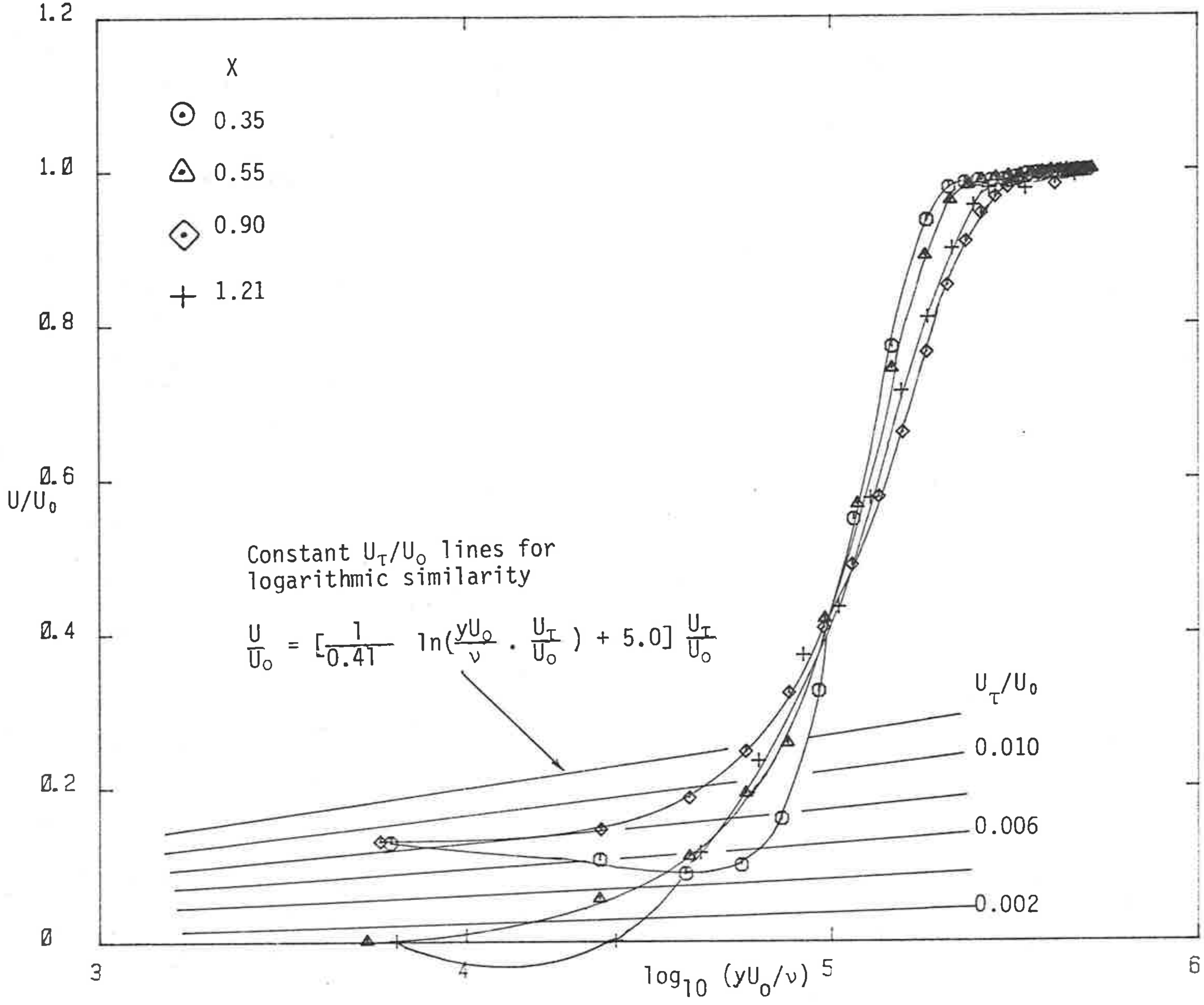

FIGURE 5.24(a) : VELOCITY PROFILES ON CLAUSER PLOT, D_C = 0.86, D_0 = 0.76, M_I = 0.35, $\bar{J}$ = 0.47

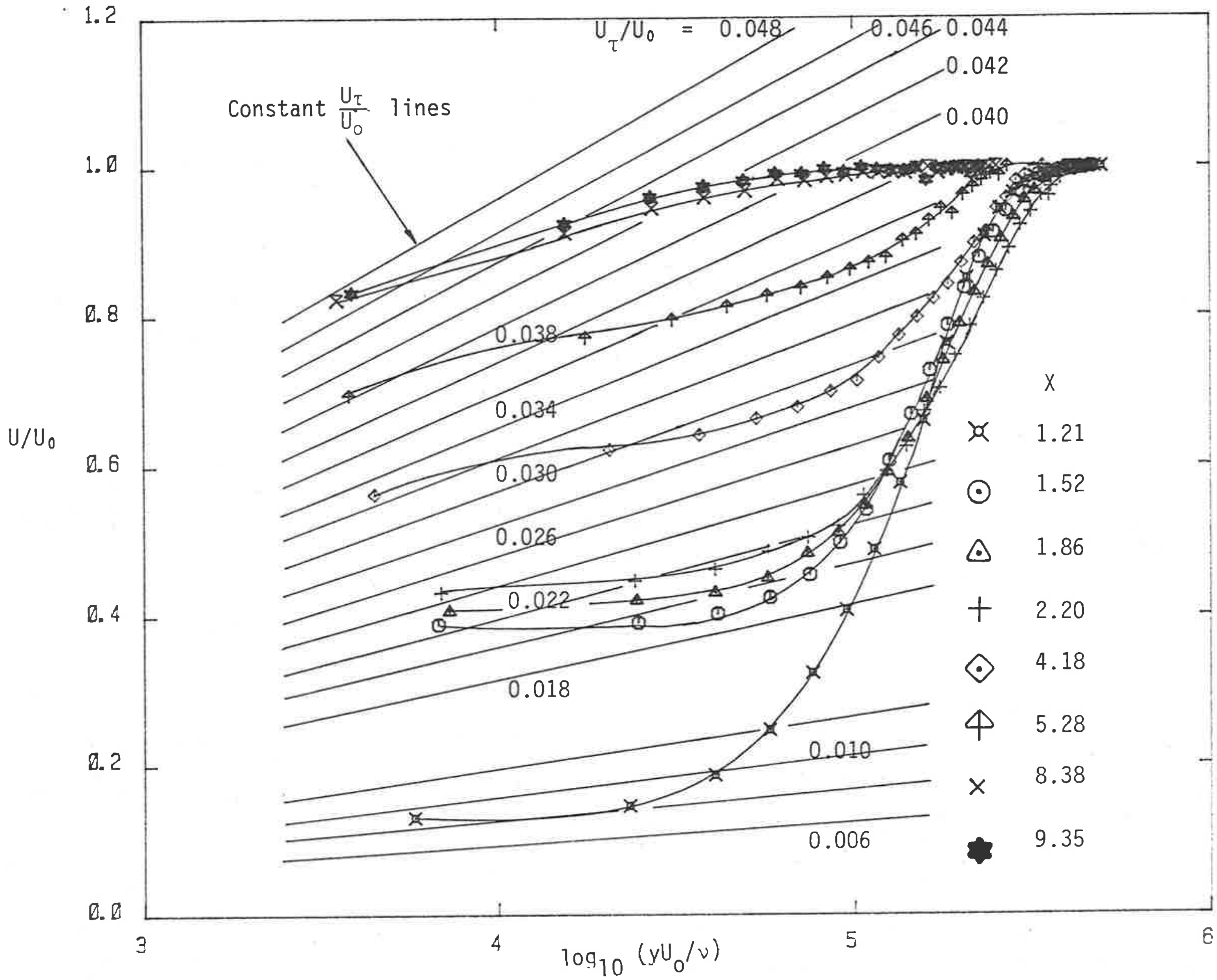

FIGURE 5.24(b) VELOCITY PROFILES ON CLAUSER PLOT, D_C = 0.86, D_υ = 0.76, M_I = 0.35, $\bar{J}$ = 0.47

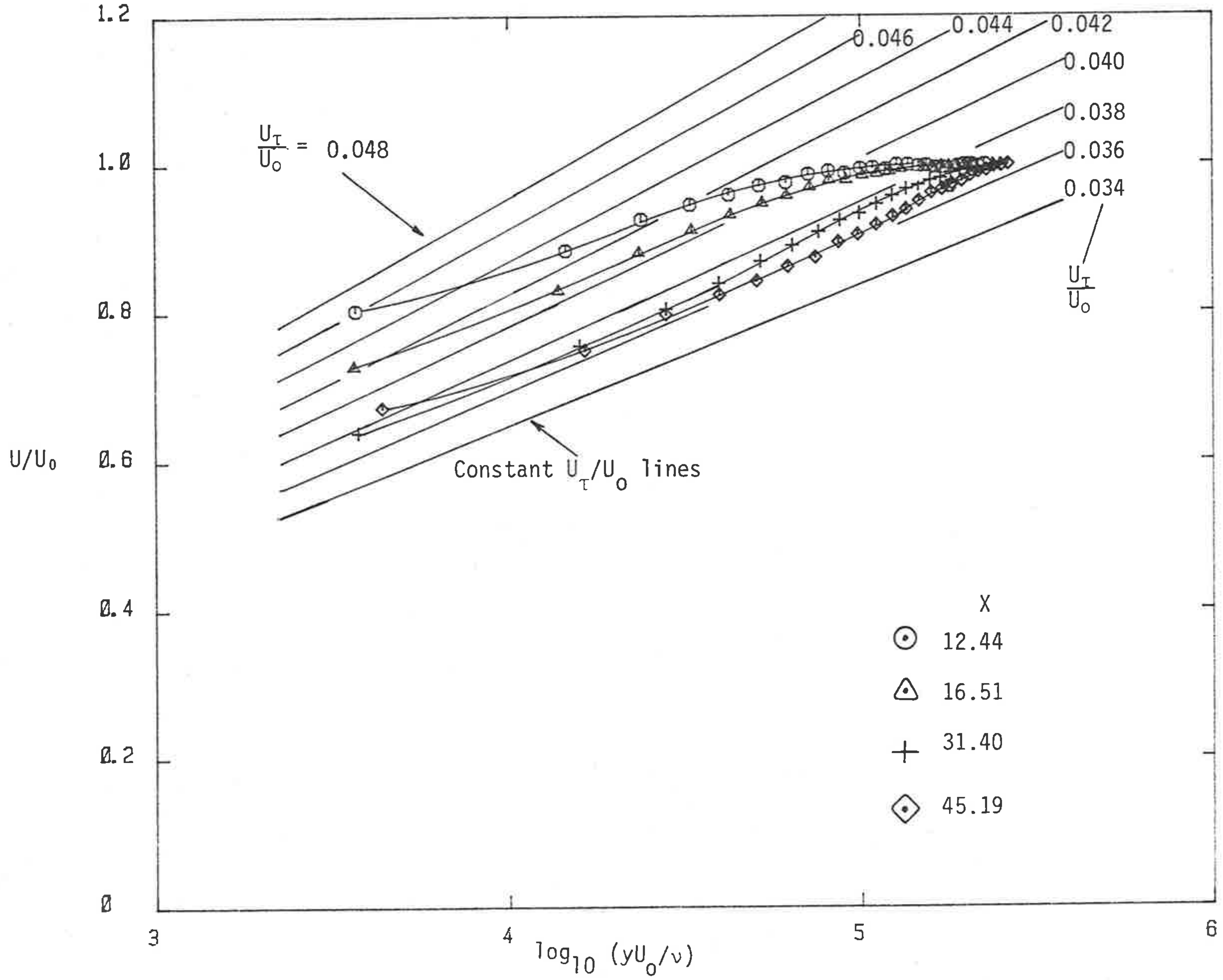

FIGURE 5.24(c) : VELOCITY PROFILES ON CLAUSER PLOT, D_C = 0.86, D_0 = 0.76, M_I = 0.35, $\bar{J}$ = 0.47

Stratford (1959), Simpson, Strickland and Barr (1977), and Schofield (1983) have shown for their two dimensional flows that as the turbulent boundary layer approaches separation the extent of the logarithmic region gradually decreases; the work of Simpson, Chew and Shivaprasad (1981) shows that at the streamwise position where intermittent separation is first observed a logarithmic region no longer exists. Following reattachment a logarithmic region is re-established and increases with distance downstream (Bradshaw and Wong, 1972, and Schofield, 1983).

Mean velocity profiles of the separated, reattaching and recovering flow (zones 3 and 4) in the present turbulent pipe flow with $D_0 = 0.76$ and $D_C = 0.86$ are shown on Clauser plots (U/U_0 against $\log_{10}(yU_0/\nu)$ together with lines of constant U_τ/U_0 corresponding to logarithmic wall similarity) in Figures 5.24(a), (b) and (c). The same data in terms of U^+ and Y^+ coordinates are shown in Figures 5.25(a) and (b) and corresponding results for $D_0 = 0.76$, $D_C = 0.39$, in Figure 5.26(a) and (b). Values of U_τ used in the profile comparison are those based on fence gauge measurements, shown in Figures 5.16 and 5.17.

If the fence-gauge data for U_τ/U_0 are accepted, then, as might be expected, for the separated flow ($X < 1.3$) there is a considerable mismatch between the profiles on the Clauser plot and the logarithmic wall similarity line which would correspond to the measured U_τ/U_0 value, since the latter is characteristic of the wall stress in the reversed flow. In the separated flow and immediately downstream of reattachment, there are not enough data points to allow a definite statement about the existence of a logarithmic region to be made. However, for $\underset{\sim}{X} > 16$ a logarithmic region is clearly evident, and the

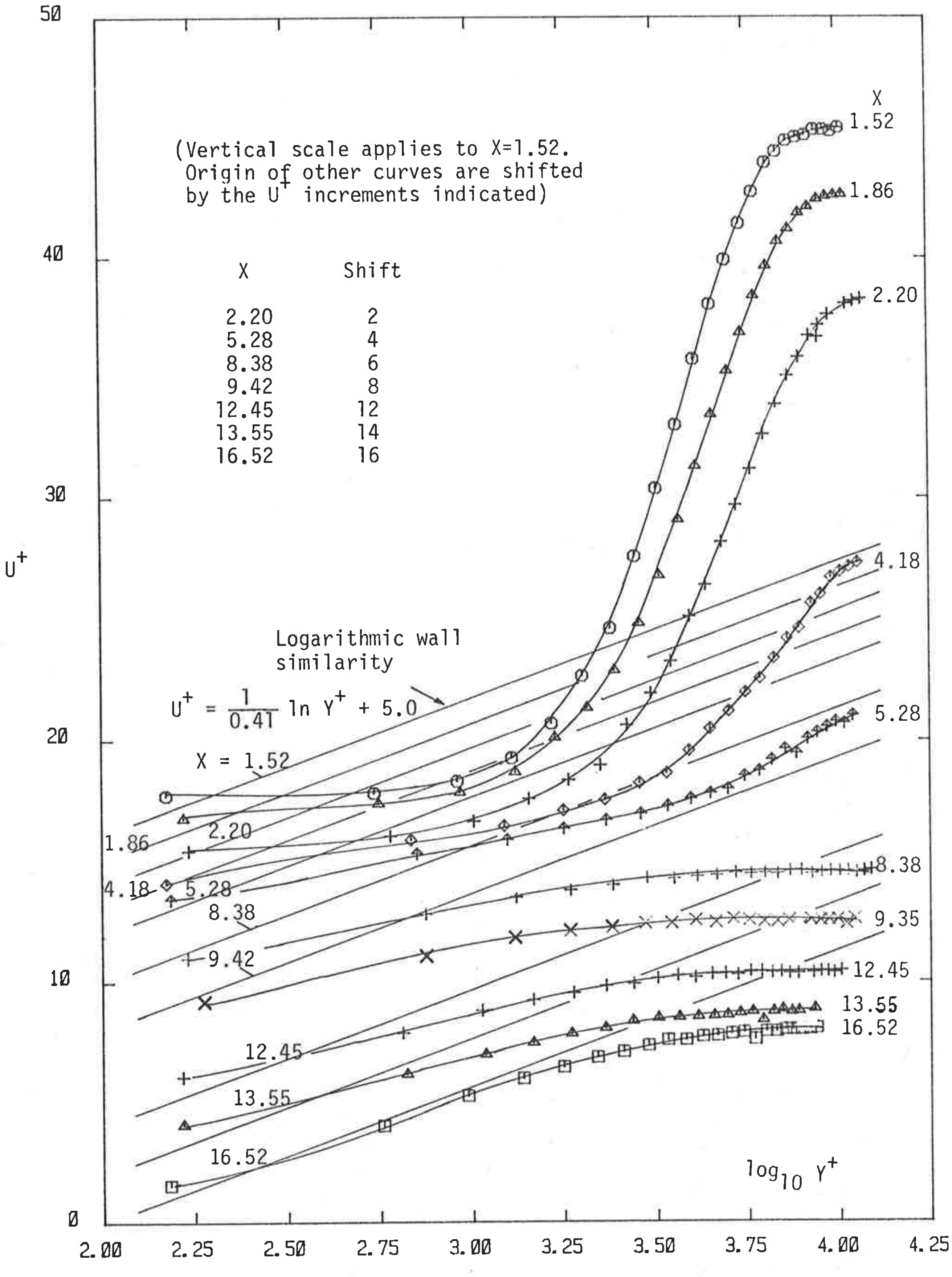

FIGURE 5.25(a) : MEAN VELOCITY DISTRIBUTION IN UNIVERSAL FORM

$D_o = 0.76$, $D_c = 0.86$, $M_I = 0.35$, $\bar{J} = 0.47$

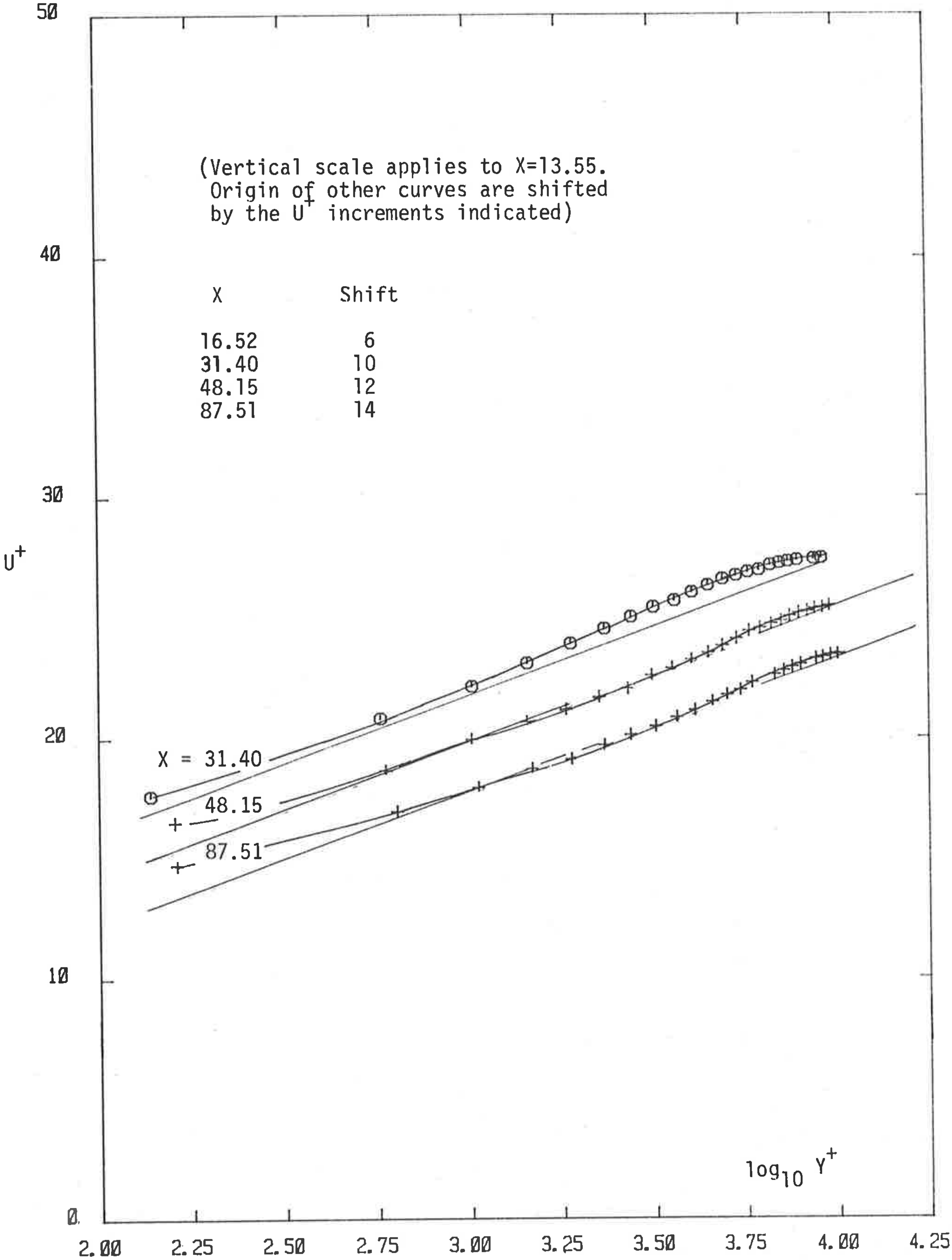

FIGURE 5.25(b) : MEAN VELOCITY DISTRIBUTION IN UNIVERSAL FORM, $D_0 = 0.76$, $D_c = 0.86$, $M_I = 0.35$, $J = 0.47$

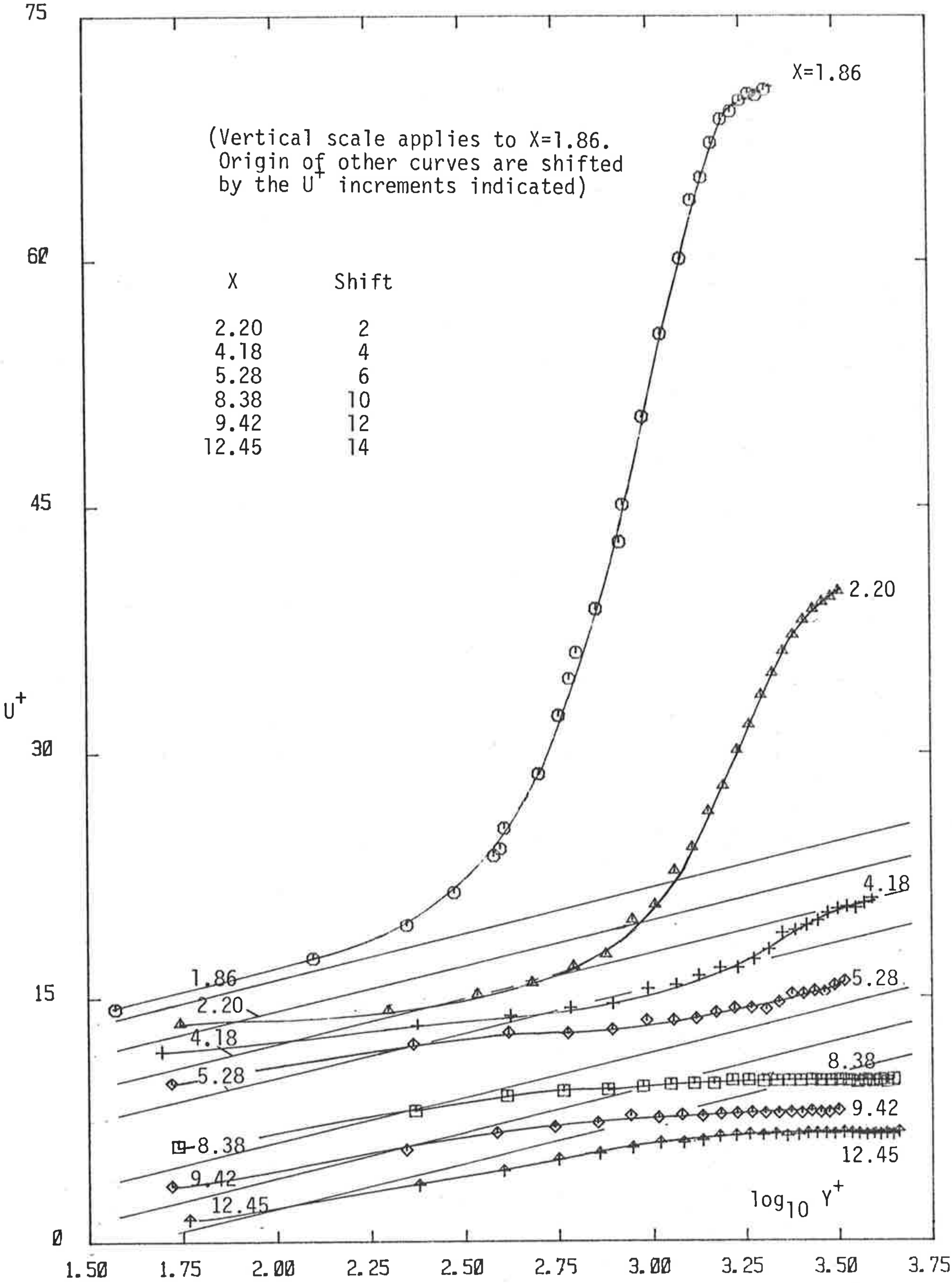

FIGURE 5.26(a) : MEAN VELOCITY DISTRIBUTION IN UNIVERSAL FORM
$D_0 = 0.76$, $D_c = 0.39$, $M = 0.10$, $J = 0.15$

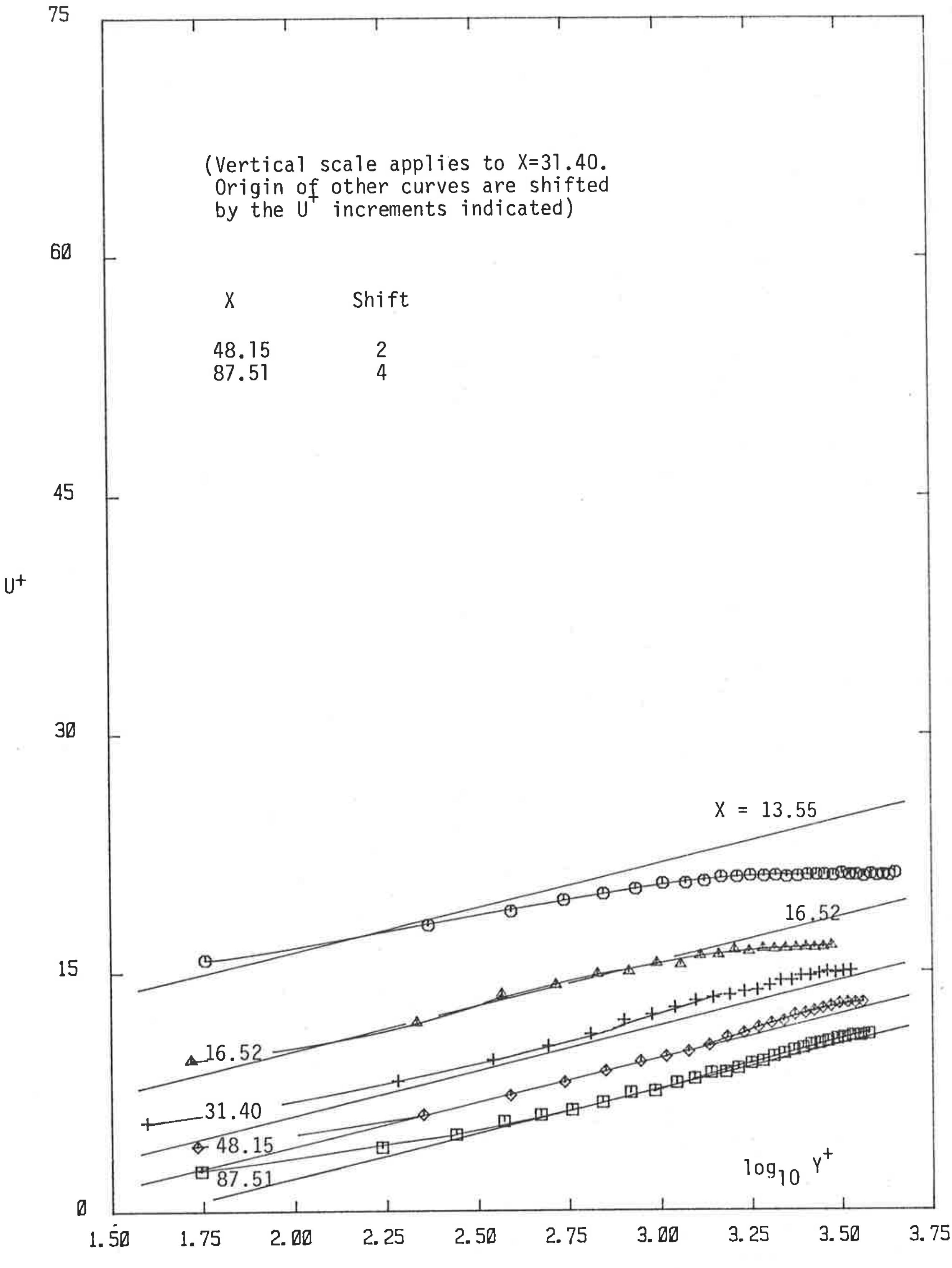

FIGURE 5.26(b): MEAN VELOCITY DISTRIBUTION IN UNIVERSAL FORM
$D_o = 0.76$, $D_c = 0.39$, $M_I = 0.10$, $J = 0.15$

general form of the development of the the profiles is consistent with the existence of a logarithmic region at least for X values greater than about 4.

Just after reattachment a large wake component is observed; it becomes less dominant as the flow progresses downstream, being still present at $X = 5.28$ but not at $X \geq 8.38$. The doubly inflexional character of the velocity profiles referred to earlier (p.182) in discussion of Figure 5.19 now appears as a dip below the logarithmic line at all streamwise locations, $X \leq 5.28$. For $8.38 \leq X \leq 16.52$ the profiles lie completely below the log line; and for $X \geq 31.4$ they have regained the small wake component typical of fully-developed equilibrium flow. Similar dips have been observed by Bradshaw and Wong (1972) and by Kim, Kline and Johnston (1980), in two-dimensional flows. The dip indicates that the flow is not in local equilibrium and that the local wall-shear velocity, U_τ, used as the inner velocity scale, is not the proper scale over the whole flow cross-sectcion. Bradshaw and Wong point out that, since the gradient of the total shear stress $\partial\tau/\partial y$ is positive near the wall in the reattachment region, the local equilibrium formula of Townsend (1961),

$$\frac{\partial u}{\partial y} = \frac{(\tau/\rho)^{1/2}}{Ky} \tag{5.29}$$

would predict a velocity gradient even higher than would the corresponding formula based on the logarithmic value $(\tau_w/\rho)^{1/2}/Ky$, rather than the lower value observed experimentally on the wall side of the dip. They concluded that the length scale in this region is not Ky, but one increasing more rapidly with y. This was confirmed by Eaton and Johnston (1980) from their measurements downstream of a backward facing step: they found the mixing length in the region $y/\delta < 0.2$ to be much larger than Ky.

This is attributable to the large scale imposed on the flow close to the wall by the approach to the wall in the reattachment process of the large eddies of the free separated shear layer. This form of scale variation seems to be the reason for both the dip below the log-law and also the disappearance of the wake component from the velocity profiles at $8.38 \leqslant X \leqslant 16.52$.

5.8.1 Velocity profiles in the Region of Adverse Pressure Gradient Downstream of Reattachment ($1.5 \lesssim X \lesssim 6$)

As discussed earlier in this section, it is known that the logarithmic law is valid in a turbulent boundary layer approaching separation and that the the logarithmic region gradually decreases in extent and has disappeared at separation. Stratford (1959) reported measurements in a two-dimensional turbulent boundary layer in a state of incipient separation, with a velocity profile not containing a logarithmic region but having a half-power law of the form

$$U = \text{const}(\alpha y)^{1/2} + \text{const}(\alpha \nu)^{1/3} \qquad (5.30)$$

where

$$\alpha = \frac{1}{\rho}\frac{dP}{dx} \, . \qquad (5.31)$$

The form of this velocity profile, and difficulties associated with both inner-layer velocity distributions based on U_τ and velocity-defect relations of the form

$$\frac{U_0 - U}{U_\tau} = \phi(y/\delta) \qquad (5.32)$$

in turbulent boundary layers in adverse pressure gradients approaching separation, where $U_\tau \to 0$, suggest that U_τ is not an appropriate velocity scale for separating and separated layers; and this notion was subsequently accepted by a number of investigators. One formulation based on an alternative length scale, which gives a good description of a considerable body of experimental data, is that of Perry and Schofield (1973) who proposed universal empirical correlations for the inner and outer regions of adverse-pressure-gradient boundary layers near separation. Their correlations apply to all types of such layers, whether they are in equilibrium or not, but are limited to cases where $\tau_m/\tau_w > 1.5$. The velocity scale used is $U_m = \sqrt{\tau_m/\rho}$, based on the maximum shear stress τ_m, rather than the wall scale $U_\tau = \sqrt{\tau_w/\rho}$. The correlation, which describes the outer 90% of the mean velocity profile (outside the law-of-the-wall region), is given by

$$\frac{U_o-U}{U_s} = 1 - 0.4(y/\Delta)^{1/2} - 0.6\sin\left(\frac{\pi y}{2\Delta}\right) , \qquad (5.33)$$

where

$$U_s = 8.0(\Delta/L)^{1/2}U_m, \qquad (5.34)$$

$$\Delta = 2.86\delta^* (U_o/U_s) , \qquad (5.35)$$

and L is the distance from the wall at which the maximum shear stress occurs.

Near the wall, the equation takes the form (see Perry and Schofield, 1973)

$$\frac{U}{U_o} = 0.47\left(\frac{U_s}{U_o}\right)^{3/2}(y/\delta^*)^{1/2} + 1 - \frac{U_s}{U_o} . \qquad (5.36)$$

Whilst the widest application of the Perry and Schofield correlation has so far been to separating and separated two-dimensional boundary layers in adverse pressure gradients, here its applicability to the separated and reattaching pipe flow in the adverse-pressure-gradient region

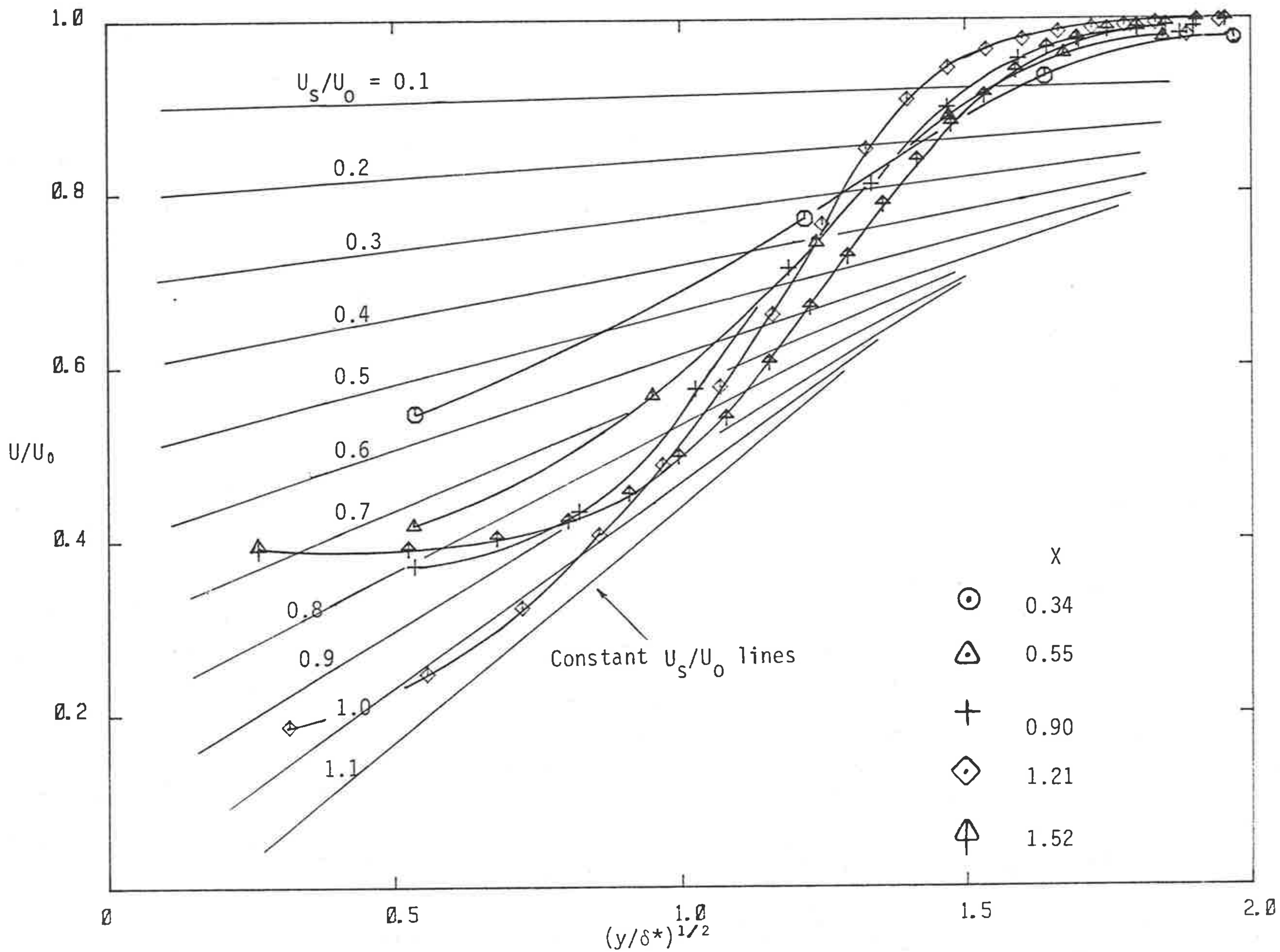

FIGURE 5.27(a) : HALF-POWER DISTRIBUTIONS, $D_C = 0.86$, $D_0 = 0.76$, $M_I = 0.35$, $\bar{J} = 0.47$

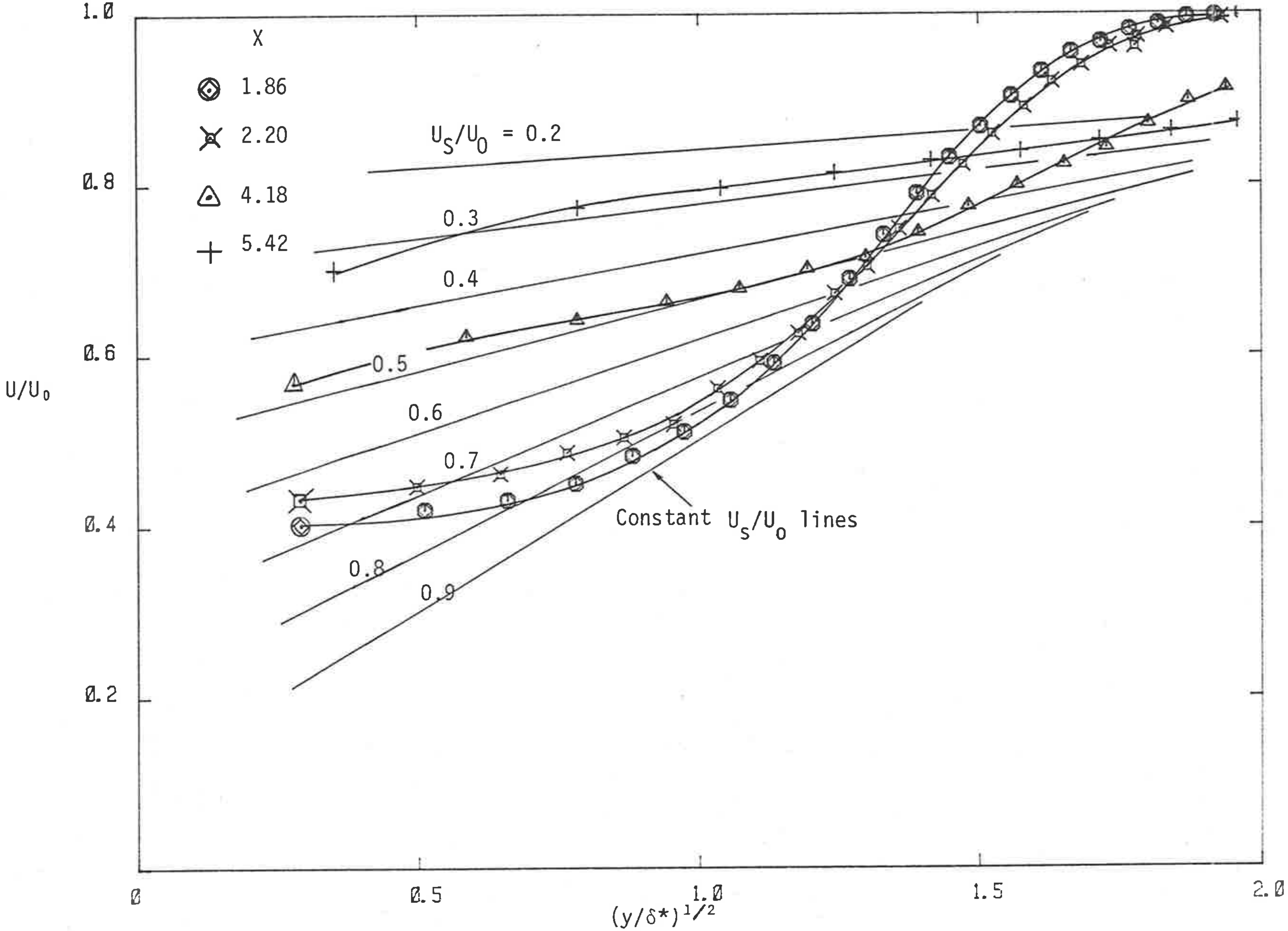

FIGURE 5.27(b) : HALF-POWER DISTRIBUTIONS, D_C = 0.86, D_0 = 0.76, M_I = 0.35, $\bar{J}$ = 0.47

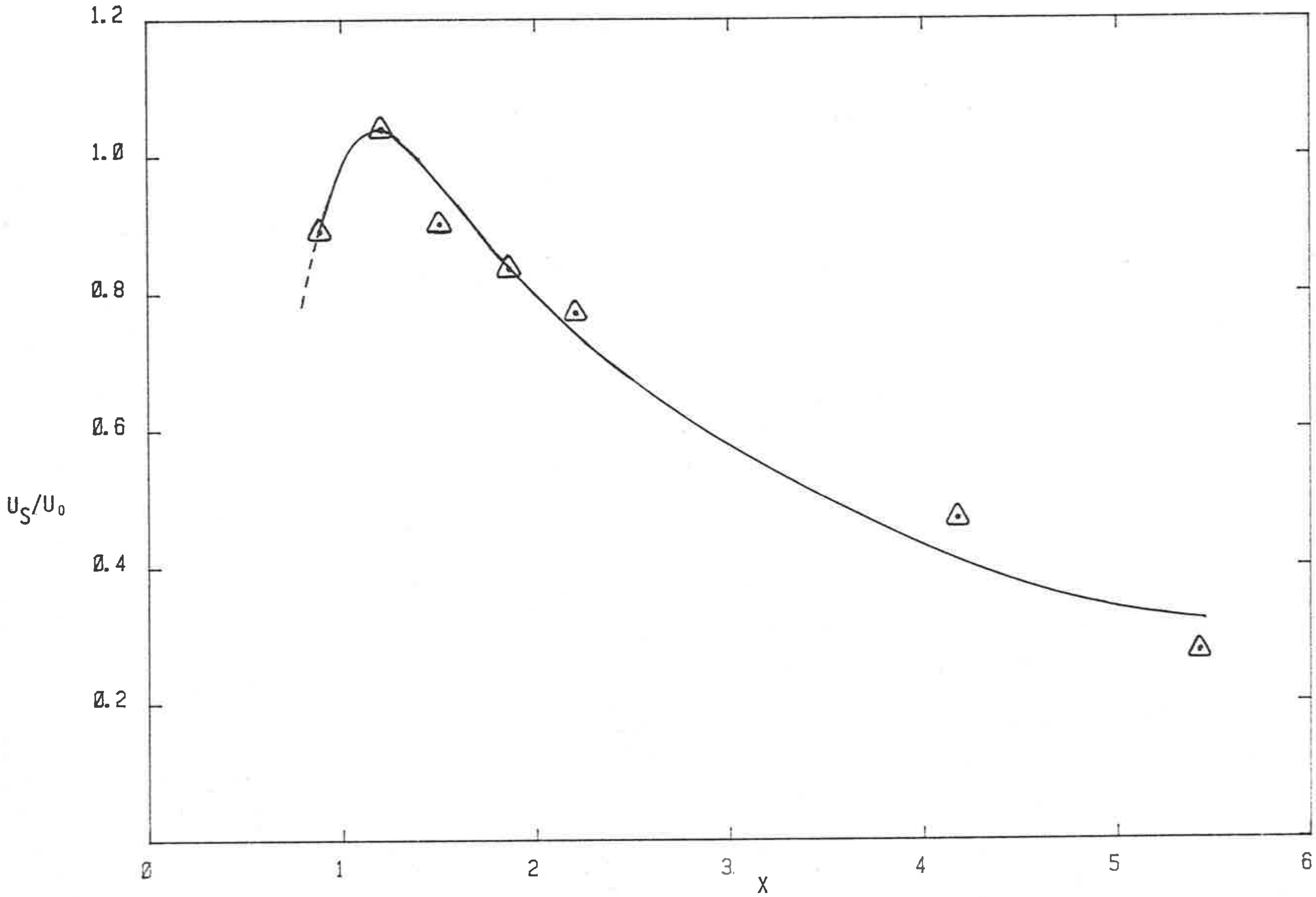

FIGURE 5.28: VARIATION OF VELOCITY RATIO , U_S/U_0 WITH STREAMWISE DISTANCE

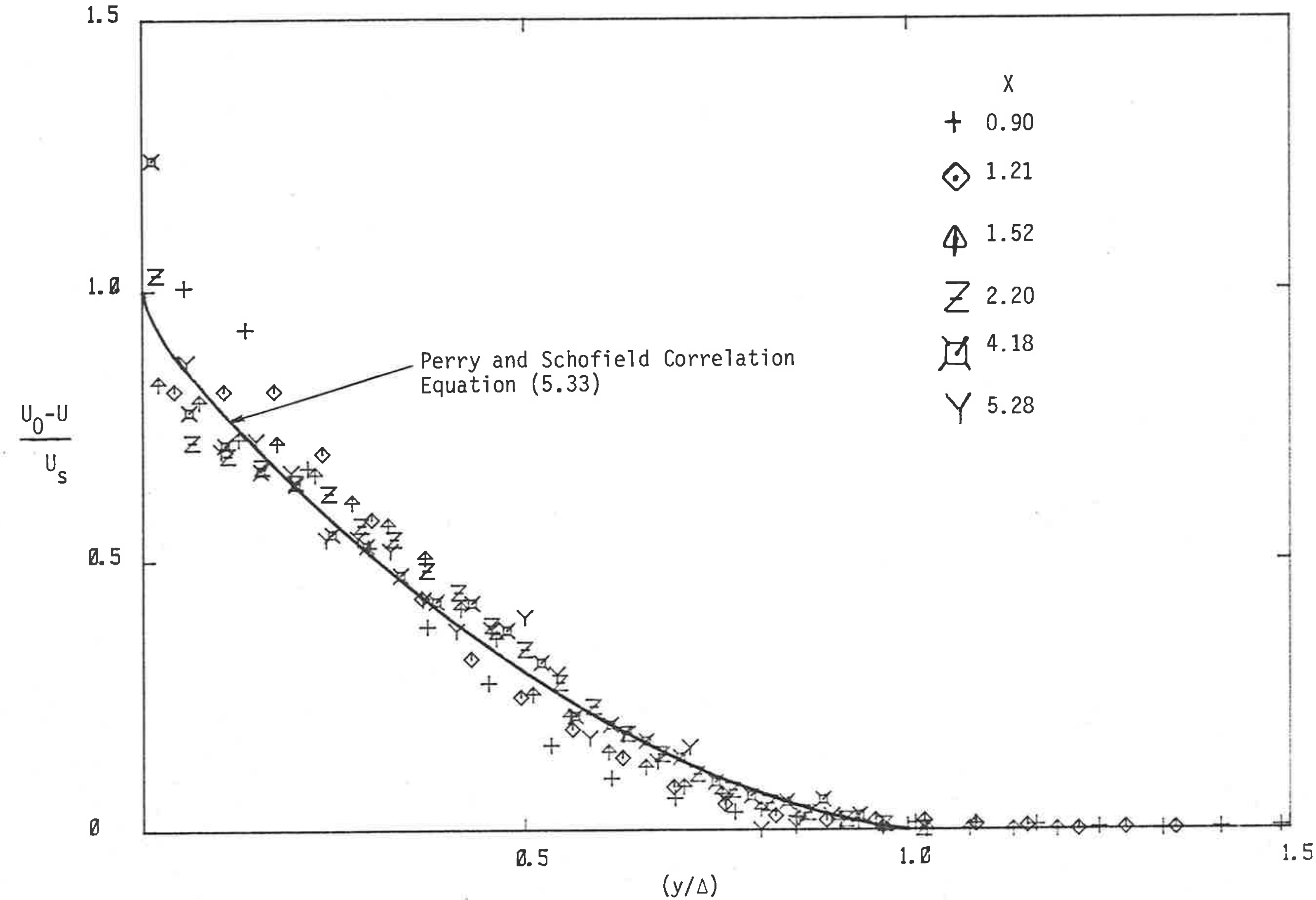

FIGURE 5.29(a) : MEAN VELOCITY PROFILES ON PERRY & SCHOFIELD, (1983) DEFECT-LAW AXES, $D_c = 0.39$, $D_0 = 0.76$
$M_I = 0.10$, $\bar{J} = 0.15$

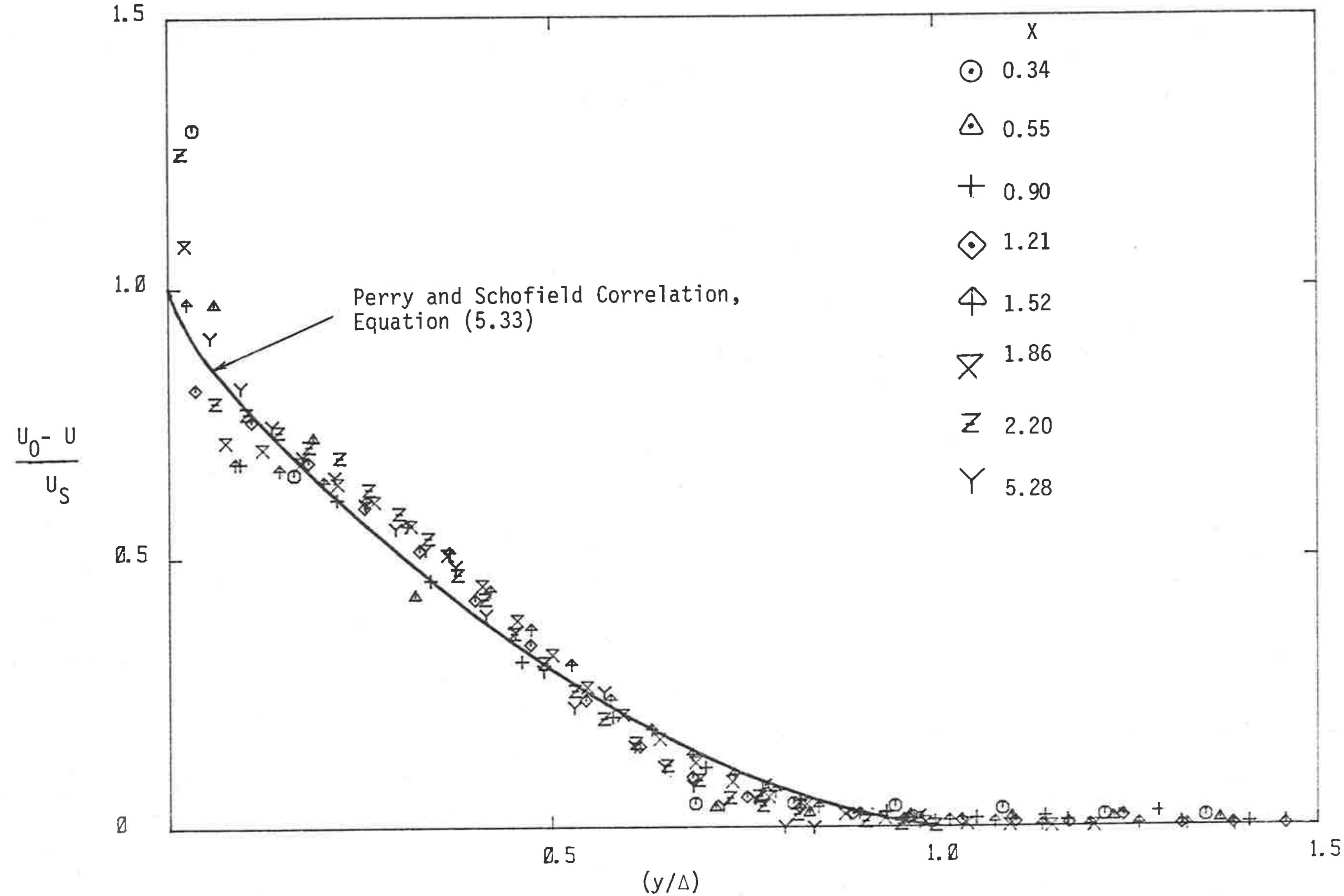

FIGURE 5.29(b) : MEAN VELOCITY PROFILES ON PERRY & SCHOFIELD, (1983) DEFECT-LAW AXES, $D_C = 0.86$, $D_0 = 0.76$, $M_I = 0.35$

$\bar{J} = 0.47$

extending from $X = 0$ to $X \approx 6$ downstream of the orifice plate will be examined.

The velocity ratio U_S/U_0 is determined by plotting the mean velocity profile on the coordinates U/U_0 versus $(y/\delta^*)^{1/2}$, and comparing it with the family of straight lines given by equation (5.36), for various constant values of U_S/U_0, in a similar way to the determination of U_τ/U_0 from a Clauser plot. For the mean velocity profiles in the reversed-flow region, the distance y is measured from the zero-velocity point in the layer. Velocity profiles in this form, for the flow $D_0 = 0.76$, $D_C = 0.86$, are shown in Figures 5.27(a) and (b).

For small X, that is just after separation, the available data points do not define the profile well over the y values where a half-power dependence might be expected. However, as the reattachment region is approached ($X \rightarrow\sim 1.5$) a half-power region becomes identifiable and its extent becomes greater as X increases. The expectation based on equation (5.33) would be that at separation or reattachment U_S/U_0 would approach 1.0 as $U_\tau \rightarrow 0$, and that the logarithmic region would disappear and the half-power region extend to the wall (Simpson, Strickland and Bar, 1977 and Schofield, 1983). The present profiles do not show a half-power dependence down to the wall in the vicinity of reattachment, owing, presumably, to the fact that the approach to separation or reattachment implied by equation (5.33) is different from that associated with the intermitent flow reversal in the real flow.

The variation of the velocity ratio U_S/U_0 with X is shown in Figure 5.28. Schofield (1983) has concluded that the value

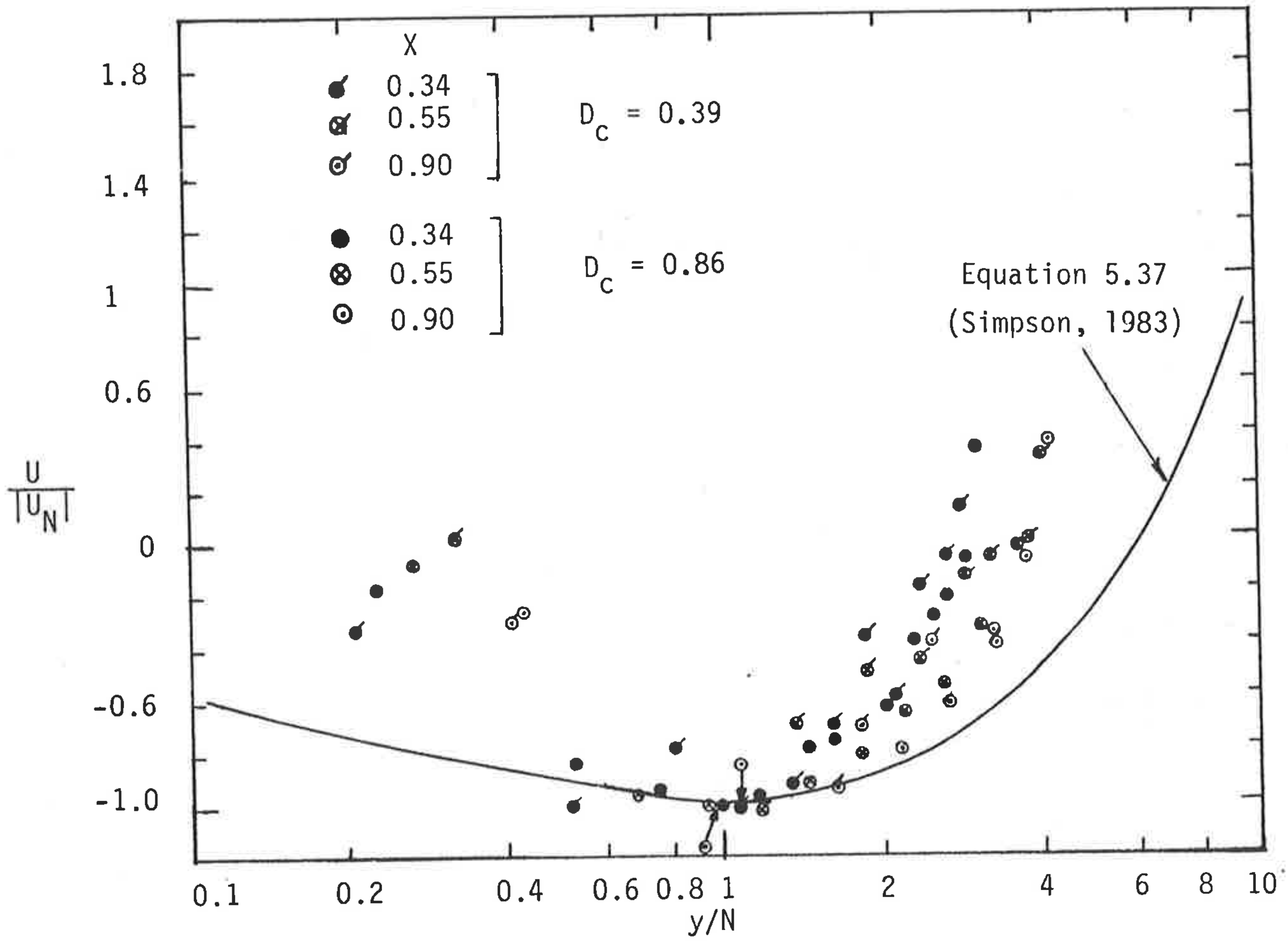

FIGURE 5.30a : NORMALIZED BACKFLOW MEAN VELOCITY, D_o = 0.76

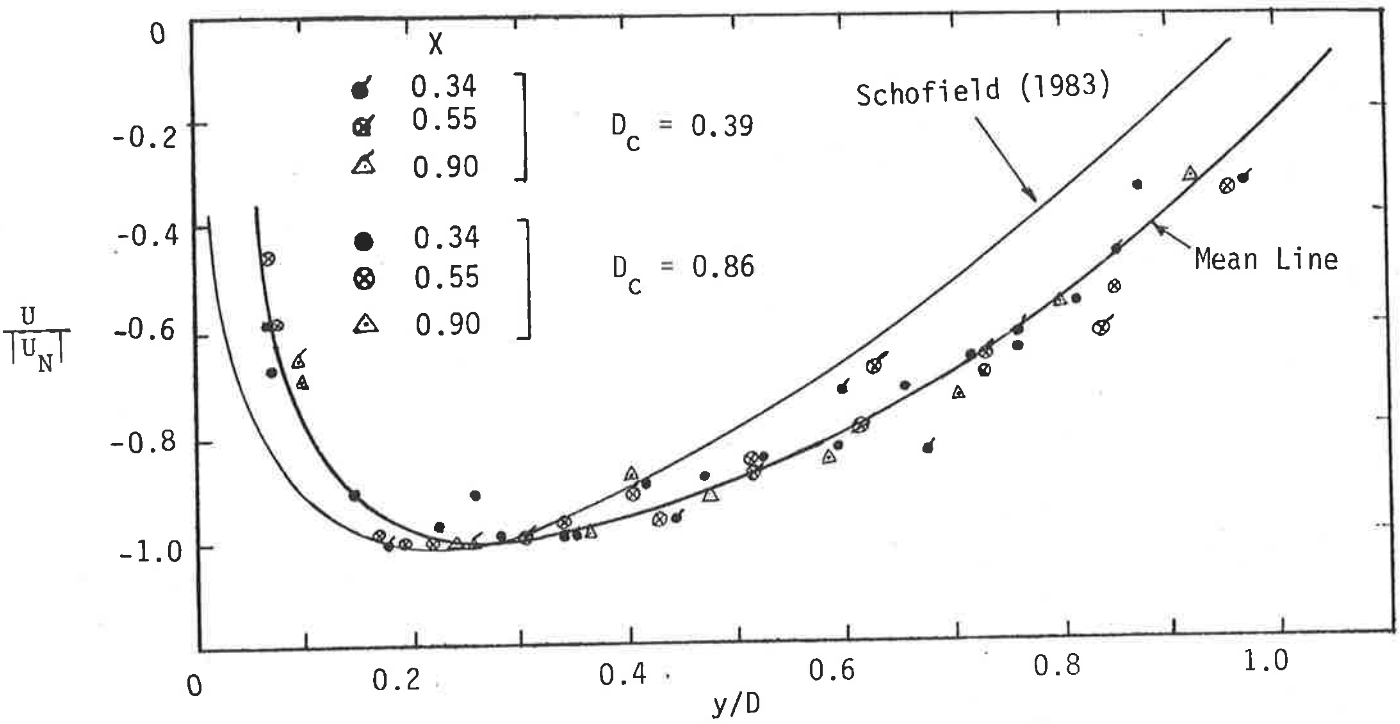

FIGURE 5.30b : NORMALIZED BACKFLOW MEAN VELOCITY, D_o = 0.76

of U_S/U_0 characterising separation and detachment of a two-dimensional turbulent boundary layer is about 1.18, rather than the value 1.0 indicated by equation (5.33); the value obtained here for pipe flow appears to be rather less, namemly 1.03.

Mean velocity profiles for the entire layer beyond the zero-velocity line are shown in defect form as $(U_0-U)/U_S$ versus y/Δ for $X \leq 5.4$ in Figures 5.29(a) and (b) for two flow conditions. Perry and Schofield's correlation, equation (5.33), is also shown. A good collapse of the data for both the flow speeds is obtained and equation (5.33) gives a fair representation of them in both the separated and reattaching flow regions. The present work therefore indicates that disturbed turbulent pipe flows also exhibit similarity of the type proposed by Perry and Schofield for two-dimensional flows.

5.8.2 Back Flow Mean Velocity Profiles

On the basis of his laser anemometer measurements in the back-flow region of a separating two-dimensional turbulent boundary layer, Simpson (1983) concludes that the mean backflow region consists of a viscous wall layer, an overlap region between the viscous and outer regions and the outer backflow region. He showed that a good collapse of mean-velocity data is obtained (particularly for $y/N < 1$) when U and y are normalised by the magnitude of the maximum negative mean velocity $|U_N|$ and its distance from the wall N, respectively. For $0.02 \leq y/N \leq 1$, Simpson proposes the relation

$$\frac{U}{|U_N|} = A\left(\frac{y}{N} - \ln\left|\frac{y}{N}\right| - 1\right) - 1, \qquad (5.37)$$

where $A = 0.3$.

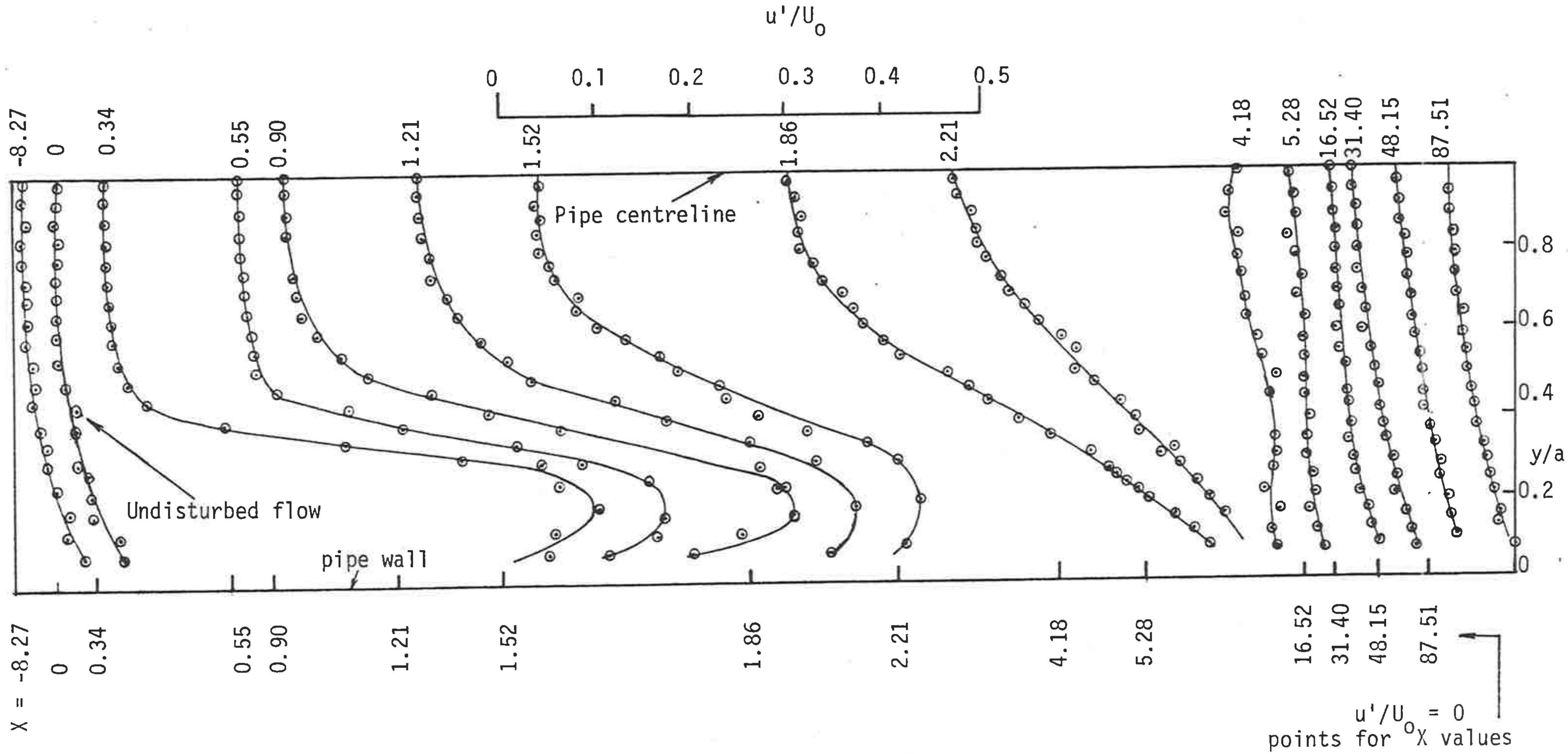

FIGURE 5.31 : STREAMWISE TURBULENCE PROFILES
(D_o = 0.72, D_c = 0.39, M_I = 0.10, $\overline{J}$ = 0.15)

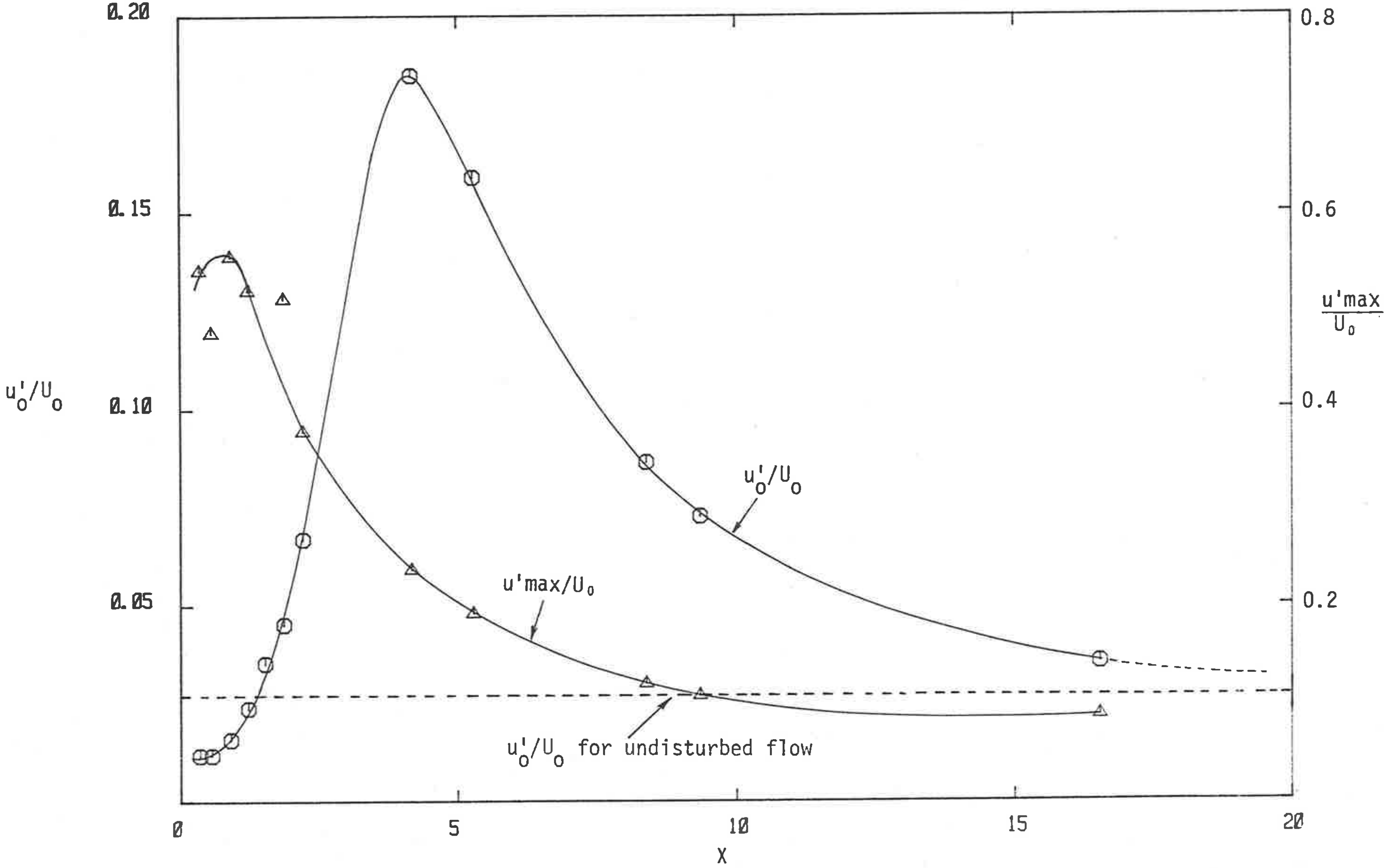

FIGURE 5.32 : VARIATION OF u_o'/U_o and u_{max}'/U_o WITH STREAMWISE DISTANCE

Schofield (1983) suggests that the distance from the wall to the maximum backflow velocity is a length scale related more to the wall region than to the backflow as a whole; he therefore proposes that a better length scale is the total backflow thickness, D.

Backflow velocity profiles in terms of Simpsons's correlation parameters for the flows $D_0 = 0.76$, $D_C = 0.86$ and 0.39 are shown in Figure 5.30(a). [Simpson's relation, equation (5.37), is also shown.] There is a fair collapse of the data, despite the fact that confidence in pitot tube measurements in reversed flow may not be very high. However, agreement between equation (5.37) and the experimental data is poor. A better collapse of the data is obtained, when y is non-dimensionalised by D (Figure 5.30(b)), as suggested by Schofield; but again, there is not good agreement between the pipe-flow data and the two-dimensional results.

5.9 Streamwise Turbulence Intensity

Measurements of streamwise turbulence intensity, expressed in terms of the local centre-line mean velocity as $u'/U_0 = \sqrt{\overline{u^2}}/U_0$, were made with a calibrated, single-wire, hot-wire anemometer.

A preliminary measurement on the pipe centre-line in undisturbed pipe-flow, in the absence of an orifice plate, gave a value there of 2.72%, in good agreement with the 2.63% indicated by the data of Laufer (1954).

Radial distibutions of u'/U_0 for the flow $D_0 = 0.72$, $D_C = 0.39$, with a Reynolds number based on pipe diameter of 1.5×10^5, for various streamwise distances in the range $-8.27 < X < 87.51$, are shown in Figure 5.31. Upstream of the orifice, the distribution of u'/U_0 is similar to that of the undisturbed flow.

Variation with X of the maximum turbulence intensity u'_{max}/U_0 at a given cross-section and turbulence intensity at the pipe centre-line, u'_0/U_0 is shown in Figure 5.32. Downstream of the orifice u'_0/U_0 increases with X to a maximum value at X ≈ 4.1 and then drops off, at first rapidly, up to X ≈ 10, and then more slowly.

The maximum value of u'_{max}/U_0 occurs at y/a = 0.18, X ~ 1.2, just upstream of reattachment; in the reattachment region the peak moves slightly away from the wall towards the pipe centre-line (Figure 5.31). The highest value measured is about 55%, rather higher than the 44% observed downstream an orifice plate with D_0 = 0.25 (Reynolds number 10^4 - 10^5) by Dyban and Epik (1970). However, both these values are considerably higher than the maximum values generally observed in two-dimensional flows, e.g. 20.5% by Eaton and Johnston (1980) in flow over a backward-facing step, and 19.5% by Symth (1979) for turbulent flow over a plane symmetric sudden expansion (although these values are referred to the mean flow velocity upstream of the discontinuity and would be higher in terms of local mean velocity).

It should be noted that in the separated flow, owing to the high turbulence intensity and also curvature of the streamlines, the results may be subject to large errors, particularly once the local turbulence intensity exceeds about 25% (Chandrsuda and Bradshaw (1981)). Kim, Kline and Johnston (1980) estimate the uncertainties in u' to be less than 10% in the region where u'/U_0 is less than 0.2 and about 20% where u'/U_0 is about 0.4.

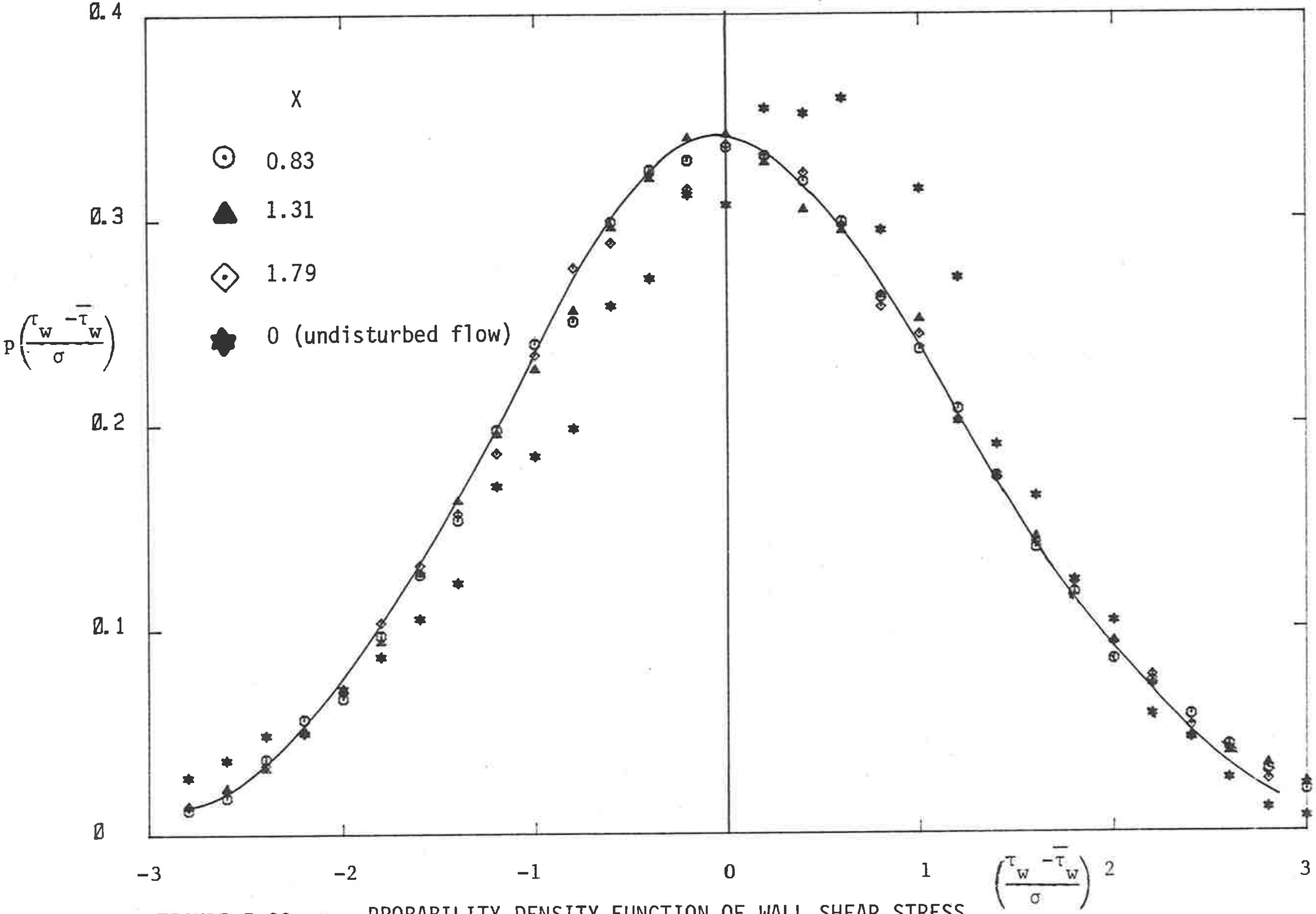

FIGURE 5.33 : PROBABILITY DENSITY FUNCTION OF WALL SHEAR STRESS $\left(\frac{\tau_w - \bar{\tau}_w}{\sigma}\right)$

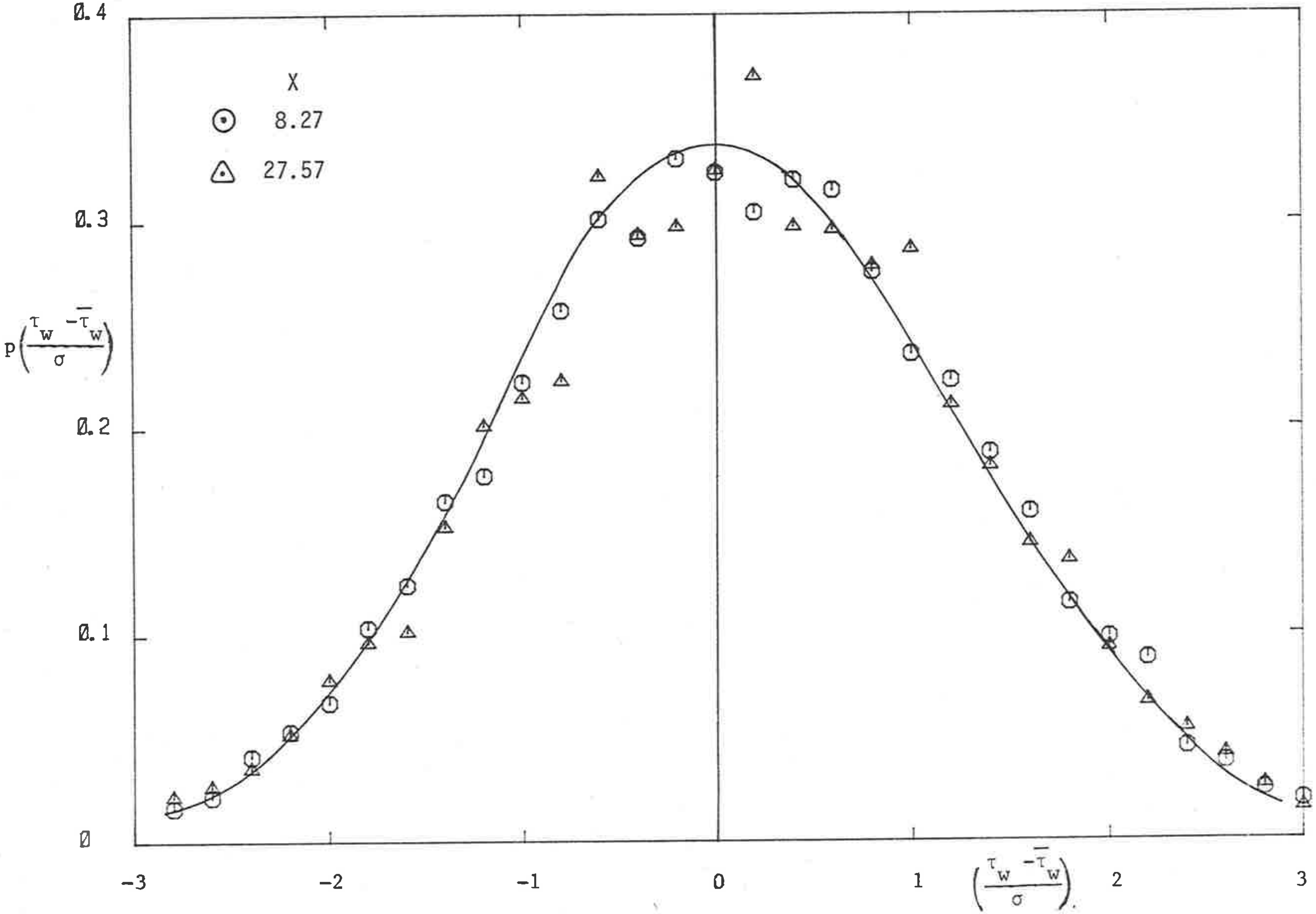

FIGURE 5.34 : PROBABILITY DENSITY FUNCTION OF WALL SHEAR STRESS

At $X \approx 48$, the distribution of u'/U_0 has reverted to a form nearly the same as that for the undisturbed flow.

5.10 Probability Distribution of Wall Shear Stress Fluctuations

Probability distributions of the instantaneous wall shear stress in the separated-flow region, close to the mean reattachment position and further downstream for the flow $D_0 = 0.76$, $D_C = 0.86$ have been obtained from surface fence gauge measurements. For this purpose, 25,600 samples were collected over a total time of 300 seconds at $X = 0.83$, 1.31, 1.79, 8.27 and 27.57 and also at $X = 0$ for the case of undisturbed flow.

The probability distribution curves for $X = 1.31$ ($\sim X_R$), 0.83 and 1.79 are shown in Figure 5.33. Variations in τ_W measured by the fence gauge are equivalent to maximum excursions of x_R about the mean position of about ± 0.2d with a standard deviation of about 0.07d. The probability distribution is nearly Gaussian. Measurements with a laser anemometer by Simpson (1976) in a two-dimensional separating boundary layer show that velocities very close to the wall, in the region of backflow, also approximately follow the Gaussian distribution. Eaton and Johnston (1980) used a pulsed-wire probe in the separated-flow region to measure the probability distribution of the velocity close to the wall (which also represents the wall shear stress) and their measurements also show it to be symmetric near the mean reattachment point; but downstream and upstream of reattachment point the distributions are skewed in the positive and negative directions respectively. The present measurements show that the wall shear stress distribution in the separated-flow region and also some distance downstream of reattachment is symmetric. The probability distributions at $X = 8.27$ and 27.57 are skewed in the same direction as that for undisturbed flow measured at $X = 0$ (compare Figures 5.33 and 5.34) - as expected, since in this region the flow is asymptotically approaching a fully-recovered undisturbed state.

5.10 Summary of Results and Conclusions

Mean flow characteristics in the fully-developed turbulent pipe-flow approaching an orifice plate, in the region of separated flow and in the flow downstream of reattachment up to and beyond distances at which an undisturbed fully developed pipe flow regime is again established, have been studied for a wide range of orifice sizes characterised by D_0. It has been shown that the overall flow characteristics can be specified by an initial Mach number M_I in the undisturbed flow approaching the orifice and the non-dimensional mass flow rate parameter J. The experimental results obtained can be summarised as follows.

(1) The mean positions of reattachment and separation points, expressed in terms of pipe diameters as X_R, X_{S1} and X_{S2} or in terms of the radial height of the orifice as x_R/h, x_{S1}/h and x_{S2}/h are functions of orifice size D_0 and the Reynolds number, Re. Over the small Reynolds number range studied, x_R/h, x_{S1}/h and x_{S2}/h appear to be unique functions of Reynolds number, Re_h, based on the radial height of the orifice h. The reattachment length decreases from about 12h to about 9h as Re_h increases from 3×10^4 to 7×10^4.

(2) Mean static pressure distributions in the separated-flow and reattachment regions downstream of the orifice are fairly closely similar for all orifices in the form of a pressure coefficient $C_p = (p-p_{min})/(p_{max}-p_{min})$ as a function of the streamwise coordinate non-dimensionalised by the reattachment length, x/x_R, except for slight dependence on orifice size D_0 in the region $1.3 \leqslant x/x_R \leqslant 3.6$.

(3) Clauser chart, Preston tube and surface fence measurements give consistent wall shear stress results in the region $X \geqslant 16.5$. In the region $2 \leqslant X \leqslant 16.5$, the Preston tube and the fence gauge still give fairly consistent values.

(4) Downstream of reattachment, the wall shear stress increases to a maximum value at about $X \approx 7.7$ and then falls off to a value typical of the undisturbed flow at $x \approx 30$. Its recovery to the undisturbed-flow value is therefore not monotonic.

(5) The wall shear stress has significant negative values in the separated-flow regions both upstream and downstream of the orifice plate.

(6) In the separated-flow region the central forward-flow portions of the mean velocity profiles exhibit a region where U varies as $y^{1/2}$. Between the central forward flow and the wall there is a region of backflow with a maximum backflow velocity of 26% of the centre line value. The two regions are separated by a line of zero velocity the shape of which scales on the reattachment length x_R. The locus of the position of maximum reverse velocity scales in a similar way. In the backflow region, mean velocity scales roughly on the maximum reverse velocity U_N and its distance N from the wall, but a better collapse of the data is obtained when the distance N is replaced by the total thickness of the backflow D.

(7) Downstream of reattachment the mean velocity profiles have both a logarithmic region and a half-power region. The extent of the logarithmic region increases with increasing X. Away from the wall the profile dips below the line of logarithmic similarity, indicating that the flow is not in local equilibrium and that the local wall shear velocity is not the proper velocity scale throughout the layer.

(8) In the region of adverse pressure gradient (the separated and reattaching flow downstream of the orifice), Perry and Schofield's velocity-defect correlation for two-dimensional flows, which utilizes length and velocity scales based on the maximum shear stress (rather than the wall shear stress), appears to be applicable.

(9) The large wake component present in the mean velocity profile at reattachment becomes less dominant further downstream and at $X = 8.38$ no wake component is evident. A small wake component then develops as equilibrium flow is again approached.

(10) The streamwise development of displacement thickness δ^*, momentum thickness θ, $H = \delta^*/\theta$ and the Clauser parameter G suggest that the recovery process which begins at the end of the reattachment region is quite slow and that the flow only reaches equilibrium again after about 48 pipe diameters.

(11) The probability density distribution of wall shear stress in the separated-flow region and reattachment zone appears to be symmetric, and can be closely approximated by a Gaussian distribution. Further downstream the distribution becomes skewed and approaches the skewed distribution typical of undisturbed flow.

CHAPTER 6

WALL PRESSURE FLUCTUATIONS

6.1 Introduction

Measurements of the power spectral density and rms value of the wall pressure fluctuations in the initially undisturbed flow, the separation and reattachment regions, and in the re-established fully-developed flow in the pipe have been made at various flow speeds and orifice sizes. They cover the frequency range of 20-20,000 Hz, streamwise distances $-12.9 \leq X \leq 84.5$, orifice plates sizes $0.62 \leq D_0 \leq 0.83$, and flow speeds corresponding to choke sizes $0.58 \leq D_C \leq 0.86$ as shown in Figure 6.1. In dimensional form, the power spectral density is expressed throughout as $\phi_p(f)$ the mean square pressure per unit frequency bandwidth (Pa^2/Hz); so that the mean square pressure $\overline{p^2}$, is given by

$$(p')^2 = \overline{p^2} = \int_0^\infty \phi_p(f)\, df. \tag{6.1}$$

The data are also presented in the form of the non-dimensional power spectral density, $\Phi_p = \phi_p(\omega) U_I / q_I^2 a$ (where $\phi_p(\omega) = \phi_p(f)/2\pi$) as a function of Strouhal number $\Omega = \omega a/U_I$, where $q_I = 1/2\, \rho_I U_I^2$, ω is the circular (radian) frequency, and U_I and ρ_I are the mean flow velocity and fluid density on the pipe centreline at the reference position, $X = -3.8$. Other forms of scaling are then introduced as required.

6.2 OVERALL ROOT MEAN SQUARE WALL PRESSURE FLUCTUATION

The combinations of orifice plate and choke for which overall rms wall pressure fluctuation have been made are given in Table 6.1.

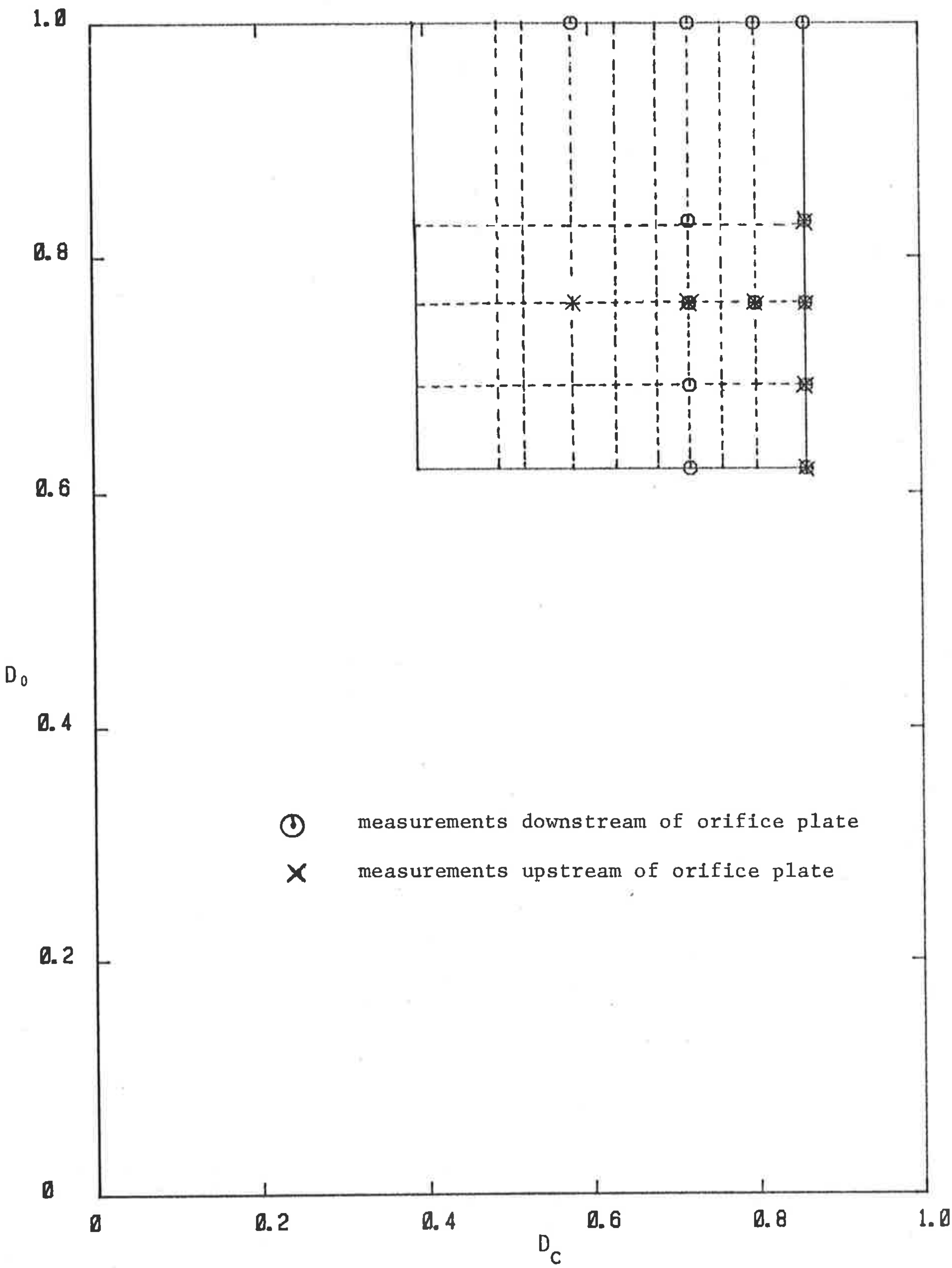

FIGURE 6.1 : RANGE OF MEASUREMENTS WITH WALL PRESSURE TRANSDUCER

TABLE 6.1

RANGE OF p' MEASUREMENTS

D_C	D_0 0.62	0.69	0.76	0.83
0.58			✓	
0.72	✓	✓	✓	✓
0.80			✓	
0.86	✓	✓	✓	✓

Measurements were made at streamwise intervals ΔX less than 0.2 in the separated-flow region, but at larger intervals (greater than 1.0) in other zones of the flow. To check the circumferential uniformity of the wall pressure field, measurements were always made at four circumferential positions (90° apart); at all X, ϕ_p was found to be independent of the circumferential position (within 0.5 dB). Figure 6.2 shows typical sets of results in various flow zones. All the data presented are those obtained from a Bruel and Kjaer 1/4" microphone.

Variation of p'/q_I with streamwise distance X for one orifice plate, D_0 = 0.76, and flow speeds given by chokes D_C = 0.58, 0.72 and 0.86 is shown in Figure 6.3, while Figure 6.4 shows p'/q_I variation with X for the orifice plates, D_0 = 0.62-0.83 and flow speed corresponding to one choke, D_C = 0.86. As would be expected, the lower the D_0 of the orifice plate, the more intense is the acoustic and turbulence field downstream, and the higher p'/q_I.

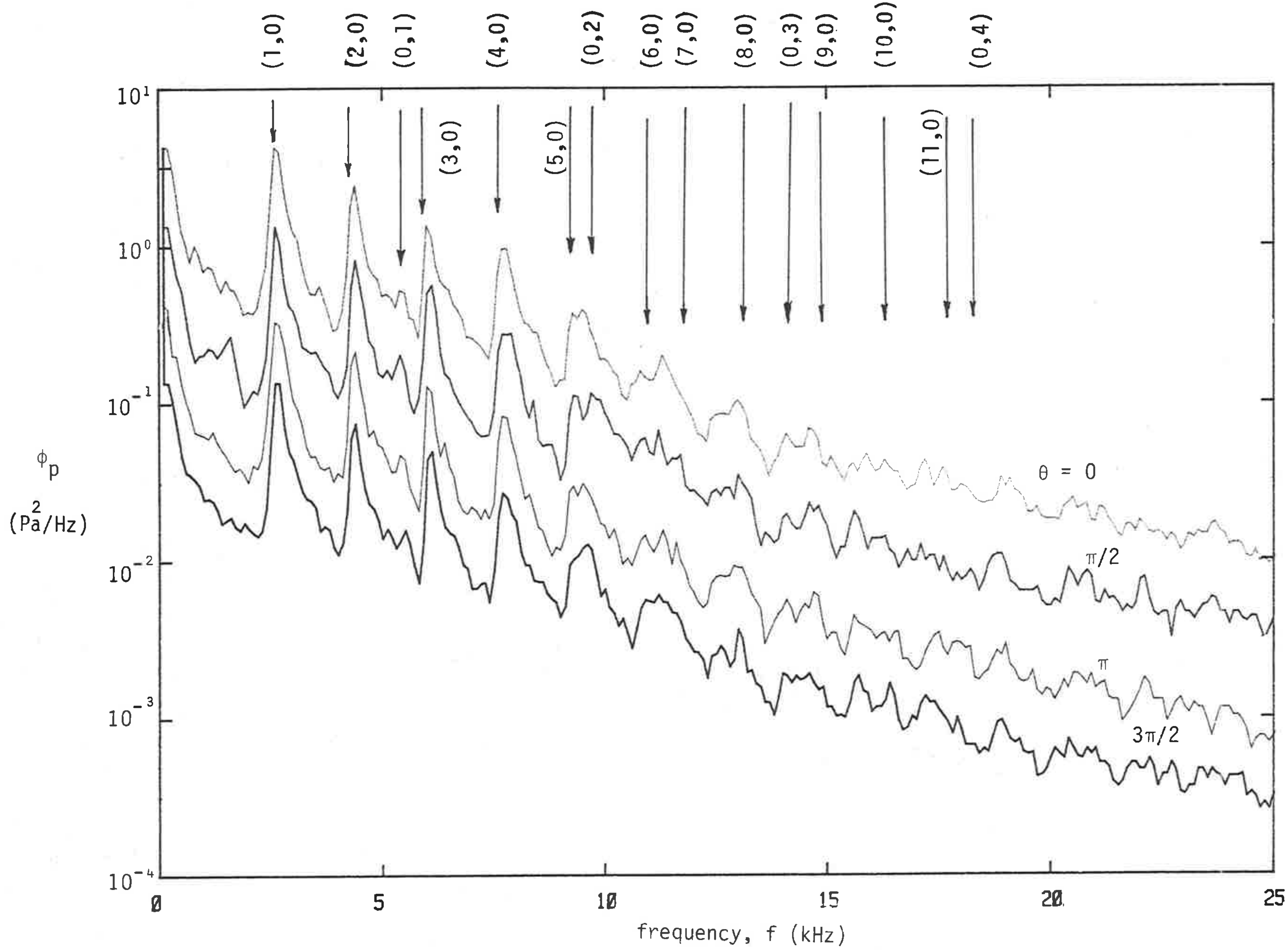

FIGURE 6.2a: WALL PRESSURE SPECTRA AT X = -0.8, D_c = 0.86, D_0 = 0.76, M_I = 0.35, $\overline{J}$ = 0.47

(Last three curves each shifted down by half a scale unit)

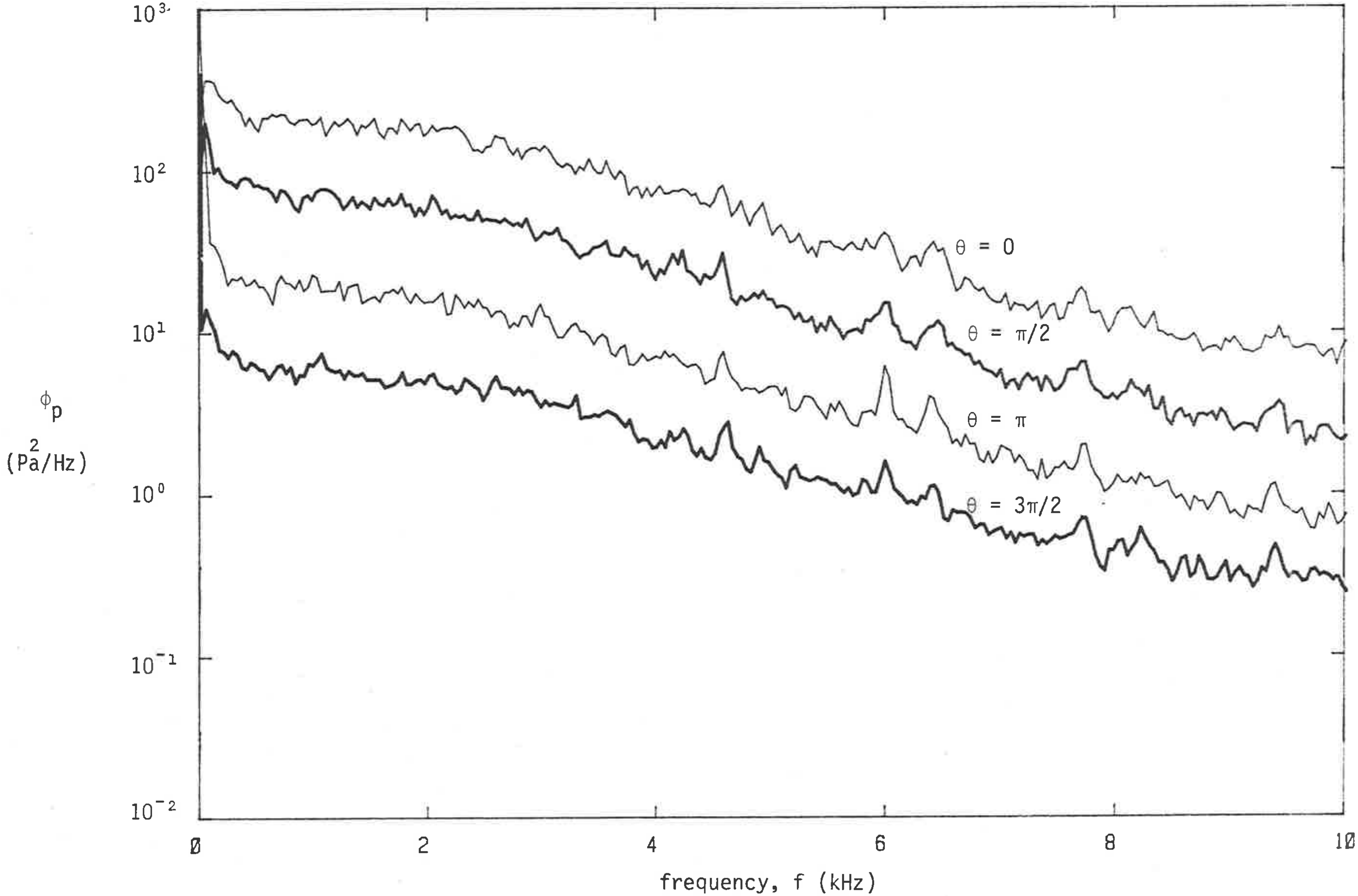

FIGURE 6.2b : WALL PRESSURE SPECTRA AT X = 1.03, D_c = 0.72, D_0 = 0.76, M_I = 0.29, $\overline{J}$ = 0.40

(last three curves each shifted down by half a scale unit)

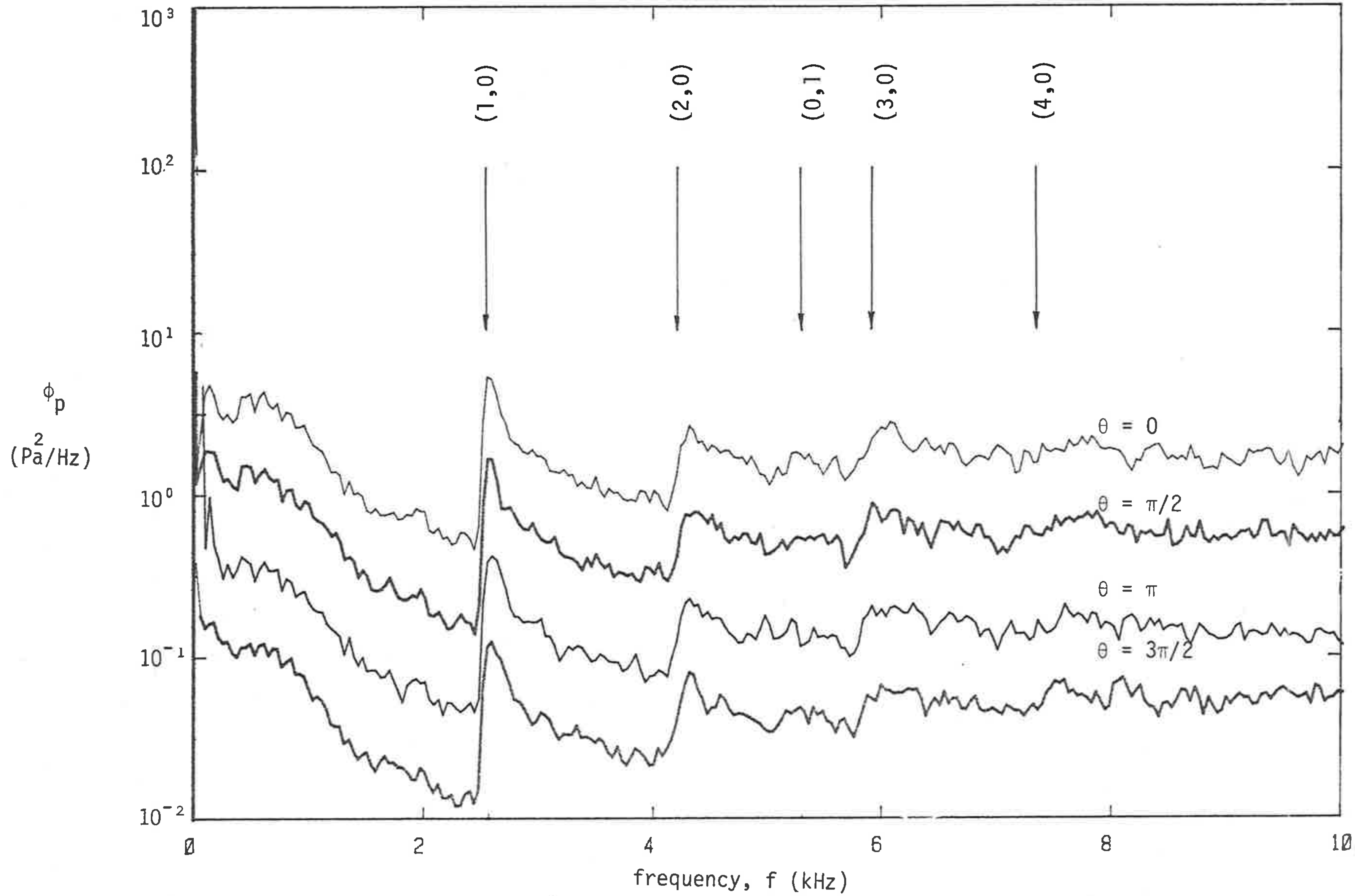

FIGURE 6.2c : WALL PRESSURE SPECTRA AT X = 22.06, D_c = 0.86, D_0 = 0.76, M_I = 0.35, $\overline{J}$ = 0.47

(Last three curves each shifted down by half a scale unit)

For $D_C = 0.72$, the maximum of p'/q_I occurs in the range of X between 1.17 and 1.24 for the various flow rates, just upstream of the mean position of the re-attachment point indicated by the fence gauge measurements. Previous measurements of wall pressure fluctuations in separated flow, summarized by Mabey (1971), generally indicate the occurrence of a maximum value of p'/q_0 some distance upstream of re-attachment (where q_0 is based on a free stream velocity); and on average this maximum value occurs at a distance downstream of the separation point of about 0.84 times the streamwise length of the separation bubble. A similar value, $x/x_R \approx 0.9$ was found by Fricke (1971) for the separation of a turbulent boundary layer produced by a surface fence. Lines for $X = X_R$ and $X = 0.91\ X_R$ on Figures 6.4 and 6.5 show that for the present data the location of the maximum p'/q_I is close to $x/x_R = 0.91$ for all flow conditions investigated.

At flow speed $D_C = 0.86$, $M_I = 0.34$ (Figure 6.4) the maximum value of p'/q_I observed here varies from 0.45 to 0.13 as D_0 varies from 0.62 to 0.83, while for $D_0 = 0.76$ for flow speeds $D_C = 0.58$-0.86 ($M_I = 0.21$-0.34) (Figure 6.3) it is ~ 0.20. These values appear to be considerably higher than those given by Mabey ($\lesssim 0.1$), but would be reduced to $p'/q_0 \simeq 0.04$ to 0.05 if p' were non-dimensionalised by q_0 based on local centreline flow velocity rather than q_I. On the other hand, Bull and Norton (1981) obtained a maximum value of p'/q_0 for a 90° mitred bend of 0.33, based on q_0 at $X = 52.8$, which would be equivalent to an even higher value based on q_I.

p'/q_I values for the same orifice-plate/choke combinations as in Figures 6.3 and 6.4 are shown in Figures 6.5 and 6.6 for larger values of X. It will be noted that p'/q_I continues to decrease at a constant rate of ~ 0.9 dB/metre even after fully-developed flow has been re-established after about 48 diameters downstream of the orifice.

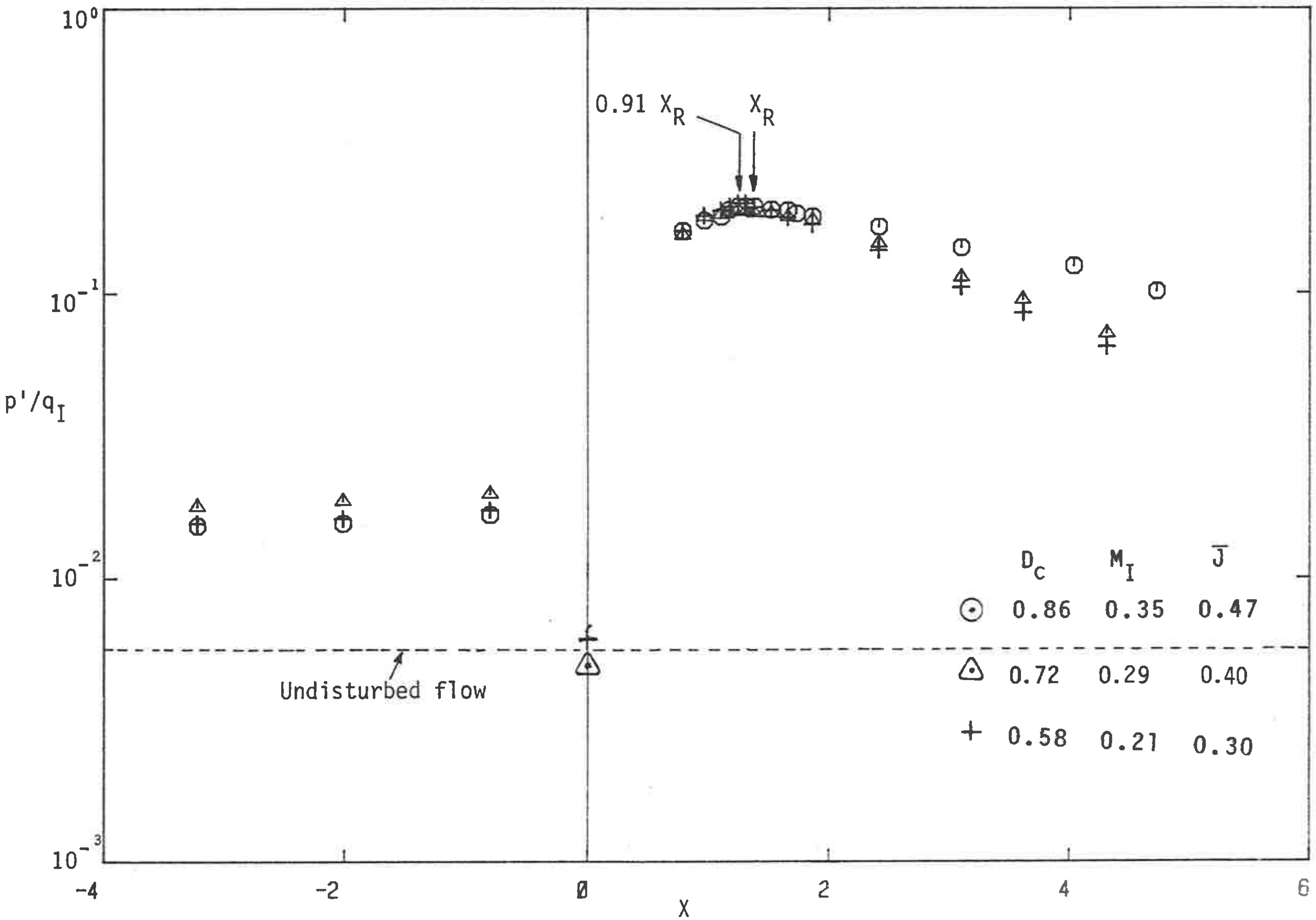

FIGURE 6.3 : VARIATION OF RMS PRESSURE FLUCTUATION WITH STREAMWISE DISTANCE, D_0 = 0.76

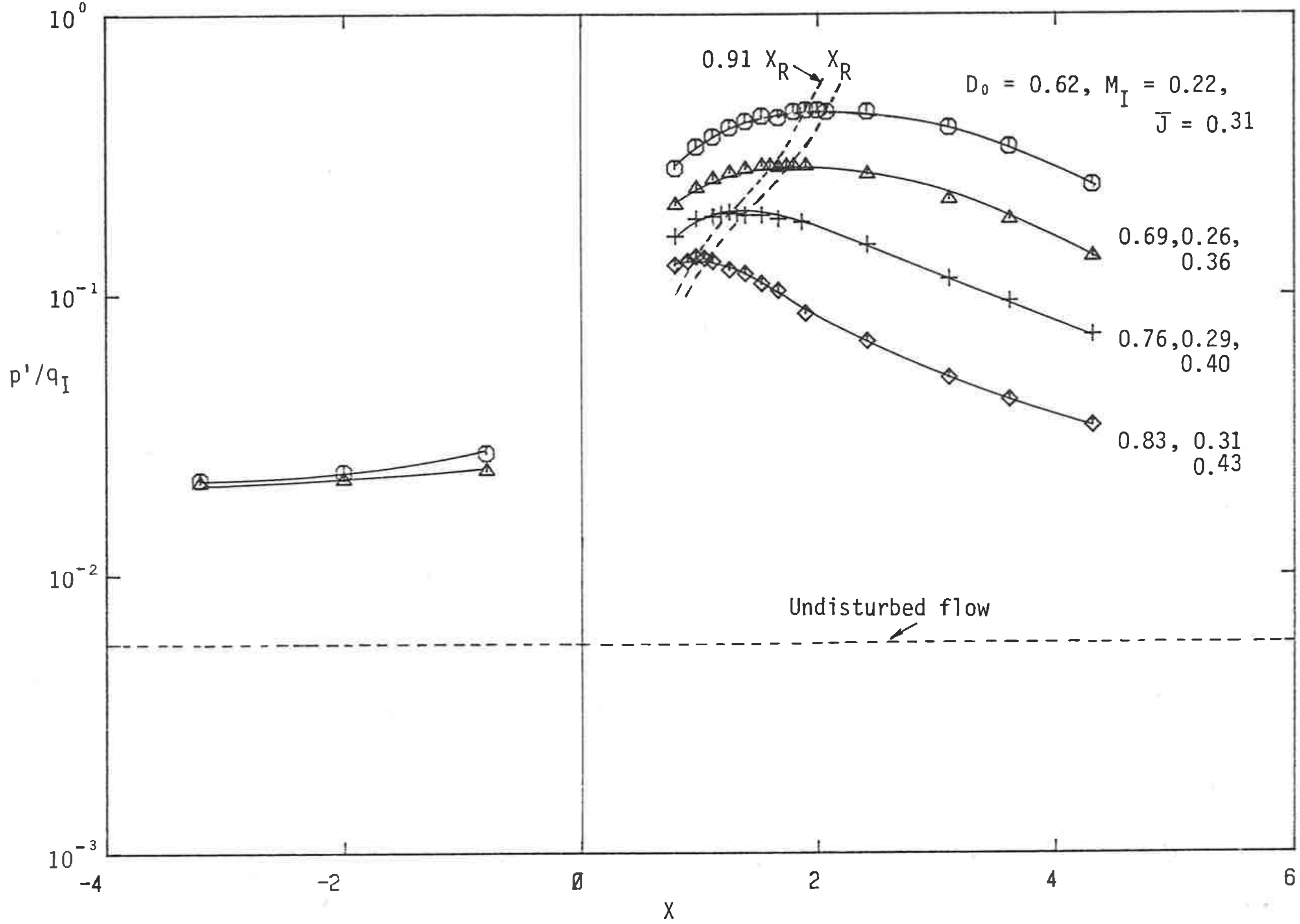

FIGURE 6.4 : VARIATION OF RMS PRESSURE FLUCTUATION WITH STREAMWISE DISTANCE, D_c = 0.72

The data of Bull and Norton (1981), for a 90 mitred band in the same flow rig, for $X \sim 12$ and 52, lead to a similar attenuation rate.

The excess of the measured p' values at large X, where the effects of the disturbance on the flow itself have died out, over those of undisturbed pipe flow is interpreted as being due to an internal propagating sound field, generated by the disturbance and radiated away from it, superimposed on the now re-established pipe flow. This is in accord with findings of earlier investigations of the effects of strong disturbances, e.g. that of Bull and Norton (1981) of the flow downstream of a mitred bend.

In the region of flow separation downstream of the orifice plate, where pressure fluctuation levels are very high, the pressure levels might be expected to be related to the maximum values of dynamic pressure in the mean flow at the vena contracta of the separated jet, $q_J = {}^1/_2\, \rho_J U_J^2$ (where ρ_J and U_J are respectively the fluid density and velocity at this point). Figures 6.3 and 6.4 also suggest that the variation of p' in this region depends on the re-attachment length x_R rather than the pipe diameter. In fact, a collapse of all data presented in Figures 6.3 and 6.4 for this region is obtained in the form of p'/q_J as a function of x/x_R (Figure 6.9(b)).

It will be seen later that the wall pressure fluctuations at large distances upstream and downstream of the orifice are predominantly acoustic, with a relatively low level turbulence pressure contribution. In these regions the acoustic component p'_{ac}, obtained by subtracting the hydrodynamic component from the total according to the relation

$$p'_{ac} = [p'^2 - (cq_0)^2]^{1/2} \tag{6.2}$$

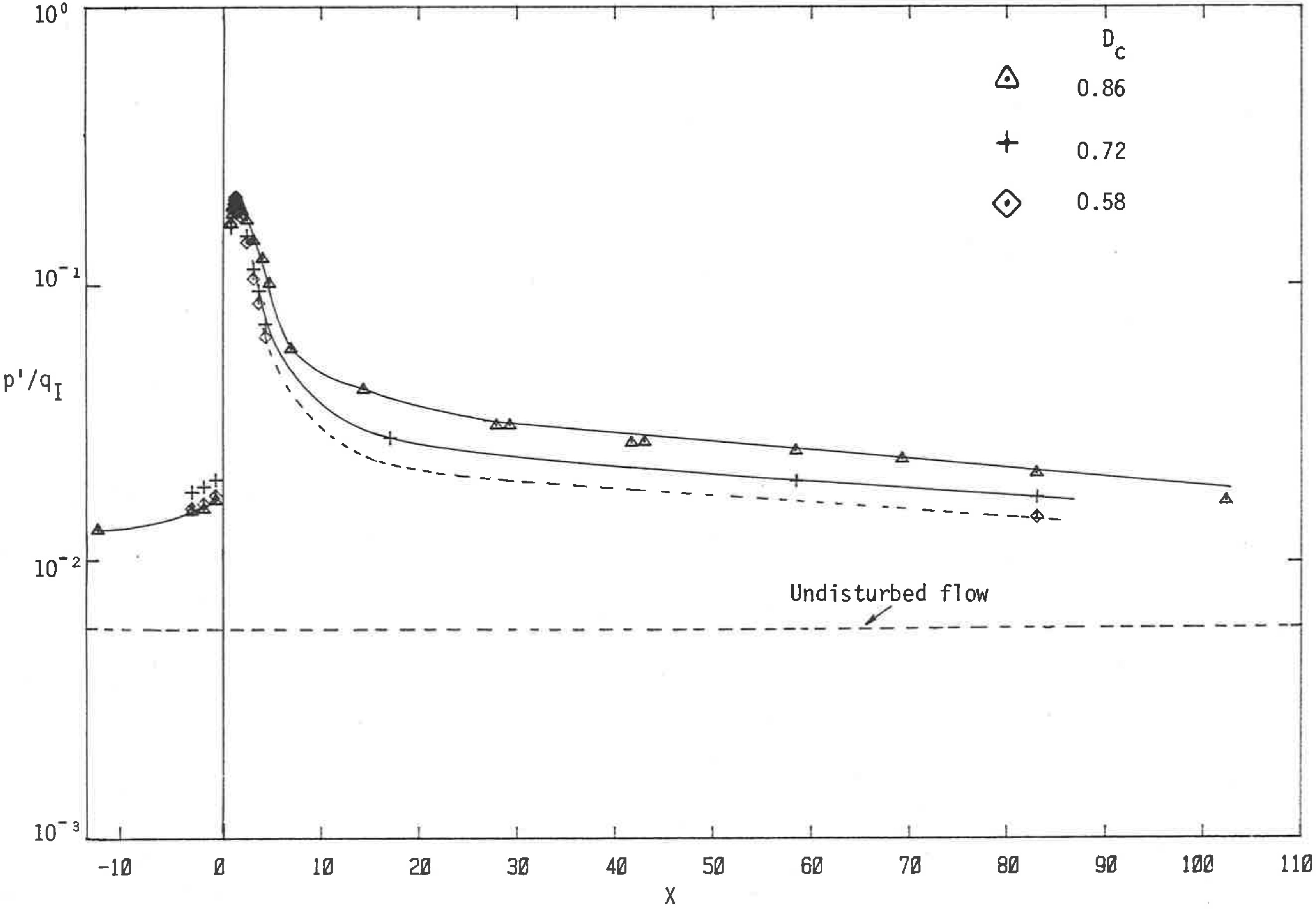

FIGURE 6.5 : VARIATION OF RMS PRESSURE FLUCTUATION WITH STREAMWISE DISTANCE, D_0 = 0.76

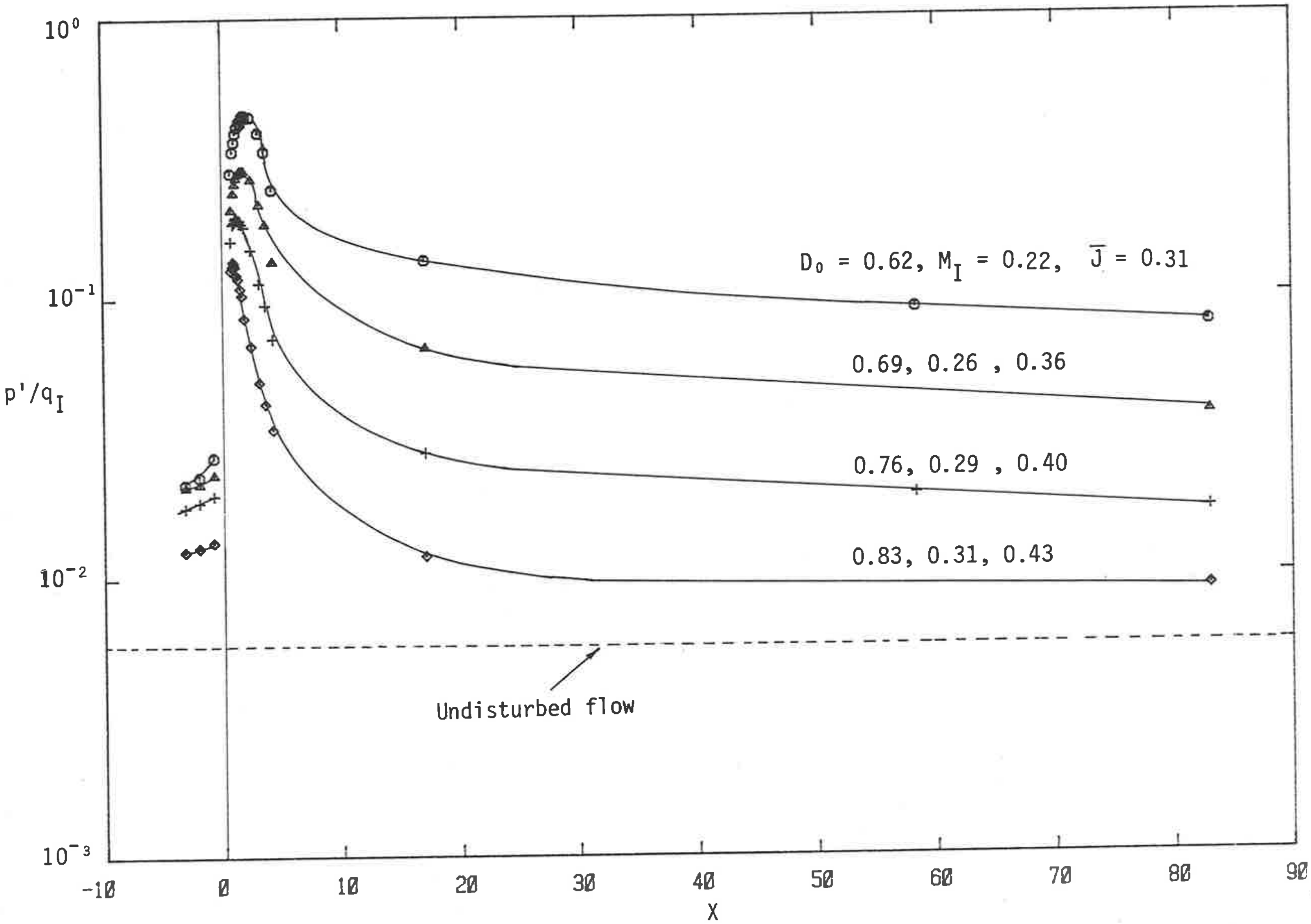

FIGURE 6.6 : VARIATION OF RMS PRESSURE FLUCTUATION WITH STREAMWISE DISTANCE, D_c = 0.72

(where c is the value of p'/q_0 corresponding to undisturbed pipe flow, typically 0.006), might also be expected to depend on q_J.

Values of p'_{ac}/q_J at the upstream positions X = -0.83 and -8.96 are plotted as a function of the maximum jet Mach number M_J in Figure 6.7, which indicates that this relationship is independent of both D_C and D_0. For the most part (with the obvious exception of results for $D_0 = 0.76$, $D_C = 0.58$) p'/q_J appears to be inversely proportional to M_J. The variation of $(p'/q_J)M_J$ with X is shown in Figure 6.9(a), and this parameter appears to correlate the data quite well.

p'_{ac}/q_J values at X = 83.0 are shown as a function of M_J in Figure 6.8. In this downstream region the values depend on both D_0 and D_C in addition to M_J. Results for a given orifice ($D_0 = 0.76$) show a weak dependence on M_J, namely $M_J^{0.3}$. On the other hand, for a given choke ($D_C = 0.72$) the values are strongly dependent on orifice size, varying inversely as D_0^4. The data of Figure 6.8 therefore suggest that p'_{ac}/q_J varies as $M_J^{0.3}/D_0^4$. The combination $(p'_{ac}/q_J)D_0^4/M_J^{0.3}$ appears to give a good correlation of data at all downstream positions $X \gtrsim 4$ (Figure 6.9(c)).

Figure 6.9 is therefore a composite plot which gives the variation of rms pressure throughout the flow. Overall p' values can be obtained from the p'_{ac} data by supplementing them with undisturbed flow turbulence pressures in accord with equation (6.2).

6.3 WALL PRESSURE SPECTRA

The power spectral density ϕ_p of the wall pressure fluctuations has been measured upstream and downstream of the orifice plates for the combinations of orifice size and choke size, in the ranges $D_0 = 0.62\text{-}0.83$ and $D_C = 0.58\text{-}0.86$, shown in Table 6.2. Measurements have been made directly by using the Hewlett Packard spectrum analyser,

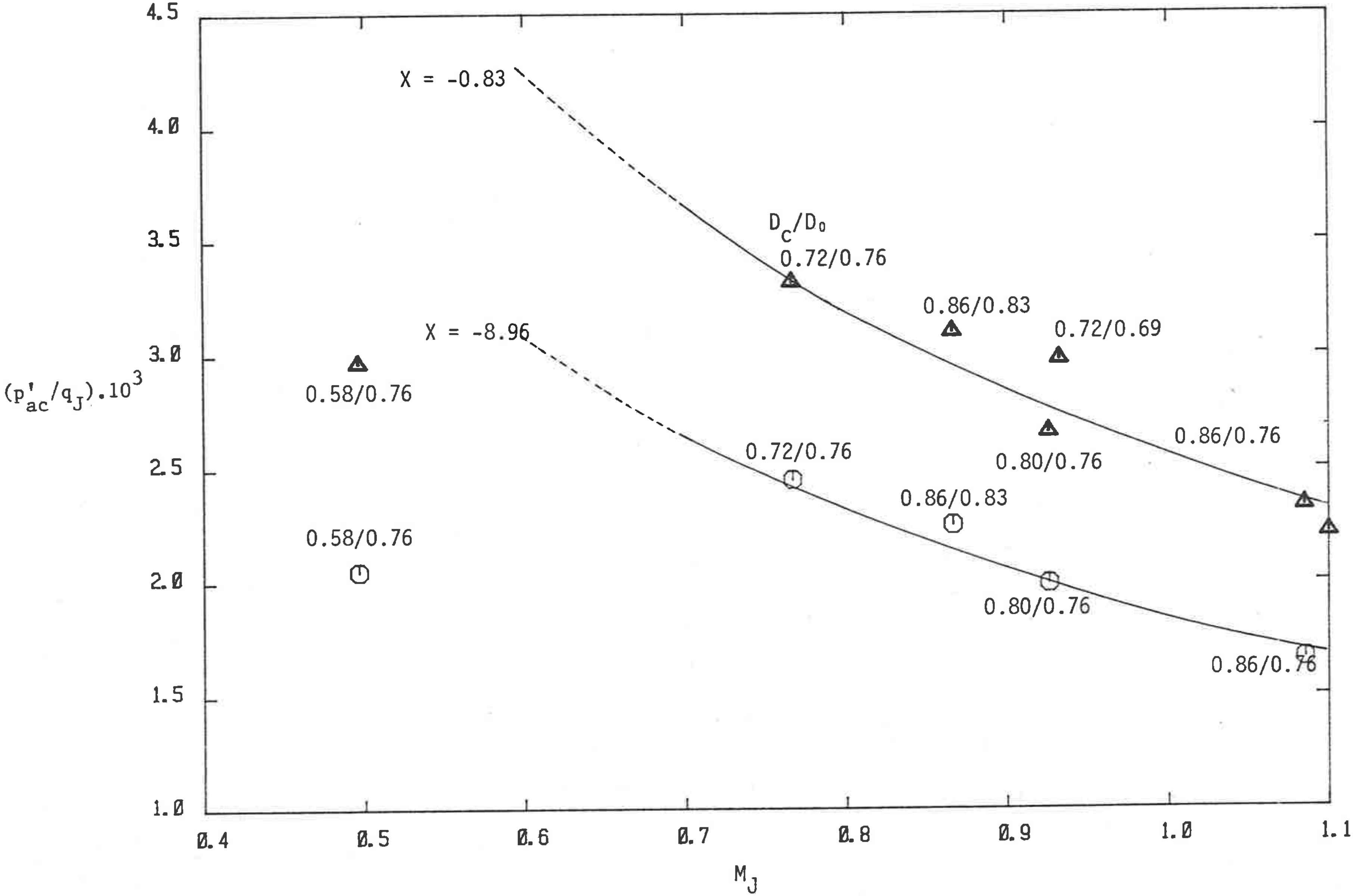

FIGURE 6.7 : VARIATION OF ACOUSTIC COMPONENT OF PRESSURE FLUCTUATION WITH M_J UPSTREAM OF ORIFICES

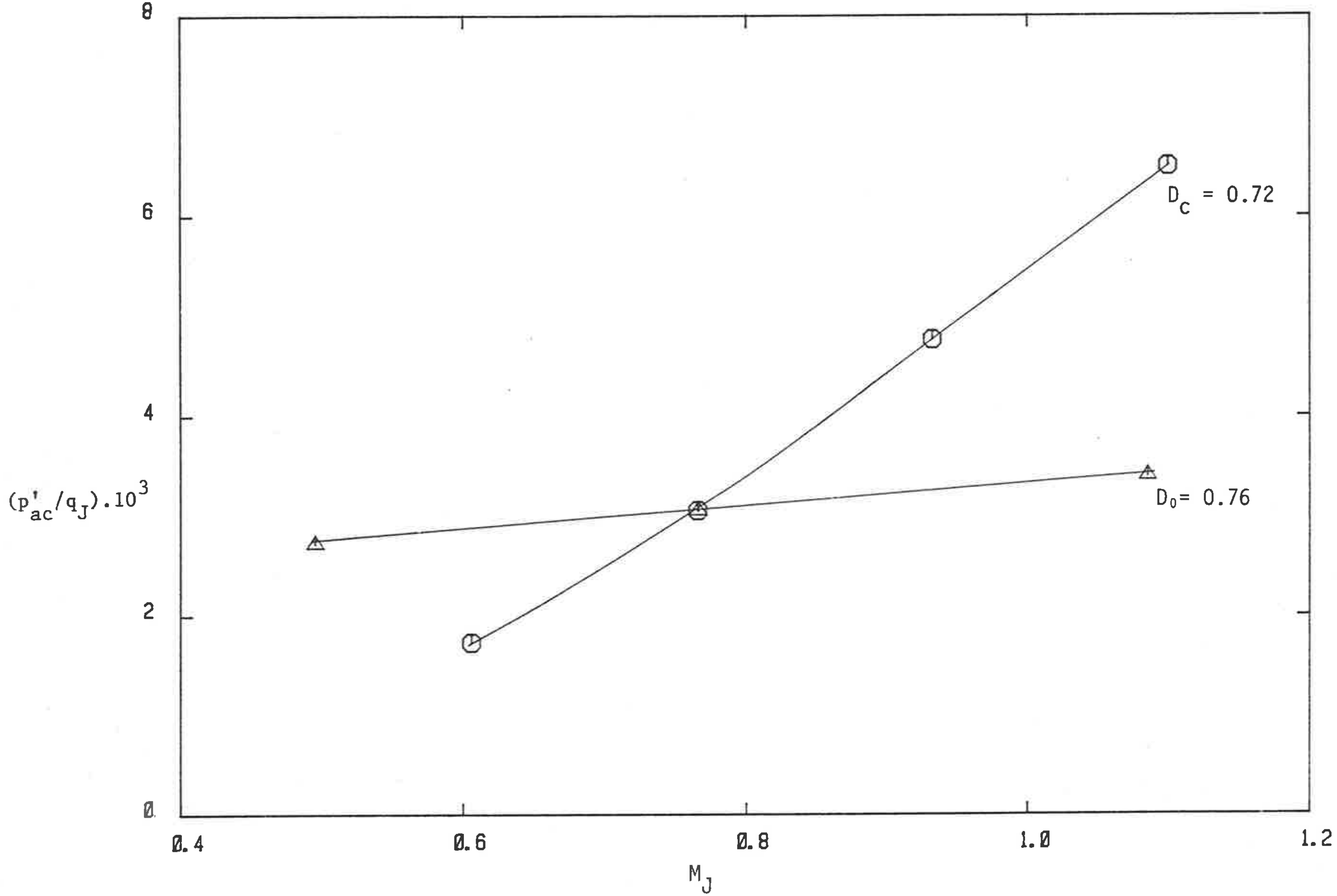

FIGURE 6.8 : VARIATION OF ACOUSTIC COMPONENT OF PRESSURE FLUCTUATION WITH M_J AT X = 83.0

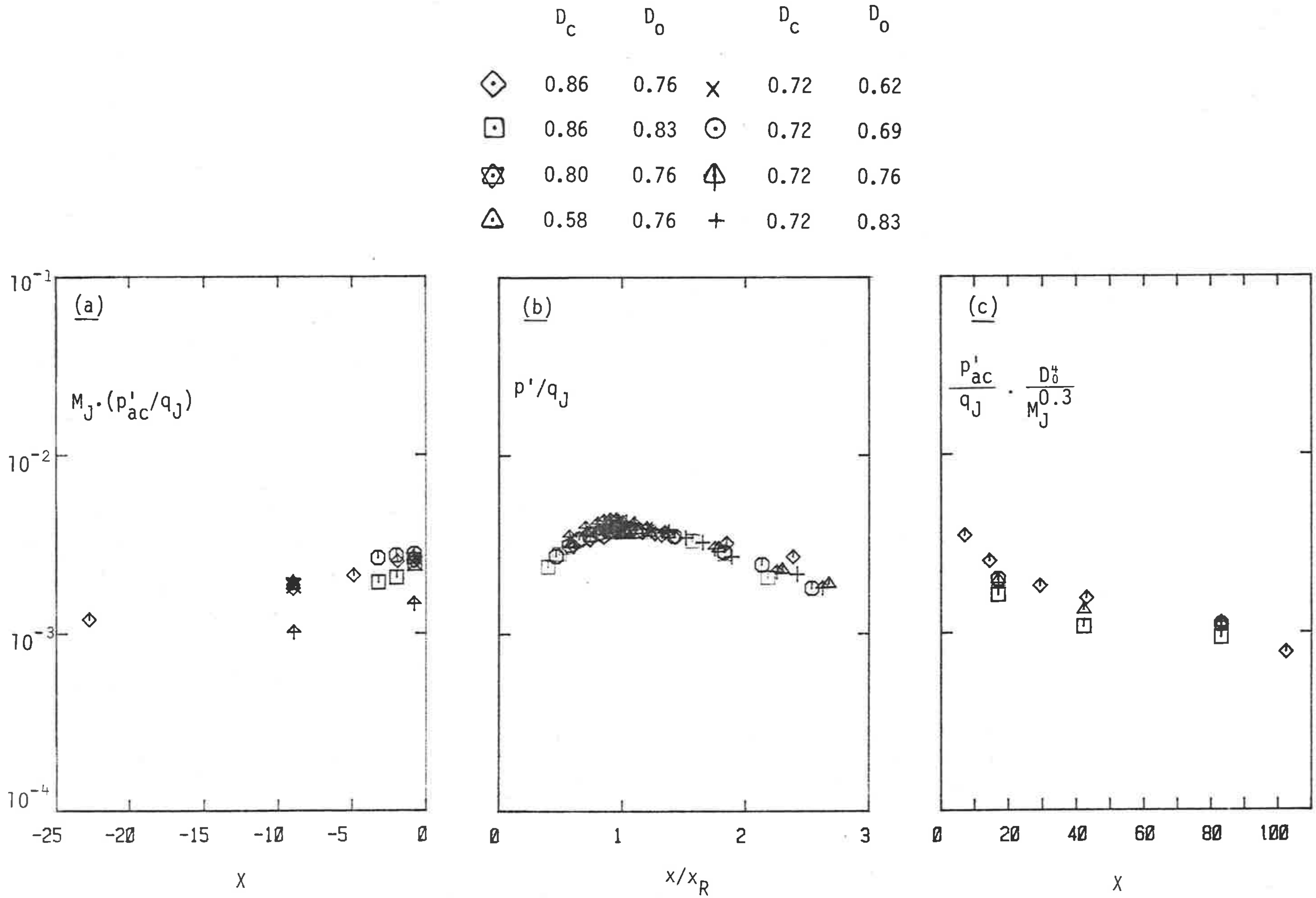

FIGURE 6.9 : SCALING OF RMS PRESSURE FLUCTUATIONS

TABLE 6.2

SPECTRAL MEASUREMENT COMBINATION

D_C \ D_0	0.62	0.69	0.76	0.83
0.58			√	
0.72	√	√	√	√
0.80			√	
0.86	√	√	√	√

and also by digitization and Fast Fourier Transformation of analogue pressure signals recorded on a RACAL tape recorder. The overall bandwidth (span) of measurements is limited to 25 kHz in the former method and 10 kHz in the latter. A constant bandwidth of 100 Hz (with frequency span of 25 kHz) is obtained with the Hewlett Packard spectrum analyser. Digitizing the tape recorded signal gives a resolution bandwidth of 2.4 Hz, and sixteen such frequency bands were combined to give a constant total bandwidth of 39 Hz with a corresponding normalised random error of 10%. The pressure sensor was a Brüel and Kjaer 1/4" microphone throughout.

The measuring range covers $-22.7 \leq X \leq 102$, the measuring points being closest together in the separated region. For presentation of results the whole flow region is divided into four parts:

i) separated flow region (zone 3);

ii) recovery region (zone 4);

iii) beyond $X = 48$, where the fully developed flow is re-established (zone 5); and

iv) upstream of the orifice plate (zones 1 and 2).

6.3.1 Separated Flow Region $0.78 \leq X \leq 1.3$ (Zone 3)

The closest point to the downstream face of the orifice plate, at which measurements can be made, is $X = 0.78$; therefore ϕ_p could not be measured at or upstream of the secondary separation point (refer to Figure 5.1, general flow picture).

The pressure fluctuations have a broad spectrum with sharp peaks at frequencies corresponding to the cut-off frequencies of higher order acoustic modes in the pipe, which are marked on the various figures. The peaks can be fairly clearly identified with the modal cut-off frequencies even though they are generally not more than about 2dB higher than the basic spectral level.

The variation of the pressure spectrum with downstream distance X in the separated flow region, for a given orifice and flow rate $D_0 = 0.76$ and $D_c = 0.86$, is shown in Figure 6.10.

It is clear from this figure that the spectral level of pressure fluctuations in the separated-flow region is considerably higher than that for the no-orifice case, in accord with the large increase in p' over that for undisturbed flow. As we have seen in Section 6.1, p' is a maximum just upstream of re-attachment, and it is evident from Figure 6.10 that this is associated with the rise in Φ_p in the low frequency region up to $\Omega = 10$, as X increases from 0.78 to 1.30; there is not much change in Φ_p for $\Omega > 10$.

Figure 6.11 shows the effect of flow rate on the spectrum for a given orifice ($D_0 = 0.76$) at each of the two positions $X = 1.03$ and 1.30. In each case data are shown for

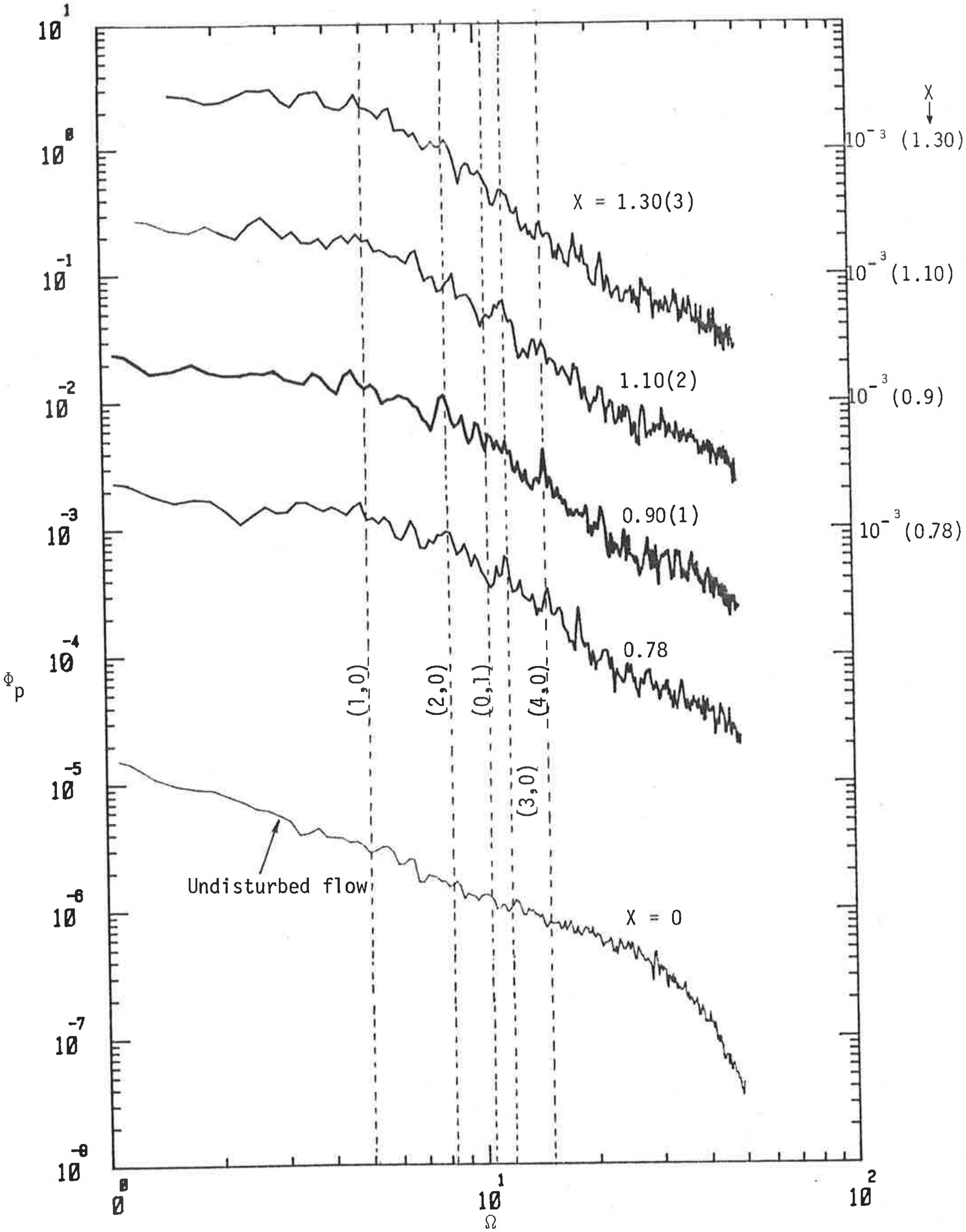

FIGURE 6.10 : WALL PRESSURE SPECTRA IN SEPARATED REGION, D_C = 0.86, D_0 = 0.76, M_I = 0.35 , $\overline{J}$ = 0.47

(Top three curves are each shifted up by one scale unit)

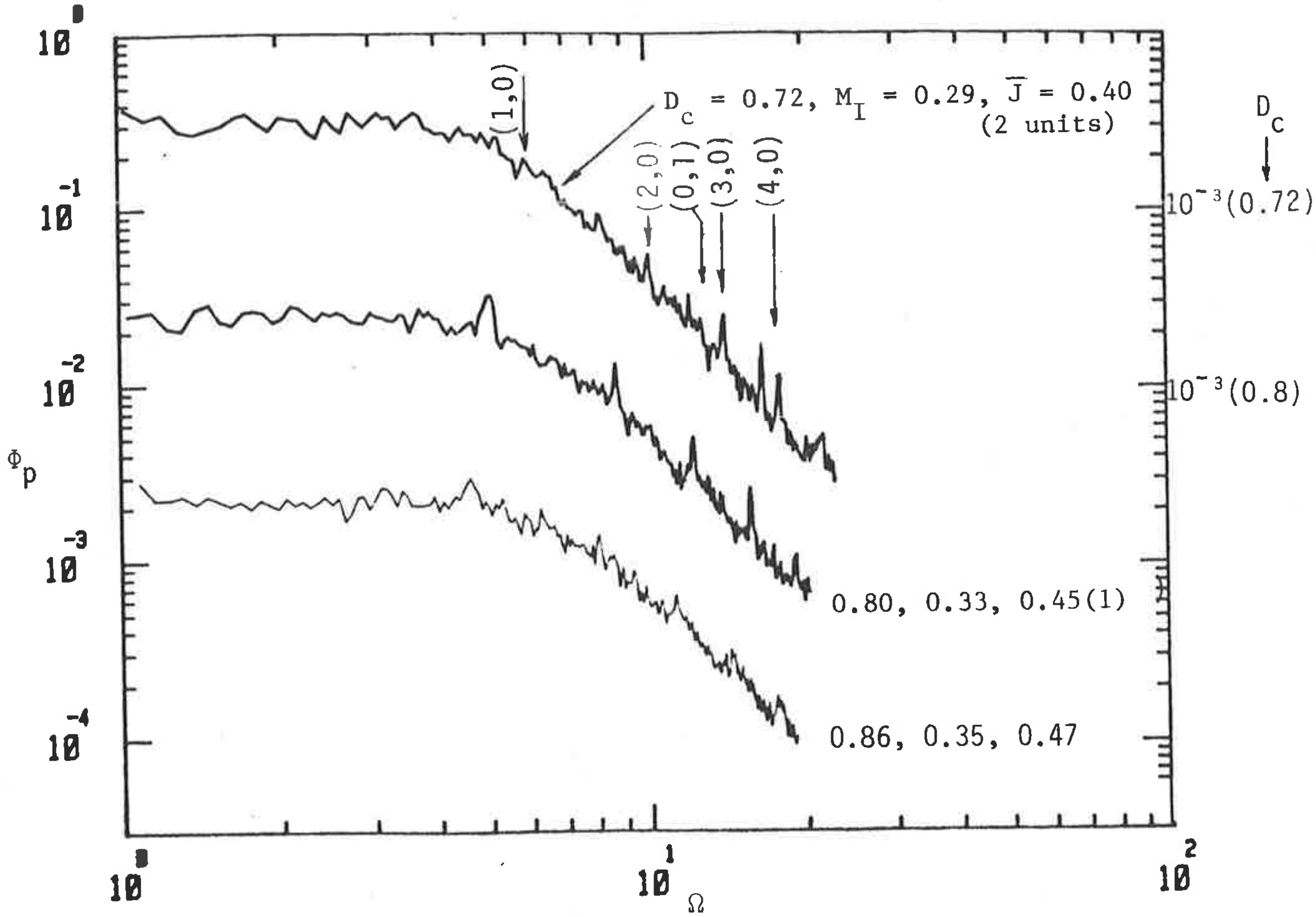

FIGURE 6.11a : WALL PRESSURE SPECTRA AT X = 1.03, D_0 = 0.76
(Top two curves are each shifted up by a scale unit)

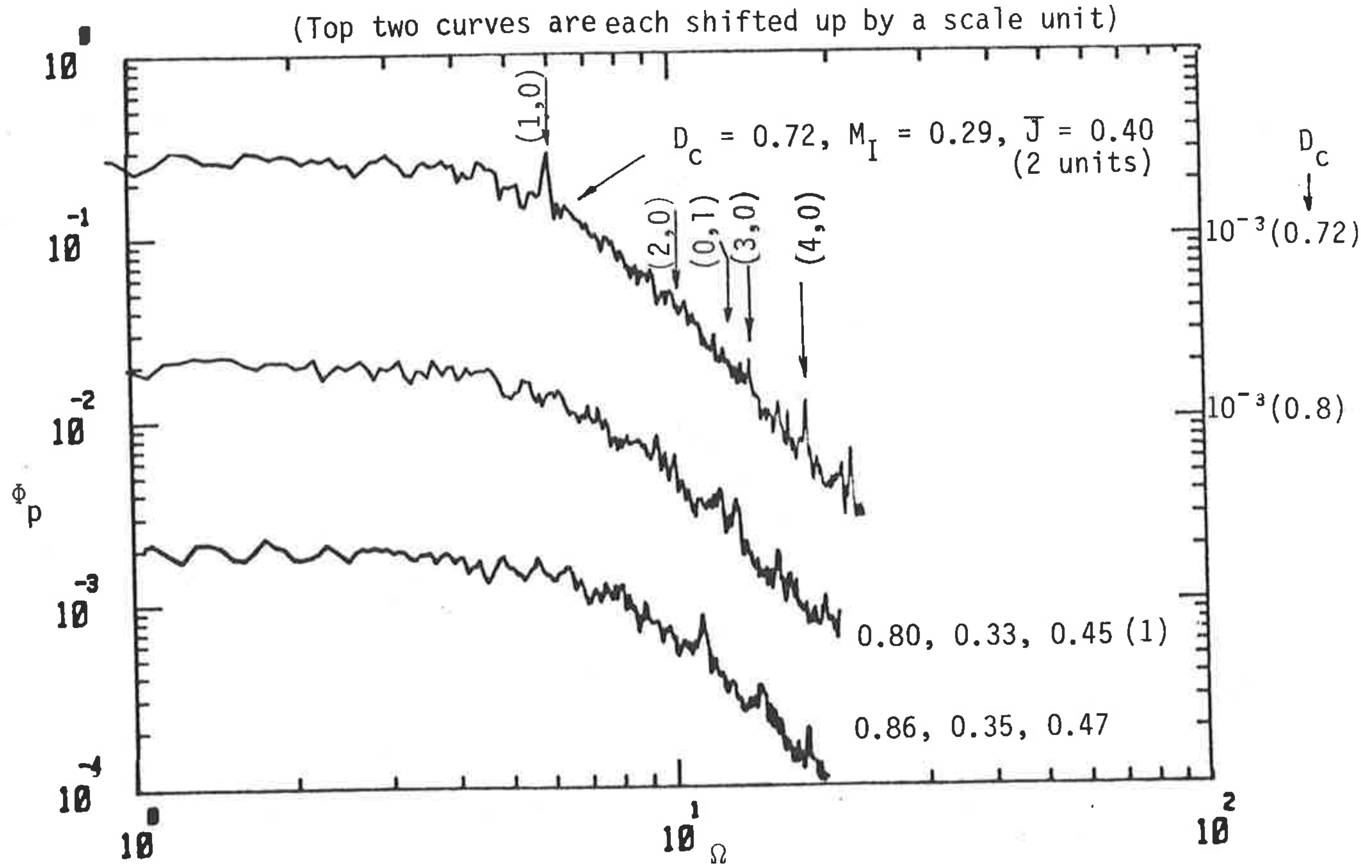

FIGURE 6.11 b : WALL PRESSURE SPECTRA AT X = 1.30, D_0 = 0.76
(Top two curves are each shifted up by one scale unit)

the flow rates corresponding to $D_C = 0.72$, 0.80 and 0.86. The spectra are very similar at the two locations, and the effect of increasing flow rate is a small decrease in Φ at low frequencies ($\Omega \lesssim 7$) and a small increase at high frequencies ($\Omega \gtrsim 7$).

The effect of orifice size for a given choke ($D_C = 0.86$) at the same two streamwise positions is shown in Figure 6.12.

All the spectra of Figures 6.11 and 6.12 are replotted in Figure 6.13 in the form $\phi_p(\omega)U_J/q_J^2 a$ v. $\omega a/U_J$, suggested by the p' scaling for this region found in Section 6.2. At both positions this appears to be a valid form of scaling.

6.3.2 Flow Recovery Region Downstream of reattachment $1.3 \leqslant X \leqslant 50$ (Zone 4)

This region extends from just downstream of reattachment to the region where the mean flow velocity profile has reverted to the undisturbed state. Again, measurements are presented showing variation with X for a given orifice and choke ($D_0 = 0.76$, $D_C = 0.86$), Figures 6.14(a) and (b), for a given orifice ($D_0 = 0.76$) with different chokes ($D_C = 0.72$, 0.80) at several X positions, Figure 6.15, and for a given choke ($D_C = 0.72$) with different orifice sizes at $X = 17.02$, Figure 6.16.

Figures 6.14(a) and (b) show that the excess of the spectral levels over those for undisturbed flow is greatest close to reattachment and then decreases with increasing X. Up to $X = 4.13$, the spectrum is broad band with small peaks corresponding to higher order acoustic modes; at larger X the acoustic contributions to Φ_p become much more prominent, as the turbulence levels relax towards their undisturbed flow values.

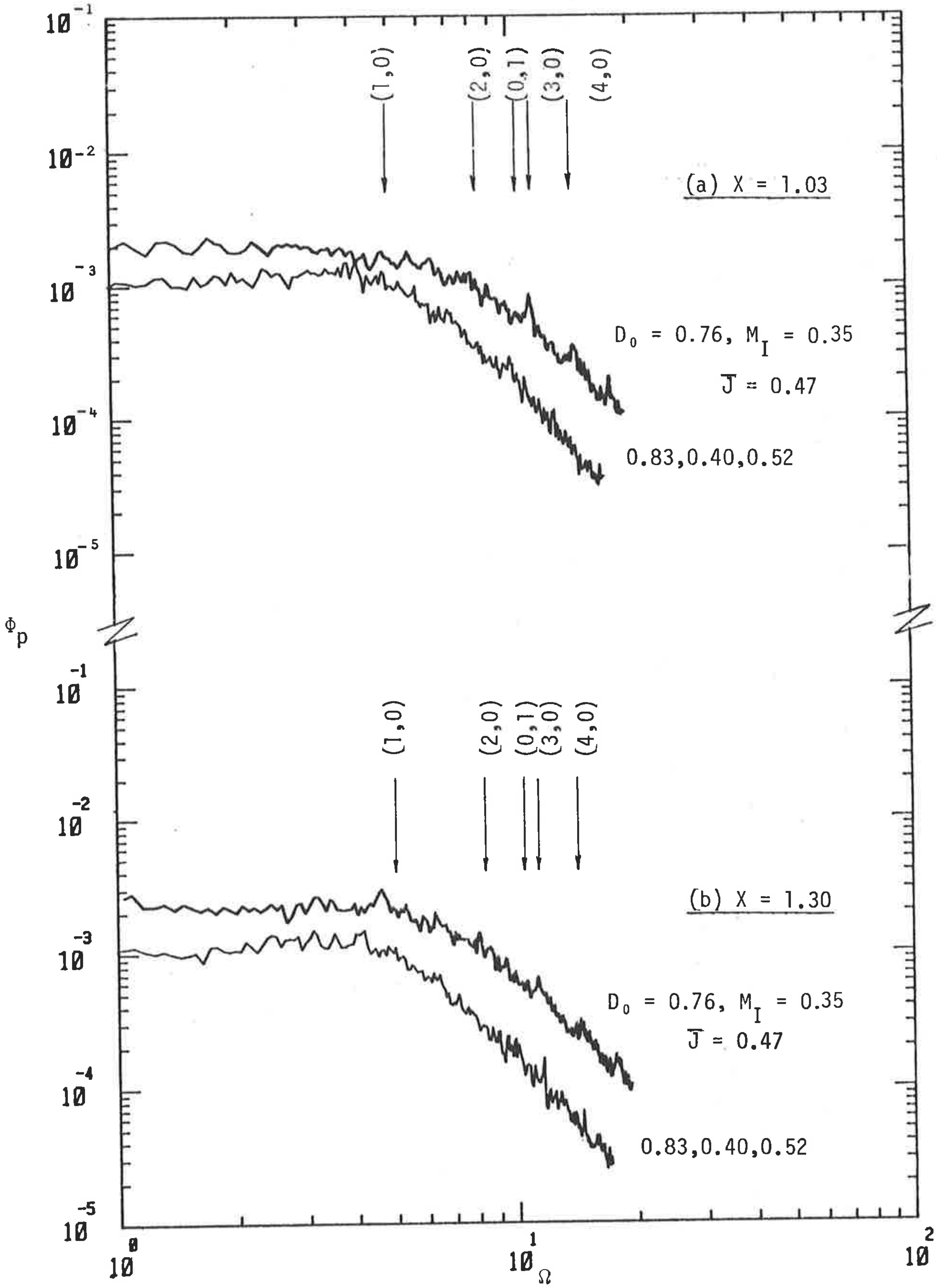

FIGURE 6.12 : WALL PRESSURE SPECTRA, D_c = 0.86

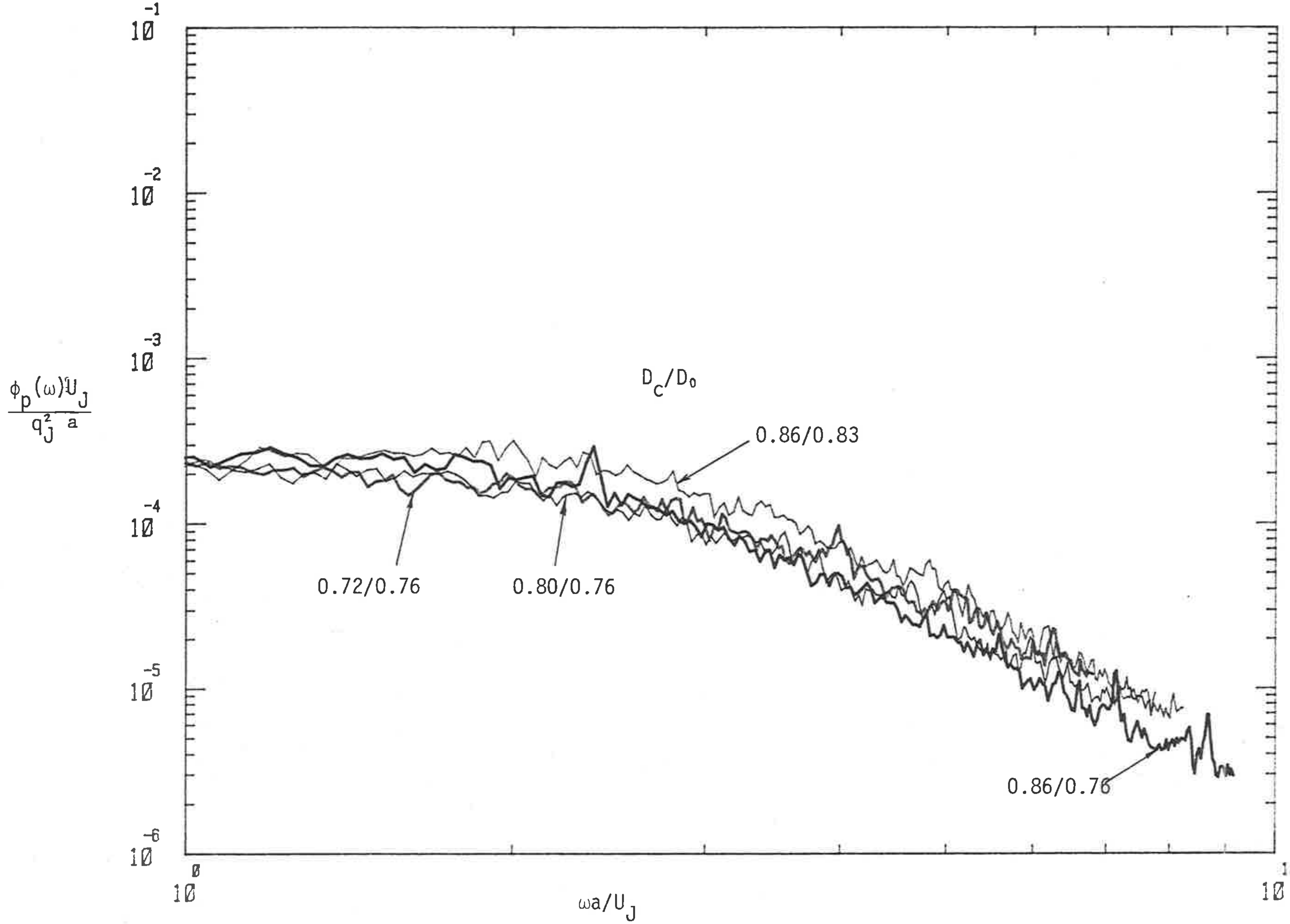

FIGURE 6.13(a) : WALL PRESSURE SPECTRA AT X = 1.03

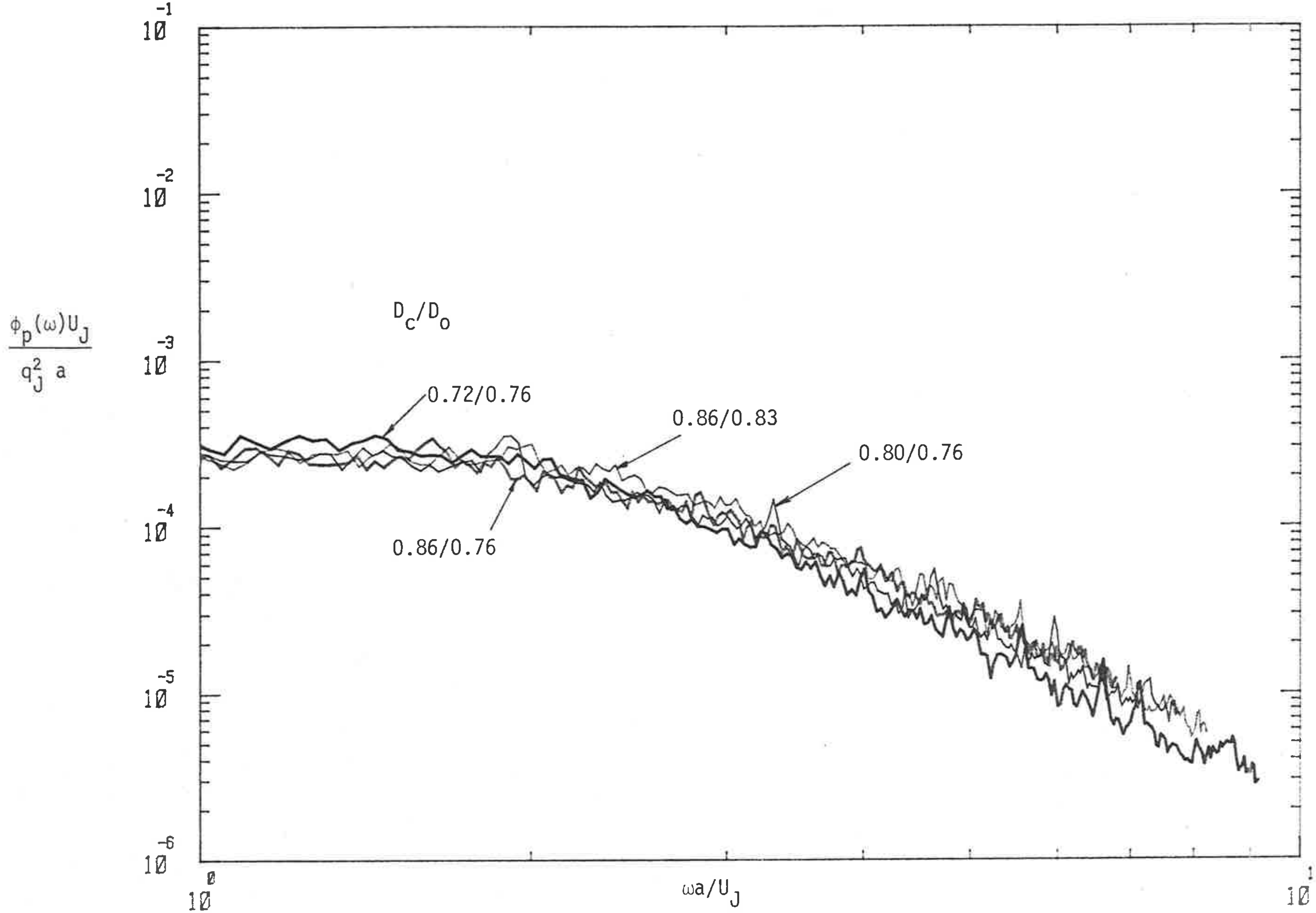

FIGURE 6.13(b) : WALL PRESSURE SPECTRA AT X = 1.30

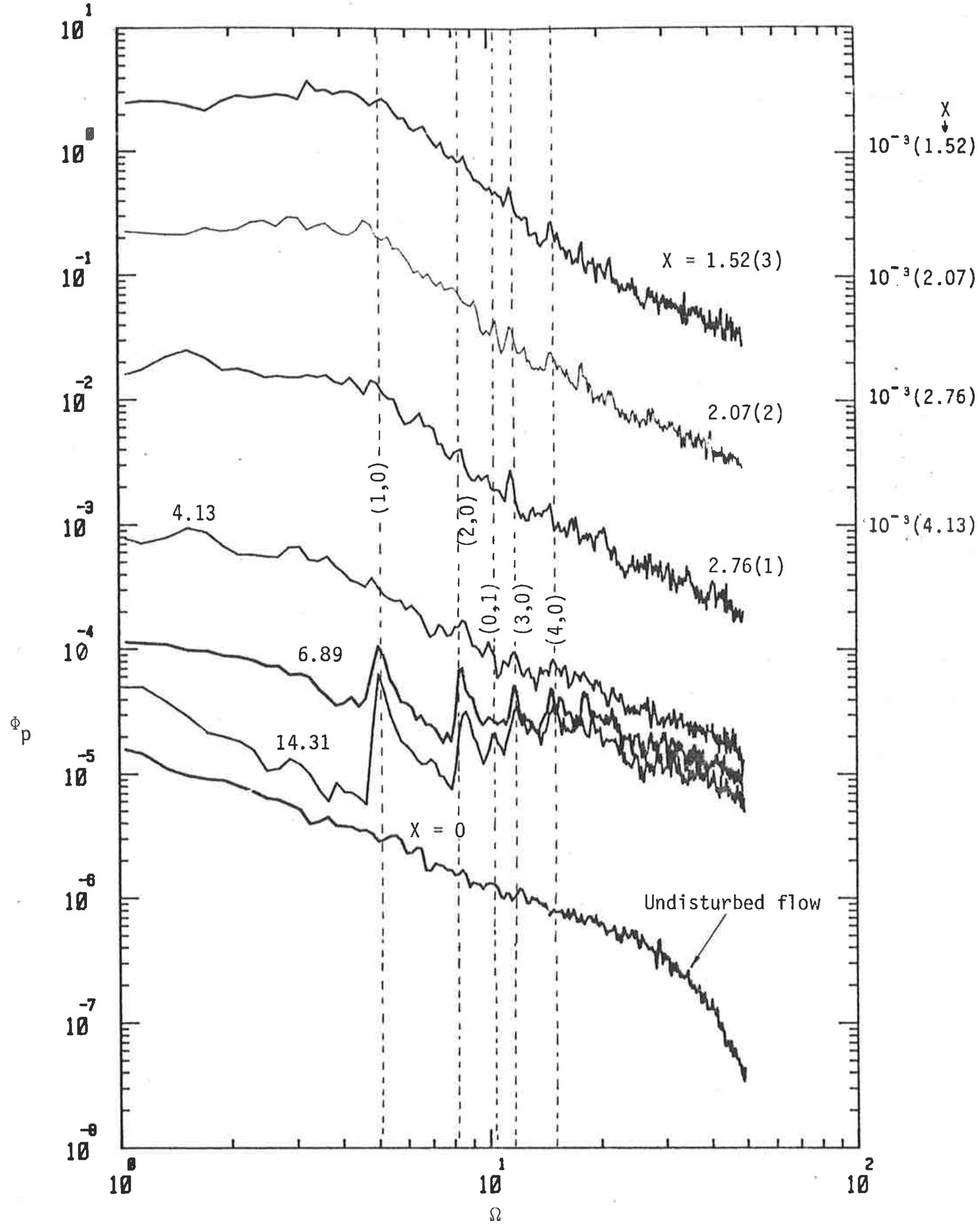

FIGURE 6.14(a) : WALL PRESSURE SPECTRA, D_c = 0.86, D_o = 0.76, M_I = 0.35, $\overline{J}$ = 0.47

(Top three curves are each shifted up by one scale unit)

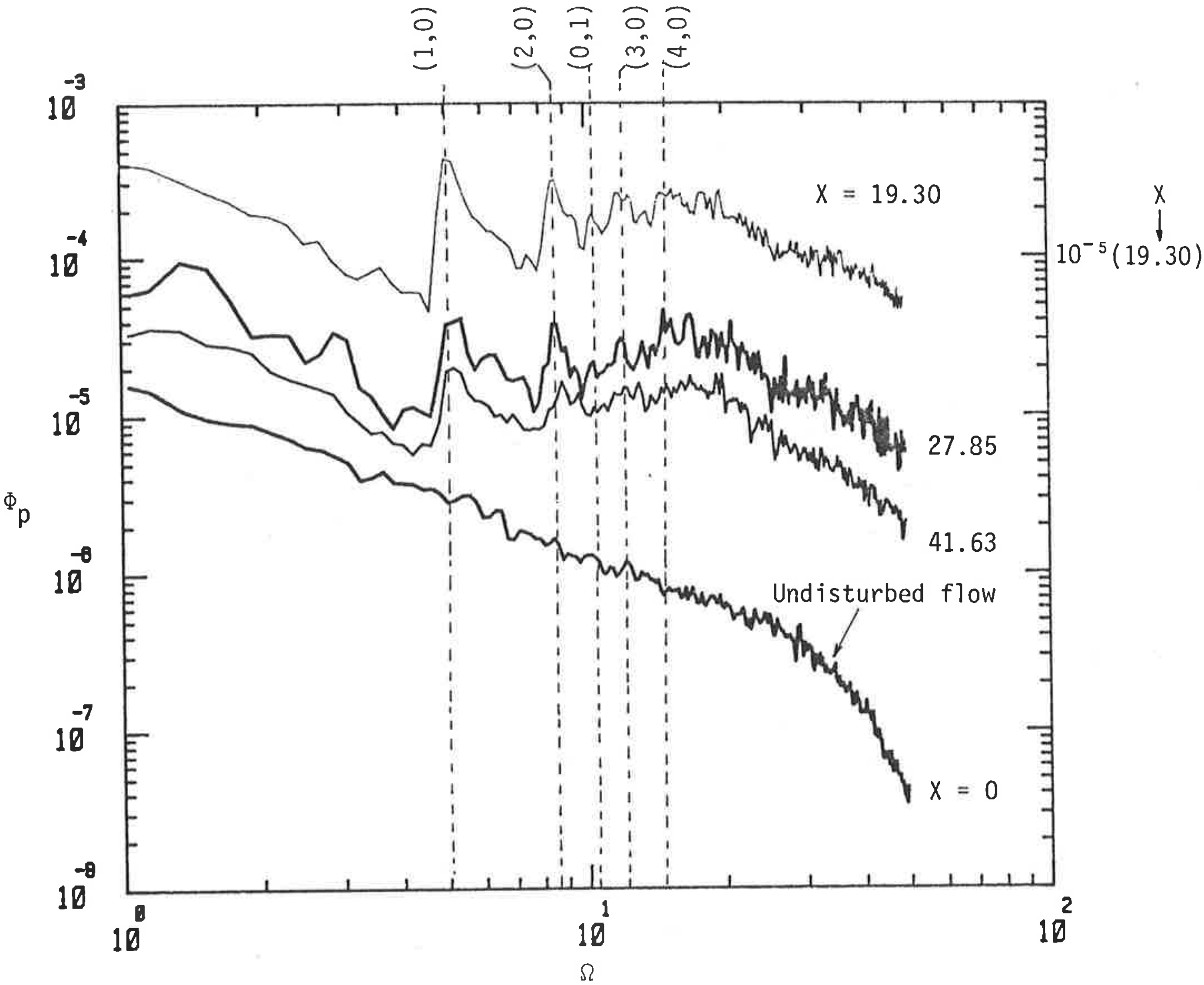

FIGURE 6.14(b): WALL PRESSURE SPECTRA, D_c = 0.86, D_0 = 0.76, M_I = 0.35, $\overline{J}$ = 0.47

(top curve is shifted up by one scale unit)

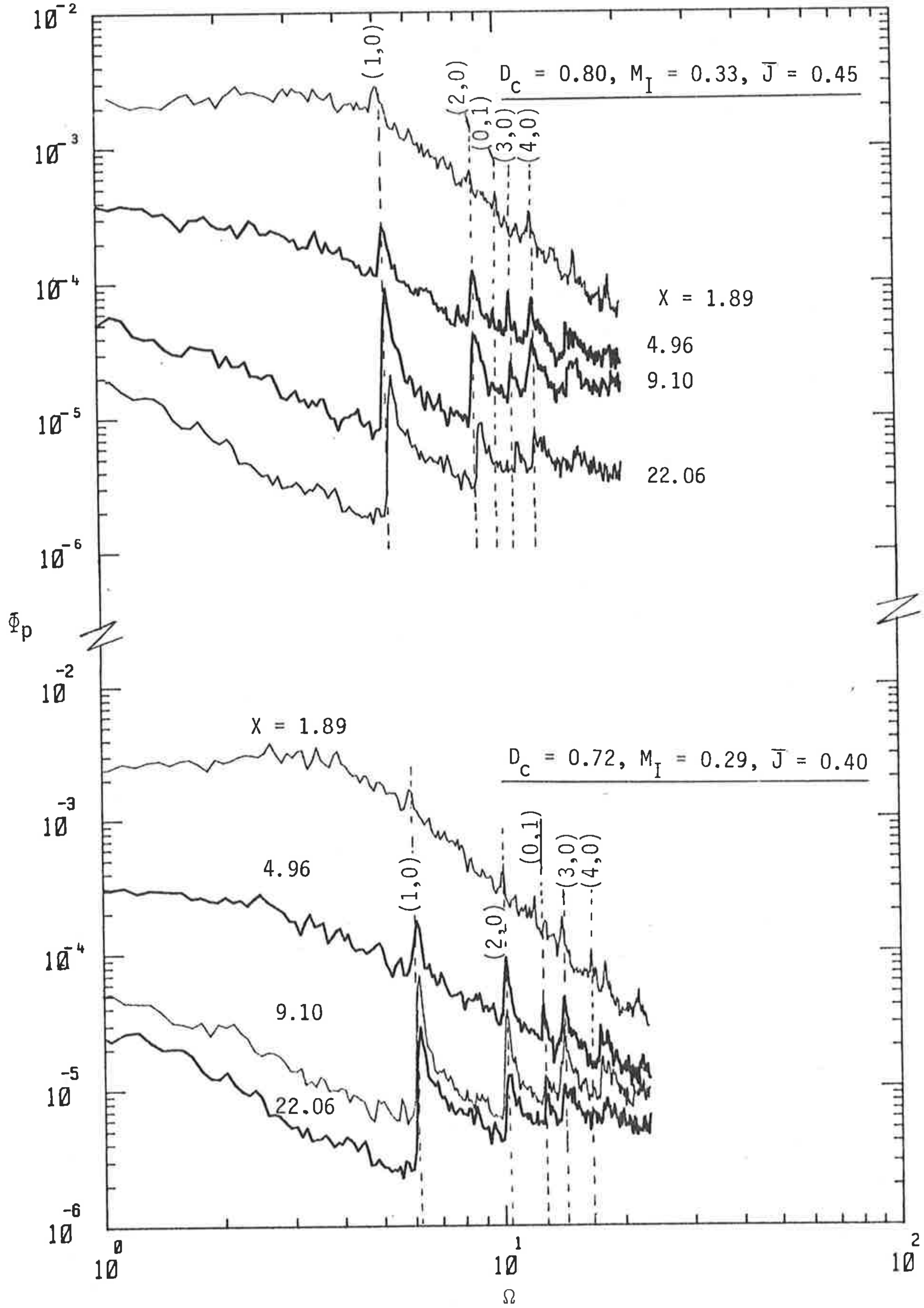

FIGURE 6.15 : WALL PRESSURE SPECTRA, D_o = 0.76

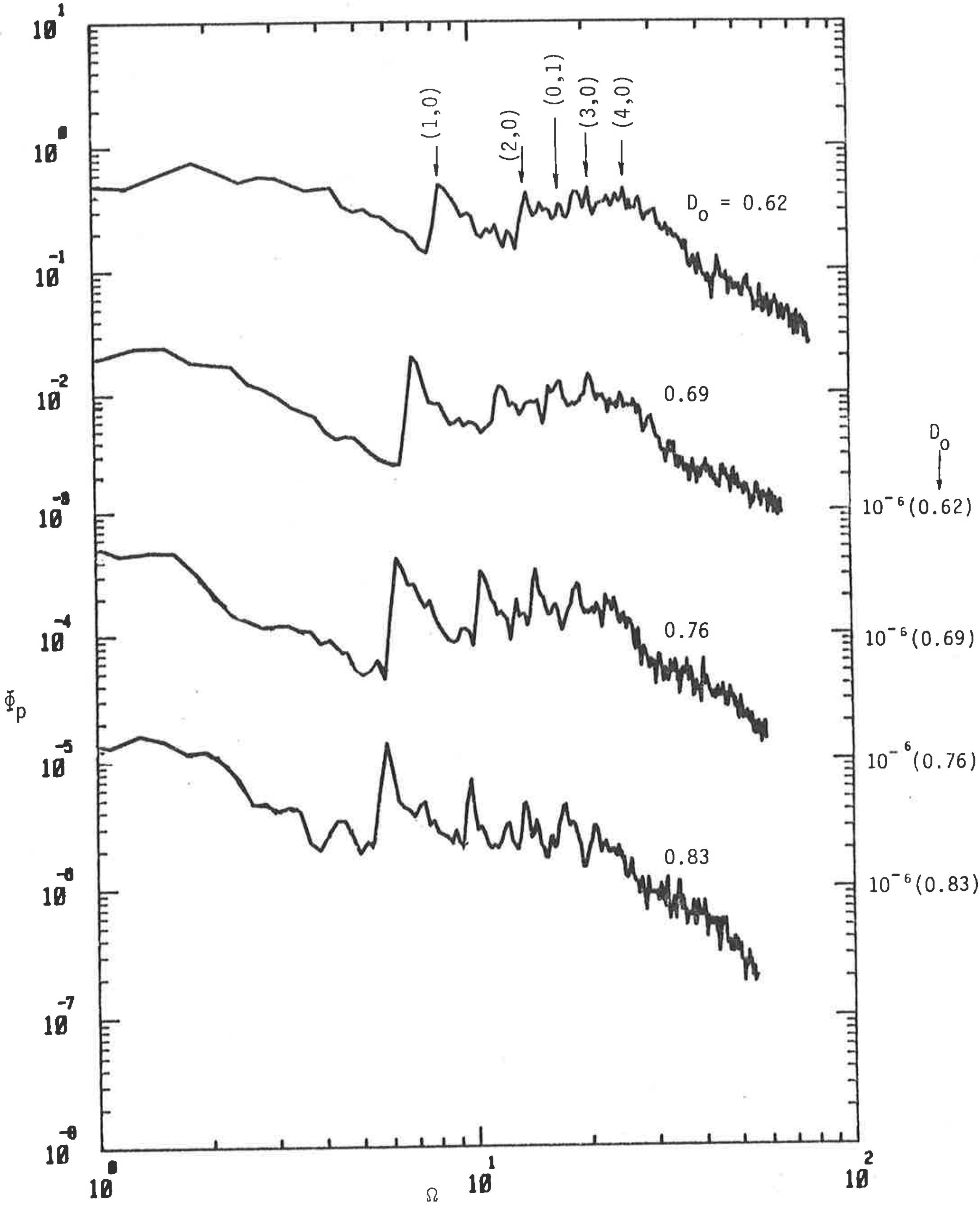

FIGURE 6.16 : WALL PRESSURE SPECTRA AT X = 17.02, D_c = 0.72

(Top three curves are each shifted up by one scale unit)

It should be noted from Figure 6.14 that the cut-off frequencies both non-dimensional and dimensional (since U_I is constant in this figure) of the higher order acoustic modes which are indicated by the sharp spectral peaks are the same for all values of X.

The effect of orifice size, in this region, is shown clearly by Figure 6.16 to be an increase in spectral level as D_0 is decreased. This trend, which implies that the orifice diameter has a significant effect on the coupling between the excitation provided by the disturbed flow and the acoustic modes in the pipe which are excited by it, is consistent with the p' measurements. It is also notable that the spectral peaks corresponding to the cut-off frequencies of the higher order acoustic modes are affected by choke size but not by the orifice size (which is consistent with the fact that the streamwise distribution of Mach number in this region for $X \gtrsim 5$ is fixed by D_C and independent of D_0). Although this is not evident from all the non-dimensional spectra of Figures 6.14 to 6.16, it is clear from dimensional spectra for the four orifice sizes, such as those shown in Figures 6.17 and 6.18.

These observations suggest that the spectra in this region are a function of some form of modified Helmholtz number, with spectral levels scaling in a similar way to that appropriate to p' in this region. This suggests a correlation in the form of $(\phi_p(\omega)c_e/q_J^2 a)(D_0^8/M_J{}^{0.6})$ as function of $(\omega a/c_e)(1-M_e^2)^{-1/2}$. The factor $(1-M_e^2)^{-1/2}$, as will be seen later, accounts for the effect of flow on the cut-off frequencies of the acoustic modes, M_e being an effective Mach

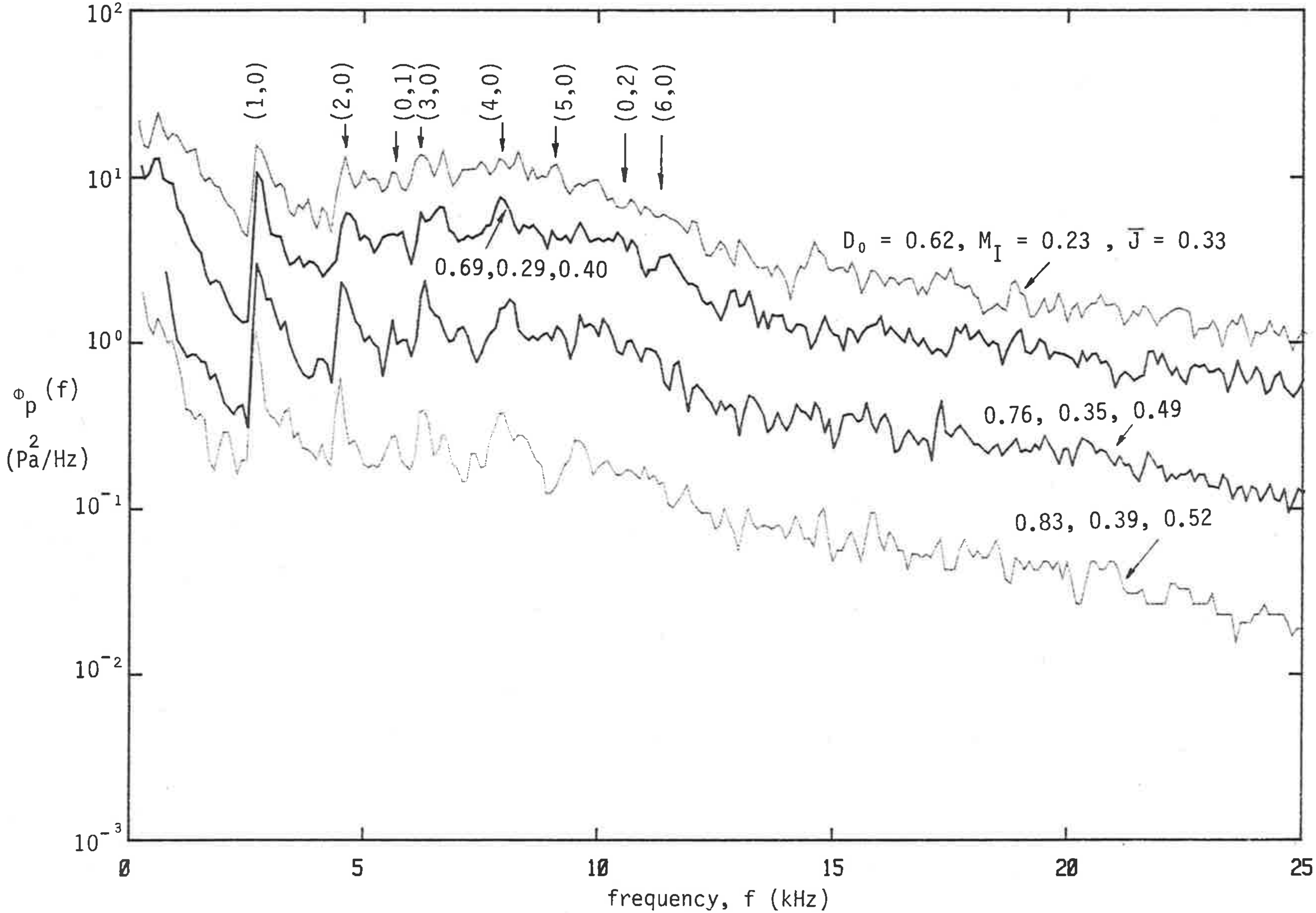

FIGURE 6.17 : WALL PRESSURE SPECTRA, D_c = 0.72, X = 17.02

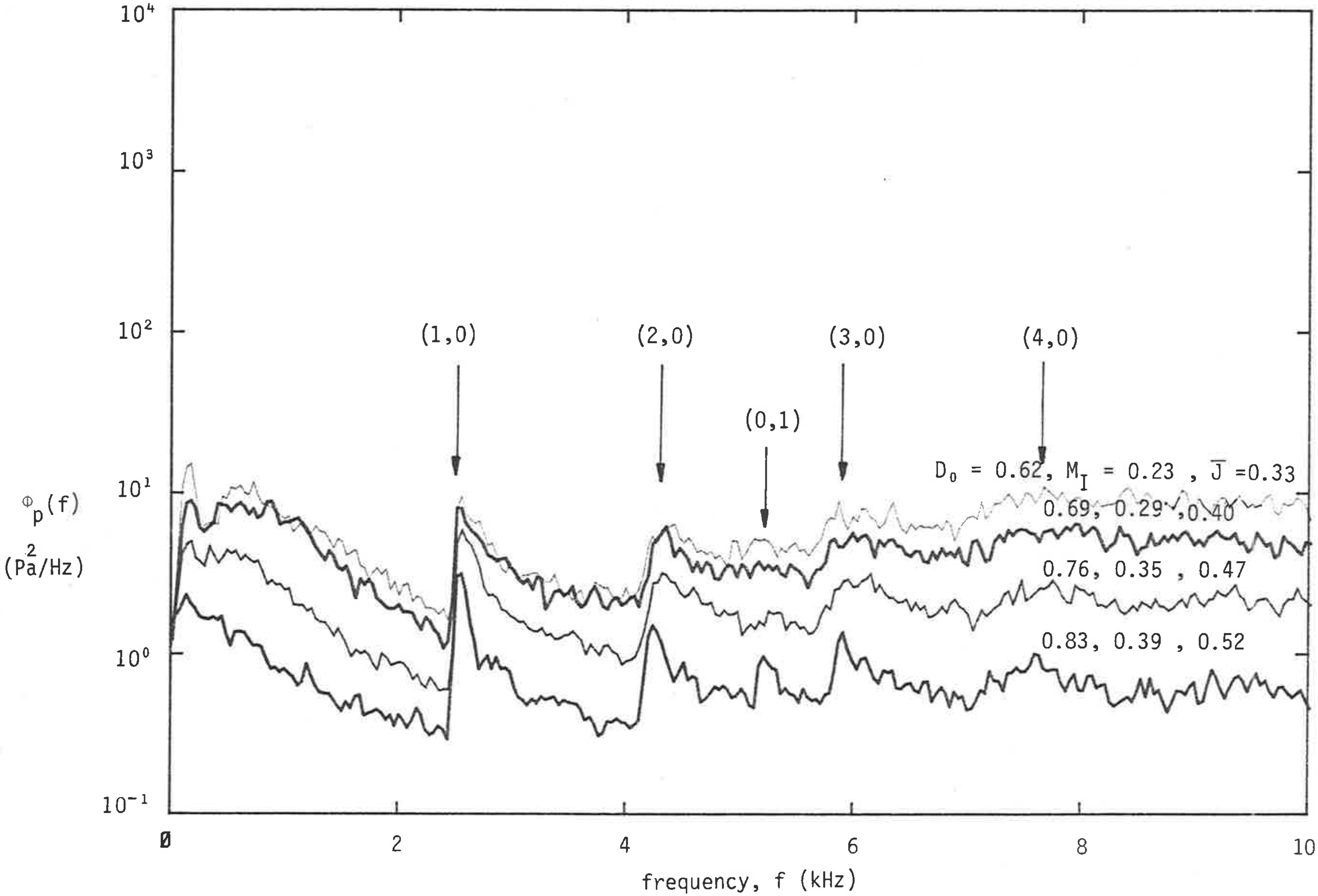

FIGURE 6.18 : WALL PRESSURE SPECTRA, D_c = 0.86, X = 13.23

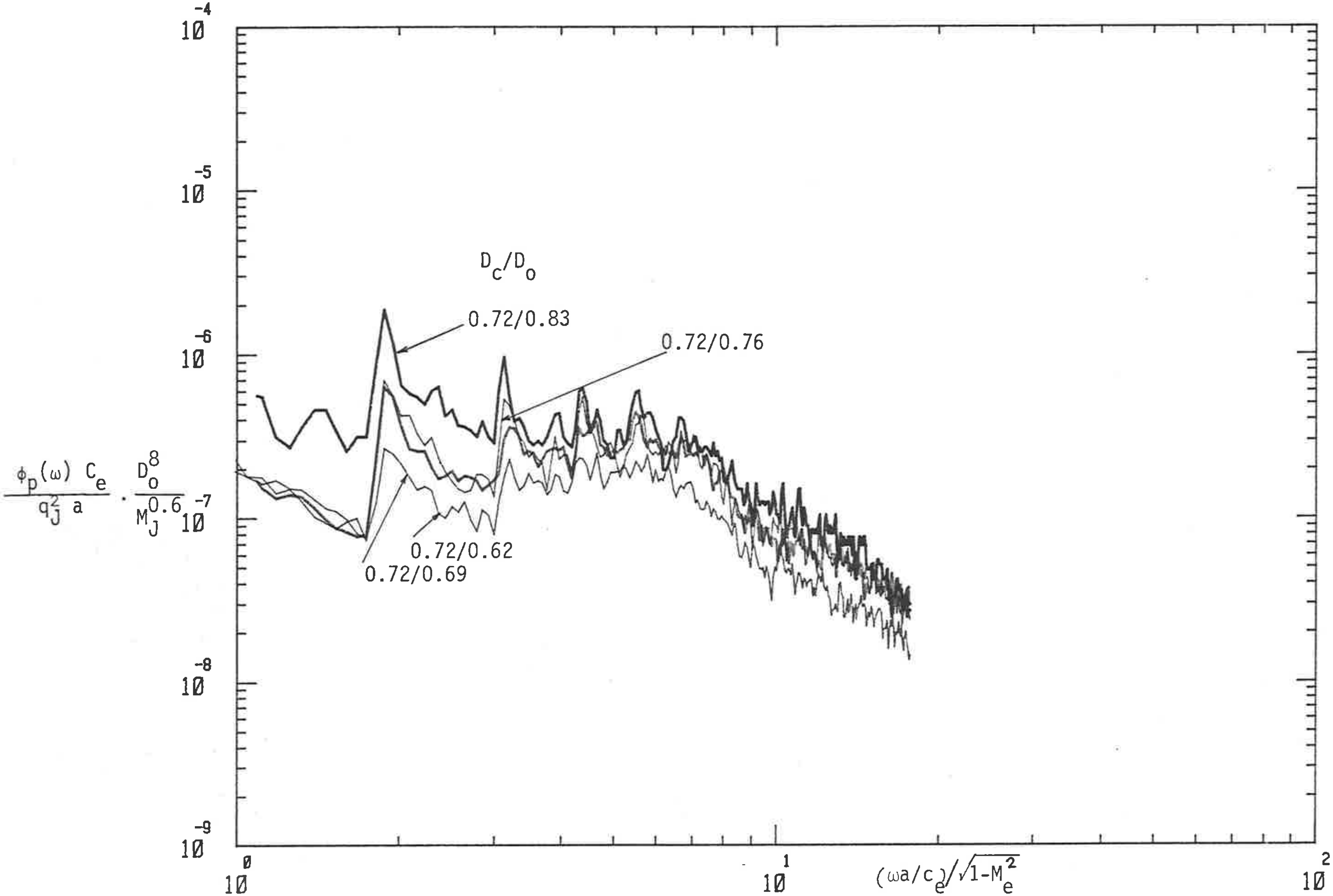

FIGURE 6.19 : WALL PRESSURE SPECTRA AT X = 17.02

number of the shear flow and c_e the corresponding sonic speed. Figure 6.19 shows that scaling of the spectral data in this way leads to a fairly good collapse.

6.3.3 Region of re-established fully-developed turbulent flow $X \geqslant 48$ (Zone 5)

Since the acoustic contribution to the pressure spectrum is already dominant further upstream in zone 4, the regaining by the flow itself of an essentially undisturbed character is not expected to influence the resultant spectra significantly. It can be seen in Figure 6.20, for $D_c = 0.86$, $D_0 = 0.76$, that the variation of the spectra with X in this region is very similar to that already seen in Figure 6.14 for zone 4. The figure also shows that the drop in p', with increasing X, results from progressive attenuation of the high frequency end of the spectrum.

Results for $D_c = 0.72$ with orifice sizes $D_0 = 0.62$-0.83 at $X = 83.05$, Figure 6.21, show that the effect of orifice size here is similar to that observed at $X = 17.02$, i.e. increasing the spectral level with decrease in D_0. Dimensional modal cut-off frequencies are again independent of orifice size for a given choke. Spectral scaling will take the same form as that already discussed for zone 4 (Section 6.3.2).

6.3.4 Region upstream of the orifice plate (zones 1 and 2)

The dependence of Φ_p on X in the range $-22.75 \leqslant X \leqslant -0.83$ for a given choke and given orifice, $D_c = 0.86$, $D_0 = 0.76$, is shown in Figure 6.22. Measurements at $X = -0.83$ for one orifice ($D_0 = 0.76$) and various chokes are presented in Figure 6.23, and for one choke ($D_c = 0.86$) and various orifices in Figure 6.24.

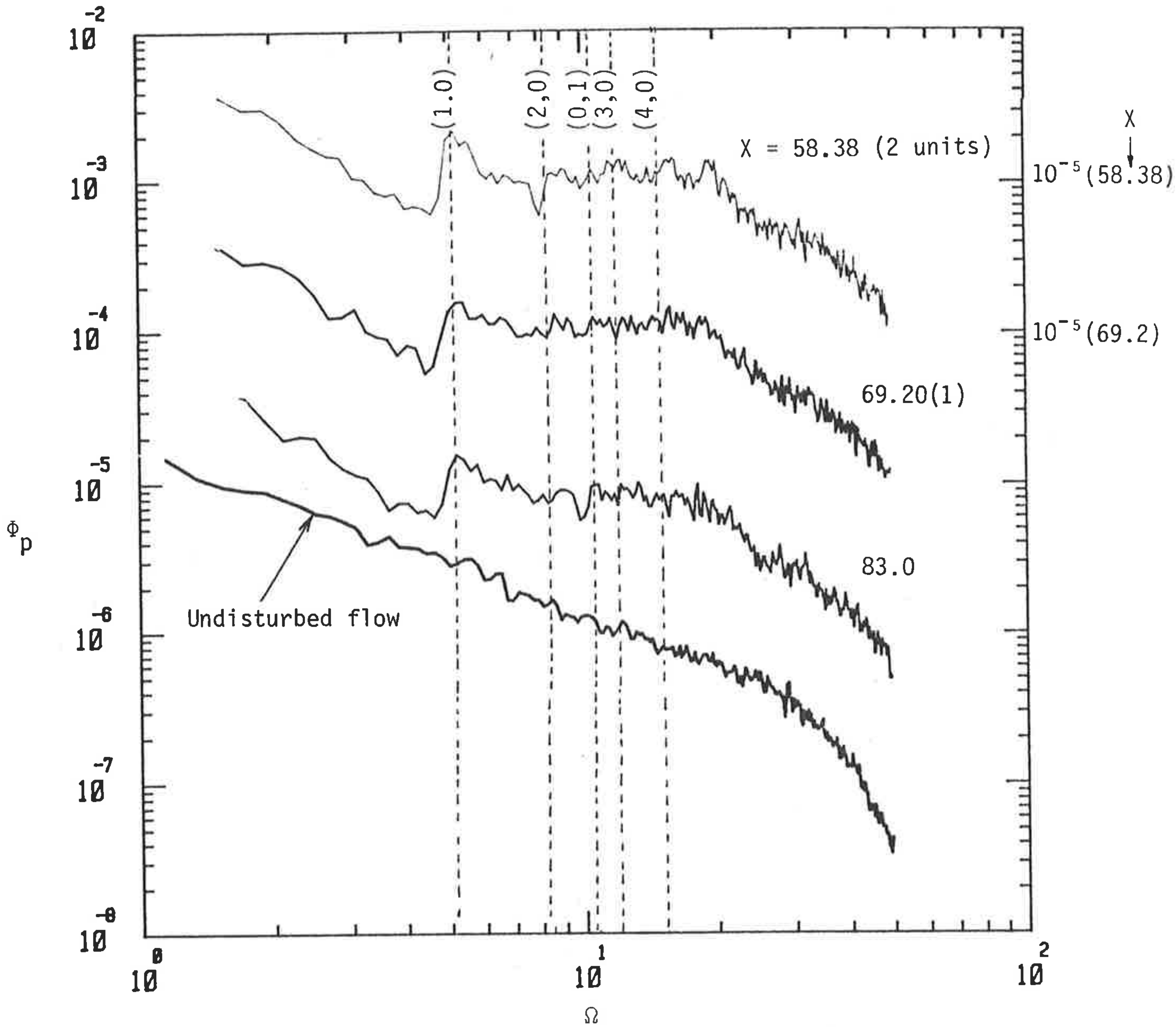

FIGURE 6.20: WALL PRESSURE SPECTRA, D_C = 0.86, D_0 = 0.76, M_I = 0.35, $\bar{J}$ = 0.47

(Top two curves are each shifted up by one scale unit)

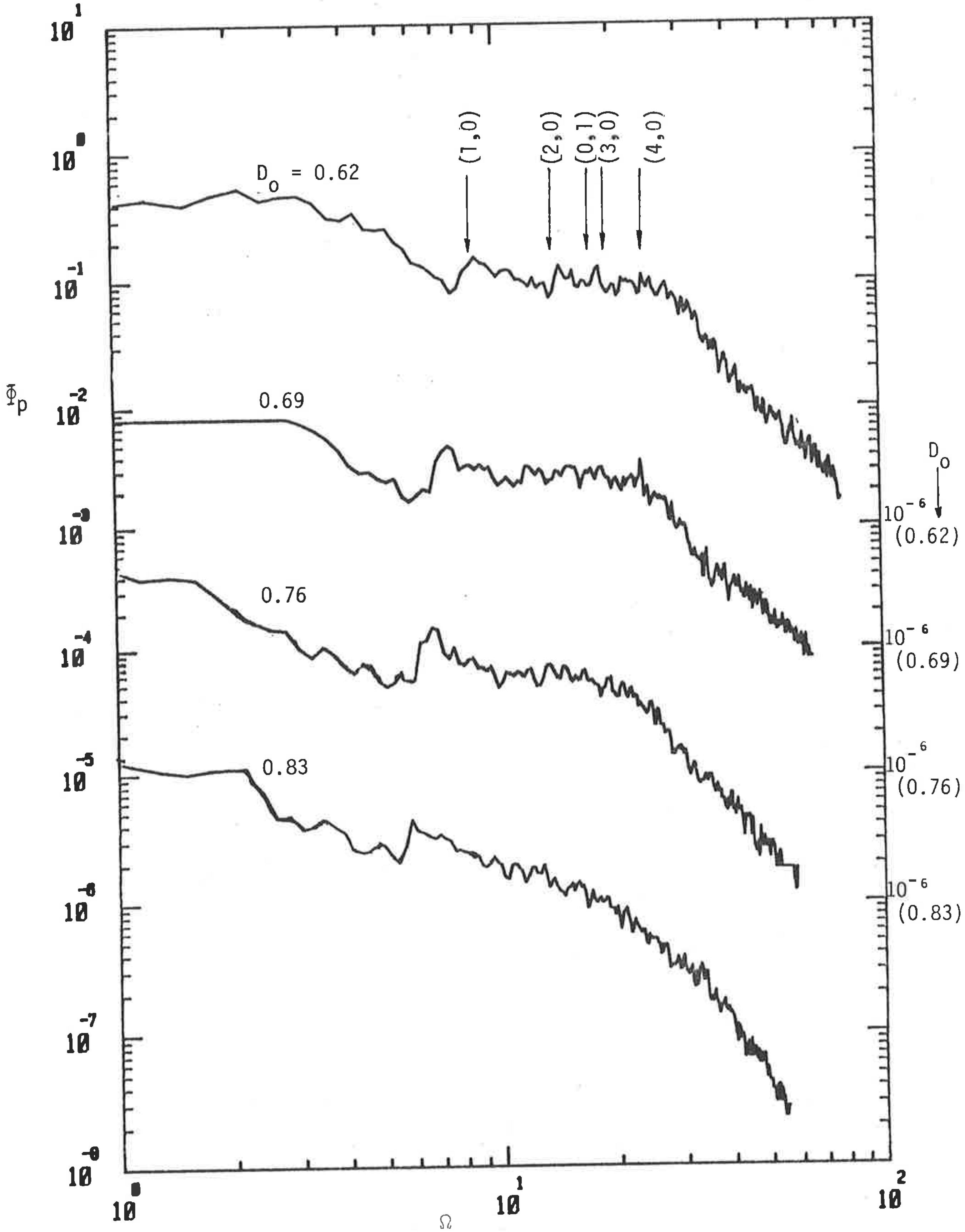

FIGURE 6.21 : WALL PRESSURE SPECTRA AT X = 83.05, D_c = 0.72
(Top three curves are each shifted up by one scale unit)

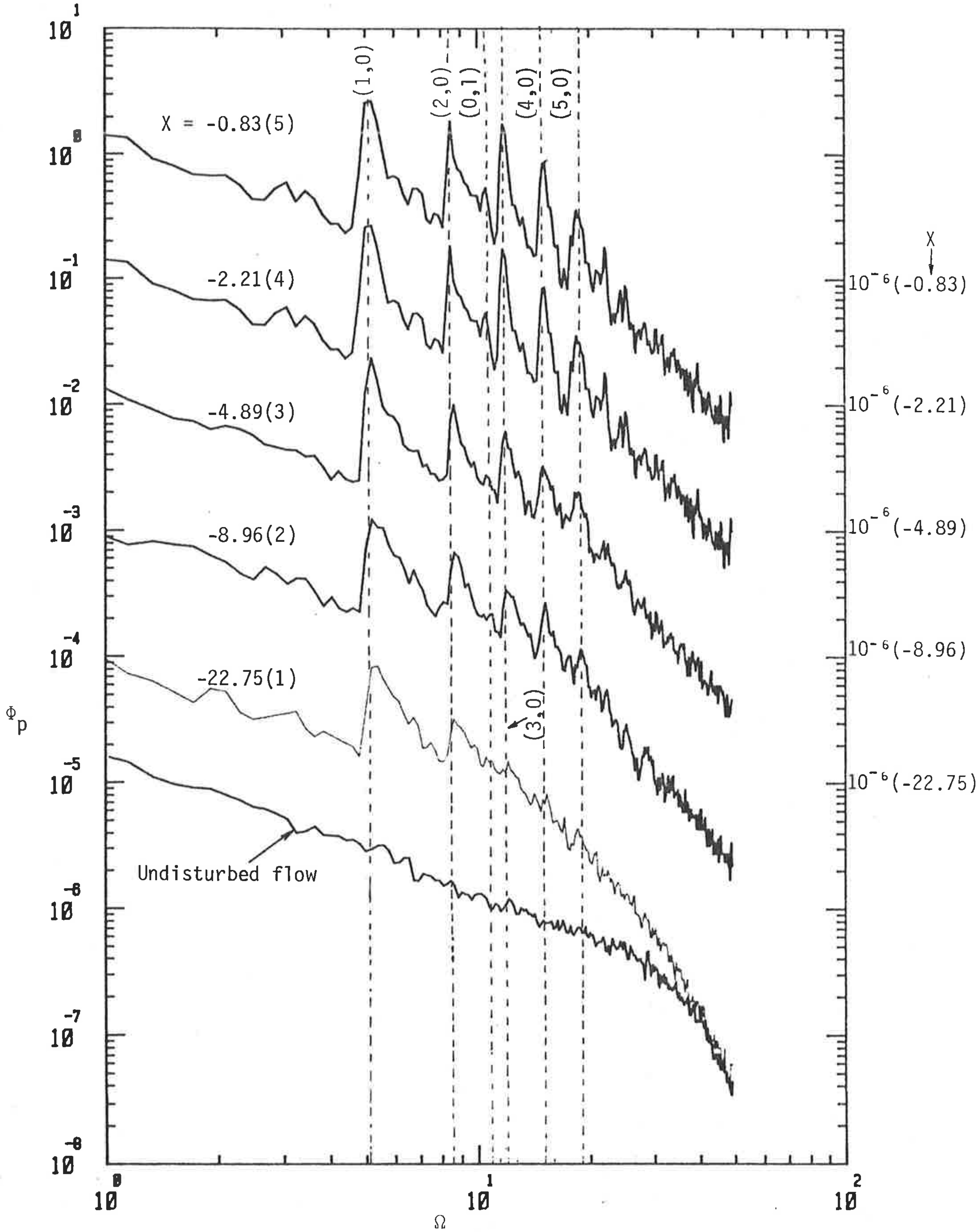

FIGURE 6.22: WALL PRESSURE SPECTRA, D_C = 0.86, Do = 0.76, M_I = 0.35 $\bar{J}$ = 0.47

(Each curve, except undisturbed flow, is shifted up by one scale unit)

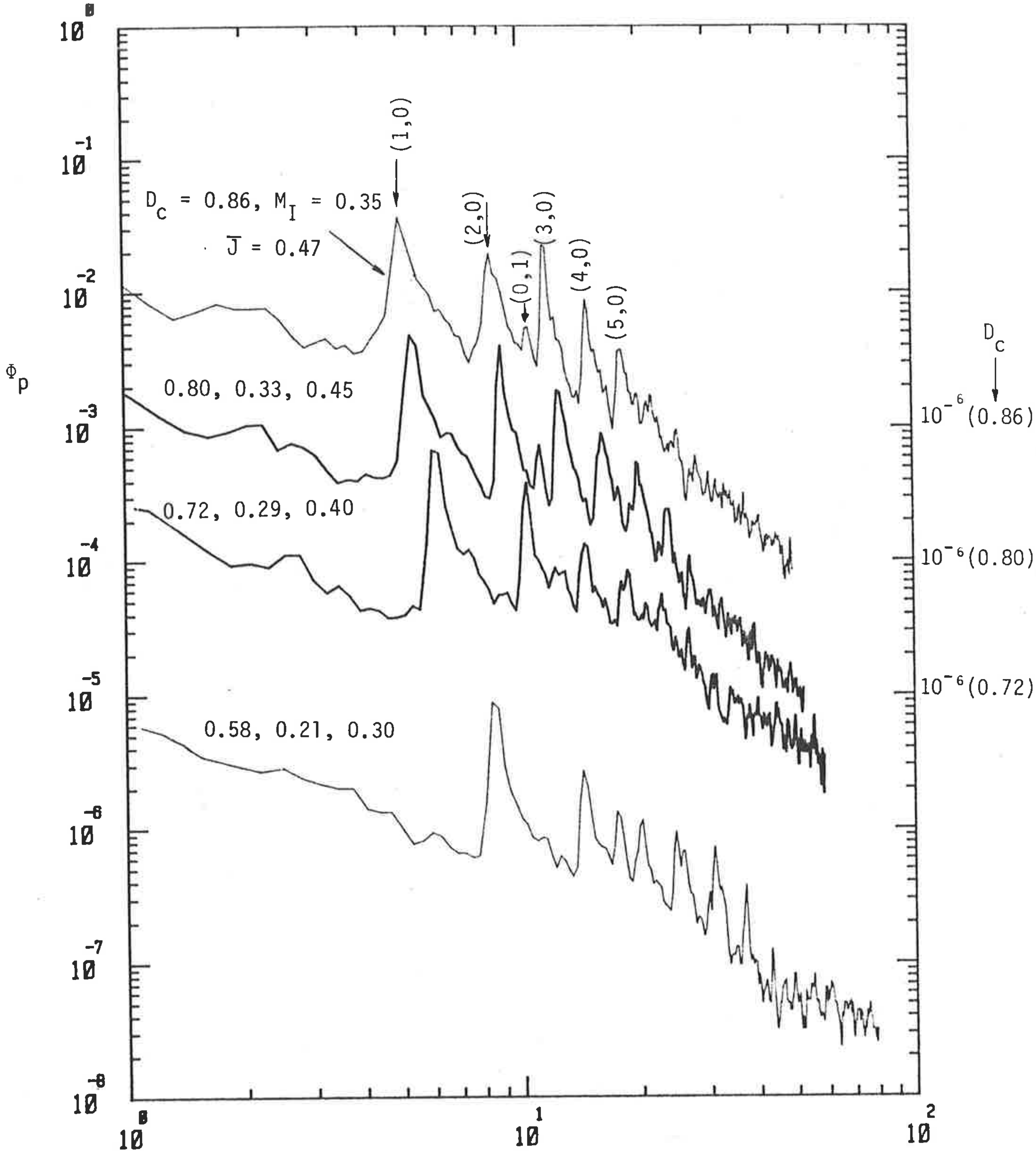

FIGURE 6.23 : WALL PRESSURE SPECTRA, D_0 = 0.76, X = -0.83

(Top three curves are each shifted up by one scale unit)

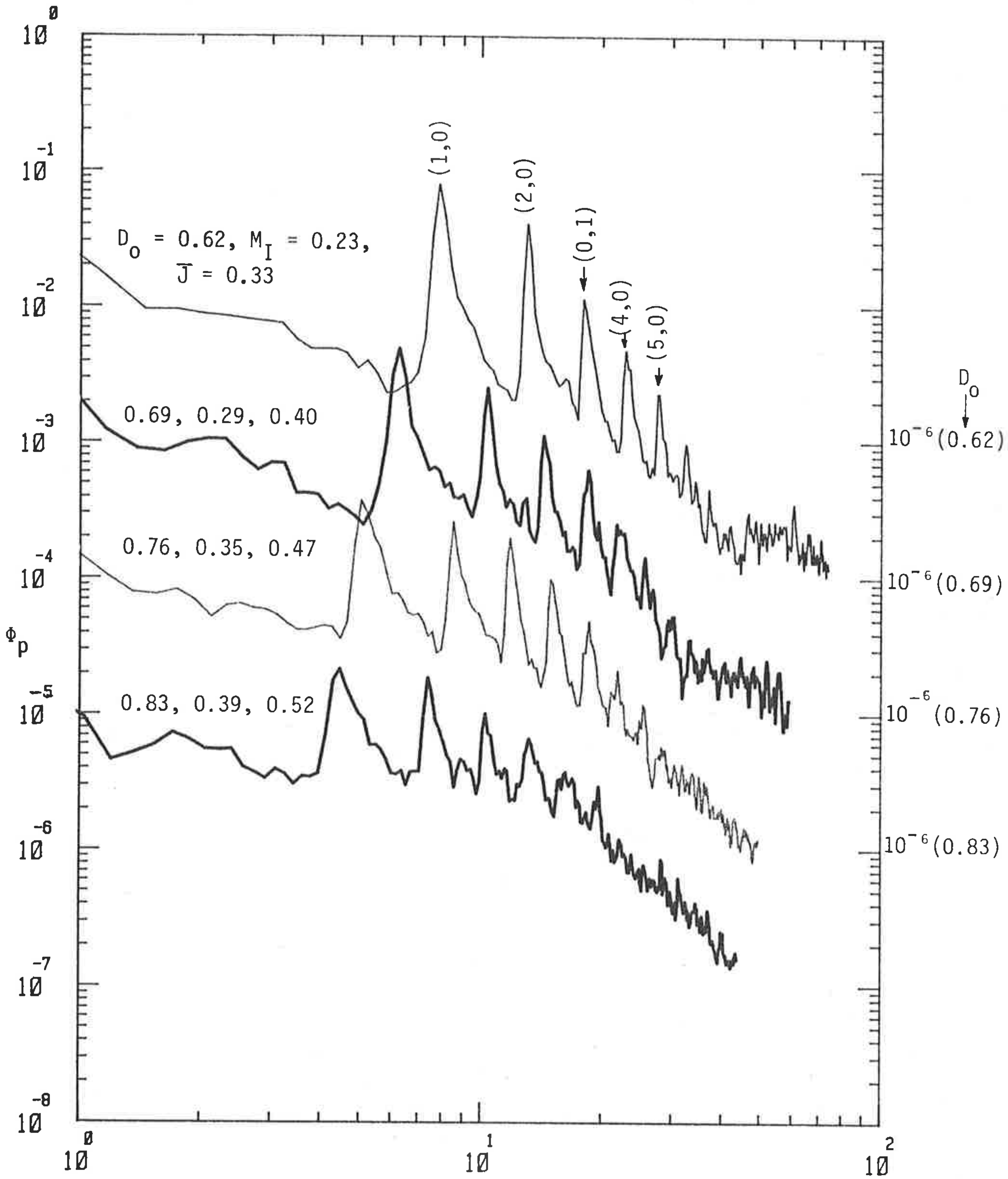

FIGURE 6.24 : WALL PRESSURE SPECTRA AT X = -0.83, D_c = 0.86

(Top three curves are each shifted up by one scale unit)

Upstream of the disturbance, when the flow speed and level of turbulence are low, the acoustic field makes the dominant contribution to both p' and ϕ_p, as is evident from Figure 6.22. Φ_p drops with increasing distance upstream (X becoming more negative), the rate of attenuation being greater at higher frequencies. It may also be noted that the Strouhal number Ω corresponding to cut-off of a given higher order acoustic mode is independent of X.

The effect of increasing flow speed, Figure 6.24, is to increase Φ_p. The decrease in the value of Ω corresponding to the cut-off frequencies of the higher order modes is due mainly to different values of U_I, but in this case, as can be seen Figure 6.25, where the results for $D_0 = 0.76$, at $X = -8.96$ are plotted, there is a slight decrease in the corresponding dimensional frequency with the (slight) increase in flow speed.

The effect of orifice size on the dimensional cut-off frequencies of the acoustic modes is illustrated in Figure 6.26 where the dimensional spectra at $X = -0.83$ are shown for $0.62 \leq D_0 \leq 0.83$ and $D_C = 0.86$. Unlike downstream, where the dimensional frequencies corresponding to the higher order acoustic mode peaks are independent of D_0, the frequencies here decrease with increase in D_0. Even though the streamwise distribution of Mach number is fixed by a given choke and is independent of D_0, M_I and U_I upstream of the orifice do vary with D_0, increasing as D_0 increases. The observed decrease in frequencies is therefore associated with an increase in M_I.

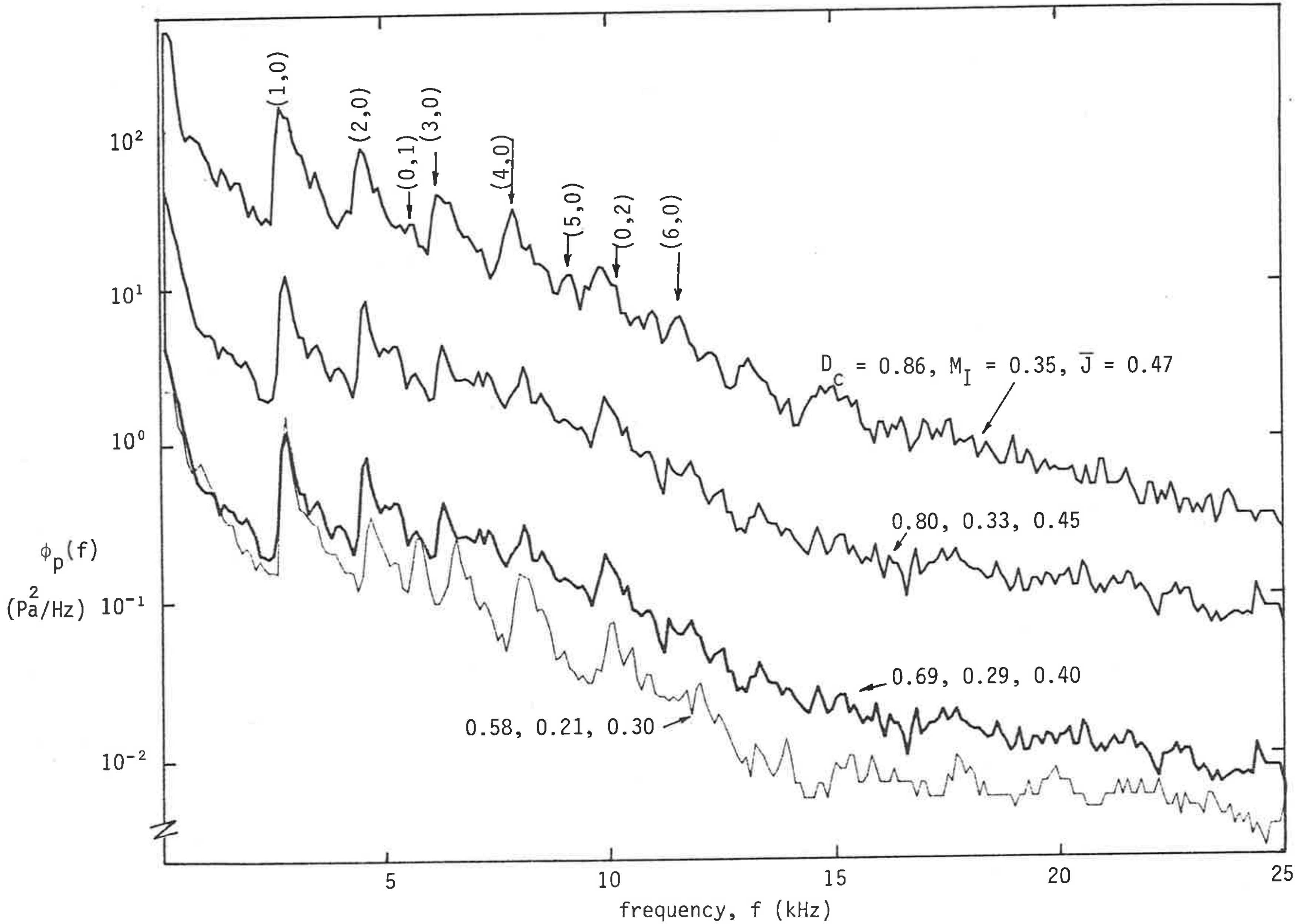

FIGURE 6.25 : WALL PRESSURE SPECTRA AT X = -8.96, D_0 = 0.76

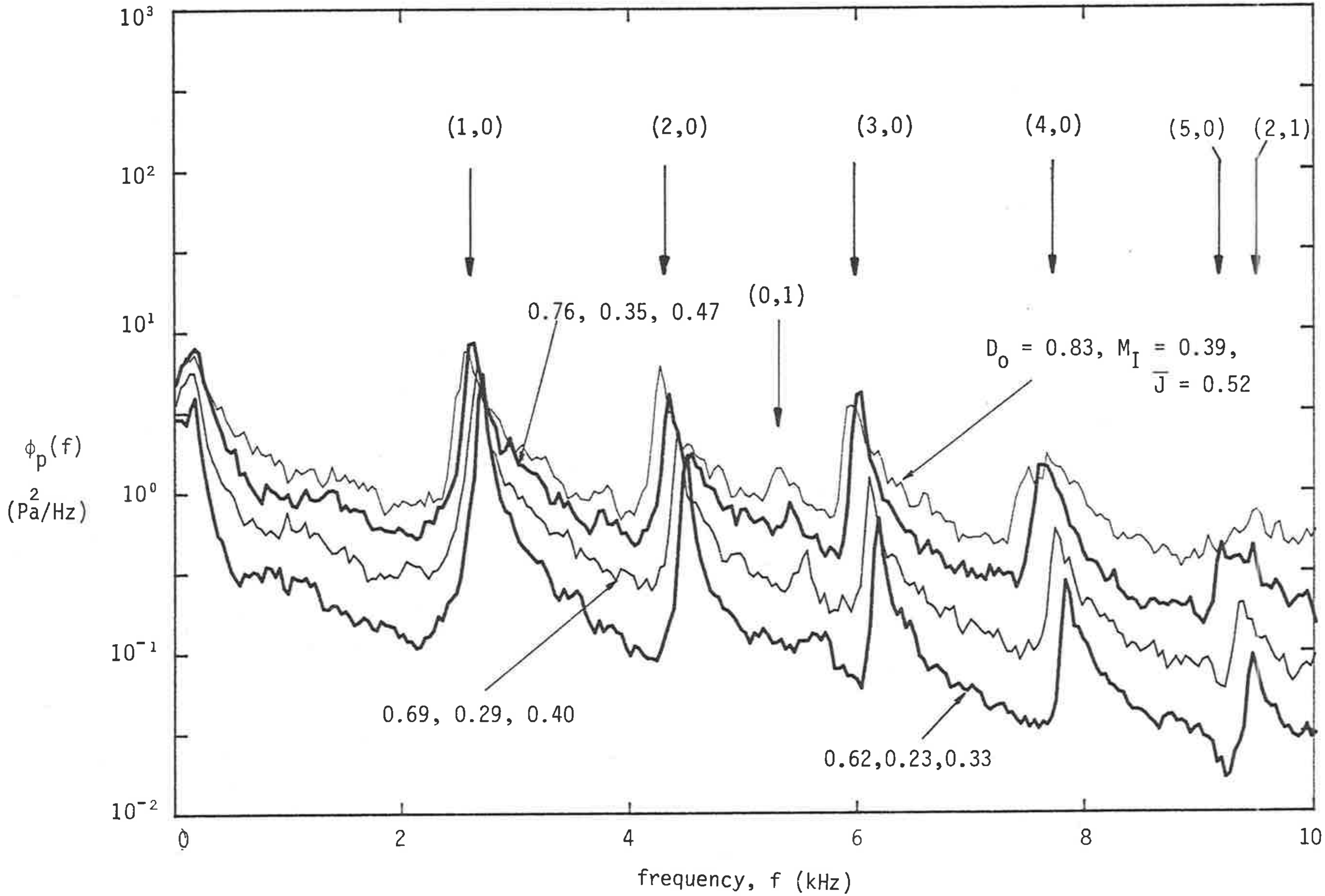

FIGURE 6.26 : WALL PRESSURE SPECTRA, X = -0.83 , D_c = 0.86

From the observed scaling of p'_{ac}/q_J with M_J in this upstream region and in the light of the discussion of the form of the spectrum in zone 4, spectra can be expected to correlate on the basis of $(\phi_p(\omega)c_e/q_J^2 a).M_J^2$ as a function of $(\omega a/c_e)(1-M_e^2)^{-1/2}$, where now M_e and c_e will be an equivalent Mach number and speed of sound for the flow in this region. This is borne out by Figure 6.27.

6.4 MODAL AMPLITUDES AND CUT-OFF FREQUENCIES

The disturbed turbulent pipe flow generates velocity and pressure fluctuations which, combined with the mean flow in the pipe, generate a sound field which propagates as plane waves and higher order acoustic modes in the pipe system. Therefore the overall wall pressure fluctuation is a combination of two pressure fields: a turbulent pressure field and an acoustic pressure field. At low frequencies, $\omega a/c \leqslant 1.84$, only plane waves can propagate. This fundamental plane wave propagation in the streamwise direction takes place with the wave front normal to the pipe axis and with acoustic pressure uniform over the cross-section of pipe. Cross-correlation techniques can be used to separate hydrodynamic pressure fluctuations from the acoustic pressure fluctuations associated with plane waves. But this technique is useful only up to frequencies corresponding to $\omega a/c = 1.84$, as, beyond this, higher order acoustic modes start propagating.

Higher order acoustic modes have different radial and circumferential patterns of acoustic pressure amplitude variation, which result from multiple reflection of acoustic pressure waves from the wall. Thus the pressure patterns for these modes are not uniform over the pipe cross-section (Chapter 2). Higher order modes propagate only at frequencies higher than their cut-off frequencies, but if the noise generated by the disturbance extends over a wide frequency range many such modes will be propagating simultaneously inside the pipe.

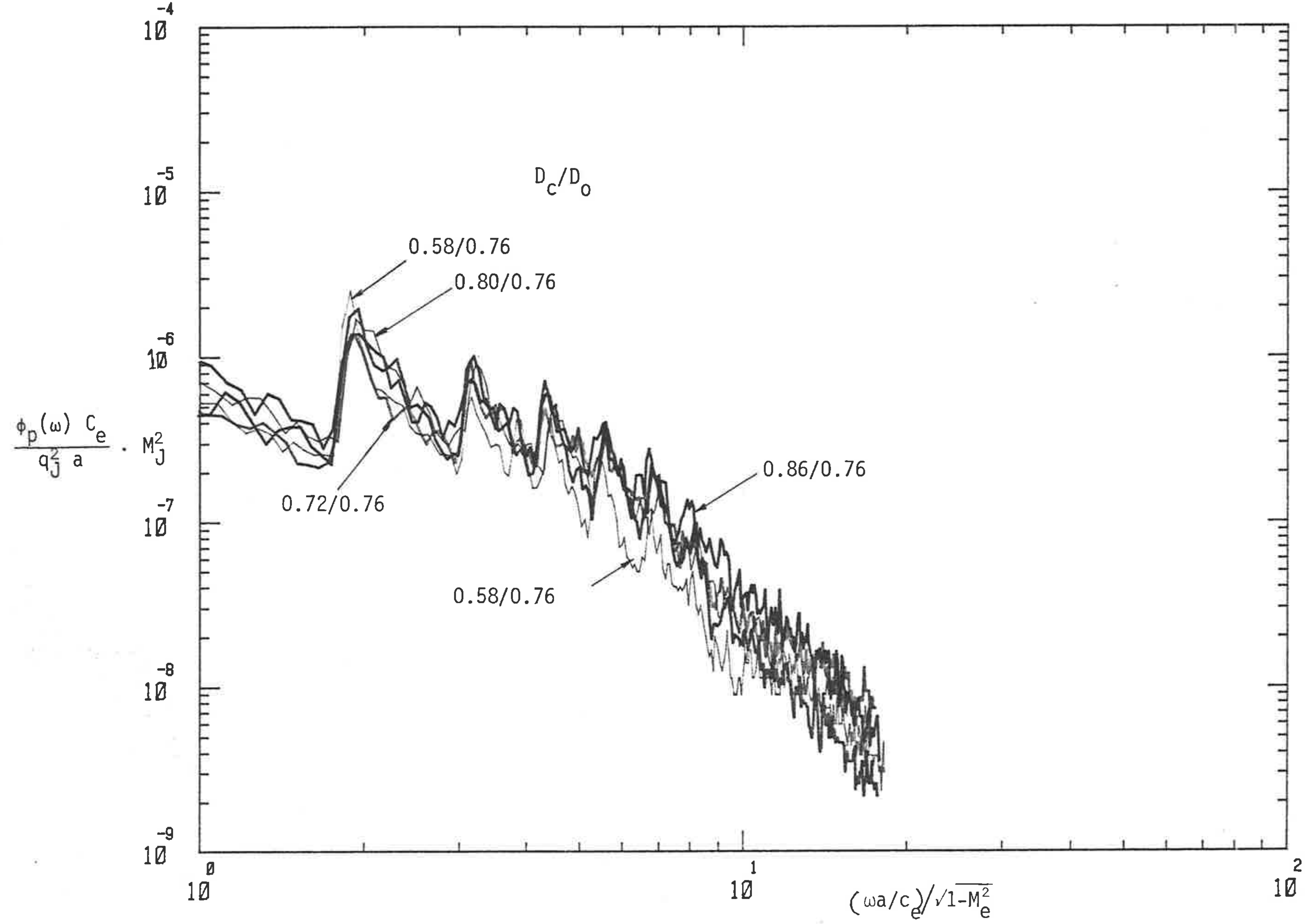

FIGURE 6.27 : WALL PRESSURE SPECTRA AT X = -8.96

The general aim of this part of the investigation is to study the attenuation and cut-off frequencies of the acoustic modes, at various streamwise locations, with a view to identifying those characteristics of the flow which determine the details of the wave system which is set up.

For example, we have seen that the flow Mach number may vary from a small value in the flow approaching the orifice to a very high value (of the order of unity or somewhat greater) in the separated jet downstream of the orifice and back to a small to moderate value at the downstream end of the piping system; since the cut-off frequencies of the higher order acoustic modes are reduced from their no-flow values by a factor of $\sqrt{1-M_e^2}$, (where M_e is some effective Mach number), one question arising, where there is such a large variation of Mach number from upstream to downstream, is which Mach number will determine the cut-off frequencies of the acoustic modes which are excited.

Cross-correlation techniques in filter bands used by Goff (1955), Bolleter and Chanaud (1971), Karvelis (1975) and Bull and Norton (1981), can show whether the acoustic energy is being propagated in a plane wave mode or higher order mode. However, due to the dispersive nature of higher order modes, cross-correlation cannot directly give the acoustic pressures associated with particular modes. Karvelis (1975) applied cross-correlation techniques to filter bands where only plane-wave propagation is possible ($\omega a/c < 1.84$), while Norton (1979) extended their application to the determination of the plane wave component of the wall pressure fluctuations in filter bands containing higher order modes, using the fact that the group velocity of the higher order modes is less than the sonic propagational speed of plane waves. Norton extracted the components of wall pressure fluctuations associated with the higher order modes in various filter bands by subtracting the turbulence and plane wave components from the total wall pressure fluctuations in those bands. Kerschen and Johnston (1981) have developed a technique to separate broadband (as well as discrete frequency) noise propagating inside a circular pipe into acoustic duct modes. The acoustic modes are separated by weighted combinations of the instantaneous outputs of pressure sensors, spaced around the pipe circumference. Considerable simplification to the technique occurs when there is no correlation between different circumferential modes. This technique has been used in the present investigation. An additional advantage of the technique is that, as an incidental to the generation of a modal spectrum, it leads to identification of the frequency at which the mode starts propagating.

Initially piezoelectric transducers were used for modal separation measurements, but owing to problems experienced in matching their sensitivities, and because of their sensitivity to structural vibrations, they were replaced by Brüel and Kjaer 1/4" microphones.

6.4.1 Acoustic modal spectra

The basis of Kerschen and Johnston's technique of modal separation is as follows.

The instantaneous wall pressure fluctuation, p, at point r, θ, x and time t, is the sum of the acoustic pressure fluctuation p_{ac} and the turbulence (hydrodynamic) pressure fluctuation p_h:

$$p(t;r,\theta,x) = p_{ac}(t;r,\theta,x) + p_h(t;r,\theta,x) \ . \qquad (6.3)$$

Both p_h and p_{ac} are stochastic processes, being random functions of space and time, and p is therefore also a stochastic process. Any one of these three pressures can be represented as a stochastic Fourier-Stieltjes integral of the form (refer to Fig. 2.1 for the coordinate system)

$$p(t;R,\theta,x) = \int_{-\infty}^{\infty} e^{i\omega t} dZ_p(\omega;R,\theta,x), \tag{6.4}$$

where the dZ_p satisfy the orthogonality condition

$$\begin{aligned}\overline{dZ_p(\omega;R,\theta,x)\ dZ_p^*(\omega';R,\theta,x)} &= \phi_p(\omega;R,\theta,x),\ \omega = \omega' \\ &= 0,\ \omega \neq \omega'.\end{aligned} \tag{6.5}$$

Consider first the case of no flow when only acoustic pressure fluctuations occur. If it is assumed that the acoustic waves are propagating in the +x-direction and the frequency of interest is bounded, i.e. modes of higher order than M are cut-off, then, with equation (2.4), equation (6.4) for the acoustic pressure at the pipe wall at x = 0 can be written in terms of the acoustic pipe modes as

$$\begin{aligned}p_{ac}(t;\theta) = \int_{-\infty}^{\infty} e^{i\omega t}\{ d\tilde{Z}_0(\omega) + \sum_{m=1}^{M} [\cos(m\theta) d\tilde{Z}_m^A(\omega) \\ + \sin(m\theta) d\tilde{Z}_m^B(\omega)]\},\end{aligned} \tag{6.6}$$

where
$$d\tilde{Z}_m^A(\omega) = \sum_n P_{mn}(R) dZ_{mn}^A(\omega). \tag{6.7}$$

If, in addition, there is no correlation between different circumferential modes, the acoustic pressure spectrum is independent of circumferential location. Kerschen and Johnston (1981b) have shown that, in this case, to separate circumferential modes up to order M, the pressure spectrum needs to be measured at 2M circumferential locations, given by $\theta = \ell\pi/M$, $\ell = 0,1,2,3,\ldots,(2M-1)$.

Combination of instantaneous pressure transducer outputs then gives

$$\frac{1}{2M}\sum_{\ell=0}^{2M-1} p_{ac}(t,\theta_\ell) = \int_{-\infty}^{\infty} e^{i\omega t} d\tilde{Z}_0(\omega) = P_0(t) \qquad (6.8)$$

$$\frac{1}{M}\sum_{\ell=0}^{2M-1} p_{ac}(t,\theta_\ell)\cos\left(\frac{m\ell\pi}{M}\right) = \int_{-\infty}^{\infty} e^{i\omega t} dZ_0(\tilde{\omega}) = P_m^A(t),$$

$$m = 1,2,..,(M-1),$$

and

$$\frac{1}{2M}\sum_{\ell=0}^{M-1} p_{ac}(t,\theta_\ell)(-1)^\ell = \int_{-\infty}^{\infty} e^{i\omega t} d\tilde{Z}_M^A(\omega) = P_M^A(t).$$

The total power spectral density of all A (cosine) m-order modes is now given in terms of the individual modal spectral densities ϕ_{mn} by

$$\tilde{\phi}_m^A(\omega) = \sum_n P^2{}_{mn}(R)\phi_{mn}(\omega), \qquad (6.9)$$

with a similar expression for the B (sine) m-order modes. $\tilde{\phi}_m^A$ and $\tilde{\phi}_m^B$, which are in general the power spectral densities of $P_m^A(t)$ and $P_m^B(t)$ respectively, are in this case equal, and the overall spectral density of m-order modes $\tilde{\phi}_m$ becomes equal to $\frac{1}{2}(\tilde{\phi}_m^A + \tilde{\phi}_m^B) = \tilde{\phi}_m^A$.

When the acoustic pressure fluctuations occur in the presence of turbulent flow and the total pressure fluctuation is given by equation (6.3), the combinations of pressure transducer outputs corresponding to equations (6.8) are

$$
\left.
\begin{aligned}
p_0(t) &= \frac{1}{2M}\sum_{\ell=0}^{2M-1} p(t,\theta_\ell) = P_0(t) + \frac{1}{2M}\sum_{\ell=0}^{2M-1} p_h(t,\theta_\ell) \quad , \\
p_m(t) &= \frac{1}{M}\sum_{\ell=0}^{2M-1} p(t,\theta_\ell)\cos\left(\frac{m\ell\pi}{M}\right) \\
&= \overset{A}{P}_m(t) + \frac{1}{M}\sum_{\ell=0}^{2M-1} p_h(t,\theta_\ell)\cos\left(\frac{m\ell\pi}{M}\right), \\
&\qquad\qquad m = 1,2,\ldots,(M-1), \\
\text{and} \\
p_M(t) &= \frac{1}{2M}\sum_{\ell=0}^{2M-1} p(t,\theta_\ell)(-1)^\ell = \\
&= \overset{A}{P}_M(t) + \frac{1}{2M}\sum_{\ell=0}^{2M-1} p_h(t,\theta_\ell)(-1)^\ell .
\end{aligned}
\right| \qquad (6.10)
$$

The power spectral densities of the combinations of transducer outputs $p_m(t)$ appearing on the L.H.S. of these equations will therefore include a turbulence contribution in addition to the acoustic modal power spectral density of $P_m(t)$. Kerschen and Johnston's result is that the power spectral densities of these combined transducer signals of equation (6.10) are

$$
\left.
\begin{aligned}
&\tilde{\phi}_0(\omega) + \frac{1}{2M}\phi_h(\omega), \\
&\overset{\sim A}{\phi}_m(\omega) + \frac{1}{M}\phi_h(\omega), \\
&\text{and} \\
&\overset{\sim A}{\phi}_M(\omega) + \frac{1}{2M}\phi_h(\omega),
\end{aligned}
\right| \qquad (6.11)
$$

respectively, where $\phi_h(\omega)$ is the power spectral density of the turbulence pressure fluctuations at the measuring station (and assumed to be independent of θ), provided that the turbulence and acoustic pressures are uncorrelated and provided there is negligible correlation between the hydrodynamic pressure fluctuations themselves at different circumferential locations.

Thus, for the procedure to yield accurate measurements of the acoustic modal spectra, it is necessary that, in general,

$$\tilde{\phi}^{A}_{m}(\omega) >> \frac{1}{M}\,\phi_h(\omega), \qquad (6.12a)$$

and for the order zero and M modes

$$\tilde{\phi}^{A}_{m}(\omega) >> \frac{1}{2M}\,\phi_h(\omega). \qquad (6.12b)$$

In the present work, four pressure transducers (1/4" Brüel and Kjaer microphones) spaced at 90° intervals have been used, and therefore modes of order up to (2,0) can be separated.

With M = 2, the signal combination corresponding to equation (6.10) are

$$p_0(t) = \frac{1}{4}[p(t,0) + p(t,\pi/2) + p(t,\pi) + p(t,3\pi/2)], \qquad (6.13a)$$

$$p_1(t) = \frac{1}{2}[p(t,0) - p(t,\pi)], \qquad (6.13b)$$

and

$$p_2(t) = \frac{1}{4}[p(t,0) - p(t,\pi/2) + p(t,\pi) - p(t,3\pi/2)]. \qquad (6.13c)$$

At frequencies below the cut-off frequencies of the (0,1), (3,0) and (6,0) modes respectively the spectra of $p_0(t)$, $p_1(t)$ and $p_2(t)$ will be

$$\left.\begin{array}{l} \phi_{0,0} + \frac{1}{4}\phi_h, \\ \phi_{1,0} + \frac{1}{2}\phi_h, \\ \text{and} \\ \phi_{2,0} + \frac{1}{4}\phi_h. \end{array}\right| \qquad (6.14)$$

Providing that the assumptions made in deriving equations (6.10) are valid and the inequality (6.12) is fulfilled, the power spectral densities of the (0,0), (1,0) and (2,0) acoustic duct modes, $\phi_{00}(\omega)$, $\phi_{10}(\omega)$ and $\phi_{20}(\omega)$ should therefor be obtained by taking the spectra of the functions defined by equations (6.13).

The various assumptions made in deriving these results will now be listed and discussed.

(a) The pipe is terminated anechoically, so that only downstream propagating sound waves are present.
Previous work on the present flow rig indicates that this condition is well approximated as a result of the action of the sonic choke at the downstream end of the pipe.

(b) Acoustic and turbulent pressure fluctuations are uncorrelated.

This assumption has previously been made by Goff (1954), Bolleter and Chanaud (1971), Karvelis (1975) and Norton (1979), all of whom used cross correlation techniques to separate acoustic and turbulent components of the wall pressure fluctuations, and Kerschen and Johnston (1981a). Kerschen and Johnston argue that acoustic pressures will be uncorrelated with the local hydrodynamic pressure fluctuations if the measuring station is far away from the region of flow separation where the acoustic pressures are generated. Karvelis (1975) concluded that the interaction between turbulent and acoustic pressure fluctuations is of the second order since

(i) their length and time scales are not of the same order of magnitude, and

(ii) the turbulent pressure fluctuations form an exponentially decaying random field convected at a large fraction of the mean velocity, whereas the acoustic pressure fluctuations propagate at the local speed of the sound.

(c) Circumferential correlation of turbulent pressure fluctuations is negligible for the transducer spacings used.

Correlation between the hydrodynamic fluctuations at different circumferential locations could be significant at very low frequencies. However, the lateral narrow-band correlation coefficient for the turbulent pressure fluctuations is typically $e^{-0.7\omega\eta/U_c}$ (η = lateral separation distance) = $e^{-0.7\theta He/M_o}$, where Helmholtz number He = $\omega a/c$ (i.e. Ω of Chapter 2). For M_o = 0.5, He = 1.84 (corresponding to the cut-off frequency of the (1,0) mode) and $\theta = \pi/2$, the correlation coefficient is 0.003, indicating that for present purposes this correlation can be ignored.

(d) Different higher order acoustic modes are not correlated. Kerschen and Johnston (1981a) show that the acoustic pressure spectrum will be independent of circumferential position only if the various acoustic modes are uncorrelated. Invariance of the spectrum with circumferential location therefore represents strong evidence of the absence of such correlation. All checks on circumferential uniformity in the present work lead to the conclusion that this inter-mode correlation is negligible.

Typical results are shown in Figures 6.2(a) and (b) of spectra at four circumferential locations, $\theta = 0, \pi/2, \pi, 3\pi/2$, at positions upstream and downstream of the orifice plate D_0 = 0.76 with choke D_C = 0.86. The spectra clearly have a strong acoustic content, as indicated by the sharp rises at frequencies corresponding to various higher order acoustic modes, and in each set the p' values obtained by integration agree to within less than 2% and the four spectra are virtually identical.

In addition, by similar arguments to those in (b) above, since the group velocity of the higher order modes is always less than the speed of sound, plane waves and higher order modes can be expected to be uncorrelated (Norton, 1979).

(e) Acoustic pressure fluctuations are large compared with hydrodynamic fluctuations.

If assumptions (b), (c) and (d) are valid, the spectra of $p_0(t)$, $p_1(t)$ and $p_2(t)$ are given by (6.14). In the present work, the inequalities (6.12a) and (6.12b) are satisfied in some regions of the flow but not others; details will be given later in discussion of experimental results.

The experimental results obtained in the present work will now be discussed.

Modal separation measurements have been made with orifice sizes D_0 = 0.62 to 0.83 and flow speed with D_C = 0.58 to 0.86 (refer to Table 6.3), embracing the region, $-22.75 \leq X \leq 47$ (at small intervals (18mm) in the separated-flow region and at a larger interval away from it). For FFT analysis with a frequency range up to 10 kHz, the analogue-recorded data were collected for a total time of 5.6 seconds. The spectra obtained by FFT were averaged over a band width of 39 Hz. For

Table 6.3

Choke and orifice combinations for modal spectra measurements

D_C	D_O			
	0.62	0.69	0.76	0.83
0.58*			✓	
0.72			✓	
0.80			✓	
0.86	✓	✓	✓	✓

*upstream only

each measuring station, the overall spectrum was also taken using the Hewlett-Packard Spectrum analyser with at least one circumferential location and occasionally checked for all four microphones spaced at 90° intervals. These direct spectral measurements were made with a maximum frequency range of 25 kHz and a band-width of 150 Hz, with a 'Hanning' passband window; the overall spectrum was averaged for at least 128 sets of data (each set consisting of 1024 samples). Comparisons were also made of the spectrum obtained by FFT of the tape-recorded signal and that obtained by feeding the same signal directly to the HP spectrum analyser set to a 10 kHz span. The spectra so obtained always agreed to within less than ± 0.5 dB.

For these tests it was only possible to mount the instrumentation section carrying all four microphones at a fixed position about 76 pipe diameters from the inlet bellmouth.

The pipe section carrying the orifice plate on the sleeve was therefore shifted, upstream and downstream, in relation to the microphone section. A minimum pipe length of 56 pipe diameters upstream of orifice was always maintained but in cases of measurements upstream and downstream, close to the orifice, a longer upstream length (~ 76 pipe diameter) was used. However, there was no similar constraint on mounting the microphone section with only two microphones (allowing separation of the (1,0) mode) installed. Therefore a few checks were made, by comparing both wall pressure spectra and modal spectra for the (1,0) mode, obtained with two different combinations of upstream and downstream lengths. The comparison was made at two locations downstream of the orifice plate, X = 13.2 and 19.2, for D_0 = 0.76, D_C = 0.86; no effect of the length changes could be detected.

Matching of microphones was repeatedly checked by measuring spectra of $p_1(t)$ (which requires only two microphones) from both available pairs of microphones. Virtually identical results could always be produced in this way.

The variation with X of the overall wall pressure spectrum and the spectra obtained by analysis of the $p_0(t)$, $p_1(t)$, and $p_2(t)$ signals corresponding to the combinations given by equation (6.13), for the case of flow with D_0 = 0.76, D_C = 0.86, is shown in Figures 6.28 and 6.29. Spectra at locations upstream of the orifice are given in Figure 6.28 and those downstream in Figure 6.29. Although measurements were made at all positions given in Table 6.3, only a selection of results, which adequately represent the variation with X which occurs, is presented. Furthermore, results are given for only one orifice/choke combination, as an exactly similar variation is observed for all other combinations, listed in Table 6.3, which were tested.

In the discussion of modal separation procedures in Section 6.4.1, discussion of assumption (e), which has to be satisfied if the acoustic modal spectral densities themselves are to be measured accurately, was left until this point. It will be seen that, while, in the present work, the inequalities (6.12a) and (6.12b) are not always satisfied, spectra of the $p_0(t)$, $p_1(t)$ and $p_2(t)$ signals, even in those cases, may still yield useful information about relative turbulence and acoustic levels.

The spectra in zone 1 all have the same character as that for X = -1.93 which is given in Figure 6.28b. Peaks corresponding to the cut-off frequencies of the acoustic modes are very prominent, indicating that, in this case, the inequalities (6.12a,b) are generally satisfied. Coincidence of the $p_0(t)$ and overall spectra shows that this is so at very low frequencies; but the divergence of the two as frequency increases indicates that both turbulence pressures and acoustic plane waves then make significant contribution to the overall spectrum. A level difference of 3dB between the $p_1(t)$ and $p_2(t)$ spectra below the (1,0) mode cut-off frequency is in accord with hydrodynamic contribution of $\phi_h/2$ and $\phi_h/4$ respectively to these spectra, as predicted by (6.14). Comparison of the spectra of $p_1(t)$ and $p_2(t)$ with the overall value indicates that the (1,0) and (2,0) modes dominate the spectrum near their cut-off frequencies but that at other frequencies

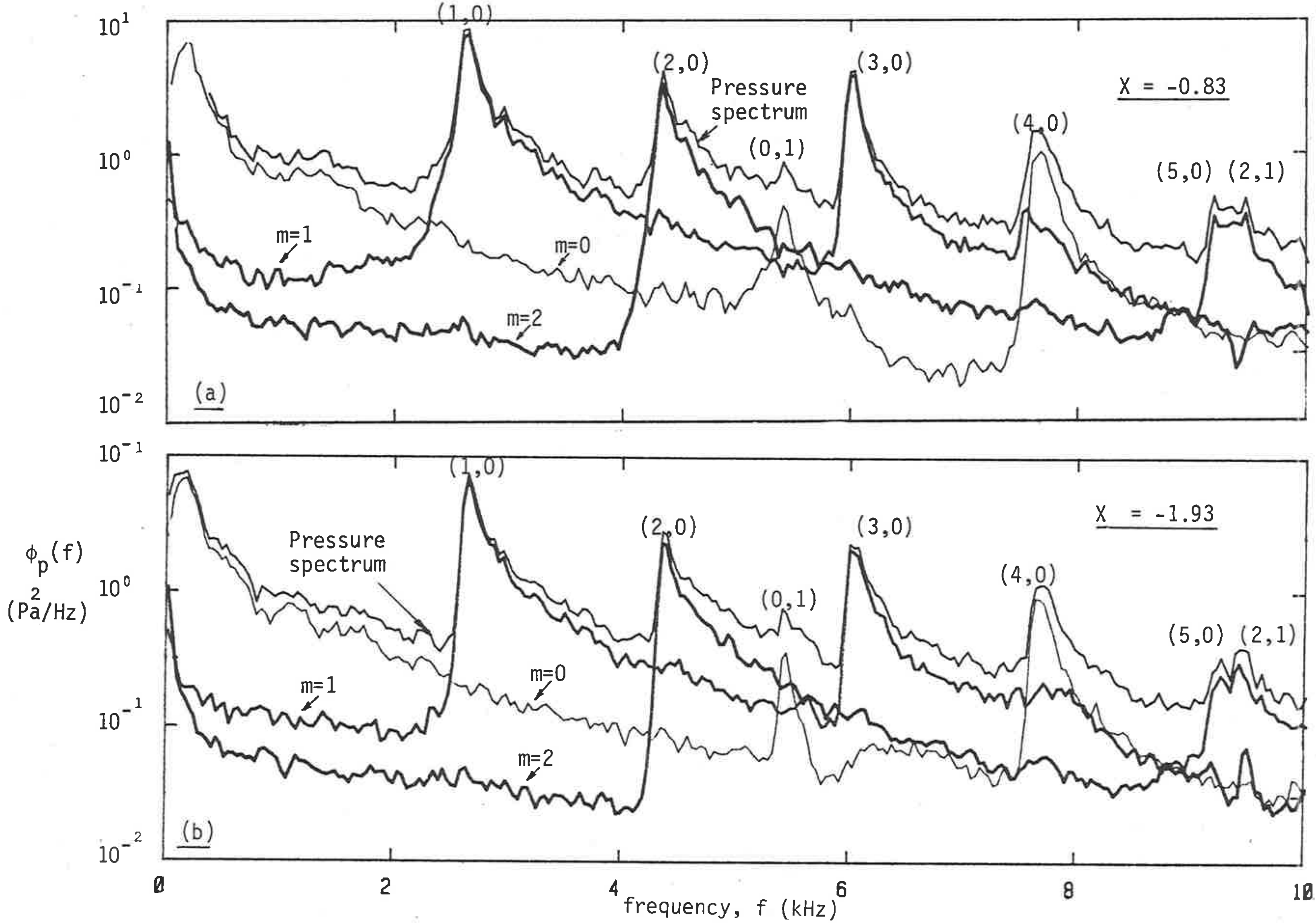

FIGURE 6.28 : MODAL SPECTRA, D_c = 0.86, D_o = 0.76, M_I = 0.35, $\overline{J}$ = 0.47

more than one acoustic mode makes a significant contribution to the overall level.

Similar remarks apply to Figure 6.28a for X = -0.83 in the separated flow region in zone 2 upstream of the orifice.

Dominance of the acoustic pressures in zones 1 and 2 is in accord with the earlier discussion (Section 6.2) that in these zones the acoustic pressure levels are determined by the high mean flow dynamic pressure in the separated jet downstream of the orifice q_J while the hydrodynamic pressure fluctuations are determined by the relatively low local dynamic pressure q_I.

Spectra for X = 0.79 and 1.31 in the separated flow region, zone 3, are shown in Figures 6.29a and b. In both cases, although there is some evidence of acoustic mode peaks, the spectra are clearly dominated by hydrodynamic pressure fluctuations: the $p_1(t)$ spectrum is about 3dB below and both the $p_0(t)$ and $p_2(t)$ about 6dB below the overall spectrum over almost the whole frequency range, implying that the $\phi_h/2$ and $\phi_h/4$ terms of (6.14) are dominant. The only evidence of identifiable acoustic modes of significant spectral level is at low frequencies where the $p_0(t)$ spectrum rises above that of $p_2(t)$: the two figures show growth in the level of the (0,0) plane wave mode extending to higher frequencies as X increases.

Figure 6.29c for X = 1.89 just downstream of flow reattachment in zone 4 shows that hydrodynamic pressure fluctuations are still generally dominant, although the influence of the (0,0) mode now extends to still higher frequencies than in zone 3.

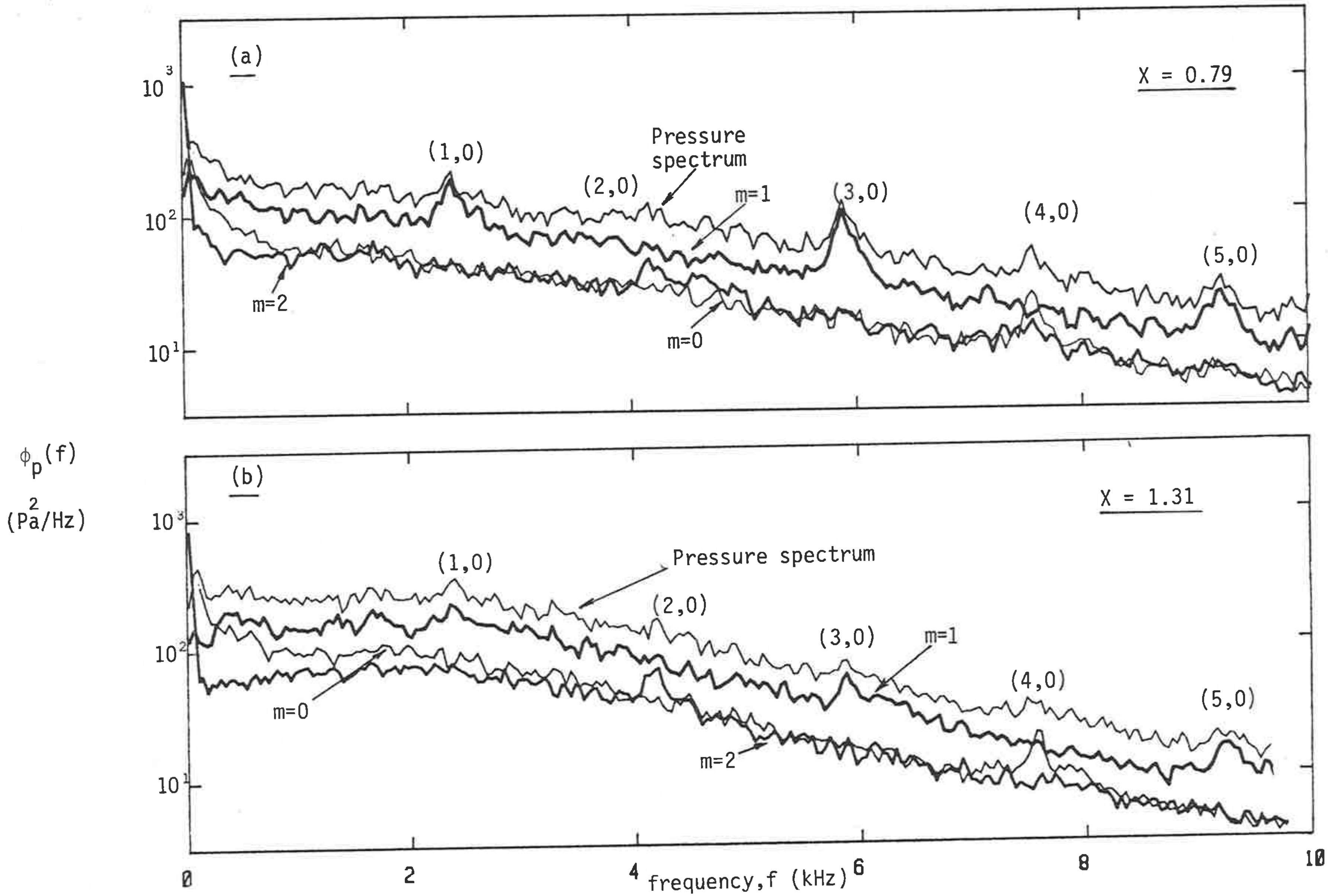

FIGURE 6.29 : MODAL SPECTRA, D_c = 0.86, D_o = 0.76, M_I = 0.35, J = 0.47

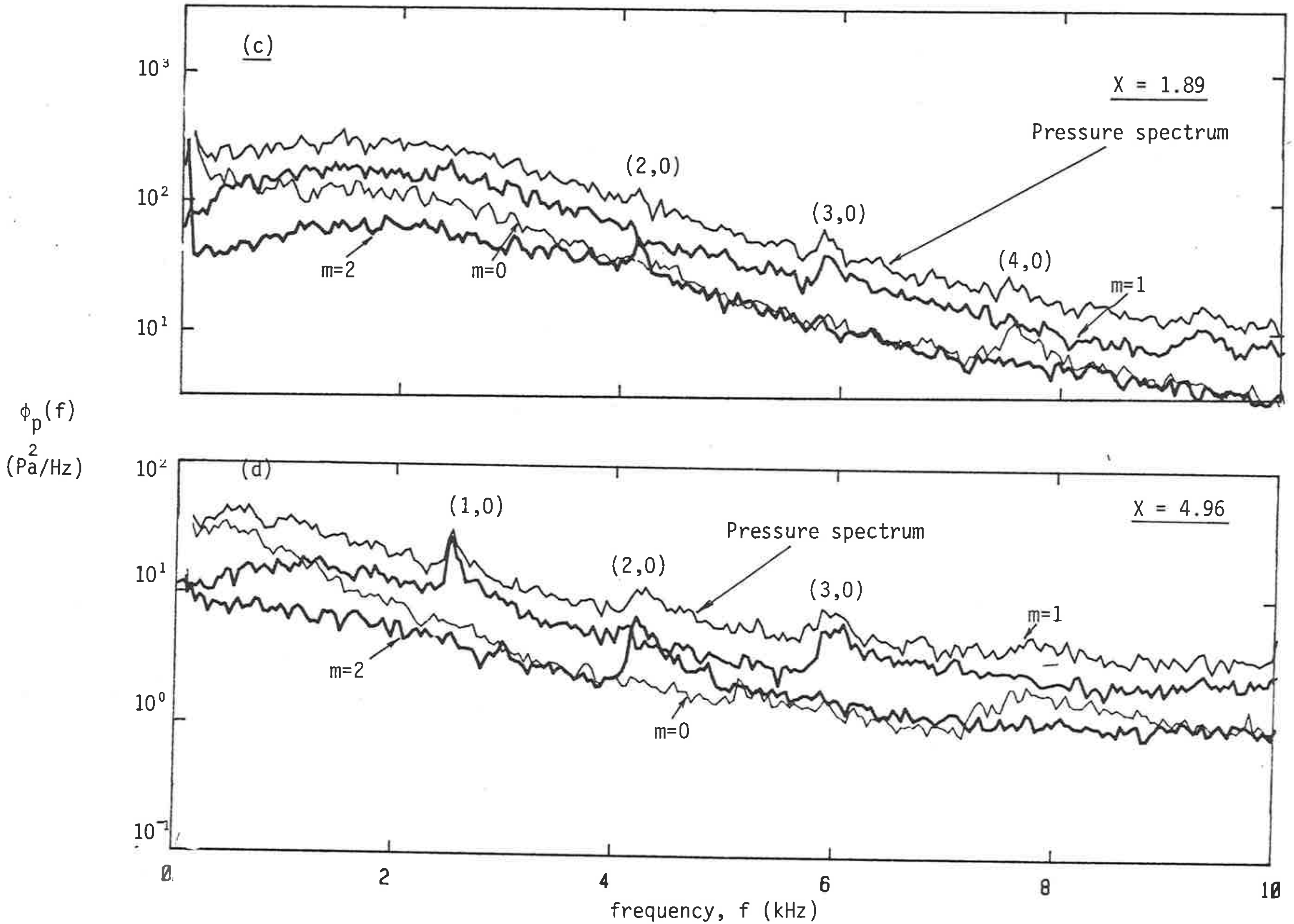

FIGURE 6.29 : MODAL SPECTRA, D_c = 0.86, D_o = 0.76, M_I = 0.35, $\overline{J}$ = 0.47

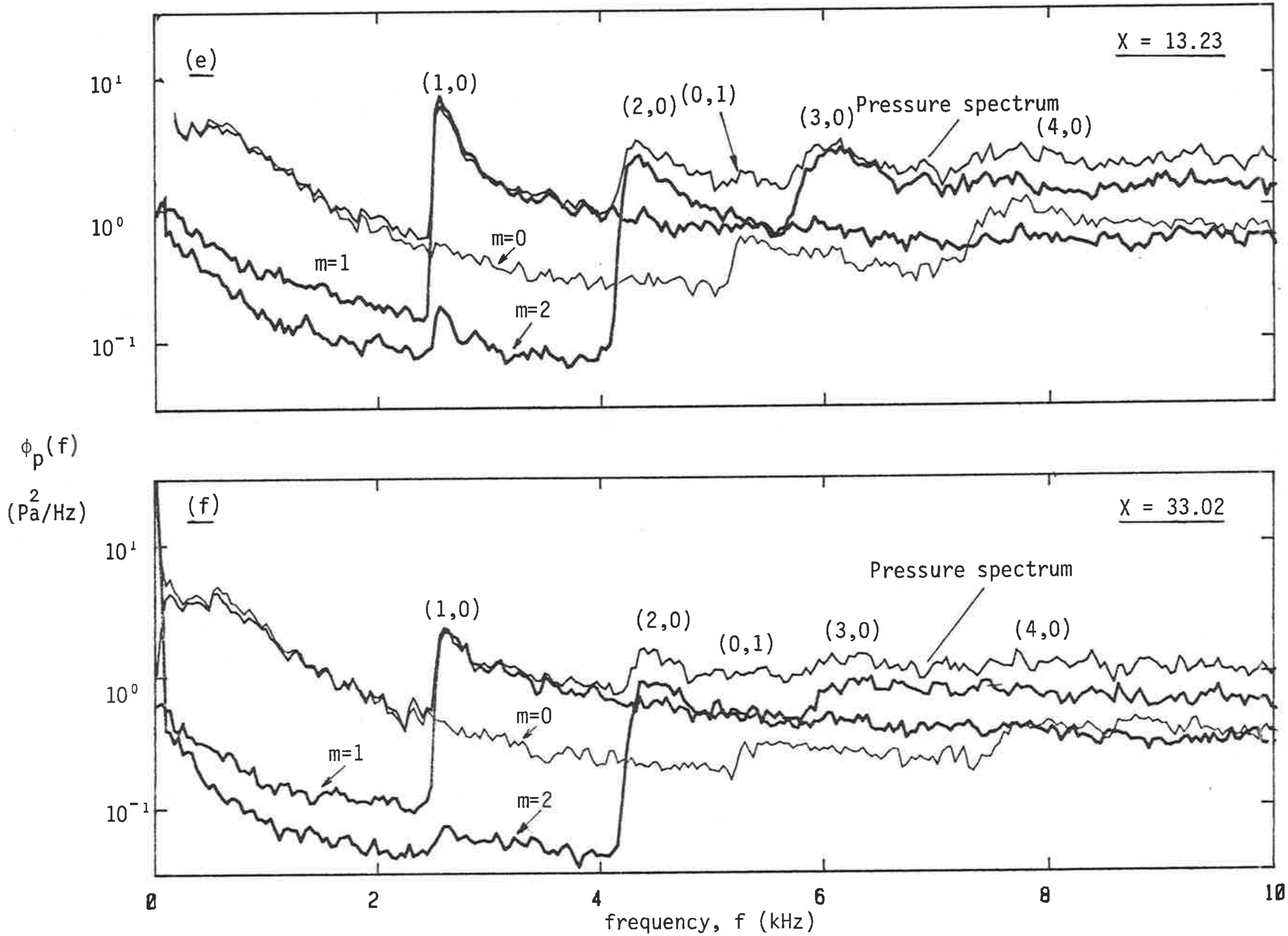

FIGURE 6.29 : MODAL SPECTRA, D_c = 0.86, D_o = 0.76, M_I = 0.35, $\bar{J}$ = 0.47

At X = 4.96 (Figure 6.29d), acoustic spectral peaks are becoming more clearly defined. Acoustic contributions have become dominant by X ~ 9 and remain so at all greater X. As can be seen in Figures 6.29e and f, the acoustic levels of the (0,0) and (1,0) modes are essentially equal to the overall levels at all frequencies up to that at which the (2,0) mode becomes propagational. At frequencies above the cut-off of the (2,0) mode acoustic pressures are still dominant, but there are significant contributions to the overall spectral level from both (1,0) and (2,0) modes.

So far the discussion has been confined to frequencies at which only (0,0), (1,0) and (2,0) modes can be separated by four pressure transducers. The $p_0(t)$ combination does not eliminate (0,n) modes and the (0,1) mode appears in all the spectra presented. It should however eliminate all modes with m > 0; the appearance of what appears to be a (4,0) mode peak in its spectrum seems to indicate (since other indications are that the four transducers are accurately matched) that for some reason the orientation of the nodal diameters for this mode is not completely random in this flow. The $p_1(t)$ combination should eliminate all modes for which m is even (including m = 0), but all modes for m odd will appear; while the $p_2(t)$ signal should not contain contributions from any modes for which m is odd or a multiple of four. In one or two cases (e.g. Figure 6.29e) cancellation of the (1,0) contribution to the (2,0) spectrum is not perfect. Modal spectral level of modes of higher order than (2,0) can be determined, from the $p_0(t)$, $p_1(t)$ and $p_2(t)$ spectra, at their cut-off frequencies where the increment in spectral level can be positively identified. Use is made of this later in determining the attenuation of the various modes with X at their cut-off frequencies.

6.4.2 Acoustic mode identification

In the pressure spectra, higher order acoustic modes can generally be identified by the step increase in power spectral density which occurs at their cut-off frequencies. However, this becomes more difficult in the higher frequency region, as the modes become more closely spaced.

Resolution can be improved by making use of the phase differences (0° or 180°) in the pressure at two points on the pipe wall separated by 180°, which are characteristic of the various modes. These, together with the no-flow cut-off frequencies and with-flow cut-off frequencies for $M_e = 0.24$ are listed in Table 6.4. The relative phase of the pressure signals from two 1/4" Brüel and Kjaer microphones, mounted in the pipe wall at opposite ends of a pipe diameter, in narrow filter bands, is obtained from the HP spectrum analyser. The relative phase of the two signals is given by the analyser within ± 10 degrees. The basic display of the instrument is ± 200 degrees with cycling taking place nominally at ± 180 degrees; the 20 degrees of hysteresis minimizes the extent to which the display bounces between ± 180°. With the spectrum analyser being used in its two-channel mode, the number of samples in each set of data acquired drops from 1024 to 512 per channel; and consequently the signals were averaged over at least 200 sets.

Table 6.4

Phase difference for signals from two diametrically opposite microphones for various higher order modes and their cut-off frequencies (for D_c = 0.86, D_0 = 0.76 ; upstream propagation)

Mode	Phase Difference	No-flow cut-off frequency, $(f_{co})_{NF}$ (kHz)	$\sqrt{1-M_e^2}\ (f_{co})_{NF}$ (for M_e = 0.24)
(1,0)	✓	2.772	2.691
(2,0)	-	4.598	4.464
(0,1)	-	5.769	5.600
(3,0)	✓	6.325	6.140
(4,0)	-	8.006	7.772
(1,1)	✓	8.027	7.793
(5,0)	✓	9.659	9.377
(2,1)	-	10.097	9.802
(0,2)	-	10.563	10.254
(6,0)	-	11.924	11.575
(3,1)	✓	12.068	11.715
(1,2)	✓	12.850	12.474
(7,0)	✓	12.915	12.537
(4,1)	-	13.976	13.567
(8,0)	-	14.525	14.100
(2,2)	-	15.010	14.571
(0,3)	-	15.317	14.869
(5,1)	✓	15.839	15.376
(9,0)	✓	16.127	15.656
(3,2)	✓	17.082	16.583
(1,3)	✓	17.625	17.110
(6,1)	-	17.668	17.152
(10,0)	-	17.722	17.204
(4,2)	-	19.094	18.536
(11,0)	✓	19.312	18.748
(7,1)	✓	19.471	18.902
(2,3)	-	19.829	19.249
(0,4)	-	20.060	19.474
(12,0)	-	20.896	20.285
(5,2)	✓	21.059	20.444
(8,1)	-	21.252	20.631
(3,3)	✓	21.960	21.318
(1,4)	✓	22.378	21.724
(13,0)	✓	22.476	21.819
(6,2)	-	22.987	22.315
(9,1)	✓	23.016	22.343
(11,3)	-	24.035	23.333
(14,0)	-	24.052	23.349
(2,4)	-	24.612	23.893
(10,1)	-	24.764	24.040
(0,5)	-	24.798	24.073
(7,2)	✓	24.886	24.159
(15,0)	✓	25.625	24.876

Phase measurements were made with the orifice $D_0 = 0.76$, and choke $D_C = 0.86$ at X = -2.01, -12.8, 19.3 and 29.2, for a frequency span of 25 kHz, at a bandwidth of 150 kHz. For a better resolution measurements were also made for a frequency span of 10 kHz, which allows the bandwidth to be reduced by a factor of 2.5 to 60 Hz. Results for X = -2.01 are shown as an example in Figures 6.30 and 6.31. These show that modal cut-off frequencies can still be determined from phase changes when the modes are scarcely discernible in the pressure spectrum itself.*

6.4.3 Attenuation of Higher Order Modes

Even in a hard-walled pipe attenuation, of acoustic waves propagating inside a pipe, with streamwise distance will occur as a result of the effects of viscosity and heat conduction at the pipe wall.

If pipe wall vibrations are excited by the internal sound field, attenuation of acoustic waves will also occur due to sound energy transmitted through the pipe wall. Further increases in attenuation may be expected when a turbulent pipe flow is present, owing to the effects of convection and interaction of sound and turbulence. Convection is expected to result in greater attenuation for upstream than for downstream propagation.

In contrast to the propagation of plane waves, the higher order modes propagate with a group velocity less than sonic speed, by multiple reflections from the pipe wall, and for this reason one would expect the higher order modes to suffer greater attenuation than plane waves.

* However, cut-off frequencies of all modes can not be obtained from phase plots, but only those at which a change from 0 degree to 180 degrees or 180 degrees to 0 degree occurs (i.e. (1,0), (2,0), (3,0), (4,0), (5,0), (2,1), (3,1) etc. modes).

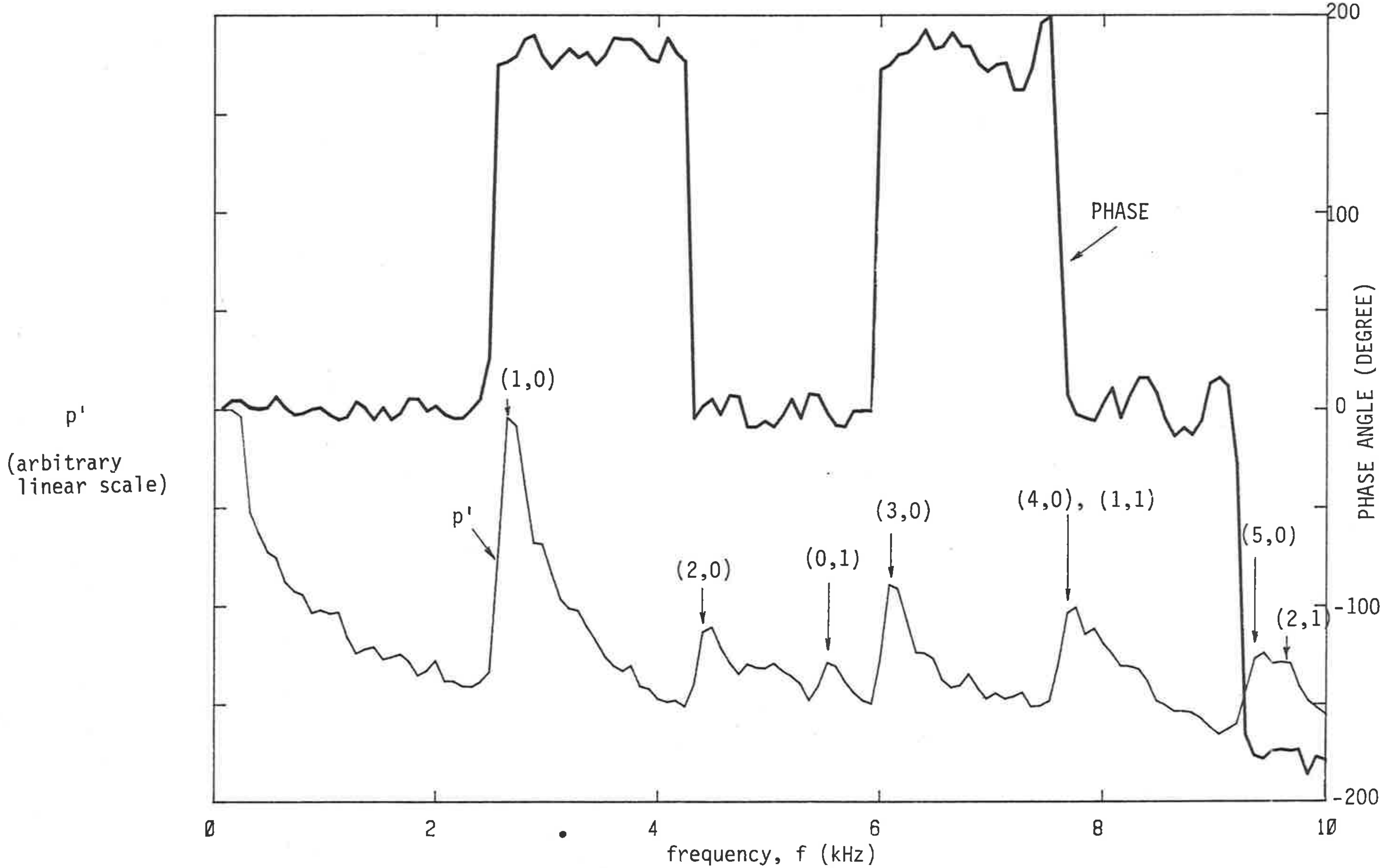

FIGURE 6.30 : WALL PRESSURE SPECTRUM AND PHASE RELATIONSHIP BETWEEN SIGNALS FROM TWO DIAMETRALLY OPPOSITE MICROPHONES (D_c = 0.86, D_o = 0.76, M_I = 0.35, $\overline{J}$ = 0.47, X = -2.01) BANDWIDTH 60 Hz

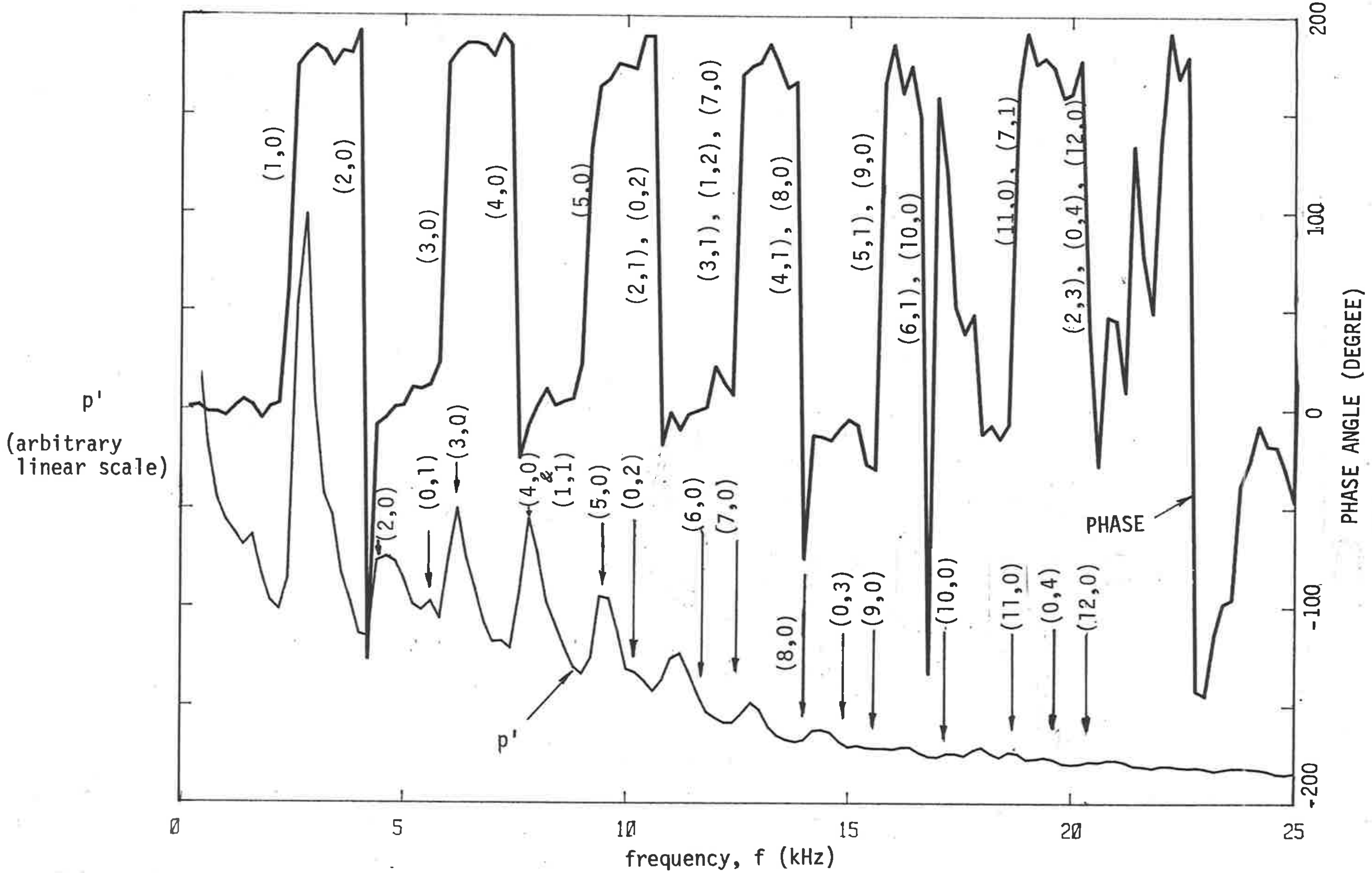

FIGURE 6.31 : WALL PRESSURE SPECTRUM AND PHASE RELATIONSHIP BETWEEN SIGNALS FROM TWO DIAMETRALLY OPPOSITE MICROPHONES (D_c = 0.86, D_o = 0.76, M_I = 0.35, $\bar{J}$ = 0.47, X = -2.01), BANDWIDTH 150 Hz

However, there is little systematic information available on attenuation of acoustic waves, and higher order modes in particular, in a hard-walled pipe carrying turbulent flow. Beatty (1950) has derived theoretical results for attenuation of higher order modes due to the effects of viscosity and heat conduction (by expressing them as small equivalent normal acoustic wall admittances), but in the absence of flow. Doak and Vaidya (1970) extend the small admittance analysis to the case of uniform mean flow, but no effects of turbulence are included. As far as viscous and thermal effects are concerned, these analyses indicate that the (0,n) (symmetric) modes will have the lowest attenuation rates of all higher order modes, and that attenuation rates will increase with both m and n.

Ingard and Singhal (1974) have derived an expression for the attenuation of plane waves in turbulent pipe flow. Their result is that the attenuation over a distance of X pipe diameters is given by

$$0.17\,\frac{M_0}{1 \pm M_0}.\,X \quad \text{dB.} \tag{6.15}$$

Positive and negative signs refer to downstream and upstream propagation respectively; so that the attenuation rate is higher for upstream propagation than downstream. They verified this expression, which is independent of frequency, by a series of tests at various flow Mach numbers. Their work also shows that, for frequencies typical of higher order modes, attenuation due to turbulent pipe flow will be greater than that due to viscous and thermal effects for all flow Mach numbers greater than about 0.1. However, the theoretical work by Crighton (1970) and further experimental work by Karvelis and Reethof (1974), which is discussed by Karvelis (1975) suggests that equation (6.15) may give an overestimate of the attenuation by factors as much as 10 at low Mach numbers.

In the present work the attenuation of higher order modes can be determined from modal spectra at various streamwise locations. The modal amplitude at cut-off is determined by subtracting the hydrodynamic pressure level immediately before cut-off from the peak value reached immediately after. Results for orifice plate $D_0 = 0.76$ with flow speed $D_C = 0.86$ are shown in Figure 6.32. All the modes attenuate rapidly in the reattachment and the recovery region up to $X \simeq 5$. Beyond that, the (m,0) mode is attenuated at a constant rate of about 0.2 dB per pipe diameter. The (0,n) mode for which no mean line is shown on the figure, appears to be attenuated at a slower rate, but, with the scatter in the data presented, this cannot be said with certainty. The effect of flow speed with $D_0 = 0.76$ is illustrated by Figures 6.33 and 6.34 and of orifice size with $D_C = 0.86$ by Figures 6.35 and 6.36. Results are shown for both upstream and downstream propagation. The figures indicate that all (m,0) modes are attenuated at about the same rate and that neither flow speed nor orifice size has any significant effect.

However, the attenuation rate, at distances well removed from the orifice, is significantly higher for upstream than for downstream propagation; the values are, respectively, about 0.3 and 0.2 dB/pipe diameter.

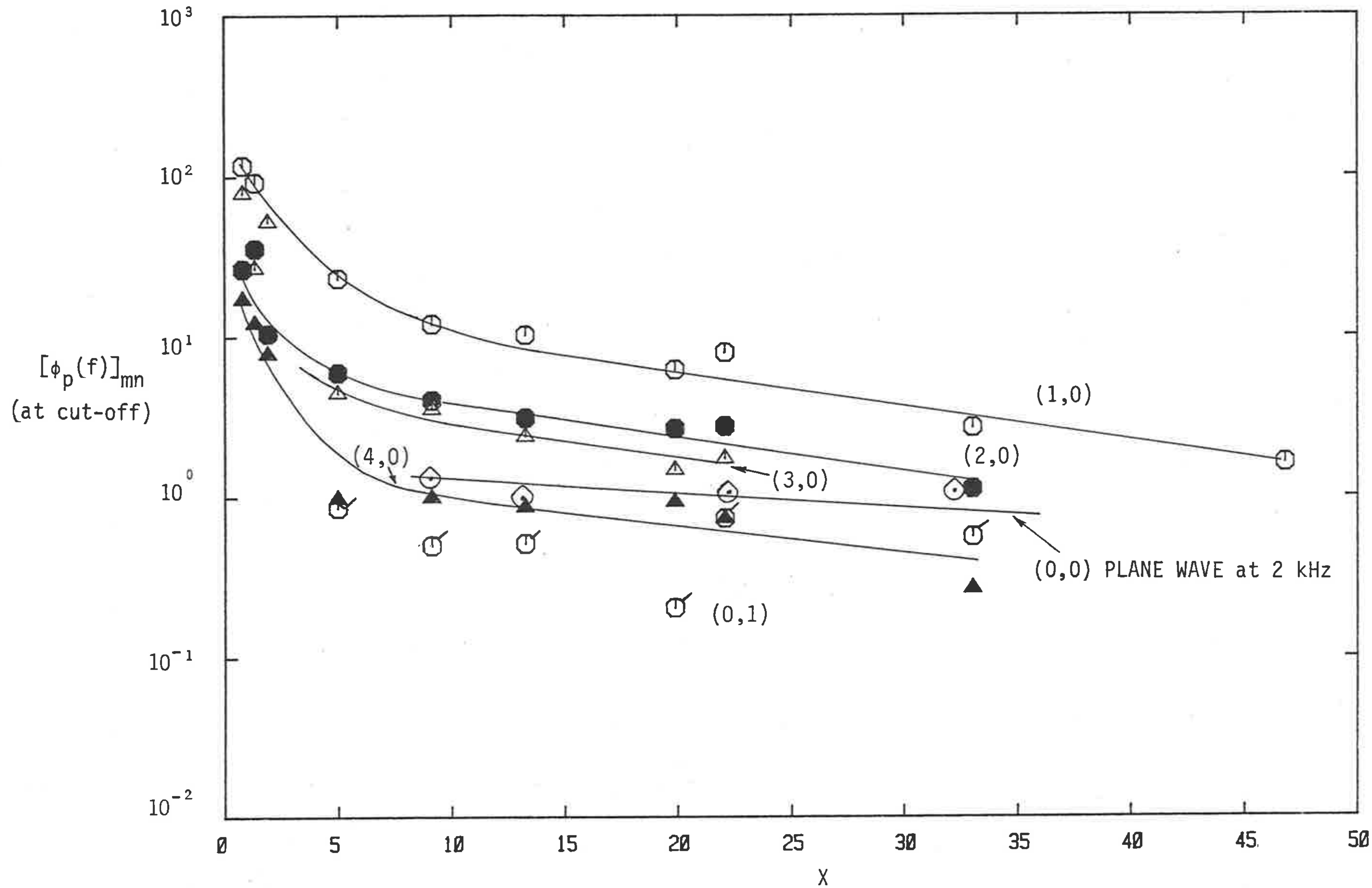

FIGURE 6.32 : CUT-OFF MODAL AMPLITUDE VARIATION WITH STREAMWISE DISTANCE, D_o = 0.76, D_c = 0.86, M_I = 0.35, $\bar{J}$ = 0.47

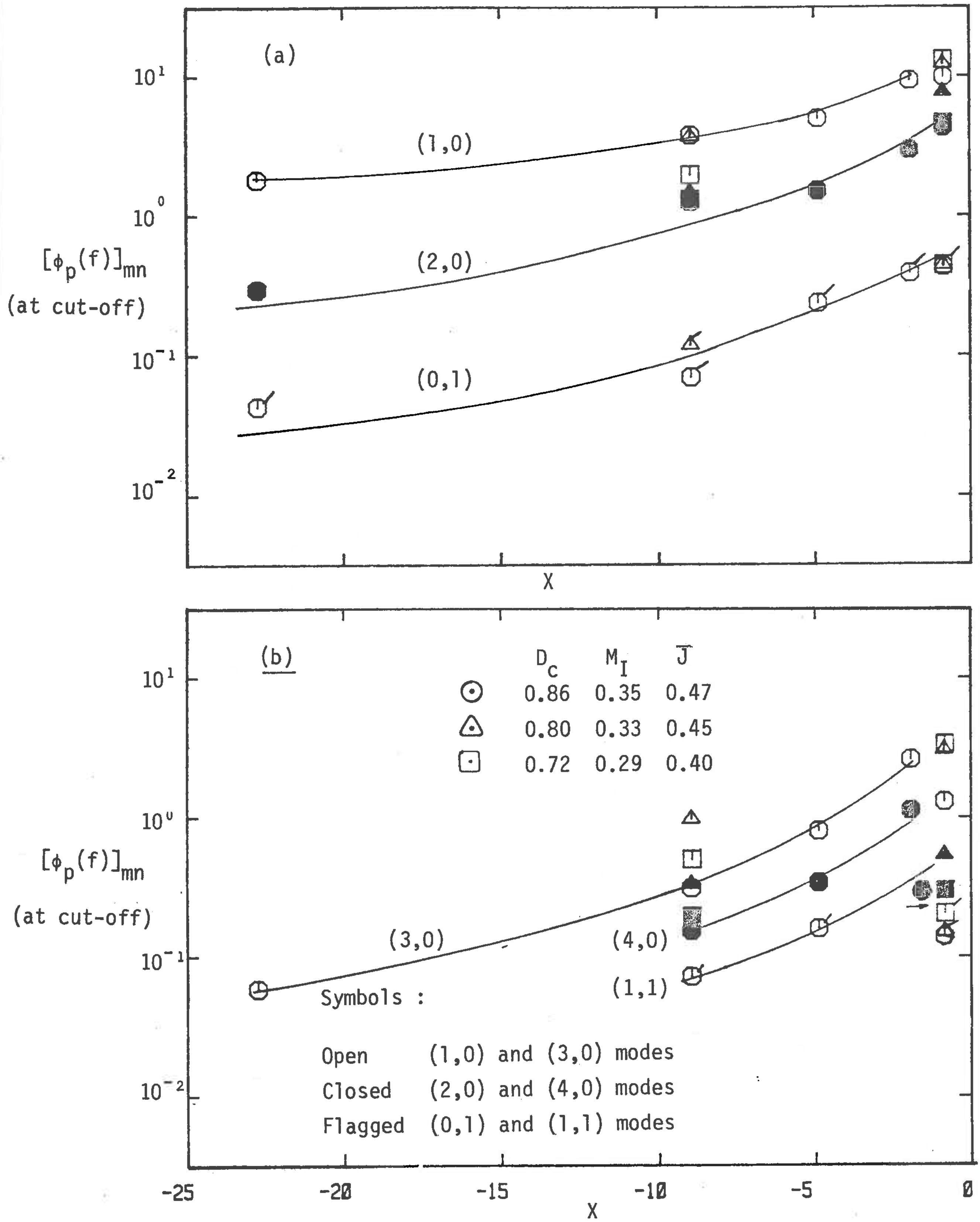

FIGURE 6.33 : EFFECT OF FLOW SPEED ON CUT-OFF MODAL AMPLITUDE VARIATION WITH STREAMWISE DISTANCE UPSTREAM OF ORIFICE PLATE, D_o = 0.76

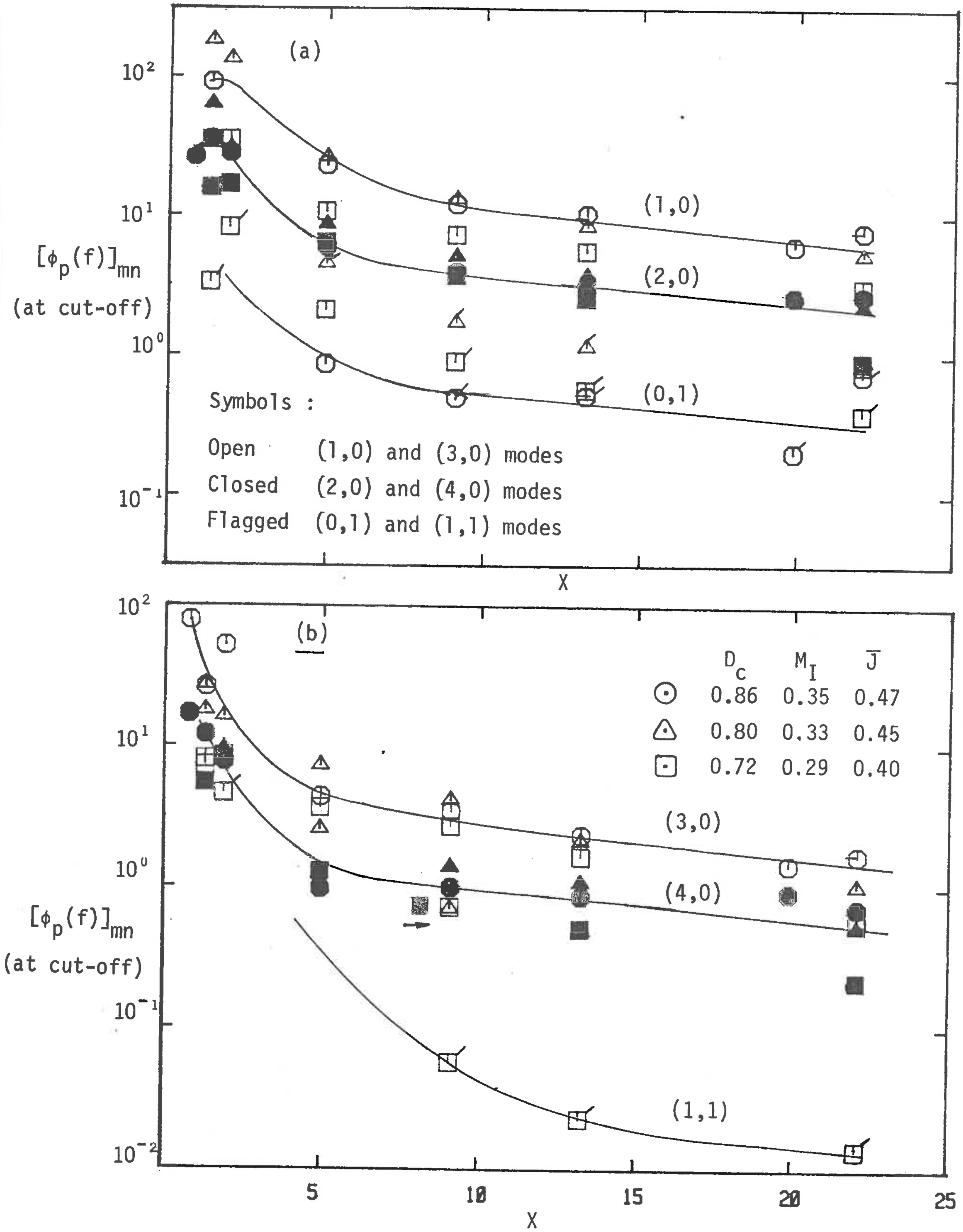

FIGURE 6.34 : EFFECT OF FLOW SPEED ON CUT-OFF MODAL AMPLITUDE VARIATION WITH STREAMWISE DISTANCE DOWNSTREAM OF ORIFICE PLATE, D_o = 0.76

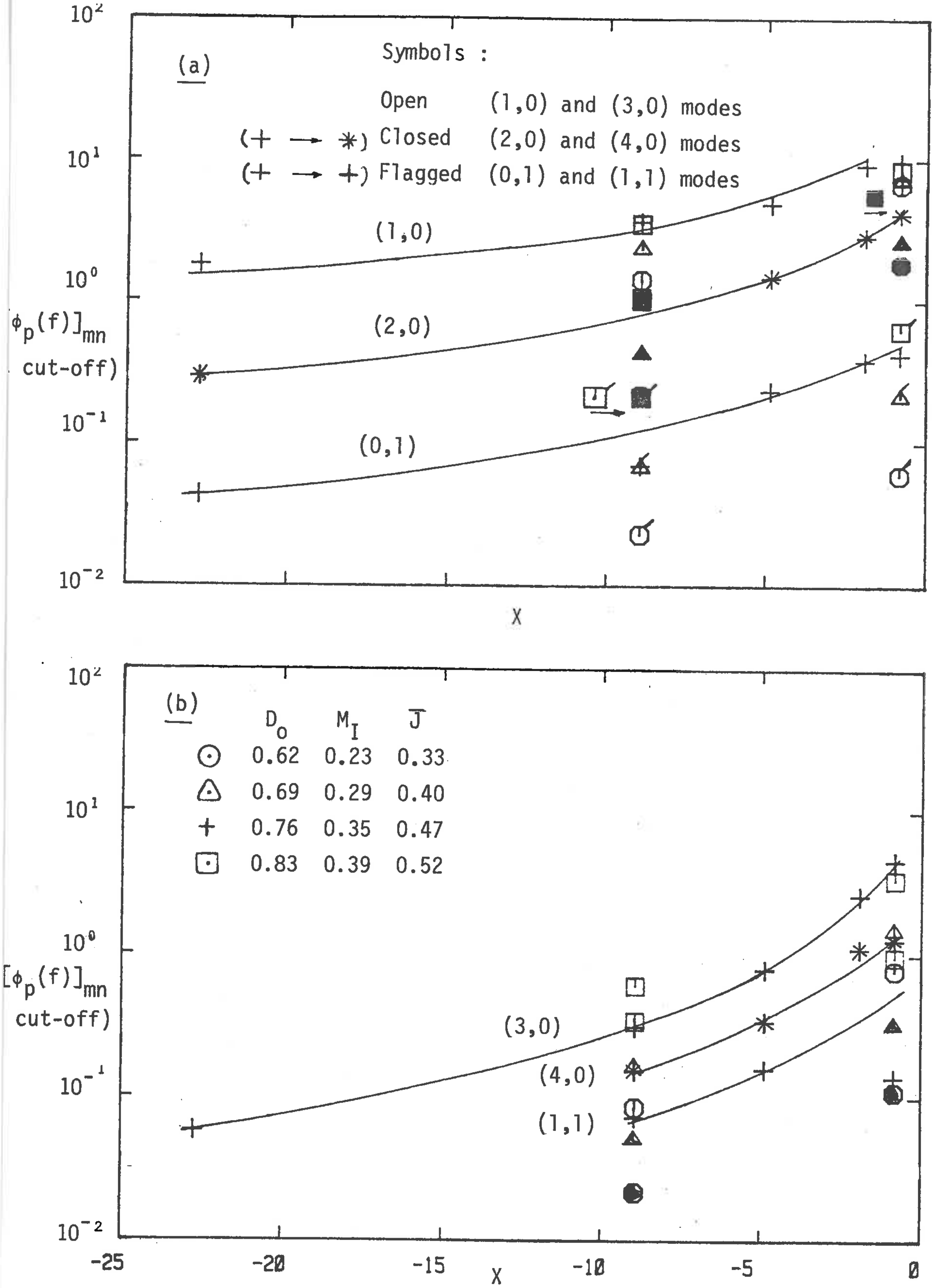

FIGURE 6.35 : EFFECT OF ORIFICE SIZE ON CUT-OFF MODAL AMPLITUDE VARIATION WITH STREAMWISE DISTANCE UPSTREAM OF ORIFICE PLATE, D_c = 0.86

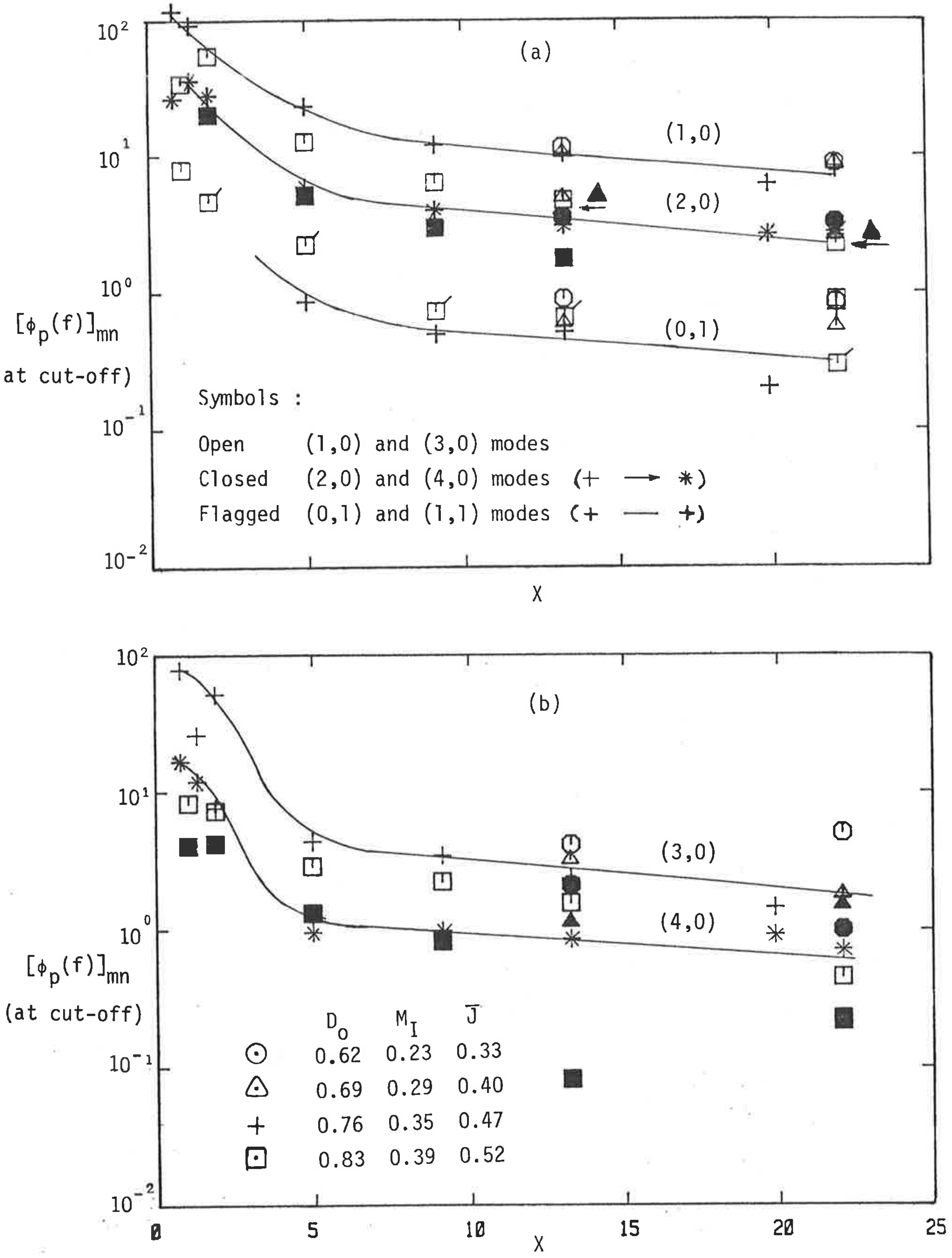

FIGURE 6.36 : EFFECT OF ORIFICE SIZE ON CUT-OFF MODAL AMPLITUDE VARIATION WITH STREAMWISE DISTANCE DOWNSTREAM OF ORIFICE PLATE, D_c = 0.86

6.4.4 Modal Cut-off Frequency

Cut-off frequencies f_{co} for the higher order acoustic modes, obtained from the modal spectra, for D_c = 0.58-0.86 and orifice plate D_0 = 0.76, and for D_c = 0.86 with all four orifice plates (D_0 = 0.62, 0.69, 0.76 and 0.83) are shown in Figure 6.37. The measurements cover the range $-22.75 \leqslant X \leqslant 46.8$. In Figure 6.37 the mean lines shown are for the D_c = 0.86, D_0 = 0.76, data only. [It should be noted that as a result of more detailed subsequent measurements, the data presented here, and their intepretation, differ somewhat from those presented by Bull and Agarwal (1984).]

For $X \gtrsim 3$, f_{co} is independent of X and independent of orifice size for all modes; it appears to depend only on D_c or M_E (and it should be noted that the centre-line Mach number M_0 is essentially equal to M_E for all $X \gtrsim 7$). The f_{co} are lower than the no flow values, $(f_{co})_{NF}$, and the difference increases with increasing M_E. For $0 \leqslant X \lesssim 3$, f_{co} decreases with X up to about $X = X_R$, where it reaches a minimum value. It then rises rapidly and within about half a pipe diameter reaches its constant downstream value.

For $X \lesssim -3$, f_{co} is constant but its value is higher than the corresponding downstream value for the same mode. In contrast to the downstream behaviour, f_{co} varies with orifice size for a given choke; its values appears to be determined by M_I. Closer to the orifice and in the separated-flow region, $-1.0 \lesssim X \leqslant 0$, a lower value of f_{co} is obtained.

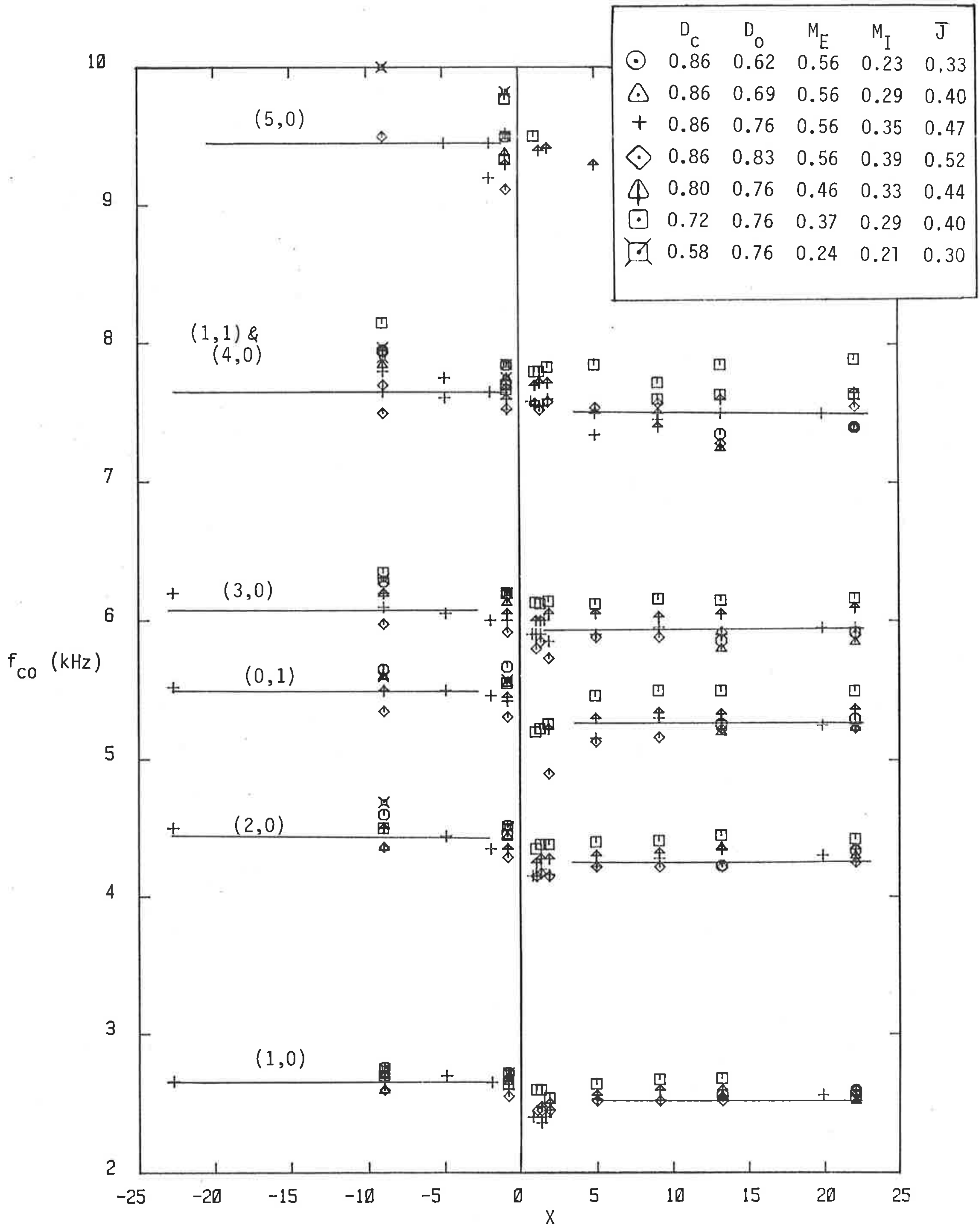

FIGURE 6.37 : VARIATION OF MODAL CUT-OFF FREQUENCIES WITH FLOW RATES AND STREAMWISE DISTANCE (Mean lines apply to D_c = 0.86, D_o = 0.76 data only)

The characteristics of f_{co} shown by Figure 6.37 are consistent with those indicated by other data which have been discussed in the context of the pressure spectra in Section 6.3.

In the idealised case of uniform flow in a pipe with Mach number M, the Helmholtz numbers ($\omega a/c$) at the cut-off of the acoustic modes are reduced below their corresponding no-flow values (κ_{mn} a) by a factor of $\sqrt{1-M^2}$; and the theoretical work presented in Chapter 2 shows that when the velocity distribution is that of fully-developed pipe flow the reduction factor becomes $\sqrt{1-M_e^2}$ where M_e is an effective Mach number, which is very closely given by the average Mach number over the velocity profile:

$$M_e = \frac{1}{R} \int_0^R M(r)dr \ . \qquad (6.16)$$

Numerical values of the ratio $A = M_e/M_0$ of M_e to the Mach number on the pipe centreline, obtained in Chapter 2 range between 0.90 and 0.91.

The experimental results which have been presented show that cut-off frequencies are reduced as flow Mach number increases, but it remains to relate the observed values quantitatively to identifiable flow parameters. On the basis of the foregoing, the Helmholtz number at cut-off of the (m,n)th mode should be given by

$$(\omega a/c_e) = (\kappa_{mn}a)\sqrt{1-M_e^2} \qquad (6.17)$$

where c_e is the speed of sound in the flow at the effective Mach number M_e.

For the flow in the present work, which is induced from a constant-condition reservoir (the atmosphere), the assumption of constant total temperature throughout gives

$$c_e = [\gamma RT_r/(1 + \frac{\gamma-1}{2} M_e^2)]^{1/2}$$

$$= c_r/(1 + \frac{\gamma-1}{2} M_e^2)^{1/2}. \qquad (6.18)$$

where c_r is the speed of sound under reservoir conditions. The cut-off frequencies can then be expressed as

$$(\omega a/c_r) = (\kappa_{mn}a)[(1-M_e^2)/(1 + \frac{\gamma-1}{2} M_e^2)]^{1/2}. (6.19)$$

Thus, if the value of the Helmholtz number $(\omega a/c_r)$ corresponding to a modal cut-off frequency is determined, the effective Mach number can be found by solving equation (6.19).

Values of $\omega a/c_r$ at cut-off for various acoustic modes at $X = 13.2$ in flows with $D_c = 0.86$ and $D_0 = 0.62$-0.83 are plotted against the theoretical no-flow values $(\kappa_{mn}a)$ in Figure 6.38. As previously indicated, the values are almost identical for all orifice sizes, and an almost identical plot is obtained for all downstream $X \gtrsim 3$. From the graph $\omega a/c_r = 0.91\ \kappa_{mn}a$ and equation (6.19) then gives $M_e = 0.39$. Figure 6.39 is a similar plot for the section $X = -8.96$ upstream of the orifice plate with $D_c = 0.86$ and $D_0 = 0.62$-0.83. It shows the variation of cut-off frequency with D_0, and a similar graph is obtained for all X.

M_e values derived from the experimental data, for various flow conditions, well upstream and downstream of the orifices, are shown in Table 6.5.

An example of the lower cut off frequencies obtained closer to the orifice is shown by Figure 6.40 for $X = -2.01$ with $D_c = 0.86$ and $D_0 = 0.76$: in this case $(\omega a/c_r) = 0.95\ (\kappa_{mn}a)$.

Table 6.5

Effective Mach Numbers, M_e, away from Disturbed-flow Region

Choke size D_C	Orifice size D_0	Downstream		Upstream	
		M_e	M_E	M_e	M_I
0.58	0.76	-	0.23	0.14	0.21
0.72	0.76	0.25	0.37	0.19	0.29
0.80	0.76	0.33	0.46	0.22	0.33
0.86	0.62	0.39	0.56	0.14	0.23
0.86	0.69	0.39	0.56	0.18	0.29
0.86	0.76	0.39	0.56	0.24	0.35
0.86	0.83	0.39	0.56	0.30	0.39

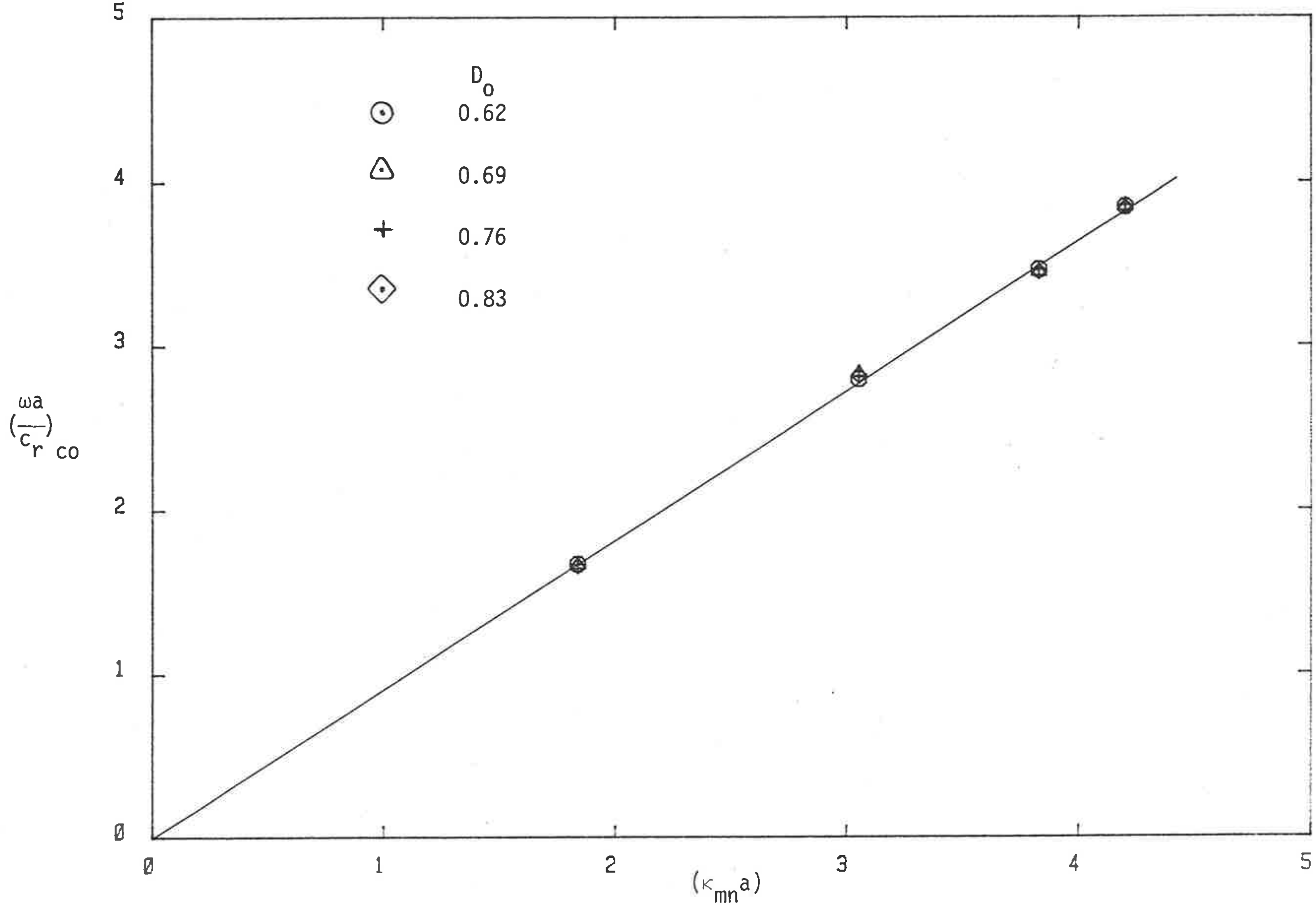

FIGURE 6.38 : MODAL CUT-OFF FREQUENCIES DOWNSTREAM OF THE ORIFICE X = 13.2 , D_c = 0.86

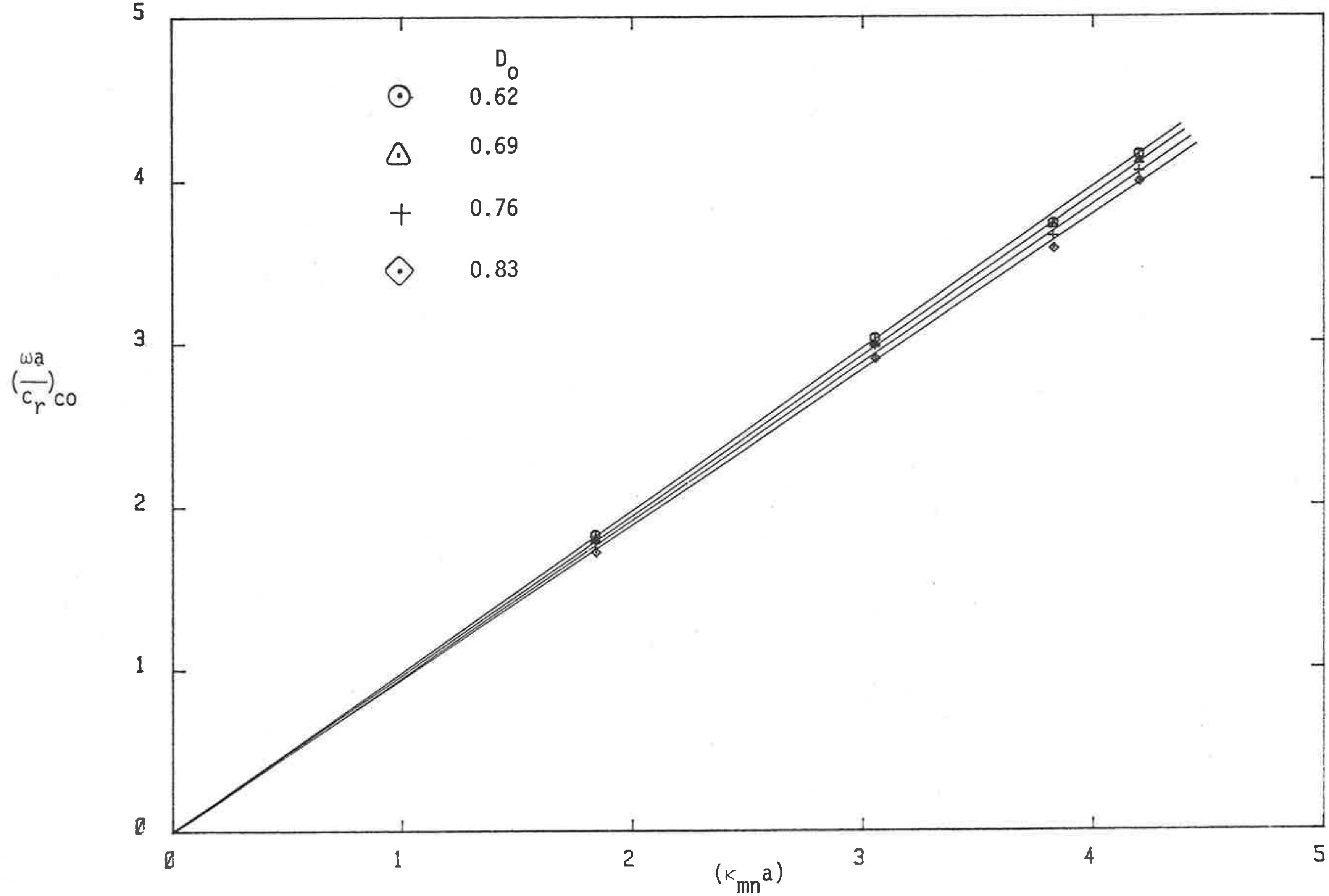

FIGURE 6.39 : MODAL CUT-OFF FREQUENCIES UPSTREAM OF THE ORIFICE, D_c = 0.86, X = -8.96

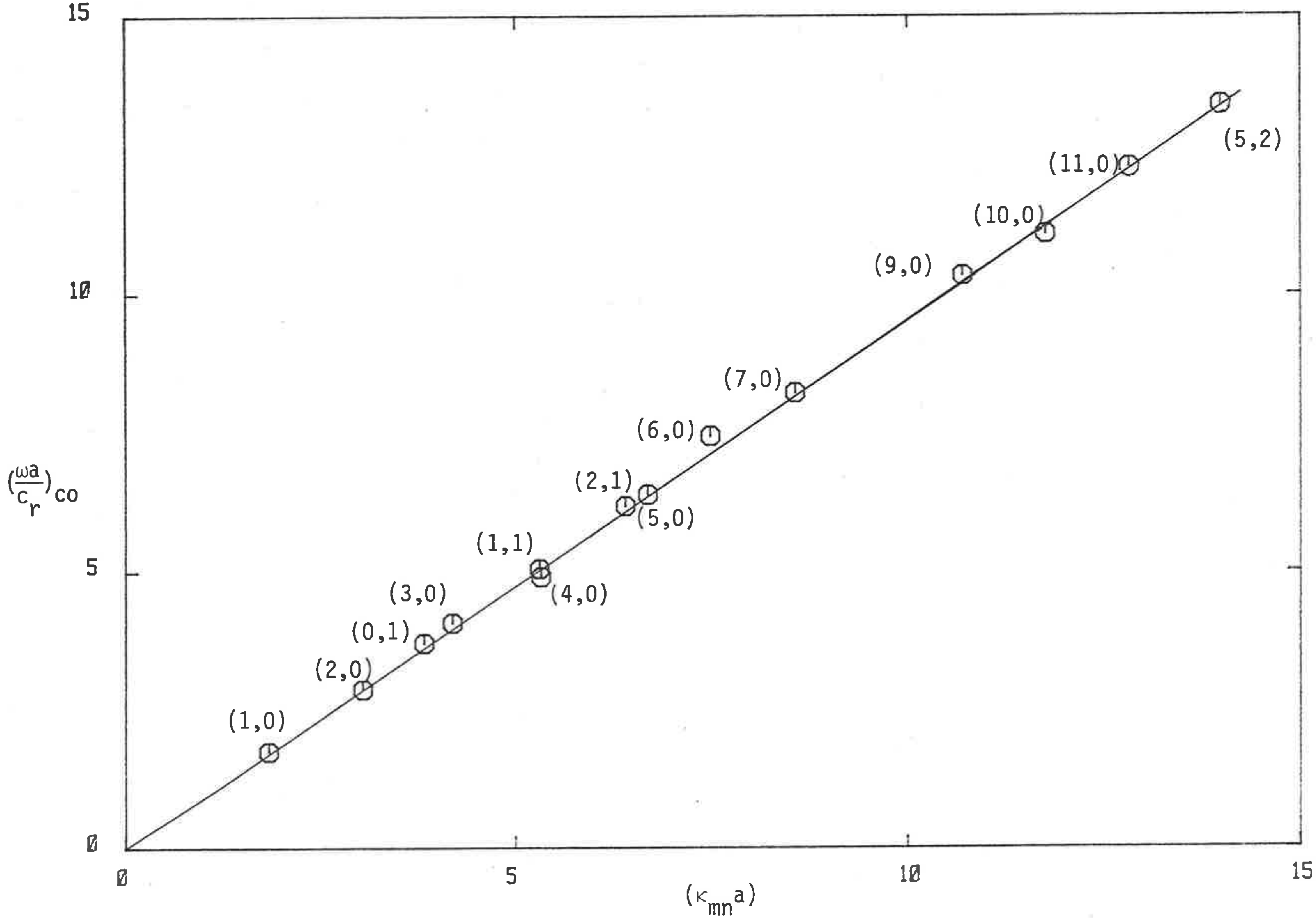

FIGURE 6.40 : MODAL CUT-OFF FREQUENCIES UPSTREAM OF THE ORIFICE FROM MODAL SPECTRA (PHASE MEASUREMENTS) AT X = -2.01, D_c = 0.86, D_o = 0.76, M_I = 0.35, $\bar{J}$ = 0.47

The effective Mach number M_e is plotted against M_I for upstream measurements and against M_E for downstream measurements in Figure 6.41. The figure shows that for both upstream and downstream data $A = M_e/M_I$ or M_e/M_E is about 0.7, in contrast to the theoretical value 0.90-0.91 for fully-developed turbulent pipe flow. Thus in the regions away from the flow disturbance the value of A is lower and the value of the cut-off frquency (which can be expressed as $(f_{co})_{NF}\sqrt{1-(AM_o)^2}$) higher than would be expected for acoustic propagation in a fully-developed velocity profile. This suggests that the sound radiated from the sources in the disturbed-flow region is effectively high-pass filtered in the near vicinity of the source; so that the apparent cut-off frequencies in the regions $X \lesssim -3$ and $X \gtrsim 3$ are in reality those higher values of regions closer to the source. This interpretation appears to be consistent with the substantial deviations, in the disturbed-flow region, of the mean-velocity profiles from that characteristic of undisturbed fully-developed flow, and with the observed variation of apparent cut-off frequency with X through the disturbed region. [It should also be noted that this, of course, implies that the lowest frequency sound in a given mode propagating away from the source is not determined by the flow conditions in the nominally undisturbed-flow regions well away from the source, as previously suggested by Bull and Agarwal (1984).] The low modal cut-off frequencies observed in the separated-flow region are interpreted as those of non-propagating (evanescent) acoustic modes.

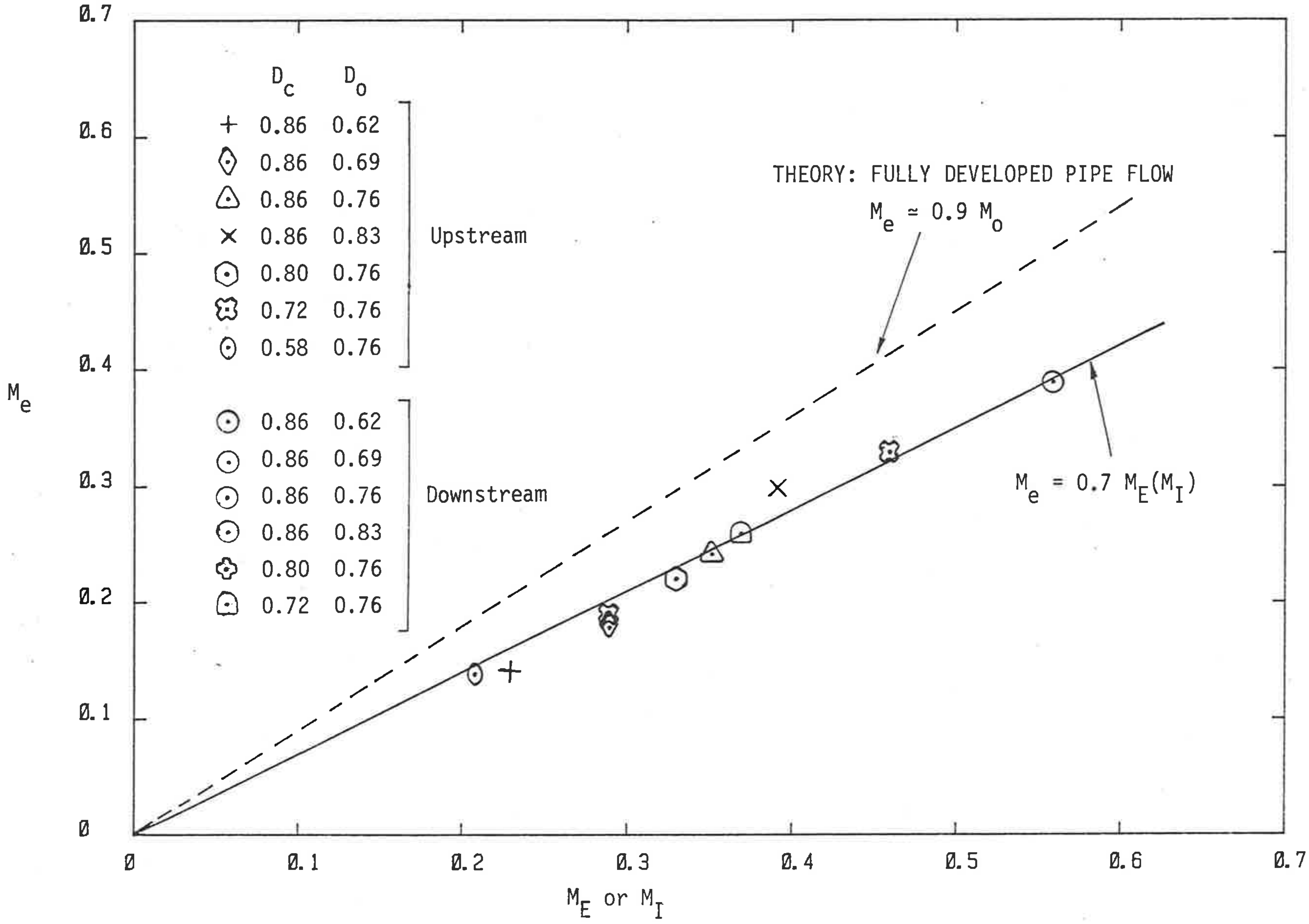

FIGURE 6.41 : EFFECTIVE FLOW MACH NUMBER

6.5 Summary and Conclusions

In this chapter the results of measurements of various characteristics of the wall pressure fluctuations in fully-developed turbulent pipe-flow, disturbed by an orifice plate, have been presented. The main results concerning the properties and structure of the resulting fluctuating pressure field are as follows.

(1) From the mean flow measurements (Chapter 5) it is known that the flow approaching the orifice retains the properties of undisturbed flow until it is quite close to it, and that, following the disturbance, the mean-velocity and turbulence profiles revert to their undisturbed states at some distance downstream ($X \gtrsim 48$). In both these nominally undisturbed regions, the local hydrodynamic pressure fluctuations should also be those characteristic of undisturbed fully-developed pipe flow. But, in both regions, the values of rms pressure and its power spectral density are, in fact, much higher than those for the undisturbed flow. The difference is attributed to propagating acoustic waves generated by the flow disturbance produced by the orifice plate.

(2) The intensity of the fluctuating pressure field in the separated-flow and reattachment region $0 \lesssim X \lesssim 1.5$ is determined by the maximum mean-flow velocity U_J in the free jet issuing from the orifice.

The overall rms wall-pressure p' scales with the dynamic pressure q_J in the jet, and, consistent with this, the wall-pressure spectra show similarity in the form of $\phi_p(\omega)U_J/q_J^2 a$ as a function of the Strouhal number $\omega a/U_J$.

The rms pressure reaches a maximum value of $p'/q_J = 0.06$ at a distance downstream of the orifice plate of about 90% of the flow reattachment length for all orifice plates and flow rates.

It appears that in this region turbulence and both propagating and non-propagating acoustic modes all contribute to the pressure fluctuations.

(3) The acoustic component of the overall rms pressure fluctuation in the nominally undisturbed flow upstream of the orifice (obtained by reducing the measured mean square value by the corresponding truly-undisturbed-flow value) is dominant and appears to scale as q_J/M_J. While the reason for the occurrence of the factor $1/M_J$ is not clear, the result does indicate that the sound field in this region is radiated from and determined by conditions in the separated-flow region downstream of the orifice. This conclusion is suported by the quite good collapse of the (unmodified) spectral data in the form $\phi(\omega)c_e M_J^2/q_J^2 a$ against $(\omega a/c_e)/\sqrt{1-M_e^2}$.

(4) The acoustic component of the overall rms pressure fluctuation is also dominant in the reattached and recovering flow downstream of the orifice and shows a dependence on $M_J^{0.3}\, q_J/D_0^4$, indicating that the sound field in this region also originates from the separated-flow region closer to the orifice. The corresponding (unmodified) spectra show a consistent form of scaling; a fair collapse of data is obtained in the form $\phi_p(\omega)c_e D_0^8/q_J^2 a M_J^{0.6}$ against $(\omega a/c_e)/\sqrt{1-M_e^2}$.

(5) The presence of the acoustic field is evidenced by the presence in the wall-pressure spectra of sharp peaks, the frequencies of which can be identified with those corresponding to the onset of propagation of the various orders of acoustic mode which can be generated within a circular pipe.

The peaks are not very prominent in the separated-flow region, indicating a major contribution to the pressure fluctuations in this region also by turbulence or non-propagating acoustic modes or both. They are very prominent in spectra both upstream of the orifice and in the reattached and recovering flow downstream. This is consistent with the dominance of acoustic pressure fluctuations over turbulence pressure fluctuations in these regions noted in (3) and (4) above.

(6) The cut-off frequencies of the various acoustic modes in the presence of flow, as obtained from overall and modal spectra of the wall-pressure fluctuations, differ from the corresponding no flow values by a factor of $\sqrt{1-M_e^2}$ where M_e is an effective flow Mach number. The spectra show quite close overall similarity when related to the non-dimensional frequency $(\omega a/c_e)/\sqrt{1-M_e^2}$ based on this same factor.

(7) In the nominally undisturbed flow well upstream of the orifice the apparent cut-off frequencies of the acoustic modes are the same at all streamwise locations, and a similar effect is observed in the recovering flow well downstream of the orifice. However the apparent cut-off frequency for a given mode is significantly higher upstream than downstream. The data suggest that the observed constancy is attributable to a high-pass filtering effect of the disturbed flow in the vicinity of the orifice, rather than to the true cut-off characteristics of the shear flow in the regions themselves. The behaviour is consistent with the observation of a minimum cut-off frequency for each mode at a position within the separated-flow region.
Apparent local variations in cut-off frequency in the region of disturbed flow appear to be associated with presence of evanescent acoustic modes.

(8) Modal spectra at various streamwise locations show that, for downstream propagation, (m,0) modes seem to have a constant rate of attenuation (0.2 dB/metre) while the (0,n) modes are attenuated at a lower rate. The attenuation for upstream propagation, is higher by about 50% (~ 0.3 dB/metre). Within the accuracy of measurement, flow speed does not seem to have a significant effect on the attenuation rate.

CHAPTER 7

VELOCITY SPECTRA

7.1 Introduction

The aims of this part of the investigation are

1) to determine the zones in which higher order acoustic modes are detectable in the spectra of the axial velocity fluctuations, and to identify the detectable modes;
2) to compare the measured radial distributions of modal acoustic particle velocity amplitude with the theoretical values derived from the corresponding modal pressure variation (see again Section 2.7.5);
3) to supplement the information on modal cut-off frequencies and effective flow Mach numbers obtained from wall pressure fluctuation measurements.

The theoretical relation between the axial component of acoustic particle velocity u and acoustic pressure is given by equation(2.56), Chapter 2. In most cases equation (2.57), which is exact for uniform flow, is expected to be a good approximation. Then the radial distribution of u will be similar to that of the pressure modified by the mean-velocity distribution through the term (c_ϕ - U).

Results presented in Chapter 6 for the overall wall-pressure spectrum when it is dominated by acoustic pressure fluctuations, and more particularly those for modal spectra, indicate that the maximum power spectral density in any given acoustic mode occurs at the cut-off frequency of that mode. If the velocity spectra are to provide similar information on cut-off frequencies, the behaviour of the acoustic particle velocity must be similar to that of the pressure and also peak at the modal cut-off frequency. However, this need not necessarily occur, and the actual behaviour must be determined from the experimental data.

The experimental spectral results which are presented are those measured with a single 5μm diameter tungsten hot wire. The hot wire probe was the same as that used for the measurements of the rms streamwise velocity fluctuation presented in Chapter 5, but in the present work the wire was uncalibrated.

The axial velocity fluctuation u to which the hot wire is subjected is the sum of a turbulence velocity fluctuation and an acoustic velocity fluctuation:

$$u = u_{ac} + u_h, \tag{7.1}$$

(where u_{ac} and u_h are the axial components of acoustic and hydro-dynamic fluctuations respectively), but the hot-wire output is not simply a function of u. A number of factors determine how closely its output represents u only.

The single hot wire responds essentially only to streamwise flow fluctuations; its output will therefore in general represent axial flow fluctuations, although it should be noted this will not be strictly accurate where streamlines of the flow are significantly inclined to the pipe axis.

It is generally acepted, following Kovasznay (1950) and Morkovin (1956), that in a compressible flow a hot wire responds primarily to mass flux (ρU) and total temperature (T_t) fluctuations. Thus

$$\frac{E'}{E} = S_{\rho u}\frac{(\rho U)'}{\rho U} + S_{T_t}\frac{T_t'}{T_t}, \tag{7.2}$$

where E is the voltage output of the hot-wire bridge; primes indicate fluctuations, and $S_{\rho u}$ and S_{T_t} are sensitivity coefficients. However, there is some uncertainty about the relative magnitudes of the sensitivities and their dependence on Mach number. Rose and McDaid (1977) and others have concluded that $S_{\rho u}$ is insensitive to Mach number variation at moderate subsonic and transonic speeds and that S_{T_t} becomes small compared with $S_{\rho u}$ at high wire overheat ratios; but the findings of Ardonceau (1984) are at variance with both these conclusions. Thus, while total temperature variations in turbulence are small and so for turbulence measurements the second term in equation (7.2) can normally be neglected, for acoustic fluctuations it can only be neglected if S_{T_t} is indeed small; and in view of the uncertainty about Mach number dependence of the sensitivities, direct comparisons of dimensional spectral levels obtained with an uncalibrated hot-wire at different flow locations, with different mean-flow Mach numbers, must be made with caution.

Even if the contribution of total-temperature fluctuations to the hot-wire response can be neglected, the hot-wire output is still a measure of mass flux rather than velocity fluctuation. In the case of turbulent fluctuations, (ρ'/ρ) is approximately equal to $(\gamma-1)M^2(u/U)$ (Kovasznay, 1950; Settles et al., 1982); thus (with $\gamma = 1.4$) density fluctuations will be responsible for about 40% of the mass flux fluctuation at $M \simeq 1$ and significantly less at lower Mach numbers. However, in the case of acoustic fluctuations, because the relation between particle velocity and density (or pressure) variations is not simple for higher-order modes and will in general be frequency-dependent, there is no simple way of resolving the hot-wire signal into its particle velocity and density fluctuation components. Both at the pipe centre-line (when $\partial U/\partial r = 0$) and near the pipe wall (where $\partial p/\partial r \simeq 0$), equation (2.56) reduces to equation (2.57). From that relation it can be shown that the mass flux fluctuations will be dominated by the particle velocity contribution in the wall region, but that, on the centre-line, particle velocity and density fluctuation contributions will be of the same order (and opposite sign).

Here the hot-wire signal will be interpreted as roughly representing u as given by equation (7.1) but it must be borne in mind that this is subject to the significant restrictions which have been outlined.

Because, for these measurements, the hot wire was uncalibrated, the results presented are restricted to the following two forms:

(i) the power spectral density $\phi_u(\omega)$, non-dimensionalised in the form

$$\Phi_u = \frac{\phi_u(\omega)U_o}{a\ \overline{u^2}} , \qquad (7.3)$$

as a function of Strouhal number,

$$\Omega = \frac{\omega a}{U_o} , \qquad (7.4)$$

where U_o is the mean flow velocity on the pipe centre-line and the normalisation is such that

$$\int_0^\infty \Phi_u d\Omega = 1; \qquad (7.5)$$

and

(ii) relative values of $\phi_u(f)$ as a function of the dimensional frequency f.

Measurements upstream of the orifice (up to X = -16.8) and downstream in the separated flow region, recovery region, and re-established equilibrium region (X > 48) have been made with the orifice and choke combinations indicated in Figure 7.1. The spectra have been obtained

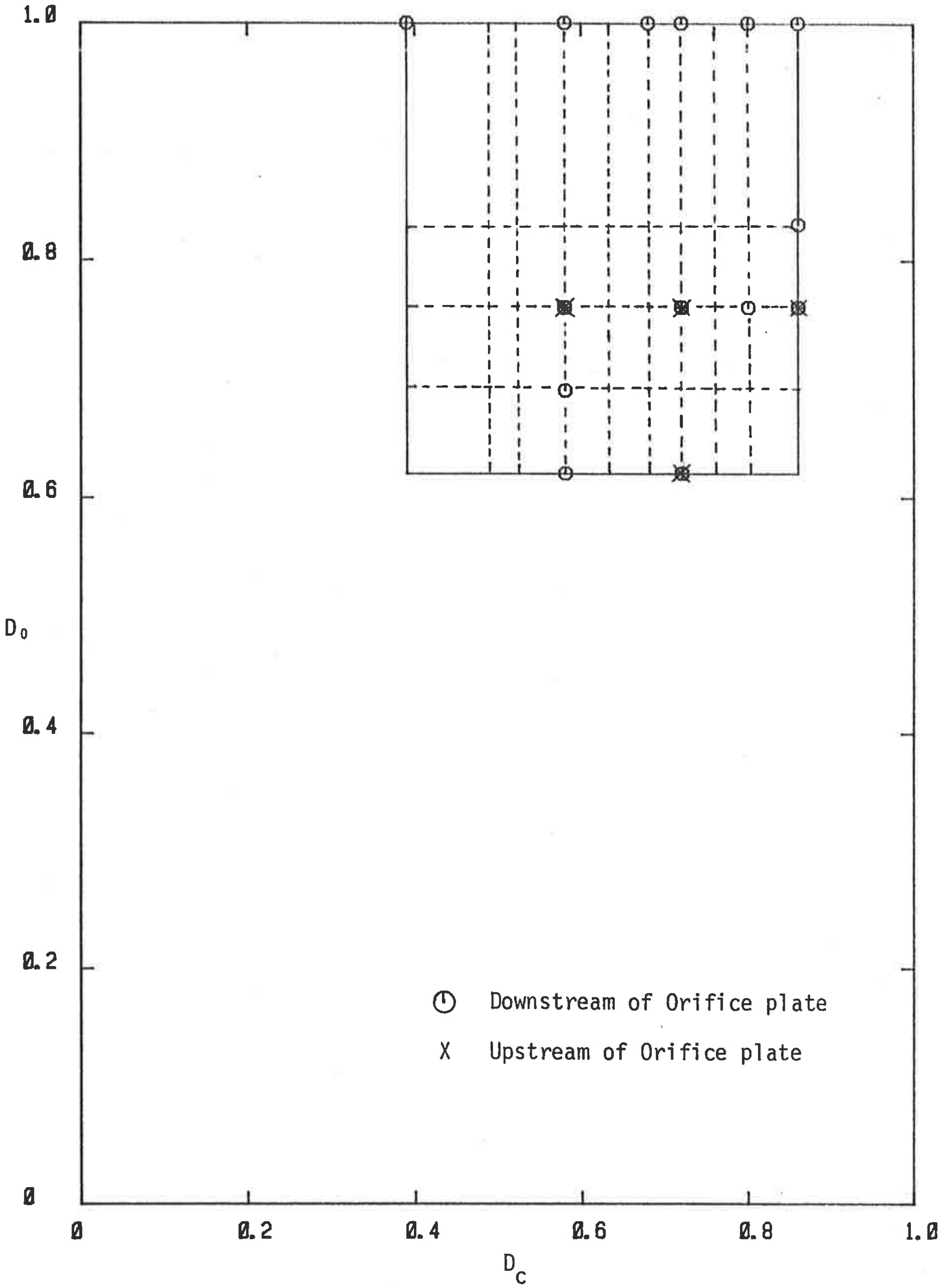

FIGURE 7.1 : RANGE OF MEASUREMENT WITH HOT WIRE ANEMOMETER

either by directly digitizing the hot wire signal (after low pass filtering with a 4-pole Butterworth filter) using the 12-bit data acquisition system or by using the Hewlett-Packard spectrum analyser.

7.2 Velocity Spectrum in Undisturbed Flow at Various Reynolds Numbers

Velocity spectra at the pipe centre-line at X = 0 for the case of the undisturbed flow, over a range of flow speeds (given by the chokes D_c = 0.39 - 0.86), are given in Figure 7.2. The Reynolds numbers, based on pipe diameter, are in the range 1.54 - 6.64 × 10^5. The u' spectrum of Laufer (1954) obtained at a pipe-flow Reynolds number of 5 × 10^5 is also shown. The spectral distributions are similar to each other and generally in close agreement with the measurements of Laufer except at high frequencies, where the present results show a somewhat more rapid drop with frequency for $\Omega \gtrsim 30$.

Spectra at various radial positions (y/a = 0.074, 0.28 and 0.691) at the flow speed given by the choke, D_c = 0.86 (Re = 6.64 × 10^5) are shown in Figure 7.3. Laufer's measurements at the same radial locations for Re = 5 × 10^5 are shown; again there is quite reasonable agreement except at high frequencies.

7.3 Streamwise Variation of Axial Velocity Fluctuations on the Pipe Centre-Line

The spectral measurements given in this section embrace the range of streamwise distances $-16.81 \leqslant X \leqslant 86.54$ with the choke D_c = 0.86, and $-16.81 \leqslant X \leqslant 2.20$ with two other chokes, D_c = 0.58 and 0.72; the data are for three orifice plates D_0 = 0.62, 0.69 and 0.76.

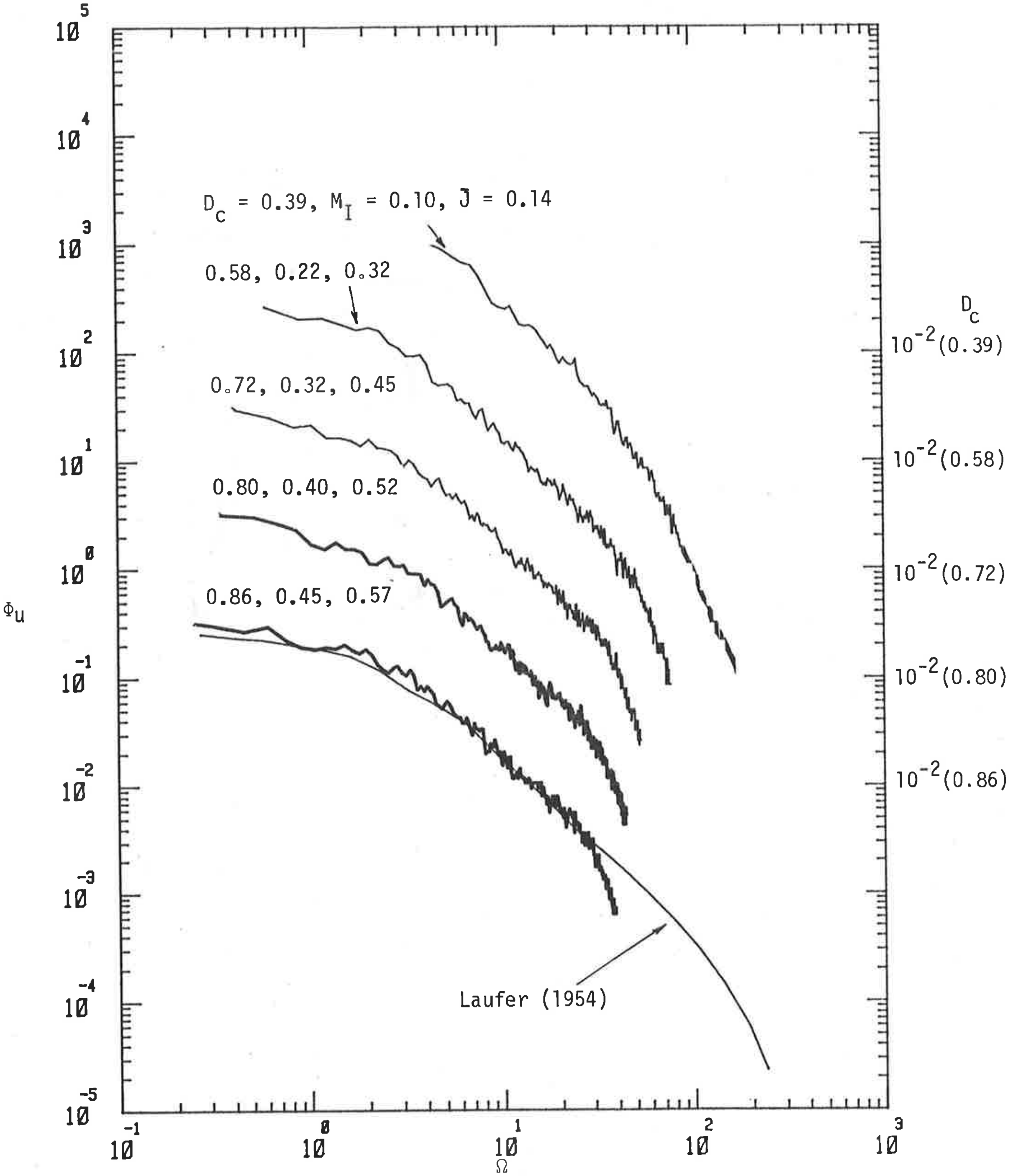

FIGURE 7.2 : NON-DIMENSIONAL VELOCITY SPECTRA AT THE PIPE CENTRELINE X = 0 IN UNDISTURBED FLOW

(Top four curves are each shifted up by one scale unit)

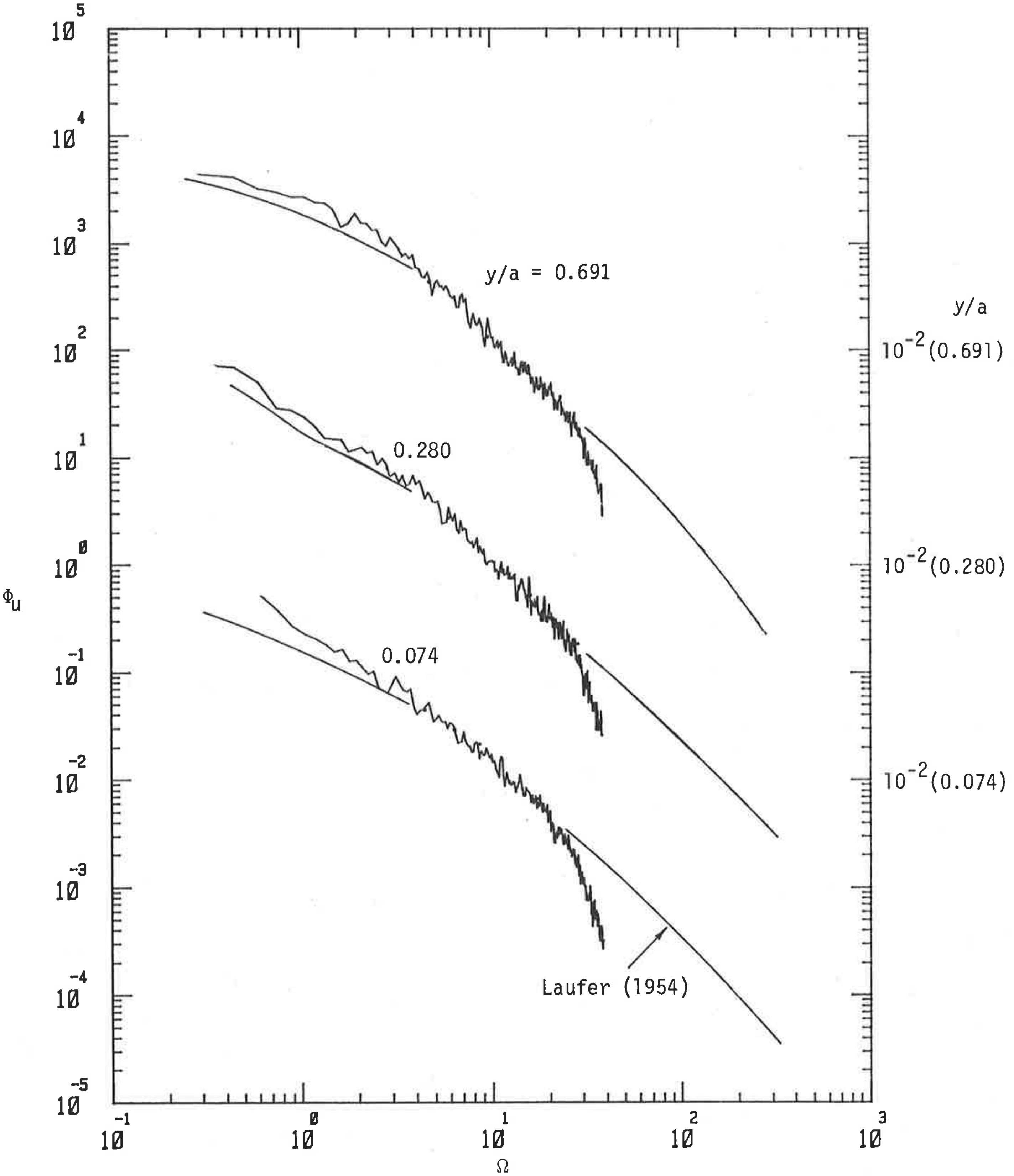

FIGURE 7.3 : NON-DIMENSIONAL VELOCITY SPECTRA IN UNDISTURBED FLOW AT $X = 0$, $D_c = 0.86$, $M_I = 0.45$, $J = 0.57$

(Top two curves are shifted up by two scale units)

In the case of uniform flow the distributions of acoustic pressure for the various acoustic modes are given by equation (2.4) as

$$p(r, \theta, x) = (A_{mn}\cos m\theta + B_{mn}\sin m\theta)J_m(\kappa_{mn}r)e^{i(k_x x-\omega t)}.$$

Since $J_m(0) = 1$ for $m = 0$ and $J_m(0) = 0$ for $m \geqslant 1$, it follows that p will be zero on the pipe centre line ($r = 0$) for all modes except those for which $m = 0$. A similar result is obtained from the numerical solutions for fully-developed pipe flow. Also, since $\partial U/\partial r = 0$ at $r = 0$, equation (2.56) reduces exactly to equation (2.57) at $r = 0$.

Therefore on the pipe centreline, only (0,n) modes should be detectable.

7.3.1 <u>Separation region ($X < X_R$, Zone 3)</u>

Spectra on the pipe centre line, at various streamwise positions, for flow with $D_0 = 0.76$ and $D_C = 0.72$ are shown in Figure 7.4.

The figure shows sharp spectral peaks at frequencies sufficiently close to the cut-off frequencies of the (0,n) modes for them to be associated with these modes. The frequencies of the peaks do not change with streamwise distance, but there is a rapid reduction of modal amplitude of the higher order acoustic modes relative to the background turbulence level as $X \to X_R$ (1.31). We have seen that pressure and velocity fluctuations both reach maximum values in this vicinity, and this suggests that the effect results from increased turbulence level rather than attenuation of the acoustic modes.

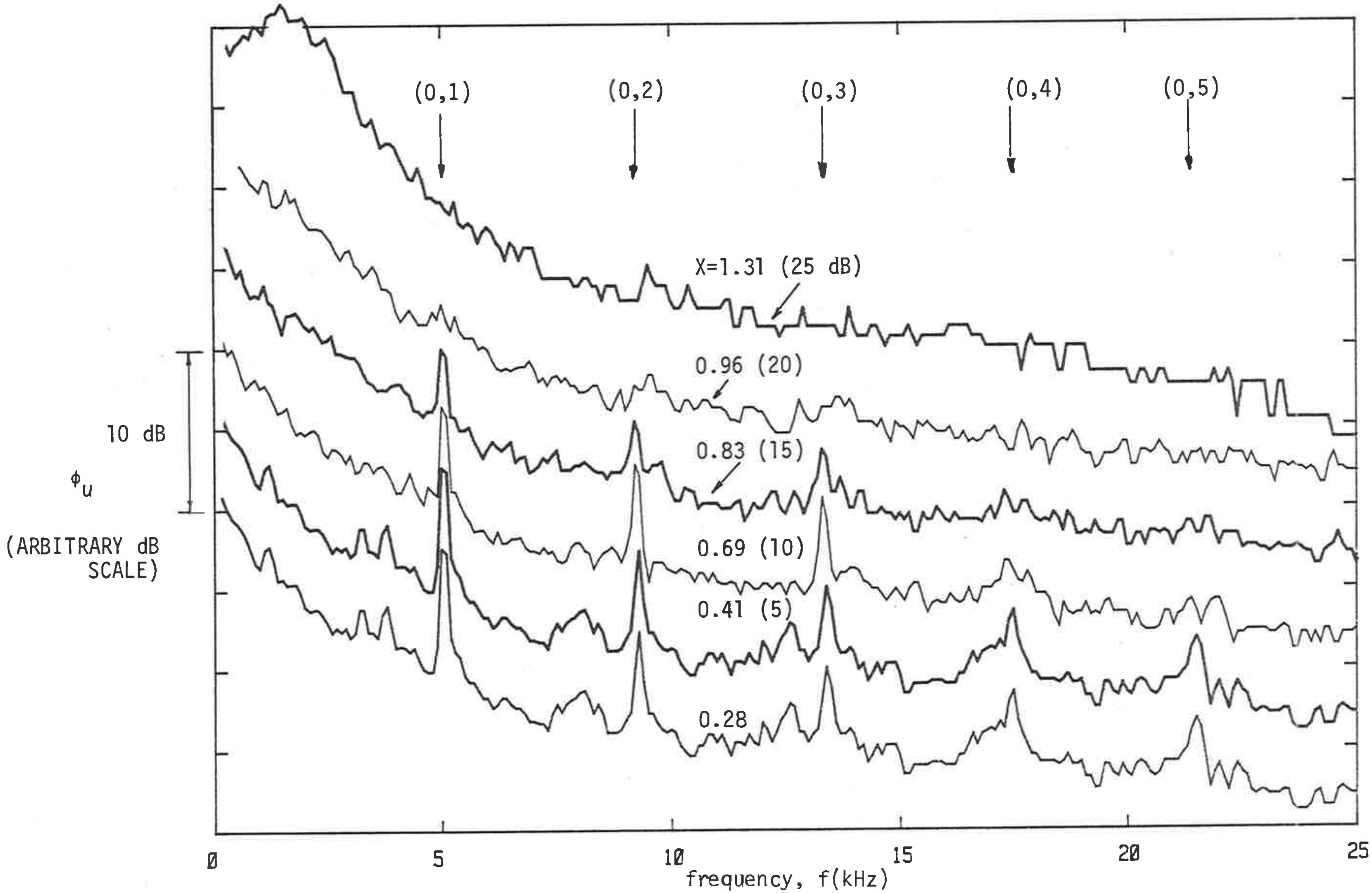

FIGURE 7.4 : VELOCITY SPECTRA IN SEPARATED REGION AT $y/a = 1.0$, $D_c = 0.72$, $D_o = 0.76$, $M_I = 0.29$, $\overline{J} = 0.40$

(Top five curves are each shifted up as shown)

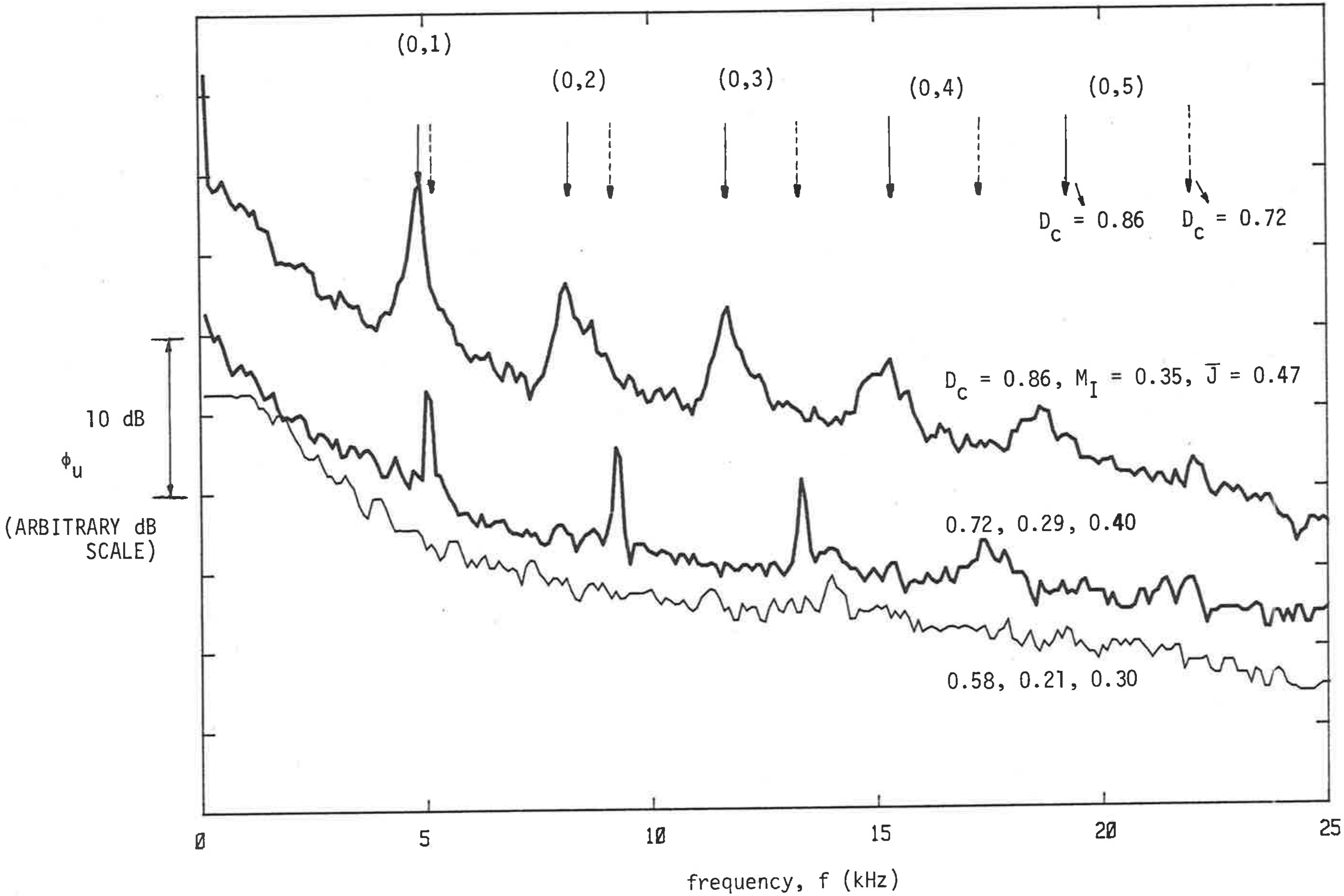

FIGURE 7.5 : VELOCITY SPECTRA IN SEPARATED REGION AT y/a = 1.0, X = 0.55, D_o = 0.76

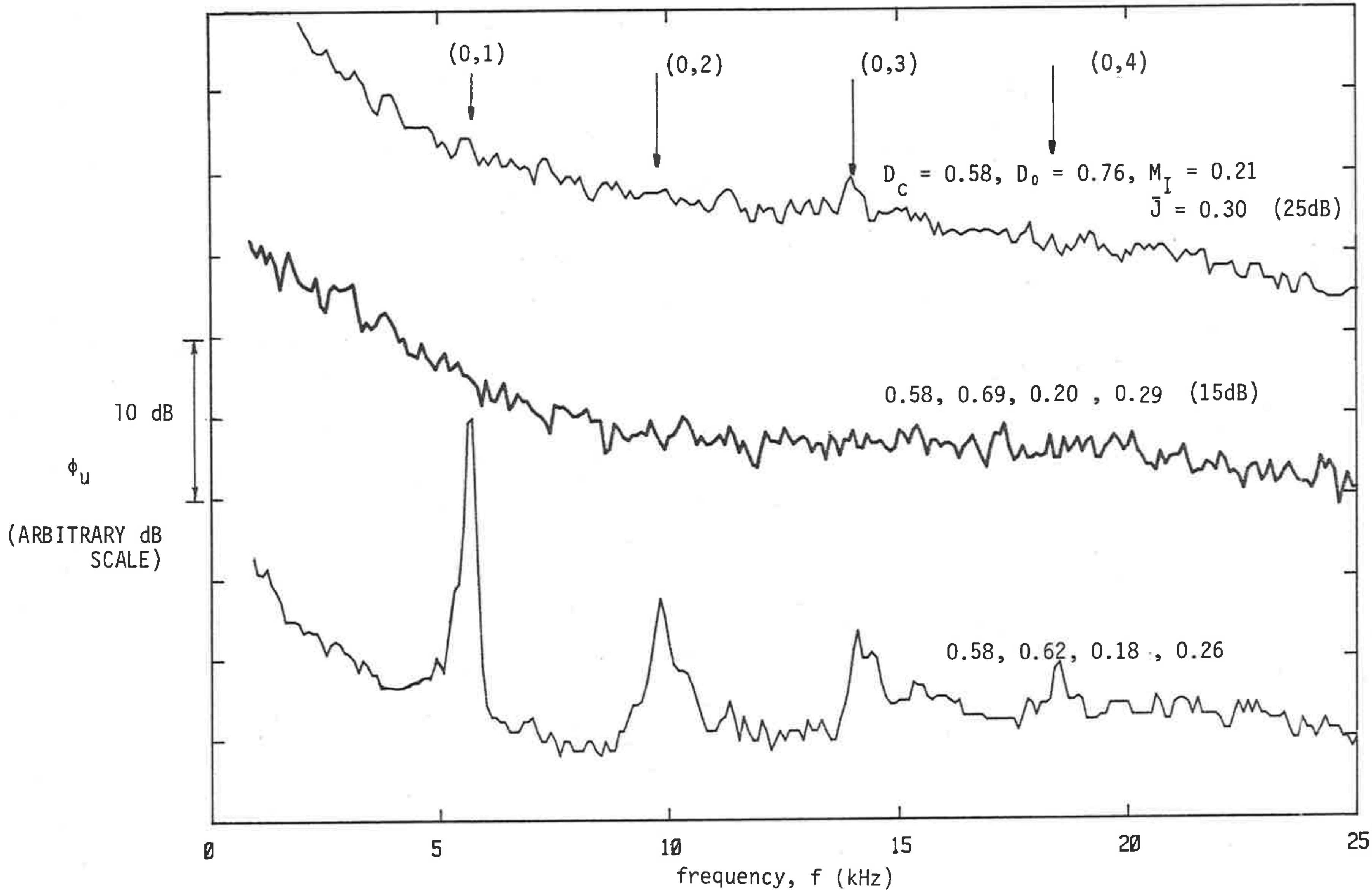

FIGURE 7.6 : VELOCITY SPECTRA AT y/a = 1.0, X = 0.55

(Top two curves are each shifted up as shown)

Spectra for the orifice plate $D_0 = 0.76$ at $X = 0.55$ with the flow speeds given by chokes $D_C = 0.58$, 0.72 and 0.86 (Figure 7.5) are generally similar to those shown in Figure 7.4, except that the (0,n) spectral peaks can be identified for the chokes $D_C = 0.72$ and 0.86 but not for 0.58. In line with the general dependence of cut-off frequencies on Mach number, the frequencies of the spectral peaks take on lower values as the flow rate increases.

At the same position, variation of orifice size for a given choke ($D_C = 0.58$) leads to turbulence spectral levels increasing with D_0 at a greater rate than acoustic levels (Figure 7.6); so that acoustic spectral peaks are evident with $D_0 = 0.62$ but not with $D_0 = 0.69$ or $= 0.76$.

7.3.2 Recovery region ($X_R < X < 48$, Zone 4)

Variation of spectra with X in this region, for $D_0 = 0.76$ with $D_C = 0.86$, is shown in Figure 7.7. Peaks corresponding to higher-order acoustic modes are evident only at $X = 1.61$. Thereafter the spectrum is dominated by turbulence and the level increases up to $X = 4.24$, and then falls continuously with increasing X (which is consistent with the u' measurements with $D_0 = 0.76$ and $D_C = 0.39$, Chapter 5). At $X = 45.19$, the spectrum is nearly the same as that of the undisturbed flow. Additional data, for $D_0 = 0.76$ with $D_C = 0.72$ (Figure 7.8) show similar spectra, but in this case acoustic modes are not really discernible even at $X = 1.47$.

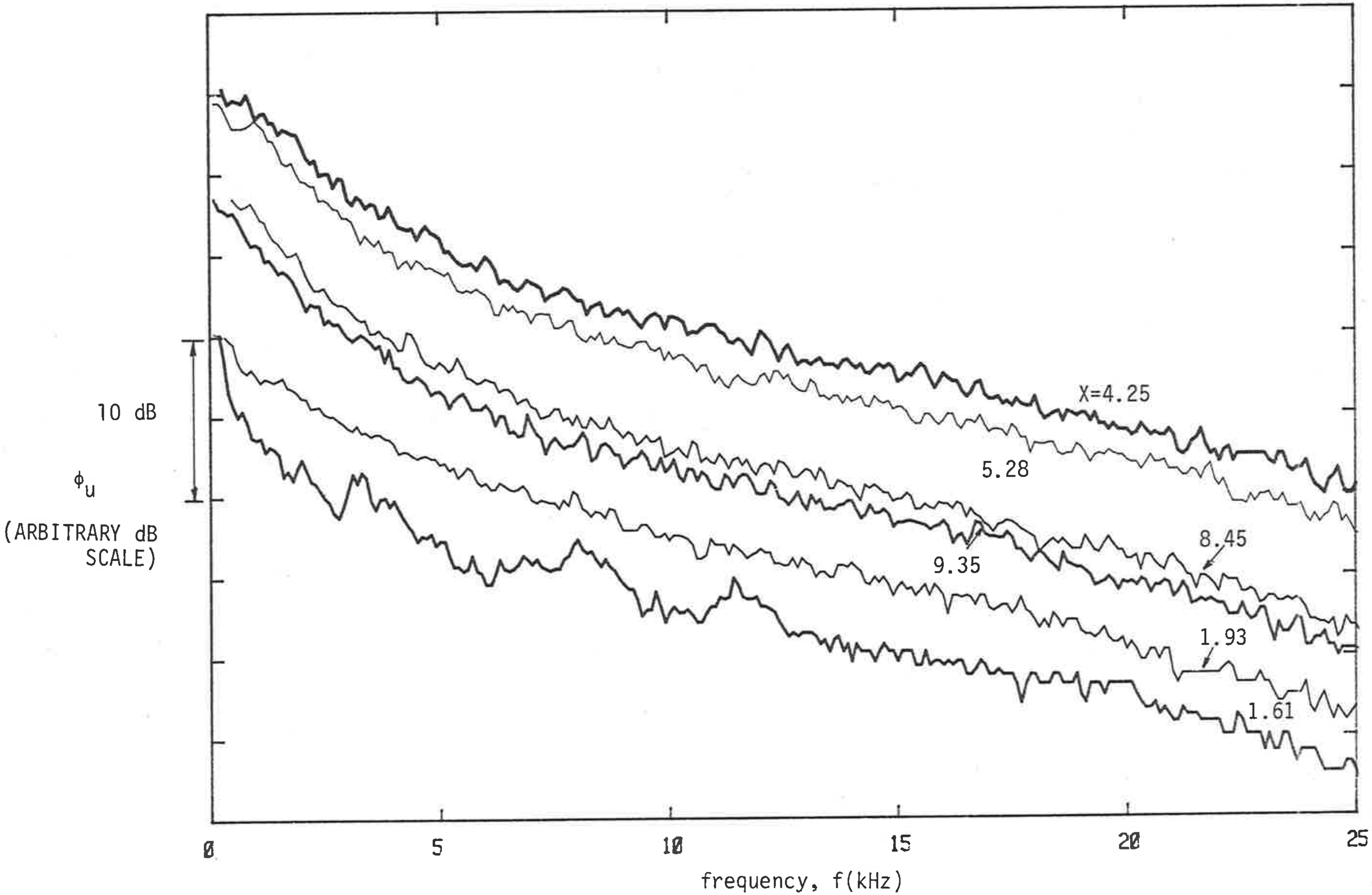

FIGURE 7.7a : VELOCITY SPECTRA IN RECOVERY REGION (ZONE 4) AT $y/a = 1.0$, $D_c = 0.86$, $D_o = 0.76$, $M_I = 0.35$, $\overline{J} = 0.47$

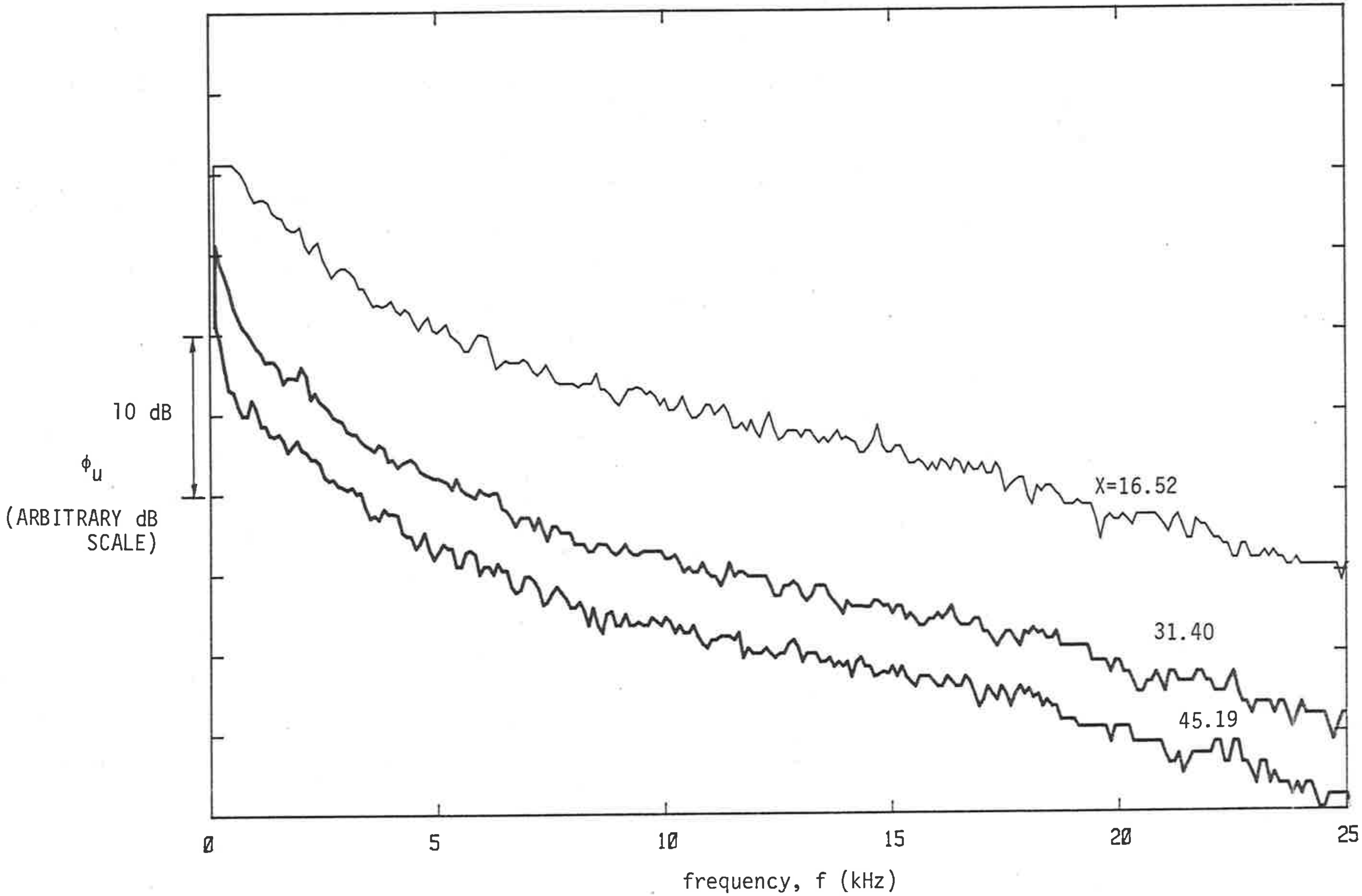

FIGURE 7.7b : VELOCITY SPECTRA IN RECOVERY REGION (ZONE 4) AT $y/a = 1.0$, $D_c = 0.86$, $D_o = 0.76$, $M_I = 0.35$, $\overline{J} = 0.47$

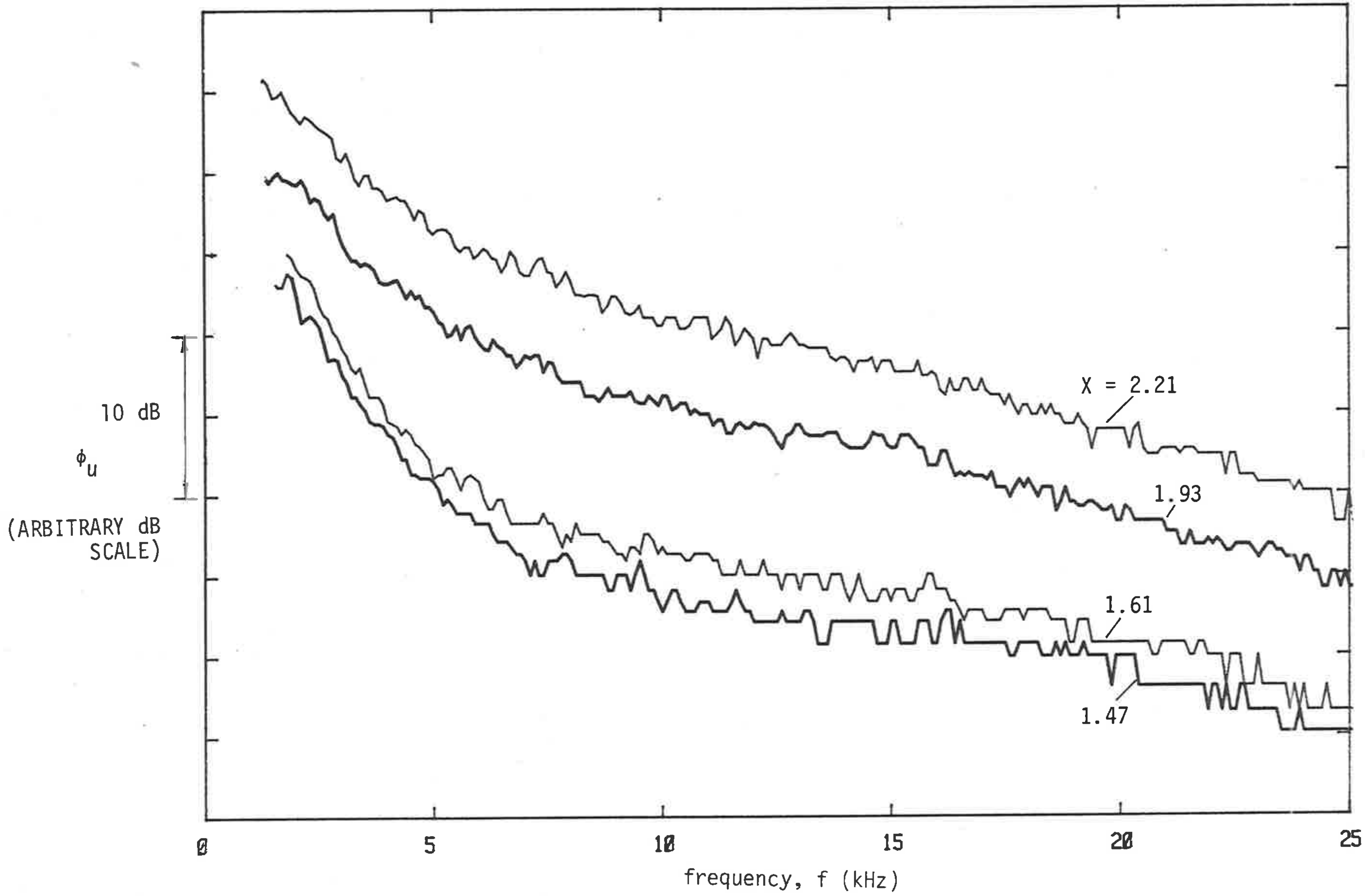

FIGURE 7.8 : VELOCITY SPECTRA IN RECOVERY REGION (ZONE 4) AT $y/a = 1.0$, $D_c = 0.72$, $D_o = 0.76$, $M_I = 0.29$, $\overline{J} = 0.40$

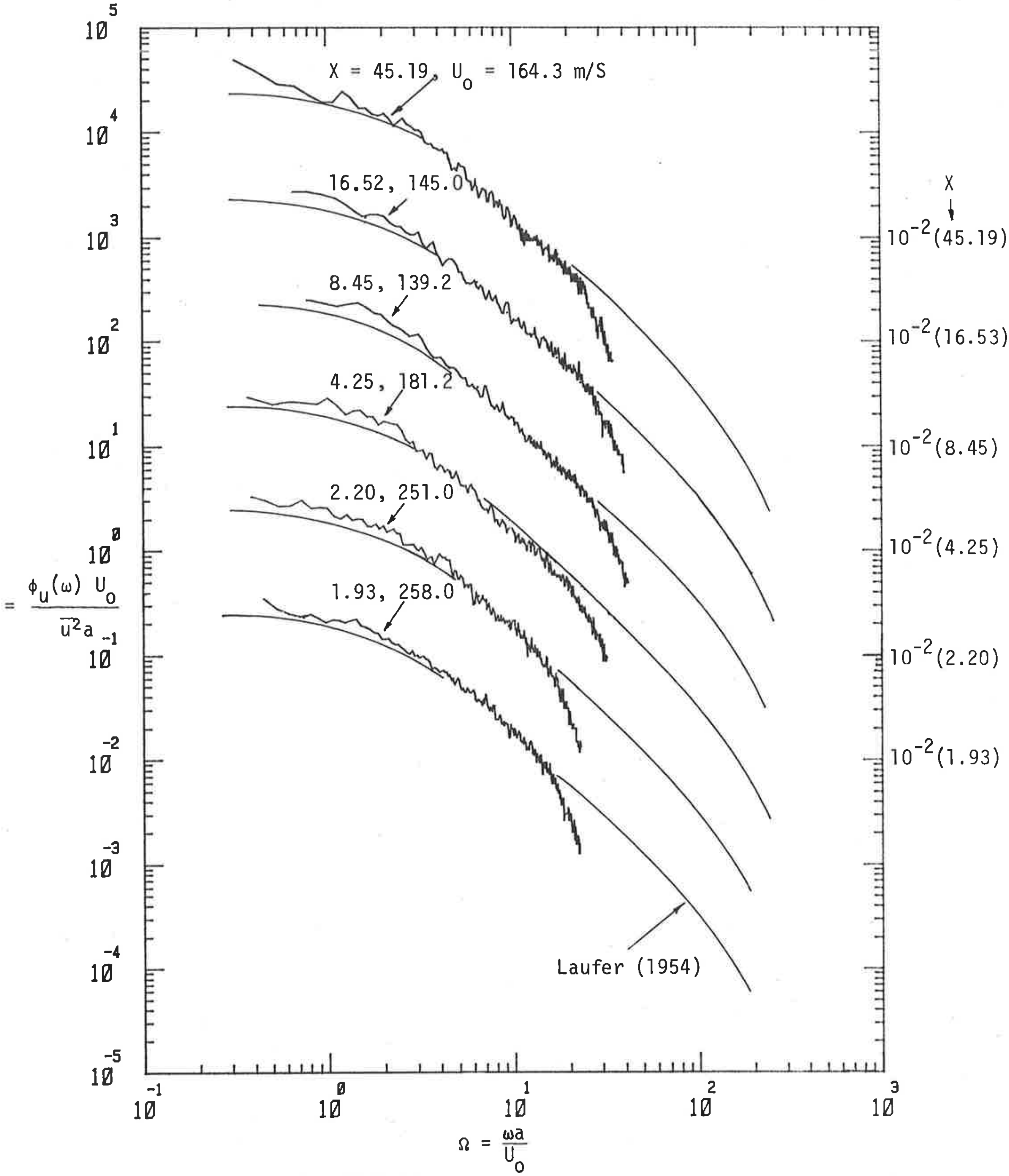

FIGURE 7.9 : NON-DIMENSIONAL VELOCITY SPECTRA AT $y/a = 1.0$, $D_c = 0.86$
$D_o = 0.76$, $M_I = 0.35$, $\overline{J} = 0.47$

Spectra of Figure 7.7 in non-dimensional form, for locations $X > 1.93$ at which higher order acoustic modes are not evident, together with Laufer's (1954) results for undisturbed flow are shown in Figure 7.9. Except at high frequencies there is a strong similarity between the two.

7.3.3 Fully developed flow re-established ($X > 48$, Zone 5)

The spectrum at $X = 86.54$ for the flow with $D_0 = 0.76$ and $D_C = 0.86$ and for the undisturbed flow at $X = 0$ are shown in Figure 7.10, in both dimensional and non-dimensional form. It is evident that in this region the velocity spectrum is turbulence-dominated and not significantly affected by either the flow disturbance or the acoustic field which is superimposed on the flow.

7.3.4 Flow upstream of the orifice (Zones 1 and 2)

Velocity spectra upstream of the orificie plate for the flow with $D_C = 0.86$ and $D_0 = 0.76$ (Figure 7.11) show no significant change with X over the range = -16.82 to -1.65. No discrete peaks corresponding to the higher order acoustic modes are evident. Similar results are obtained for different orifice sizes and flow speeds. Data for $D_0 = 0.76$ with $D_C = 0.58$, 0.72 and 0.86 and for $D_0 = 0.62$ and $D_C = 0.86$ are shown in Figure 7.12. No acoustic peaks are present in the spectra and the effect of flow speed and orifice size is merely to change the spectral level in accord with changes in the mass flow rate. The spectra of Figures 7.11 and 7.12 in non-dimensional form, Figures 7.13 and 7.14, are again similar to that of undisturbed flow.

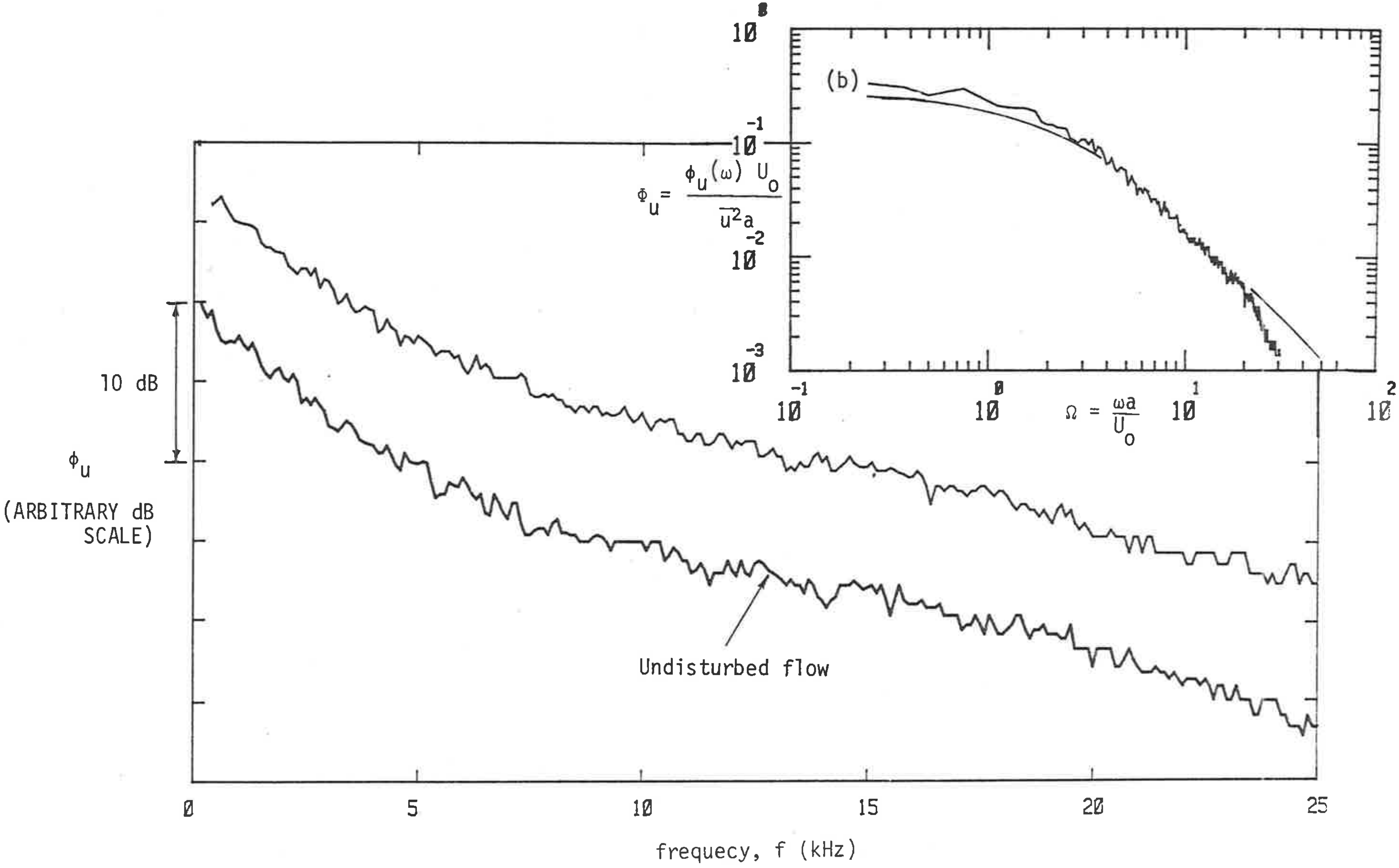

FIGURE 7.10a : VELOCITY SPECTRA AT $y/a = 1.0$, $X = 86.54$, $D_c = 0.86$, $D_o = 0.76$, $M_I = 0.35$, $\bar{J} = 0.47$
(Top curve is shifted up by 10 dB)

7.10b : NON-DIMENSIONAL SPECTRA, $U_o = 184.2$ m/s

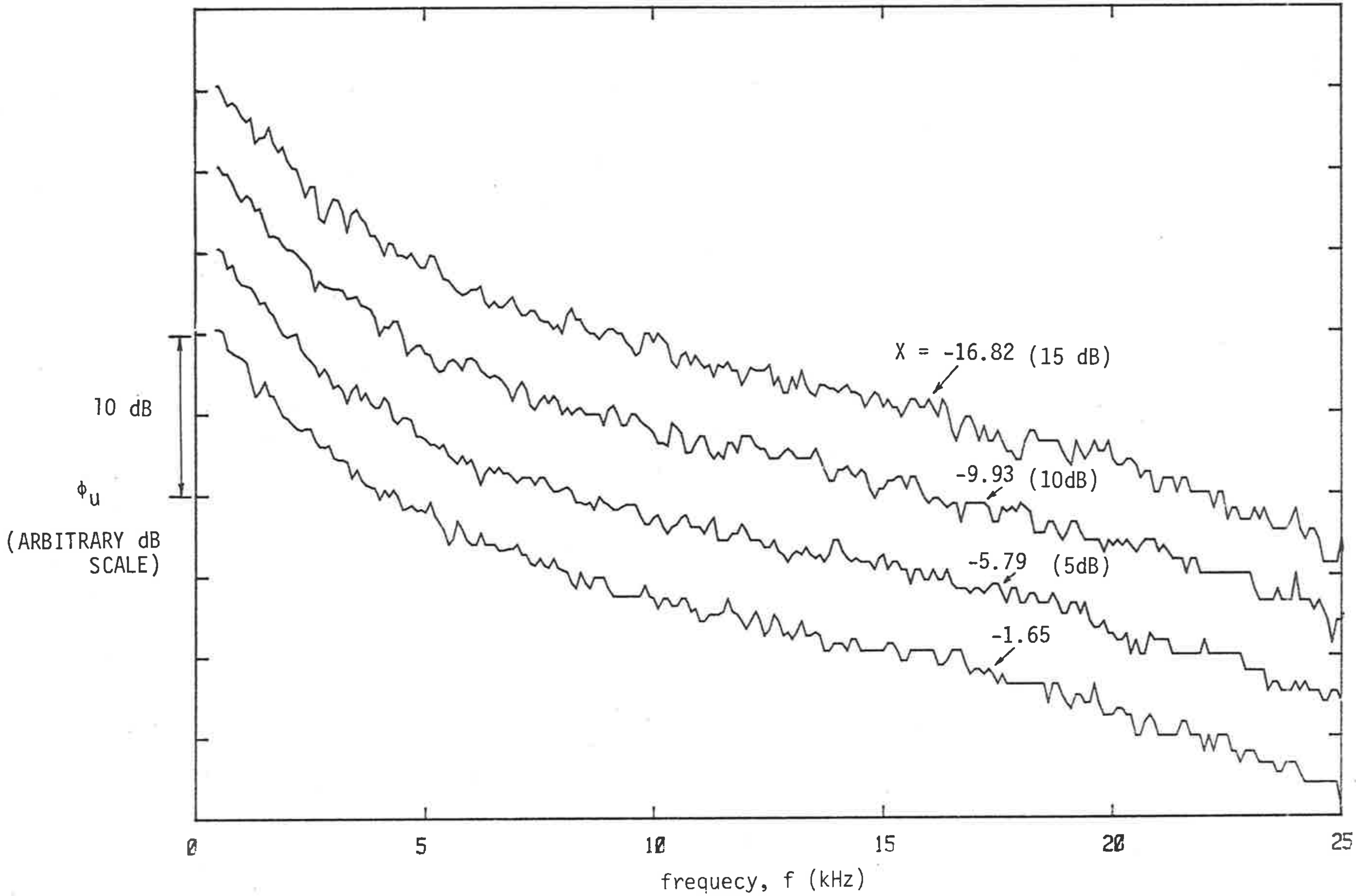

FIGURE 7.11 : VELOCITY SPECTRA AT y/a = 1.0, D_C = 0.86, D_O = 0.76, M_I = 0.35, $\overline{J}$ = 0.47

(Top three curves are each shifted up by 5 dB)

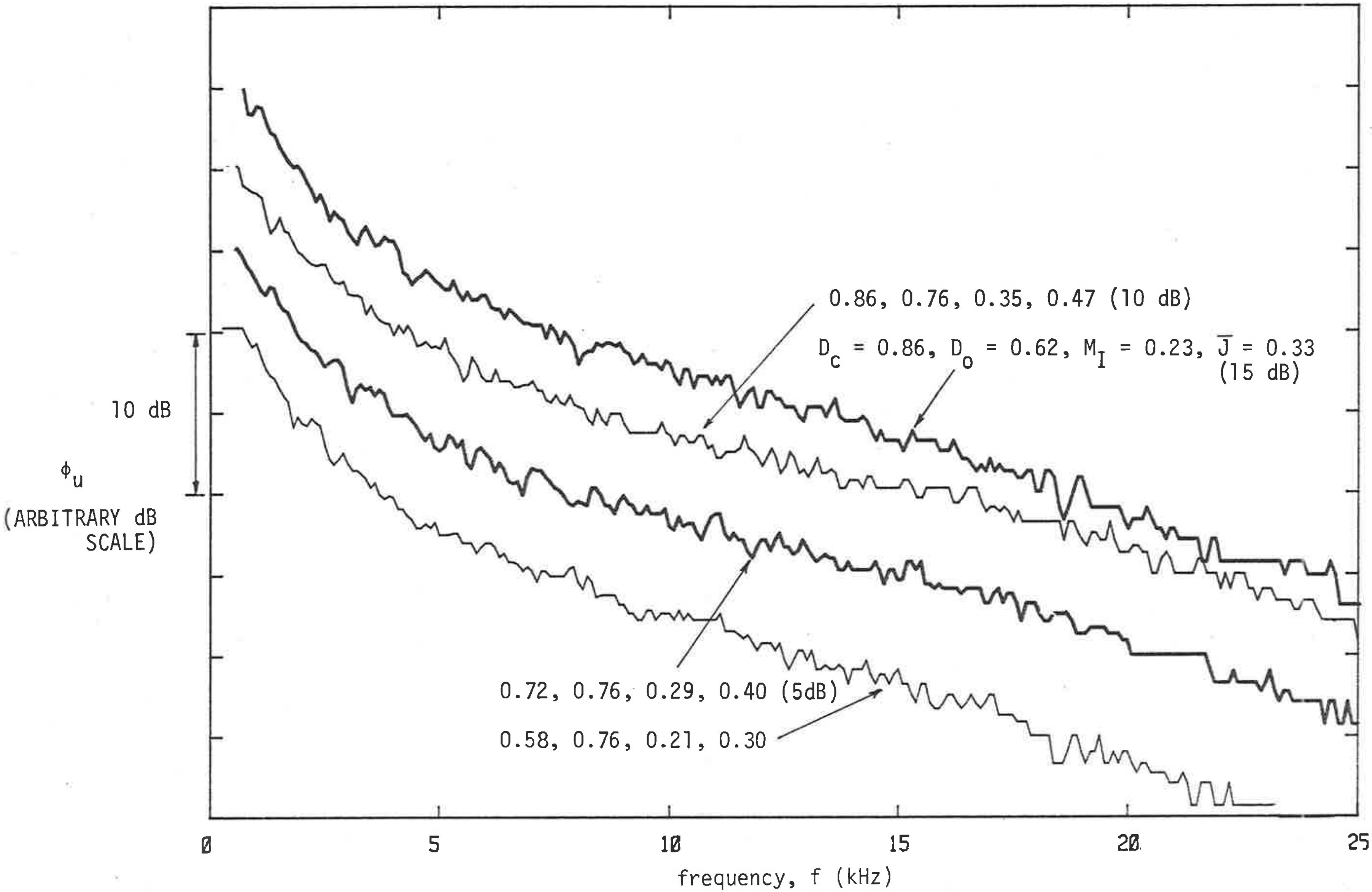

FIGURE 7.12 : VELOCITY SPECTRA AT $y/a = 1.0$, $X = -1.65$

(Top three curves are each shifted up by 5 dB)

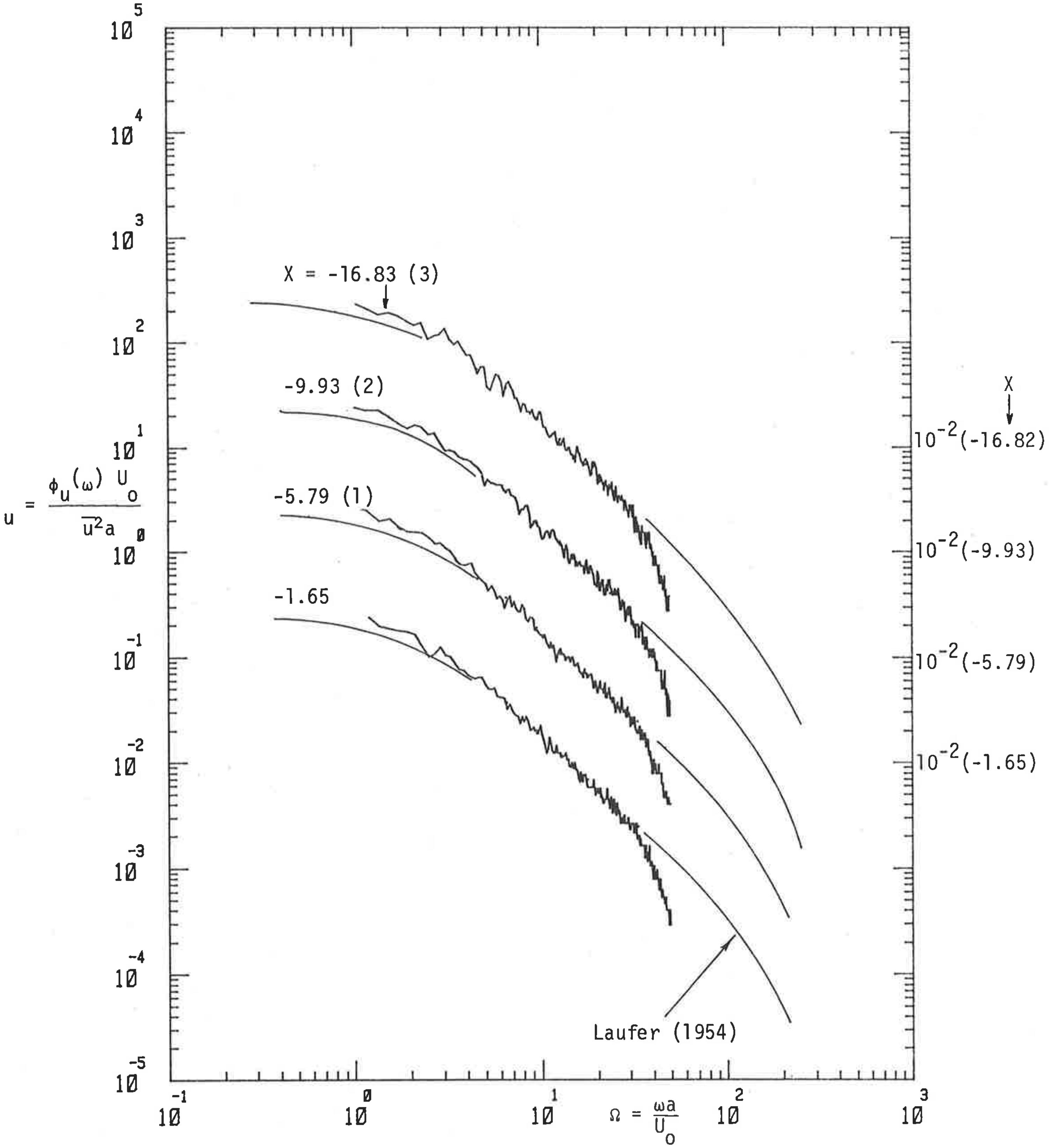

FIGURE 7.13 : NON-DIMENSIONAL VELOCITY SPECTRA AT $y/a = 1.0$, $D_c = 0.86$, $D_o = 0.76$, $M_I = 0.35$, $\overline{J} = 0.47$

(Top three curves are each shifted up by one unit)

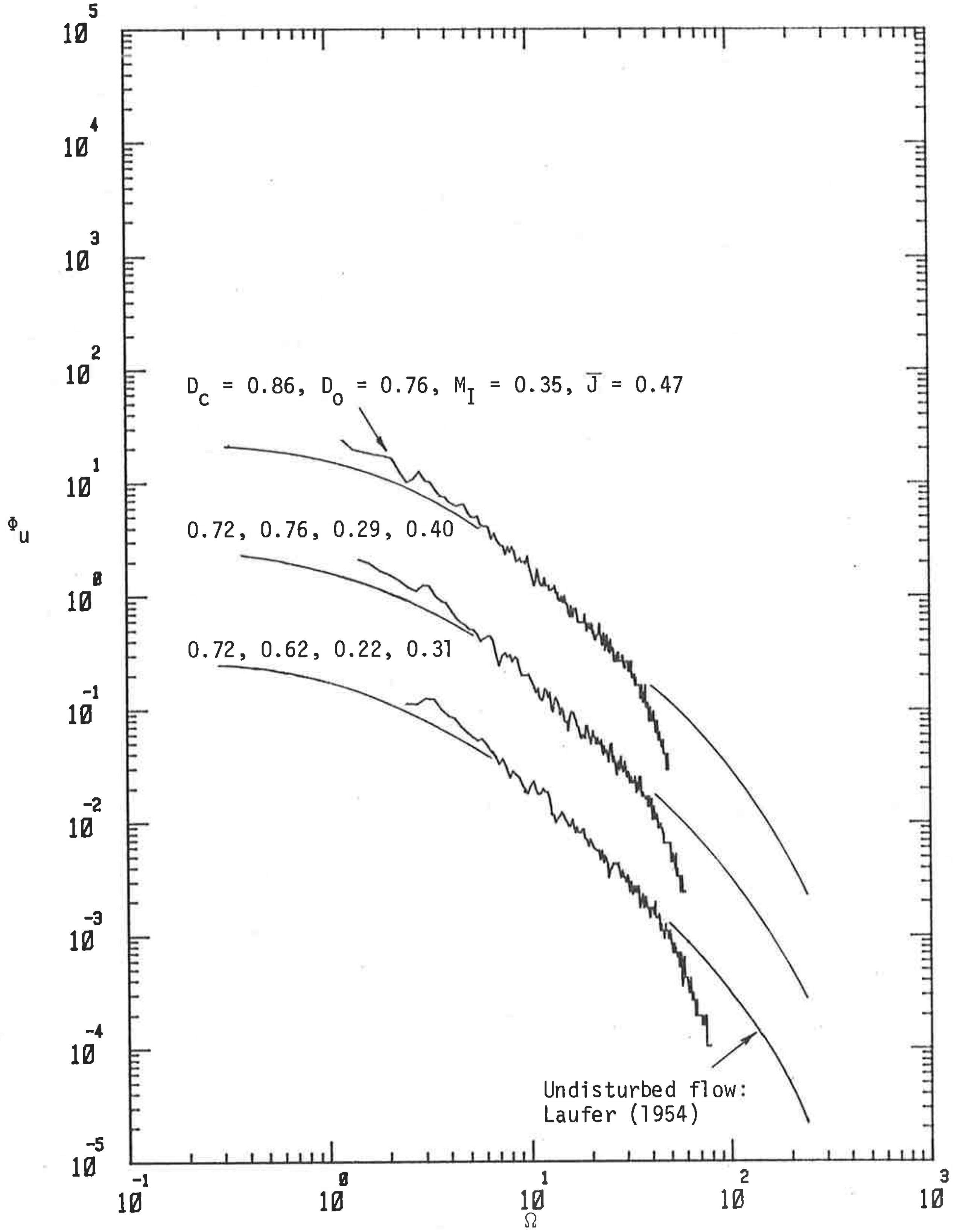

FIGURE 7.14 : NON-DIMENSIONAL VELOCITY SPECTRA AT y/a = 1.0, X = -1.65

7.4 Variation of Velocity Fluctuations with Radial Distance from the Pipe Wall

All the experimental data presented in this section are for the orifice plate $D_0 = 0.76$ in combination with the choke $D_C = 0.86$.

7.4.1 Downstream of the orifice

Spectra measured at eleven radial positions at X = 0.55, within the separated flow region, are shown in Figure 7.15. There is clearly a dominance of turbulence velocity fluctuations near the wall at y/a = 0.074, 0.16 and 0.25. There is a suggestion of very weak acoustic peaks in the spectrum at y/a = 0.33, but such peaks only become clearly visible at y/a = 0.5. They can be clearly seen in all spectra for $0.50 \leq y/a \leq 1.0$. At these positions most of the first fifteen higher-order modes (up to (8,0)) can be detected, but beyond this it is generally hard to distinguish the peaks. Pairs of modes such as (6,0) and (3,1), and (1,2) and (7,0), cannot be separated as their cut-off frequencies are very close together. For $y/a \geq 0.74$ the (m,0) modes are progressively reduced in magnitude while the (0,n) modes are increasing in magnitude. At y/a = 1.0, i.e. at the pipe centre line, as expected, only (0,n) modes are present. Changes in the spectra with X, moving from the separated-flow region through reattachment (X = 1.31) and some distance into the recovery region (X = 1.93) are shown in Figure 7.16 for four different radial positions. Spectra at X = 1.31 and 1.93 are similar and most of them are dominated by turbulent fluctuations; the only clearly distinguishable peaks at these two positions are those corresponding to (0,n) modes which can be seen at y/a = 0.83 for X = 1.31. The main effect associated with

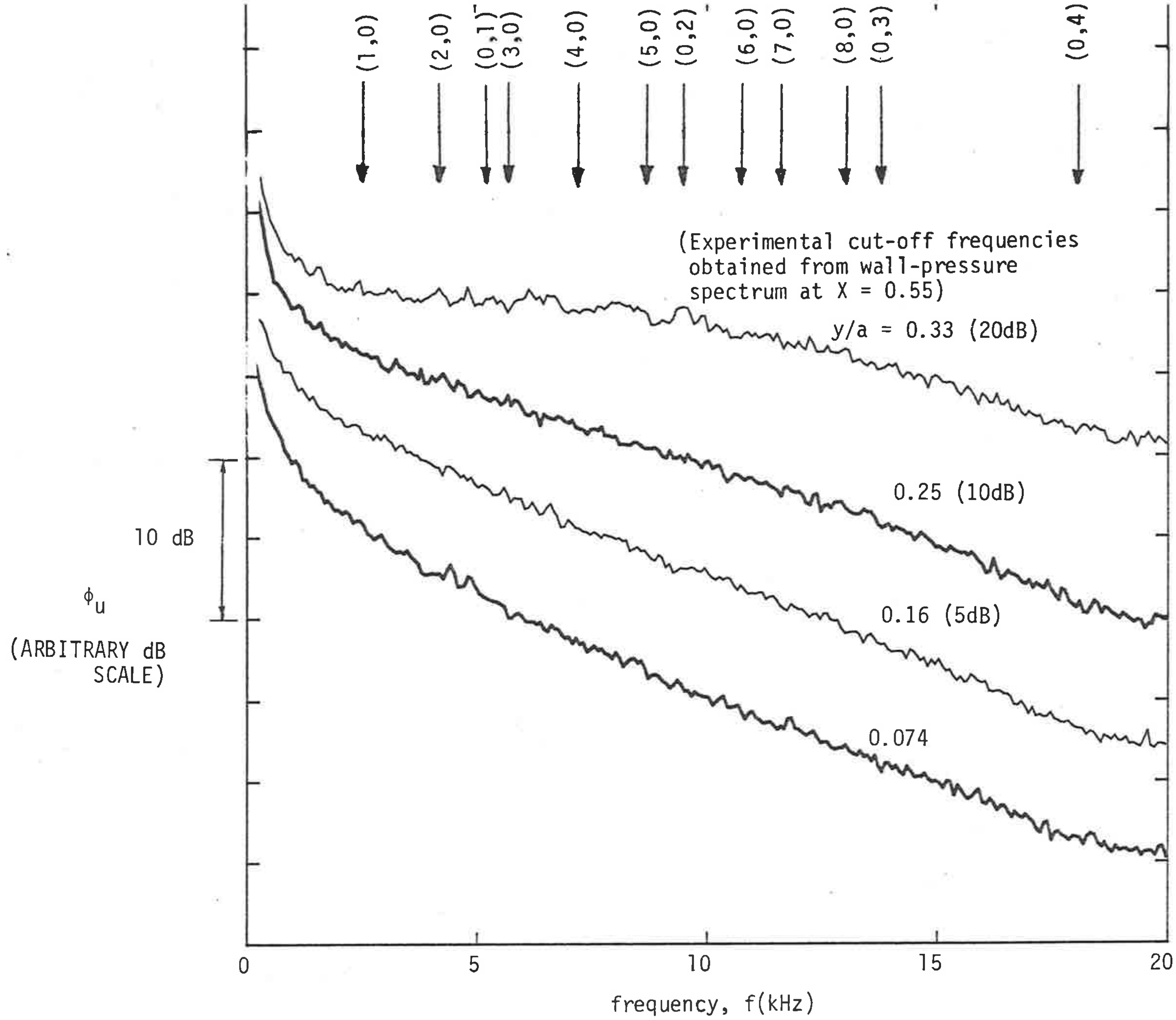

FIGURE 7.15a : VELOCITY SPECTRA AT X = 0.55, D_c = 0.86, D_o = 0.76, M_I = 0.35, $\bar{J}$ = 0.47

(Top three curves are each shifted up as shown)

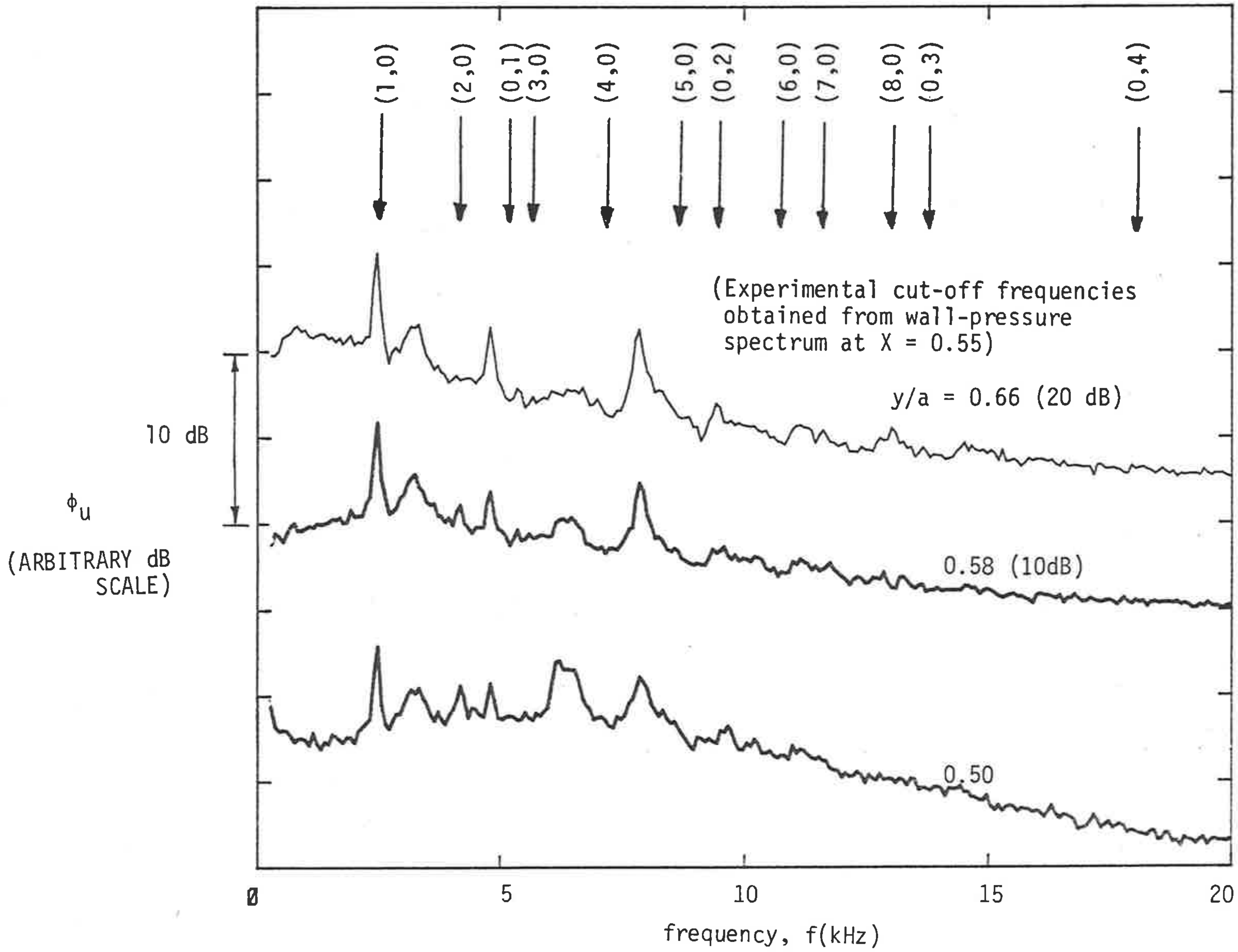

FIGURE 7.15b : VELOCITY SPECTRA AT X = 0.55, D_c = 0.86, D_o = 0.76, M_I = 0.35, $\overline{J}$ = 0.47

(Top two curves are each shifted up as shown)

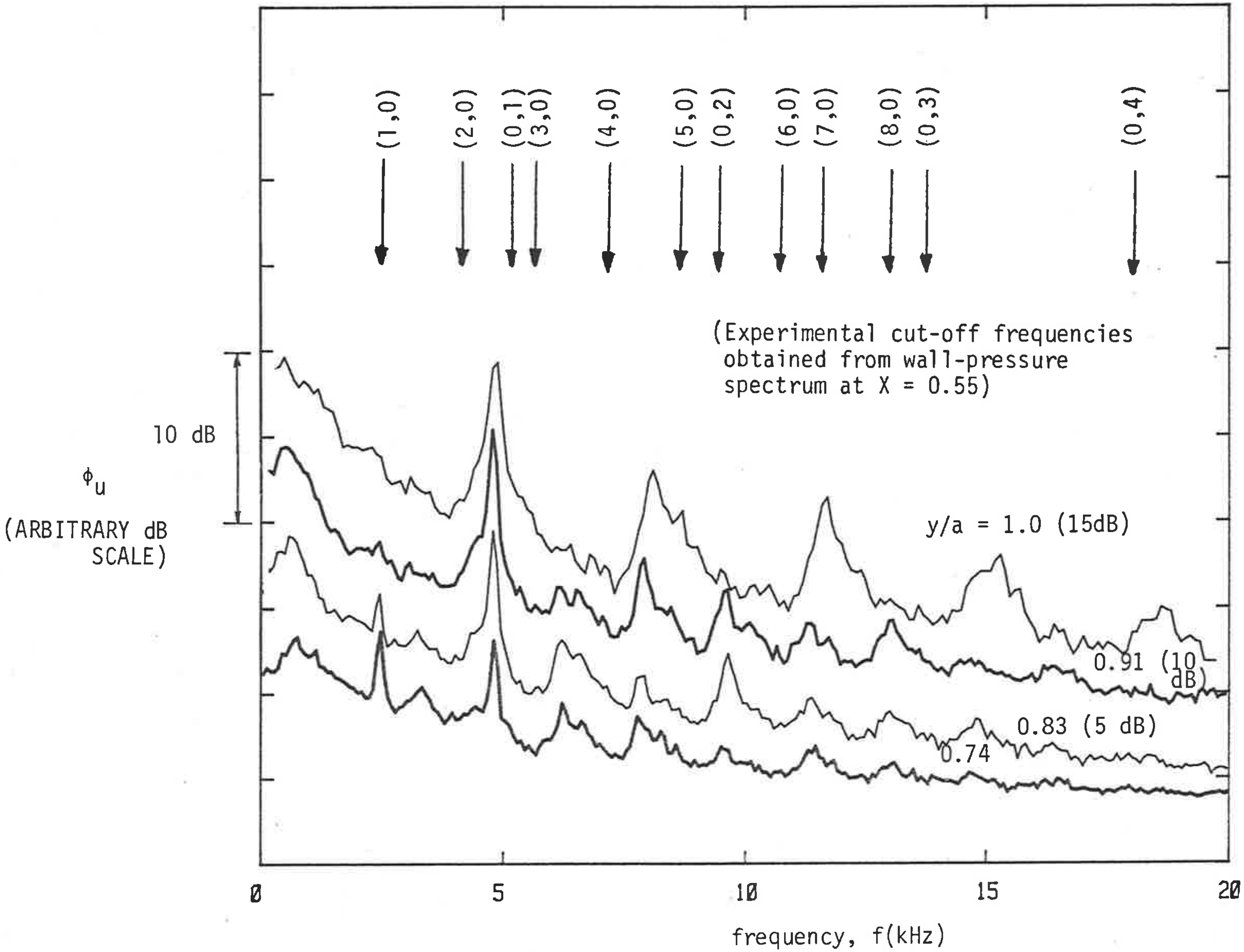

FIGURE 7.15c : VELOCITY SPECTRA AT X = 0.55, D_c = 0.86, D_o = 0.76, M_I = 0.35, $\overline{J}$ = 0.47

(Top three curves are each shifted up as shown)

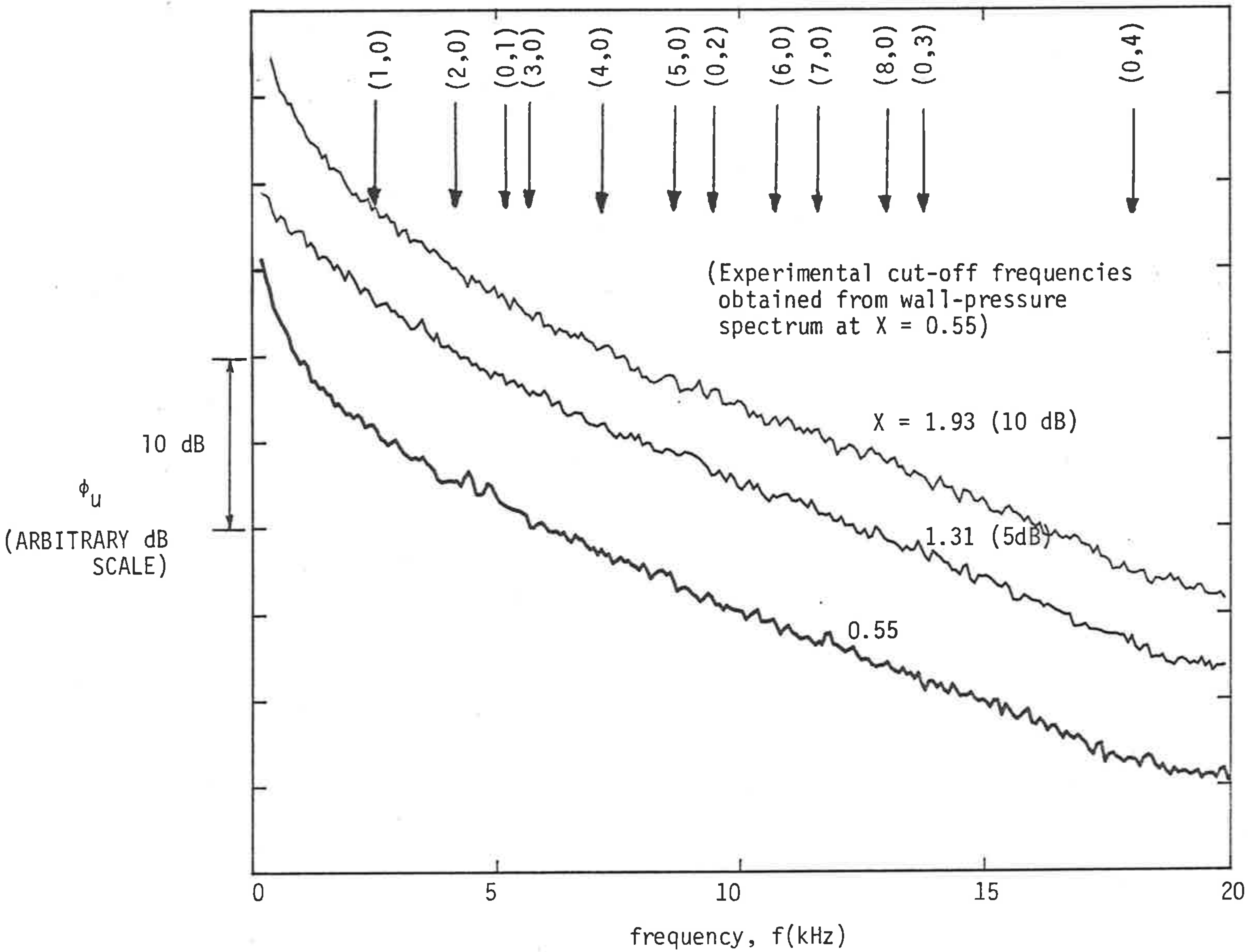

FIGURE 7.16a : VELOCITY SPECTRA AT $y/a = 0.074$, $D_c = 0.86$, $D_o = 0.76$, $M_I = 0.35$, $\bar{J} = 0.47$

(Top two curves are each shifted up as shown)

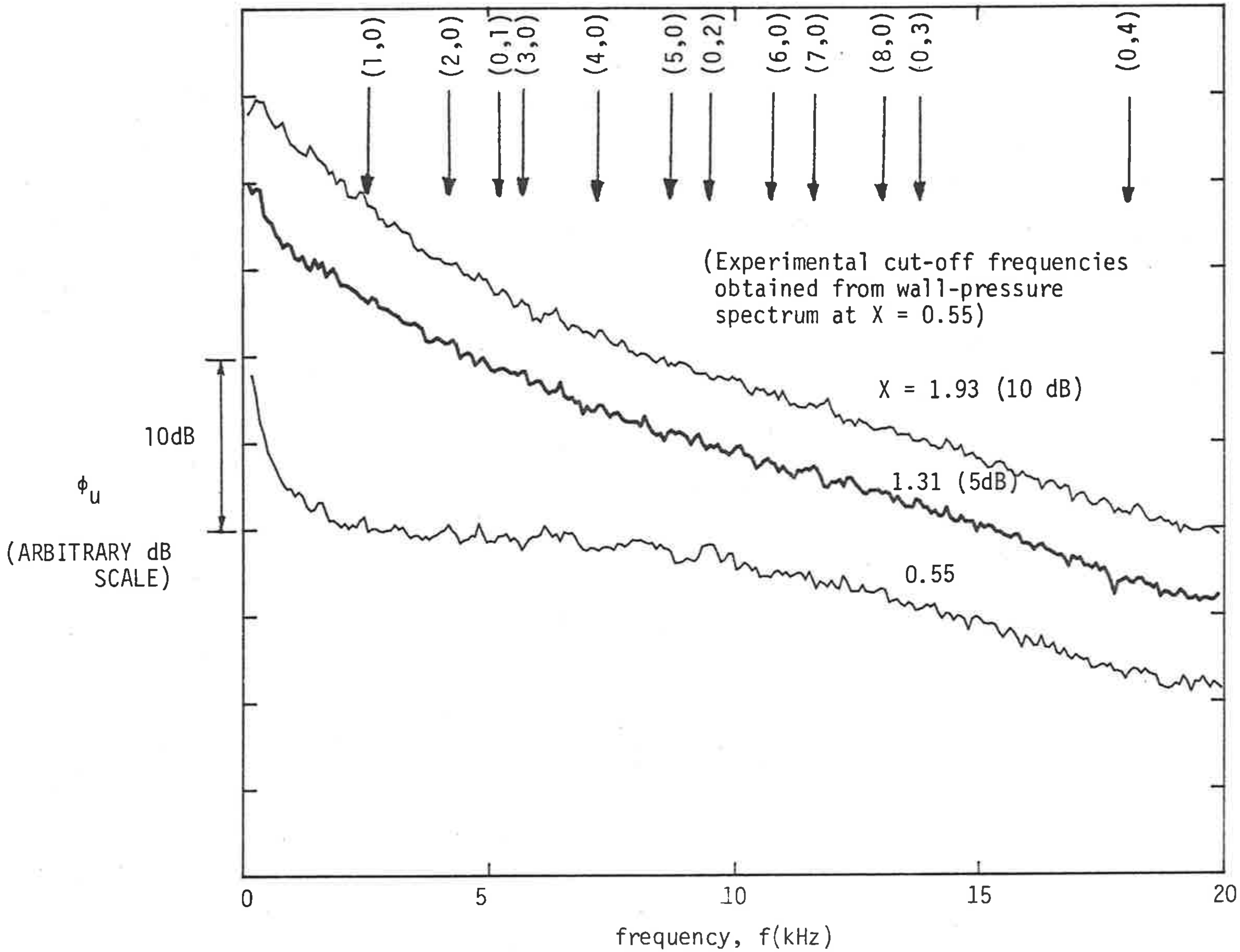

FIGURE 7.16b : VELOCITY SPECTRA AT y/a = 0.33, D_c = 0.86, D_o = 0.76, M_I = 0.35, $\overline{J}$ = 0.47

(Top two curves are each shifted up as shown)

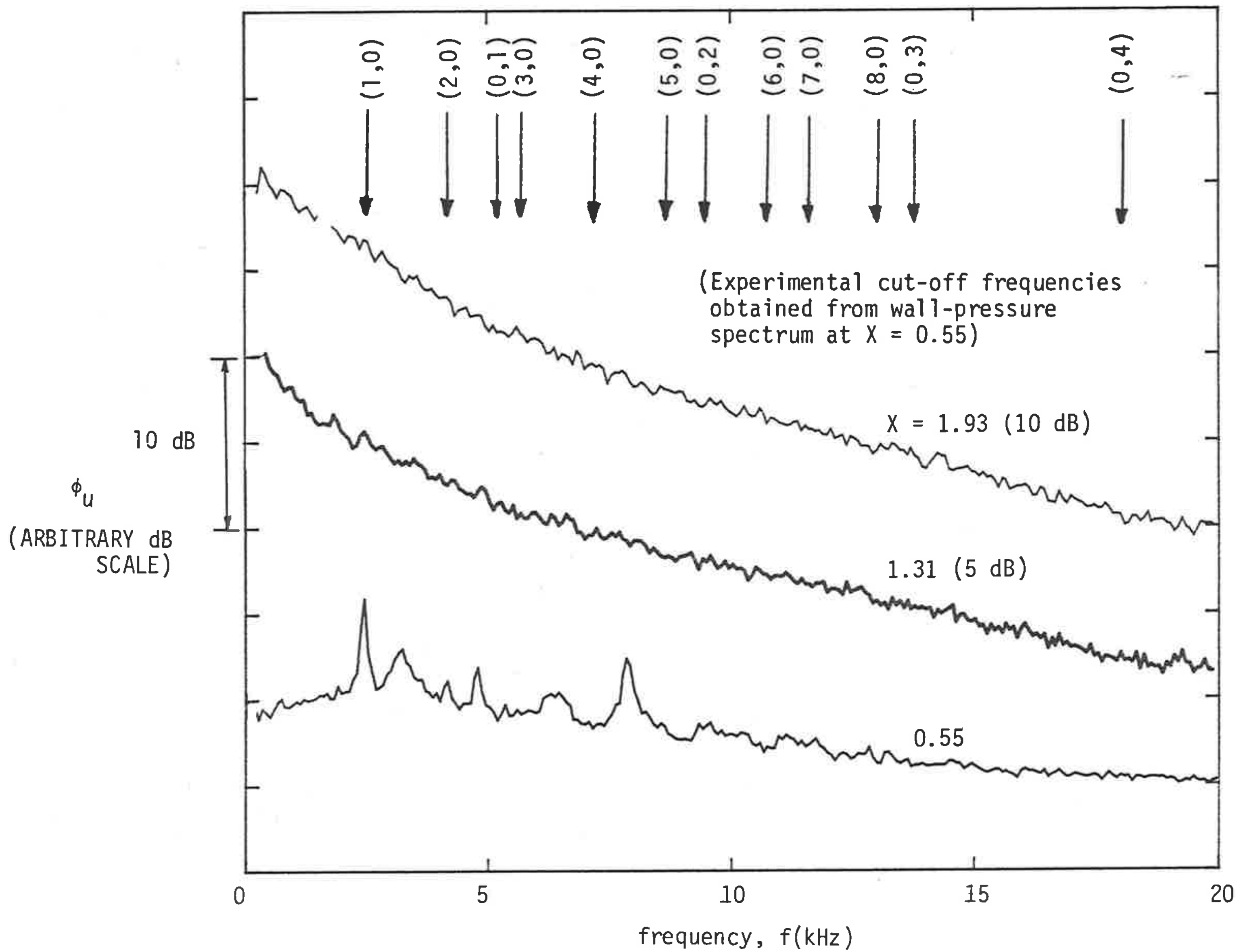

FIGURE 7.16c : VELOCITY SPECTRA AT y/a = 0.58, D_c = 0.86, D_o = 0.76, M_I = 0.35, $\overline{J}$ = 0.47

(Top two curves are each shifted up as shown)

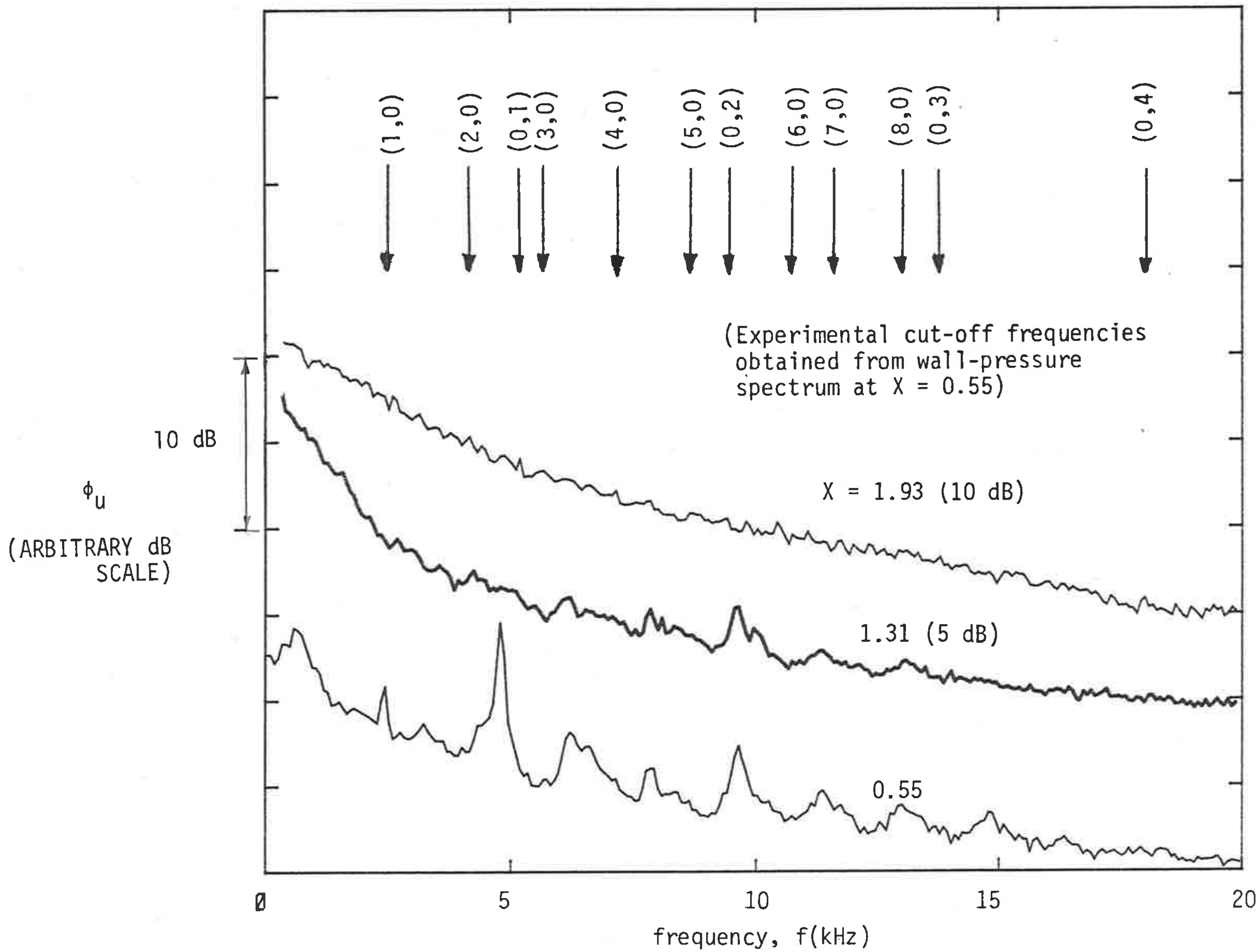

FIGURE 7.16d : VELOCITY SPECTRA AT $y/a = 0.83$, $D_c = 0.86$, $D_o = 0.76$, $M_I = 0.35$, $\overline{J} = 0.47$

(Top two curves are each shifted up as shown)

increasing X is the change in shape of the spectrum, particularly at low frequencies, which occurs between $X = 0.55$ and 1.31.

Cut-off frequencies shown on Figures 7.15 and 7.16 are experimental values obtained from wall-pressure spectra at the same streamwise positions.

At $X = 31.4$ (Figure 7.17) spectra measured at radial positions $0.074 < y/a < 0.66$ do not show any obvious acoustic spectral peaks. In non-dimensional form the spectra are similar to those for undisturbed pipe flow (except at high frequencies) in the central region of the pipe and a little less so closer to the pipe wall (Figure 7.18).

7.4.2 Upstream of the orifice

Spectra at $X = -1.65$ and -16.82 for $y/a = 0.074$, 0.28, 0.41, 0.58 and 0.91 are shown in Figures 7.19 and 7.20. No spectral peaks corresponding to the higher order acoustic modes are evident. The extent of similarity of the non-dimensional spectra (Figure 7.21) to those of the undisturbed flow is comparable to that observed at $X = 31.40$ well downstream of the orifice (Figure 7.18).

7.5 Regions where Higher-order Acoustic Modes are Detectable in Velocity Spectra

The regions where higher-order acoustic modes are detectable in the spectral data which have been presented in this chapter are indicated in Figure 7.22. It can be seen that detectability is confined to the separated-flow region (zone 3, Figure 5.1); it extends over the whole pipe radius close to the downstream side of the orifice plate, but shrinks towards the pipe centre-line as X increases.

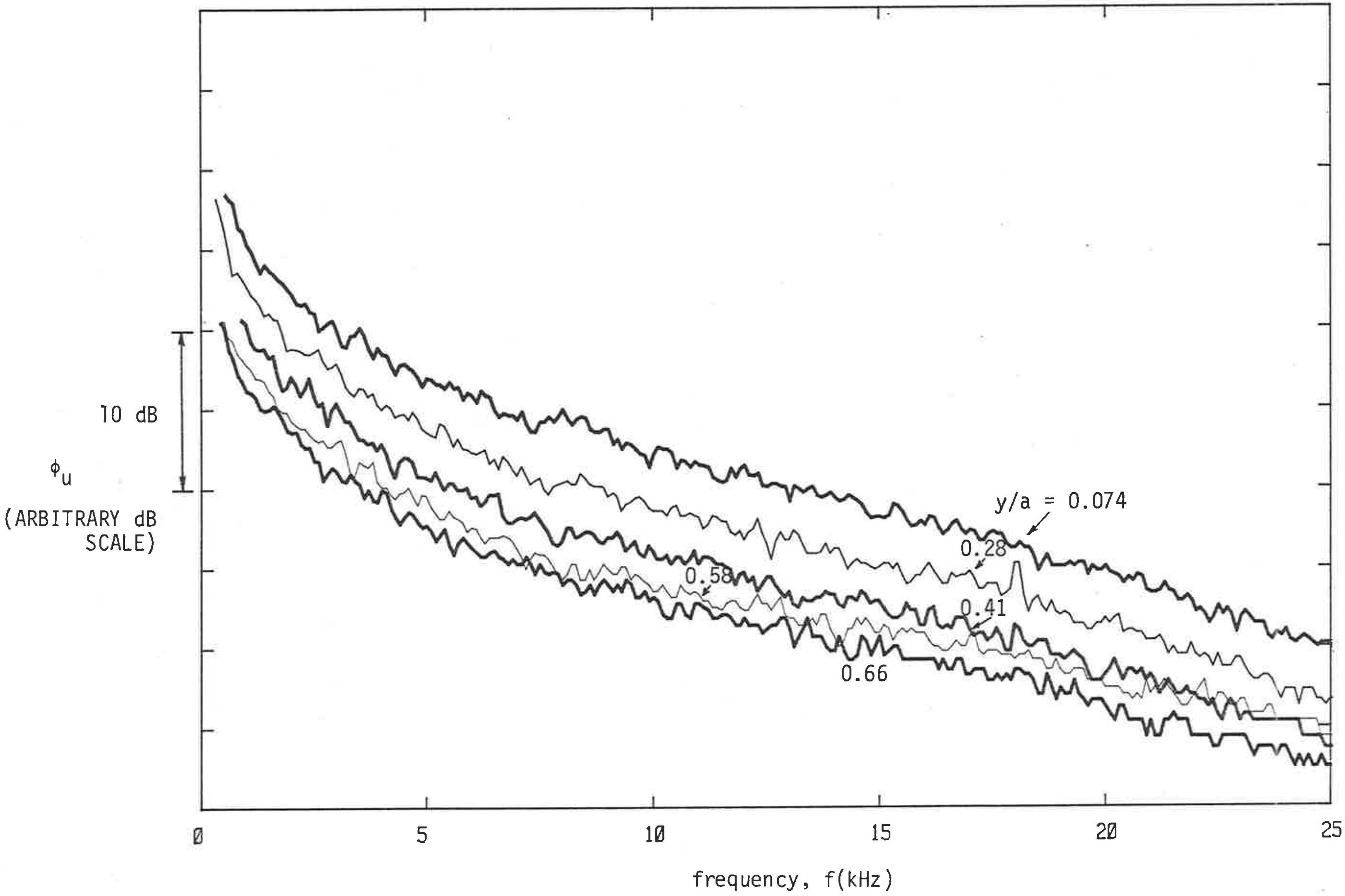

FIGURE 7.17 : VELOCITY SPECTRA AT X = 31.40, D_c = 0.86, D_o = 0.76, M_I = 0.35, $\bar{J}$ = 0.47

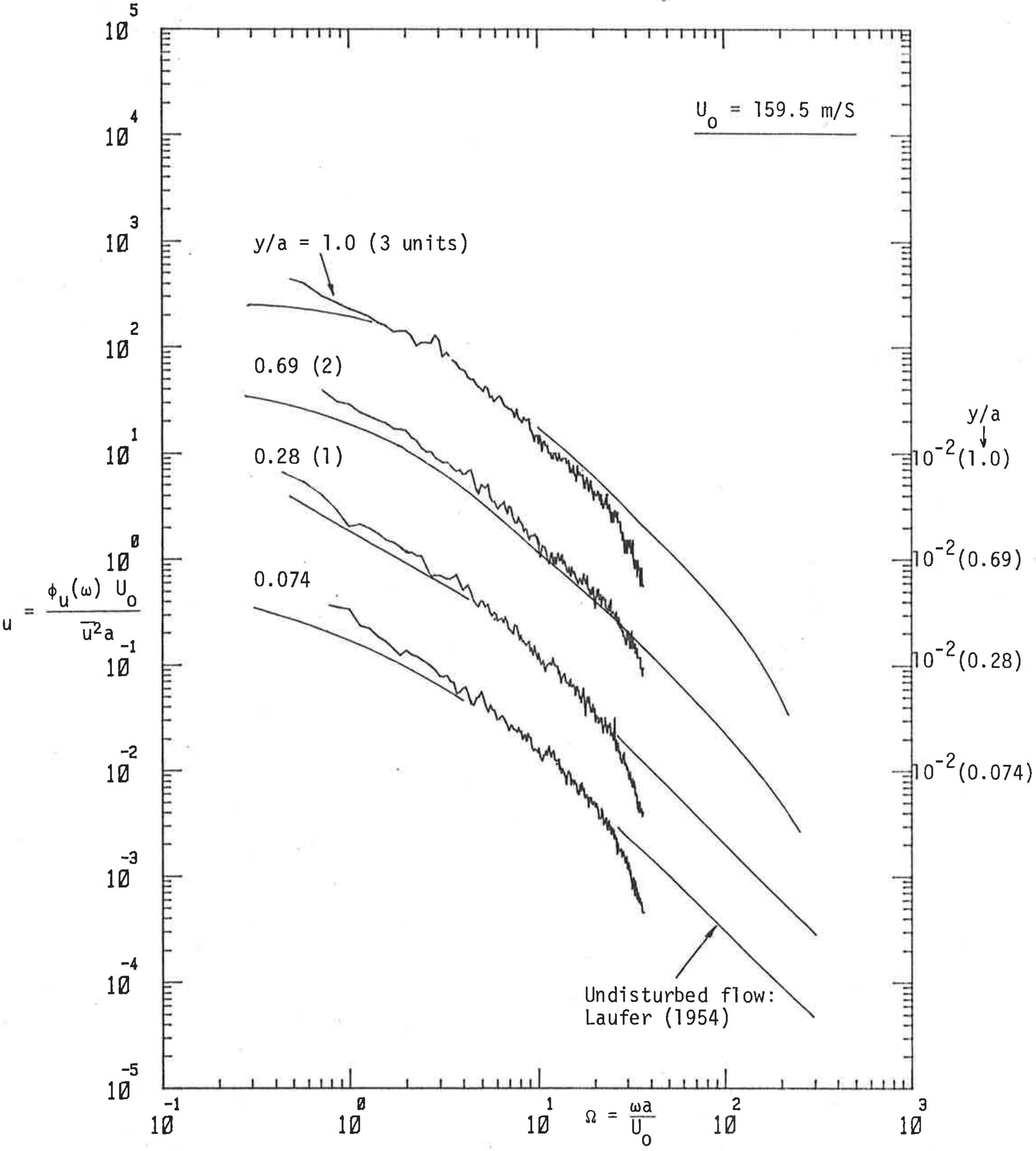

FIGURE 7.18 : NON-DIMENSIONAL VELOCITY SPECTRA AT X = 31.40, D_c = 0.86, D_o = 0.76, M_I = 0.35, $\overline{J}$ = 0.47

(Top three curves are each shifted up by one scale unit)

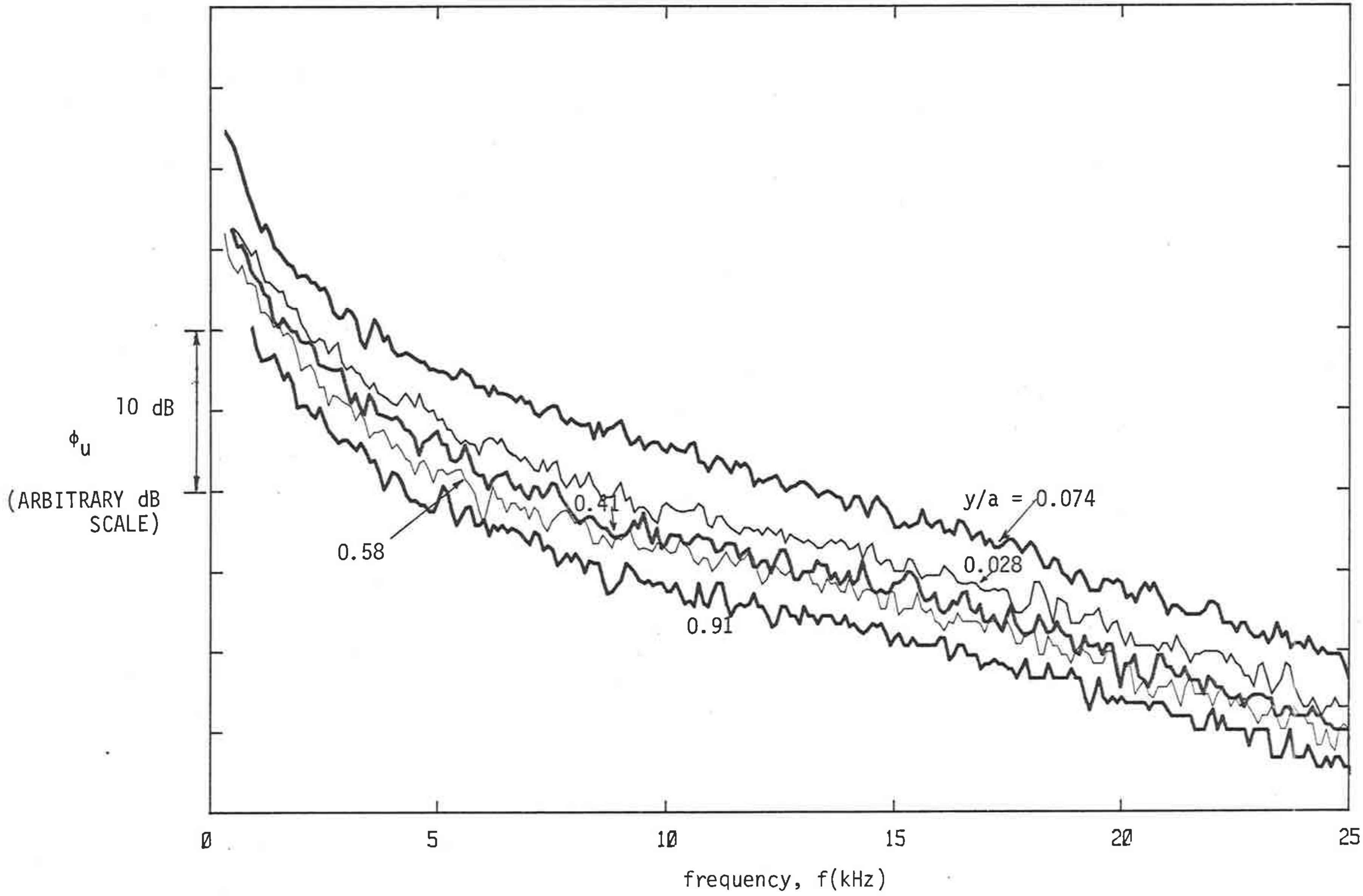

FIGURE 7.19 : VELOCITY SPECTRA AT X = -1.65, D_c = 0.86, D_o = 0.76, M_I = 0.35, $\overline{J}$ = 0.47

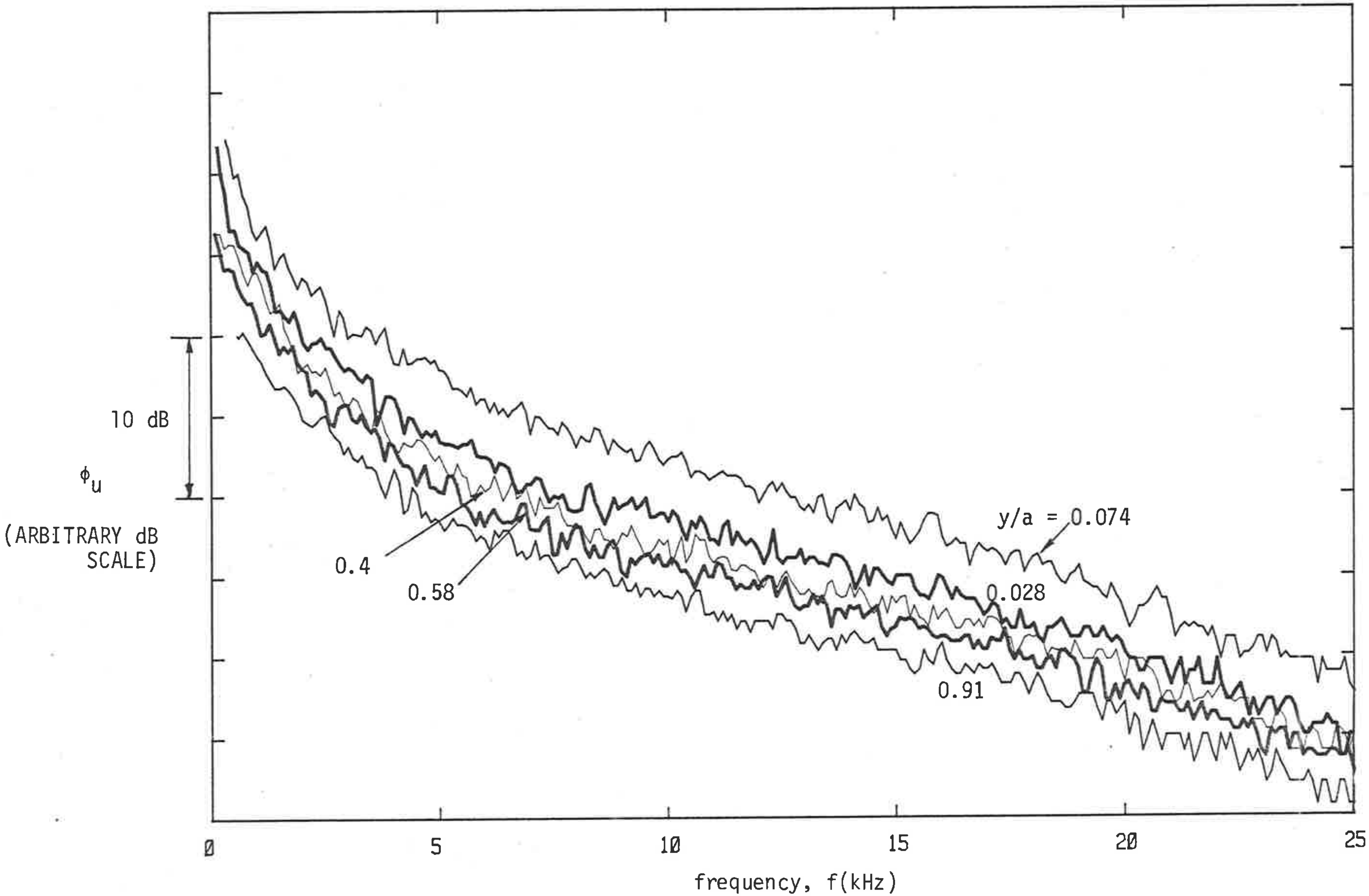

FIGURE 7.20 : VELOCITY SPECTRA AT X = -16.82, D_c = 0.86, D_o = 0.76, M_I = 0.35, $\overline{J}$ = 0.47

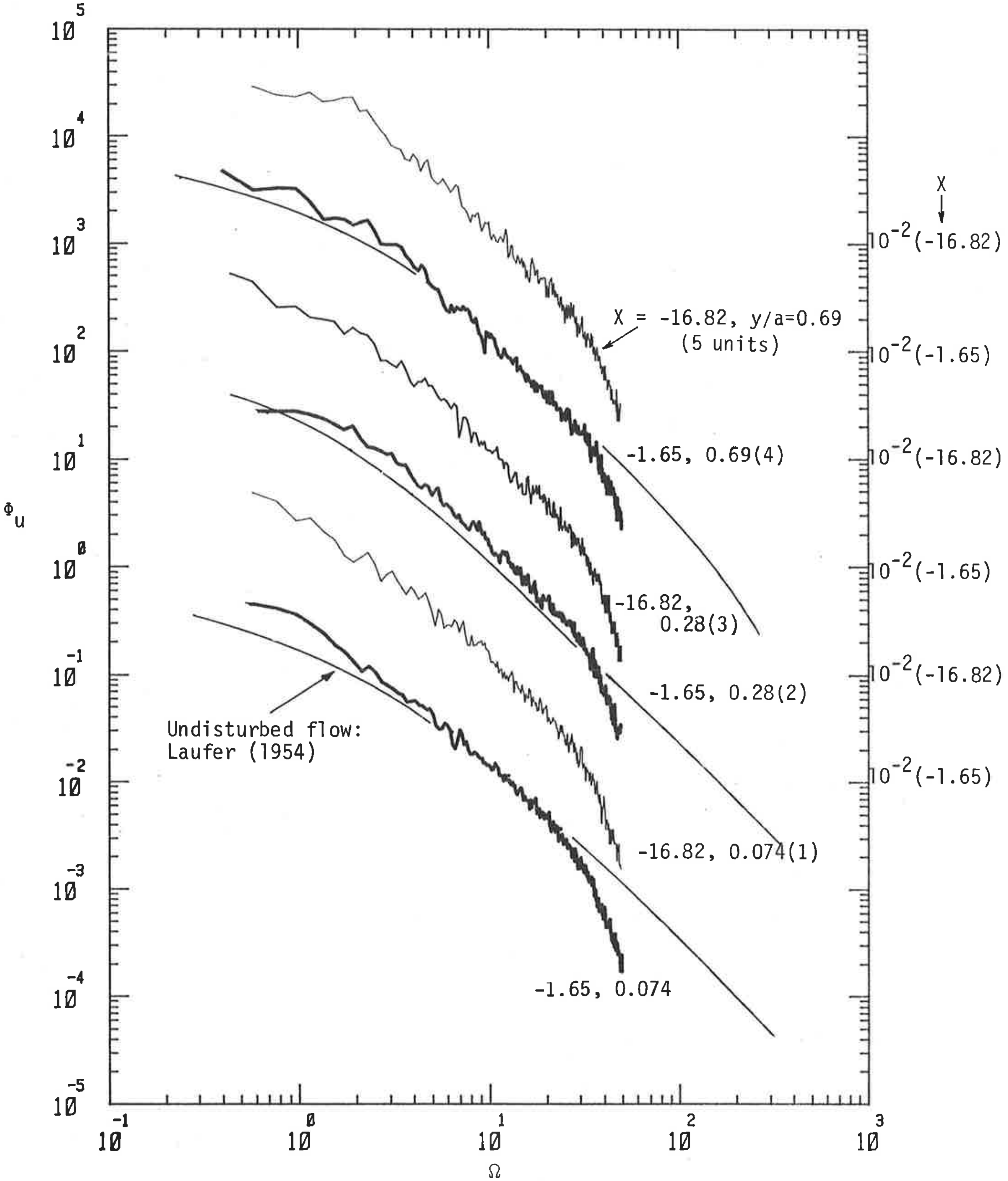

FIGURE 7.21 : NON-DIMENSIONAL VELOCITY SPECTRA, D_c = 0.86, D_o = 0.76, M_I = 0.35, $\bar{J}$ = 0.47

(Top five curves are each shifted up by one scale unit)

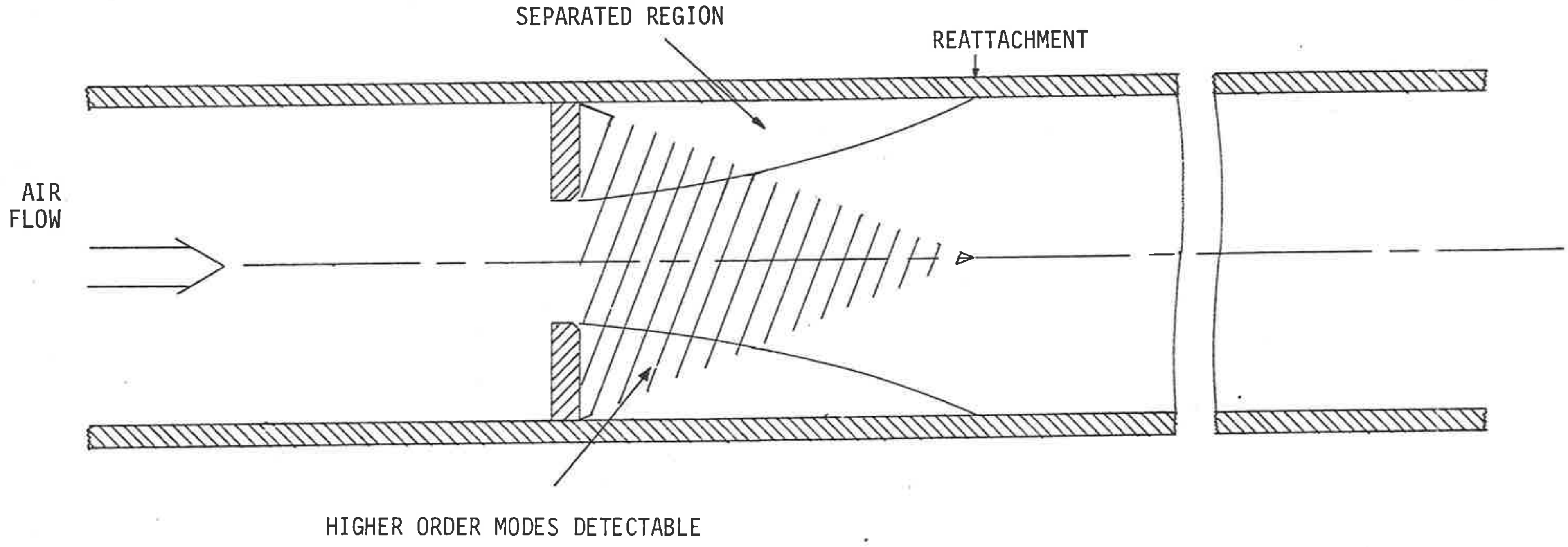

FIGURE 7.22 : REGION WHERE HIGHER ORDER ACOUSTIC MODES ARE DETECTABLE IN VELOCITY SPECTRUM

7.6 Modal Amplitudes and Cut-off Frequencies

7.6.1 Radial distributions of modal amplitude of axial particle velocity and acoustic pressure

In view of the fact that higher-order modes are detectable in the velocity spectra only in the separated-flow region, comparison of the experimental modal distributions of acoustic particle velocity with those derived from acoustic pressure distributions calculated for undisturbed fully-developed flow must be made with some reservation. However, acoustic mode shapes in the separated-flow region can be expected to be not too different from those in the fully-developed flow for the comparison still to be of interest.

Theoretical pressure distributions for the (1,0), (2,0), (3,0), (0,1) and (0,2) modes at their cut-off frequencies are shown in Figure 7.23(a); the corresponding distributions of axial particle velocity calculated by the approximate relation, equation (2.57), are shown in Figure 7.23(b).

The calculated particle-velocity distributions are compared with those derived from the experimental spectral data for $X = 0.55$ in Figure 7.24. It can be seen that there is a broad consistency between the theoretical and measured mode shapes.

7.6.2 Cut-off frequencies

Because of the limited region in which the higher-order acoustic modes are detectable, the velocity spectra do not add greatly to the information on with-flow cut-off frequencies obtained from the wall-pressure spectra. Table 7.1 summarises the velocity data for the (0,n) modes with $n = 1\text{-}4$; they

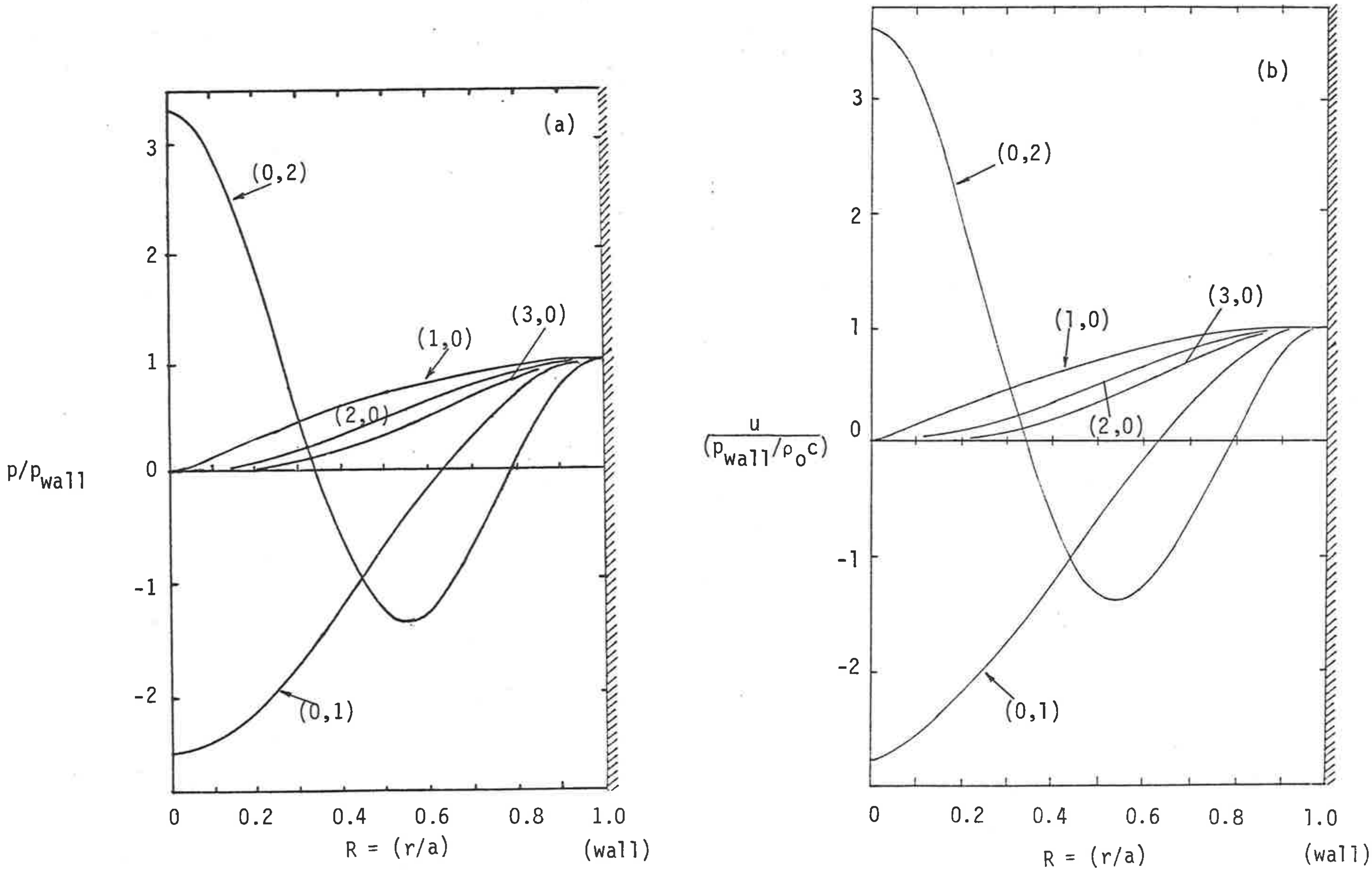

FIGURE 7.23 : THEORETICAL ACOUSTIC PRESSURE AND MODAL PARTICLE VELOCITY AMPLITUDE VARIATION ACROSS PIPE RADIUS FOR $M_o = 0.45$, $\Omega = \Omega_{co}$

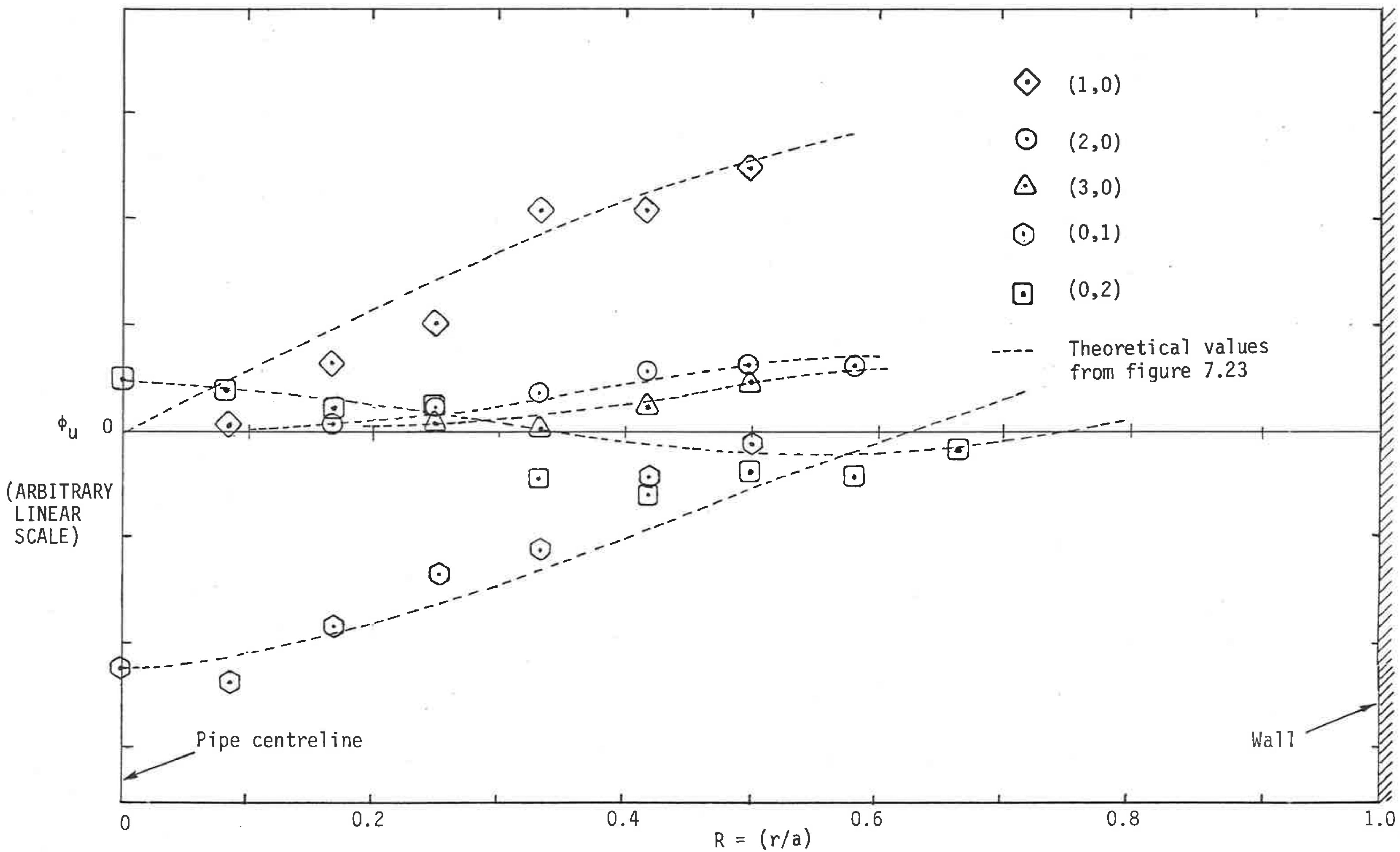

FIGURE 7.24 : THEORETICAL AND EXPERIMENTAL VARIATION OF MODAL PARTICLE VELOCITY AMPLITUDE AT X = 0.55, D_c = 0.86, D_o = 0.76, M_I = 0.35, $\overline{J}$ = 0.47

apply to X = 0.55, although the data of Figure 7.4 indicate that the modal peak frequencies do not change perceptibly with X over the range 0.28 < X < 0.83.

TABLE 7.1

MODAL PEAK FREQUENCIES IN VELOCITY SPECTRA, X = 0.55

D_c	D_0	M_0	Mode	Frequency of Modal Peak f (kHz)	Frequency of Modal Peak $(\frac{\omega a}{c_r})$	Average M_e	A $=M_e/M_0$
0.58	0.62	0.49	(0,1)	5.6	3.7	0.32	0.65
			(0,2)	9.8	6.5		
			(0,3)	14.1	9.4		
			(0,4)	18.6	12.4		
0.72	0.76	0.79	(0,1)	5.0	3.3	0.46	0.58
			(0,2)	9.2	6.1		
			(0,3)	13.3	8.9		
			(0,4)	17.4	11.5		
0.86	0.76	1.07	(0,1)	4.8	3.1	0.60	0.56
			(0,2)	8.1	5.4		
			(0,3)	11.7	7.8		
			(0,4)	14.9	9.9		

Where comparisons of the frequencies, given in Table 7.1, at which modal peaks in the velocity spectra occur, with corresponding cut-off frequencies obtained from wall-pressure spectra, Figure 6.37, can be made, they show that the two are not the same: for the (0,1) mode, at least, the velocity peak appears to occur at a frequency less than the modal cut-off frequency. The interpretation of this is not clear, particularly as the comparison is confined to the region of disturbed flow.

Table 7.1 also shows non-dimensional values of the modal peak frequencies as $(\omega a/c_r)$, and the corresponding values of M_e

and $A = M_e/M_0$ derived from them by equation (6.19) as if the velocity peaks did correspond to cut-off frequencies. The values of A are very much lower than the theoretical values (0.90 - 0.91) for undisturbed fully developed flow and also lower than the reduced value (0.70) derived from the wall-pressure spectra. Since the mean-velocity profiles do not change greatly with flow Mach number, the value of A at a given streamwise position X might be expected to be independent of the flow speed. The values given in Table 7.1 show this expectation is roughly fulfilled.

7.7 Summary and Conclusions

The results presented lead to the following conclusions.

(1) The presence of acoustic modes is shown up by peaks in the axial velocity-fluctuation spectra at frequencies close to, but apparently not equal to, the modal cut-off frequencies.

(2) The acoustic modes are detectable, above the turbulent velocity fluctuations, only in the separated-flow region downstream of the orifice.⊛

(3) The frequencies of the modal peaks appear to be independent of streamwise and radial position within the separated-flow region, and decrease as flow rate increases in a similar way to cut-off frequencies.

(4) To the limited extent that comparisons can be made, the measured mode shapes for axial acoustic particle velocity are similar to theoretical shapes derived from calculated acoustic pressure distributions.

(5) Very soon after flow reattachment and within only a few pipe diameters of the orifice plate, the velocity spectrum is completely dominated by turbulent fluctuations and its shape becomes very similar to that for undisturbed flow.

⊛ There is rapid reduction of modal amplitude of the acoustic modes relative to the background turbulence level as $X \rightarrow X_R$. This effect appears to result from increased turbulence level rather than attenuation of acoustic modes.

CHAPTER 8

FLUCTUATIONS IN SEPARATED REGION

8.1 Introduction

As has been discussed in Chapter 5, the reattachment region is highly unsteady. The separated shear layer grows into the recirculating flow and curves sharply in the reattachment zone and impinges on the wall. Bradshaw and Wong (1972) suggested that at reattachment eddies bifurcate, part travelling upstream and part downstream. McGuinness (1978) observed low frequency static pressure fluctuations in the separation bubble at the entrance of a pipe and concluded that these fluctuations are caused by eddies moving upstream in the low speed recirculating flow. Knisely and Rockwell (1982) studied the low frequency oscillations in cavity flow and observed that they are caused by feedback of disturbances from the impingement point. Studies by Eaton and Johnston (1982) of flow over a backward facing step using a thermal tuft, Simpson, Strickland and Barr (1977) using a laser anemometer and flow visualisation work of Smits (1982) confirm the existence of low frequency oscillations and also the interpretation that the eddies deflect alternately upstream and downstream in the reattachment region.

This Chapter is concerned with the nature and cause of low frequency motion of the separation bubble in the region downstream of the orifice plate. Mean positions of separation and reattachment points are derived from measurements of γ_p, the fraction of time for which the flow is in the downstream direction at a given point on the surface. Reattachment and separation points are defined as the points with 50% downstream flow (Eaton, Jeans, Ashjaee and Johnston, 1979, Simpson 1981); these are also points where the mean wall shear stress and mean flow velocity gradient are zero, and, therefore, where the mean velocity at a small finite distance from the wall would also approach zero. The output of a single hot-wire anemometer is always positive, regardless of the flow direction, being characteristic of the heat transfer from the wire. Therefore a single hot-wire anemometer is direction-insensitive and cannot be used to give an unambiguous indication of flow reversal or separation. To overcome this problem, dual wire or dual film anemometers have been used. In dual wire probes, the heated wake of one hot wire can be sensed by the second wire directly behind it. The difference in the two hot wire signals serves as the indicator of the flow direction, because the relative magnitude of the two hot wire outputs depends on which wire is in the wake of the other. Günkel, Patel and Weber (1971), Cook and Redfearn (1975) and Jerome, Guitton and Patel (1971) used probes of this kind in highly turbulent and reversing flows. Horstman and Rose (1977), Mier and Kreplin (1971) and McCroskey and Durbin (1972) used a similar technique with dual surface films to detect the flow direction.

Recently, three wire probes, where the wake of a central heated wire is detected by temperature-sensing wires on either side of it, have been used. Rubensin, Okuno, Mateer and Brosh (1975) used buried wire skin friction gauges of this type. Downing (1972) mounted the temperature-sensor wires at right angles, so as not to disturb the flow over the heater wire, but this made the probe unable to cope with the lateral components of velocity. Eaton, Jeans, Ashjaee and Johnston used a three wire probe in the flow behind a backward facing step. Their system consists of a hot wire heater and sensor elements operated as resistance thermometers. The pulsed wire probe of Bradbury and Castro (1971) is a one dimensional velocity sensor, but it has a limitation on the maximum velocity it can measure for a given wire spacing (e.g. 14 m/s for 1.25mm). Carr and McCroskey (1979) used a three element probe, operating all the wires as constant temperature anemometers, and thereby obtaining a velocity signal from the heater wire in addition to the direction from the temperature-sensor wires.

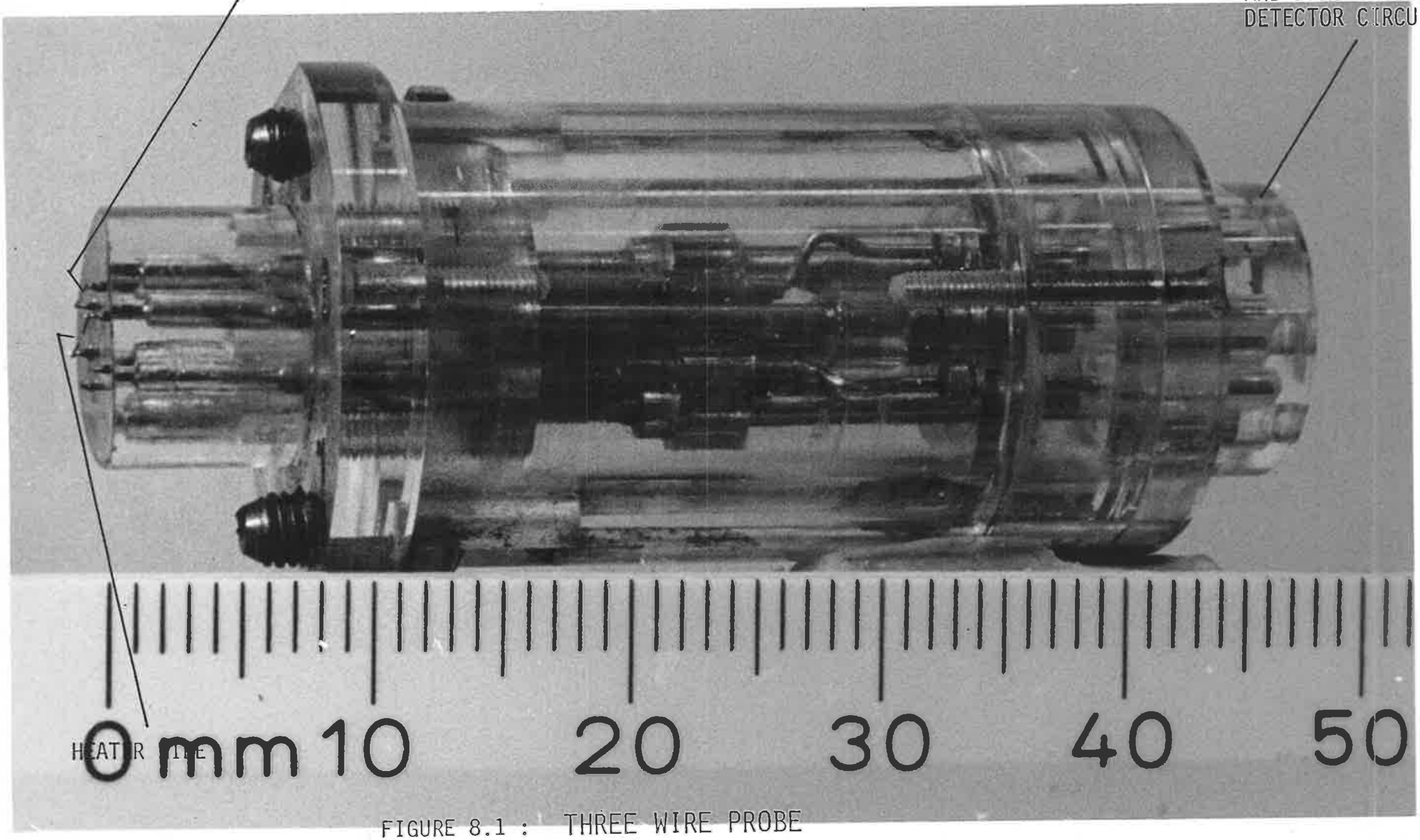

FIGURE 8.1 : THREE WIRE PROBE

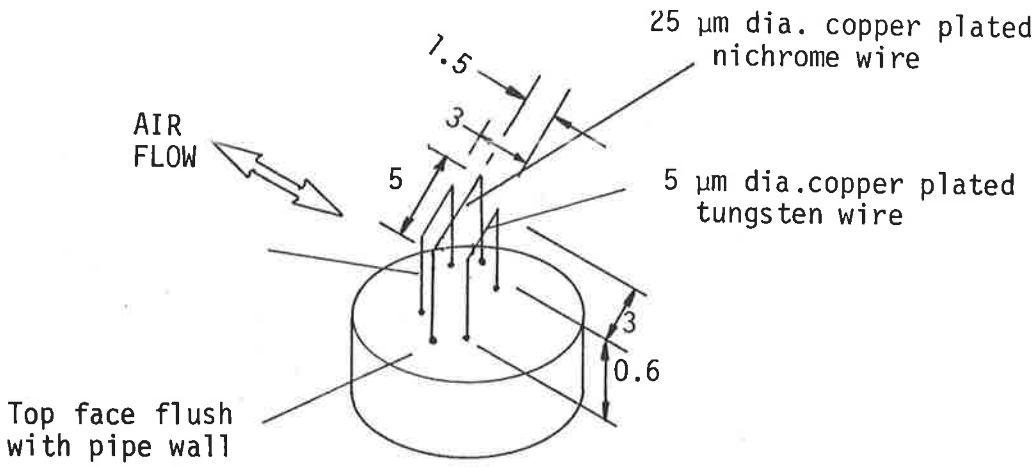

(a) Wire Geometry

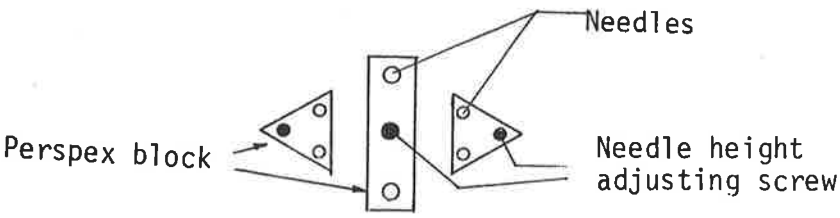

(b) Plan of geometry of needle and adjusting screw geometry

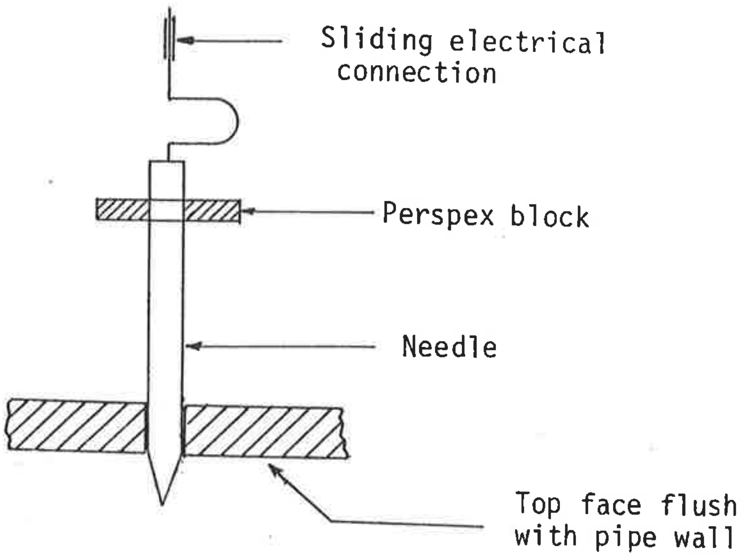

(c) Electrical connection to needles

FIGURE 8.2 : THREE-WIRE PROBE DETAILS

(all dimensions in mm)

Shivaprasad and Simpson (1982) used a modified three-wire probe similar to the one described by Eaton, Jeans, Ashjaee and Johnston, but of somewhat different geometry, to give the indication of the instantaneous direction of the flow velocity.

8.2 Probe Design and Operating Details

The probe used in the present investigation is shown in Figure 8.1. It consists of three parallel wires, a central, heated, velocity-sensing wire and two temperature-sensing wires, each mounted on a pair of sewing needles (0.2mm diameter). The probe body is made of perspex and the top surface, which is exposed to the flow, is machined to match the profile of the pipe. Each set of needles is mounted on a separate perspex block; a screw from the bottom winds the perspex block up or down, thereby adjusting the height of the needles protruding from the top surface of the probe. This arrangement and the needle spacings are shown in Figure 8.2. A flexible sliding contact (to take care of misalignments in the hole) for the electrical connections, is provided for each needle.

The temperature-sensors are tungsten wires, 5 μm in diameter, copper plated at each end, with a sensing length of ~ 1.5 mm. The heater and velocity-sensing wire used is nichrome, 25 μm in diameter, also with a 1.5mm sensing length and copper plated ends. All wires are soft soldered to the needles. The probe fits in the instrumentation holes of the pipe section (Figure 3.4) and once mounted becomes an integral part of the test surface. The needles can protrude through the clearance holes in the face of the outer shell up to 6 mm, to facilitate the mounting of the wires. Connections to the wires are provided through pins in the outer shell of the probe.

The heater wire is operated at high temperature, ~ 600-700°C, by a DISA constant temperature, 55M10 bridge. Since nichrome has a low temperature coefficient, ~ 0.0004, this requires an overheat ratio of only about 1.25, for a power dissipation of 8-10 watts. The choice of 25 μm diameter wire was a compromise between wires of larger diameter, which were ruled out on account of poor frequency response and the problem of soft soldering them to the needles, and smaller size wires, e.g. 5μm, which have to be operated at high overheat ratios (> 1.8) and therefore tend to burn out frequently. The wire is left on for several hours, before use, to stabilize. Typical resistances of heater and temperature-sensor wires are 3.4 Ω and 6.3 Ω respectively. By taking both the temperature-sensor wires from the same batch, it is possible to match their resistances within about ± 0.2 ohm. Measurements were made with 1-1.5 amp current through heater wire; this heater current was found to be adequate, and above this γ_p was found to be independent of heater current.

Initial trials with the temperature-sensor wires operating as constant-current and constant-temperature anemometers (at low overheats ~ 1.1) were not very successful, as in both cases the wires were too sensitive to velocity fluctuations. It was difficult to separate changes in output due to flow from those due to the heated wake. Therefore an electronic circuit similar to that used by Eaton, Jeans, Ashjaee and Johnston was adopted (Figure 8.3). The two temperature wires form two arms of a Wheatstone bridge network, the other two arms being fixed 5kΩ resistors. To adjust for small differences in the temperature-sensor resistances, the probe is mounted in the pipe with flow (and heater wire CTA turned off) and the resistor connected in series with one of the wires adjusted until null bridge output is obtained. The output from the Wheatstone bridge is amplified 1000 times and then fed to a zero-crossing detector, which gives an output of 0 or -9 volts

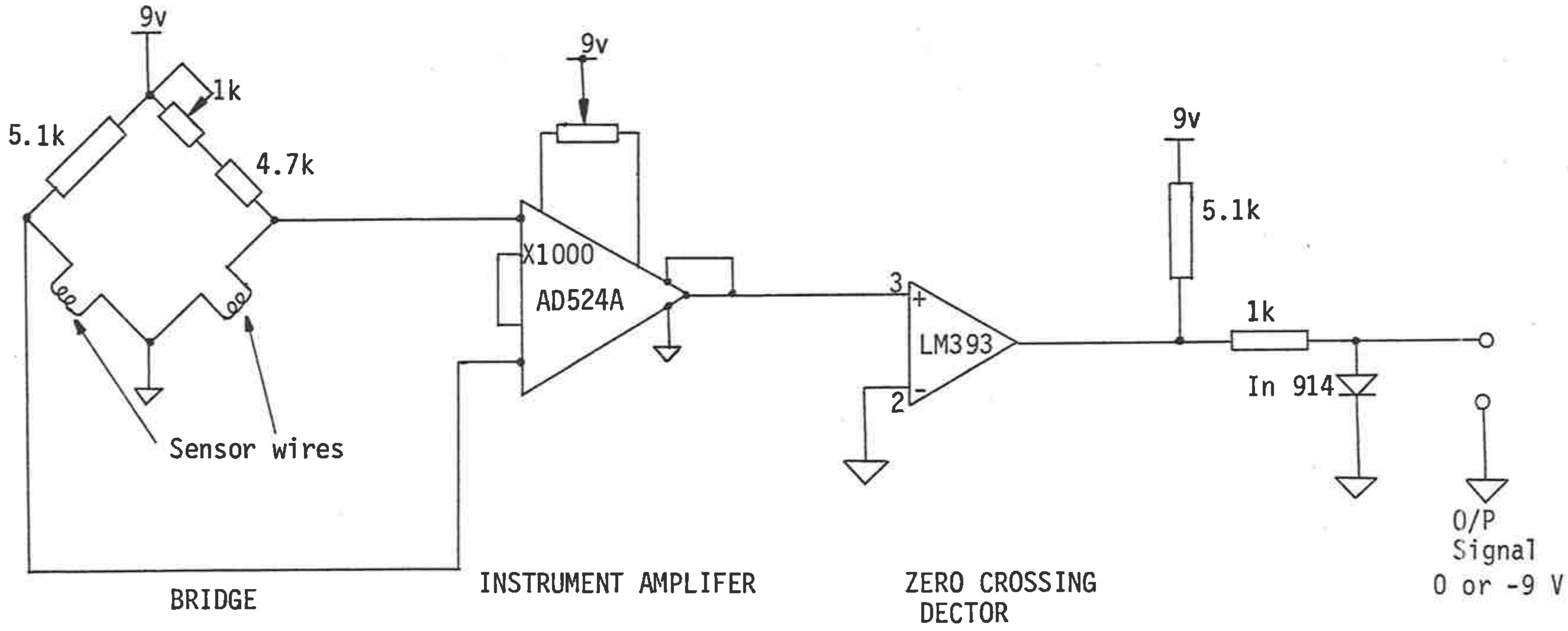

FIGURE 8.3 : THREE-WIRE PROBE DIRECTION DETECTOR

depending upon whether the output of Wheatsone bridge is positive or negative (i.e. which wire is hotter). The offset of the amplifier was adjusted till the output signal fluctuated between zero and -9V. An output of -9 volts was selected so that the signal could be directly fed to the 12-bit A/D converter.

If there is no temperature difference between the wires, electronic noise will cause the output to switch between 0 and -9V at high frequency. The signal due to the temperature difference between the wires is always greater than the electronic noise (2-3mV). Although the null voltage from the Wheatstone bridge and offset adjustment on the amplifier were quite stable, they were checked before each run.

All three wires were set at a distance of 0.6mm from the pipe wall for the present measurements.

8.3 Measurement of Mean Reattachment length

The probe has been used to measure γ_p and also the velocity signal from the heater wire, for the flows D_0 = 0.62, 0.69 and 0.76, D_c = 0.72 and 0.86. For this purpose, the signal from the CTA is fed through a 20dB attenuator (because the signal from the hot wire is generally more than 7 volts and the amplifier provides a maximum of 7 volts offset) and offset amplifier to one channel of the 12 bit A/D converter. The signal from the direction-detector circuit is fed to another channel of the same A/D converter (Figure 8.4). The attenuator and amplifier combination is calibrated using a very stable voltage source (Datel type DVC 8500). For sampling rates greater than 2kHz the rate does not seem to make any difference in the value of γ_p, but a higher sampling rate, 5 kHz or 15 kHz, was used to allow the hot wire signal to be reconstructed.

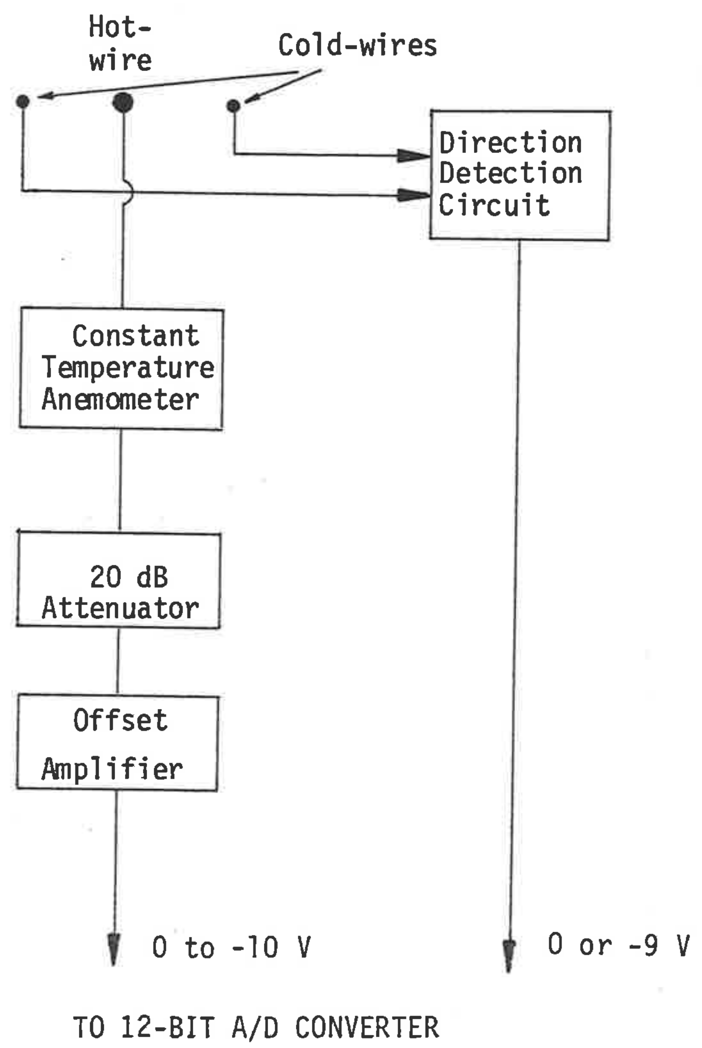

FIGURE 8.4 : THREE-WIRE PROBE DATA ACQUISITION PROCEDURE

Measurements downstream the orifice plates have been obtained for a series of streamwise locations at intervals of 10-25mm. Data from several runs each of about 5 seconds duration have been averaged to give percentage downstream flow for any given location. The maximum difference in the averaged value of γ_p was less than 5% between successive runs for the same position and even lower with larger averaging time. To check the geometrical symmetry, the probe was rotated by 180° and the γ_p measurements reflected. Again the variation in the value of γ_p was less than 5%.

Variation of γ_p with the streamwise distance X, for the flow $D_0 = 0.82$, $D_C = 0.86$, is shown in Figure 8.5. Measurements were continued up to the point X = 2.62, where the entire flow is in downstream direction, i.e. $\gamma_p = 1$. At about half way along the length of the separation bubble γ_p reaches a minimum of about 3%, i.e. the flow is predominantly in the upstream direction; γ_p does not seem to reach zero, indicating that the flow is never entirely in the upstream direction. γ_p rises steeply beyond this point and at $X \approx 2.6$, $\gamma_p = 1$. Results obtained by surface fence gauge for this flow are also shown on Figure 8.5. There is a remarkable similarity in the general shape of the two curves, and the mean positions of the reattachment point (γ_p = 50% and $\Delta P = 0$) obtained by two methods are nearly the same.

γ_p values obtained for the flows D_0 = 0.62, 0.69 and 0.76 with $D_C = 0.86$ are shown in Figure 8.6. A curve for the lower flow speed obtainted with flow $D_0 = 0.62$, $D_C = 0.72$ is also included. In general the curves are similar, with the γ_p= 50% crossing shifting upstream with increasing flow rate (or increasing D_0 for a given choke). Reattachment lengths derived from these measurements and the surface fence gauge results are very close to each other (Figure 8.6).

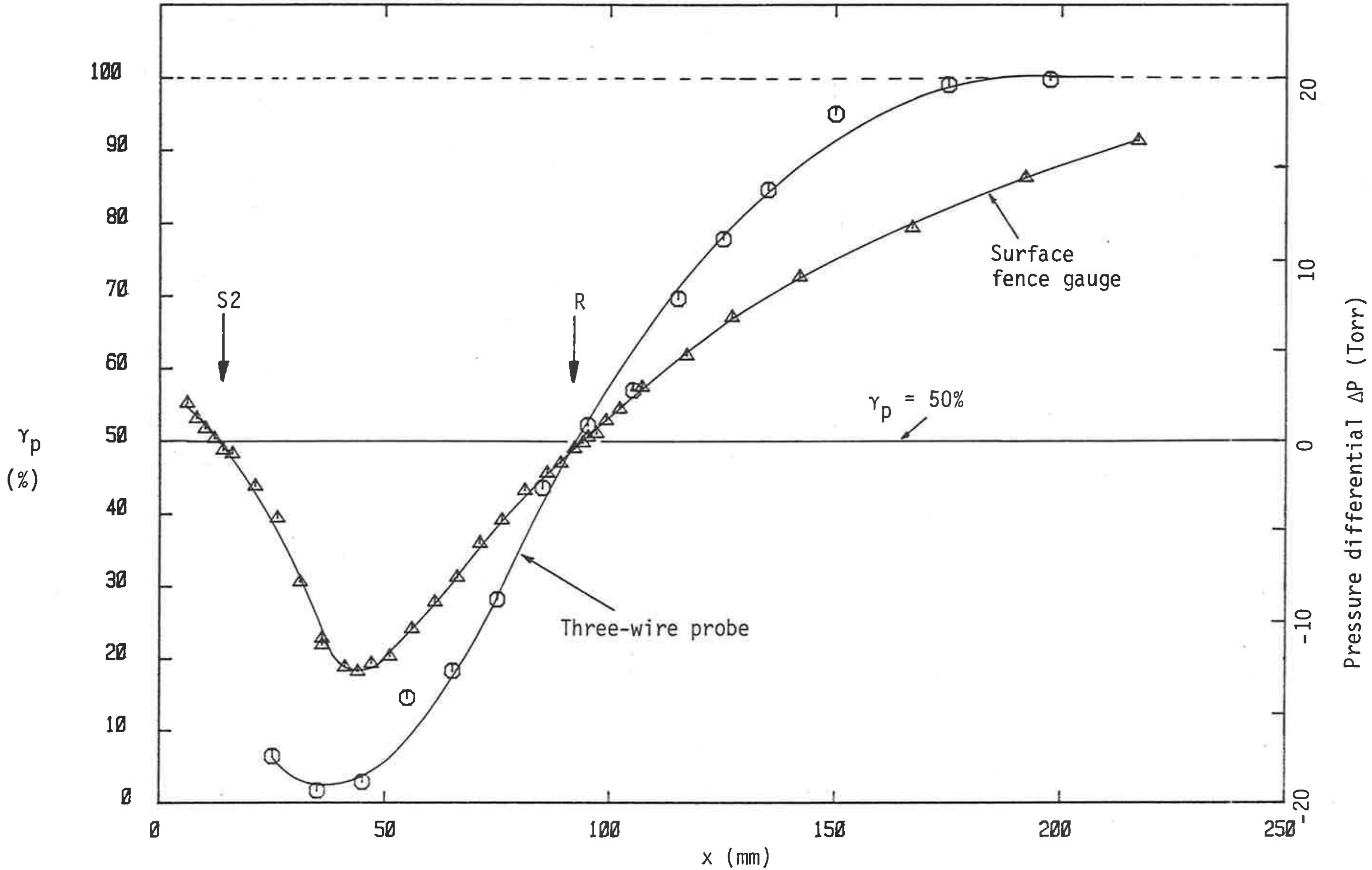

FIGURE 8.5 : MEAN REATTACHMENT LENGTH OBTAINED FROM THREE WIRE PROBE AND SURFACE FENCE GAUGE

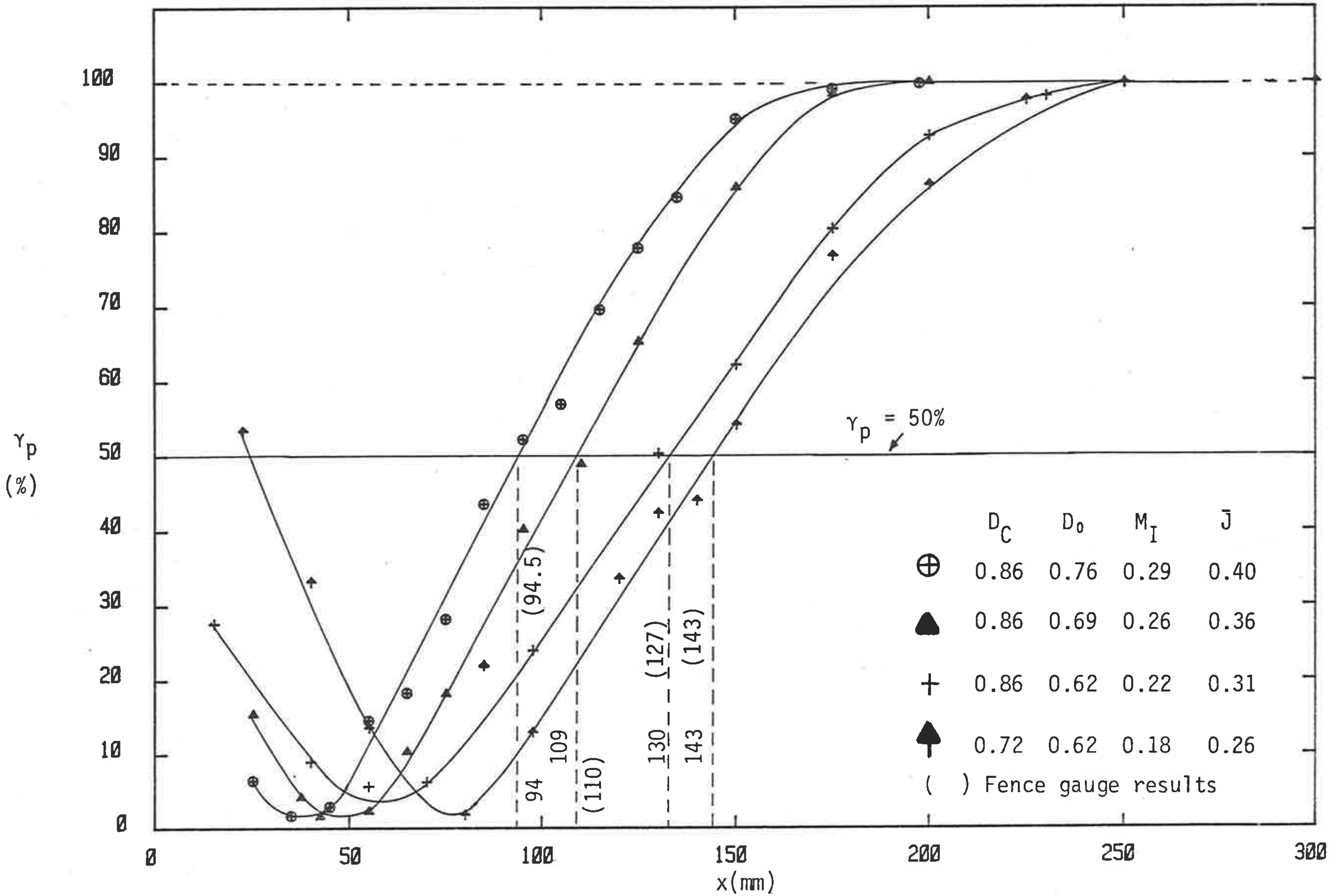

FIGURE 8.6 : PERCENTAGE FORWARD FLOW NEAR REATTACHMENT

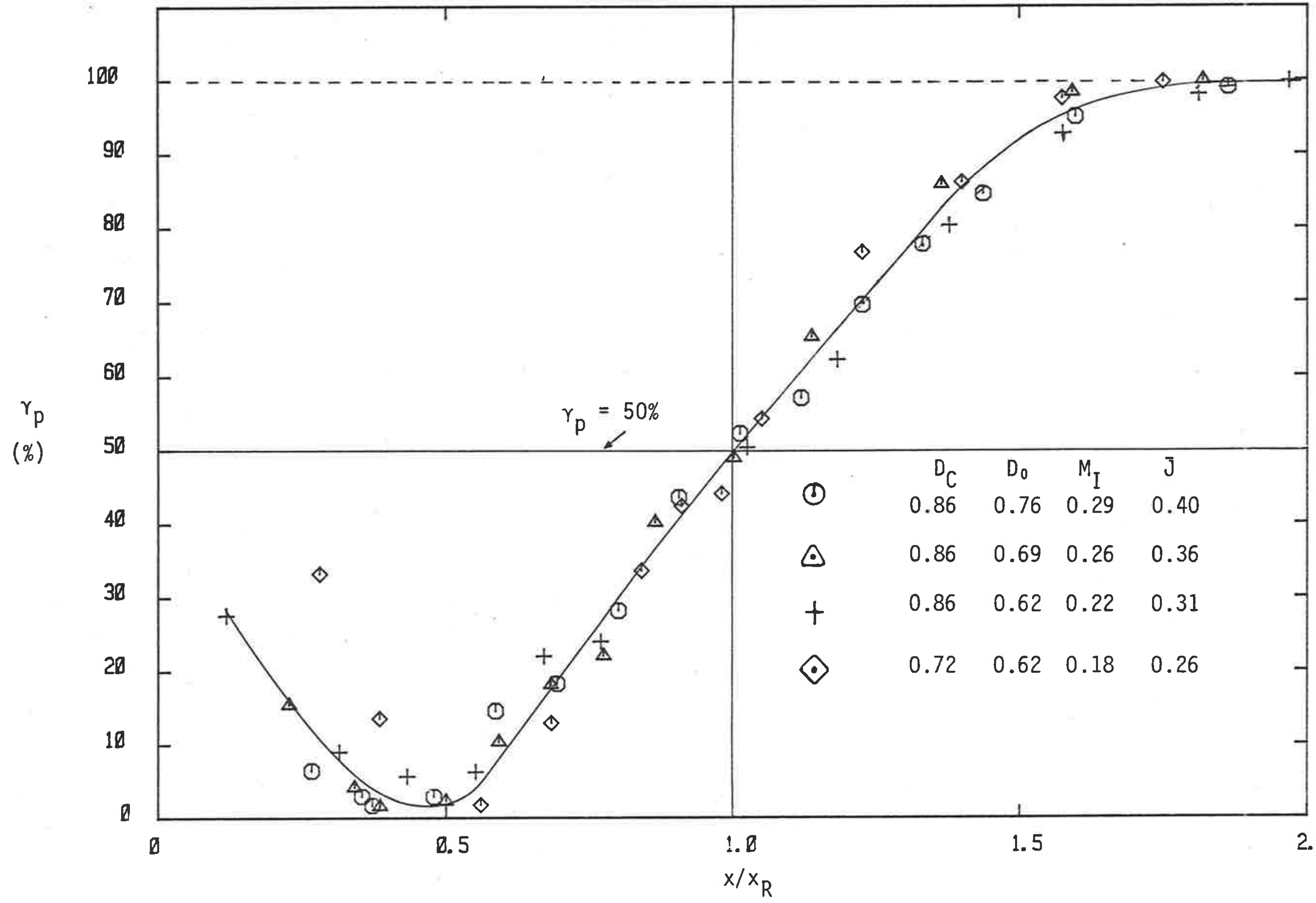

FIGURE 8.7 : PERCENTAGE FORWARD FLOW NEAR REATTACHMENT

A good collapse of the data, for a given choke, is obtained when γ_p is plotted against the streamwise coordinate normalized by the mean reattachment length x/x_R (Figure 8.7).

The measurements of γ_p indicate that the zone between the minimum γ_p (where the flow is almost totally upstream) and the point where it reaches 1 (flow completely downstream) extends from about 0.6 x_R upstream of the reattachment point to about 0.8 x_R downstream.

The results from the three wire probe indicate that this technique provides a very accurate measurement of the mean reattachment length.

8.4 Hot-Wire Signal

The voltage from the hot wire and the switching signal from the zero-crossing detector circuit, at various streamwise positions for the cases of the flow speed and orifice size investigated, were essentially simultaneously recorded (actually sequentially with a maximum time delay of 4 microseconds). An uncalibrated hot wire was used and it is assumed that during the duration of recording (~ 1 second), there was no drift in the hot-wire signal.

The hot-wire signal and the output from the zero-crossing detector at three streamwise locations downstream of the orifice plate, X = 0.76, 1.31 and 1.6 (i.e. at reattachment and slightly away from it upstream and downstream) in the flow D_0 = 0.72, D_c = 0.86, are shown in Figures 8.8, 8.9 and 8.10. The extent of the downstream flow is clearly evident from the zero-crossing detector signal: at X = 0.76 the flow is predominantly in an upstream direction; at X = 1.31 (i.e. reattachment), the extent of downstream and upstream flow seems to be the same; and at X = 1.86, the flow is clearly dominantly downstream with only occasional flow going in the

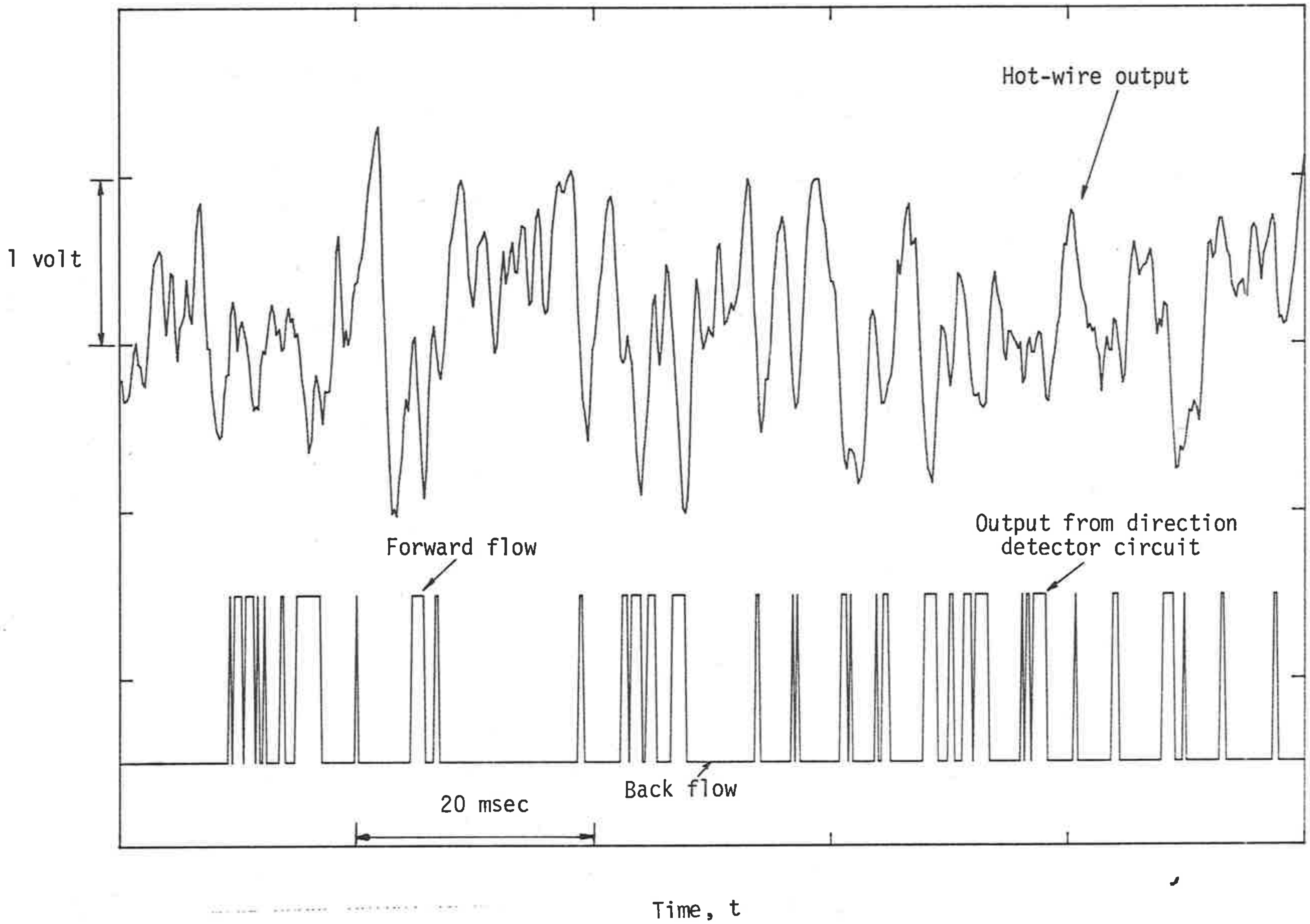

FIGURE 8.8 : THREE-WIRE PROBE OUTPUT IN SEPARATED REGION AT X = 0.76, D_c = 0.86, D_o = 0.76, M_I = 0.35, $\overline{J}$ = 0.47

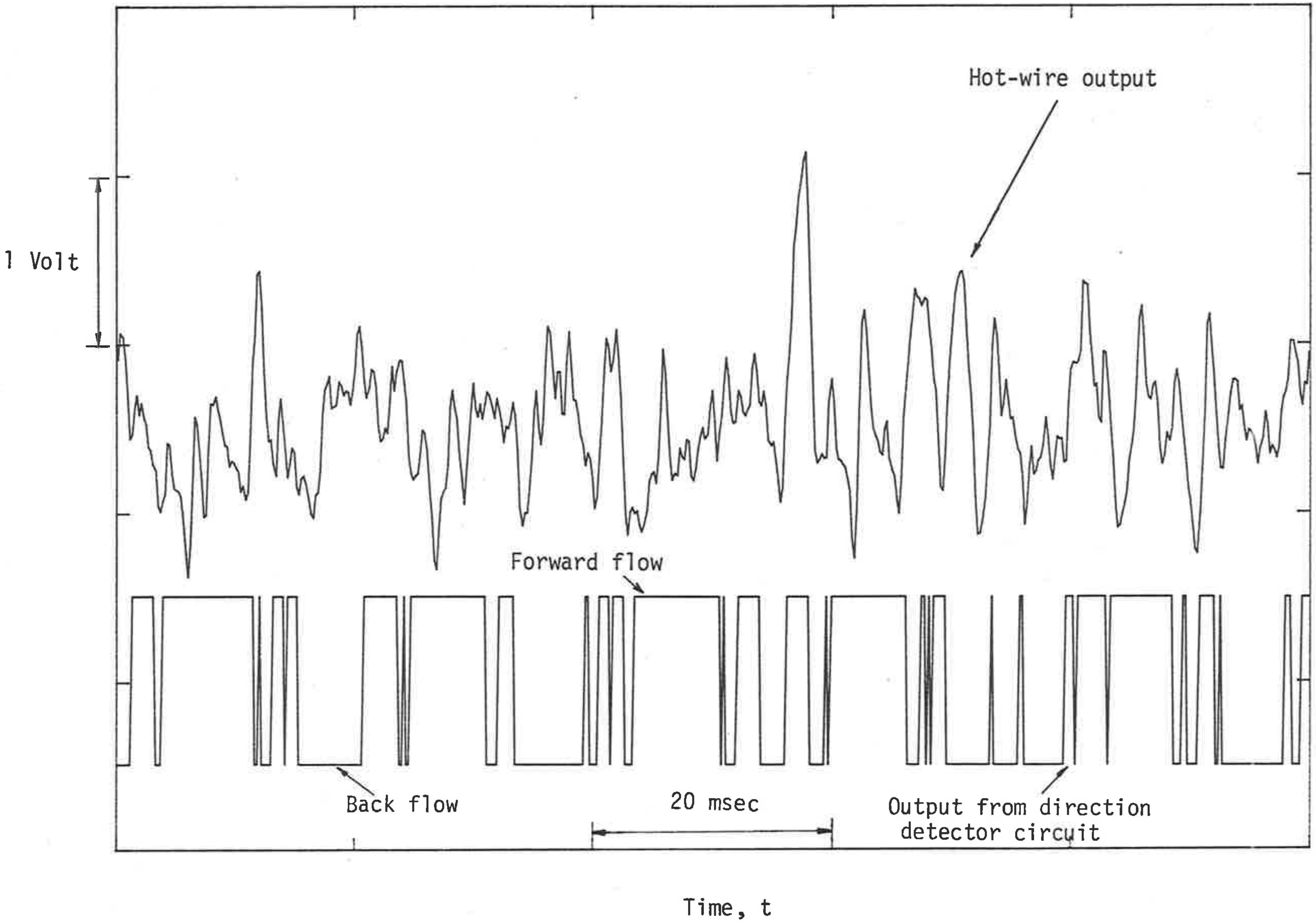

FIGURE 8.9 : THREE-WIRE PROBE OUTPUT NEAR REATTACHMENT AT $X = 1.31$, $D_c = 0.86$, $D_o = 0.76$, $M_I = 0.35$, $\bar{J} = 0.47$

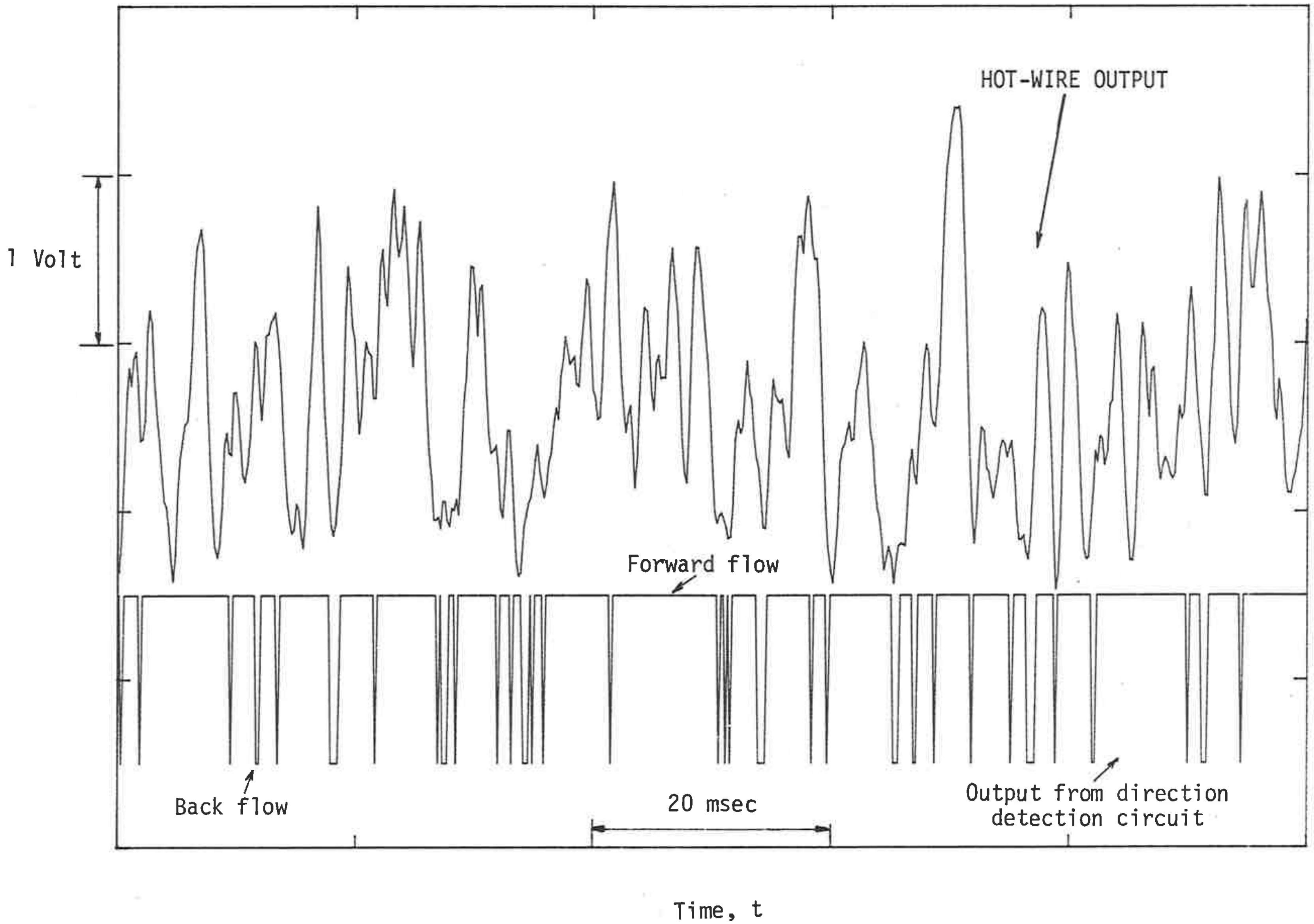

FIGURE 8.10 : THREE-WIRE PROBE OUTPUT DOWNSTREAM OF REATTACHMENT AT X = 1.86, D_C = 0.86, D_O = 0.76, M_I = 0.35, $\overline{J}$ = 0.47

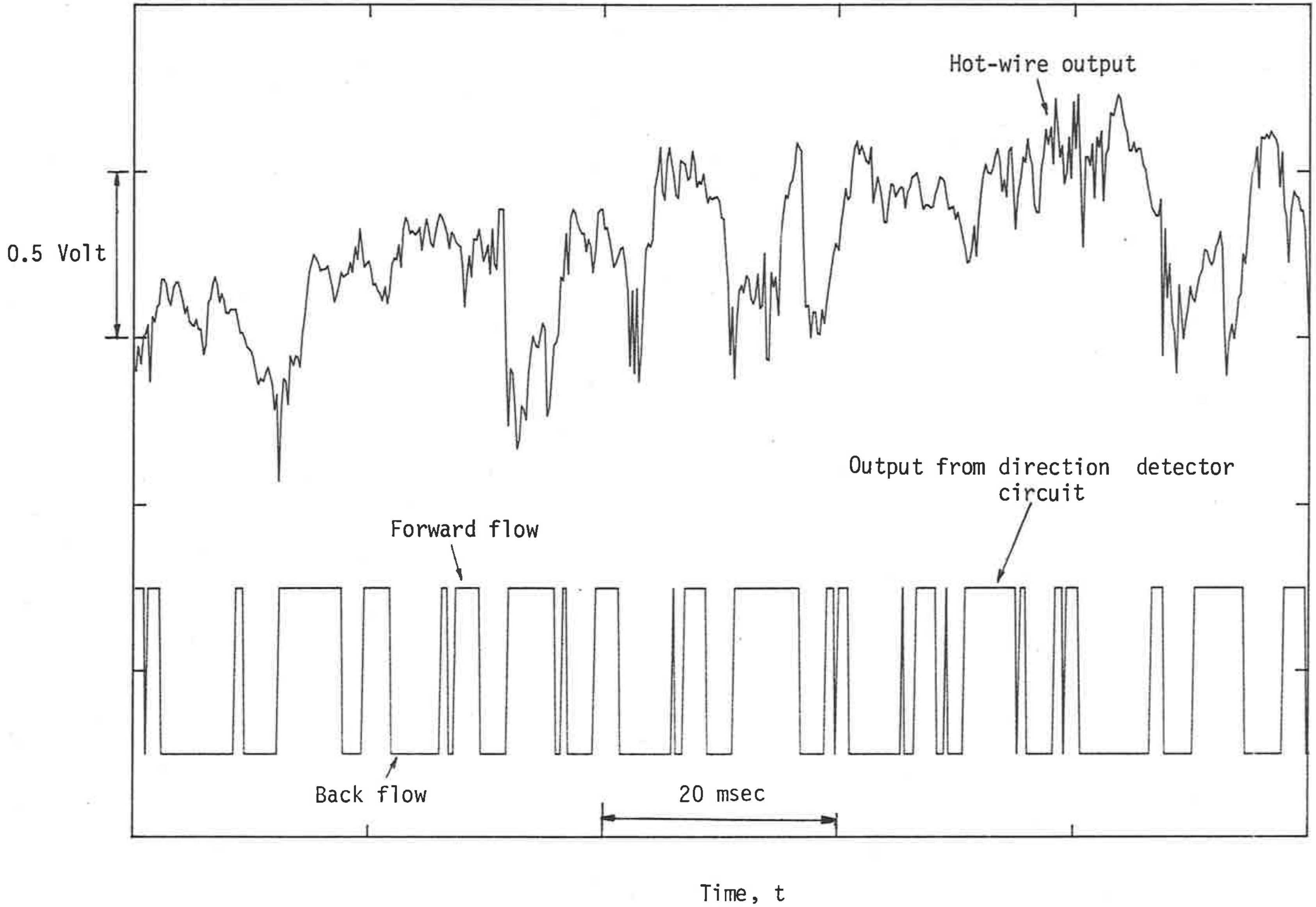

FIGURE 8.11 : THREE-WIRE PROBE OUTPUT NEAR REATTACHMENT AT X = 1.93, D_c = 0.72, D_o = 0.62, M_I = 0.29, $\bar{J}$ = 0.40

upstream direction. Hot-wire and direction signals at X = 1.93 (~ X_R) for D_C = 0.72 and D_0 = 0.62 are also shown, in Figure 8.11 The curve is very similar to that for the previous case (Figure 8.9).

Where the direction signal indicates a flow reversal, the hot-wire signal can be clearly seen to be going to a minimum (but, because of the hot-wire characteristic, not to zero).

8.5 Low Frequency Oscillation

The existence of low frequency motion in separated flow has been observed in the flow downstream a backward-facing step (Eaton and Johnston (1981)), in the flow through a sharp bend in a fully developed turbulent pipe-flow (Tunstall and Harvey, 1966), and in the flow through an orifice (McGuinness, 1978). These low frequency oscillations appear to be responsible for the high turbulence intensity in the separated region. Low frequency oscillations are not visible in the wall pressure spectra or velocity spectra measured with an overall bandwidth of 0-25 kHz, as the filter pass-band is then 150 Hz in the case of the H.P. spectrum analyser and 38 Hz in the case of tape-recorded data. Therefore the spectrum in the separated-flow region, in the low frequency range 0-25 Hz, has been obtained by analysing the output of a Barocell connected to a static pressure tapping in the pipe wall, using the H.P. spectrum analyser. In this frequency range a bandwidth of 0.15 Hz is obtained; smaller bandwidths were not possible as the sampling rate is reduced in inverse proportion to the frequency span, and at frequency spans less than 0-25 Hz, the time for collection of one set of data (1024 samples) exceeds the time for which the flow remains choked. The spectrum obtained for the flow D_0 = 0.72, D_C = 0.86, measured at X = 0.76, is shown in Figure 8.13. Several

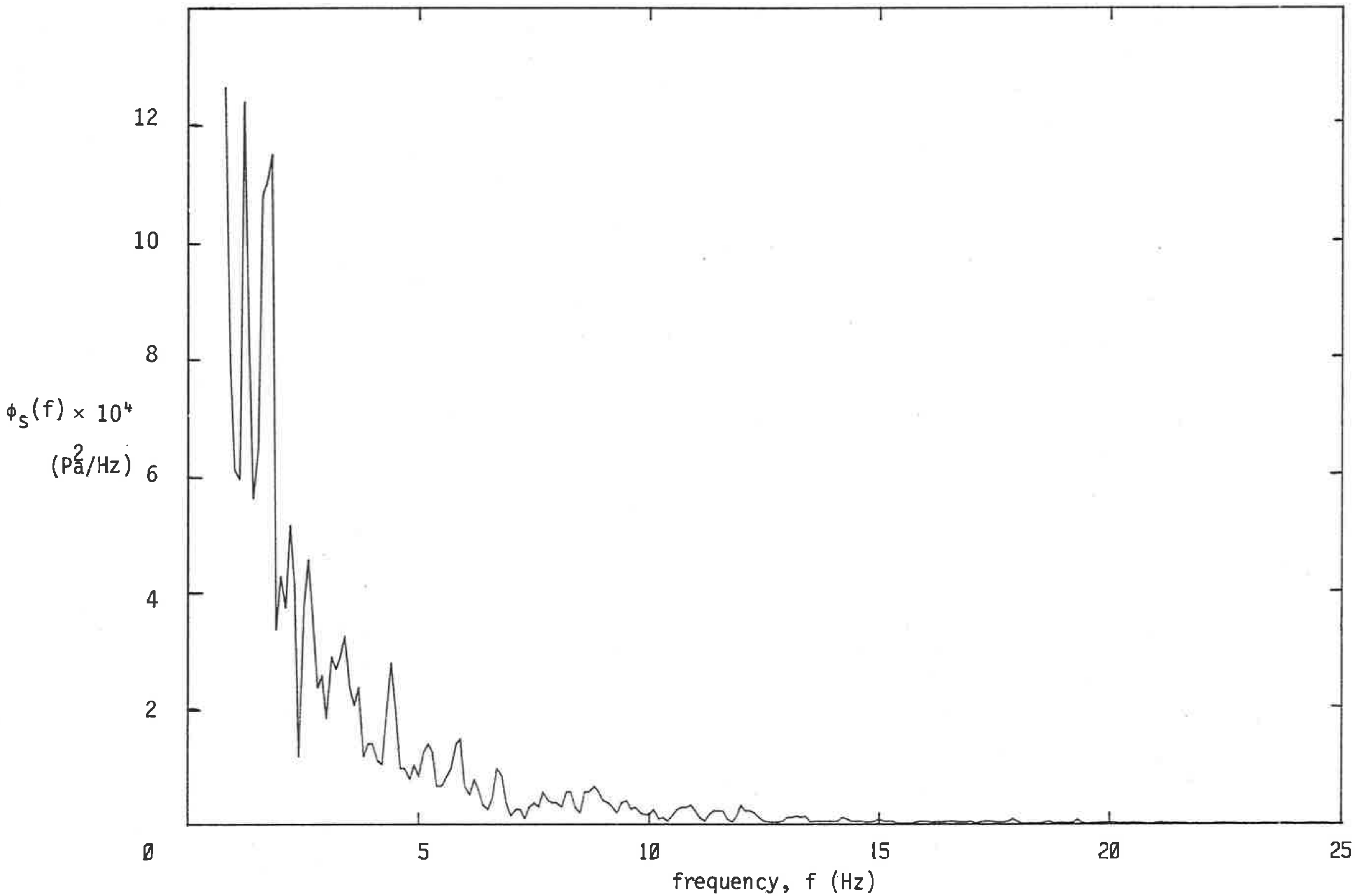

FIGURE 8.12 : SPECTRUM OF WALL PRESSURE FLUCTUATION IN SEPARATED REGION AT X = 0.76, D_c = 0.86, D_o = 0.76, M_I = 0.35, $\bar{J}$ = 0.47

low frequency peaks are evident in the spectrum, particularly the ones at 1.2 Hz, 1.8 Hz. However too much significance should not be read into these: it should be pointed out that the effect of variation of flow parameters on the spectrum has not been investigated here, and it should be noted that Eaton and Johnston (1980) in a similar investigation of flow over a backward-facing step found no well-defined periodicity in the flow reversals.

8.6 Summary and Conclusions

Results of measurements made with a three-wire probe in the separated-flow region allow the following conclusions to be drawn.

(1) Values for the mean reattachement position, defined as the 50%-downstream-flow point, are in very good agreement with those measured by the surface fence gauge (Chapter 5).

(2) The variation of the fraction of time for which the flow is in the downstream direction γ_p with streamwise position in the separated and reattaching flow is a function of x/x_R only.

(3) The position of the reattachment point and the flow in the recirculation zone are subject to random low frequency oscillation.

CHAPTER 9

DISCUSSION AND CONCLUSIONS

This investigation has been concerned with the characteristics of the flow and associated acoustic field in fully-developed turbulent pipe flow with flow separation caused by an orifice plate. Detailed experimental results for mean-flow velocity profiles, wall pressure and axial velocity fluctuations in the disturbed flow region and far from it; i.e. upto and beyond the position where a fully-developed turbulent pipe flow has been re-established and upstream of the disturbance, are presented. Specific conclusions relating to various sections have been presented in earlier chapters. In this section the conclusions are summarised and the more important conclusions about the overall problem are discussed.

As discussed in the literature survey very little work on the flow structure, generation and propagation of higher order modes in fully-developed turbulent pipe flow with flow separation due to an orifice plate, has been reported. In particular there has been very little attempt to study the streamwise variation of modal amplitude and cut-off frequencies of higher order acoustic modes generated in the pipe due to the flow disturbance and also their variation with flow rate. The main conclusions are as follows.

(1) In the pipe, the centreline Mach Number (M_I) is essentially constant for some considerable distance upstream of the orifice and falls slightly below M_I as the flow contracts to pass through the orifice. Just downstream of the orifice the Mach number reaches its maximum value and then falls very rapidly reaching a local minimum value at about $X \simeq 7$. With further increase in X it rises, at first more rapidly (zone 4) than frictional effects can account for and then in zone 5, for $X \gtrsim 48$ at a rate determined

entirely by frictional effects. The streamwise development of mean velocity profiles, displacement thickness δ^*, momentum thickness θ, shape parameter $H(\delta^*/\theta)$ and the Clauser parameter also suggest that the flow after disturbance reaches equilibrium again after about 48 pipe diameters.

The flow Mach number further downstream, just upstream of the choke is determined by the ratio of throat area of the choke to the cross-sectional area of the pipe i.e. by D_c^2 and is independent of the orifice size, D_o.

(2) In the flow approaching the orifice, a fully developed velocity profile exists (but diverging from it very close to the orifice plate). In the region of reversed flow downstream of the orifice after separation the central forward-flow portions of the mean velocity profiles exhibit a region where U varies as $y^{\frac{1}{2}}$. Downstream of reattachment the mean velocity profiles have both a logarithmic region and a half-power region. The extent of the logarithmic region increases with increasing X. In the region of adverse pressure gradient, Perry and Schofield's velocity-defect correlation for two-dimensional flow, which utilizes length and velocity scales based on the maximum shear stress (rather than the wall shear stress), appears to be applicable. Dips in the velocity profiles below the line of logarithmic similarity (upto $X \approx 16$) also indicate that the local wall shear velocity is not the proper scale throughout the layer.

(3) The mean positions of reattachment and separation points, expressed in terms of pipe diameters as X_R, X_{S1} and X_{S2} (or in terms of the radial height of the orifice as x_R/h, x_{S1}/h and x_{S2}/h) are functions

of orifice size, D_o and the Reynolds number, Re. Values for the mean reattachment position measured by surface fence gauge are in good agreement with those measured with surface hot film and three-wire probes.

(4) The flow disturbance in fully-developed turbulent pipe flow generates an intense internal sound field comprising plane waves and higher order acoustic modes, which propagates throughout the pipe system. Therefore the wall pressure field can be identified as that of fully-developed turbulent pipe flow with a superimposed acoustic field generated by the flow disturbance i.e. orifice plate. The values of overall rms pressure , p' and its power spectral density well downstream of the disturbance ($X \gtrsim 48$), where fully-developed turbulent pipe has been re-established, are much higher than those for the undisturbed flow. The difference is attributed to propagating acoustic waves generated by the flow disturbance produced by the orifice plate.

The presence of the acoustic field is also evidenced by the presence in the wall-pressure spectra of sharp peaks, the frequencies of which can be identified with those corresponding to the onset of propagation of the various orders of acoustic modes. The peaks are not very prominent in the separated flow region indicating a major contribution to the pressure fluctuations in this region by turbulence. They are very prominent in spectra both upstream of the orifice and in the reattached and recovering flow downstream. This is consistant with the dominance of acoustic pressure fluctuations over turbulence pressure fluctuations observed in these regions. Relative phase information of the pressure signals from two microphones (mounted in the pipe wall at opposite ends of a pipe diameter) has been useful to identify the acoustic modes where the modes are scarcely discernible in the pressure spectrum itself.

(5) The intensity of fluctuating pressure fields in the separated flow and reattached region $0 \leqslant X \leqslant 1.5$ is determined by the maximum mean flow velocity U_J in the free jet issuing from the orifice plate. The acoustic component of the overall rms pressure fluctuation, in the nominally undisturbed flow upstream of the orifice appears to scale on q_J/M_J and in the reattached and recovering flow downstream of the orifice shows a dependence on $M_J^{0.3}q_J/D_0^4$. These conclusions are supported by a good collapse of overall rms wall-pressure and wall-pressure spectra in these regions.

(6) In the nominally undisturbed flow well upstream of the orifice the apparent cut-off frequencies of the acoustic modes are the same at all streamwise locations and a similar effect is observed in the recovering flow well downstream of the orifice. Modal cut-off frequencies for a given mode are significantly higher upstream than downstream and are rather higher than would be expected. For both upstream and downstream data A (M_e/M_I or M_e/M_E) is about 0.70, in contrast to the theoretical value of 0.90 - 0.91 for fully developed pipe flow (as shown in Chapter 2). This indicates that modal cut-off frequencies are determined by the disturbed flow in the source region, which has a high-pass filtering effect on the sound generated. This is consistent with the observation of a minimum cut-off frequency for each mode at a position in the separated region.

(7) The cut-off frequencies of the various higher order acoustic mode in the presence of flow differ from the corresponding no flow values

by a factor of $\sqrt{1-M_e^2}$. The spectra show quite close overall similarity when related to the non-dimensional frequency $(\omega a/c_e)/\sqrt{1-M_e^2}$ based on this factor.

(8) The acoustic modes in the axial velocity spectra are detectable above the turbulence velocity fluctuations only in the separated flow region downstream of the orifice and the measured mode shapes for axial acoustic particle velocity are similar to theoretical shapes derived from calculated acoustic pressure distributions.

(9) $\Delta M\phi$, which gives a measure of the extent to which shear flow augments the phase velocity from the no-flow case at the same K_x, depends on mode order, M_o and the direction of propogation. Extensive calculated results for various modes have been presented.

The present work as discussed in the preceding paragraphs, has answered a number of questions concerning the internal sound field and its relation to the characteristics of the disturbed flow in fully-developed turbulent pipe flow with flow separation caused by an orifice plate , and represents a comprehensive investigation on the sound field in a pipe resulting from flow separation.

REFERENCES

ADAMS, E.W., JOHNSTON, J.P. and EATON, J.K. [1984], "Experiments on the Structure of Turbulence Reattaching Flows", Report MD-43, Thermosciences Division, Department of Mechanical Engineering, Stanford University.

ALLAN, W.K. [1970], "Velocity Distribution in Turbulent Flow", Journal of Mechanical Eng. Science, 12, (6), pp.391-399.

ARDONCEAU P.L. [1984], "The Structure of Turbulence in a Supersonic Shock-Wave/Boundary-Layer Interaction", AIAA Journal, 22(9), pp.1254-1262.

BACK, L.H. and ROSCHKE, E.J. [1972], "Shear-Layer Flow Regimes and Wave Instabilities and Reattachment Lengths Downstream of an Abrupt Circular Channel Expansion", Trans. of ASME, Journal of Applied Mechanics, September, pp.677-681.

BANNISTER, F.K. and MUCKLOW, G.F. [1948], "Wave Action following Sudden Release of Compressed Gas from a Cylinder", Proc.Inst.Mech.Engineers, Vol. 159, pp.269-300.

BEATTY, R.E. Jr. [1950], "Boundary Layer Attennuation of Higher Order Modes in Rectangular and Circular Tubes", The Journal of the Acoustical Society of America, 222(6), pp.850-854.

BELLHOUSE, B.J. and SCHULTZ, D.L. [1966], "Determination of Mean and Dynamic Skin Friction, Separation and Transition in low-speed Flow with a Thin-film heated Element", Journal of Fluid Mechanics, 24, pp.379-400.

BENDAT, J.S. and PIERSOL, A.G. [1971], "Random Data : Analysis and Measurement Procedures", Wiley-Interscience, New York.

BOLLETER, U. and CHANAUD, R.C. [1970], "Propagation of Fan Noise in Cylindrical Ducts", The Journal of The Acoustical Society of America, 49(3), pp.627-638.

BOLLETER, U. and CROCKER, M.J. [1971], "Theory and Modal Spectra in Hard-Walled Cylindrical Ducts", The Journal of The Acoustical Society of America, 51(5), pp.1439-1447.

BRADBURY, L.J.S. and CASTRO, I.P. [1971], "A Pulsed-Wire Technique for Velocity Measurements in Highly Turbulent Flows", Journal of Fluid Mechanics, 49(4), pp.657-691.

BRADSHAW, P. [1971], "An Introduction to Turbulence and its Measurement", Pergamon Press.

BRADSHAW, P. and WONG, F.Y.F. [1972], "The Reattachment and Relaxation of a Turbulent Shearlayer", Journal of Fluid Mechanics, 52, pp.113-135.

BRITISH STANDARD 1042 Part I : 1964, "Orifice Plates, Nozzles and Venturi Tubes".

BROWN, G.L. [1967], "Proceedings of the 1967 Heat Transfer and Fluid Mechanics Institute", 361-8 (Ed. Olfe, D.B. and Van Atta, C.W.), Stanford University Press.

BROWN, G.L. and DAVEY, R.F. [1971], "The Calibration of Hot Films for Skin Friction Measurements", The Review of Scientific Instruments, 42(11), pp.1729-1731.

BULL, M.K. [1969], "Mean Shear Layer in a Constant Presure Turbulent Boundary Layer", AIAA Journal, 7(2), pp.354-362.

BULL, M.K. and AGARWAL, N.K. [1983a], "Propagation of Acoustic Waves in Fully Developed Turbulent Pipe Flow", Proceedings of the 11th International Congress on Acoustics, Paris.

BULL, M.K. and AGARWAL, N.K. [1983b], "Characteristics of Flow Separation Due to an Orifice Plate in Fully Developed Turbulent Pipe Flow", Proceedings of the Eighth Australasian Fluid Mechanics Conference (Newcastle, NSW), 1, 4B, pp.1-4.

BULL, M.K. and AGARWAL, N.K. [1984], "The Mechanisms of Pipe-Flow Noise Generation Due to Internal Flow Separation", Proceedings of the Internoise 84, Honolulu, 1, pp.261-264, [Ed. Making, G.C.]

BULL, M.K. and LANGEHEINEKEN, TH. [1981], "On the Wall Pressure Field in Turbulent Pipe Flow", Report No. 73, Max-Planck-Institut fur Stroemungs forschung, Goettingen.

BULL, M.K. and NORTON, M.P. [1981], "On the Hydrodynamic and Acoustic Wall Pressure Fluctuations in Turbulent Pipe Flow due to a 90° Mitred Bend", Journal of Sound and Vibration, 76(4), pp.561-586.

BULL, M.K. and THOMAS, A.S.W. [1976], "High Frequency Wall-Pressure Fluctuations in Turbulent Boundary Layers", The Physics of Fluids, 19, (4), pp.597-599.

CARR, L.W. and McCROSKEY, W.J. [1979], "A Directional Sensitive Hot-Wire Probe for Direction of Flow Reversal in Highly Unsteady Flow", ICIASF '79 Record, pp.154-162.

CHANDRSUDA, C. and BRADSHAW, P. [1981], "Turbulence Structure of a Re-attaching Mixing Layer", Journal of Fluid Mechanics, 110, pp.171-194.

CLAUSER, F.H. [1954], "Turbulent boundary layer in Adverse Pressure Gradients", Journal of Aero. Sciences, 21, pp.91-108.

COLES, D. [1954], "The Problem of the Turbulent Bounday Layer", Z.Cingen. Math. Phys. 5, pp.181-203.

COLES, D. [1956], "The Law of the Wake in the Turbulent Boundary Layer", Journal of Fluid Mechanics, 1, pp.191-226.

COOK, N.J. and REDFEARN, D. [1975], "Calibration and Use of a Hot-Wire Probe for Highly Turbulent and Reversing Flows", Journal of Industrial Aerodynamics, 1, pp.221-231.

COOLEY, J.W. and TUKEY, J.W. [1965], "An Algorithm for the Machine Calculation of Complex Fourier Series", Math.Comput.19(90), pp.297-301.

CRIGHTON, D.G. [1970], Hydrodynamic Noise Lecture Notes, Pennsylvania State University (quoted by Karvelis (1975)).

CREMER, L. [1955], "Theory of Transmission loss of Cylindrical Shells", (in German), Acustica, 5, pp.245-256.

DAVIES, P.O.A.L., FISHER, M.J. and BARRATT, M.J. [1962], "The Characteristics of the Turbulence in the Mixing Region of a Round Jet", Journal of Fluid Mechanics, 15, pp.337-367.

DOAK, P.E. and VAIDYA, P.G. [1970], "Attenuation of Plane Wave and Higher Order Mode Sound Propagation in Lined Ducts", Journal of Sound and Vibration, 12(2), pp.201-224.

DOWNING, P.M. [1972], "Reverse Flow Sensing Hot Wire Anemometer", Journal of Physics E : Scientific Instruments, 5, pp.849-851.

DYBAN, Y.P. and EPIK, E.Y. [1970], "Effect of Turbulence on Calculating Heat Transfer Downstream of an Orifice in a Tube", Heat Transfer - Soviet Research, 2(1), pp.11-16.

EATON, J.K., JEANS, A.H., ASHJAEE, J. and JOHNSTON, J.P., [1979], "A Wall-flow Direction Probe for Use in Separating and Reattaching Flows", Trans. of ASME, Journal of Fluids Engineering, 101, pp.364-366.

EATON, J.K. and JOHNSTON, J.P. [1980], "Turbulent Flow Reattachment : An Experimental Study of the Flow and Structure Behind a Backwad-Facing Step", Report MD-39, Thermosciences Division, Department of Mechanical Engineering, Stanford University.

EATON, J.K. and JOHNSTON, J.P. [1981], "A Review of Research on Subsonic Turbulent Flow Reattachment", AIAA Journal, 19(9), pp.1093-1100.

EATON, J.K. and JOHNSTON, J.P. [1982], "Low Frequency Unsteadyness of a Reattaching Turbulent Shear Layer", IUTAM Symposium on Structure of Complex Turbulent Shear Flow, Marseille (Ed. Dumas, R. and Fulachier, L.)

ETHERIDGE, D.W. and KEMP, P.H. [1978], "Measurement of Turbulent Flow Down stream of a Rearward Facing Step", Journal of Fluid Mechanics 86, pp.545-566.

EVERSMAN, W. [1971], "The Effect of Boundary Layer on the Transmission and Attenuation of Sound in an Acoustically Treated Circular Duct", The Journal of the Acoustical Society of America, 49(5), pp.1372-1580.

EVERSMAN, W. [1972], "Representation of a 1/N Power Law Boundary Layer in the Sheared Flow Acoustic Transmission Problem", Journal of Sound and Vibration, 24(4), pp.459-469.

EVERSMAN, W. [1973], "Approximation for Thin Boundary layers in the Sheared Flow Duct Transmision Problem", Journal of Acoustical Society of America, 53 (5), pp.1346-1350.

FRICKE, F.R. [1971], "Pressure Fluctuations in Separated Flows", Journal of Sound and Vibration, 17(1), pp.113-123.

FRICKE, F.R. and STEVENSON, D.C. [1968], "Pressure Fluctuations in a Separated Flow Region", The Journal of Acoustical Society of America, 44(5), pp.1189-1200.

FULLER, C.R. [1978], "Propagation and Reactive Attenuation of Low Frequency Sound in Hard-Walled Ducts with and Without Flow", Ph.D. Thesis, University of Adelaide.

GUNKEL, A.A., PATEL, R.P. and WEBER, M.E. [1971], "A Shielded Hot-Wire Probe for Highly Turbulent Flows and Rapidly Reversing Flows", Ind.Eng. Chem. Fundamental 10(4), pp.627-631.

GOFF, K.W. [1955], "The Application of Correlation Techniques to some Acoustical Measurements", Journal of the Acoustical Society of America, 50(1), pp.236-242.

GOLDSTEIN, S. [1955], "Modern Developments in Fluid Dynamics", Dover Publications, New York.

HARRIS, R.W. and LEDWIDGE, T.J. [1974], "Introduction to Noise Analysis", Pion Ltd., London.

HAYAKAWA, K., SMITS, A.J. and BOGDONOFF, S.M. [1982], "Turbulence Measurements in Two Shock-Wave/Shear layer Interactions", IUTAM Symposium on Structure of Coupling Turbulent Shear Flow, pp.279-288 (Ed. Dumas, R., and Fulacher, L.).

HAYAKAWA, K., SMITS, A.J. and BOGDONOFF, S.M. [1984], "Turbulence Measurements in a Compressible Reattaching Shear Layer", AIAA Journal, 22(7), pp.889-895.

HECKL, M. [1958], "Experimental Investigation of the Transmission Loss of Cylinders", (in German), Acustica, 8, pp.259-265.

HERSH, A.S. and CATTON, I. [1970], "Effect of Shear Flow on Sound Propagation in Rectangular Ducts", The Journal of the Acoustical Society of America, 50 (3), Part 2, pp.992-1003.

HORTSMAN, C.C. and ROSE, W.C. [1977], "Hot Wire Anemometry in Transonic Flow", AIAA Journal, 15(3), pp.395-401.

*

HYLAND, C.E. [1978], "Noise Generation due to Orifices in Pipework with Flow", Master of Eng. Science Thesis, University of Adelaide.

INGARD, UNO and SINGHAL, VIJAY, K. [1974], "Sound Attenuation in Turbulent Pipe Flow", The Journal of Acoustical Society of America, 55(3), pp.535-538.

JEROME, F.E., GUITTON, D.E. and PATEL, R.P., [1970], "Experimental Study of the Thermal Wake Interference Between Closely Spaced Wire of a X-Type Hot wire Probe", The Aeronautical Quarterly, May, pp.119-128.

KARVELIS, A.V. [1975], "An Experimental Investigation of the Wall Pressure Fluctuations in Piping Containing Simple Control Devices", Ph.D. Thesis, Pennsylvania State University.

KERSCHEN, E.J. and JOHNSTON, J.P. [1980], "Modes Selective Transfer of Energy from Sound Propagating inside Circular Pipes to Pipe Wall Vibration", The Journal of Acoustical Society of America, 67(6), pp.1931-1934.

KERSCHEN, E.J. and JOHNSTON, J.P. [1981a], "Modal Content of Noise Generated by a Coaxial Jet in a Pipe", Journal of Sound and Vibration, 76(1), pp.95-115.

KERSCHEN, E.J. and JOHNSTON, J.P. [1981b], "A Modal Separation Measurement Technique for Broadband Noise Propagating Inside Circular Ducts", Journal of Sound and Vibration, 76(4), pp.499-515.

KIM, J., KLINE, S.J. and JOHNSTON, J.P. [1978], "Investigation of a Reattaching Turbulent Shearlayer; Flow over a backward facing Step", Report MD-37, Thermoscience Div., Dept., of Mechanical Engineering,

KIM, J., KLINE, S.J. and JOHNSTON, J.P. [1980], "Investigation of a Reattaching Turbulent shearlayer; Flow over a backward facing Step", Transactions of the ASME, Journal of Fluid Engineering, 102, pp.364-366. Stanford University.

* Howe, M.S. [1979], "The Interaction of Sound with Low Mach Number Wall Turbulence with Application to Sound Propagation in Turbulent Pipe Flow", Journal of Fluid Mechanics, 94, pp.729-744.

KNISELY, C. and ROCKWELL, D. [1982], "Self-sustained Low Frequency Components in an Impinging Shear Layer", Journal of Fluid Mechanics, 116, pp.157-186.

KO, S.H. [1972], "Sound Attenuation in Acoustically lined Circular Ducts in the Presence of Uniform Flow and Shear Flow", Journal of Sound and Vibration, 22(2), pp.193-210.

KO, S.H. [1973], "Theoretical Prediction of Sound Attenuation in Acoustically lined Annular Ducts in the Presence of Uniform Flow and Shear Flow", The Journal of the Acoustical Society of America, 54(6), pp.1592-1606.

KONSTANTINOV, N.I. and DRAGNYSH, G.L. [1955], "The Measurement of Friction Stress on a Surface", Energomashinestroenic, 176, pp.191-200.

KOVASZNAY, L.S.G. [1950], "The Hot-Wire Anemometer in Supersonic Flow", Journal of the Aeronautical Sciences, 17, pp.565-572.

KREYSZIG, E. [1972], "Advanced Engineering Mathematics", John Wiley & Sons.

KUHN, G.F. [1974], "Sound Transmission through Ducts with and Without Flow", University of Southampton, I.S.V.R., Tech. Rept. 65.

KUHN, G.F. and MORFEY, G.L. [1976], "Noise due to fully Developed Turbulent flow exhausting from straight and bent pipes", Journal of Sound and Vibration, 44(1), pp.27-35.

LANGEHEINEKEN, TH. [1977], "Experimentelle Untersuchung der Wanddruckschwankungen einer ausgebildeten turbulenten Rohrstroemung". Max-Planck-Institut fuer Strö~~e~~mungsforschung, Goettingen. Bericht 106/1979.

LANGREN, D.D. and SPARROW, E.M. [1967], "Flow Separation on Redevelopment Downstream of an End-Cap Orifice in a Tube", Trans. of ASME, Journal of Basic Engineering, March, pp.233-235.

LAU, J.C., FISHER, M.J. and FUCHS, H.V. [1972], "The Intrinsic Structure of Turbulent Jets", Journal of Sound and Vibration, 22(4), pp.379-406.

LAUFER, J. [1954], "The Structure of Turbulence in Fully Developed Pipe Flow", N.A.C.A. Tech. Rep. 1174, pp.417-434.

LAUFER, J. and McCLELLAN, R. [1956], "Measurements of Heat Transfer from Fine-wires in Supersonic Flow", Journal of Fluid Mechanics 1(2), pp.276-289.

LIEPMAN, H.M. and ROSHKO, A. [1956], "Elements of Gasdynamics", John Wiley & Sons, New York.

LIM, K.B. [1971], "A Study of Pressure Fluctuations in Turbulent Shear Flows Under the Effects of Mean Pressure Gradients", Ph.D. Thesis, University of Adelaide.

MABEY, D.G. [1972], "Analysis and Correlation of Data on Pressure Fluctuations in Separated Flow", Journal of Aircraft, 9(9), pp.642-645.

MASON, V. [1969], "Some experiments on the Propagation of Sound Along a Cylindrical Duct Containing Flowing Air", Journal of Sound and Vibration, 19(2), pp.208-226.

McCROSKEY, W.J., DURBIN, E.J. [1972], "Flow Angle and Shear Stress Measurements Using Heated Films and Wires", Trans. of ASME, Journal of Basic Engineering, March, pp.46-52.

McGUINESS, M. [1978], "Flow with a Separation Bubble-Steady and Unsteady Aspects", Ph.D. Dissertation, Cambridge University.

MIER, H.U. and KREPLIN, H.P. [1980], "Experimental Investigation of the Boundary Layer Transition and Separation on a Body of Revolution", Z.Flugwiss. Weltraumforsch 4(2), pp.65-71.

MIKHAIL, M.N. and ABDELHAMID, A.N. [1973a], "Transmission and Far Field Radiation of Sound Waves in Analysis from Lined Ducts Containing Shear Flow", AIAA Paper No. 73-1013.

MIKHAIL, M.N. and ABDELHAMID, A.N. [1973b], "Shear Flow Effect on the Propagation and Attenuation of Sound Waves in an Acoustically Treated Annular Duct", Division of Aerothermodynamics, Report No. ME-73-2, Carleton University, Canada.

MORSE and INGARD [1968], "Theoretical Acoustics", McGraw-Hill, New York.

MORFEY, C.L. [1971], "Transmission Through Duct Walls of Internally Propagated Sound", Proc. 7th International Congress on Acoustics, Paper 24, A9, Budapest.

MORKOVIN, M.W. [1956], "Fluctuations and Hot-Wire Anemometry in Compressible Fluids", AGARDograph, No. 24.

MUGRIDGE, B.D. [1969], "The Measurement of Spinning Acoustic Modes Generated in an Axial Flow Fan", Journal of Sound and Vibration, 22, pp.487-506.

MUNGUR, P. and PLUMBLEE, H.E. [1969], "Propagation and Attenuation of Sound in a Soft Walled Annular Duct Containing a Sheared Flow", NASA, SP-207, pp.305-327.

MURTHY, V.S. and ROSE, W.C. [1978], "Wall Shear Stress Measurements in a Shock-Wave Boundary Layer Interaction", AIAA Journal 16(7), pp.667-672.

MOODY, L.F. [1944], "Friction Factor for Pipe Flow", Trans. of ASME, 66.

MOORE, C.J. [1979], "Measurements of Radial and Circumferential Modes in Annular and Circular Ducts", Journal of Sound and Vibration, 62(2), pp.235-256.

NAYFEH, A.H., KAISER, J.E. and TELIONIS, D.P. [1975], "Acoustics of Aircraft Engine-Duct Systems", AIAA Journal, 13(2), pp.130-153.

NORTON, M.P. [1979], "The Effect of Internal Flow Disturbances on the Vibration Response of and the Acoustic Radiation from Pipe", Ph.D. Thesis, University of Adelaide.

OWER, E. and PANKHURST, R.C. [1977], "The Measurement of Air Flow", 5th edition, Pergamon Press, Oxford.

OWEN, F.K. and BELLHOUSE, B.J. [1970], "Skin Friction Measurements at Supersonic Speeds", AIAA Journal, 8, pp.1358-1360.

PATEL, V.C. [1965], "Calibration of the Preston Tube and limitations on its use in pressure gradients", Journal of Fluid Mechanics, 23(1), pp.185-206.

PERRY, A.E. and SCHOFIELD, W.H. [1973], "Mean Velocity and Shear Stress Distributions in Turbulent Boundary Layers", The Physics of Fluids, 16(12), pp.2068-2074.

PERRY, A.E. and FAIRLIE, B.D. [1975], "A Study of Turbulent layer Separ ation and Reattachment", Journal of Fluid Mechanics, 69(4), pp.657-672.

PLUMBLEE, H.E. [1973], "A Theoretical and Experimental Study of Sound Attenuation in an Annular Duct", AIAA paper No. 73-1005.

PLUMBLEE, H.E. and DEAN, P.D. [1973], "Sound Measurements within and in the Radiated Field of an Annular Duct with Flow", Journal of Sound and Vibration, 28(4), pp.715-735.

PRIDMORE-BROWN, D.C. [1958], "Sound Propagation in a Fluid Flowing Through an Attenuation Duct", Journal of Fluid Mechanics, 4, pp.393-406.

RENNISON, D.C. [1976], "The Vibrational Response of and the Acoustic Radiation from thin Walled Pipes, Excited by Random Fluctuating Pressure Fields", Ph.D. Thesis, University of Adelaide.

RUBESIN, M.H., OKUNO, A.F., MATEER, G.G. and BROSH, A. [1975], "A Hot Wire Surface Gauge for Skin Friction and Separation Detection Measurements", NASA TM-62, p.465.

SAVKAR, S.D. [1971], "Propagation of Sound in Ducts with Shear Flow", Journal of Sound and Vibration, 19(3), pp.355-372.

SCHOFIELD, W.H. [1981], "Equilibrium Boundary Layers in Moderate to Strong Adverse Pressure Gradients", Journal of Fluid Mechanics, 113, pp.91-122.

SCHOFIELD, W.H. [1983], "On Separating Boundary Layers", Mechanical Engineering Report No. 162, Aeronautical Research Laboratories, Melbourne.

SCHLICHTING, H. [1955], "Boundary Layer Theory", Pergamon Press.

SCHUBERT, G. and CORCOS, G.M. [1967], "The Dynamics of Turbulence near a Wall according to a Linear Model", Journal of Fluid Mechanics, 29, pp.113-135.

⊛ Rose, W.C. and Mcdaid, E.P. [1977], "Turbulence Measurement in Transonic Flow", Proc. of the AIAA 9th Aerodynamic Testing Conference, Arlington, Texas.

SETTLES, G.S., WILLIAMS, D.R., BACA, B.K. and BOGDONOFF, S.M. [1982], "Reattachment of a Compressible Turbulent Free Shear Layer", AIAA Journal, 20(1), pp.60-67.

SHANKAR, P.N. [1972a], "Acoustic Refraction and Attenuation in Cylindrical and Annular Ducts", J. of Sound and Vibration, 22(2), pp.233-246.

SHANKAR, P.N. [1972b], "Sound Propagation in Duct Shear Layers", Journal of Sound and Vibration, 22(2), pp.221-232.

SHIVPRASAD, B.G. and SIMPSON, R.L. [1982], "Evaluation of a Wall-Flow Direction Probe for Measurements in Separated Flows", Trans of ASME, Journal of Fluids Engineering, 104, pp.162-166.

SIMPSON, R.L. [1975], "Interpreting Laser and Hot-Film Anemometer Signals in a Separating Boundary Layer", AIAA Journal, 14, pp.124-126.

SIMPSON, R.L. [1981], "Review - A Review of Some Phenomena in Turbulent Flow Separation", Trans.of ASME, Journal of Fluid Engineering, 103, pp.520-533.

SIMPSON, R.L. [1983], "A Model for the Backflow Mean Velocity Profile", AIAA Journal, 21(1), pp.142-143.

SIMPSON, R.L., CHEW, Y.T. and SHIVAPRASAD, B.G. [1981], "The Structure of a Separating Turbulent Boundary Layer; Part 1. Mean Flow and Reynolds Stress", Journal of Fluid Mechanics, 113, pp.23-51.

SIMPSON, R.L., STRICKLAND, H.J. and BARR, P.W. [1977], "Features of Separating Turbulent Boundary Layer in the Vicinity of Separation", Journal of Fluid Mechanics, 79(3), pp.553-594.

SMITS, A.J. [1982], "A Visual Study of a Separation Bubble", Flow Visualisation II, Hemisphere Publishers, N.Y., pp.247-251.

SMYTH, R, [1979], "Turbulent Flow over a Plane Symmetric Sudden Expansion", Trans. of ASME, Journal of Fluids Engineering, 101, pp.348-353.

SPENCE, D.A. and BROWN, G.L. [1968], "Heat Transfer to a Quadratic Shear Profile", Journal of Fluid Mechanics, 33(4), pp.753-773.

Stephens, R.W.B. and Bate, A.E. [1966], " Acoustics and Vibrational Physics", St. Martin's Press, New York.

STRATFORD, B.S. [1959], "An Experimental Flow with Zero Skin-Friction throughout its Region of Pressure Rise", Journal of Fluid Mechanics, 5(1), p.17.

THOMAS, A.S.W. [1977], "Organised Structure in the Turbulent Boundary Layer", Ph.D. Thesis, University of Adelaide.

TOWNSEND, A.A. [1976], "The Structure of Turbulent Shear Flow", Cambridge University Press, (2nd edition).

TUNSTALL, M.J. and HARVEY, J.K. [1968], "On the Effect of a Sharp Bend in a Fully Developed Turbulent Pipe Flow", Journal of Fluid Mechanics, 34(3), pp.395-608.

VAGT, J.D. and FERNHOLZ, H. [1973], "Use of Surface Fences to Measure Wall Shear Stress in Three-Dimensional Boundary Layers", Aeronautical Quarterly,

WALTER, J.L. [1979], "Coincidence of Higher-Order Modes - A Mechanism of the Excitation of Cylindrical Shell Vibrations via Internal Sound" Ph.D. Thesis. Pennsylvania State University.

WATTS, D.G. [1962], "A General Theory of Amplitude Quantization with Applications to Correlation Determination", Inst. Elec.Eng. Proc. 109(C), pp.209-214.

WINDROW, B. [1956], "A Study of Rough Amplitude Quantization by Means of Nyquist Sampling Theory", I.E.E. Trans., Circuit Theory, CT-3 (2), pp.266-270.

WINTER, K.G. [1977], "An Outline of the Techniques available for the Measurements of Skin Friction in Turbulent Boundary Layers", Prog. Aerospace Sci., 18, pp.1-57.

ADDENDUM

Page Nos. 358, 362, $\gamma_p = 1$; should be read as $\gamma_p = 100\%$.